Proceedings 2006 eleventh annual symposium of the IEEE/LEOS Benelux Chapter, November 30 - December 1, 2006, Eindhoven, The Netherlands

PROCEEDINGS 2006

Eleventh Annual Symposium of the IEEE/LEOS Benelux Chapter

Thursday November 30 / Friday December 1, 2006
COBRA Institute
Eindhoven University of Technology
The Netherlands

Editors

A.M.J. Koonen, X.J.M. Leijtens,
H.P.A. van den Boom, E.J.M. Verdurmen, J. Molina Vázquez

Organized by

Eindhoven University of Technology
in association with IEEE/LEOS

Supported by

COBRA Institute
Newport
Spectra-Physics
Ocean Optics
LASER 2000
BFi OPTiLAS
Genexis
Simac

Published by IEEE/LEOS Benelux Chapter
Eindhoven University of Technology
Department of Electrical Engineering
Division of Telecommunication Technology and Electromagnetics
Den Dolech 2
P.O. Box 513
5600 MB Eindhoven
The Netherlands

Phone +31 (0)40 2473451
Fax +31 (0)40 2455197
www http://tte.ele.tue.nl
www http://leosbenelux.org

Keywords integrated optics, photonics, lasers, lightwave technology, non-linear optics, optical communication, optical materials, photonic crystals, nanophotonics, quantum electronics

---

CIP-DATA LIBRARY TECHNISCHE UNIVERSITEIT EINDHOVEN

Proceedings

Proceedings 2006 eleventh annual symposium of the IEEE/LEOS Benelux Chapter : November 30 - December 1, 2006, Eindhoven, The Netherlands / editors A.M.J. Koonen, X.J.M. Leijtens, H.P.A. van den Boom ... [et al.] - Eindhoven : Technische Universiteit Eindhoven, 2006.
ISBN-10: 90-6144-989-8
ISBN-13: 978-90-6144-989-8
NUR 959
Trefw.: geintegreerde optica / optische telecommunicatie / fotonica / lasers.
Subject headings: integrated optics / optical communication / microwave photonics / lasers.

Preface

This year it is the privilege of Eindhoven University of Technology to host the 11th Annual Symposium of the IEEE/LEOS Benelux Chapter.

The Chapter was founded in 1996, and is thus this year celebrating its first decennium. The LEOS fields of interest are spanning a wide range of optical techniques: lasers and integrated optics, optical fibres, optical communication systems and devices, optical sensors, physics of novel materials, polymers and inorganic materials, nonlinear optics, quantum electronics and quantum optics.

Since its establishment, the Chapter aims to promote the LEOS fields of interest in the Benelux (Belgium, the Netherlands, and Luxembourg), as well as in the neighbouring countries Germany and France, by stimulating interaction between scientists and engineers working in universities, industry, and other research institutes. The activities of the Chapter encompass presentations by invited speakers, workshops, thematic meetings, and the Annual Symposium. The Symposium has been organised yearly since 1996, and is the most prominent event of the Chapter. It provides an excellent forum for young researchers to exchange their latest information, and to promote the research going on in the Benelux region to a wide public.

In 2006, the Symposium again is arranged as a two-day event. In the evening of Nov. 30th, there will be an invited talk by dr. van den Hoven of Genexis, one of the fine examples of successful optical industries in the Netherlands. Thereafter the spectrum of activities in broadband research in our COBRA Institute will be presented, including the ones in the National Research Centre Photonics within COBRA. The evening program is continued with a poster session, and the opportunity to meet informally with drinks and some light snacks. On Friday Dec. 1st, the program features two invited talks, given by the distinguished LEOS lecturers prof. Plant of McGill University and dr. Notomi of NTT Basic Research Labs. It also has two parallel sessions of four oral paper presentations each, which were selected from the large number of submitted papers. Also a second poster session will be held. As has been become a nice tradition, by the end of the day there will be an award ceremony for the Best Poster.

The Symposium organising committee would like to thank the invited speakers and presenters of regular and poster papers, for their valued contributions. It is this kind of interaction which constitutes the spirit of our Chapter. Also we thank the Program Committee for their hard work in selecting the papers, and the many other volunteers who helped to put this Symposium together. Finally, let us thank the organisations which through their generous support made this Symposium feasible: the COBRA Institute, Newport, Spectra-Physics, LASER 2000, BFi OPTiLAS, Genexis, Ocean Optics and Simac Electronics.

We trust the Symposium will offer you a valuable platform for interaction and encourage you to take the opportunity for lively discussions with your fellow researchers

and other colleagues in the LEOS field.

On behalf of the Symposium organising committee,

Ton Koonen - Symposium chairman
Henrie van den Boom - Symposium vice chairman
Xaveer Leijtens - chairman LEOS Benelux Chapter

Eindhoven, Nov. 9, 2006

Program Committee

Prof. Ton Koonen, chairman	Technische Universiteit Eindhoven
Dr. Xaveer Leijtens	Technische Universiteit Eindhoven
Prof. Alfred Driessen	Universiteit Twente
Dr. René de Ridder	Universiteit Twente
Dr. Taco Visser	Vrije Universiteit Amsterdam
Prof. Geert Morthier	Universiteit Gent
Prof. Peter Bienstman	Universiteit Gent
Prof. Patrice Mégret	Faculté Polytechnique de Mons
Dr. Marc Wuilpart	Faculté Polytechnique de Mons
Prof. Hugo Thienpont	Vrije Universiteit Brussel
Prof. Jan Danckaert	Vrije Universiteit Brussel
Prof. Philippe Emplit	Université Libre de Bruxelles
Dr. Thomas Erneux	Université Libre de Bruxelles

Organizing Committee

Prof. Ton Koonen, chairman
Ir. Henrie van den Boom, vice-chairman
Dr. Xaveer Leijtens, chairman LEOS Benelux Chapter
Dr. Harm Dorren
Pauline van Gelder-Hoen
Ir. Bas Huiszoon
Dr. Fouad Karouta
Susan de Leeuw-Jeffery
Dr. Richard Nötzel
Dr. Huug de Waardt

Contents

Posters: Integrated Optics 73

The Dynamic Bandwidth of Fiber-to-the-Home

G.N. van den Hoven, E.G.C. Pluk

Genexis B.V. Eindhoven, Netherlands
info@genexis.eu
http://www.genexis.eu

Fiber-to-the-Home (FTTH) can provide end-users with virtually unlimited bandwidth, and at the same time liberating the end-user from the clutches of a single service provider. This paper will present two examples of dynamic bandwidth in optical networks, showing the advantages offered to the user, today and tomorrow. The first example shows how the transparency of Ethernet traffic allows the dynamic configuration of services. The second example introduces a new concept for the dynamic reconfiguration of bandwidth, using multiple wavelengths.

Broadband Communication research activities at the COBRA Institute

A.M.J. Koonen

COBRA Institute, Eindhoven University of Technology,
P.O. Box 513, NL5600MB Eindhoven, The Netherlands
a.m.j.koonen@tue.nl

The activities in the COBRA Institute encompass research on novel materials, devices and systems for broadband communication. Novel optical materials enable ultra-fast multi-functional integrated optical circuits. With these, high-capacity fast-routing networks are investigated, as well as versatile fibre access and in-home networks, and their applications. The activities in the area of optical communication are within the heart of the institute. An overview will be given how these activities fit within the entire field of research of COBRA, illustrated with some recent research highlights, and of COBRA's future research directions.

Agile All-Photonics Networks – A Vision of Optical Networks for 2012 and Beyond

David V. Plant

Dept. of Electrical & Computer Engineering
McGill University
Montreal, Quebec, Canada
plant@photonics.ece.mcgill.ca

Recent advances in fiber optic technology have prompted researchers to envision a future all-photonic network that is capable of supporting multiple access and services at very high bit rates. The confluence of optical transmission and optical network functions opens up new paradigms for network architectures that are enabled by emerging photonic technologies. Characteristics of these architectures and technologies that distinguish them from existing ones include: (1) networks in which the transmission of information is based on optical packets (burst-switched or packet-switched networks, with and without all-optical header recognition), (2) optical code-division multiplexing for allocating bandwidth-on-demand in bursty, asynchronous traffic environments, and (3) practical implementations for optical generation, shaping, and processing. In these all-photonic multi-access networks, any node can use a designated time slot to send a packet to any other node in the network. The bursty nature of these networks imposes new design constraints on transmitters, receivers, and optical components. We review various system and technology considerations for such networks.

All Optical Control of Light by Photonic Crystal Nanocavities

Masaya Notomi

NTT Basic Research Laboratories
Photonic Nanostructure Research Group
3-1 Morinosato-Wakamiya, Atsugi, 243-0198 JAPAN
notomi@nttbrl.jp / notomi@will.brl.ntt.co.jp
http://www.brl.ntt.co.jp/people/notomi

Recently, various aspects of the performance of photonic crystals have rapidly progressed, such as waveguide loss and cavity Q. Thanks to these advances, various forms of all-optical control of light is becoming possible using photonic crystals. In this talk, I will first review our recent achievement in ultrasmall and ultrahigh-Q nanocavities. Next I will show the realization of all-optical switches and bistable memories using photonic-crystals nanocavities. Third, we will discuss possible applications of these functions. One is the application for all-optical digital processing chips. Second is dynamic control of light which leads to interesting novel ways of controlling fundamental properties of light, such as adiabatic wavelength conversion and optomechanical energy conversion.

LOW COST HIGH CAPACITY DATA TRANSMISSION OVER PLASTIC OPTICAL FIBRE USING QUADRATURE AMPLITUDE MODULATION

J. Yang, X. Li, M.S. Alfiad, A.M.J. Koonen, H.P.A. van den Boom

COBRA Institute, Eindhoven University of Technology, The Netherlands

P.O. Box 513, NL 5600 MB Eindhoven, The Netherlands

Phone +31 40 2475653, fax +31 40 2455197, e-mail J.Yang@tue.nl

While a data transmission system based on step-index multi-mode plastic optical fibre (POF) is potentially of very low cost, it is also severely bandwidth-limited. To circumvent the bandwidth limitation, Quadrature Amplitude Modulation (QAM) may be used to realize high capacity data transmission. Three different QAM systems with large-core step-index plastic optical fibre are proposed. They are Direct QAM, Baseband/subcarrier emulated QAM, and Wavelength-sliced emulated QAM. The performances of the three systems have been analyzed by computer simulations. Based on the simulation results, the technical feasibility for those system concepts is assessed in order to select the optimal configuration. A simple Direct QAM system has been set up. Measurements have been carried out with different optical sources; a 658 nm laser diode and a 520 nm SLED. A vector signal generator is employed as QAM modulator and the quality of the I and Q signals was measured by a vector signal analyzer. 90 Mbit/s over 100 meter step-index plastic optical fibre with a core diameter of 1 mm has been achieved with an error vector magnitude less than 3%.

Introduction

The 1 mm PMMA Step-Index Polymer Optical Fibre (SI-POF) is an attractive medium in short-range communication networks. It combines the advantages of the normal optical fibre (high bandwidth, EMI immunity) with the simple installation which makes it cost efficient [1]. The large 1mm core makes the handling of the optical access network by non-professionals possible while the cheap PMMA and the simple step-index structure give low fibre production costs. Hence, PMMA SI-POF with 1 mm core diameter will be investigated in the recently started European joint R&D project POF-ALL – "Paving the Optical Future with Affordable Lightening-fast Links" [2]. Since the target of the POF-ALL project is to realize at least 100Mbit/s over 300 meter length, QAM is considered due to the severely bandwidth-limited 1 mm PMMA SI-POF [3]. The QAM modulation scheme conveys data by coding the data on two orthogonal carrier channels. A larger eye opening can be expected for the QAM transmission with the same link power budget compared to other multi-level transmissions because of the more even distribution of the points in the modulation constellation. The other reason why QAM signaling is selected for the high capacity POF link is that QAM technology has been already widely deployed in wireless LAN standards, such as the IEEE 802.11x family, in digital video broadcast systems on coaxial cable networks (DVB-C), and for fast internet in cable modem systems such as DOCSIS. Thus, the high speed QAM signal modulation and demodulation chips can be lower cost thanks to the large market of wireless LANs and cable modems.

QAM system implementation options

Three different QAM systems for the 1mm SI-POF system are proposed. They are Direct QAM, Baseband/subcarrier emulated QAM (SC-QAM), and Wavelength-sliced emulated QAM (WS-QAM) [3]. The first option Direct QAM is depicted in Fig.2a), and the spectrum allocation for Direct QAM is shown in Fig.2b). When the data rate is R and a QAM-2^N scheme is used, the passband QAM signal spectrum is centred on the carrier fc and occupies in practice a bandwidth of about $1.4R/N$. So the carrier frequency fc needs to be larger than $0.7R/N$, and therefore the bandwidth of the POF link should be at least $1.4R/N$. The second option, termed 'baseband/subcarrier emulated QAM' (SC-QAM) and depicted in Fig.2a), emulates QAM by modulating I and Q signals on two different subcarriers., e.g. the I signal in baseband and the Q signal in a passband centred around the carrier frequency fc. The spectrum needed for SC-QAM is more than $2.1R/N$ as shown in Fig.2b) which is much wider than that for the Direct QAM option. The carrier frequency fc should exceed $1.4R/N$ while the bandwidth of the POF link should be at least $2.1R/N$. The third option is 'wavelength-sliced emulated QAM' and is depicted in Fig.3a). Two SLEDs are used to generate two orthogonal channels by wavelength slicing. Crosstalk may occur due to overlap in the spectra. So additional signal processing has to be deployed to eliminate the crosstalk. The electrical signal spectra of the I and Q signal are both in baseband, as shown in Fig.3b). Hence this option requires the least bandwidth of the POF link, namely only $0.7R/N$.

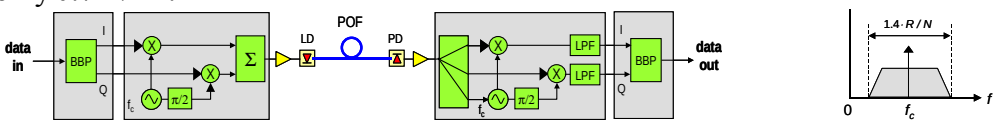

a) system concept

b) spectrum

Fig. 2 Direct QAM

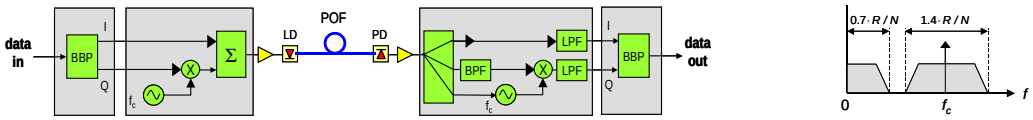

a) system concept

b) spectrum

Fig. 3 Baseband/subcarrier emulated QAM

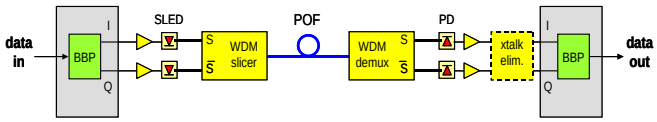

a)system concept

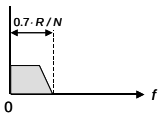

b) spectrum

Fig. 4 Wavelength-sliced emulated QAM

Performance analysis of QAM system options

The performances of the QAM system options have been analyzed by computer simulations. Based on the simulation results, the technical feasibility for those system concepts is assessed in order to select the optimal configuration. Due to the limitation of bandwidth, we focus on the Direct QAM and WS-QAM.

Within the simulation program VPI Transmission Maker, the two systems are both implemented with 100 meter multi-mode fibre. For a good comparison of Direct QAM and WS-QAM, the parameters are set to be the same. In both systems, the bit rate is set to be 128 Mbit/s using QAM-64 signals, implying a symbol rate of 21.3 MBaud. A laser

diode with a wavelength of 650 nm and average output power of 5 mW was assumed. A raised cosine filter was used for pulse-shaping and has a roll-off factor β=0.2. The carrier frequency fc=30MHz for Direct QAM.

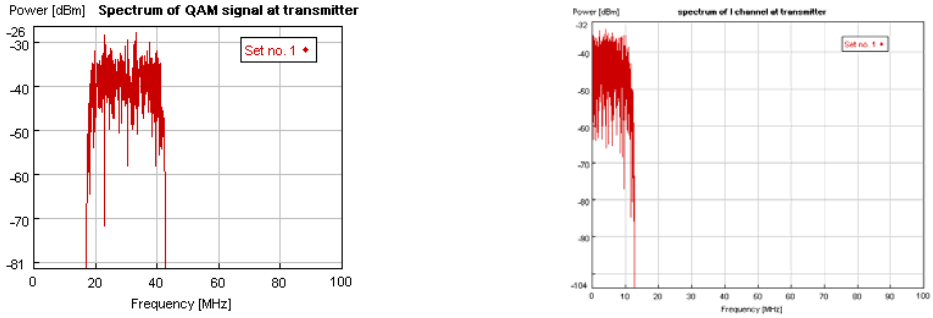

a) Spectrum of Direct QAM b) Spectrum I channel of WS-QAM

Fig. 5 The spectrum of QAM signal after transmitter

The first simulation results are shown in Fig.5. The occupied bandwidths of the two different QAM implementations in the transmitter have been calculated. From Fig.5a), the QAM signal makes use of 25.6MHz bandwidth. Since the Direct QAM is transmitted in the passband and the carrier frequency fc=30MHz, the needed bandwidth of POF link is around 42MHz while it can be 25.6MHz in an ideal case. On the other hand, the two orthogonal carriers for WS-QAM are separated by different wavelengths so the QAM signal can be transmitted as baseband signal. The required bandwidth in the transmitter is therefore not more than 13MHz, which is only half of the Direct QAM passband signal.

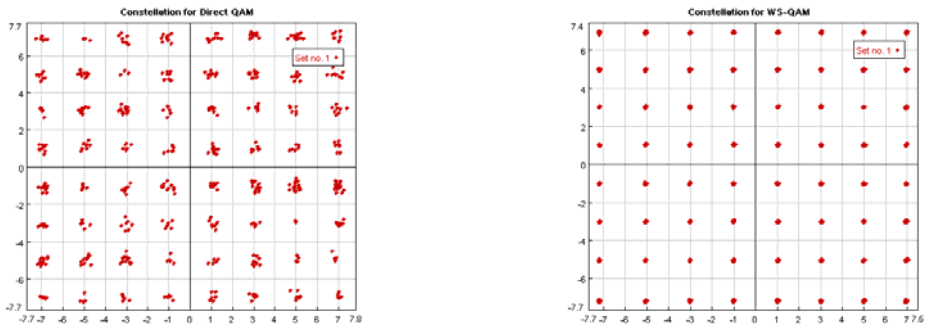

a) Constellation for Direct QAM b) Constellation for WS-QAM in I channel

Fig. 6 The Constellation for QAM signal after transmitter

After the matched raised cosine filter, the constellation diagrams are shown for these two QAM implementations in Fig.6. Obviously, the constellation points of Direct QAM are more scattered than that of WS-QAM because the I and Q subcarriers are more independent to each other in the WS-QAM system, which implies more orthogonality in the transmission.

Experiment Results

An experimental Direct QAM system has been setup for the measurement of the error vector magnitude (EVM) which is an indication of the quality of the QAM signal. The optical source is directly intensity-modulated by the 64-QAM signal and the optical signal is detected by a large-area silicon PIN photodiode. A 658nm Fabry Perot laser diode and a 520nm green SLED are both tested as the optical source, both emitting

5.5mW optical power. The symbol rate is fixed at 15.0 MS/s. So the bit rate of the system is 90Mbit/s since the number of bits per symbol *N*=6 for 64-QAM. The optimal cases in the experiments are shown in Fig.7. With the laser diode, the error free transmission can reach 100 meter and the measured EVM was 1.723%, well less than the limitation of 5% for error free transmission in case of 64 QAM. With the 520nm green SLED, the system can only achieve 50 meter for error free transmission while the measured EVM was 2.881%.

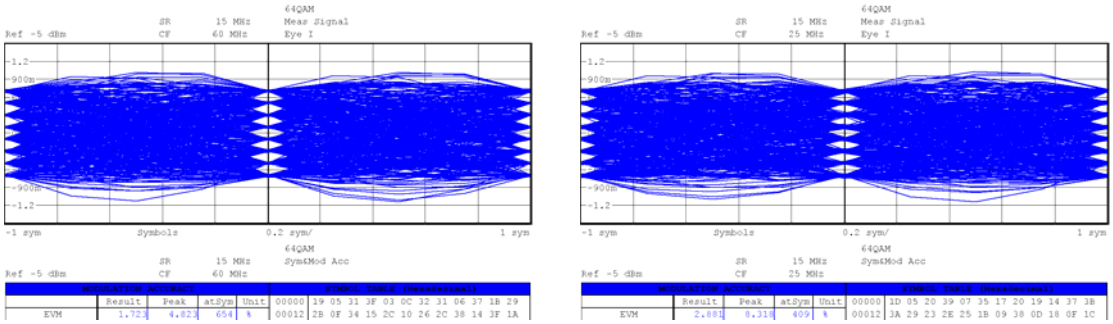

a) With 658nm laser diode, 100m POF b) With 520nm green SLED, 50m POF

Fig. 7 The eye diagram and measured EVM

Conclusions

From theoretical analysis, the QAM technique may be a good option for realizing a low cost but high capacity POF link. The technical feasibility of system solutions employing Direct QAM and WS-QAM have been analyzed for data rates of 128Mbit/s on a 1 mm core SI-POF link with a length of 100 meter. The WS-QAM system scheme seems better because of the high bandwidth efficiency. Experiments with measurements have been carried out with a simple Direct QAM system according to the simulations. Error free 90Mbit/s QAM transmission has been realized with a 650nm laser diode over 100 meter while the system can reach 50 meter with a 520nm green SLED as the optical source.

References

[1] A.M.J. Koonen, H.P.A. van den Boom, A. Ng'oma, M. Garcia Larrode, J. Zeng, G.D. Khoe, "POF Application in Home Systems and Local Systems", Proc. POF 2005, Hong Kong, Sep. 19-22, 2005, pp. 165-168.

[2] http://www.ist-pof-all.org

[3] A.M.J. Koonen, X. Li, J. Zeng, H.P.A. van den Boom, "High capacity data transport over plastic optical fibre links using quadrature modulation", Proc. ICAT 2006, Cambridge (UK), June 21-22, 2006, pp. 69-72

[4] D. Càrdenas, A. Nespola, R. Gaudino, S. Abrate, C. Lezzi, "FTTH in Italy: the FastWeb access infrastructure and its possible evolution with new PMMA-SI-POF media converters", IEE Conference on Access Technologies, 21-22 June 2006, Abington Hall, Cambridge, UK

[5] W. Daum, J. Krauser, P. Zamzow, O. Ziemann, "Polymer optical fibers for data communications", Springer (2002)

Embedded OTDR Monitoring of the Fiber Plant behind the PON Power Splitter

W. Chen, B. De Mulder, J. Vandewege and X.Z. Qiu

Ghent University, INTEC/IMEC, St.-Pietersnieuwstraat 41, B-9000 Gent,

Email: wei.chen@intec.ugent.be

We present a laboratory prototype which verifies a novel embedded optical time-domain reflectometry (OTDR) approach. It integrates inexpensive fiber monitoring functionality into an optical network unit (ONU) transceiver module of passive optical networks (PONs). The prototype includes a laser module, an analog front-end, a reconfigurable digital control platform with back-end data processing and a graphic user interface. The prototype demonstrates accurate OTDR measurements of two cascaded sections of optical fibers behind a power splitter representing a PON drop fiber section. Experiments show backscattering curves and Fresnel reflections where signal-to-noise ratio was improved by signal processing.

Introduction

For tomorrow's broadband optical access networks, the point-to-multipoint (P2MP) network architecture has best cost to performance ratio and its deployment is gaining momentum fast. A time division multiplexing (TDM) P2MP network contains optical power splitters between an optical line termination (OLT) and optical network units (ONUs) (Fig. 1). Time slots are allocated for the upstream traffic from each ONU to the OLT, during which the ONU transmits upstream data in bursts, rather than continuously. The burst-mode ONU data transmitter comprises an optical laser module and a laser driver. The large scale of modern PONs makes cost-efficient fiber monitoring from the ONU side desirable, to reduce the operation and maintenance costs. By integrating OTDR (optical time-domain reflectometry) functionality into optical transceiver modules, the embedded OTDR becomes an integral part of the network, which can be accessed by the PON management plane to monitor and test the quality of the physical layer.

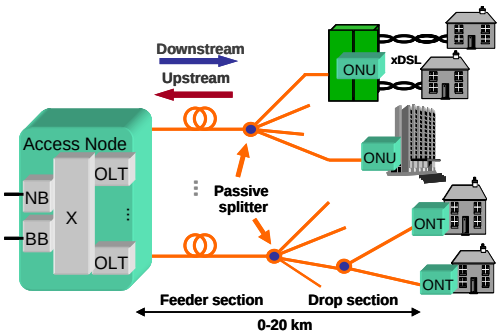

Fig. 1. Fiber network with TDM P2MP topology

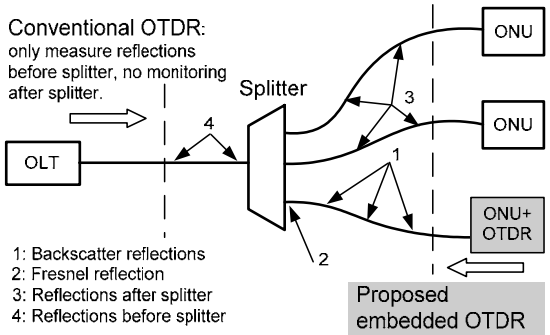

Fig. 2. Proposed embedded OTDR can monitor fiber drops without ambiguities

Conventional PON fiber monitoring is performed by OTDR measurements at the OLT side (Fig. 2). However, this suffers from reduced sensitivity due to high splitting losses and from ambiguous results due to the superposition in time of multiple OTDR traces originating from different ONU drop sections. To monitor the fiber status and locate a fault in the drop section more accurately, the better choice is to integrate an OTDR unit

in the ONU. As the high split ratio of P2MP networks makes the cost of the ONU a dominant decision criterion, a recent concept for low-cost ONU-embedded OTDR reuses the existing ONU data laser diode (LD) and laser driver [1]. This reduces the cost to a certain extent as no dedicated OTDR laser and driver are required, but an additional coupler and photo detector are still needed.

This paper presents a novel technique called FiberMon for embedding OTDR into existing data transmitters, suitable for monitoring the fiber plant of a wide range of TDM optical networks in the background, during network operation. The OTDR hardware is purely electronic, integrated inside the burst-mode optical transmitters (BM-Tx), and does not require extra (electro-)optical components. An original FiberMon prototype was built containing an optical front-end, a reconfigurable digital platform and graphic user interface (GUI). Experimental results prove the functionality and the feasibility of embedded OTDR. The FiberMon technique is developed with PON (passive optical network) specifications in mind [2], but is in fact quite generic.

The FiberMon Embedded OTDR Concept

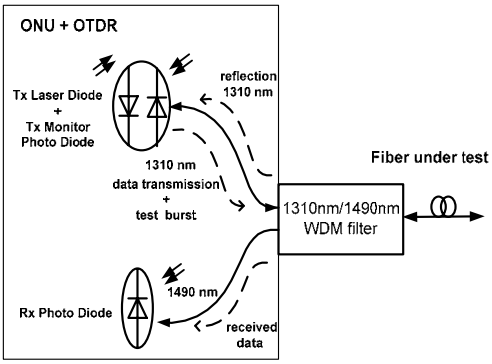

Fig. 3. The optical architecture of an ONU

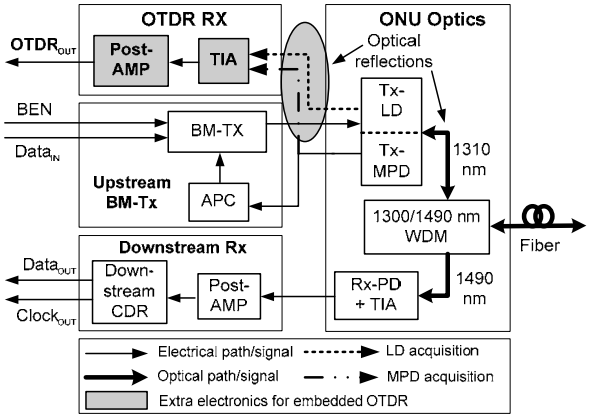

Fig. 4. A PON ONU transceiver with embedded OTDR

Fig.3 shows the ONU optics, with the 1310nm reflection to be used for OTDR. Reflection-tolerant Fabry-Pérot (FP) lasers with integrated monitor photo diode (MPD), and vertical-cavity surface-emitting lasers (VCSELs), are cost-effective in a PON ONU, as the expensive integrated optical isolator can be omitted. During data transmission the LD emits light bursts and the MPD monitors the emitted optical power, serving the automatic power control (APC) loop. During the idle time window between two bursts, the LD can transmit an OTDR test signal after which the LD and/or MPD act(s) as an OTDR photo detector to receive the optical reflections. Fig. 4 shows a PON ONU transceiver with embedded OTDR unit. It consists of ONU optics, upstream 1310 nm BM-Tx, downstream 1490 nm receiver (Rx) and 1310 nm OTDR Rx. This OTDR hardware doesn't need any additional OTDR optics and only requires a limited amount of extra electronics. If there are no suitable idle time windows, FiberMon can perform OTDR measurements in the background by processing the optical echo signals caused by the data bursts themselves. LD and/or MPD then receive(s) the optical reflections immediately after emission of a data burst. Mathematical analysis and simulation have proven that the response of a pulse with arbitrary width can be converted into the standard step response, when the OTDR front-end is sufficiently linear [3]. In this way, fully non-intrusive OTDR can be performed that does not interfere with the ongoing traffic nor penalize the network performance.

Experimental prototype

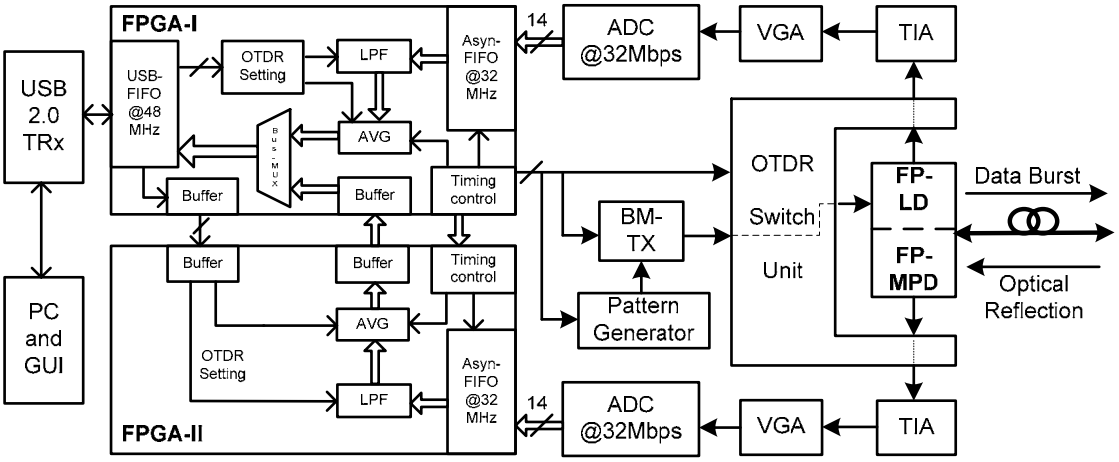

Fig. 5. Block diagram of experimental prototype

Fig. 5 shows the block diagram of the experimental prototype. The selected LD, a 1310 nm InGaAsP/InP FP laser chip, is mounted in a coaxial package with a MPD and a single-mode fiber pigtail. The OTDR switch unit (OSU) performs a fast switchover between two states: transmit mode and monitoring mode. During transmit mode, the BM-Tx connects to the forward-biased LD and modulates it with the input data signal. After transmission, the OSU shuts down the LD very quickly, and connects the OTDR analog front-end (OAF) to the LD and/or the MPD. The transient time of the OSU switchover is made short. An OTDR TIA bandwidth of 5 MHz trades-off spatial resolution and noise reduction. A variable gain amplifier (VGA) matches the input range of the analog-to-digital conversion (ADC) to the level of the received optical reflections. The ADC samples the amplified reflection signal at 32 Mbps with a 14-bit resolution, offering ample dynamic range to detect the optical events in a PON network. Performing the OTDR measurement simultaneously on both FP-LD and FP-MPD channels is interesting because it can provide a more efficient fiber monitoring with substantial averaging. For this purpose two Virtex-II FPGAs perform real-time processing, one on each channel, and provide OTDR data path connectivity between the OAF and GUI. The FPGA modules are programmed by the computer through a USB 2.0 transceiver (TRx) in a daisy chain. Both FPGAs and ADCs are synchronized to each other. FPGA-I is the master and contains a hardware counter that provides accurate timing for the OTDR measurements. FPGA-I and FPGA-II communicate bi-directionally to deliver measurement data and to set OTDR parameters. During initialization, FPGA-I receives commands and parameters from the GUI, parses them and performs the corresponding configuration of the real-time OTDR processing blocks in FPGA-I and FPGA-II. These tasks include loading low-pass filter (LPF) coefficients, setting averaging and interleaving, and defining the width of the injected pulse and the length of fiber under investigation. During operation, both FPGAs receive a large amount of reflection samples simultaneously. Asynchronous FIFOs (first-in first-out memories) in both FPGAs will store this OTDR trace momentarily. After filtering and averaging, the USB-FIFO transfers them to the computer. An updated OTDR trace is shown on the GUI, which runs on a Linux based PC platform, and the dataset is saved for further backend data processing.

Measurement results

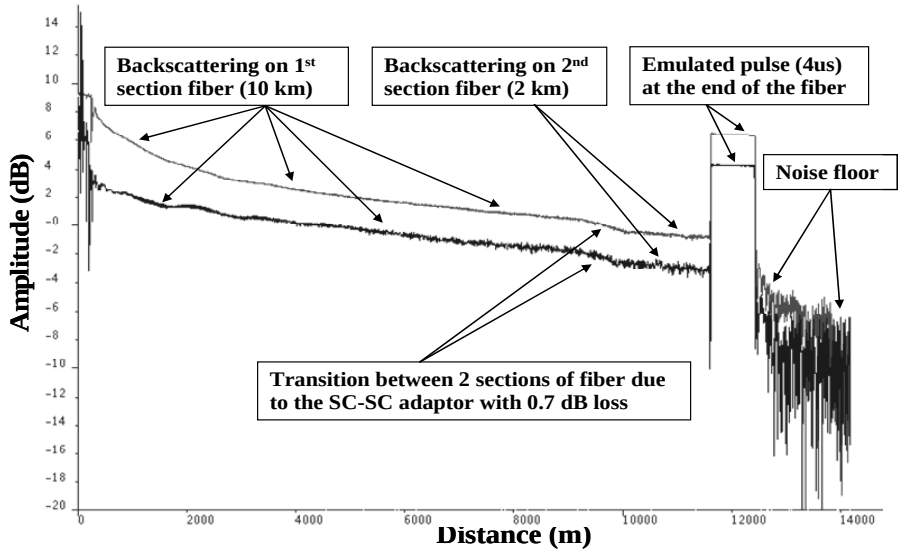

Fig. 6. Measured OTDR curves in log scale on FP-LD and FP-MPD simultaneously from the proposed experimental prototype

The prototype hardware was connected to two cascaded sections of ITU-T G652 compliant single-mode optical fiber with a similar backscatter constant and attenuation: a first section of 10 km, and a second of 2 km with a Fresnel reflector at the end. Pulses with 3 dBm peak optical power were injected repeatedly into the test fiber. In order to improve the signal-to-noise ratio (SNR), an averaging function and low-pass filtering block were activated in the FPGAs. The top OTDR trace on Fig. 6 is measured from an FP-LD with 0.12 A/W responsivity, the bottom one from a FP-MPD with 0.033 A/W responsivity. The two linear sections with 10 km and 2 km length in Fig. 6 result from Rayleigh backscattering. A transition region can be noticed with a width of 4 µs, which indicates an SC-SC adaptor with 0.7 dB loss. At the end of the fiber, the Fresnel reflector can be clearly distinguished with a 4 µs width emulated pulse [3]. By simultaneously measuring on both the FP-LD and the FP-MPD, a relatively stable combined optical reflection is obtained, and the polarization dependency of a FP laser module can be compensated considerably.

Conclusions

It has been shown how an original experimental prototype performs the embedded OTDR measurements. The SNR improved embedded OTDR curve with 12 km G652 single-mode optical fiber was obtained by the use of the proposed embedded method. This technique and experimental prototype will be used in the future work to perform further OTDR measurements of the PON system.

References

[1] H. Schmuck, J. Hehmann, M. Straub and Th. Pfeiffer, "Embedded OTDR techniques for cost-efficient fibre monitoring in optical access networks", in Proceedings of the ECOC 2006.

[2] "Gigabit-capable Passive Optical Networks (GPON): Physical Media Dependent (PMD) layer specification", ITU-T Recommendation G.984.2, Mar. 2003.

[3] B. De Mulder, W. Chen, J. Bauwelinck, J. Vandewege and X.Z. Qiu, "Non-Intrusive Fiber Monitoring of TDM Optical Networks", to be published by IEEE JLT, Jan. 2007.

Performance of Maximum Likelihood Sequence Estimation in 10 Gb/s Transmission Systems with Polymer Optical Fiber

S.C.J. Lee(1), F. Breyer(2), S. Randel(3), B. Spinnler(3), I.L. Lobato Polo(4), D. van den Borne(1), J. Zeng(1), H.P.A. van den Boom(1), A.M.J. Koonen(1)

(1) COBRA Research Institute, Univ. of Technology Eindhoven, Eindhoven, the Netherlands, e-mail: s.c.j.lee@tue.nl; (2) Institute of Communications Engineering, Univ. of Technology Munich, Munich, Germany; (3) Siemens AG, Corporate Technology, Information and Communications, Munich, Germany; (4) Siemens AG, Program and System Engineering, Munich, Germany

The 120 µm core-diameter perfluorinated graded-index polymer optical fiber (GI-POF) is gaining interest for use in local area networks (LAN) such as enterprise or datacenter backbones to support 10 Gigabit Ethernet (10GbE). In this paper, the performance of MLSE equalization on a 100 m GI-POF transmission link operating at 10.7 Gb/s is investigated.

Introduction

Rapid increase of data traffic in data communication applications has pushed the demand for high-capacity and low-cost optical networks for use in local area networks (LAN), such as enterprise or datacenter backbones [1,2]. The use of 10 Gigabit Ethernet (10GbE) in such cases will often require a new installation, because the commonly used CAT-5 copper cables are unsuitable for 10GbE transmission over sufficiently long distances. Although this can be solved by upgrading the cable infrastructure to CAT-6A copper cables, it may not be a future-proof solution.

A promising alternative is the use of fiber optic cables, such as multimode silica fibers. However, short-reach LAN requires very cost-efficient solutions. This makes the use of most optical fibers impractical due to the associated high installation costs. In comparison to multimode silica fibers, the perfluorinated graded-index polymer optical fiber (GI-POF) with 120 µm core-diameter is a promising alternative because the large core-diameter allows large alignment and dimensional tolerances for components. Furthermore, it still allows the use of standard high-speed transmitters and detectors at wavelengths of 850 and 1300 nm. The GI-POF thus offers ease of use and installation, with clip-on connectors requiring minimal training or specialist equipment for termination. Furthermore, cables made from GI-POF are extremely flexible, offering a bending radius of 5 mm compared with 25 mm for silica fiber cables and 30 mm for CAT-6A copper cables.

Due to bandwidth limitations caused by modal dispersion in large-core multimode fibers, 10 Gb/s data transmission on such 120 µm perfluorinated GI-POF is limited to distances less than 100 m [3]. Recent research advances in electrical equalization for 10 Gigabit Ethernet multimode fiber (MMF) links show the possibility to compensate for such modal dispersion, yielding significant performance improvement [4,5].

In this paper, we investigate the performance improvement for a 100 m transmission link with 120 µm perfluorinated GI-POF operating at 10.7 Gb/s, when electrical equalization in the form of maximum likelihood sequence estimation (MLSE) is used. It is well known that for all equalization schemes, MLSE achieves the best performance [6]. These results can therefore be seen as a performance bound for using electrical equalization to combat modal dispersion.

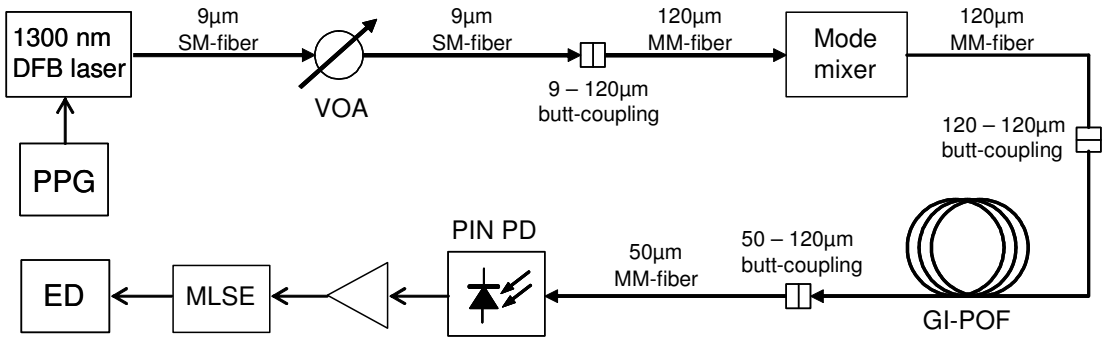

Fig. 1: Experimental Setup.

Experimental Setup

The experimental setup of the GI-POF transmission system is shown in Fig. 1. A directly modulated 1300 nm distributed feedback (DFB) laser with standard single-mode fiber pigtail is used as the transmitter. This laser is modulated with a non return-to-zero 2^{15}-1 pseudorandom bit sequence at 10.7 Gb/s (PPG). A variable optical attenuator is placed after the laser to adjust the power level. Before coupling into the GI-POF, a mode mixer is used. This mode mixer consists of 50 cm of the same type of GI-POF wound 10 times around a cylinder with 20 mm diameter. Using such a mode mixer stabilizes the transmission system, because of the over-filled mode launch.

After the mode mixer, the optical power is launched into 100 m of perfluorinated GI-POF. The GI-POF used is a commercial fiber with 0.185 numerical aperture, 120 µm core-diameter, and 500 µm total diameter including cladding. The attenuation is approximately 40 dB/km at a wavelength of 1300 nm. For the back-to-back measurement, the GI-POF is left out of the experimental setup (compare Fig. 1).

At the receive end, a 50 µm silica multimode fiber (MMF) pigtailed InGaAs PIN detector is used, leading to a 3.5 dB coupling loss due to core-size mismatch between the GI-POF (120 µm) and the silica MMF (50 µm). After electrical amplification, the received signal is fed into a commercial MLSE module [7]. This MLSE module comprises a 3 bit A/D converter operating at a two-fold sampling speed (21.4 GSamples/s) and a four-state (2 symbols memory) Viterbi decoder. Finally, the output of the MLSE is fed to the error detector (ED).

Experimental Results

Fig. 2a and b show the measured bit-error ratio (BER) values after transmission at 10.7 Gb/s over 100 m of GI-POF plotted against time without and with MLSE, respectively. These BER values are measured every second for a total time period of 900 seconds and a received optical power of -7.5 dBm. It can be seen that BER values around 10^{-3} are reduced to 10^{-7} when MLSE is employed. As the measured BER values with MLSE are several orders of magnitude better than the limit of forward error correction (FEC), which is commonly used in 10 Gb/s transmission systems, error-free transmission can be achieved under all circumstances.

The measured BER curves depicted in Fig. 2c compare the performances of the system with and without MLSE in the same 100 m GI-POF transmission link operating at 10.7 Gb/s. Each plotted BER value corresponds to the mean of 300 measured values obtained every second. At a BER of 10^{-4}, the 100 m GI-POF system with MLSE has a 6 dB better receiver sensitivity than without MLSE. For the back-to-back measurements

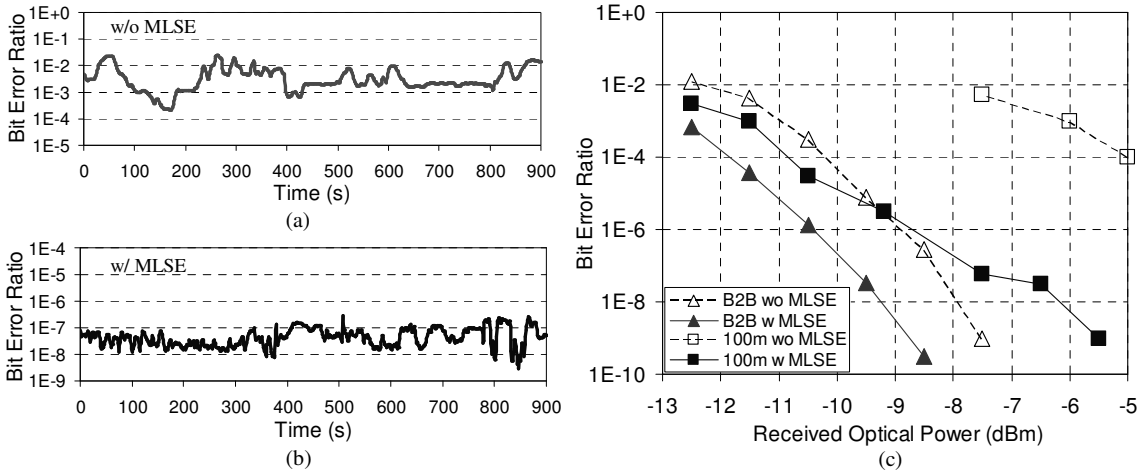

Fig. 2: (a) BER vs. time for 100 m GI-POF without MLSE at 10.7 Gb/s and -7.5 dBm received optical power; (b) same as a., but with MLSE; (c) comparison of MLSE performance for the back-to-back case and transmission over 100 m GI-POF.

without GI-POF, the system performs 2 dB better with MLSE as a result of impairments due to the directly modulated laser and modal dispersion introduced by the mode mixer.

Conclusions

We've shown a 6 dB better receiver sensitivity (at a BER of 10^{-4}) for a 100 m GI-POF link operating at 10.7 Gb/s, using MLSE to combat the influence of modal dispersion. This shows that the system's power budget can be improved by 6 dB when electrical equalization is employed, implying that the GI-POF can support 10 Gigabit Ethernet transmission over distances larger than 100 m. Together with the additional advantages of mechanical robustness, relaxed alignment tolerances and easy, low-cost installation, this makes the GI-POF a promising solution for future enterprise and datacenter backbone networks.

References

[1] C.M. DeCusatis, "Fiber optic cable infrastructure and dispersion compensation for storage area networks," IEEE Communications Magazine, vol. 43, pp. 86-92, March 2005.

[2] S. Randel, S.C.J. Lee, B. Spinnler, F. Breyer, H. Rohde, J. Walewski, A.M.J. Koonen, and A. Kirstädter, "1 Gbit/s Transmission with 6.3 bit/s/Hz Spectral Efficiency in a 100 m Standard 1 mm Step-Index Plastic Optical Fibre Link Using Adaptive Multiple Sub-Carrier Modulation," Proc. ECOC'06, PDP Th4.4.1 (2006).

[3] G. Giaretta, W. White, M. Wegmueller, R.V. Yelamarty, T. Onishi, "11Gb/sec Data Transmission Through 100m of Perfluorinated Graded-Index Polymer Optical Fiber," Proc. OFC'99, PDP, PD14-1 (1999).

[4] P. Pepeljugoski, J. Schaub, J. Tierno, J. Kash, S. Gowda, B. Wilson, H. Wu, A. Hajimiri, "Improved Performance of 10 Gb/s Multimode Fiber Optic Links Using Equalization," Proc. OFC'03, ThG4 (2003).

[5] C. Xia, M. Ajgaonkar, and W. Rosenkranz,"On the Performance of the Electrical Equalization Technique in MMF Links for 10-Gigabit Ethernet," IEEE J. Lightwave Technol., vol. 23, pp. 2001-2011, June 2005.

[6] J.G. Proakis, Digital Communications. New York: McGraw-Hill, 2001.

[7] A. Färbert, S. Langenbach, N. Stojanovic, C. Dorschky, T. Kupfer, C. Schulien, J.P. Elbers, H. Wernz, H. Griesser, C. Glingener, "Performance of a 10.7 Gb/s Receiver with Digital Equaliser using Maximum Likelihood Sequence Estimation," Proc. ECOC'2004, PD-Th4.1.5 (2004).

Optical Code Sensing Multiple Access / Collision Detection (OCSMA/CD) on a Passive Optical Network Employing a Single Spectral En/Decoder

B. Huiszoon, H. de Waardt, G.D. Khoe and A.M.J. Koonen

COBRA Research Institute, Eindhoven University of Technology, 5600MB Eindhoven, The Netherlands

In this paper, we propose the concept of optical code-sense multiple access / collision detection to upgrade an optical code division passive optical network with minor modifications to transparently deploy Ethernet (or packet) based services.

Introduction

Optical Code-Sense Multiple Access / Collision Detection (OCSMA/CD) is a novel Medium Access Control (MAC) protocol in the optical physical layer (PHY). OCSMA/CD has its primary and most attractive application to transparently run Ethernet (or packet) based services on fiber-optic networks which employ Optical Code Division Multiplexing (OCDM) or Optical Code Division Multiple Access (OCDMA). Previous work on Ethernet MAC protocols for a PON focused on optical carrier-sense [1-3]. For a code division network this obviously does not result in correct detection of collisions unless multiple wavelength channels are used per destination. However this leads to a significant increase in network complexity moreover to an inefficient usage of optical bandwidth.

A Passive Optical Network (PON) shared-fiber architecture is envisaged to provide optical transparency in the access network layer. Network nodes have to be able to sense each other's activities in order for the MAC protocol to work. In [1] the cyclic properties of an Arrayed Waveguide Grating (AWG) are used. However, this imposes a fixed WDM scheme onto the PON. In [2] an isolator is placed at a star coupler which also reflects optical power onto the fiber of the source. Such a solution introduces a self-jamming effect. This effect also occurs in [3] although it is used for peer-to-peer or shared LAN networking. We upgrade the passive splitter in PON with a second coupler stage to have directional coupling. In other words the optical power is reflected to all-but-own fibers. Collision detection in such systems is straightforward [4]. Moreover the network is kept wavelength agnostic which in combination with wavelength agnostic Optical Networking Units (ONUs) results in a fully dynamic Wavelength Division Multiplexing (WDM) scheme.

Cost-efficiency and photonic integration are key in order for a code division network to be commercially attractive. We consider spectral amplitude coding of a cost-efficient incoherent optical source such as a Light Emitting Diode (LED). This type of OCDMA is therefore referred to as Spectral Amplitude Encoded OCDMA (SAE OCDMA). A low complexity integrated en/decoder based on Mach-Zehnder Interferometers (MZIs) was proposed in [5]. Such en/decoder is reciprocal thus the existing setup can be upgraded with the code-sense functionality by only adding few components rather than adding a separate circuit. Besides, having the sensing and transmission functionality in one device reduces the processing time which increases the network efficiency.

In this paper the SAE OCDMA PON concept is introduced, featuring wavelength routing, a code-sensing MAC protocol, and collision detection. Simulation results confirm the principle of operation.

Spectral Amplitude Encoded OCDMA PON with Wavelength Routing

In this section the general concept of SAE OCDMA on PON is introduced and a network scenario is given. The scenario not only considers a single PON connected to the CO but also multiple PONs connected. Wavelength routing of code labeled channels is suggested in the subnet of PONs. In code division networks an orthogonal code is usually assigned to each user but it can also be used to address the destination. In latter case, collisions are at stake and a MAC protocol is required.

Spectral amplitude encoding of incoherent optical sources was first proposed in [6]. The encoded spectrum is used in a Spectral Shift Keying (SSK) modulation format. In SSK a binary one is represented by the encoded pattern and a binary zero by the complementary (π shifted) version, or vice versa. As such, the filter pattern uniquely identifies a user but at the same time it represents the data flow. At the receiver the mixed SSK signals of different users is launched into one of the inputs of the decoder. Balanced detection is used at the receiver to maximize the auto-correlation for a code match and to minimize the cross-correlation for no code match. Only with such an SSK setup full rejection of multiple user interference is achieved. A significant improvement was made in [5] which proposed an integrated MZI based cascade chain as encoder and decoder. Parallel processing of up and downstream encoded data is required at the CO for truly asynchronous medium access. Recently a tree structure has been demonstrated which cost-efficiently provides such functionality [7].

The central office is not limited to just a single PON but it may have multiple PONs connected. If each PON operates on its own (dynamically) assigned wavelength, all-optical Wavelength Routing (WR) maximizes the throughput in the CO's subnet of PONs. We aim at no wavelength conversion at the CO to increase the end-to-end optical transparency. It also simplifies the network scenario. As a result the SSK signal is transmitted on the wavelength of the destination PON (lambda_out) by using the optical orthogonal code of the addressee. If the code labeled wavelength channel is routed correctly, the broadcast-and-select properties of PON and OCDMA ensure that the addressee receives its data. It is clear that a collision may occur at an aggregation point when multiple ONUs simultaneously transmit data to a similar destination. Data not intended for nodes outside the "home" PON is sent on the assigned wavelength (lambda_home) with the ONU's own optical orthogonal code. Collisions may also occur if peer-to-peer communication is enabled between two ONUs in the same PON.

Spectral Amplitude Encoded OCDMA PON with Collision Detection

Fig. 1 shows the architecture of the SAE OCDMA PON. The necessary upgrades for code sensing abilities are denoted with a grey background and dotted outline. Code sensing is implemented in the optical PHY to lower the complexity in the protocol stack. The autocorrelation peak of any transmission on a set code is detected. The presence of optical power is sufficient to establish that a collision has taken place.

A tunable Band-Pass Filter (BPF) is used in combination with a Superluminescent LED (SLED) to select a transmission wavelength band at the ONU. An isolator between

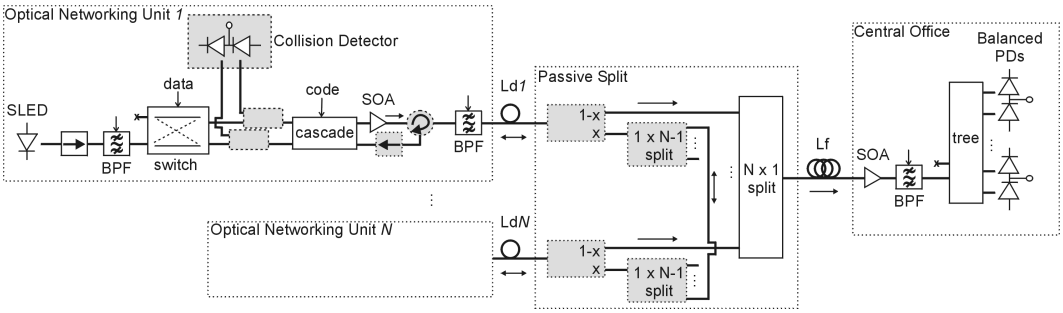

Fig. 1: Spectral Amplitude Encoded OCDMA Passive Optical Network with Wavelength Routing and Collision Detection

the BPF and SLED prevents reflections that degrade performance and blocks downstream signals used by the collision detector. A switch is used for SSK modulation by switching the optical signal either to the upper or the lower input of the cascade. One of the outputs of the cascade is then amplified by a Semiconductor Optical Amplifier (SOA). A second tunable BPF is set to a similar band as the first filter and suppresses out-of-band downstream wavelength channels and ASE noise added by the SOA. To upgrade the ONU node design with collision detection only few extra components are required. Firstly, two couplers couple part of the received optical field to a (balanced) collision detection unit. Secondly, a circulator is added to split upstream and downstream traffic before the SOA. The downstream reflected optical field might saturate the SOA such that the required gain for the upstream traffic can not be provided. An extra isolator makes sure secondary upstream traffic is not passed through the SOA. The design of the ONU allows cost-efficient photonic integration which is of key importance. Many efforts are made towards the integration of the circulator and isolator [8,9].

The passive Nx1 splitter is modularly upgraded for power reflection to all-but-own fibers. It is common to reflect at the passive splitter to avoid excessive delays in collision detection due to the long length of the feeder fiber (Lf) with respect to the distribution fibers (Ld) of the PON**.** The modular solution proposed for star couplers in [10] has been modified to suit a 1xN splitter. Major difference is that most optical power has to be coupled towards the CO and smaller portions have to be coupled towards the ONUs. The passive Nx1 splitter is extended with two extra couplers per distribution fiber. The coupling ratio x of the first coupler is a variable to optimize the setup. The second coupler has a 1xN-1 equally distributed splitting ratio. The tree structure is placed at the CO to simultaneously decode each individual SSK channel. An SOA is used as pre-amplifier with a tunable BPF to suppress out-of-band noise. Transmission from the CO to the ONU is not considered here.

Simulation results

In this section simulation results are discussed of the system that is shown in Fig. 1. Three ONUs have been simulated where one of the three is transmitting part of its data on the code of one of the other ONUs. The coupling ratio x in the novel design of the passive splitter is set to 0.8 but can be further optimized. A two-stage cascade and a two-stage tree are used to generate and process the required code set [7]. The optical distribution and feeder fibers are replaced by attenuators and optical delay modules to avoid excessive simulation time. The results are expected not to change significantly since the fiber distances are short in case of PON in the access network layer.

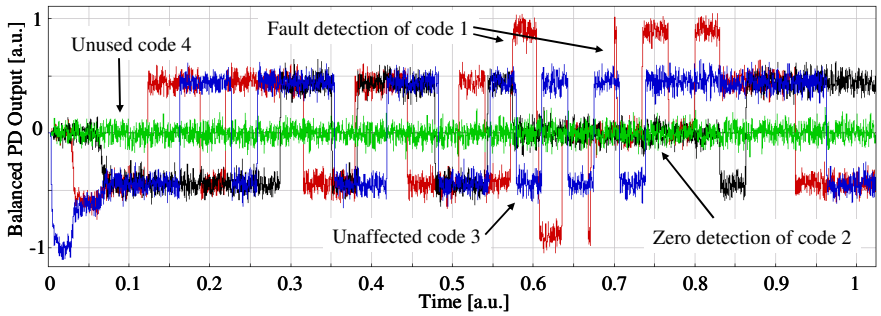

Fig. 2: Received and decoded bit streams at the Central Office

Fig. 2 shows the received bit streams at the CO. The soft capacity characteristic of OCDMA is clearly seen at the beginning of the transmissions. Adding users results in an overall reduction in Signal-to-Noise Ratio (SNR). During its data transmission, ONU 2 suddenly switches from code 2 to code 1. It is then interfering ONU 1 and vice versa. In the response at the CO this is observed by fault detection at code 1 and zero detection at code 2. This extreme case should not happen if more intelligence is added in the simulation. ONU 2 should sense the medium before actually transmitting its data. The transmission of ONU 3 on code 3 remains unaffected.

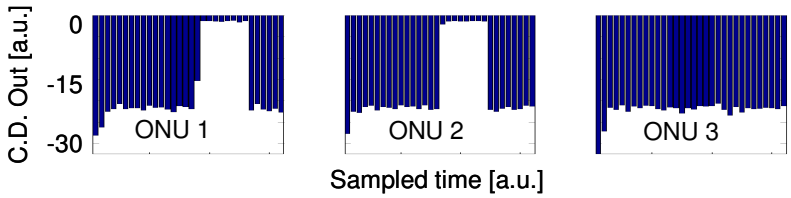

Fig. 3: Collision Detector (C.D.) output of three different ONUs

Fig. 3 shows the electrical output power of each of the three collision detection units which corresponds with Fig. 2. The high CD output of ONU 1 and ONU 2 indicate a collision is detected. The CD of ONU 3 detects no collisions.

Conclusion

We have proposed OCSMA/CD to implement Ethernet (or packet) based services on optical code division PONs. A collision detection unit is easily implemented on an existing reciprocal en/decoder at the ONU-side. The passive splitter is modularly upgraded with directional coupling to reflect optical power to all-but-own fibers.

References

[1] B.N. Desai, *et al.*, in *Proc. OFC'01*, paper WN5
[2] C.J. Chae, *et al., Photon. Technol. Lett.*, 14(5), pp. 711, 2002
[3] E. Wong, *et al.*, *Photon. Technol. Lett.*, 16(9), pp. 2195, 2004
[4] J.W. Reedy, *et al.*, *J. on Sel. Areas in Comm*, 3(6), pp. 890, 1985
[5] C.F. Lam, *et al.,* in *Proc. CLEO'98*, paper CThU4
[6] D. Zaccarin, *et al.*, *Photon. Technol. Lett.*, 4(4), pp. 479, 1993
[7] B. Huiszoon, *et al.*, to be published in *Proc. LEOS Annual'06*, paper ThW2
[8] W. Van Parys, *et al.*, in *Proc. OFC'06*, paper OFA2
[9] T.R. Zaman, *et al.*, *Photon. Technol. Lett.*, 18(12), pp. 1359, 2006
[10] T. Hermes, *Electron. Lett.*, 27(23), pp. 2136, 1991

Interactions with a photonic crystal micro-cavity using an AFM in contact or tapping mode operation

W.C.L. Hopman[1], K.O. van der Werf[2], A.J.F. Hollink[1], W. Bogaerts[3], V. Subramaniam[2], R.M. de Ridder[1]

[1]Faculty of Electrical Engineering, Mathematics and Computer Science, Mesa+ Institute for Nanotechnology, University of Twente, PO Box 217, 7500AE Enschede, The Netherlands

[2] Faculty of Science and Technology, Mesa+ Institute for Nanotechnology, University of Twente, PO Box 217, 7500AE Enschede, The Netherlands

[3]Department of Information Technology, Ghent University – IMEC, Sint-Pietersnieuwstraat 41, 9000 Gent, Belgium

In this paper we show how the evanescent field of a localized mode in a photonic crystal micro-cavity can be perturbed by a nano-sized AFM tip. Due to the high field intensities in the cavity, we can see a significant change in output power when the tip is brought into the evanescent field in either contact or tapping mode operation. We find a 4 dB modulation, when using a Si_3N_4 tip and we show that the transmittance can be tuned from 0.32 to 0.8 by varying the average tapping height.

Introduction

Photonic crystal (PhC) micro-cavities (MC) are increasingly important building blocks in integrated optics. However, the strong dependence on the geometry of the MC cavity properties demands high-resolution fabrication processes to satisfy the designers' criteria. Even though nanotechnology-based fabrication advances rapidly, errors in the fabrication process are still inevitable due to variations in the fabrication process. This has led to an increase in attention for mechanical tuning [1, 2]. In this research we focused on mechano-optical interactions through the evanescent field, which have been utilized in, for example, sensors [3] and actuators [4]. In traditional mechano-optical approaches, the size of the object placed in the evanescent field is much larger than the optical wavelength to obtain a sufficiently large phase shift while avoiding strong attenuation. However, an optical micro-resonator providing a strongly enhanced field in a small volume (that is, having a high quality factor to modal volume ratio Q/V [5]) can have a strong mechano-optical interaction with sub-wavelength-sized dielectric objects. For example, the optical transfer function of an MC realized in silicon on insulator (SOI) can be strongly affected by an object with a minimum radius as small as 10 nm in close proximity to the resonator. In this research we use a scanning atomic force microscope (AFM) [6] with a dielectric tip for the mechano-optical interactions with the MC. We show that the AFM can be used in both contact mode and tapping mode to achieve strong interactions with the PhC MC.

Design and Setup

The experiments reported in this paper were performed on a PhC MC design in SOI (220 nm device layer thickness on 1 μm buried oxide) in a triangular lattice with 440 nm period and 270 nm hole radius. For practical purposes we designed a relatively large Fabry-Perot-like cavity (~ 2 μm) terminated by two holes on each side in a PhC waveguide (see Fig. 1a). This high-finesse cavity has a Q of about 650. This Q value was sufficient for our purpose, showing already a strong interaction of the probe with

the cavity resonance, although much higher Q's can be attained, if needed, by optimizing the cavity design [5]. For feeding the PhC cavity we simply used W1 waveguides (i.e. one row of holes left out). The connecting photonic wires had a width of 600 nm, which ensures single TE-mode operation for wavelengths around 1550 nm. The structure as shown in the SEM photo in Fig. 1a, was fabricated (at IMEC, Belgium) using a process [7] involving deep UV lithography (λ = 248 nm) and reactive ion etching. The resonance wavelength was measured to be 1539.25 nm, see Fig. 1b.

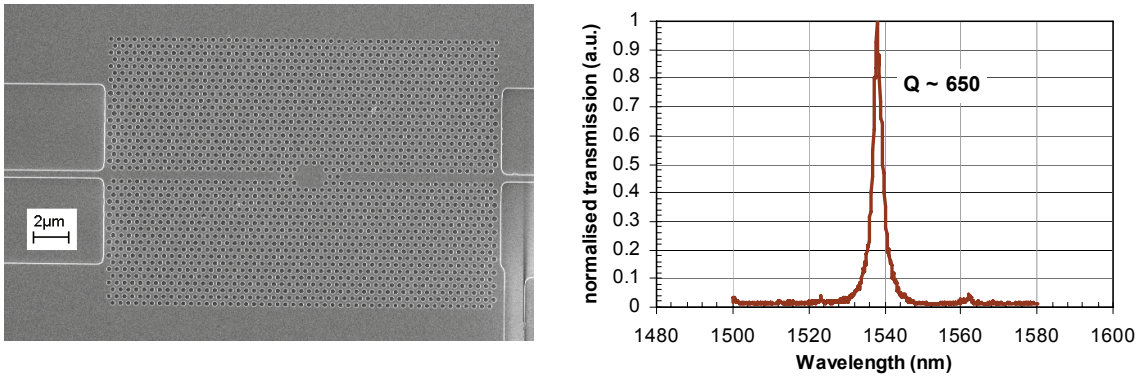

(a) (b)

Fig. 1. (a) *SEM photo of the PhC MC.* ***(b)*** *The normalized spectral response.*

A scanning probe AFM was combined with a standard end-fire transmission setup for performing the nano-mechano-optical tuning experiments. A schematic representation of the setup is shown in Fig. 2.

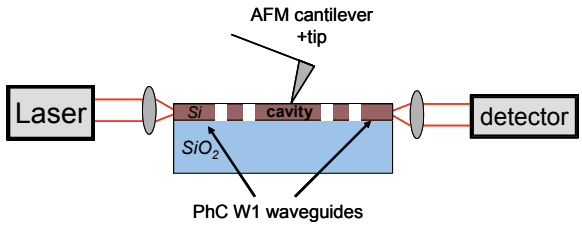

Fig.2 *A schematic representation of the dual-measurement setup.*

The AFM could be operated both in contact mode (dragging the tip over the sample) and in tapping mode. The cantilever was driven at its resonance frequency (~ 63 kHz) for tapping mode operation. The tip was scanned over the sample in a raster scan (256 x 256 points). The height (obtained from the AFM deflection signal) and the optical transmission could be determined at each raster point. By experiments [2] and modeling it was found that a small silicon nitride probe having a relatively low refractive index n (Si_3N_4, $n \cong 2.0$) can be used to map out the standing wave pattern in a PhC resonator. The probe induces a local phase shift, which results in a shift of the resonance to higher wavelengths. A drop in transmitted power can be observed, when the laser wavelength remains constant (at the initial resonance wavelength). A silicon (Si, $n \cong 3.5$) probe tip can be selected for obtaining an even higher interaction with the MC. This was also done for the tapping experiments presented in this paper.

Experiments

The size of the scanning window was set to its maximum value (20 µm) to locate the MC. By scanning in contact mode with a Si_3N_4 tip (minimum radius 10 nm) over the

sample, we obtained the structure geometry from the AFM as shown in Fig. 3a and simultaneously the transmitted power, shown in Fig. 3b. This latter figure can be interpreted as the 2-D representation of the transmitted power at the resonance wavelength versus the tip position. The dark spots corresponding to a position inside the resonator represent dips in the transmission. Outside the resonator we only find a light color, with almost no variation, because the field intensity is low at those locations.

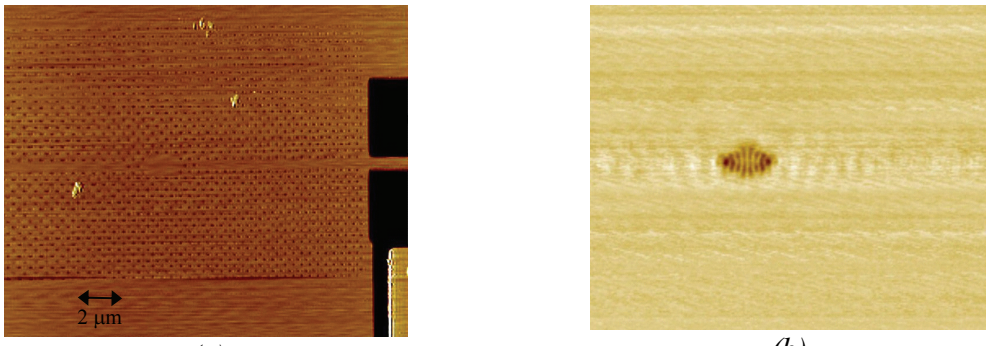

(a) *(b)*

Fig. 3. (a) *AFM height data, obtained by scanning a Si_3N_4 tip over the PhC structure in contact mode.* ***(b)*** *While scanning, the transmitted power was monitored and graphically visualized in a 2D image.*

This type of resonance imaging in a PhC MC was for the first time demonstrated in [2], where a maximum modulation of about 4 dB was found for a nano-sized Si_3N_4 probe. In principle there are two ways to improve the interaction with the cavity: the first is by increasing the size of the tip, this can for example be established by focused ion beam milling [8] of the tip; the second alternative is to select a probe having a higher refractive index, for example silicon. The disadvantage of a Si probe in contact mode compared to a Si_3N_4 probe is that the Si probe wears off at a much faster rate. As a consequence, the probe size is slightly increased at each successive scan. However, this can be avoided by operating the AFM in tapping mode if the cantilever is stiff enough.

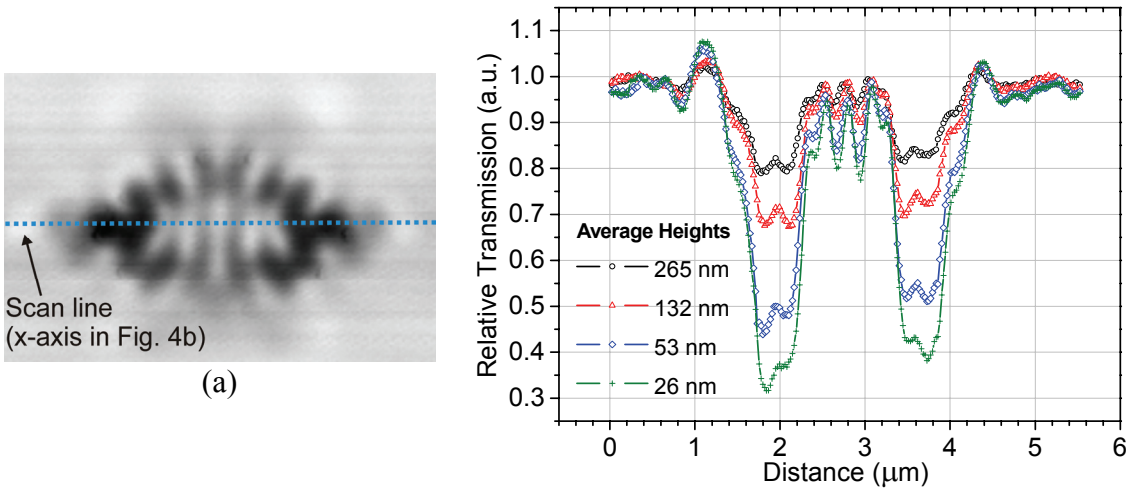

(a) (b)

Fig. 4*.* ***(a)*** *A 2D representation of the transmitted power when a Si tip is scanned over the sample in tapping mode.* ***(b)*** *The graph shows the transmission over the scan line, see (a), for 4 average tapping heights. Lowering the tapping height increases the impact on the resonance, as expected.*

The result of the scan over the MC in tapping mode is shown in Fig. 4a. The tapping amplitude for this measurement was 52 nm, resulting in an average height of 26 nm. Due to the decay of the evanescent field above the cavity, the effect of the tip on average transmitted power depends on the average tip height. Because the field has an exponentially decaying shape above the cavity, the interaction between the tip and the MC resonance will also be approximately exponentially in shape. By varying the tapping amplitude above a pre-selected position, the transmission can be carefully tuned. The shift in transmission can be related approximately to a wavelength by using the transmission spectrum shown in Fig. 1b with the assumption that the scattering losses can be neglected, which is consistent with modeling (not shown in this paper). The on/off ratio of the transmitted power can be tuned from 0.8 (265 nm average height above the sample) to a value as low as 0.32 (26 nm). The minimum value is limited here by the minimum feasible tapping amplitude (2 x 26 nm = 52 nm).

Conclusions

We have shown that it is possible to interact with a PhC MC resonance using a nano-sized dielectric AFM tip. In contact mode, using a Si_3N_4 tip, we were able to map-out the standing-wave pattern in the MC. The maximum modulation depth found was 4 dB. Furthermore we showed that the AFM can also be operated in tapping mode to tune the transmitted power and thus the resonance wavelength (neglecting scattering). The major advantage for future integrated applications is that a tip wears off at a much lower rate when operated in tapping mode. This is particularly interesting when a silicon tip is employed.

References

[1] A. F. Koenderink, M. Kafesaki, B. C. Buchler, and V. Sandoghdar, "Controlling the resonance of a photonic crystal microcavity by a near-field probe", Physical Review Letters, vol. 95, pp. 153904-1-4, 2005.

[2] W. C. L. Hopman, K. O. Van Der Werf, A. J. F. Hollink, W. Bogaerts, V. Subramaniam, and R. M. De Ridder, "Nano-mechanical tuning and imaging of a photonic crystal micro-cavity resonance", Optics Express, vol. 14, pp. 8745-8752, 2006.

[3] S. Wonjoo, O. Solgaard, and S. Fan, "Displacement sensing using evanescent tunneling between guided resonances in photonic crystal slabs", Journal of Applied Physics, vol. 98, pp. 33102-1-4, 2005.

[4] G. N. Nielson, D. Seneviratne, F. Lopez-Royo, P. T. Rakich, Y. Avrahami, M. R. Watts, H. A. Haus, H. L. Tuller, and G. Barbastathis, "Integrated wavelength-selective optical MEMS switching using ring resonator filters", IEEE Photonics Technology Letters, vol. 17, pp. 1190-2, 2005.

[5] Y. Akahane, T. Asano, B. S. Song, and S. Noda, "High-Q photonic nanocavity in a two-dimensional photonic crystal", Nature, vol. 425, pp. 944-947, 2003.

[6] K. O. Van Der Werf, C. A. J. Putman, B. G. De Grooth, F. B. Segerink, E. H. Schipper, N. F. Van Hulst, and J. Greve, "Compact stand-alone atomic-force microscope", Review of Scientific Instruments, vol. 64, pp. 2892-2897, 1993.

[7] W. Bogaerts, R. Baets, P. Dumon, V. Wiaux, S. Beckx, D. Taillaert, B. Luyssaert, J. Van Campenhout, P. Bienstman, and D. Van Thourhout, "Nanophotonic waveguides in silicon-on-insulator fabricated with CMOS technology", Journal Of Lightwave Technology, vol. 23, pp. 401-412, 2005.

[8] W. C. L. Hopman, R. M. De Ridder, S. Selvaraja, C. G. Bostan, V. J. Gadgil, L. Kuipers, and A. Driessen, "Realization of 2-dimensional air-bridge silicon photonic crystals by focused ion beam, milling and nanopolishing," presented at Proceedings of SPIE - The International Society for Optical Engineering, Strasbourg, 2006.

Electrically Injected Thin-film InGaAsP Microdisk Lasers Integrated on a Si-wafer

J. Van Campenhout[1], P. Rojo-Romeo[2], D. Van Thourhout[1], C. Seassal[2], P. Regreny[2], L. Di Cioccio[3], J.M. Fedeli[3], and R. Baets[1]

[1] Ghent University-IMEC, Department of Information Technology- Sint-Pietersnieuwstraat 41, 9000 Gent, Belgium
[2] Laboratoire d'Electronique, Microelectronique et Micro-systèmes, Ecole Centrale de Lyon, 36 Avenue Guy de Collongue, 69134 Ecully cedex-France
[3] CEA-DRT/LETI, 17 Rue des Martyrs, 38054 Grenoble cedex 9-France.
e-mail: joris.vancampenhout@intec.ugent.be

We report on electrically pumped lasing in a microdisk cavity defined in an InGaAsP-based thin film bonded on top of a silicon wafer. The top metal contact is placed in the centre of the disk, whereas the bottom contacting is done by means of a thin lateral contacting layer. In order to avoid large optical absorption in p-type contact layers, a tunnel junction was used in combination with two n-type contacts. Lasing was observed in pulsed regime with a current threshold as low as 0.55mA, for microdisks with a diameter of 6μm.

Introduction

Microdisk lasers have attracted a lot of interest lately, mostly due to their potential role as very compact light sources with low power consumption in large scale photonic integrated circuits. Several authors have reported electrically injected lasing in microdisk structures supported by a pedestal, some with lasing thresholds well below 100µA [1]-[3]. Our work focuses on the integration of these III-V microdisk lasers on a Si platform. This approach not only facilitates integration with silicon electronics but also with silicon photonics. Indeed, because of the transparency of Si at the telecommunications wavelengths, and the fact that CMOS technology can be used in the fabrication of photonic components in Silicon-on-Insulator (SOI) [4], silicon has emerged as a promising platform for photonic functions. In our approach, integration of compact active optoelectronic components on a silicon platform is done by bonding a thin III-V film on top of it. Optically pumped lasing in microdisk lasers integrated on a Si-wafer and their optical coupling to an underlying SOI-waveguide has already been demonstrated [5]. In this paper we report on electrically pumped devices.

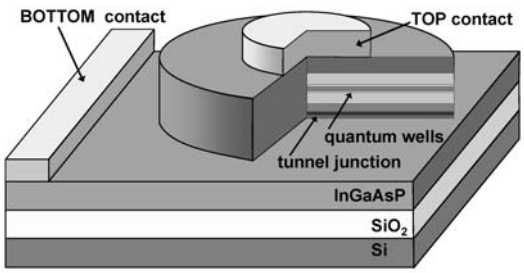

Figure 1. Microdisk laser design

Design aspects

An important design aspect of electrically injected, thin-film laser devices is the epilayer heterostructure composition: this should allow efficient carrier injection while preserving optical resonance quality (see figure 1). An important issue is how to contact

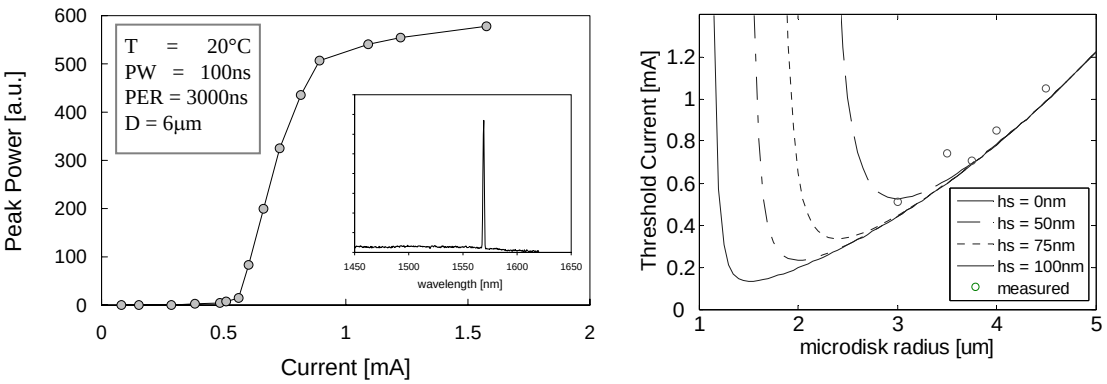

Figure 2. Left: light output vs. current for *D*=6μm, inset: lasing spectrum for I=0.75mA. Right: calculated threshold current versus disk diameter *D* and bottom contact slab thickness h_s. Circles denote measured values.

Table 1 Parameter values used in threshold current calculations

Parameter	Value	Parameter	Value	Parameter	Value
A	10^8 s^{-1}	G_0	1500 cm^{-1}	α_{int}	35cm^{-1}
B	2 10^{-10} cm^{-3} s^{-1}	n_0	1.5 $10^{18}cm^{-3}$	$\alpha_{scatter}$	5cm^{-1}
C	1.6 10^{-28} cm^{-6} s^{-1}	Γ	0.068		
η_i	0.7	d_{QW}	18nm		

the p-type layer of the pn-junction. In classic substrate lasers, this is done by means of a highly doped, low-bandgap semiconductor layer. However, these layers are very absorptive and thus not useable in a thin membrane. Therefore, we implemented a tunnel junction, in combination with a second n-type contact. This tunnel junction consists of a reverse-biased Q1.2 p++/n++-junction with layer thicknesses of only 20nm and doping levels above $10^{19}cm^{-3}$. This type of tunnel junction can have low absorption losses in combination with a low electrical resistivity [6]. We calculated an internal loss of 35/cm, mostly due to free carrier absorption in the tunnel junction. A second important aspect is the position of the metal contacts. They should be kept away form the optical field to avoid any excess absorption. In our design, the top contact is placed only in the centre of the microdisk, whereas the bottom contact is placed on a very thin n-type InP layer that extends laterally at the bottom of the microdisk. The bend losses of the microdisk resonator are highly dependent on this bottom contact layer thickness h_s. FDTD simulations show that for disk diameters *D* smaller than 6μm, h_s should be smaller than 100nm. For h_s = 50nm, disk diameters can be even as small as 4μm. The threshold current was calculated as function of these two design parameters, assuming logarithmic gain and (material) parameter values given in table 1. Results are shown in figure 2.

Fabrication and measurement Results

First, the laser heterostructure including three compressively strained InAsP quantum wells and the tunnel junction was grown by molecular beam epitaxy (MBE) on a 2 inch InP wafer. This wafer was bonded onto a Si wafer by molecular bonding (for more details, see [5]). After substrate removal, the microdisks were defined by optical lithography and were etched into the 420nm-thick bonded membrane by reactive ion

etching (RIE) using a Ti hard mask. The RIE etch was incomplete, leaving a thin bottom contact membrane of about 80nm. These structures were covered with a benzocyclobutene (BCB) film, in which contact windows were etched before depositing the top and bottom metal contact. Au-based contacts were deposited and fast-alloyed at 400°C.

Electrically injected lasing was observed for microdisks with diameters in the range 6-9μm. The P-I curve and lasing spectrum for a disk with diameter of 6μm is depicted in fig. 2 and reveals a threshold current as low as 0.55mA, and a lasing wavelength of 1570nm. For all diameters, the microdisks lase only in the radially fundamental whispering gallery modes, due to the presence of the top metal contact in the centre of the disk. For smaller top metal contacts, we also observed lasing for radially higher order modes. The current threshold as a function of diameter is also depicted in fig 2: for disk diameters smaller than 6μm, we failed to open the top contact window in the BCB-layer. However, calculated threshold current values indicate that we could reduce the threshold down to 0.25mA by reducing the diameter to 4μm. Lasing was only obtained in pulsed regime, due to the high electrical resistance of the device in combination with a poor heat sinking ability. Indeed, the voltage drop at threshold varies between 5-7V, mainly due to the non-optimal tunnel junction and non-optimal n-type metal contacts. A thermal analysis of the microdisk laser yields a thermal resistance of about 10^4 K/W for D = 6μm, what results in serious self heating. Future work includes coupling to a passive SOI-waveguide and improvement of the tunnel junction, metal contacts and etching quality.

Acknowledgements

The work of J. Van Campenhout was supported by the Research Foundation – Flanders (FWO-Vlaanderen). Part of this work was performed in the context of the EU-funded project PICMOS.

References

[1] T. Baba, M. Fujita, A. Sakai, M. Kihara, and R. Watanabe, “Lasing characteristics of GaInAsP-InP strained quantum-well microdisk injection lasers with diameter of 2-10μm,” Photon Tech Lett., vol. 9, no. 7, pp. 878–880, 1997.

[2] R. Ushigome, M. Fujita, A. Sakai, T. Baba, and Y. K. Kubun, “GaInAsP microdisk injection laser with benzocyclobutene polymer cladding and its athermal effect,” Jpn J Appl Phys, vol. 41, no. 11A, pp. 6364–6369, 2002.

[3] M. Fujita, R. Ushigome, and T. Baba, “Continuous wave lasing in GaInAsP microdisk injection laser with threshold current of 40 uA,” Electron Lett, vol. 36, no. 9, pp. 790–791, 2000.

[4] W. Bogaerts, R. Baets, P. Dumon, V. Wiaux, S. Beckx, D.Taillaert, B. Luyssaert, J. Van Campenhout, P. Bienstman and D. Van Thourhout, “Nanophotonic waveguides in silicon-on-insulator fabricated with CMOS technology”, Journ. of Lightwave Technology, Vol. 23(1), pp. 401 – 412, Jan 2005

[5] H. T. Hattori, C. Seassal, E. Touraille, P. Rojo-Romeo, X. Letartre, G. Hollinger, P. Viktorovitch, L. Di Cioccio, M. Zussy, L. El Melhaoui, and J. M. Fedeli, “Heterogeneous integration of microdisk lasers on silicon strip waveguides for optical interconnects,” Photon Tech Lett, vol. 18, no. 1-4, pp. 223–225, 2006.

[6] J. Boucart, C. Starck, F. Gaborit, A. Plais, N. Bouché, E. Derouin, J. C. Remy, J. Bonnet-Gamard, L. Goldstein, C. Fortin, D. Carpentier, P. Salet, F. Brillouet, and J. Jacquet, “Metamorphic DBR and Tunnel-Junction Injection: A CW RT Monolithic Long-Wavelength VCSEL”, Journ. Sel. Top. Quant. Elec., Vol. 5(3), pp. 520 – 529, May 1999

Size limitations of quantum dot microdisc lasers

J. Molina Vázquez, R.W. Smink, B.P. de Hon, A.G. Tijhuis, G.D. Khoe and H.J.S. Dorren

Eindhoven University of Technology, P.O. Box 513, 5600 MB, Eindhoven, The Netherlands
(Email: j.molina.vazquez@ieee.org)

We calculate the whispering gallery modes in a microdisc laser with an InGaAsP/InP quantum dot gain medium. We find that the combination of large quantum dot gain bandwidth and strong field confinement provides support for several lasing modes. The effect of the microdisc dimensions on the lasing modes' properties is explored. Finally, we investigate the necessary microdisc and quantum dot properties to optimise the trade-off between the reduction in the microdisc's dimensions, which is required for high integration density, and the lasing modes' properties.

Introduction

The increasing speed of fibre-optic-based telecommunications has focused attention on high-speed optical processing of digital information. Complex optical processing requires a high-density, high-speed, low-power optical memory. Recently, a fast, low-power optical memory element based on coupled micro-ring lasers occupying an area of 720 μm^2 was demonstrated [1].

Semiconductor microdisc lasers are of great interest because of their small cavity volume, high cavity quality factors for whispering gallery modes, cleavage-free cavities, excellent wavelength selectivity and ultralow threshold [2]. These characteristics can be enhanced by using quantum dots (QDs) in the semiconductor's gain medium since they offer fast response to external pumping [3], low threshold, high characteristic temperature and large gain bandwidth [4].

During the last decade, whispering gallery modes in microdisc lasers have been theoretically and experimentally investigated [2,3,5–7]. However, the theoretical models in [5–7] are simplified to a two-dimensional problem neglecting the wavevector dispersion in the axial direction. In addition, these models have not been used to explore the size limitations of microdisc lasers, which is crucial in determining their integration potential for large scale memory applications. Finally, to the best of our knowledge, there has been no theoretical investigation of microdisc lasers in the full three-dimensional space with a QD active region.

Model

We consider a disc with a dielectric-air boundary supported by a post with an active region consisting of ten QD layers as that depicted in Fig. 1. Lower order modes suffer from large losses due to their low confinement within the disc. Hence, we are only interested in high order modes where the light propagates along the edge of the disc, and therefore the coupling of the field into the supporting post can be neglected. Due to the symmetry of the problem, we use a cylindrical coordinate system. This imposes Bessel-type solutions for the field in the radial direction. We solve Maxwell's equations in three dimensions,

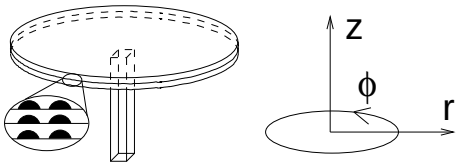

Fig. 1. Multiple layered quantum dot microdisk laser and coordinate system.

for transverse electric (TE) modes, using the method of Borgnis' potentials [8]. In the angular direction we assume clockwise and counter-clockwise propagating plane waves. In the axial direction the field consists of a cosine solution inside the disc and decaying exponential functions outside. Finally, in the radial direction the field is described by Bessel functions of complex order k_ϕ.

Note that the order of the Bessel is equal to the wavevector for the field propagating in the angular direction. Hence, in order to account for the losses due to the field radiating out of the disc, one must solve the field equations for complex k_ϕ. In the literature, one finds simplified solutions consisting of Bessel functions of integer order [5–7], which results in an over-estimation of the field confinement.

The computation of the Bessel functions is an essential element in our model. Since both the order and argument of the Bessel function can be complex, we perform the computation of the Bessel functions using their integral representations [9] with well chosen integration paths as described in [10].

To calculate the QD steady state gain and carrier-induced refractive index change, we compute the susceptibility of the gain medium taking into account the QD inhomogeneous broadening due to different alloy composition, the different QD confined levels, and their corresponding dipole matrix elements [11]. The electronic structure of the QDs is given by an anisotropic parabolic confinement potential as suggested by photoluminescence spectra [12]. The anisotropy in the confinement potential arises from the disc-shape of the dots giving stronger confinement in the growth direction. Finally, the polarization dephasing due to carrier-carrier interaction via Auger processes is calculated as in [13,14].

Results

Fig. 2 shows the calculated QD gain and carrier-induced refractive index dispersion for 10 layers with a QD density of 4×10^{10} cm^{-2} having 105 meV ($\sim$180 nm) energy level separation, which can be achieved using small size QDs. The gain and index can be scaled proportionally to the number of QD layers. The background index is 3.390, which corresponds to that of $In_{0.72}Ga_{0.28}As_{0.61}P_{0.39}$ [15]. A carrier density of 10^{12} cm^{-2} provides gain in both the ground and excited states. Also shown, are different lasing modes that can co-exist due to the broad gain bandwidth. Other modes are also obtained but their low field confinement within the disc and small spectral overlap with the QD gain forbids them from lasing. Due to the small carrier-induced refractive index from the QDs, the microdisc mode profiles are predominantly determined by the microdisc's material index and dimensions. Hence, one can modify the QD properties to provide the largest gain at the mode wavelength of interest. For example, one could engineer QDs with a gain spectrum that matches the 8th and 10th modes shown in Fig. 2, which are close to the

telecommunications wavelengths of 1.30 μm and 1.55 μm.

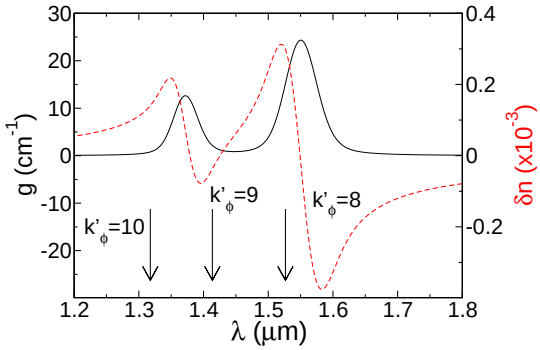

Fig. 2. Quantum dot gain (solid) and carrier-induced refractive index (dashed) spectra. Also shown are the lasing modes for the 1 μm radius and 200 nm height disc.

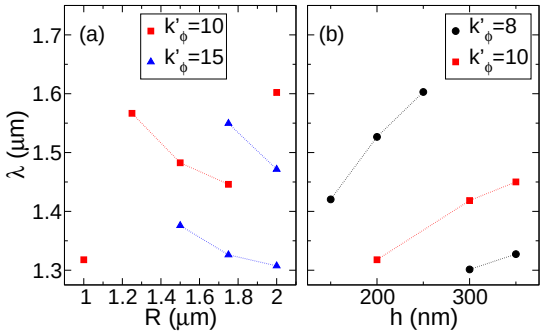

Fig. 3. Mode wavelength dependence on (a) disc radius, and (b) disc height, for the 8th (circles), 10th (squares) and 15th (triangles) modes. The lines give an aid to the reader.

The radius of the disc is varied from 0.50 μm to 2.00 μm for a fixed disc height of 200 nm, and the height is varied from 50 nm to 350 nm, for a fixed radius of 1 μm. Fig. 3 shows the mode wavelength dependence on the disc radius and height for modes within the wavelength range of 1.30 μm to 1.70 μm. It is clear how the mode wavelength decreases with increasing radius and increases with increasing height. We found that for disc radii below 1 μm or disc heights smaller than 200 nm there are no lasing modes. This is because only low order modes, whose field confinement inside the disc is low and correspondingly have large loss, can exist in the microdisc within the chosen wavelength range. Note that the modes in Fig. 3 will not always correspond to a lasing mode since this will depend on the QD gain at a particular wavelength. However, as mentioned earlier, one can tune the QD properties to provide better overlap between the gain spectrum and the mode of interest. From these results, one can calculate that the smallest memory element based on coupled QD microdisc lasers will have an area of $\sim$6.28 μm^2 and a thickness of 150 nm for the given material.

Finally, Fig. 4 shows the mode profiles for the 7th, 11th and 15th modes in the disc with 1.50 μm radius and 200 nm height. One can see the formation of whispering gallery modes for the higher order modes [Figs. 4(a) and 4(b)], with very low losses due to the strong field confinement.

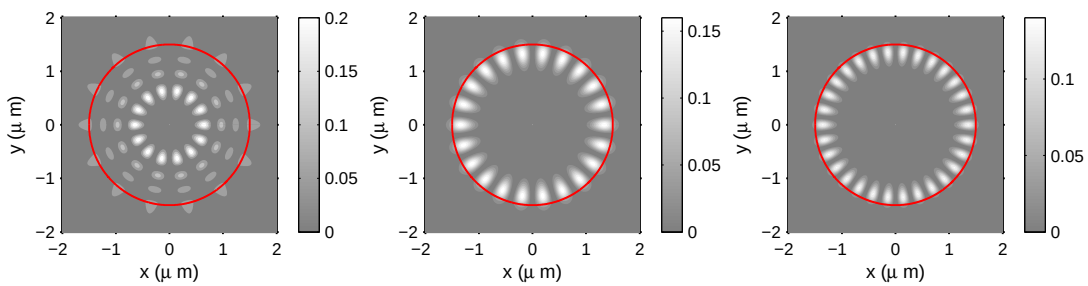

Fig. 4. Quantum dot microdisc laser (solid ring) modes with $k'_\phi = 7$ (left), $k'_\phi = 11$ (centre), and $k'_\phi = 15$ (right) for a disc with 1.50 μm radius and 200 nm height.

Conclusions

The lasing modes in quantum dot microdisc lasers have been numerically calculated and the dependence of the mode wavelength on the disc radius and height explored. We found that the smallest memory element based on coupled quantum dot microdisc lasers will require an area larger than $\sim 6.28 \mu m^2$ and a thickness greater than 150 nm for the material studied. This shows that quantum dots microdisc lasers are promising candidates for high density, large scale optical memories.

References

[1] M.T. Hill, *et al.*, *Nature*, vol. **432**, pp. 206–209, 2004.

[2] M. Fujita, *et al.*, *Electron. Lett.*, vol. **36**, pp. 790–791, 2000.

[3] K. J. Luo, *et al.*, *Appl. Phys. Lett.*, vol. **78**, pp. 3397–3399, 2001.

[4] D. Bimberg, *et al.*, *IEEE J. Select. Topics Quantum Electron.*, vol. **3**, pp. 196–205, 1997.

[5] N. C. Frateschi and A. F. J. Levi, *J. Appl. Phys.*, vol. **80**, pp. 644–652, 1996.

[6] M. Fujita, *et al.*, *IEEE J. Select. Topics Quantum Electron.*, vol. **5**, pp. 673–681, 1999.

[7] E. I. Smotrova and A. I. Nosich, *Opt. Quantum Electron.*, vol. **36**, pp. 213–221, 2004.

[8] K. Zhang and D. Li, *Electromagnetic theory for microwaves and optoelectronics*, Springer, Berlin, 1998.

[9] N. M. Temme, *Special Functions: an Introduction to the Classical Functions of Mathematical Physics*, Wiley-Interscience, Chichester, 1996.

[10] R. W. Smink, *et al.*, *Proc. Int. Conf. Electromag. in Advanced Applications & European Electromag. Struct. Conf.*, ISBN 88-8202-094-0, pp. 931–934, 2005.

[11] J. Molina Vázquez, *et al.*, *Optical and Quantum Electronics*, vol. **36**, pp. 539–549, 2004.

[12] G. Park, *et al.*, *Appl. Phys. Lett.*, vol. **73**, pp. 3351–3353, 1998.

[13] H. H. Nilsson, *et al.*, *Phys. Rev. B*, vol. **72**, pp. 205331, 2005.

[14] J. Molina Vázquez, *et al.*, *IEEE J. Quantum Electron.*, vol. **42**, pp. 986–993, 2006.

[15] F. Fiedler and A. Schlachetzki, *Solid State Electron.*, vol. **30**, pp. 73–83, 1987.

Efficient coupling structures for integration of pillar photonic crystals with ridge waveguides

A.A.M. Kok, R. Meneghelli, J.J.G.M. van der Tol and M.K. Smit

COBRA, Eindhoven University of Technology, Den Dolech 2,
P.O. Box 513, 5600 MB, Eindhoven, The Netherlands

We present 2D FDTD simulations of the coupling from a conventional optical waveguide to a photonic crystal waveguide and vice versa. Firstly, the optimum radius of the waveguide rods is determined for pillar photonic crystals surrounded by air and with a polymer layer stack. Secondly, the transmission of the waveguides with the coupling structures is simulated. The bandwidth obtained at 95% transmission is $\simeq 20$nm for the pillars in air, increasing to $\simeq 50$nm if the polymer layer stack is implemented.

Introduction

Photonic crystals show a huge potential for decreasing the dimensions of planar photonic integrated circuits. However, photonic crystal-based components can only be successfully integrated with conventional optical integrated circuits if the losses are comparable or lower than those of existing components.

We aim for the integration of pillar photonic crystals in photonic integrated circuits based on InP/InGaAsP technology, operating around $\lambda = 1.55$ µm. A square lattice of high-index rods in a low-index medium gives rise to a large band gap for TM polarization. In order to reduce the losses of pillar photonic crystals in air, we implement a polymer layer stack between the rods. The core layer is a polyimide with a high refractive index, which is sandwiched between two polymer layers of low refractive index [1]. In this way we create optical guiding in between the semiconductor pillars, reducing the out-of-plane diffraction, and thus the propagation losses of the structure.

Furthermore, the losses can be significantly reduced by optimizing the coupling from the ridge waveguide to the photonic crystal waveguide and vice versa [2]. In this paper we present two-dimensional FDTD calculations of a simple butt coupler.

Photonic crystal waveguides

The conventional photonic integrated circuit imposes restrictions on the material system that is used for the photonic crystals. The substrate consists of InP with a refractive index of $n_{\mathrm{InP}} = 3.196$ and the guiding layer is InGaAsP, with an index of $n_{\mathrm{InGaAsP}} = 3.435$. The guiding layer is 500 nm thick, and it has an InP top cladding of 1 µm. The polymer layer stack that is implemented to create optical guiding between the pillars, consists of poly(hexafluoroisopropyl)methacrylate (PHFIPMA), with an index of $n_{\mathrm{PHFIPMA}} = 1.38$ and the polyimide PI2737, with an index of $n_{\mathrm{PI2737}} = 1.64$.

Full 3D simulations are necessary when designing photonic crystal-based devices, but these require substantial computational power. To get an indication of the influence of the different parameters, the first optimization is done in 2D. To account for the third dimension, the effective index method is applied. The effective index of the fundamental TM mode of the III-V layer stack is $n_{\mathrm{eff,III\text{-}V}} = 3.332$ and that of the polymer layer stack

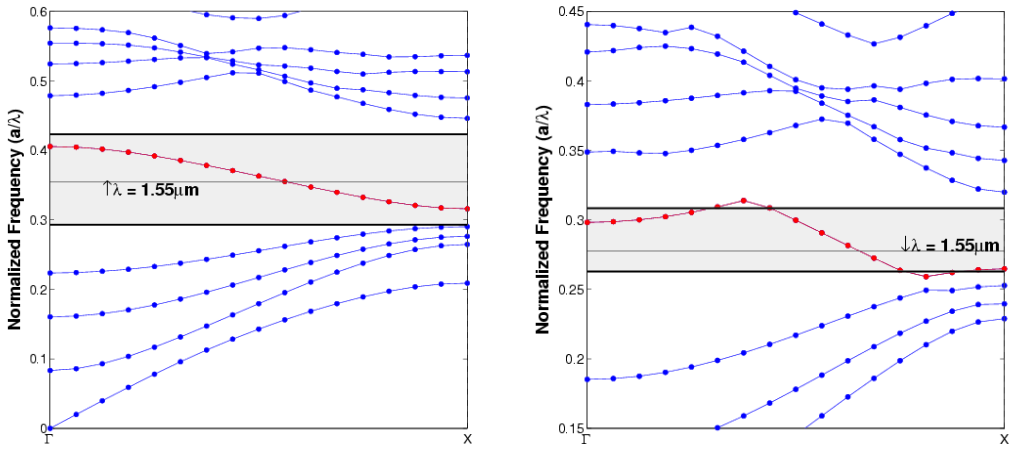

(a) Pillars in air

(b) Pillars in polymer

Figure 1: Band diagrams for photonic crystal waveguides; (a) for pillars in air, and (b) for pillars embedded in a polymer layer stack.

is $n_{\text{eff,polymer}} = 1.49$.
The largest possible band gap is obtained for $r/a = 0.20$ in the case of pillars in air, where r represents the pillar radius and a the lattice constant. The ratio increases to $r/a = 0.22$ if the polymer layer stack is implemented. From the center frequency of the band gap, and keeping in mind that the operating wavelength is 1.55 μm, the optimal lattice constant and the corresponding pillar radius are derived. For the lattice of pillars in air, this results in $a = 550$ nm and $r = 110$ nm, whereas in the case of pillars in polymers we derived $a = 430$ nm and $r = 95$ nm. The smaller dimensions of the latter crystal are due to the increase of the average refractive index, causing a decrease in the effective wavelength inside the structure.
Introducing a line defect in the photonic crystal, by changing the radius of a row of pillars, creates a guided mode inside the band gap. To choose the defect radius, we compared the calculated band diagrams in ΓX direction of varying defect radii. Fig. 1(a) shows the band diagram of the photonic crystal waveguide of pillars in air, with a defect radius of 175 nm. Fig. 1(b) show the analogue graph for pillars in a polymer stack, where the optimal defect radius is 170 nm. The optimal radii are chosen to have a steep but uniform slope around the wavelength of interest, which is indicated in the graphs as well. Note that in the case of pillars in polymers the guided mode of the line defect also exists outside 2D band gap.

Coupling structure

The simplest structure to couple light from a ridge waveguide into a photonic crystal waveguide, is to place the two types of guiding structures directly in front of each other. This configuration is depicted in Fig. 2. The input ridge waveguide is tapered down to the diameter of the line defect pillars and the output ridge waveguide can be tapered again to the width that is required in the photonic integrated circuit.
The transmission of this structure is calculated using the 2D FDTD method of CrystalWave, a commercially available software package. To calculate the transmission, we

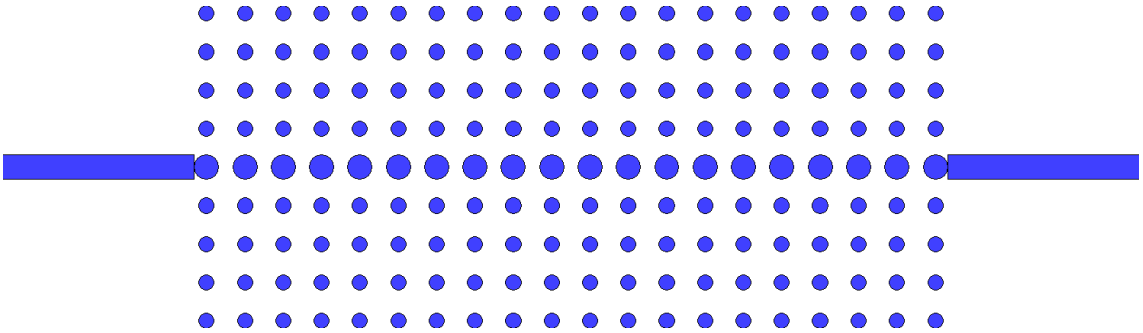

Figure 2: Top view of the coupling structure.

excite the fundamental mode of the input waveguide. By placing sensors in the ridge waveguides, we can extract the optical input and output powers. The transmission is given by dividing the optical power in the fundamental mode (propagating in forward direction) at the output waveguide sensor by that at the input waveguide sensor. The length of the photonic crystal waveguide is 20 periods, and the length of the input and output ridge waveguides corresponds to 5 times the lattice constant.

To optimize the transmission of the structures, the distance between the end facets of the ridge waveguides and the photonic crystal waveguide can be varied. Fig. 3(a) shows the transmission of the structure with pillars in air. In the graph, one curve shows the case where the ridge waveguide touches the first defect pillar. The second curve represents the optimal situation, with a distance of 100 nm between the ridge waveguide and the photonic crystal waveguide. For zero distance, the light couples directly to the first pillar of the photonic crystal waveguide. However, if we apply a gap between the two waveguide types, a cavity is created, making the coupling more wavelength-dependent. This effect is clearly visible in the transmission graph. The fact that the transmission exceeds 1 is due to the simulation method; the excitation is not exactly at the same location as the input sensor, so the output sensor might capture light that is not passing through the input sensor, e.g. because some light is reflected from the edges, back to the output sensor. It can be concluded that the distance between the ridge waveguides and the photonic crystal waveguide is an important parameter in the optimization of the coupling structure. The bandwidth at 95% transmission is in the order of 20 nm for a distance of 100 nm. Although we obtain a high transmission, the losses will increase when taking into account the third dimension.

The transmission of the photonic crystal waveguide of pillars embedded in a polymer layer stack is optimized following the same procedure. The transmission of that structure is shown in Fig. 3(b). Introducing the polymer layer stack increases both transmission and bandwidth considerably. The shifting of the modulation peaks when changing the distance between both types of waveguides in the coupler, indicates that they are due to Fabry-Pérot resonances. For the pillars in air, the guided mode extends outside the band gap, and this enables transmission outside the band gap. The bandwidth at 95% transmission is in the order of 55 nm for an optimized distance between the two types of waveguide of 45 nm.

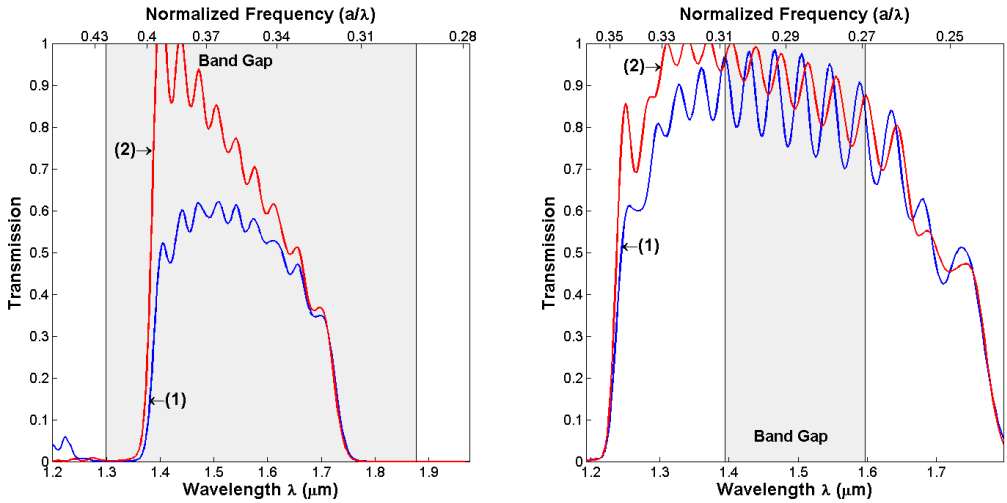

(a) Pillars in air

(b) Pillars in polymer

Figure 3: Transmission for the butt coupler; (a) for pillars in air, and (b) for pillars embedded in a polymer layer stack. Curve (1) shows the transmission of the butt coupler with zero distance between ridge waveguide and photonic crystal waveguide, whereas curve (2) shows the result for optimized distance, being 100 nm for pillars in air and 45 nm for pillars in polymers.

Conclusions

We have determined the optimal geometrical parameters for a photonic crystal waveguide based on InP/InGaAsP pillars. To reduce the waveguide losses, a polymer layer stack is implemented. The transmission of a coupling structure from a conventional ridge waveguide to a photonic crystal waveguide and vice versa is optimized, based on 2D simulations. A high transmission is obtained, over a bandwidth that is sufficiently large for the application in photonic integrated circuits. Implementation of the polymer layer stack increases both transmission and bandwidth considerably.
Full 3D simulations are in preparation to complete the design of the photonic crystal waveguides. We are planning to fabricate the couplers and to compare transmission measurements to the simulation results.

Acknowledgement

This research is supported by NanoImpuls, a nanotechnology program of the Dutch Ministry of Economic Affairs. The authors would like to thank Dr. R.W. van der Heijden for his support.

References

[1] A.A.M. Kok, E.J. Geluk, M.J.H. Sander-Jochem, J.J.G.M. van der Tol, Y.S. Oei and M.K. Smit, "Two-dimensional photonic crystals based on InP rods", *Proc. IEEE/LEOS Symposium (Benelux Chapter)*, 2005, pp. 273–276.

[2] P. Bienstman, S. Assefa, S.G. Johnson, J.D. Joannopoulos, G.S. Petrich and L.A. Kolodziejski, "Taper structures for coupling into photonic crystal slab waveguides", *J. Opt. Soc. Am. B*, vol. 20(9), 2003.

Integrated Waveguide Device for Picosecond Pulse Amplification and Spectral Shaping

M.J.R. Heck, E.A.J.M. Bente, Y. Barbarin, A. Fryda, H.D. Jung, Y.S. Oei, R. Nötzel, D. Lenstra and M.K. Smit

COBRA Research Institute, Technische Universiteit Eindhoven,
Postbus 513, 5600 MB Eindhoven, The Netherlands

We report on the simulation, design and characterization of a new device, named IRIS. It is designed for increasing the optical bandwidth of picosecond pulses to enable further pulse compression or shaping. The IRIS device consists of a concatenated array of semiconductor optical amplifiers and saturable absorbers. It is realized in the InP/InGaAsP material system for the 1550nm range.

Simulations and measurements on the realized IRIS devices show increased spectral broadening as compared to an SOA of equivalent length. Moreover simulations show that pulse peak amplification is over two times higher and ASE output levels are lower by about two orders of magnitude, making it a promising short pulse amplifier.

Introduction

Pulsed lasers with a coherent broad optical spectrum are attractive sources for use in arbitrary waveform generators [1], dense wavelength division multiplexing systems, optical code-division multiple-access (O-CDMA) systems [2] and frequency comb generation. Such systems can be realized on a single photonic integrated circuit when semiconductor mode-locked lasers (MLLs) are used as the pulsed source. Nowadays monolithic MLLs are able to produce pulses with durations down to 1-2ps, having a corresponding spectral width of up to 2nm [3]. By changing the design or operating conditions the spectrum can be broadened, leading to non-transform limited pulses [4,5].

To increase the optical bandwidth of picosecond pulses further, amplification and highly non-linear fibers are often used. In a photonic integrated circuit a semiconductor optical amplifier (SOA) is a possible option, though at the expense of increasing the noise in a system and the broadening that can be achieved is limited.

In this paper we present our IRIS device [6] which we have designed to add bandwidth to an optical picosecond pulse, for applications as mentioned above. We compare the performance of a number of configurations of the IRIS device with an SOA of the same length, both theoretically and experimentally.

IRIS device

The IRIS device consists of a series of equal pairs of one SOA section and one saturable absorber (SA) section, as schematically depicted in Fig. 1(a). Such devices have been realized using InP/InGaAsP bulk gain material, operating at wavelengths in the region of 1.55μm. The sequence of SOAs and SAs is fabricated by etching a shallow ridge waveguide of 2μm width in the bulk gain material. To suppress lasing, the waveguide is oriented at the Brewster angle for the fundamental mode with the facets which have also been antireflection coated. To create electrical isolation between the SOAs and SAs, the most highly doped part of the p-cladding layers is etched away using a dry RIE etch

process. The isolation section between the SOA and SA has a length of 10µm (shorter SAs) to 20µm (longer SAs). Two gold metal pads alternately contact the waveguide sections to create two common contacts for the SOAs and SAs respectively (as can be seen in the photograph in Fig. 1(b)). Amplification and absorption are realized by a forward or reverse electrical bias of the diode respectively. We have designed and realized a number of different device configurations with a varying length ratio between the SOA and SA (up to 50%) and number of SOA/SA pairs (5, 10 or 20). We have added SOAs on the same chip for reference purposes. The fabrication technology of the IRIS device is fully compatible with the technology to fabricate MLLs as presented in [4]. This allows for further integration of the MLLs with the IRIS device.

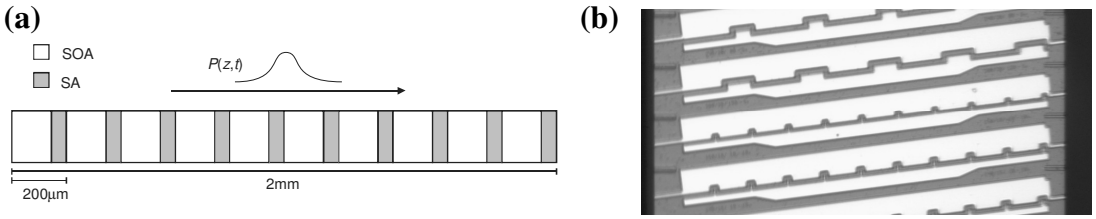

Fig. 1: (a) Schematic overview of the IRIS configuration used in the simulations. An input pulse (denoted by $P(z,t)$) enters from the left side, entering an SOA and exiting from the right-hand side. The ratio of the SOA and SA length within the 200µm section is varied. (b) Photograph of the realized devices, showing different configurations.

Simulation results

We have simulated the IRIS configuration as pictured in Fig. 1(a). In the simulations the ratio between the SOA and SA lengths is varied, but the number of SOA/SA pairs is fixed at ten. Isolation sections in between the SOA and SA are not taken into account. Input pulses have a duration of 2ps and a peak power of 0.1W, which are representative values for pulses generated by semiconductor MLLs. The pulse repetition rate studied here is 'long' as compared to the carrier recovery time (i.e. propagation of a single pulse is simulated).

To simulate picosecond pulse propagation through the device we use the model we have presented in [5], extended with ASE fields. The model is made bidirectional, to simulate ASE and laser fields propagating in both directions, and assumes zero reflection at the facets.

After propagation of the pulses through the IRIS device, the simulated spectra of the output show an increase in bandwidth compared to the simulation result of an equally long SOA. This is presented in Fig. 2(a). In Fig 2(b) the detailed evolution of the spectrum as a function of total SOA current is presented for the device that produces the highest bandwidth (140µm/60µm configuration) in Fig. 2(a). The increase in spectral broadening for this device is over five times, i.e. 17nm as compared to a maximum of 3nm for an SOA. The main reason for this increase in broadening is that under these operating conditions the temporal broadening of the pulse in the IRIS device is minimized, much like the situation in a passively mode-locked laser. Because of this the change in the carrier depletion takes place in the shortest time. As a result the self-phase modulation is maximized [5]. A second important result is that the ASE level in the output is reduced by about two orders of magnitude as compared to the output from an SOA (Fig. 2(c)). The gain depletion due to the ASE is therefore also significantly

reduced. These features make the IRIS device a promising candidate for a short pulse optical amplifier.

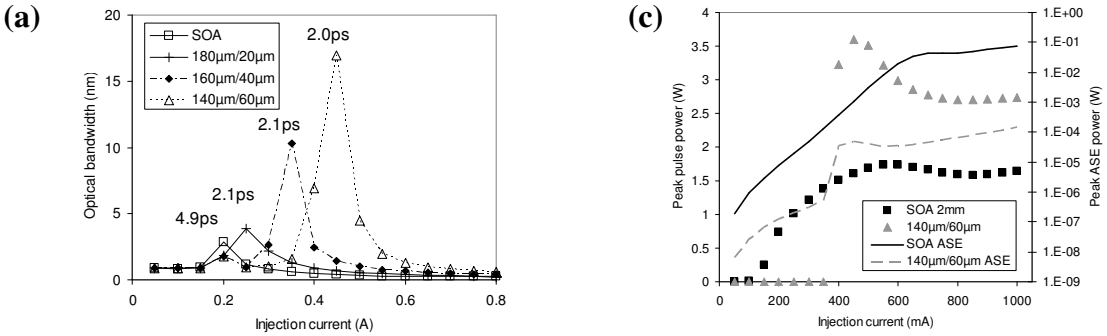

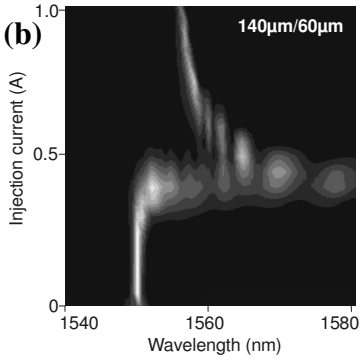

Fig. 2: Simulation results for IRIS devices where input pulses have a duration of 2ps and a peak power of 0.1W. The input pulses are transform limited. (a) Calculated spectral broadening (FWHM) of three configurations (10 pairs of SOA/SA with respective lengths as mentioned in the inset) compared to an SOA of 2mm length. (b) A picture of the development of the shape of the spectrum of the 140µm/60µm configuration as a function of the injection current. The spectral intensity in (b) is normalized and coded from black up to white. In (a) corresponding output pulse durations at maximum broadening are shown. (c) The calculated peak pulse transmission of the 140µm/60µm configuration compared to that of an SOA and their respective maximum ASE levels.

Experimental results

Spectra of short pulses that have propagated through one of several designs of IRIS devices have been measured. Most results were obtained with the devices with 20 pairs of SOA/SA sections, so this set is presented here. The TE polarized input pulses have a peak power of approximately 0.08W, a duration of 2.5ps and a repetition rate of 10GHz. The experimental results are presented in Fig. 3(a) and agree qualitatively with the simulated results in two aspects. First the total SOA current values at which the increase in spectral broadening of the device output starts to occur, increases with longer SA lengths. Secondly, the spectra obtained with the IRIS devices show increased maximum broadening for the shorter SA lengths (60µm/10µm and 55µm/15µm configuration, Fig. 3(a)) when compared to an SOA, namely 4nm and 3nm respectively. As our devices are not packaged, the injection current is pulsed to avoid excessive heating of the device. Additional spectral broadening is expected for the devices with longer SAs at higher injection currents (above 660mA, which was the limit of our setup), as predicted by the simulations. The experimental results in Fig. 3 do not show the spectral narrowing at higher injection currents, as predicted by the simulations results presented in Fig. 2(a,b). Experimentally we observed the dependency of the spectrum on the reverse bias voltage on the SA sections. In the simulations this voltage dependency is not taken into account explicitly [5]. Increasing the voltage on the SA decreases the modulation depth in the spectra (Fig. 3(b)). This feature makes the spectrum more suitable for applications as mentioned above. The equalization of the spectrum needs less intensity modulation, either by absorption or by amplification of the separate spectral components.

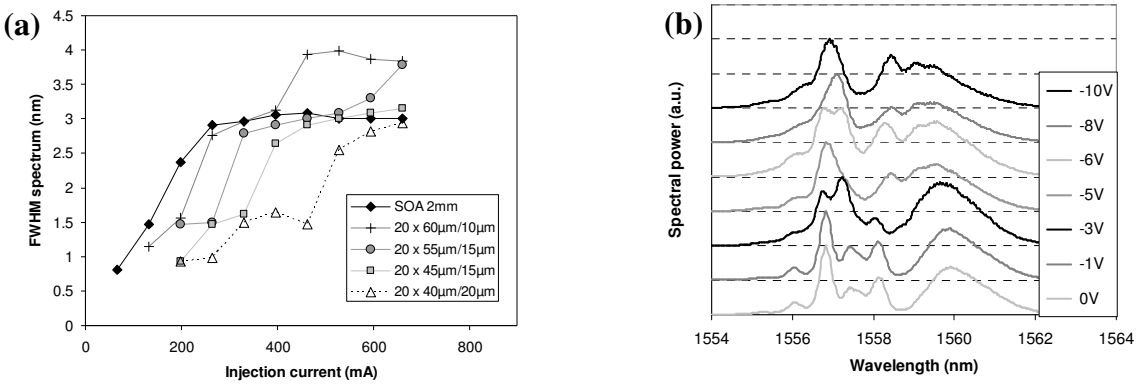

Fig. 3: (a) Measured spectral widths (FWHM) for different IRIS configurations with 20 SOA/SA pairs. The applied reverse bias on the SAs is -1V. The injection current is supplied by a pulsed source, using 300ns pulses and 1% duty cycle. (b) Normalized output pulse spectra after propagation through a configuration with short SAs (20x 60µm/10µm), applying different reverse bias voltages.

Conclusion

We have theoretically and experimentally investigated a new device concept, called IRIS, which we have designed for adding bandwidth to a short pulse. The fabrication and processing technology can be compatible with that of a MLL, which enables monolithic integration of a MLL with an IRIS device.

Simulations show that the device performance with respect to adding bandwidth to picosecond pulses is better than that of an SOA of equivalent length, with calculated bandwidths of up to five times as large (17nm as compared to 3nm). Measurements on realized devices agree qualitatively with our simulations, showing increased performance (4nm compared to 3nm), but the measured range of injection currents is limited by the current source.

Furthermore the simulations show that in the process of amplification a picosecond pulse can be compressed inside the IRIS device, whereas these pulses broaden inside an SOA. Moreover ASE noise levels are suppressed about two orders of magnitude, making the IRIS device a promising short pulse amplifier.

This research is supported by the Towards Freeband Communication Impulse of the technology program of the Dutch Ministry of Economic Affairs and by the Dutch NRC-Photonics program.

References

[1] K. Takiguchi, K. Okamoto, T. Kominato, H. Takahashi and T. Shibata, “Flexible pulse waveform generation using silica-waveguide-based spectrum synthesis circuit,” Electron. Lett., vol. 40, no. 9, pp. 537-538, 2004

[2] C. Ji, R.G. Broeke, Y.Du, J. Cao, N. Chubun, P. Bjeletich, F. Olsson, S. Lourdudoss, R. Welty, C. Reinhardt, P.L. Stephan and S.J.B. Yoo, “Monolithically integrated InP-based photonic chip development for O-CDMA systems,” IEEE J. Select. Topics Quantum Electron., vol. 11, no. 1, pp. 66-77, Jan./Feb. 2005

[3] R. Kaiser, B. Hüttl, H. Heidrich, S. Fidorra, W. Rehbein, H. Stolpe, R. Stenzel, W. Ebert, and G. Sahin, “Tunable monolithic mode-locked lasers on InP with low timing jitter,” IEEE Photon. Technol. Lett., vol. 15, no. 5, pp. 634–636, May 2003.

[4] Y. Barbarin, E.A.J.M. Bente, M.J.R. Heck, Y.S. Oei, R. Nötzel and M.K. Smit, “Characterization of a 15 GHz integrated bulk InGaAsP passively modelocked ring laser at 1.53µm,” accepted for publication in Optics Express

[5] M.J.R. Heck, E.A.J.M. Bente, Y. Barbarin, D. Lenstra and M.K. Smit, “Simulation and design of integrated femtosecond passively mode-locked semiconductor ring lasers including integrated passive pulse shaping components,” IEEE J. Quantum Electron., vol. 12, no. 2, Mar.-Apr. 2006.

[6] M.J.R. Heck and E.A.J.M. Bente, NL patent application

Ring resonator-based single-chip 1x8 optical beam forming network in LPCVD waveguide technology

L. Zhuang[1], C. G. H. Roeloffzen[1], R. G. Heideman[2], A. Borreman[2],
A. Meijerink[1], W. van Etten[1]

[1]University of Twente, Faculty of Electrical Engineering, Mathematics and Computer Science, Telecommunication Engineering group, P.O. Box 217, 7500 AE, Enschede, The Netherlands

[2]LioniX B.V., P.O. Box 456, 7500 AH, Enschede, The Netherlands

Optical ring resonators (ORRs) are good candidates to provide continuously tunable delay in optical beam forming networks (OBFNs) for phased array antenna systems. Delay and splitting/combining elements can be integrated on a single optical chip to form an OBFN. A state-of-the-art 1×8 OBFN chip has been fabricated in LPCVD waveguide technology. It is designed with 1 input and 8 outputs, between which a binary-tree topology is used. A different number of ORRs (up to 7) are cascaded for each output. In this paper, the principle of operation is explained and demonstrated by presenting measurements on the 1×8 OBFN chip.

1 Introduction

Beam forming for broadband RF signals can be achieved by means of a phased-array antenna working with an optical beam forming network (OBFN). This OBFN consists of optical splitting/combining circuitry and delay elements, which need to be continuously tunable in order to achieve continuous beam angle control. Moreover, in order to support relatively broadband RF signals, the delay elements should have a flat magnitude response and a linear phase response in the corresponding frequency range. To meet these requirements, optical ring resonators (ORRs) appear to be good candidates due to their continuous tunability, and well-known advantages of integrated optics [1]-[5]. This paper demonstrates the advantages of optical beam forming using integrated ORRs, by explaining its operating principles, and by presenting some measurement results on an actual ORR-based 1×8 OBFN chip. The chip is realized in LPCVD planar optical waveguide technology [6].

2 Principles of Ring resonator-based optical beam forming networks

A. Optical ring resonator (ORR) delay elements

A single ring resonator has a periodic bell-shaped group delay response. The peak delay value and its position are determined by the coupling coefficient κ and the additional round-trip phase shift ϕ of the ring, respectively. An ORR delay element shows an inherent trade-off between peak delay and bandwidth. The bandwidth of the delay element can be increased, however, by cascading multiple ORR sections, as illustrated in the inset of Fig. 1. Since the group delay responses of the individual sections simply add up, the total delay response can be flattened by properly tuning the ORRs, as illustrated in Fig. 1. The bandwidth of the delay element can be extended by adding more sections, and the peak-peak ripple of the group delay response in the flattened frequency band can be decreased by decreasing the difference between the resonance frequencies of the rings

[1],[3]–[5]. Measurements on a 3-ring optical delay device realized in LPCVD waveguide technology have been presented in [5], showing good agreement with theory.

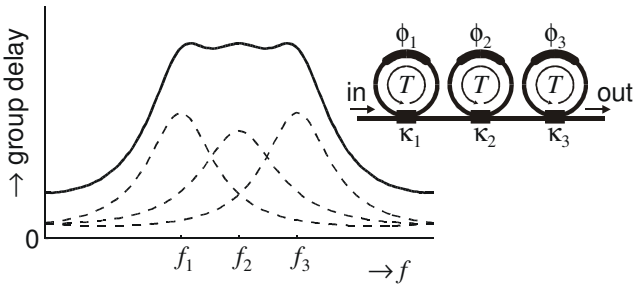

Fig. 1. *Theoretical group delay response of three cascaded ORR sections. The dashed lines represent the group delay responses of the individual sections. Inset: cascade of three ORRs with round-trip delay T, additional round-trip phase-shifts ϕ_i and power coupling coefficients κ_i.*

B. Optical beam forming network (OBFN)

When the optical delay elements are integrated together with signal processing circuitry, an OBFN is obtained. In order to reduce the number of tuning elements, a binary tree OBFN topology is considered instead of the straightforward parallel OBFN. An ORR-based 1x8 OBFN has been proposed, consisting of 3 stages with in total 12 ORRs and 7 tunable splitters, as shown in Fig. 2.

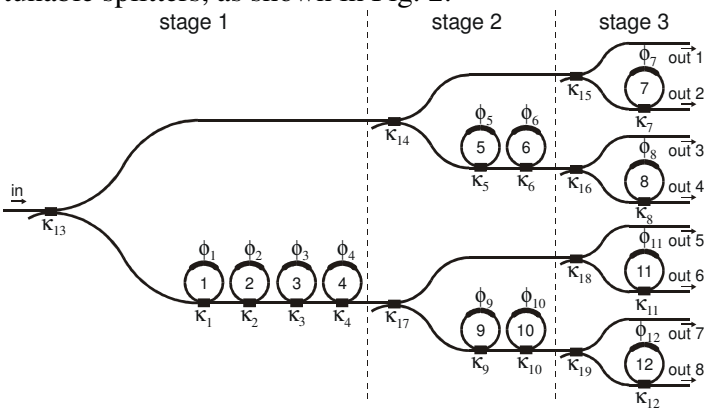

Fig. 2. *Binary tree-based 1×8 optical beam forming network for a phased-array transmitter system, consisting of 12 ORRs and 7 tunable splitters.*

3 Device design and realization

The complete beam forming operation can be integrated into one optical chip [7]. The actual design of the 1×8 OBFN has been divided in the design of elementary basic building blocks: bent waveguides, Mach-Zehnder interferometers (MZIs) for the tunable coupling and splitting function, and the tapered waveguide end-faces. Next, the most promising building blocks have been selected and fabricated using the TripleX^{TM} technology [6]. The actuation of the couplers, splitters and phase shifters is done thermo-optically, allowing tuning of the resonance frequency of the ORR, tuning of the delay, and tuning of the splitting ratio, within 1 ms. Fig. 3 shows a photograph of a realized 1×8 OBFN chip. The chip length is 4.85 cm and the chip width is 0.95 cm.

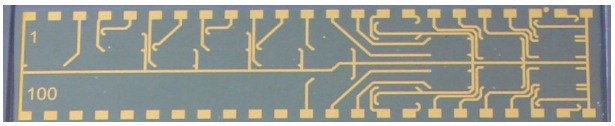

Fig. 3. *Photograph of the 1×8 OBFN chip. The bondpads and electrodes are clearly visible.*

A single 1×8 OBFN as depicted in Fig. 2 requires 31 heaters (two tuning elements for each ORR and one for each splitter) and therefore at least 31 electrodes and one ground electrode to drive the heater elements.

4 Measurements

The optical group delay responses at each output of the 1×8 OBFN chip have been measured by means of the phase-shift method, using the setup that is shown in Fig. 4.

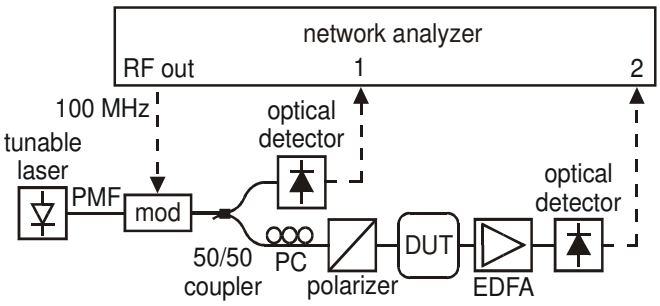

Fig. 4. *Group delay measurement setup. DUT: Device under test, EDFA: erbium-doped fiber amplifier, mod: external Mach-Zehnder intensity modulator, PC: polarization controller, PMF: polarization-maintaining fiber.*

The Agilent PNA network analyzer generates an electrical 100 MHz RF signal, which modulates the monochromatic light from the Santec tunable by means of an external $LiNbO_3$ Mach-Zehnder-based intensity modulator. The modulated optical signal is splitted by means of a fiber splitter. One part is detected and directly led back to the network analyzer. The other part is re-polarized and coupled into the device under test (DUT), such that the 1×8 OBFN is investigated for TE-polarized light. The eight output powers are subsequently measured by moving the fiber to the desired output ports. An erbium-doped fiber amplifier is used to boost the optical power, which is measured by means of a second detector and led to the network analyzer. The network analyzer measures the RF phases $\varphi_1(\lambda)$ and $\varphi_2(\lambda)$ of the output signals of the optical detectors for different laser wavelengths λ. The group delay response is estimated from these results by calculating

$$\tau_g(\lambda) = \frac{\varphi_1(\lambda) - \varphi_2(\lambda)}{2\pi f_{RF}}, \tag{1}$$

where f_{RF} is the frequency of the electrical signal (100 MHz in our case). Note that this is a relative group delay response: it is biased by an eventual path length difference between the two paths from the 50/50 coupler to the inputs of the network analyzer. The average powers at the outputs of the OBFN chip were measured using an HP 81532A Power Meter (not shown in Fig. 4). With this setup the group delay responses at each output of the OBFN chip have been measured over one FSR of 14 GHz, which corresponds to a ring circumference of 1.2 cm and a group index of 1.8. Measurements have been carried out with different settings for the heating elements. The measurement results prove that the waveguide loss is « 1 dB/cm. Fig. 5 shows the measured group delay responses at the outputs 2 to 8 of the OBFN, which demonstrate the delay generation of one single ring up to 7 cascaded rings. As a 1×8 OBFN, each output is required to give a different delay value over a common frequency band, in order to satisfy the condition of beam forming. Fig. 5 demonstrates linearly increasing delays from outputs 2 to 8 of the 1×8 OBFN chip, considering output 1 as the zero delay reference. The coupling coefficients and round-trip phase-shifts of the rings are tuned such that the delays cover a bandwidth of 2.5 GHz, with the largest delay value of approximately 1.2 ns (corresponding to 36 cm of physical distance in air) and delay ripple of approximately 0.1 ns (3 cm). Since the 1x8 OBFN chip is designed such that each of the 3 stages can be measured separately, in practice the final delay responses at the outputs are achieved by tuning every stage to a flattened delay response over a common frequency band before they add up.

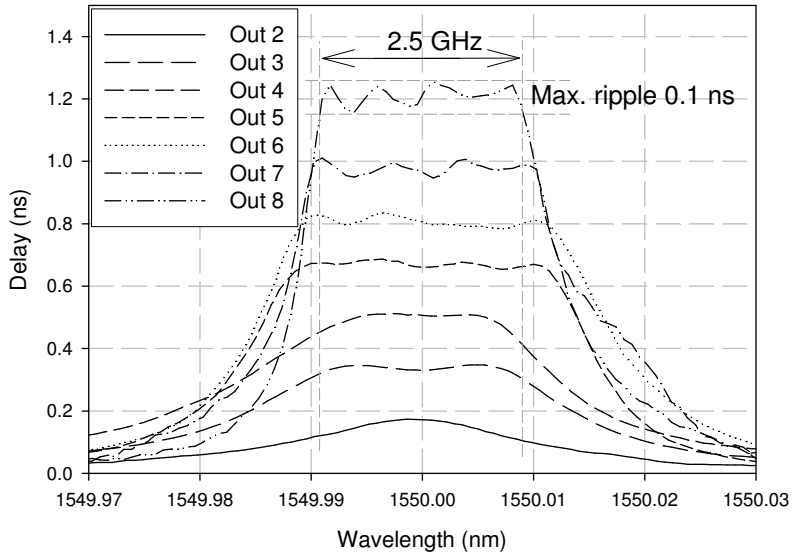

Fig. 5. *Measured group delay responses at different outputs of the 1x8 OBFN chip.*

5 Conclusion

Group delay responses at each output of the ORR-based 1×8 OBFN chip realized in LPCVD waveguide technology have been measured. The measurement results are in good agreements with theory. Delay generation of up to 7 cascaded rings for optical beam forming is demonstrated with a maximum delay of 1.2 ns, with a bandwidth of 2.5 GHz, and ripple of 0.1 ns. To our knowledge, this is the first single-chip demonstration of eight-element optical beam forming with true time delay and continuous tunability.

Acknowledgements

This work was part of the Broadband Photonic Beamformer project and the IO-BFN project, both supported by the Dutch Ministry of Economic Affairs, SenterNovem project number IS052081 and NIVR project number PEP 61424, respectively.

References

[1] G. Lenz, B. J. Eggleton, C. K. Madsen, R. E. Slusher, "Optical delay lines based on optical filters," *IEEE J. Quantum Electron*., Vol. 37, No. 4, April 2001, pp. 525–532.

[2] J. E. Heebner, V. Wong, A. Schweinsberg, R. W. Boyd, D. J. Jackson, "Optical transmission characteristics of fiber ring resonators," *IEEE J. Quantum Electron.*, Vol. 40, No. 6, June 2004, pp. 726–730.

[3] M. S. Rasras et al., "Integrated resonance-enhanced variable optical delay lines," *IEEE Photon. Technol. Lett.*, Vol. 17, No. 4, April 2005, pp. 834–836.

[4] L. Zhuang, C. G. H. Roeloffzen, W. van Etten, "Continuously tunable optical delay line," *Proc. of the 12th IEEE/CVT Symp. in the Benelux*, Enschede, The Netherlands, November 2005.

[5] C. G. H. Roeloffzen, L. Zhuang, R. G. Heideman, A. Borreman, W. van Etten, "Ring resonator-based tunable optical delay line in LPCVD waveguide technology," *Proc. of the 9th IEEE/LEOS Symp. in the Benelux*, Mons, Belgium, December 2005, pp. 79–82.

[6] R. G. Heideman, A. Melloni, M. Hoekman, A. Borreman, A. Leinse, F. Morichetti, "Low loss, high contrast optical waveguides based on CMOS compatible LPCVD processing: technology and experimental results," *Proc. of the 9th IEEE/LEOS Symp. in the Benelux*, Mons, Belgium, December 2005, pp. 71–74.

[7] L. Zhuang, C. G. H. Roeloffzen, R. G. Heideman, A. Borreman, A. Meijerink, W. van Etten, "Single-chip optical beam forming network in LPCVD waveguide technology based on optical ring resonators," *Proc. of the International Topical Meeting on Microwave Photonics (MWP'2006)*, Grenoble, France, 3-6 October 2006, p. F1.4.

A nanophotonic NEMS-modulator in Silicon-on-Insulator

J. Roels(1), I. De Vlaminck(2), D. van Thourhout(1), L. Lagae(2), D. Taillaert(1), R.Baets(1)

(1) Ghent University –IMEC, Department of Information Technology (INTEC),

St-Pietersnieuwstraat 41, 9000 Ghent – Belgium

Contact = joris.roels@intec.ugent.be

(2) IMEC, Kapeldreef 75, B-3001 Leuven, Belgium,
also at ESAT/INSYS, KULEUVEN, Belgium

In order to achieve fast all optical switching in communication networks, a compact, low cost, integrated optical switch is needed. Nanophotonic integrated circuits in silicon-on-insulator (high-index contrast) are well-suited for this purpose. Nevertheless it is hard to obtain a strong light modulation effect in silicon.

In this paper we demonstrate light modulation by moving a nanophotonic waveguide (NEMS = nano-electromechanical system). We also fabricated and characterized passive directional couplers. Both achievements are an important step towards a 2x2 nanophotonic NEMS-switch.

I. Introduction

Optical signal processing components need to be down-scaled to the size of electrical components in order to be economically competitive. However current photonic integrated circuits (PIC) are fairly large compared to their electronic counterparts. This is because the on-chip optical waveguides typically have a low index contrast, and therefore the light is weakly confined in the large waveguide core (core diameter >> 1μm). As a result waveguides need a large bend radius and signal processing components typically consume lots of valuable (expensive) chip area. Nanophotonic waveguides confine light into a submicron core area by using a very high refractive index contrast. Therefore the size of the PICS can be reduced by an order of magnitude.

Silicon-on-Insulator (SOI) is an attractive material system for such nanophotonic waveguides because of the high refractive index contrast between the silicon top layer (n=3.48) and the silica (=SiO_2) cladding (n=1.45). Moreover SOI makes it possible to integrate photonic components with electronics and offers CMOS-compatible, cost reducing fabrication.

The last 5 years many compact passive optical components in SOI have been successfully demonstrated [1,2]. However it is hard to obtain compact active optical components in SOI since the refractive index of silicon does not exhibit a strong electro-optic or thermo-optic modulation effect [3]. In this paper we discuss a concept for a waveguide switch based on an optical directional coupler with moving arms.. Moving on-chip structures with submicron size are often called NEMS (Nano-electro mechanical Systems). Optical NEMS are a new and exciting research domain that requires the combination of several engineering fields like electromagnetism, mechanical engineering and nanophotonics.

Electrostatic actuation

We will make the waveguide move by the principle of electrostatic actuation (Figure 1). A voltage is applied between a silicon waveguide and an electrode. The waveguide is partially suspended in air so that a stringlike structure is created. The electrode and string from electrical point of view act like the plates of a capacitor and electrical charges with opposite signs are formed upon them. These charges cause an attractive Coulomb force F_{elek} between the string and the electrode. The balance between F_{elek} and the counteracting mechanical spring force F_{elek} finally results in a translation of the waveguide string. When the translation exceeds a critical value (approximately one third of the original gap between string and electrode) instability occurs and the string irreversibly snaps down to the electrode (pull-in), which should be avoided.

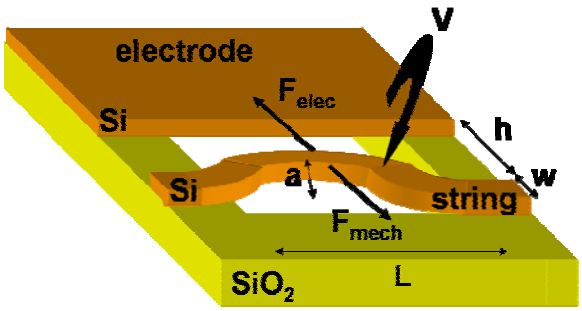

Figure 1: principle of electrostatic actuation

Switching principle

The waveguide switch is based on the principle of a passive directional coupler. The physical behavior of such a directional coupler is described by the theory of supermodes or a coupled mode theory [4]. When two waveguides are brought in sufficiently close proximity the mode profiles of their guided eigenmodes will have an overlap. Under that conditions a periodical exchange of light power between the two waveguides will take place. When we excite one waveguide with unity power (P_{in}=1) the power that is coupled into the not-excited waveguide (P_{cross}) is given by (with L the length of the coupling section, see Figure 2, right):

$$P_{cross} = \sin^2\left(\frac{\pi L}{2L_c}\right)$$

Lc is a parameter that is called the "effective coupling length" and it is defined as the length of the coupling section that is needed to couple all light into the not-excited waveguide (P_{cross} =1). Lc can be calculated from the theory of supermodes when the effective mode indices of the supermodes are known [4].

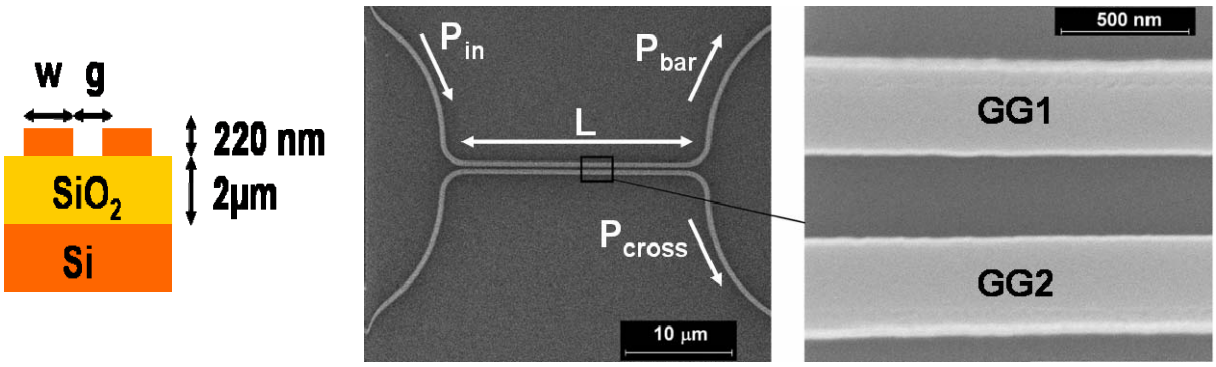

Figure 2: directional coupler: cross-section (left), SEM-picture + detail (right)

In a high-index contrast material system the parameter Lc is very sensitive to small changes in the gap distance g. Figure 3 (left) shows a simulation of Lc in function of the gap distance g for some typical design parameters. The simulation was performed with the help of a full vectorial 3D-mode solver. It is clear from the picture that changes as small as 100nm cause a doubling of Lc and therefore cause a full switch of the light from one waveguide to another.

In order to verify the above described theory we fabricated and characterized some passive directional couplers in SOI with coupling sections L varying from 0 to 28µm with an interval of 3.5 µm. The results are shown in Figure 3 (right). We found an excellent agreement between our measurements and the sine square dependency predicted by the theory of supermodes and the coupling mode theory.

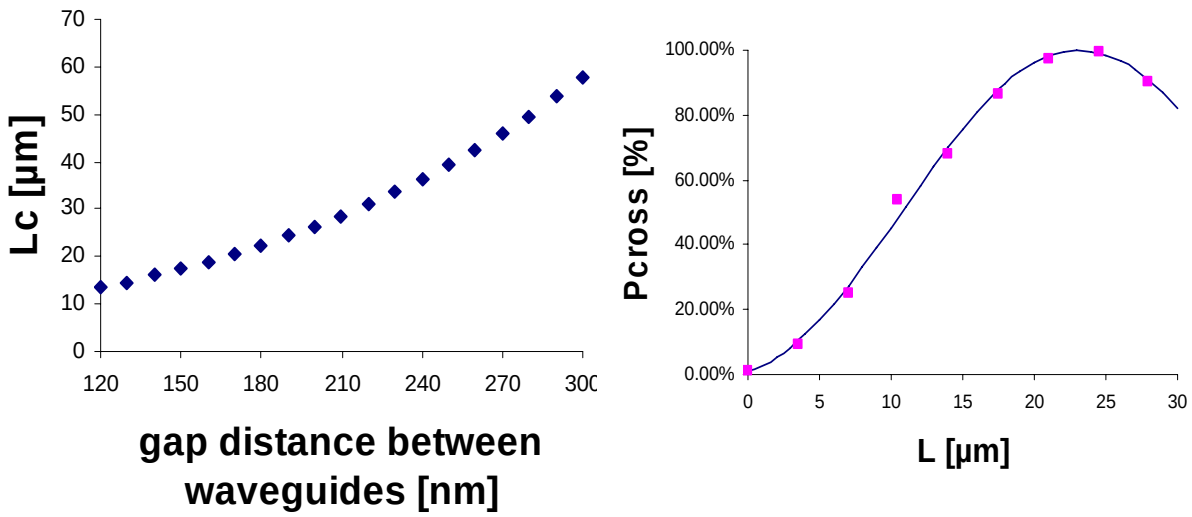

Figure 3: Simulation of Lc in function of g with w=400nm at λ=1.55µm (left); Measurement of P_{cross} (squares, right) + theoretical fitting (full line, right) at λ=1.57 µm

It should be stressed that for high-index contrast material systems it is not trivial to find such a good agreement between theory and measurements since slight aberrations in the fabrication generally cause uncomplete coupling (P_{cross} max < 1). To our knowledge it is the first time that such matching results are reported in literature for directional couplers fabricated with DUV (Deep Ultra Violet, see Fabrication) in SOI.

Fabrication

A DUV-process (Deep Ultra Violet) with submicron resolution was developed using the CMOS-facilities of IMEC to define the required patterns in the top silicon layer. This process is described in detail elsewhere [1]. To create an active NEMS-device in a second step the waveguides need to be partially underetched so that a suspended structure is created. This was done using a resist mask and buffered HF which provides a selective silica etch. Finally aluminium was evaporated to define electrical contact areas.

An optical NEMS-modulator

In order to demonstrate modulation by moving waveguides we fabricated the device shown in Figure 4 (left). Both the electrode and waveguide are suspended in air. By applying a voltage between the electrode and the waveguide they move closer to each other and more light will leak out of the waveguide so we expect a drop of the measured transmission P_{out}/P_{in}. Indeed we measured a decrease of 20% when a voltage of 15V was applied.

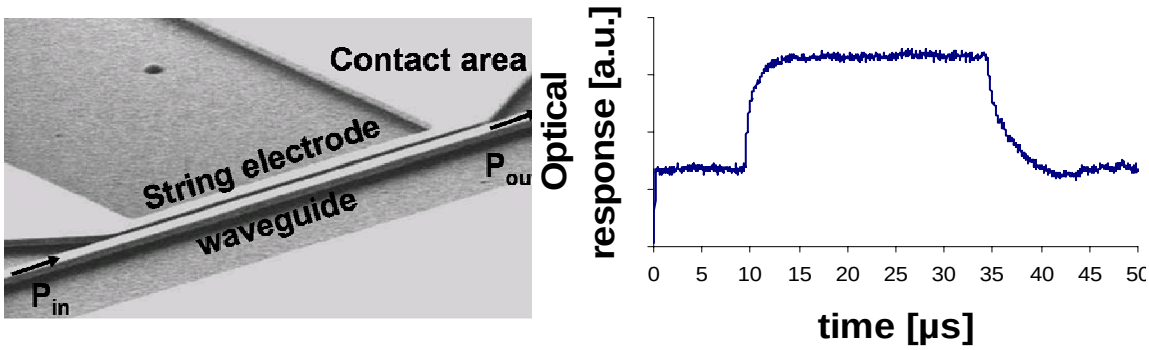

Figure 4: SEM-picture NEMS-device (left) + measurement dynamic optical response (right)

We also did experiments on the dynamic behavior. Figure 4 (right) shows the dynamical optical response when a square voltage wave is applied to the device. We can clearly see that switching times are in the order of 3-5µs. A SEM-analysis has shown that during the experiments pull-in has taken place which complicates the analysis of the results. Nevertheless we believe that the measured switching times are dominated by (purely) electrical charging effects and that the measured shape of the optical response corresponds to the typical exponential shape with RC-time constant that is found when a capacitor C is loaded over a resistor R. We can conclude from this experiment that for our future devices we need a better control of the contact resistance (lower the resistance to decrease the RC-time constant) and the driving voltage (to avoid pull-in). That way we expect to measure subµs switching times.

Conclusion

In this paper we discussed on-chip optical switching using a NEMS-approach in a high-index contrast material system. We have fabricated and characterized passive directional couplers and found an excellent agreement between theory and measurements. We also fabricated a NEMS-device and discussed the observed dynamics. Both results are important steps towards compact NEMS-switches in Silicon-on-Insulator that we will demonstrate in the near future.

References

[1] W. Bogaerts, Nanofotonische golfgeleiders en Fotonische Kristallen in Silicium-op-Isolator, PhD-thesis, 2004 University of Ghent

[2] Dumon, P., et al., Compact wavelength router based on a Silicon-on-insulator arrayed waveguide grating pigtailed to a fiber array, Optics Express, 2006. **14**(2): p. 664-669.

[3] R.S. Jacobsen, Strained silicon as a new electro-optic material, Nature 2006, **441**(7090): p. 199-202.

[4] Märtz R, Integrated Optics, Design and Modeling, 1995, Boston, London: Artech House

Multimode Waveguides of Photodefinable Epoxy for Optical Backplane Applications

M.B.J. Diemeer, L.T.H. Hilderink, H. Kelderman and A. Driessen

University of Twente, Integrated Optical Microsystems Group, P.O. Box 217, Enschede, the Netherlands

We developed photodefined, multimode-fiber compatible waveguides based on epoxies. These waveguides will be embedded in backplane PCB's for optical interconnect applications using 850 nm VCSELs as light sources. Apart from very low loss, the material selection took into account, PCB compatibility and low yellowing due to high temperature processing (for PCB lamination and soldering). The waveguides showed losses < 0.06 dB/cm at 832 nm and 633 nm. Their loss increase after aging (1 hr at 185 °C) was limited to 0.04 dB/cm at 850 nm. Waveguides realized on FR-4 (epoxy-fiberglass) PCB material are demonstrated.

Introduction

The continuous increase of the microprocessor clockrate (expected clockfrequency ~10^{10} Hz in 2011), in addition to the continuous increase of data rates in optical transmission systems, has created a bottleneck in high- end systems like servers, and telecom switches, at the interconnect between cards over their PCB (Printed Circuit Board) backplane. In those systems, aggregate data rates of multiple Tbps have to be transported via the backplanes over a typical distance of about 0.5 m. and with such bandwidth-distance products, the electrical data transmission through a copper line is touching its fundamental limit around 20 Gbps. Optical transmission via waveguides offers the potential of a much larger capacity. Therefore, there is worldwide an intense research activity ongoing to realize Optical Backplanes. These are backplanes with an embedded multimode polymeric optical waveguide layer, equipped with in- and output couplers, fabricated with PCB compatible, low-cost fabrication techniques [1,2].

In [3] we reported on a photodefinable epoxy formulation with attractive properties for Optical Backplane applications. However, a drawback of this material is its increase of attenuation at 850 nm from 0.1 dB/cm to 0.4 dB/cm due to yellowing after the high temperature processing step (1 hr, 180 °C) which is applied in PCB lamination process. The high content of the aromatic diglycidyl ether of bisphenol-A (DGEBA) prepolymer in the formulation can largely be held responsible for that. Therefore, we have replaced most of the aromatic epoxy by (saturated) cycloaliphatic epoxies which are known to yield less yellowing after aging. This paper shows the superior properties of the new formulation.

Cycloaliphatic epoxy formulation

An important requirement is the solid nature of the epoxy material for the waveguide core. This prevents the latent image of photoacid catalyst that is formed in the epoxy matrix after masked uv- exposure to fade by diffusion. Moreover, a solid core material layer is required for contact masking.

A cycloaliphatic epoxy prepolymer (code name CHEP) was identified as a suitable material. It features, apart from a low epoxy equivalent weight, a high glass transition temperature of about 200 °C (cured polymer) and a low content of ionic impurities.

A drawback of (cyclo) aliphatic epoxies is their relatively low refractive index (n~1.5), compared to aromatic (e.g. DGEBA) epoxies (n~1.6). This makes it difficult to find cladding materials, which should have indices 0.013 lower than the core material in order to make waveguide channels having a numerical aperture (NA) that is compatible with multimode fibers (50 μm core, NA= 0.2).
Therefore CHEP for the core material was blended with DGEBA to raise its index. To reduce the sensitivity for cracking as a result of the high glass transition temperature, a polyol was added to the formulation. This additive is known to improve the polymer flexibility. In addition, it enhances the cure rate. We applied a high-purity triol. Other additives are an anti-oxidant, an adhesion promoter and a flow and leveling additive. Fig. 1 shows the refractive index at 830 nm of the CHEP-DGEBA-triol film waveguides as a function of DGEBA content as measured with a prism coupler (Metricon).

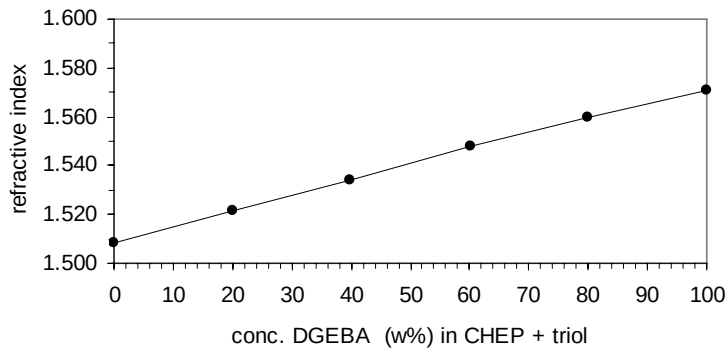

Fig. 1. Refractive index @ 850 nm of CHEP film waveguides as a function of DGEBA content.

From fig. 1, it can be seen that at about 20% DGEBA concentration the required refractive index contrast of 0.013, with undoped CHEP as cladding, can be obtained.
Fig. 2a is a SEM picture of photodefined waveguide core showing very smooth sidewalls and a rectangular cross-section. Fig. 2b shows a microscope picture of waveguides (~40 μm thick and wide) embedded in an undoped CHEP cladding as deposited onto a FR-4 PCB substrate. Excellent planarization can be observed.

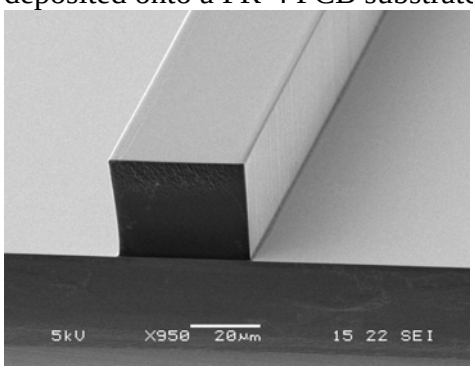

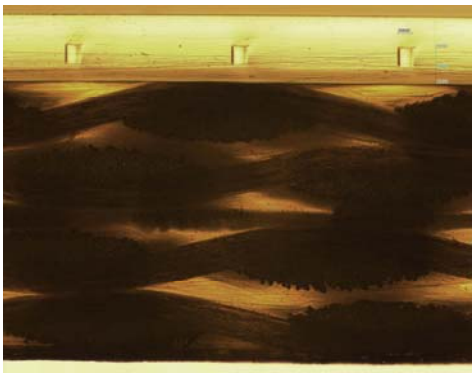

Fig. 2a. SEM picture of a CHEP-DGEBA-triol core. Fig. 2b. Microscope picture of embedded waveguides deposited onto a FR-4 PCB substrate; the fiberglass yarn is clearly visible.

Apart from cracks, the polyol also reduces the UV exposure time. The amount of photoinitiator (triarylsulfonium hexafluorophosphate) could be reduced with 50% while keeping the exposure time in the mask aligner (Karl Süss MA55) the same. This will be

beneficial for the reduction of yellowing by photoinitiator residues after high temperature processing.
To allow for accurate loss measurements of CHEP-based waveguides, a very long (103.6 cm) coiled up waveguide, combined with a short (7.2 cm) reference waveguide was made on a 4'Pyrex wafer. The long waveguide is a Fermat spiral as shown in fig. 3a. The radius of the two inner loops is 15 mm.

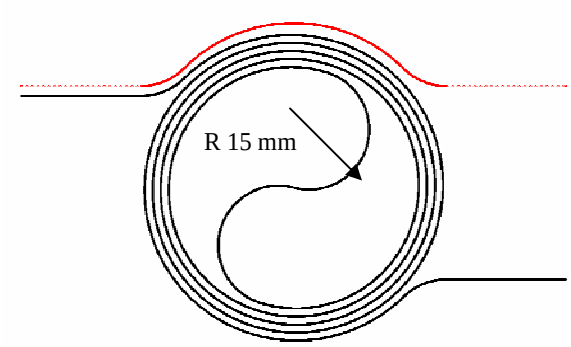

Fig. 3a. Fermat spiral and reference waveguide.

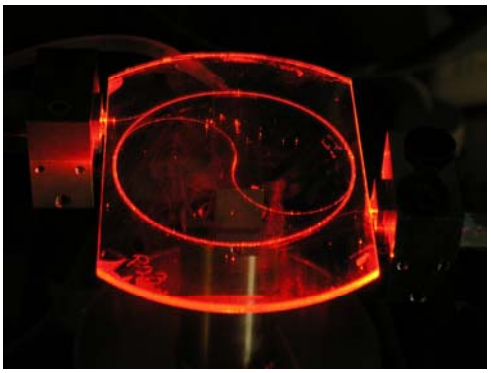

Fig. 3b. Stray light at 633 nm from the spiral.

A relatively high contrast waveguide, with an index difference of 0.03 (NA=0.3) has to be made for this structure in order to keep bend losses in the inner loops to negligible values. To that end, we combined the 20% DGEBA doped CHEP core with a CHEP cladding doped with a low refractive index, difunctional epoxy siloxane. The core was spincoated and photodefined directly onto the Pyrex wafer, and the photocurable cladding was used to adhere a cover Pyrex wafer onto this to protect the waveguide and to allow for dicing of endfaces. Fig. 3b shows the stray light at 633 nm emitted by the waveguide as recorded by a digital camera. The propagation loss at 633 nm was derived from the variation of the intensity in the individual channels as a function of the propagation distance as taken from a small section of a zoomed-in picture (fig. 4a). This is plotted in fig. 4b and yields a propagation loss of 0.04 dB/cm.

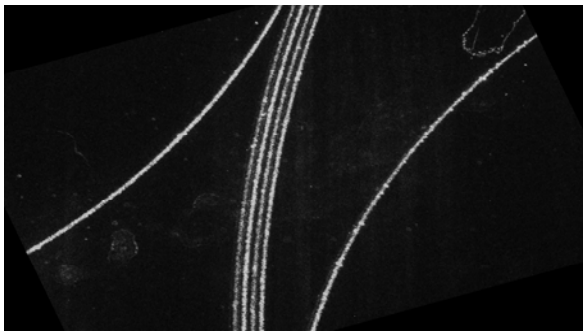

Fig. 4a: Stray light (@633 nm).
Note the alternation in back and forth running channels.

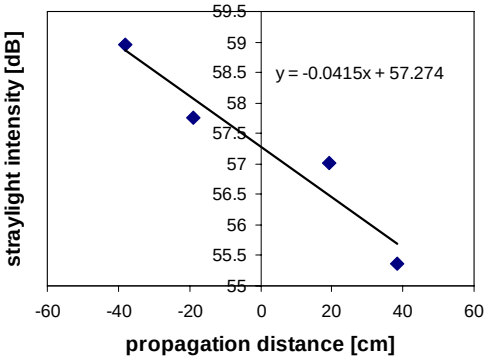

Fig. 4b: Stray light intensity vs. path length.
The zero reference is placed in the centre.

In addition, propagation loss measurements were performed at laser wavelengths of 633 nm and 832 nm using butt-coupled multimode input/output fibers. The propagation loss was derived from the differences in insertion loss (IL) and path length between the

spiral and the reference channel. The loss at 633 nm show good correspondence with the stray light measurement result. These results are listed in table 1.

Table 1. Measured propagation losses

Wavelength [nm]	From IL [dB/cm]	Stray light [dB/cm]
633	0.05	0.04
832	0.06	

The spectral dependence of the propagation loss was as measured by injecting white light in the waveguides and analyzing the output using an optical spectrum analyzer (Spectro 320, Instrument Systems). The spectrum have been calibrated on measurement at 633 nm as given in Table 1. The measurement has been repeated after thermal aging of the sample for 1 hour at 185 °C. The results as presented in fig. 4a and 4b show losses around 0.05 dB/cm between 600 and 700 nm and between 800 and 850 nm, while the loss increase after thermal aging is limited to 0.04 dB/cm at wavelengths >700 nm.

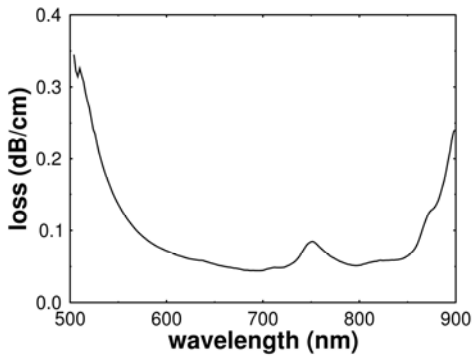

Fig. 4a. Spectral dependence of the prop. loss.

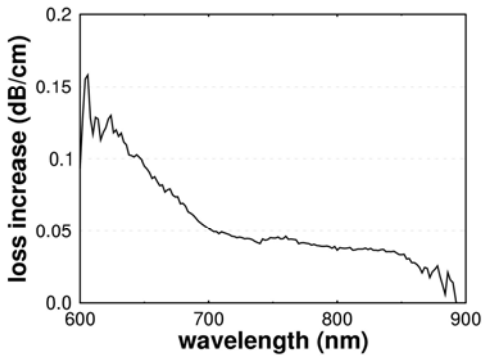

Fig. 4b. Loss increase after thermal aging (1hr at 185 °C).

Conclusion

We have presented attractive multimode photodefinable epoxy waveguides for Optical Backplane applications. Multimode-fiber compatible waveguides on FR-4 PCB substrate material have been demonstrated. A propagation loss of <0.06 dB/cm at 850 and 633 nm has been measured. Thermal aging at 185 °C for 1 hour yields a loss increase of < 0.04 dB/cm at wavelengths >700 nm.

Acknowledgement

The authors acknowledge the financial support of STW (project TOE 6986).

References

[1] C. Berger, R. Beyeler, G.-L. Bona, R. Dangel, L. Dellmann, P. Dill, F. Horst, M. Kossel, C. Menolfi, T. Morf, B. J. Offrein, M. L. Schmatz, T. Toifl, and J. Weiss, "Optical links for printed circuit boards," in 16th Ann. Meeting of IEEE Lasers & Electro-Optics Soc., October 26-30, Tucson, AZ, USA, 2003.

[2] B. J. Offrein, C. Berger, R. Beyeler, R. Dangel, L. Dellmann, F. Horst, T. Lamprecht, N. Meier, J. Kash,, "High bandwidth board-level parallel optical interconnects for server applications," Proc. 32-th ECOC, vol. 3, paper We4.2.1, pp. 483-485, Sept. 24-28, Cannes, Fr., 2006.

Beyond the Size Limit on Cavity Solitons with Left-Handed Materials

L. Gelens,[1] P. Tassin,[1] G. Van der Sande,[1,2] I. Veretennicoff,[1] P. Kockaert,[3] M. Tlidi,[2] D. Gomila[4] and J. Danckaert[1]

[1]Department of Applied Physics and Photonics, Vrije Universiteit Brussel, Pleinlaan 2, B-1050 Brussel, Belgium

[2]Optique non linéaire théorique, Université Libre de Bruxelles, CP 231, Campus Plaine, B-1050 Bruxelles, Belgium

[3]Service d'optique et acoustique, Université Libre de Bruxelles, CP 194/5, 50, Av. F. D. Roosevelt, B-1050 Bruxelles, Belgium

[4]Institut Mediterrani d'Estudis Avançats (IMEDEA, CSIC-UIB), Campus Universitat Illes Balears, E-07122 Palma de Mallorca, Spain

We propose a technique to produce cavity solitons with arbitrarily small diameter by placing a nonlinear left-handed material in a Fabry-Perot resonator together with a traditional nonlinear material. This configuration allows engineering the diffraction strength. Considering the typical nonlocal behaviour of the nano-structured left-handed metamaterial, we develop a mean-field model describing the spatiotemporal evolution of this system. We focus our numerical studies on the influence of the nonlocality on the size and linear stability of these localised structures as the diffraction strength is decreased. A minimal width beyond the diffraction limit is discovered and applications are discussed.

Introduction

Transverse localised structures in nonlinear optical cavities – often referred to as cavity solitons (CSs) – have been predicted and demonstrated in a large number of systems [1,2]. Such structures have been suggested for use in optical data storage and information processing. Typically, diffraction constrains their size to be of the order of the square root of the diffraction coefficient.

Some of us have shown recently that the diffraction coefficient of a nonlinear optical resonator can be engineered by inserting a left-handed material in the cavity [3]. The value of the diffraction coefficient can then be reduced to arbitrarily small values by tuning the relative thicknesses of right-handed and left-handed material layers. As, in the Lugiato-Lefever equation, length scales with the diffraction coefficient, this system potentially allows for CSs beyond the size limit imposed by natural diffraction. However, intuitively, one expects that the sub-wavelength structure of left-handed metamaterials will impose a new limit on the width of CSs. Here, we investigate the consequences of this shorter space scale on the properties of CSs.

Linear nonlocality

Technically, the Lugiato-Lefever equation can be derived from a perturbation analysis applied to Maxwell's equations in a nonlinear Kerr medium. The diffraction term arises as a first-order contribution and higher order spatial derivates can be neglected with respect to the diffraction term. However, when the diffraction coefficient is tuned to

small values, higher order terms should be taken into account. The nonlocal linear polarisation, for example, results in an additional term in the Lugiato-Lefever equation,

$$\frac{\partial E}{\partial t} = -(1+i\theta)E + E_{in} + i\Gamma|E|^2 E + i\mathcal{D}\nabla_\perp^2 E + \iint \sigma(\mathbf{r}_\perp - \mathbf{r}_\perp^{'})E(\mathbf{r}_\perp^{'})d^2\mathbf{r}_\perp^{'}, \quad (1)$$

which couples the electric field envelopes at different transverse locations. We assume that this term can be expanded in a series of spatial derivatives of E:

$$\iint \sigma(\mathbf{r}_\perp - \mathbf{r}_\perp^{'})E(\mathbf{r}_\perp^{'})d^2\mathbf{r}_\perp^{'} = \sigma_0 E + \sigma_1 \nabla_\perp^2 E + \sigma_2 \nabla_\perp^4 E + \ldots \quad (2)$$

The first two terms in Eq. (2) will contribute to the phase velocity and the diffraction effects, respectively. Keeping only the next higher order effect, we finally arrive at

$$\frac{\partial E}{\partial t} = -(1+i\theta)E + E_{in} + i\Gamma|E|^2 E + i\mathcal{D}^{(1)}\nabla_\perp^2 E + i\mathcal{D}^{(2)}\nabla_\perp^4 E, \quad (3)$$

where $\mathcal{D}^{(1)}$ and $\mathcal{D}^{(2)}$ describe the diffraction strength and the strength of the nonlocal effects, respectively.

Linear stability analysis

When examining the homogeneous, stationary solutions of Eq. (3), it is found that the output-field vs. input-field can have a mono- and bistable characteristic. The study here is limited to the monostable region. At higher background intensities a modulational instability gives rise to the appearance of CSs. A linear stability analysis has been performed on these homogeneous, stationary solutions, showing that the modulational instability depends critically on the dimensionless parameter η, defined by the ratio of the nonlocality vs. the diffraction: $\eta = \mathcal{D}^{(2)}/\mathcal{D}^{(1)2}$.

For $\eta > 0$, it is possible to predict the width of the CSs in the limit of small diffraction:

$$\Lambda_+ = 2\pi\sqrt{2\eta\mathcal{D}^{(1)}} = 2\pi\sqrt{\frac{2\mathcal{D}^{(2)}}{\mathcal{D}^{(1)}}}. \quad (4)$$

Eq. (4) predicts that the CS-width increases with decreasing $\mathcal{D}^{(1)}$, while the classical diffraction limit (without the nonlocal term) predicts a decreasing width. This suggests the existence of a minimal CS-width for an optimal value of the diffraction coefficient $\mathcal{D}^{(1)}$. In order to determine this optimum, numerical simulations are needed. It is always possible that the CS with optimal width is unstable. This information shall also be provided by the numerical simulations.

For $\eta < 0$, we find that the CS-width will still decrease with increasing diffraction strength $\mathcal{D}^{(1)}$, but that due to the width will eventually saturate at

$$\Lambda_{\lim} = 2\pi\sqrt[4]{-\frac{\mathcal{D}^{(2)}}{2-\theta}}. \quad (5)$$

Stability and minimal width of cavity solitons

In order to find stationary, localised solutions of Eq. (3) and their stability, we follow a Newton method [4]. The radial form of Eq. (3) is discretised, from which a set of nonlinear coupled complex equations is found. Spatial derivatives are calculated in the Fourier space by using a Fast Fourier Transform and taking zero boundary conditions. With an appropriate initial condition, the Newton-Rhapson method converges to a solution of this set of equations. This initial condition is found by performing a 2D spatiotemporal simulation of a radial version of Eq. (3). This approach is extremely accurate and automatically generates the Jacobian operator, which provides insight into the stability of the solutions. This method also allows finding unstable solutions and thus creating full bifurcation diagrams.

In Figure (1), bifurcation branches of the CSs are shown as a function of the background intensity of the homogeneous, stationary solutions I_s and the maximum intensity of the solitons (for $\theta = 1.23$). The lowest, solid line represents the stable homogeneous solution. For $\eta > 0$ [Figure 1 (a)], the branches expand to lower intensities for increasing values of η, also enlarging the region of stability (solid line). This trend is reversed at a certain η, narrowing the stability region with larger values of η. For $\eta < 0$ [Figure 1 (b)], the branches always shift to higher I_s and the region of stability narrows with increasing values of $|\eta|$. Note also that in both cases the peak intensity of the CSs diminishes with increasing $|\eta|$. This is a first sign of broadening of the CSs.

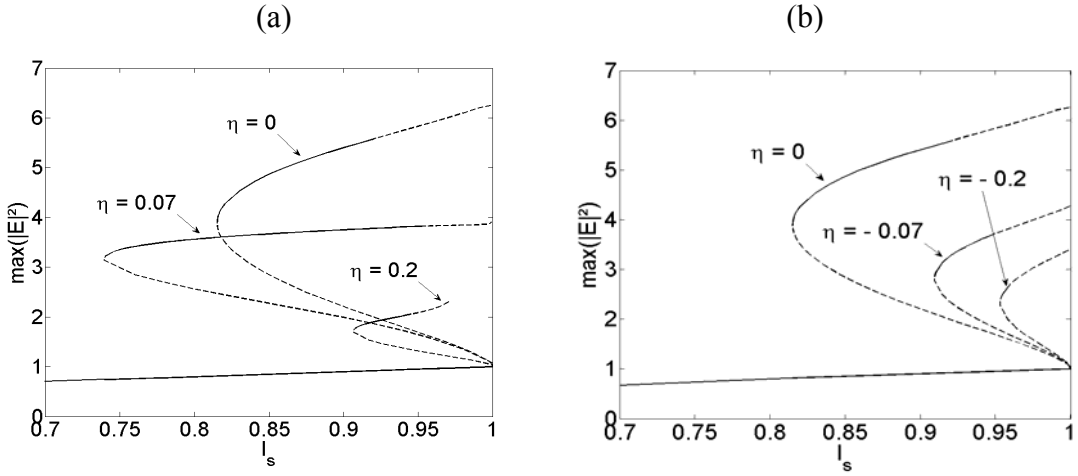

Figuur 1: Bifurcation diagrams with a detuning θ = 1.23 and for different values of η, with η (a) positive and (b) negative. The lowest solid line is the stable homogeneous solution. The branches above are CSs. Solid lines represent stable CSs, dashed lines unstable CSs.

To find the minimal CS-width, a renormalised full width at half maximum (FWHM) is defined:

$$\xi = d_{FWHM} / \sqrt[4]{\left|\mathcal{D}^{(2)}\right|}. \tag{8}$$

This renormalization allows getting a general result that only depends on the detuning θ. The renormalised FWHM of the stable CSs is plotted in Figure (2). For $\eta = 0$, the solid lines give the width for the lowest and highest values of I_s for which the CS is stable.

We find that smaller $\mathcal{D}^{(1)}$ correspond to narrower CSs. When taking into account linear nonlocality (dashed lines), the linear dependency is lost and the FWHM saturates around $\xi = 3$ for both positive [Figure 2 (a)] and negative [Figure 2 (b)] values of η. For too large values of $|\eta|$ ($|\eta|^{-1/2} < 2$), the CS branch becomes entirely unstable. This Figure provides us with the minimal width and the corresponding optimal value, which is mainly determined by the scaling law [Eq. (4), (5)] and by the loss of stability.

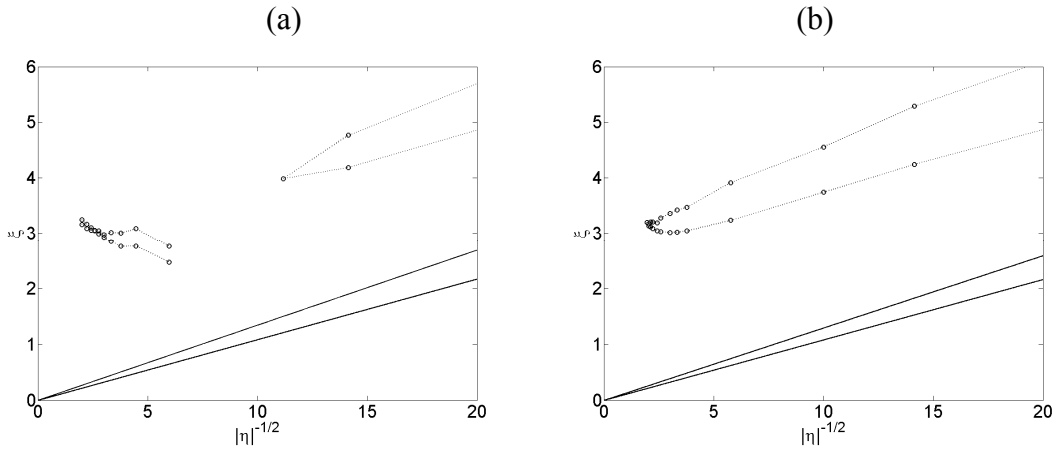

Figuur 2: The renormalised FWHM in function of $|\eta|^{-1/2}$ for (a) positive η and (b) negative η.

Conclusion

The ultimate physical limit on the width of cavity solitons in a diffraction-compensated system is investigated. This limit is due to the destabilisation of the cavity solitons caused by the nonlocal interaction of the electric field with the left-handed metamaterial in the cavity.

Acknowledgements

We acknowledge support from the Belgian Science Policy Office (project IAP 5/18). L.G. and P.T. are Ph.D. fellows of the Research Foundation – Flanders (FWO). G.V. is a Postdoctoral fellow of the Research Foundation – Flanders (FWO). M. T. is a Research Associate of the Fond National de la Recherche Scientifique (FNRS).

References

[1] S. Trillo and W. Torruellas, Spatial Solitons, Berlin: Springer-Verlag, 2001.

[2] S. Barland, J.R. Tredicce, M. Brambilla, L.A. Lugiato, S. Balle, M. Giudici, T. Maggipinto, L. Spinelli, G. Tissoni, T. Knödl, M. Miller, and R. Jäger, Nature,Vol. 419, pp. 699-702, 2002.

[3] P. Kockaert, P. Tassin, G. Van der Sande, I. Veretennicoff, and M. Tlidi, Phys. Rev. A, Vol. 74, 033822, 2006.

[4] W. J. Firth, G. K. Harkness, A. Lord, J. M. McSloy, D. Gomila, and P. Colet, J. Opt. Soc. Am. B, Vol. 19, pp. 747-752, 2002.

[5] D. Gomila, Dynamics of Spatial Structures in Nonlinear Optics, Ph.D. Thesis, IMEDEA-UIB, 2003.

Use of weakly titled fiber Bragg gratings for strain sensing purposes

C. Caucheteur[1], C. Chen[2], J. Albert[2], P. Mégret[1]

[1] Faculté Polytechnique de Mons, Service d'Electromagnétisme et de Télécommunications, Boulevard Dolez 31, 7000 Mons, Belgium

[2] Carleton University, Department of Electronics, Colonel By Drive 1125, K1S 5B6 Ottawa, Canada

Weakly tilted fiber Bragg gratings with grating planes tilted at small angles with respect to the fiber axis couple light to backward going core and cladding modes. Their transmitted spectrum is characterized by narrow resonance dips below the Bragg wavelength corresponding to the core mode coupling. We present the spectral evolution of weakly tilted fiber Bragg gratings in response to temperature changes, bending, axial strain and transversal loads. Because the cladding modes in the transmitted spectrum present different sensitivities than the core mode, the obtained results demonstrate the great potential of these gratings for temperature-insensitive strain sensing applications.

Introduction

Fiber Bragg gratings (FBG) are widely used as sensors of temperature, strain and microbending [1]. These optical sensors are compatible with structures made of composite materials; they are chemically inert and inherently immune from electromagnetic interference. However, when temperature and strain simultaneously affect an FBG, the measurement of the wavelength shift does not provide temperature-insensitive strain measurement. To discriminate these two contributions, structures such as two FBGs, superimposed FBGs, hybrid FBG with long period grating and high birefringence FBGs are required but they increase the complexity of the sensors [1].

Weakly tilted fiber Bragg gratings (TFBG) couple light both to backward propagating core mode and cladding modes [2]. The resonant wavelengths for these mode couplings depend differentially on external perturbations. This has several advantages. While the core mode (Bragg) resonance is only sensitive to axial strain and temperature, the cladding mode resonances are sensitive to the external perturbations (strain, temperature, bending, refractive index, …) [3-6].

In this paper, we analyze the evolution of the transmitted spectrum of TFBGs in response to external perturbations and we demonstrate that temperature-insensitive strain measurements are possible with such gratings.

Cladding modes coupling in TFBGs

In TFBGs, two kinds of couplings exist. The Bragg wavelength, corresponding to the self contra-propagating coupling of the core mode is given by [2]:

$$\lambda_B = \frac{2n_{eff,core}\Lambda_g}{\cos\theta} \tag{1}$$

where $n_{eff,core}$ is the effective refractive index of the core, Λ_g is the nominal grating period and θ is the internal tilt angle (Figure 1).

The resonant wavelengths of the cladding modes, corresponding to the contra-propagating coupling between the core mode and the cladding modes, are given by [2]:

$$\lambda_{cld,i} = (n_{eff,cld,i} + n_{eff,core}) \frac{\Lambda_g}{\cos\theta} \tag{2}$$

where $n_{eff,cld,i}$ is the effective refractive index of the cladding mode i, i=1, …, m with m the total number of cladding modes.
Figure 2 presents the typical transmitted spectrum of a TFBG with the cladding modes resonances situated below the Bragg wavelength. An important feature of weakly tilted FBGs is the presence of a strong "ghost mode" resonance, immediately to the left of the Bragg resonance. This ghost mode is made up of several low order cladding modes.

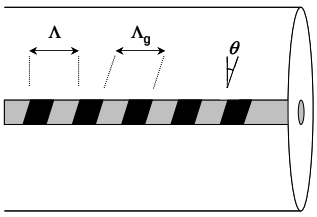

Figure 1. Schematic of a TFBG.

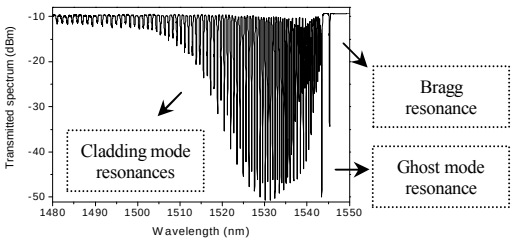

Figure 2. Transmitted spectrum of a 3° TFBG.

The experimental results presented below were obtained on TFBGs inscribed into standard single mode fiber using a pulsed laser (KrF – 248 nm) and a phase mask.

Temperature and axial strain influences on the transmitted spectrum

Figures 3 and 4 show the relative wavelength shifts of cladding modes resonances with respect to the Bragg resonance when axial strain and temperature affect a 4° TFBG. 3 differential wavelength shift regions are obtained for the strain perturbation. First, the ghost mode region appears to be very sensitive to external strain perturbations while low order cladding modes (up to 5 nm from the Bragg wavelength) have negative relative wavelength shifts. Secondly, between 5 nm and 20 nm from the Bragg resonance, the differential wavelength shift grows very linearly with mode order and with strain.

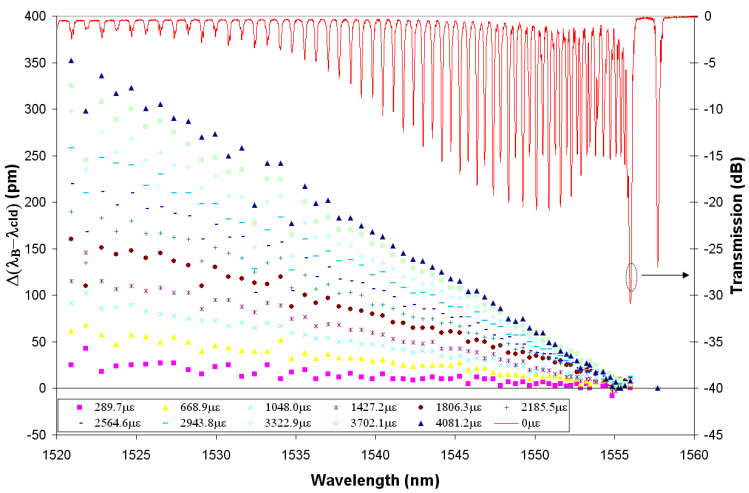

Figure 3. Transmitted spectrum of a 4° TFBG and differential wavelength shift due to strain changes.

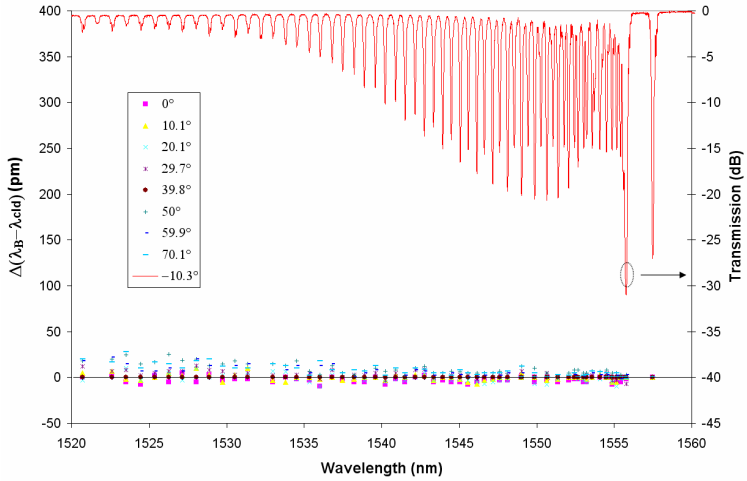

Figure 4. Transmitted spectrum of a 4° TFBG and differential wavelength shift due to temperature.

For higher order modes, further than 20 nm from the Bragg resonance, the results become irregular because the cladding mode resonances have double- and triple-peaked resonances which are difficult to follow reliably over large shifting ranges. If the same individual peak of a multi-peak resonance could be followed unambiguously, then the differential wavelength shift should continue to be linear.

On Figure 4, within the temperature range from about -10°C to 70°C, the relative cladding mode shifts are less than ± 12 pm or equivalent to an apparent ± 1.2°C drift in over ~80°C of temperature variation (except for the short wavelength region). Therefore, a temperature insensitive sensor can be made by monitoring the relative core and cladding mode wavelength shifts in the transmission spectrum.

Bending and transverse strain influences on the transmitted spectrum

Figure 5 presents the effect of a curvature on the transmitted spectrum of a 1 cm long 3° TFBG whereas Figure 6 presents the effect of a transversal load on the transmitted spectrum of a 1 cm long 4° TFBG. Unlike temperature and axial strain effects, curvatures and transversal loads affect the peak to peak amplitudes of the resonances in the transmitted spectrum. The bending mainly influences the cladding modes near the ghost mode region while transversal loads affect the whole spectrum.

In order to efficiently correlate the spectral evolution with the external perturbation, a global measurement of the area delimited by the cladding modes in the transmitted spectrum was privileged in comparison to a local detection of the cladding modes [6,7].

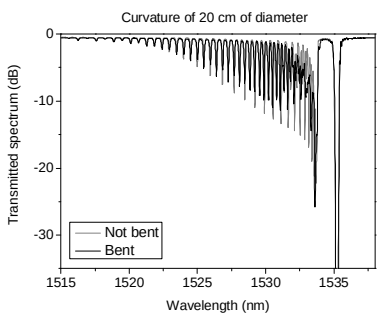

Figure 5. Effect of a curvature on the transmitted spectrum of a 3° TFBG.

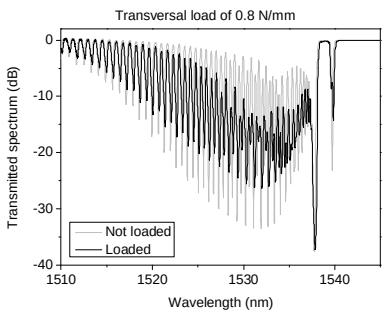

Figure 6. Effect of a transversal load on the transmitted spectrum of a 4° TFBG.

Figures 7 and 8 present the evolution of the normalized area (ratio between the area delimited by the perturbed spectrum and the reference area) in response to bending and transversal loads, respectively. In both cases, the evolution is monotonic and decreasing. We experimentally verified that the temperature influence on the value of the normalized area in the range -10°C to 70°C can be neglected. This behavior was expected since all the cladding modes present nearly the same temperature sensitivity. They are thus all shifted without significant modification of the area delimited by the cladding modes. This property provides temperature-insensitive bending and transverse strain measurements. Let us also mention that the Bragg resonance is not affected by the bending, which is not the case for transversal loads.

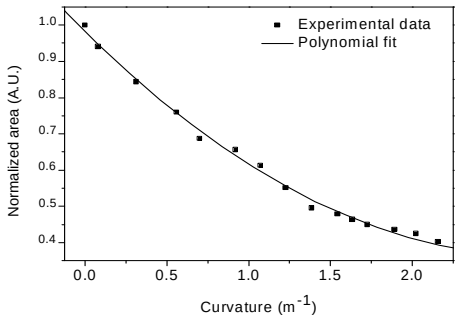

Figure 7. Evolution of the normalized area versus curvature for a 3° TFBG.

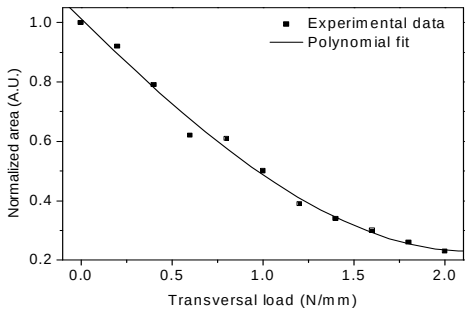

Figure 8. Evolution of the normalized area versus transverse strain for a 4° TFBG.

Conclusion

In this paper, we demonstrated that weakly tilted fiber Bragg gratings can be advantageously used for temperature-insensitive strain sensors. To measure the axial strain, a local measurement of the cladding modes was chosen whereas to measure the bending and the transverse load, a global measurement of the area delimited by the cladding modes was privileged. In both cases, a good sensitivity was obtained.

Acknowledgment

Christophe Caucheteur is supported by the *Fonds National de la Recherche Scientifique* (FNRS). Authors acknowledge the financial support of the attraction pole program IAP V/18 of the *Belgian Science Policy*.

References

[1] A. Othonos, K. Kalli, "Fiber Bragg gratings: fundamentals and applications in telecommunications and sensing", Artech House (Norwood), 1999.

[2] K.S. Lee, T. Erdogan, "Fiber mode coupling in transmissive and reflective tilted fiber gratings", Applied optics, vol. 39, pp. 1394-1404, 2000.

[3] G. Laffont, P. Ferdinand, "Tilted short-period fibre-Bragg-grating-induced coupling to cladding modes for accurate refractometer", Meas. Science and Technology, vol. 12, pp 765-770, 2001.

[4] C. Caucheteur, P. Mégret, "Demodulation technique for weakly tilted fiber Bragg grating refractometer", IEEE Photonics Technology Letters, vol. 17, n. 12, pp. 2703-2705, 2005.

[5] C. Chen, L. Xiong, A. Jafari, J. Albert, "Differential sensitivity characteristics of tilted fiber Bragg grating sensors", in Proceedings of SPIE, vol. 6004, paper 6004-13, 2005.

[6] C. Caucheteur, K. Chah, F. Lhommé, M. Blondel, P. Mégret, "Simultaneous bend and temperature sensor using tilted FBG", in Proceedings of SPIE, vol. 5855, pp. 707-710, 2005.

[7] C. Caucheteur, K. Chah, F. Lhommé, M. Blondel, P. Mégret, "Use of tilted Bragg gratings to simultaneously measure sugar concentration and temperature during the production process of sugar", in Proceedings of SPIE, vol. 5855, pp. 451-454, 2005.

Feedback phase sensitivity of a semiconductor laser subject to filtered optical feedback

H. Erzgräber[1], B. Krauskopf[2,1], D. Lenstra[3], A.P.A Fischer[4] and G. Vemuri[5]

[1]Natuur– en Sterrenkunde, Vrije Universiteit Amsterdam, The Netherlands
[2]Department of Engineering Mathematics, University of Bristol, UK
[3]Faculty of Electrical Engineering, Mathematics and Computer Science, Delft University of Technology, The Netherlands
[4]Laboratoire de Physique des Lasers, Universit Paris XIII, UMR CNRS 7538, France
[5] Indiana University-Purdue University Indianapolis, Indiana 46202-3273, USA

Filtered optical feedback (FOF) can be used to stabilize a semiconductor laser but also to generate chaotic laser emission that may find applications in chaos communication schemes. We study theoretically the dynamics the FOF laser and identify the feedback phase as an important parameter that organizes the huge degree of multi-stability in this system. A systematic experimental study of the phase effect on the dynamics is presented that is supported by theoretical findings.

Recent research in laser dynamics goes towards harnessing the nonlinear dynamical properties of semiconductor laser for new applications. Secure communication with chaotic carrier waves [1] or broad band laser sources [2] are only two examples of this vital field of nonlinear laser dynamics. A key to successfully exploiting nonlinear laser dynamics is to understand the underlying mechanisms which lead to the unstable behavior of semiconductor lasers, and to gain control over them.

Here we investigate the underlying structure of a semiconductor laser subject to filtered coherent optical feedback (FOF). First experimental and theoretical studies of the FOF laser as considered here can be found in Ref. [3; 4]. In particular in Ref. [5] the key role of the feedback phase C_p for organizing the dynamics of the FOF laser was demonstrated theoretically. In order to verify the relevance of C_p the following experiment was designed; a sketch is shown in Fig. 1. The laser is a commercially available single mode Fabry-Pérot type semiconductor laser emitting at 780 nm with a threshold current of $I_{th} = 43$ mA. Throughout the experiments the laser was operated at a pump current of $I = 70.6$ mA.The temperature of the lasers can be stabilized with an accuracy in the order of 0.01 K. The laser's frequency shift due to changes of the pump current was linear and was estimated as 3.6 GHz/mA. The filter consists of two flat mirrors with reflectivity $R =$ 70 %, respectively. The distance between the mirror was $D = 3.9 \pm 0.1$ cm, which results in a free spectral range of FSR=3.8$\pm$0.1 GHz. The finesse was measured experimentally as $f = 5 \pm 0.5$, which results in a filter width of HWHM= 385$\pm$30 MHz (half width at half maximum). Importantly, the piezo translation stage with a mechanical resolution of 20 nm allows for changes of the feedback phase with a resolution of 19 measurement points per 2π-cycle. The FOF laser was operated with very low feedback, the threshold reduction is less than 0.1 %. The feedback was controlled with a combination of a polarizer and a $\lambda/2$-plate. Finally, in total four optical isolators, with isolation better than -30 dB each, ensure clockwise propagation of the light in the feedback loop and prevent from unwanted reflections.

Figure 2 shows experimental measurements of the underlying mode structure of the FOF laser and its dependence on the detuning Δ and the feedback phase C_p. For each panel the pump current of the laser is modulated slowly with ramp and the intensity I_F of the feedback field is monitored. Increasing and decreasing parts of the pump current ramp are shown in each panel of Fig. 2. Small changes of the pump current result in a slight change of the laser frequency and therefore, in a change in the detuning between the center frequency of the filter (which is kept fixed) and the frequency of the solitary laser. Because the modulation frequency and the modulation amplitude is small, other effects can be neglected. First, we concentrate on the effect of changing detuning in Fig. 2(a). There is a maximum in I_F around zero detuning, where the laser frequency coincides with the center frequency of the filter. As the pump current changes the feedback intensity I_F changes discontinuously. Plateaus can be seen where I_F is almost constant, interrupted by sudden jumps. On each plateau the feedback intensity I_F stays almost constant because the FOF laser locks to a stable mode with almost constant frequency; we call this modes external filtered modes (EFMs). When such a mode becomes unstable or disappears the FOF laser jumps to the next adjacent EFM. Approximately 10 EFMs are found when the laser frequency in scanned over the whole filter profile. Due to hysteresis effects the situation for increasing and decreasing pump current differs quantitatively. Figure. 2(b) shows the same situation for slightly increased value of the feedback phase C_p. In particular in can be seen that the plateaus for increasing pump on the left filter flank are shifted downwards slightly, while they are shifted upwards on the right filter flank. The reverse happens for decreasing pump current. This is indicated by the arrows in the individual panels. For increasing changes of C_p the EFMs shift continuously [Fig. 2(b) to (f)]. When C_p has changed by 2π the situation of Fig. 2(a) is retained. Between each panel C_p has changed by approximately $1/3\pi$.

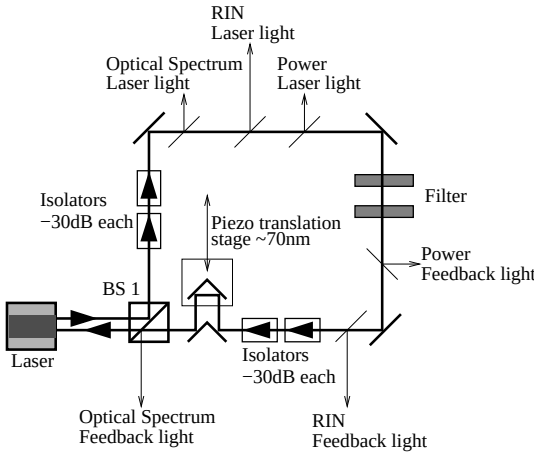

Figure 1: Setup of the FOF laser with the Fabry-Pérot filter, piezo translation stage, optical isolators. The detection for both the laser field and the feedback field consists of scanning Fabry-Pérot interferometer, fast photo diodes, electrical spectrum analyzer, digital oscilloscopes, and slow photo diodes.

We model the FOF laser with a set of rate equations for the complex envelope of the laser field E, the filter field F, and the laser inversion N given by

$$\dot{E} = (1+i\alpha)N(t)E(t) + \kappa F(t,\tau) \quad (1)$$

$$T\dot{N} = P - N(t) - (1+2N(t))|E(t)|^2 \quad (2)$$

$$\dot{F} = \Lambda E(t-\tau)e^{-iC_p} + (i\Delta - \Lambda)F(t)\,. \quad (3)$$

Here $\alpha = 5$ is the self-phase modulation parameter, $\kappa = 0.0001$ the feedback rate, $T = 100$ the electron decay rate, $P = 2.55$ the pump rate, C_p the feedback phase, $\Delta = -0.014$ the filter detuning and $\Lambda = 0.014$ the filter width (HWHM). Note that the detuning is defined

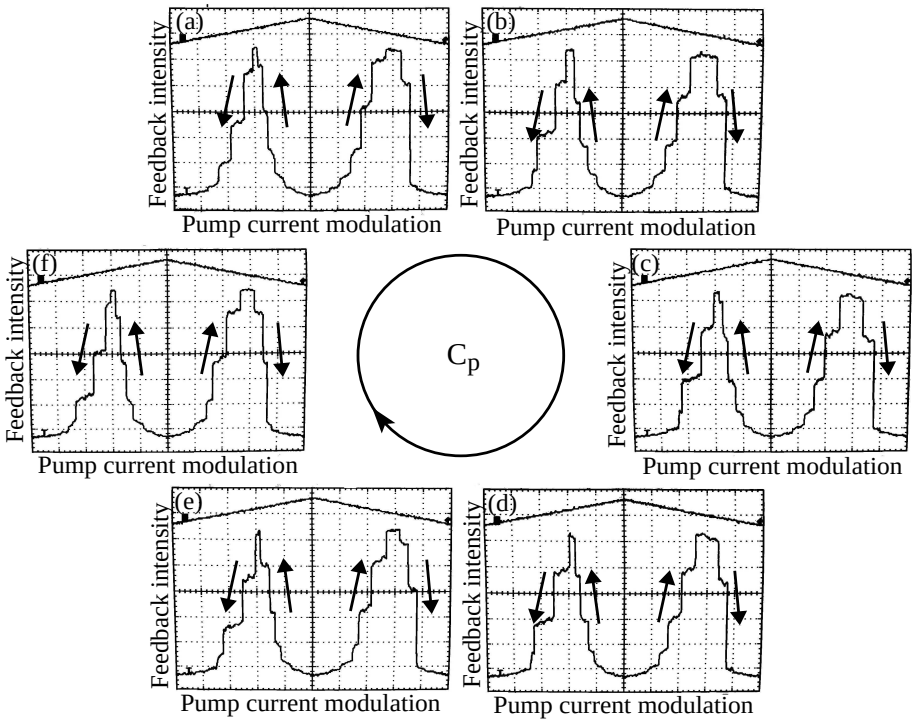

Figure 2: 2π-cycle of the EFMs. Each panel shows the intensity of the feedback light as a function of increasing and decreasing pump current. The pump current was slowly modulated with a triangular ramp, which is shown in the top part of each panel.

as $\Delta = \Omega_F - \Omega_0$, where Ω_0 solitary laser frequency and Ω_F the center frequency of the filter.

The external filtered modes are the basic solution of Eqs. (1)–(3) are CW states, with a frequency deviation ω_s from the solitary laser frequency at threshold. The amplitudes of the laser field $\sqrt{I_L}$ and the filtered feedback field $\sqrt{I_F}$ and the inversion N_s of laser are constant in time. The feedback field may have a constant phase shift ϕ.

$$E(t) = \sqrt{I_L} e^{i\omega_s t}, N(t) = N_s, F(t) = \sqrt{I_F} e^{i\omega_s t + i\phi}. \tag{4}$$

In what follows we use numerical continuation [6] to investigate the structure and stability of the EFMs as a function of the solitary laser frequency Ω_0 and the feedback phase C_p. This is shown in Fig. 3, where in each panel the feedback intensity I_F is plotted as a function of Ω_0, and C_p takes the values indicated in the panels. As Ω_0 is changed, EFMs are born and destroyed in saddle-node bifurcations $(+)$. In particular, the thick curves indicate stable EFMs which can be seen in the experiments. Once a stable EFM is lost in a saddle-node bifurcation (together with an unstable EFM) the FOF laser jumps to the adjacent stable EFM. For each value of Ω_0 more than one stable EFM can be found. This leads to hysteresis effects in for increasing and decreasing Ω_0. Moreover the EFMs change their position as the feedback phase C_p is changed, which is indicated by the arrows in each panel. Indeed in light gray curves of saddle-node bifurcations are plotted, as parameterized by the feedback phase.

In conclusion, we analyzed the external feedback modes of the FOF laser experimentally and theoretically. In particular the experimental design allowed to study the influence of the feedback phase. The experimental results could be reproduced in good agreement

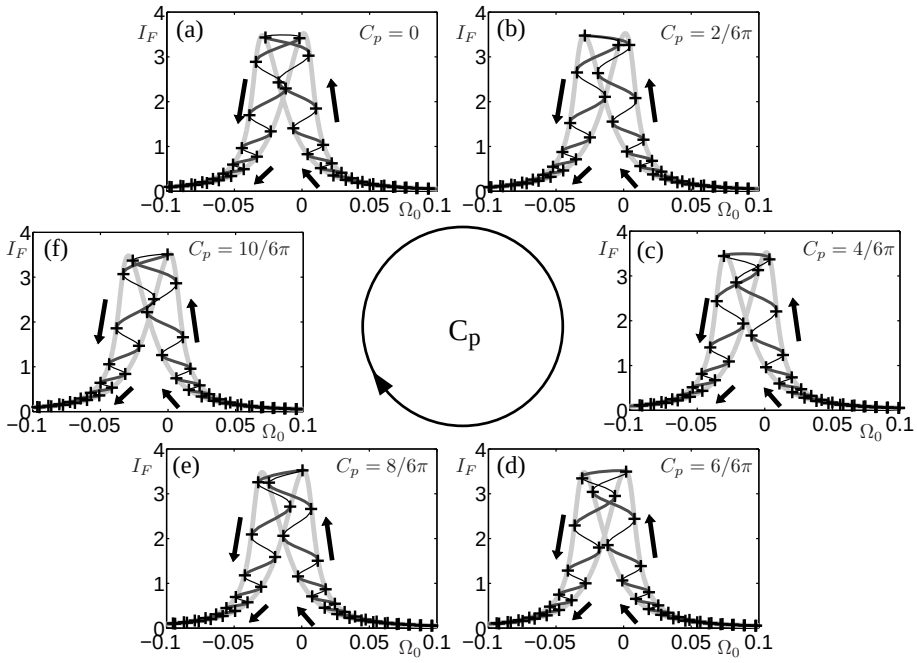

Figure 3: 2π-cycle of the EFMs as computed from Eqs. (1)–(3). Each panel shows the intensity of the feedback light as function of Ω_0. Unstable parts are black, stable parts are dark gray and saddle-node bifurcations are indicated as $(+)$. The light gray line is the saddle-node bifurcation line parameterized by C_p.

by studying a rate equation model. This is the foundation for current experimental and theoretical studies focusing on complex dynamics, for example those arising from Hopf bifurcations of EFMs for higher feedback rates.

References

[1] A. Argyris, D. Syvridis, L. Larger, V. Annovazzi-Lodi, P. Colet, I. Fischer, J. García-Ojalvo, C.R. Mirasso, L. Pesquera, and K.A. Shore. Chaos-based communications at high bit rates using commercial fibre-optic links. *Nature*, 438:343–346, 2005.

[2] M. Peil, I. Fischer, and W. Elsäßer. Spectral broadband dynamics of semiconductor lasers with resonant short cavities. *Phys. Rev. A*, 73:023805, 2006.

[3] O.K. Andersen, A.P.A. Fischer, I.C. Lane, E.M. Louvergneaux, and S. Stolt. Experimental stability diagram of a diode laser subject to weak phase-conjugate feedback from a rubidium vapor cell. *IEEE J. Quantum Electron.*, 35:577–582, 1999.

[4] A.P.A. Fischer, O.K. Andersen, M. Yousefi, S. Stolte, and D. Lenstra. Experimental and theoretical study of filtered optical feedback in a semiconductor laser. *IEEE J. Quantum Electron.*, 36:375–384, 2000.

[5] H. Erzgräber, B. Krauskopf, D. Lenstra, A.P.A. Fischer, and G. Vemuri. Frequency versus relaxation oscillations in a semiconductor laser with coherent filtered optical feedback. *Phys. Rev. E*, 73(5):055201, May 2006.

[6] K. Engelborghs, T. Luzyanina, and G. Samaey. DDE-BIFTOOL v. 2.00 user manual: a matlab package for bifurcation analysis of delay differential equations. Technical Report TW-330, Department of Computer Science, K. U. Leuven, Leuven, oct 2001.

A Biosensor based on Surface Plasmon Interference

P. Debackere, S. Scheerlinck, P. Bienstman, R. Baets

Photonics Research Group, INTEC,
Sint-Pietersnieuwstraat 41, 9000 Gent, Belgium

We propose a new concept for surface plasmon sensing using a surface plasmon interferometer. The high field enhancement of surface plasmons near the metallic interface makes them ideal for use in bio- and chemical sensors where a very small change in refractive index should be detected. To our knowledge this is the first time that the SOI material system has been combined with the SPR technique for sensing purposes. The device is two orders of magnitude smaller than current integrated SPR sensors. We obtain a theoretical limit of detection of 10^{-6} *RIU for a component of length 10* μ*m.*

Introduction

The use of surface plasmon resonance (SPR) for biological and chemical sensing is well established. The high sensitivity of this technique to surface phenomena makes it ideal for use in real-time and label-free biosensors where very small changes in refractive index must be detected. Driven by the vision of a laboratory on a chip and its impact in numerous applications such as detection, biosensing, kinetic and binding studies and point-of-care diagnostics, extensive work has been done to miniaturize SPR biosensors. In the past decade, several integrated optical SPR sensors have been demonstrated [1, 2, 3], in which thin gold films serving as a platform for the attachment of sensing films are deposited on top of an integrated optical waveguide system. However, all integrated SPR sensors that have been investigated so far are fabricated in a material system with a low refractive index contrast, keeping typical dimensions of waveguides and optical components too large for miniaturization and consequent lab on chip applications. Working with a high refractive index material system such as silicon-on-insulator is a more straight-forward approach to meet the requirements for high-level integration and high-throughput fabrication.

Theory

The surface plasmon interferometer is schematically depicted in Fig. 1. The device consists of a gold layer embedded into the silicon membrane on top of a supporting silica layer. Upon reaching the gold-clad layer, a dielectric TM-polarized mode guided by the silicon membrane slab waveguide excites two surface plasmon modes, one at the upper and one at the lower interface of the gold layer. Due to the highly assymetric cladding layers these modes are not coupled. Therefore, their phase velocities are entirely determined by the refractive index of the upper and lower dielectric. At the end of this section, interference of the two surface plasmon modes results in a dielectric mode launched in the output waveguide. This explains the sensing functionality of the interferometer: a change in the refractive index of the medium above the gold layer results in a phase difference between the two surface plasmon modes and consequently, in a change of output intensity. For our simulations, we used an in house-developed eigenmode solver CAMFR [5]. The calculation method consists of a Fourier Modal Method algorithm, which was recently

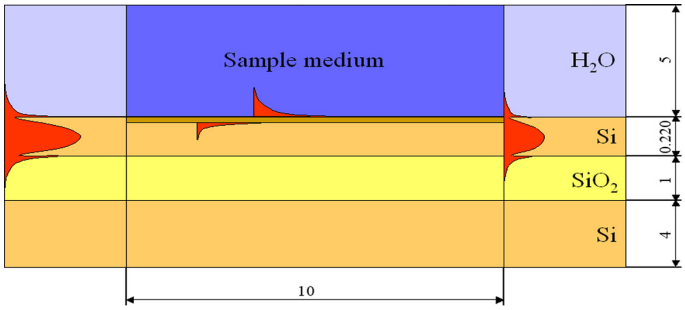

Figure 1: Schematical setup of the proposed structure, all dimension in μm

improved by adding an adaptive spatial resolution at the discontinuity points of the refractive index profile [6], that generates reliable estimates for an eigenmode solver. The reference data for the refractive index of gold was taken from [8].
Fig. 2 illustrates the interferometric nature of our device. For a sensing section of length 10 μm, the transmitted intensity of the fundamental TM mode of the silicon slab waveguide is plotted as a function of refractive index of the sample medium. For this simulation, we have chosen a wavelength of 1.55 μm, which is in the near-infrared region and suitable for biosensing applications. On the bottom of this figure, the phase difference between the two interfering waves is calculated.

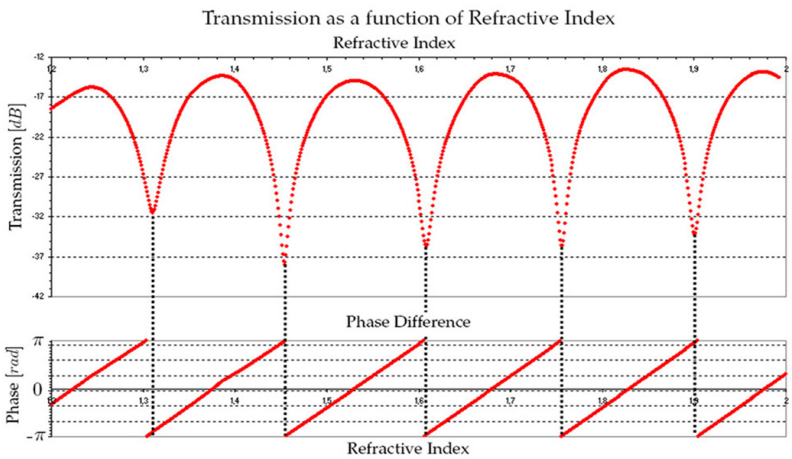

Figure 2: Transmission of the structure depicted in Fig. 1 as a function of refractive index. The length of the structure is 10 μm

Although the theory as outlined above has been presented here for a fixed wavelength and variable refractive index of the sample medium, there is a second, and perhaps more useful, method of using this device. As outlined above, the first method is to use a monochromatic input mode and monitor the output power as a function of the refractive index of the sample. This approach is known as the 'intensity measurement mode'. The second mode of operation uses a broadband input mode and as a function of the refractive index of the sample medium we monitor the position of the spectral minima in the transmission curve. This is the 'wavelength interrogation mode'.
In Fig. 3 we have simulated the response of the structure shown in Fig. 1 to a broadband incoming waveguide mode. The refractive index of the sample medium is fixed at a value of 1.33. This behavior can also be explained by comparing the phase difference between

the internal and the external plasmonmodes as can be seen in the bottom of Fig. 3.

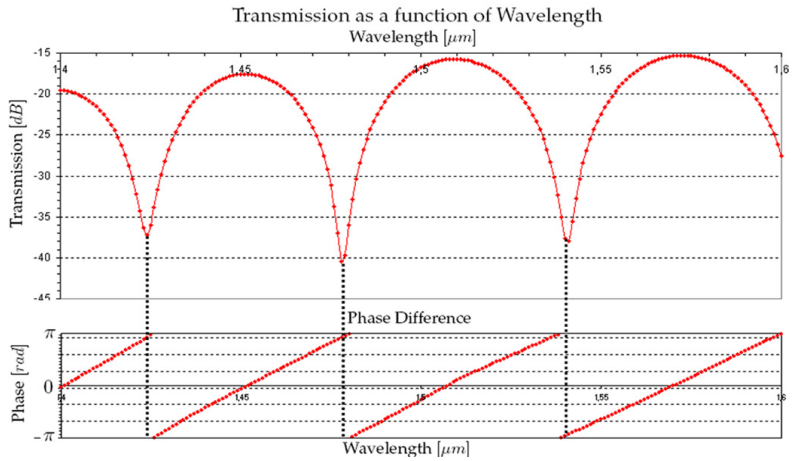

Figure 3: Transmission of the structure as a function of the wavelength, the length of the structure is 10 μm

In both modes of operation a sensor length of approximately 10 μm should suffice, which is two orders of magnitude smaller than current integrated surface plasmon sensors.

Sensitivity of the Device

If we take the intensity measurement approach to detect refractive index changes we can calculate that the sensitivity for this device reaches values of 10000 dB/RIU (refractive index unit). In conjunction with an optoelectronic system which can measure changes in the optical power of 0.01 dB, variations in the refractive index as small as 10^{-6} can be measured. Integrated surface plasmon resonance sensors in low-index contrast material systems typically boast values of 2000 dB/RIU, this corresponds to a detection limit of 5×10^{-6} RIU [3].
Taking the wavelength interrogation approach, sensitivity is defined as the shift of the wavelength for which transmission is minimal as a function of the refractive index of the sample medium ($\Delta\lambda/RIU$). From Fig. 4 one can see that the shift of the wavelength for which transmission is minimal as a function of the refractive index of the sample medium is equal to 463.5 nm per refractive index unit. According to [7] a prism based sensors has a shift of 13800 nm per refractive index unit at 850 nm, an a grating based device has a value of 630 nm per refractive index unit.
In order to demonstrate that our proposed device can detect very thin dielectric layers representative of thin protein layers, we have determined the shift of the wavelength for which the transmission is minimal as a function of the thickness of an adsorbed layer at the *Au*-sample medium interface. In Fig. 5 the adsorbed layer thicknesses varyies from 1 to 400 nm and has a refractive index of 1.34. By inspection of the slope of the curve we can estimate the dependence of the peak position on the layer thickness to be approximately equal to 6 pm/nm. This demonstrates that our device can be used to measure layer thicknesses of absorbed protein layers.

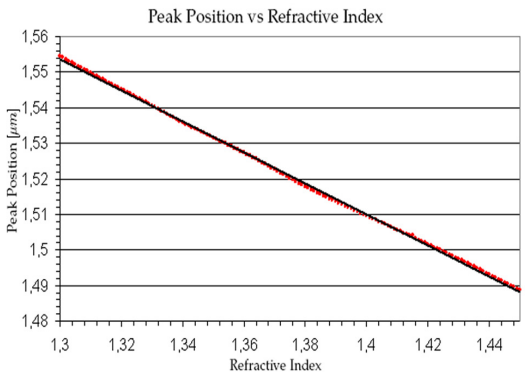

Figure 4: Shift of the resonance wavelength as a function of the refractive index of the sample medium

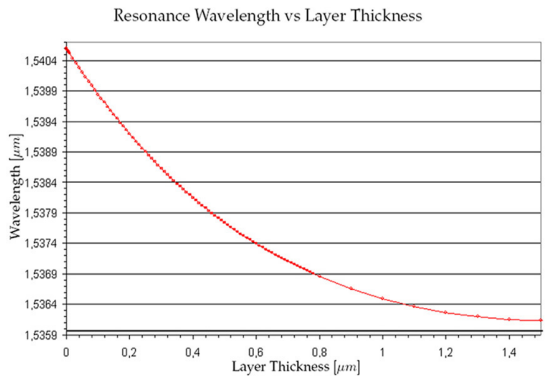

Figure 5: Shift of the resonance wavelength as a function of the thickness of the adsorbed layer

Conclusions

We have presented in this paper a novel concept for a biological sensor using surface plasmon waves. The new device was described from a theoretical point of view, and simulation results show its potential for sensing applications.

Due to its different working principle as compared to other devices, this device has a number of interesting benefits. Firstly, the device is two orders of magnitude smaller than conventional surface plasmon waveguide sensors, due to the integration into a high-index contrast material system. Secondly the device is highly tunable, due to the fact that it is based on interference rather than loss. This makes it an excellent candidate for a vast number of applications. Thirdly, the sensitivity of this device is comparable with that of state-of-the art biological sensors.

The authors believe this novel concept to be an important step toward a fully integrated surface plasmon lab-on-chip solution.

References

[1] Čtyrocký J. *et al*, "Theory and Modelling of Optical Waveguide Sensors Utilising Surface Plasmon Resonance", *Sensors and Actuators B*,**54**, pp. 66 - 73 1999.

[2] Harris Rd, Wilkinson JS, "Waveguide Surface Plasmon Resonance Sensors", *Sensors and Actuators B*,**29**, pp. 261 - 267 (1995)

[3] Homola J, Čtyrocký J, Skalský M, Hradilová J and Kolářová P, "A Surface Plasmon Resonance Based Integrated Optical Sensor", *Sensors and Actuators B*,**38-39**, pp. 286 - 290 (1997)

[4] Debackere P, Scheerlinck S, Bienstman P and Baets R, "Surface plasmon interferometer in silicon-on-insulator: novel concept for an integrated biosensor", *Optics Express*, **14**, pp.7063-7072 (2006)

[5] Bienstman P and Baets R, Optical Modelling of Photonic Crystals and VCSELs using Eigenmode Expansion and Perfectly Matched Layers", *Opt. Quantum Electron* **33**(4–5), pp. 327-341 (2001)

[6] Debackere P, Bienstman P, Baets R, "Improved ASR Convergence for the Simulation of Surface Plasmon Waveguide Modes", *to appear in special issue of Optical and Quantum Electronics on Optical Waveguide Theory and Numerical Modeling*, (2006)

[7] Homola J, Sinclair S and Gauglitz G, "Surface Plasmon Resonance Sensors: Review", *Sens. Actuators B*, **54**, pp. 3-15 (1999)

[8] Handbook of Optical Constants of Solids ,*edited by E. Palik*, Academic Press New York, (1985)

Fabrication of an electro-optic polymer microring resonator

M. Balakrishnan, E. J. Klein, M. B. J. Diemeer, A. Driessen
Integrated Optical Microsystems, MESA+Institute for Nanotechnology, P.O. Box 217, 7500 AE Enschede, The Netherlands.
M. Faccini, W. Verboom, D. N. Reinhoudt
Laboratory of Supramolecular Chemistry and Technology, MESA+Institute forNanotechnology, P.O. Box 217, 7500 AE Enschede, The Netherlands.
A. Leinse
LioniX BV, P.O. Box 456, 7500 AH Enschede, The Netherlands.

A laterally coupled electro-optic polymer microring resonator was designed and fabricated. The design consists of microrings of 200 µm radius with racetrack structures to improve the coupling between the bus waveguide and the ring. Two different fabrication schemes namely reactive ion etching (RIE) and photodefinition are presented. Thermally grown siliconoxide on conducting silicon was used as the bottom cladding. Passive ring resonance behavior has been demonstrated around 1550 nm. The through port response of the ring showed a maximum extinction of about 12 dB and a finesse of 6.

1. Introduction

Microring resonators are promising candidates for very large scale integration photonics. Polymer microring resonators are especially interesting for electro-optic (EO) modulator application in optical communication systems. Ring resonators made of EO polymers have certain advantages over inorganic materials such as $LiNbO_3$ most notably the low microwave/optical velocity mismatch allowing simple design of high speed modulation devices [1]. However, in traveling wave Mach-Zehnder high speed polymer modulators the bandwidth is limited by the loss of the several centimeter long micro-strip line [2]. On other hand in microring modulators, since the device is small the electrode size can be much smaller and as the microwave index of refraction of polymers is ~1.5 the device's high speed behavior is mainly capacitive. Hence, electrode loss is not an issue and the bandwidth is set by the electrode capacitance. In the present work laterally coupled microring resonators have been fabricated in PMMA-DR1 (Polymethylmthacryalate-Disperse red) by RIE and in SU8 (a negative photoresist) by photodefinition. Lateral coupling offers the advantage of a single mask process and allows symmetric coupling avoiding the critical alignment step in the vertically coupled resonators. The coupling between the waveguide and the ring is an important factor which determines the quality factor of the rings. In most of the laterally coupled polymer microring resonators, submicron gaps between the bus waveguides and the ring are required for sufficient coupling. These submicron gap sizes can be achieved by imprinting involving expensive E-beam lithography. In the present work we demonstrate high coupling with the gap sizes of 1 µm to 1.5 µm (which can be easily achieved by contact mask lithography) by having racetrack structures. The coupling is varied by varying the racetrack length and the gap. PMMA-DR1 is used as a test material for the realization of the design. In the final devices PMMA-DR1 will be replaced by SU8-TCVDPA (tricyanovinylidenediphenylaminobenzene) polymer which

can be photodefined utilizing the low UV absorption window of the TCVDPA chromophore [3]. TCVDPA was chosen as it was reported to have the highest photochemical stability among a large number of EO chromophores [4].

2. Device design and fabrication

Microring resonator design was made using PMMA-DR1 as the core material with a refractive index of 1.6 at 1550 nm. Silicon oxide was used as the bottom cladding and the top cladding was VSC (an UV curable epoxy with a refractive index of 1.55 at 1550 nm). The bus waveguides were 2 µm wide and 0.9 µm thick to satisfy the monomodal condition. Because of single mask processing the thickness of the ring was also 0.9 µm. For this configuration the minimum possible ring radius was 200 µm in order that the bending losses in the ring is not more than 1dB/cm. Bending loss, scattering loss, transition losses between the straight and the bend sections of the ring and material loss are the main loss mechanisms in the microring resonator. In general scattering and material losses in microring resonator are much higher and the 1 dB/cm bending loss can be negligible. The simulated transition loss is 0.4 dB per round trip. The length of the racetrack is varied from 20 µm to 240 µm and the gap size is varied form 1 µm to 1.5 µm. In the first scheme inverted ridges were made by photolithography and RIE in thermally grown siliconoxide of 8 µm thickness on conducting silicon. The conductive silicon will serve as the bottom electrode for electro-optic modulation. Silicon oxide was chosen as the bottom cladding instead of a polymer as the gaps of 1 µm can be well defined than in a polymer. PMMA-DR1 was spin coated to fill the inverted ridges. The excess slab height of PMMA-DR1 was etched back to zero by RIE as even the presence of small slab height is detrimental for the bending losses of the ring. A top cladding of VSC was spin coated on top of it. A microscope picture of the fabricated device is shown in figure 1. In the second scheme the SU8 was spin coated on silicon oxide and the structures are made by direct photodefinition. The same mask used in the scheme 1 was used as the refractive index of SU8 is comparable with PMMA-DR1 [3]. Contact lithography was done in Karl süss mask aligner. A top cladding of VSC was applied on top of the SU8 core.

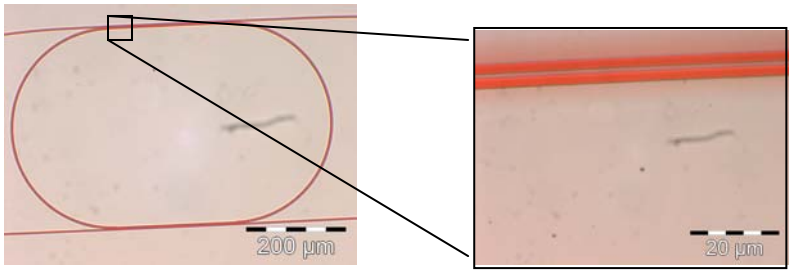

Figure 1: PMMA-DR1 microring resonator fabricated by RIE with a racetrack length of 240µm and a gap of 1 µm

3. Experiments and discussion

The microring devices were tested by coupling TE polarized light from a Erbium doped fiber amplifier (emission from 1530 nm to 1560 nm and 10 mW output power). The outcoupled light was analyzed with a spectrum analyzer. Figure 2 shows the through port response of the PMMA-DR1 microrings with a gap of 1µm for various racetrack

lengths. It can be seen from figure 2 that the extinction ratio increases with the racetrack length up to 160 µm. The highest extinction ratio of 12 dB was seen at a racetrack length of 160 nm. With further increase in racetrack length the power couples back to the bus waveguide and the extinction ratio decreases. This decrease is very rapid with further increase in the racetrack length beyond 160 nm as the power couples back to the bus waveguide and also at very high racetrack lengths the roundtrip losses of the ring becomes a dominant factor.

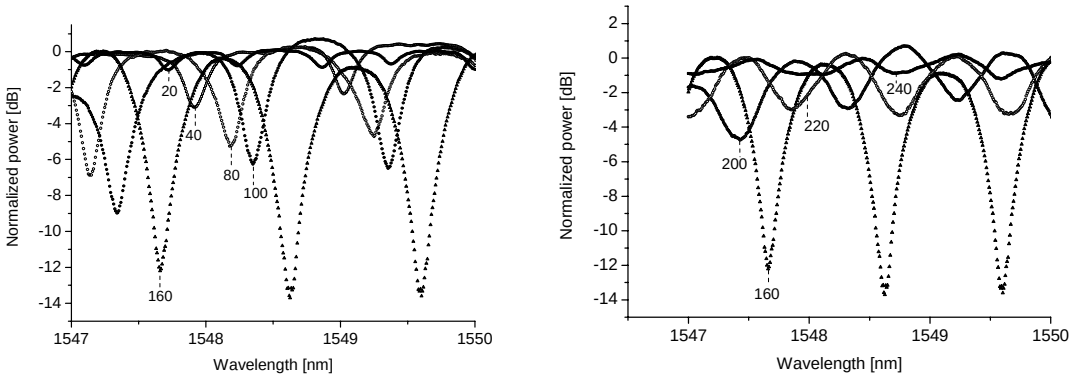

Figure 2: Through port response of PMMA-DR1 microrings of different racetrack lengths for TE polarization (Numbers shown in the graphs are the racetrack lengths in µm)

The quality factor of the resonance was measured for the device with 160 nm racetrack to be 8000 and the finesse was 6. The free spectral range (FSR) varies from 1.1 nm to 0.9 nm as the racetrack length varies from 20 nm to 240 nm. The coupling constants and the ring losses were extracted from the through port response by making a fit using Rfit software. The ring loss is 30 dB/cm. Figure 3 shows the extracted coupling constants as a function of racetrack length for different gap sizes.

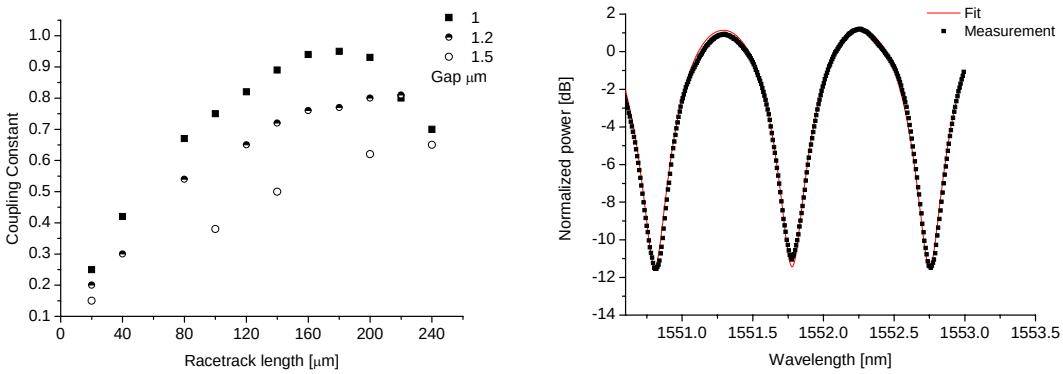

Figure 3: Coupling constants as a function of racetrack length for different gap sizes (left), Through port response of SU8 microring with a racetrack length of 180 nm and a gap of 1.5 µm for TE polarization (right)

It can be seen from the figure 3 (left) that the maximum achievable coupling constant by increasing the racetrack length is limited by the gap size. By further reducing the gap size below 1 μm coupling constant close to about 0.95 can be achieved at a much shorter racetrack length which will reduce the roundtrip losses of the ring and increase the FSR slightly.

Figure 3 (right) shows the through port response of the photodefined ring in SU8. The gap size was 1.5 μm and the race track length was 180 μm. With further optimization of the photodefinition process gaps of less than 1.5 μm can be realized. The coupling constant was found from the fit to be 0.94 and the ring loss is 19 dB/cm. When compared with the PMMA-DR1 rings with 1.5 μm gap high coupling constant is found in the SU8 rings. This is because the refractive index of SU8 is slightly less than that of PMMA-DR1 and hence the mode field expands more into the cladding. Also a reduction in the ring losses of about 10 dB/cm is seen in the photodefined rings possibly because of reduced side wall roughness together with low material absorption loss.

4. Conclusion

Laterally coupled microring resonators were fabricated in an electro-optic polymer (PMMA-DR1) and a passive material (SU8). SU8 can be loaded with TCVDPA chromophore to make it electro-optically active and can be photodefined. The coupling constant was varied by changing the racetrack length and extinction ratio of 12 dB was measured in both the material systems. This looks promising for electro-optic modulator applications.

This research work is supported by the Dutch Technology Foundation STW, Applied Science Division of NWO and the Technology Program of the Ministry of Economic Affairs and carried out within the framework of the project TOE 6067 “Broadband and wavelength selective modulators for optical communication based on electro-optic polymers”

5. References

[1] Y. Shi, C. Zhang, H. Zhang, J. Becthel, L. Dalton, B. Robinson, and W. Steier, “low half voltage polymeric electro-optic modulator achieved by controlling chromophore shape”, Science vol 288, pp 119-122, 2000.

[2] P. Rabiei, H. Steier, C. Zhang and L. R. Dalton, “Polymer microring modulators and filters”, J. of Lightwave technology, vol 20, pp 1968-1975, 2002.

[3] M. Balakrishnan, A. Driessen, M. B. J. Diemeer, M. Faccini, W. Verboom, D. N. Reinhoudt, A. Borreman, and M. J. Gilde, “Channel waveguide definition in electro-optic polymers with a novel chromophore by UV-thermal crosslinking”, Proceedings LEOS Beneulux , pp 76-79, 2004.

[4] A. G. Gonzalez, G. I. Stegeman, A. K. Y. Jen, X. Wu, M. Canva, A. C. Kowalczyk, X. Q. Zhang, and H. Z. Lackritz, “Photostability of electro-optic polymers possessing chromophores with efficient amino donors and cyano containing acceptors”, J. Opt. Soc. Am, B vol 18, pp 1846-1848, 2001.

An integrated transceiver based on a reflective semiconductor optical amplifier for the access network

L. Xu, X.J.M. Leijtens, J.H. den Besten, M.J.H. Sander-Jochem,
T. de Vries, Y.S. Oei, P.J. van Veldhoven, R. Nötzel and M.K. Smit

COBRA Research Institute, Technische Universiteit Eindhoven
Postbus 513, 5600 MB Eindhoven, The Netherlands

In this paper, a reflective transceiver is presented which monolithically integrates a wavelength duplexer, a reflective SOA (RSOA) and a detector. The first characterization shows that the wavelength duplexer obtained better than −15 dB optical isolation between the upstream and downstream signals. The polarization dependence was less than 25% of the 200 GHz (1.6 nm) channel spacing over a 50 nm wavelength range. A 750 µm long RSOA achieved around 20 dB on-chip gain, and a 30 µm long photodetector shows good responsivity of up to 0.25~0.4 A/W within a 50 nm operating range at −2V bias voltage.

Introduction

With the dramatic increase in the number of the subscribers and their demands on the speed and bandwidth capacities, the substitution at the user side of the usual media such as coaxial cable with the optical fiber is inevitable. A transceiver at the user side performs the tasks to transform the data in the download stream carried by the light inside the fiber into electrical information, and to upload the electrical data stream from the user side into the optical information suitable for the fiber transmission. The performance and cost of the transceiver will directly influence the whole system deployment. Previous research has demonstrated up to 1.25 Gbit/s transceiver (ONU) for the download and upload streams by using discrete components: a wavelength duplexer, a laser[1] or a RSOA[2] as transmitter, and a photodetector.

However, due to the cost, it is not practical to deploy such a transceiver with discrete components at the user side. In this paper, we present a reflective transceiver which monolithically integrates the above discrete components within one chip, fig. 1. This device is designed for the Dutch Broadband Photonics project, in which the wavelengths are dynamically allocated. The wavelengths which will carry the data are assigned by the local exchange, according to the network requirements. Therefore the transceiver has to be wavelength agnostic. We chose to use a RSOA as a transmitter, because in that way the wavelength is specified by the local exchange and modulated and reflected at the user side.

The module works with two wavelengths (λ_1 and λ_2) spaced 200 GHz coming from the network into the transceiver, where they will be separated by the wavelength duplexer and guided to the photodetector (λ_1) and the RSOA modulator (λ_2). The downstream data, carried by λ_1, is detected by the photodetector, while λ_2 is a continuous wave (CW) light

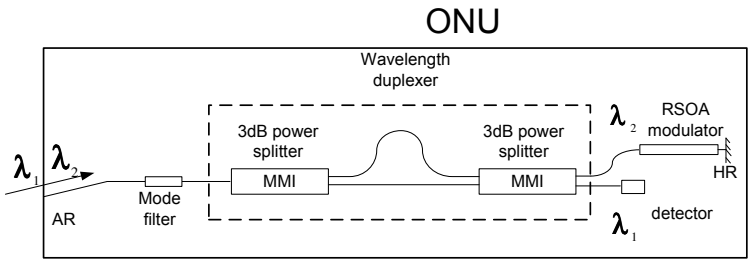

Figure 1: Integrated transceiver consisting of a wavelength duplexer, a reflective SOA modulator and a detector.

and is guided to the RSOA where it is modulated, amplified and reflected back to the network. The RSOA is realized by applying a high reflectivity coating (HR) at the one side of the chip. To avoid lasing, the other facet of the chip, where the light is coupled into and out of the device, is provided with an anti-reflection coating (AR). An angled input waveguide and a mode filter are used to further minimize the reflections from that facet. The wavelength duplexer is designed to be polarization insensitive by proper waveguide geometry design. The detailed modeling and simulation of the layers, waveguides, mode filter, and MMI can be found in [3]. The modulation of the upstream data is carried out by changing the driving current of the RSOA. The photodetector and the RSOA in this device share the same PIN layer structure, but work under the different bias conditions.

Fabrication and characterization of the transceiver

The material we used is grown on an N-type InP substrate by a three-step low pressure metal-organic-vapor-phase epitaxy (MOVPE) at 625 °C. The SOA active layer consists of 120 nm thick Q1.55 ($\lambda_{gap} = 1.55\,\mu$m) InGaAsP layer embedded between two quaternary confinement layers. The structure was covered by a 200 nm thick p-InP layer. Next, the active sections were defined by lithography and reactive ion etching (RIE) using a SiN_x layer as etching mask. In the second epitaxy step, a Q1.25 InGaAsP layer was selectively grown for the passive sections with the SiN_x mask protecting the active sections[4]. In the third epitaxy step, a 1300 nm thick p-InP cladding layer and p-InGaAs contacting layer were grown.

In the transceiver, all access waveguides, photodetector and RSOA are shallowly etched, 100 nm into the Q1.25 film layer by RIE, to minimize the transmission loss and the surface recombination. The multimode interference couplers (MMIs) and the 1.5 μm-wide Mach-Zehnder arms are etched completely through the waveguiding layer, giving stronger lateral confinement to allow for smaller radii and better fabrication tolerance for the MMIs. Polyimide was spun for passivation and planarization. By etching back the polyimide, the Ti/Pt/Au metal can be evaporated on the p-InGaAs contact layer to form the electrodes on the top and the ground (n-InP) at the backside. After annealing and cleaving, the chip was soldered on a copper chuck with a Peltier cooler for the characterization.

The first measurement was done on the duplexer, and the results are shown in fig. 2. The vertical axis shows the transmission of the duplexer, normalized to a deeply etched straight waveguide. The isolation between two datastreams is better than 15 dB. The measured channel spacing between the downstream and upstream wavelength is about 205 GHz.

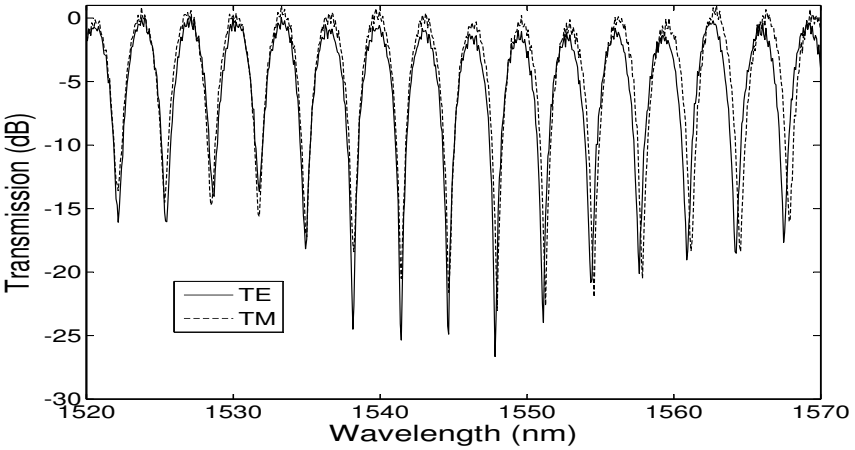

Figure 2: A polarization independent wavelength duplexer

The peak transmission shift between TE and TM polarized light is less than 25% of the 200 GHz (1.6 nm) channel spacing, within the range of 1520 nm to 1570 nm.

To obtain high gain and high signal extinction ratio, the RSOA preferably works at high injection current, but below the lasing threshold. The size of the measured RSOA is 750 μm long and 2 μm wide. The HR facet has 99% reflectivity, and the AR facet at the input side has 0.1% reflectivity. With these values, the lasing threshold of the RSOA was predicted to be around 150 mA through rate-equation-based modeling, while the measured value was about 100 mA. The cause of this discrepancy is the residual reflections. The influence of these residual reflections, together with a heating effect, was also observed on the gain curve which bends at higher injection current near to lasing threshold, as is shown in fig. 3. Several reflection cavities between active-passive butt-joints and facets are observed by analyzing a high resolution optical spectrum with a Fourier transformation[5]. In a next design, residual reflections will be further suppressed by angling the waveguides entering the active material[4], and using adiabatic curves to avoid possible reflections at waveguide junctions.

The modulation speed of the RSOA is limited mostly by the spontaneous carrier lifetime which is shortened with higher injection current. For an InP based SOA the carrier lifetime is on the order of hundreds of picoseconds, thus corresponding to GHz modulation rates.

The photodetector has the same layer structure as the RSOA, but works under reverse bias. We fabricated detectors with lengths ranging from 30 μm to 60 μm. Here we present the measurements of the 30 μm-long and 2 μm-wide detector. The dark current of the photodetector is less than 50 nA at -5 V reverse bias voltage. The measured responsivity, shown in fig. 4, is up to 0.25~0.4 A/W (corresponding to 60%~90% internal quantum efficiency if the fiber chip coupling loss is estimated at -4.3 dB) in operating range at -2 V bias. The estimated bandwidth for this detector is up to 25 GHz based on RC and carrier transit time calculation.

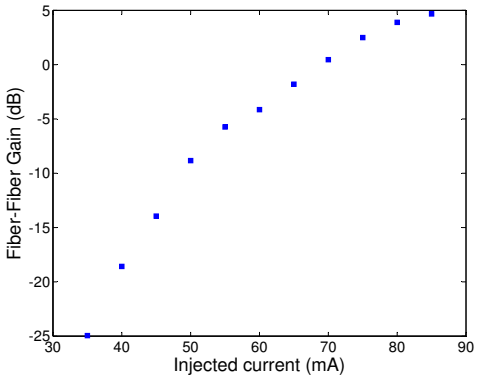

Figure 3: Measured device gain increased with the injection current for $\lambda_{peak} = 1523.6$nm, and $P_{optin} = -15$ dBm.

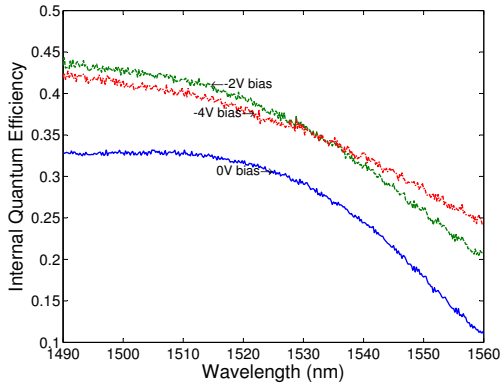

Figure 4: Responsivity of a 30 μm long detector as a function of the wavelength at different reverse-bias voltages.

Conclusion

In this paper, we realized a first integrated transceiver with a wavelength duplexer, a RSOA modulator and a photodetector. It gives better than 15 dB isolation between downstream and upstream data, and a polarization dependence smaller than 25% of the 200 GHz (1.6 nm) channel spacing within 50 nm wavelength range, over 5 dB fiber-fiber gain at 85 mA injection current, and a good responsivity for a 30 μm-long photodetector, 0.25~0.4 A/W at -2 V reverse bias.

This work is partly funded by the Dutch National Broadband Photonics Access project.

References

[1] J. Endo, M. Nakamura, Y. Umeda, and Y. Akatsu, “1.25 Gbit/s optical transceiver with high sensitivity and high speed response for GE-PON systems,” in *2005 Conference on Lasers and Electro-Optics (CLEO)*, 2005, pp. 1496–1497.

[2] J. Prat, C. Arellano, V. Polo, and C. Bock, “Optical network unit based on a bidirectional reflective semiconductor optical amplifier for fiber-to-the-home networks,” *IEEE Photon. Technol. Lett.*, vol. 17, no. 1, pp. 250–252, Jan. 2005.

[3] L. Xu, X. Leijtens, M. Sander-Jochem, Y. Oei, and M. Smit, “Modeling and design of a high-speed reflective transceiver for the access network,” in *Proc. IEEE/LEOS Symposium (Benelux Chapter)*. Mons, Belgium, Dec. 2005, pp. 137–140.

[4] Y. Barbarin, E. Bente, C. Marquet, E. Leclère, T. de Vries, P. van Veldhoven, Y. Oei, R. Nötzel, M. Smit, and J. Binsma, “Butt-joint reflectivity and loss in InGaAsP/InP waveguides,” in *Proc. 12th Eur. Conf. on Int. Opt. (ECIO ’05)*. Grenoble, France, April 6–8 2005, pp. 406–409.

[5] D. Ackerman, L. Zhang, L.-P. Ketelsen, and J. Johnson, “Characterizing residual reflections within semiconductor lasers, integrated sources, and coupling optics,” *IEEE J. Quantum Electron.*, vol. 34, no. 7, pp. 1224–1230, July 1998.

Dual-Channel Approach to Photonic Modulators in Silicon-on-Insulator Technology

V. M. N. Passaro, F. De Leonardis °, and F. Dell'Olio

Photonics Research Group, Dipartimento di Elettrotecnica ed Elettronica, Politecnico di Bari, via Edoardo Orabona n. 4, 70125 Bari, Italy

° Dipartimento di Ingegneria dell'Ambiente e per lo Sviluppo Sostenibile, Politecnico di Bari, viale del Turismo n. 8, 74100 Taranto, Italy

The well-known main methods to modulate the refractive index in silicon-based waveguides are the thermo-optic effect and the plasma dispersion effect. The latter is much faster, allowing modulation frequencies of the order of gigahertz and it is used to change both the real refractive index and optical absorption coefficient. In this paper, we analyze an improved architecture of a depletion-type device for varying the refractive index of Silicon-on-Insulator waveguides by using a four terminal p-n junction diode. The modeling and design of an optimized architecture of depletion-type photonic modulator in silicon-on-insulator is presented and discussed. Highly compact structure is demonstrated by using a novel interferometer dual-channel approach.

Device structure

Nowadays, there is an increasing interest in Silicon Photonics [1], in particular for silicon modulators [2]. For instance, Fig. 1(a) illustrates the device structure presented in literature by Gardes et al. [3]. It is a depletion-type vertical optical phase modulator integrated in a low loss Silicon-on-Insulator (SOI) rib waveguide. The device has an asymmetrical p-n structure where two slab n^+ silicon regions work as a common cathode and two p^+ polysilicon regions are joined as a common anode (four terminals). Both n^+ and p^+ regions are modeled as highly doped regions with peak doping concentrations of 1×10^{19} ion/cm^3. The optimized structure is based on a silicon thickness of 0.45 μm, etched rib waveguide 0.415 μm wide and a slab thickness of 0.1μm. The silicon slab and the bottom part of the rib have an n-type background doping concentration of 4×10^{17} ion/cm^3 and the top part of the rib has a p-type uniform doping concentration of 2×10^{17} ion/cm^3 (uniform profile, see Fig. 1a). The oxide thickness is chosen to be 1μm which ensures good optical confinement and a top silicon oxide cladding layer covers the whole structure.

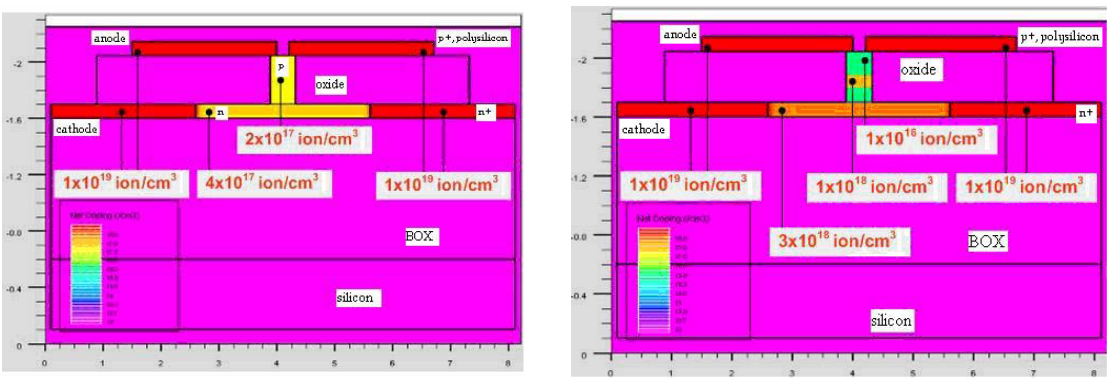

(a) (b)

Fig. 1. (a) Cross section of structure by Gardes et al. [3] and (b) modified structure of this paper.

The n^+ doped regions are situated on both sides of the wave guiding region, in the slab, 1.5 μm away from the centre of the waveguide. In general, the design was optimized in order to achieve birefringence free propagation (equal effective index for quasi-TM and quasi-TE waves in the rib), single mode condition, optimum value and positioning of *n*-type and *p*-type doping, maximum bandwidth and minimum losses. In particular, the rib width has a direct influence on the capacitance of the device, as the p-n junction is situated in the rib of the waveguide, so diminishing the rib width reduces the relevant capacitance.

Moreover, Fig. 1(b) shows the modified structure investigated in this paper. Although the four terminal approach and all sizes are the same as before, the doping profile inside the rib has been modified by including a peak *p*-type doping at center ($1x10^{18}$ ion/cm^3 over 75 nm) and reducing the *p*-type doping in the rest of the rib ($1x10^{16}$ ion/cm^3 over 110 nm at the rib top and over 165 nm at rib bottom), and increasing the *n*-type doping inside the silicon slab ($3x10^{18}$ ion/cm^3). By this doping profile, a reduction of carrier absorption inside the rib, an increase of index modulation due to stronger changes of free carrier concentrations, and an increase of breakdown voltage larger than 10 V can be simultaneously achieved together with the other advantages already mentioned (single mode, birefringence free). These results are obtained without inducing any optical loss increase, given by 2 dB/cm for 0V and 1 dB/cm for 10V of bias voltage.

The importance of this modified structure is clear when we consider the device as inserted in both arms of a 1x1 Mach Zehnder (MZ) interferometer. In Fig. 2(a) the push-pull MZ interferometer is sketched by using the depletion device of Fig. 1(a). Here four phase shifters of the same geometry are required, two of them represent the AC depletion devices, the next two are DC phase shifters and bias the device by introducing a static π-phase shift in one arm. The length of a depletion phase shifter was calculated to be 2.5 mm in order to achieve a π-phase shift when a reverse bias of 10V is applied [3]. Then, a total length of about 5 mm was obtained. In Fig. 2(b) the MZ interferometer is sketched as modified by including the device structure of Fig. 1(b) in the right arm and the same structure of Fig. 1(a) in the left arm (named as *dual-channel approach*). Each phase modulator is 2.52 mm long. The ”OFF state” is achieved by driving the AC modulator on the left at a reverse bias of 3 V and the AC modulator on the right at 4 V: this enables destructive interference at the output. The ”ON state” corresponds to AC modulators having a bias of 10V (on the left) and 0V (on the right) respectively, allowing constructive interference. Since the interferometer can be achieved by using only two AC modulators, the MZ total length should be significantly reduced.

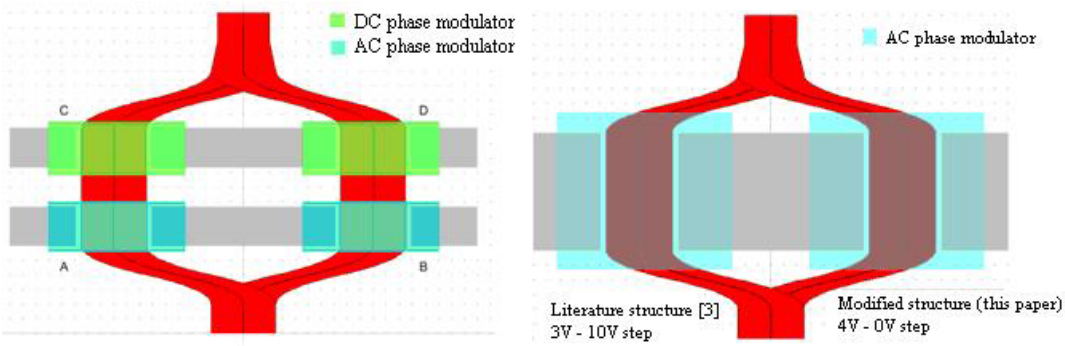

(a) (b)

Fig. 2. (a) Structure by Gardes et al. [3] and (b) dual-channel interferometer architecture.

Device modeling

The device has been electrically modeled for both its static and dynamic behavior using a commercial simulation package [4], by solving the equations which describe the semiconductor physics such as Poisson's equation and charge continuity equations for holes and electrons. This approach has been used to find the free carrier concentrations in the wave-guiding region of the device for both DC and transient biasing conditions. From those concentrations, both refractive index and absorption coefficient changes have been evaluated by using the well known Soref's equations [5]. Fig. 3 shows the refractive index change versus position along the rib for both structures (uniform and modified doping profile), respectively. An index change larger up to six times than that provided in [3] is so demonstrated.

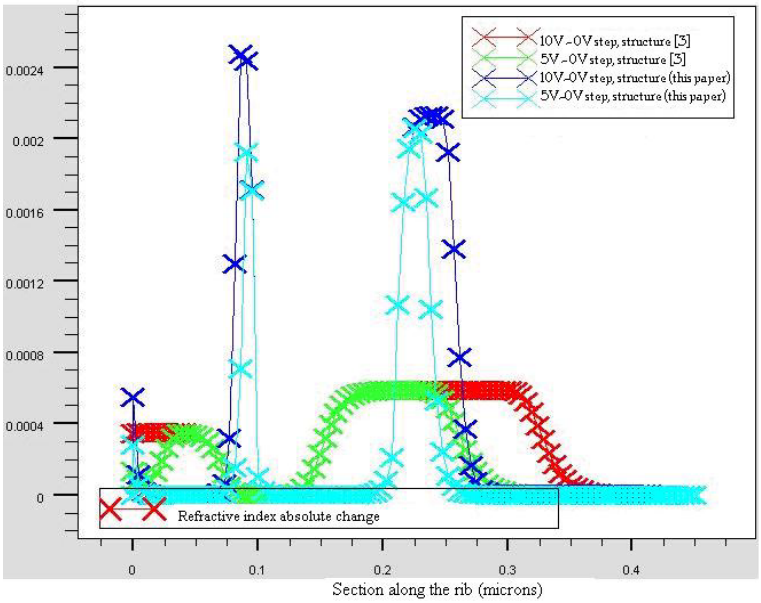

Fig. 3. Refractive index change versus rib position for both structures.

However, a very moderate increase of absorption is revealed by simulations, so keeping still low the losses.

The device has been optically modeled using the full-vectorial beam propagation method [6] at the wavelength of 1.55μm. By considering the refractive index change provided by the electrical simulation of the free carrier distribution in the p-n device, as in Fig. 3, it is possible to predict the effective index change of the waveguide for different applied voltages. The same approach has been used to characterize the phase shift against transient time, i.e. the device dynamic operation.

Fig. 4(a) shows the phase shift as a function of applied voltage achieved for the two polarizations, quasi-TE or quasi-TM, using the modified structure. Then, a phase shift of 172° for quasi-TE or 225° for quasi-TM can be obtained by applying 10 V over a simple phase shifter 2.5 mm long.

Moreover, in Fig. 4(b) the phase switch is sketched versus transient time for dual-channel MZ device, 2.52 mm long, biased in OFF-ON-OFF state for both polarizations. This dynamic study clearly gives a switching time of 8 ps and, then, a device bandwidth of about 60 GHz.

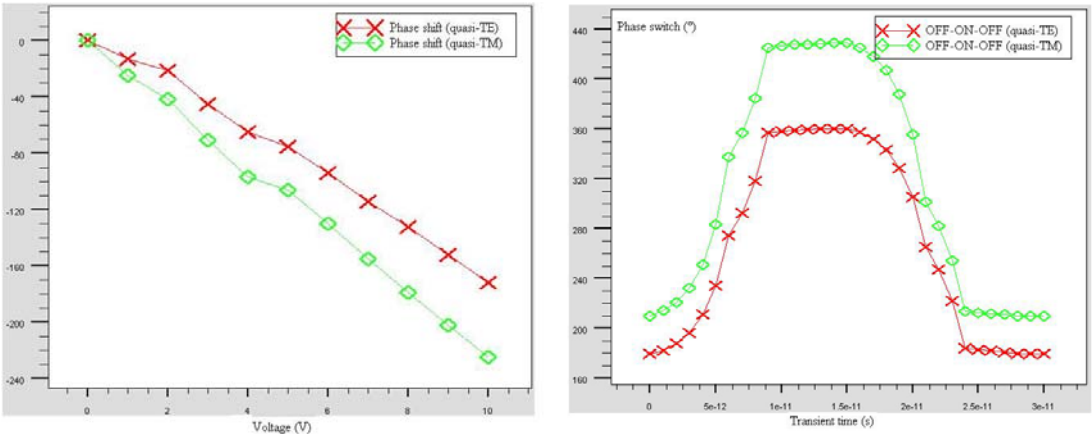

(a) (b)

Fig. 4. (a) Phase shift versus applied voltage and (b) dual-channel MZ phase switch versus transient time.

Conclusion

In this paper we have investigated an optimized architecture of a 2.52 mm long optical modulator based on a p-n junction integrated in a SOI rib waveguide for 1.55μm operation wavelength. The refractive index and the absorption coefficient of the rib waveguide are changed using the free carrier dispersion effect via depletion of a p-n junction. The doping profile inside the rib has been modified in order to achieve very large refractive index change (up to six times than in the uniform profile used in literature) and, then, large phase shifts while keeping low the absorption coefficient changes and the relevant losses. By using this optimized structure in one arm of a Mach-Zehnder interferometer and the uniform doping structure in the other arm (dual-channel approach), high performance and highly compact device has been theoretically demonstrated, including a length of about 2.52 mm, low switching time (8 ps instead of 7 ps) and large bandwidth, about 60 GHz.

References

[1] G. T. Reed, “The optical age of silicon”, Nature, vol. 427, pp. 595-596, 2004.

[2] G. T. Reed, C. E. Png, “Silicon Optical Modulators”, Materials Today, vol. 8, pp. 40-50, 2005.

[3] F.Y. Gardes, G.T. Reed, N.G. Emerson, C.E. Png, “A sub-micron depletion-type photonic modulator in silicon on insulator”, Opt. Express, vol. 13, pp. 8845-8854, 2005.

[4] ATLAS by Silvaco International Corporation, ver. 4.3.0.r, single license, 2004.

[5] R. A. Soref, B. R. Bennett, “Kramers-Kronig analysis of E-O switching in silicon”, Proc. SPIE, vol. 704, pp. 32-37, 1986.

[6] OptiBPM by Optiwave Corporation, ver. 7.0, single license, 2005.

Modeling of an All-Optical Raman Modulator in Silicon-on-Insulator Technology

F. De Leonardis and V. M. N. Passaro °

Dipartimento di Ingegneria dell'Ambiente e per lo Sviluppo Sostenibile, Politecnico di Bari, viale del Turismo n. 8, 74100 Taranto, Italy

° Photonics Research Group, Dipartimento di Elettrotecnica ed Elettronica, Politecnico di Bari, via Edoardo Orabona n. 4, 70125 Bari, Italy

The high Raman gain and small mode area in Silicon-on-Insulator (SOI) rib waveguides make the Stimulated Raman Scattering observable over the millimetre-scale interaction length, usually encountered in integrated optical devices. In this paper, we propose the theoretical study and simulation of a novel all-optical intensity modulator based on Raman effect in SOI rib waveguide, as an all-optical signal processing device highly suitable for high speed systems in order to avoid the usual bottlenecks associated with electrical-to-optical and optical-to-electrical signal conversion. Some numerical examples are given to show the device principle of operation.

Modulator architecture

The architecture of the integrated all-optical intensity modulator is shown in Fig. 1.

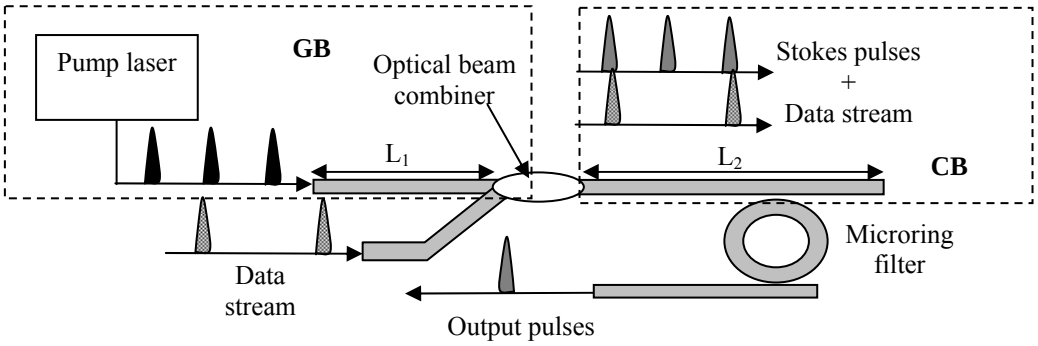

Fig. 1. Architecture of the all-optical Raman intensity modulator.

Two different blocks can be recognized, the generation block (GB), where a pump signal is launched into the SOI rib waveguide travelling over a length L_1, and a cancellation block (CB). If the pump power is large enough, a Stokes pulse is generated via Stimulated Raman Scattering (SRS). When a data stream is introduced at the optical beam combiner, the power transfer from the data to the Stokes pulses occurs if the pulses are quasi velocity-matched. Since the power transfer occurs if a space-time overlap between data and Stokes pulses is verified, the Stokes pulse will erase only the matched data pulse, selected in the cancellation block (CB) of length L_2. Finally, a selective Bragg grating or microring filter is used to extract at the output only the modulated data signal. Although this principle of operation is similar to that already presented in literature [1], here it is investigated in a totally integrated optical silicon architecture.

Since the cancellation is due to an all-optical power transfer mechanism between different optical pulses, the usual hypothesis of quasi-continuous wave operation cannot be used. In fact, it applies for experimental investigation in SOI waveguides where the

pump pulses have a full wave half maximum time width $T_{FWHM} \geq$ 1 ns, the walk-off length L_w generally exceeding the waveguide length L. However, for ultrashort pulses with $T_{FWHM} < 10$ ps, typically it holds $L_w \leq L$. SRS is then limited by the group-velocity mismatch and occurs only over distances $z \sim L_w$ even if the actual waveguide length L is considerable larger than L_w. At the same time, the nonlinear effects such as self phase modulation (SPM) and cross phase modulation (XPM) can become important and affect the evolution of both pump and Raman pulses. Thus, in this situation the time derivative cannot be neglected and appropriate numerical techniques are necessary to solve the partial differential equation system governing the mutual interaction among Stokes, pump and data pulses..

Modeling and numerical results

The goal of the proposed modeling is to include all nonlinear effects involved in the SOI device in a general and self-consistent formalism. In particular, in both GB and CB we have considered Raman effect (generation of the fundamental, first and second order Stokes waves), walk-off effect, SPM and XPM induced by Kerr effect, two photon absorption (TPA), plasma dispersion and free carrier absorption (FCA) induced by TPA. It is worth to note that the TPA effect is generated only by the pump pulse in GB, while TPA is produced in CB by the combination of the residual pump, data stream pulse and fundamental Stokes wave. Therefore, the model is constituted by a rate equation for the time dynamics of TPA generated free carriers and by a system of partial differential equations in time and space domains, written in GB section as:

$$
\begin{cases}
\frac{\partial A_p}{\partial z} + \beta_{1p}\frac{\partial A_p}{\partial t} + j\frac{1}{2}\beta_{2p}\frac{\partial^2 A_p}{\partial t^2} = -\frac{\left(\alpha_p^{(prop)} + \alpha_p^{(FCA)}\right)}{2}A_p - 0.5\beta^{(TPA)} f_{p,p}\left|A_p\right|^2 A_p + j\gamma_{p,p}\left|A_p\right|^2 A_p + \\
+ j2\gamma_{p,s0}\left|A_{s0}\right|^2 A_p + j\frac{2\pi}{\lambda_p}\Delta n_p A_p - \frac{1}{2}g_R\frac{\omega_p}{\omega_{s0}} f_{p,s0}\left|A_{s0}\right|^2 A_p \\
\frac{\partial A_{s0}}{\partial z} + \beta_{1,s0}\frac{\partial A_{s0}}{\partial t} + j\frac{1}{2}\beta_{2,s0}\frac{\partial^2 A_{s0}}{\partial t^2} = -\frac{\alpha_{s0}^{(prop)}}{2}A_{s0} - \frac{1}{2}\alpha_{s0}^{(FCA)}A_{s0} - \beta^{(TPA)} f_{s0,p}\left|A_p\right|^2 A_{s0} + j2\gamma_{s0,p}\left|A_p\right|^2 A_{s0} + j\gamma_{s0,s0}\left|A_{s0}\right|^2 A_{s0} \\
+ j\frac{2\pi}{\lambda_{s0}}\Delta n_{s0} A_{s0} + \frac{1}{2}g_{R,s0} f_{s0,p}\left|A_p\right|^2 A_{s0} - \frac{1}{2}g_{R,s0} f_{s0,s1}\left|A_{s1}\right|^2 A_{s0} \\
\frac{\partial A_{s1}}{\partial z} + \beta_{1,s1}\frac{\partial A_{s1}}{\partial t} + j\frac{1}{2}\beta_{2,s1}\frac{\partial^2 A_{s1}}{\partial t^2} = -\frac{\alpha_{s1}^{(prop)}}{2}A_{s1} - \frac{1}{2}\alpha_{s1}^{(FCA)}A_{s1} - \beta^{(TPA)} f_{s1,p}\left|A_p\right|^2 A_{s1} + j2\gamma_{s1,s0}\left|A_{s0}\right|^2 A_{s1} + j2\gamma_{s1,p}\left|A_p\right|^2 A_{s1} \\
+ j\gamma_{s1,s1}\left|A_{s1}\right|^2 A_{s1} + j\frac{2\pi}{\lambda_{s1}}\Delta n_{s1} A_{s1} + \frac{1}{2}g_{R,s1} f_{s1,s0}\left|A_{s0}\right|^2 A_{s1} - \frac{1}{2}g_{R,s1} f_{s1,s2}\left|A_{s2}\right|^2 A_{s0} \\
\frac{\partial A_{s2}}{\partial z} + \beta_{1,s2}\frac{\partial A_{s2}}{\partial t} + j\frac{1}{2}\beta_{2,s2}\frac{\partial^2 A_{s2}}{\partial t^2} = -\frac{\left(\alpha_{s2}^{(pt)} + \alpha_{s2}^{(FCA)}\right)}{2}A_{s2} - \beta^{(TPA)} f_{s2,p}\left|A_p\right|^2 A_{s2} + j2\gamma_{s2,s1}\left|A_{s1}\right|^2 A_{s2} + j\gamma_{s2,s2}\left|A_{s2}\right|^2 A_{s2} + \\
+ j2\gamma_{s2,p}\left|A_p\right|^2 A_{s2} + j2\gamma_{s2,s0}\left|A_{s0}\right|^2 A_{s2} + j\frac{2\pi}{\lambda_{s2}}\Delta n_{s2} A_{s2} + \frac{1}{2}g_{R,s2} f_{s2,s1}\left|A_{s1}\right|^2 A_{s2} \\
\frac{\partial A_{s2}}{\partial t} + j\frac{1}{2}\beta_{2,s2}\frac{\partial^2 A_{s2}}{\partial t^2} = -\frac{\left(\alpha_{s2}^{(pt)} + \alpha_{s2}^{(FCA)}\right)}{2}A_{s2} - \beta^{(TPA)} f_{s2,p}\left|A_p\right|^2 A_{s2} + j2\gamma_{s2,s1}\left|A_{s1}\right|^2 A_{s2} + j\gamma_{s2,s2}\left|A_{s2}\right|^2 A_{s2} + \\
+ j2\gamma_{s2,p}\left|A_p\right|^2 A_{s2} + j2\gamma_{s2,s0}\left|A_{s0}\right|^2 A_{s2} + j\frac{2\pi}{\lambda_{s2}}\Delta n_{s2} A_{s2} + \frac{1}{2}g_{R,s2} f_{s2,s1}\left|A_{s1}\right|^2 A_{s2}
\end{cases}
$$

Moreover, it is clear that the model involves five partial differential equations in CB section, for residual pump, data pulse, fundamental Stokes pulse, first and second order Stokes waves. They are similar to the previous ones and are not reported here.

The main design criteria selected for our device have been absence of any birefringence in nano-scale SOI rib waveguide for the fundamental Stokes wave and no excitation of higher order Stokes waves in both GB and CB sections. As an example, by assuming a pump pulse at λ_p = 1.4332 μm, the condition of free polarization for the fundamental Stokes wave (λ_{s0} = 1.5487 μm) can be obtained using a SOI waveguide with a rib total height H = 500 nm, a slab height H_s =150 nm and rib width W = 396 nm [2]. Other numerical parameters were $T_{FWHM} = 100$ ps for both pump and data pulses (1.67 Gb/s pulse rate in this case), and Raman gain $g_R = 10.5$ cm/GW. Then, the excitation of higher order Stokes waves in GB is avoided assuming a peak pump power $P_0 = 1.5$ W and a waveguide length $L_1 = 10$ mm. Fig. 2 shows the time-space evolution of data pulse in CB, with the cancellation by the fundamental Stokes pulse (see also Fig. 3).

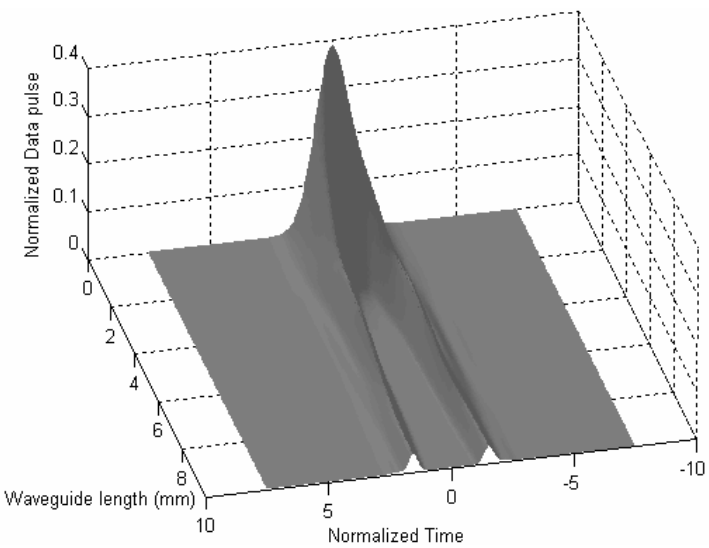

Fig. 2. Time-space evolution of data pulse in CB section.

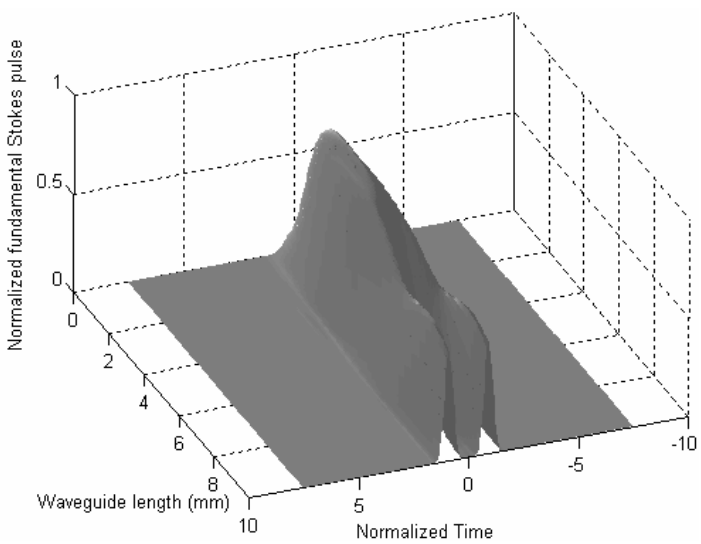

Fig. 3. Evolution of fundamental Stokes pulse in CB section.

The high cancellation rate essentially depends on the relative high level of the Stokes wave at the input of CB, as a result of the amplification process in GB. In Fig. 3 it is

visible a depletion effect of the fundamental Stokes wave as induced by the building up of the first order Stokes wave (given in Fig. 4). Then, the waveguide length can be set to $L_2 = 4$ mm in order to avoid the excitation of higher order Stokes waves. Finally, Fig. 5 shows an example of signature operation on the data stream, the cancellation inducing secondary lobes which are 5 dB down with respect to the data pulse.

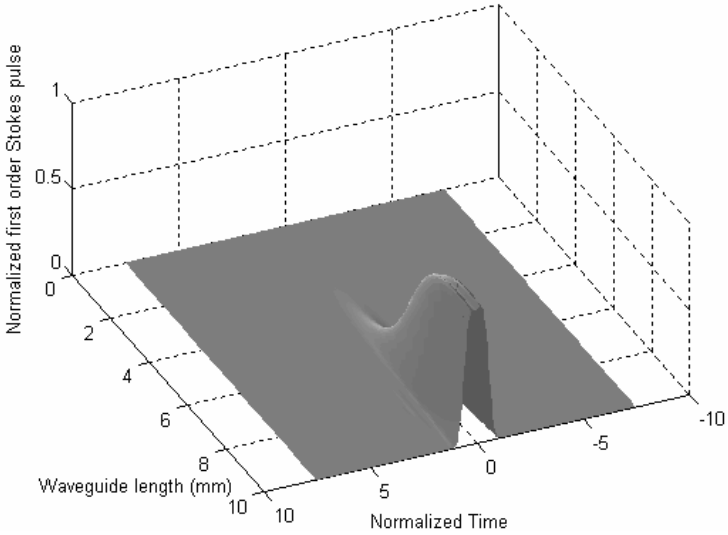

Fig. 4. Space- time evolution of first order Stokes pulse in CB section.

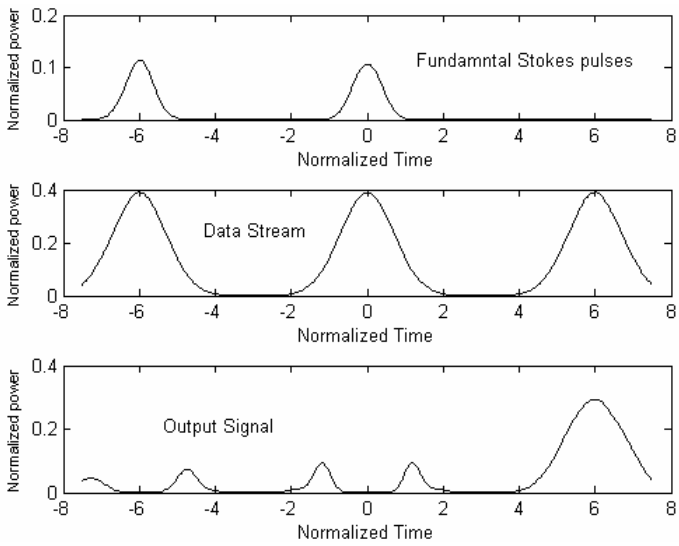

Fig. 5. Interaction between data stream and fundamental Stokes pulses.

Conclusions

In this paper the modelling of a fully integrated optical intensity modulator based on Raman effect in SOI waveguides is presented and discussed. Results are shown as an example of all-optical modulation of a fast data stream.

References

[1] G. Burdge et al., "Ultrafast intensity modulation via Raman gain for all-optical processing," Eur. Conf. on Opt. Commun. Proc., pp. 61-64, 1997.

[2] V.M.N Passaro and F. De Leonardis, "Space-Time Modelling of Raman Pulses in Silicon on Insulator Optical Waveguides", J. Lightwave Technology, vol. 24, pp. 2920-2931, 2006.

An integrated polarization splitter and converter

L.M. Augustin, J.J.G.M. van der Tol, R. Hanfoug, W. de Laat*, M.K. Smit

COBRA Research Institute, Technische Universiteit Eindhoven
Postbus 513, 5600 MB Eindhoven, The Netherlands
* ASML
Veldhoven, The Netherlands

A new design for an integrated passive polarization splitter and converter is presented. The device consists of a Mach-Zehnder Interferometer with polarization converters in both arms. The position of the converters is such that a phase difference of π radians occurs between TE and TM. This results in polarization splitting in the output coupler. The device is analyzed using the transfer matrix method and fabricated on InP/InGaAsP. First measurement results show a splitting ratio of approximately 10 *dB and a conversion of >90 %. This device can be monolitically integrated with passive and active components.*

Introduction

The polarization state of light is of ever greater importance in modern telecommunications networks. First of all a lot of components in the network are highly polarization dependent, furthermore polarization mode dispersion can degrade the transmission in an optical fiber. On the other hand, the polarization can be employed in e.g. polarization multiplexing, and polarization based filtering [1]. In all these cases, polarization splitters and converters are key-elements.

Passive polarization splitters and converters that are able to be integrated with both active and passive components are preferred. Passive polarization splitting can be achieved by loading a waveguide with metal [2], by mode-evolution [3], or by modal birefringence [4, 5]. Splitters based on the latter have the advantage that they have low loss and show a high splitting ratio. A drawback is their length (1 to 3 mm) compared to other components on the chip.

We present a short, 600 μm long, interference based splitter integrated with a polarization converter. The device consists of a Mach Zehnder Interferometer with polarization converters in both arms.

Principle

The layout of the device is depicted in fig. 1. The device is based on interference. Light

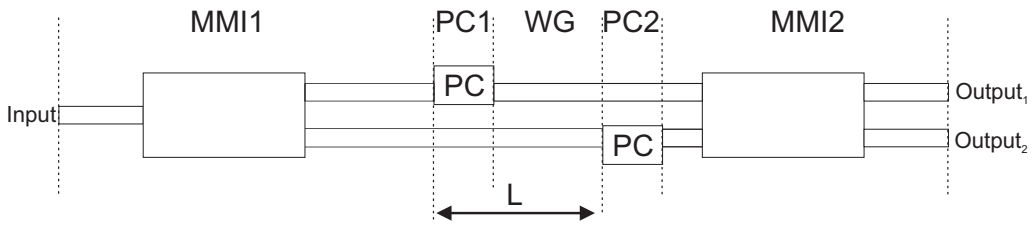

Figure 1: *Schematic of the MZI polarization splitter/converter*

coupled into the input waveguide is split into the two branches with equal power and phase. In the upper branch a polarization converter is placed that rotates the polarization 90°, so after this, the orthognal polarization propagates through this branch.
In the lower branch the light in the original polarization propagates over a distance L before being rotated in a polarization converter. The birefringence in the waveguides causes a phase shift between light in the arms and when both signals are mixed in the output MMI, the phase difference causes one polarization to appear in one of the outputs while the opposite polarization goes to the other output. To achieve the desired splitting, the phase difference between the branches needs to be $\frac{\pi}{2}$ radians, this is obtained when: $L = \frac{\pi}{2(\beta_{\mathrm{TE}}-\beta_{\mathrm{TM}})}$, here $\beta_{\mathrm{TE,TM}}$ are the propagation constants for both polarizations. The polarization converters in the arms consist of an asymmetric waveguide with a straight and a slanted sidewall [6].

Analysis

The performance of the device is analyzed using the transfer matrix method. The splitter is divided into 5 parts as shown in fig. 1: the input coupler (MMI1); a Polarization Converter in the upper arm, nothing in the lower arm (PC1); straight waveguides of length L in both branches (WG); a Polarization Converter in the lower arm, nothing in the upper arm (PC2) and the output coupler (MMI2). Simulation results with TE input as a function of the conversion of the polarization converters in the arms are shown in fig. 2(a). The

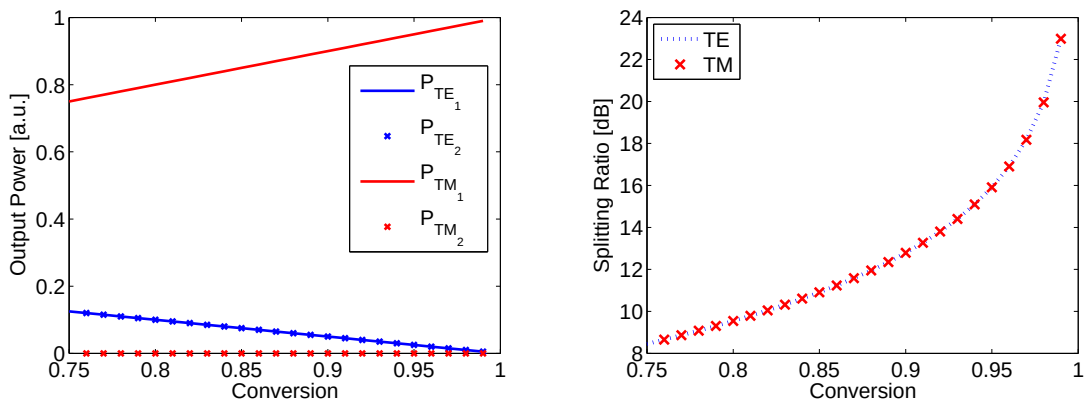

(a) Output powers (b) Splitting Ratio

Figure 2: *Simulated performance of the integrated polarization splitter/converter as a function of conversion of the polarization converters in the branches (TE input)*

TE outputs can only be zero if the conversion in the arms equals 1. If the conversion is lower, the non-converted part is split equally over the two branches, therefor the net conversion of the splitter/converter - for TE input defined as the fraction of the power in TM with respect to the total power in output port 1: $c_{net} = \frac{P_{\mathrm{TM}_1}}{P_{\mathrm{TE}_1} + P_{\mathrm{TM}_1}}$ - is always higher than the conversion of the individual converters.
The influence of the coupling coefficient of the output coupler is also investigated, but MMI's can be made tolerant to width deviations [7], so the conversion of the polarization converters in the arms is considered to be the limiting factor in the fabrication.
Fig. 2(b) shows the Splitting Ratio (Total power in wanted port / Total power in unwanted port) of the splitter for a coupling coefficient of 0.5 for MMI2. For a splitting ratio larger

than 13 dB, a conversion larger than 90% is needed.
The waveguides used are 2 μm wide, and deeply etched into a layerstack having a 300 nm InP topcladding, and a 500 nm Q(1.25) filmlayer on an InP substrate. This yields a $\Delta\beta = \beta_{TE} - \beta_{TM}$ of 0.03 μm^{-1}, so for this device a distance L of 52 μm is needed. The total length of the device, including in- and output MMI's is about 600 μm. The splitter can be made shorter by using smaller MMI's.

Fabrication

The processing of the polarization splitter is similar to the process described earlier [6]. The lithographical definition of the waveguides is made in an ASML PAS5500/250 5× reduction wafer stepper. This allows a very accurate width control, better than 20 nm on a 800 nm line. This machine is advantageous as compared to Electron Beam Lithography, because it has a large writing field, better uniformity and is suited for mass-production.
The etching of the waveguides and the straight side of the polarization converter is done in a CH_4/H_2 RIE. The slanted side is etched in a Br_2-Methanol solution. This etchant etches both InP and InGaAsP anisotropically with an angle of 54°.

Characterization

Both the integrated splitter/converter as separate polarization converters on the same chip are examined on a setup shown below. The devices are exited using an EDFA and a 2.5 nm

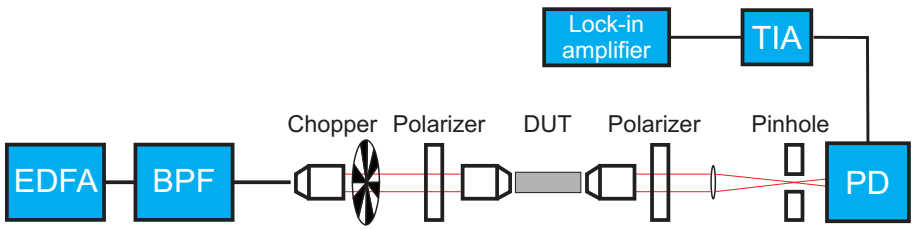

Figure 3: *Setup used for characterization of the polarization splitter and converter. BPF: Band-pass filter, PD: Photodiode, TIA: Trans impedance amplifier*

wide bandpass filter, set to a central wavelength of 1555 nm. This signal is chopped and the polarization is fixed using a polarizer. The light is coupled into the chip and the output is coupled through a polarizer to determine the output polarization. It is detected with a photodiode connected to a trans impedance amplifier and a lock-in amplifier.
The single polarization converters are measured first. The conversion as a function of the width of the device is examined. The results are shown in fig. 4(a).
A conversion of 95% can be achieved for a width of 0.75 μm. The polarization converters used in the splitter are 0.8 μm wide. According to the measurements, this converter will have a conversion of 88%.
The full splitter/converter is measured at the same wavelength. The numbers for the conversion agree well with the expected net conversion if the converters in the arms have a conversion of 88%. The difference between the splitting for TE and TM is caused by the polarization dependence of the output coupler. The coupler is not a perfect 50-50 coupler for TM. This problem is identified and can be solved in a next realization. The low numbers for the splitting ratios are caused by a small phase error (approximately 0.25 radians) in the branches.

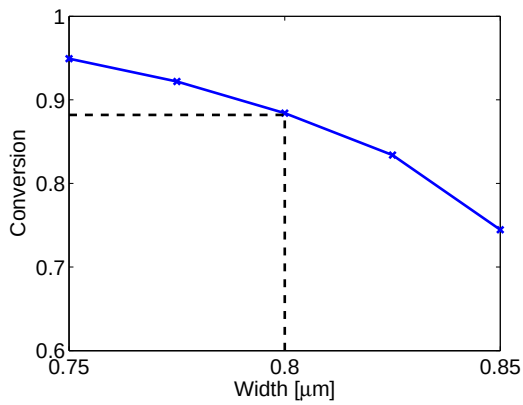

(a) Measured conversion as a function of width of polarization converter (the dashed line shows the converter used in the integrated splitter)

SR_{TE}	9.1 dB
SR_{TM}	11.4 dB
c_{TE-TM}	0.91
c_{TM-TE}	0.91

(b) Measured performance of the integrated splitter/converter

Figure 4: *Measurement results*

Conclusions

A novel type of interference based integrated polarization splitter and converter is presented. The device is analyzed using the transfer matrix method. Splitting ratios larger than 95% are expected for conversion ratios of the converters of more than 90%. The polarization converters are the limiting factor in the fabrication process. According to previous work, for a width deviation of 100 nm a conversion $>$ 90% can be achieved. The device is fabricated and first measurements show a splitting of 10 dB and a conversion of 90 %.

This research is carried out in the framework of the IST-MUFINS project. The European Commission is gratefully acknowledged for financial support. The Centre for Integrated Photonics in Ipswich, UK is kindly acknowledged for supplying the wafer for this experiment.

References

[1] R. Hanfoug, J.J.G.M. van der Tol, L.M. Augustin, and M.K. Smit, "Wavelength conversion with polarisation labelling for rejection and isolation of signals (POLARIS)," in *Proc. 11th Eur. Conf. on Int. Opt. (ECIO '03)*. Apr. 2–4 2003, pp. 105–108, Prague, Czech Republic.

[2] P. Albrecht, M. Hamacher, H. Heidrich, D. Hoffmann, H. Nolting, and C.M. Weinert, "TE/TM mode splitters on InGaAsP/InP," *IEEE Photon. Technol. Lett.*, vol. 2, pp. 114–115, Feb. 1990.

[3] J.J.G.M. van der Tol, J.W. Pedersen, E.G. Metaal, Y.S. Oei, H. van Brug, and I. Moerman, "Mode evolution type polarization splitter on InGaAsP/InP," *IEEE Photon. Technol. Lett.*, vol. 5, pp. 1412–1414, Dec. 1993.

[4] J.J.G.M. van der Tol, J. W. Pedersen, E.G. Metaal, J.-W. van Gaalen, Y.S. Oei, and F.H. Groen, "A short polarization splitter without metal overlays on InGaAsP-InP," *IEEE Photon. Technol. Lett.*, vol. 9, pp. 209–211, Feb. 1997.

[5] L.M. Augustin, J.J.G.M. van der Tol, R. Hanfoug, W. de Laat, and M.K. Smit, "Design and fabrication of a single etch-step polarization splitter on InP/InGaAsP with increased width tolerance," in *Technical Digest Integr. Photon. Res. and Apps. (IPRA '06)*, p. ITuG4, Uncasville, USA, Apr. 24–Apr. 28 2006.

[6] U. Khalique, Y. Zhu, J.J.G.M. van der Tol, L.M. Augustin, R. Hanfoug, F.H. Groen, P. van Veldhoven, M.K. Smit, M. van de Moosdijk, W. de Laat, and K. Simon, "Ultrashort polarization converter on InP/InGaAsP fabricated by optical lithography," in *Technical Digest Integr. Photon. Res. and Apps. (IPRA '05)*, p. IWA3, San Diego, USA, Apr. 11–Apr. 13 2005.

[7] M.T. Hill, X.J.M. Leijtens, G.D. Khoe, and M.K. Smit, "Optimizing imbalance and loss in 2 $\times$ 2 3-dB multimode interference couplers via access waveguide width," *J. Lightwave Technol.*, vol. 21, pp. 2305–2313, Oct. 2003.

Numerical Observations of Negative Group Velocity in a Two-port Ring-resonator Circuit and Its Potential for Sensing Applications

H. P. Uranus and H. J. W. M. Hoekstra

Integrated Optical MicroSystems (IOMS) Group, MESA+ Research Institute, University of Twente,
P.O. Box 217, 7500 AE Enschede, The Netherlands.
E-mail: h.p.uranus@ewi.utwente.nl, h.j.w.m.hoekstra@ewi.utwente.nl.

A two-port ring-resonator circuit is studied theoretically. It is shown that superluminal and negative group velocity (v_g) phenomena can occur in both a passive two-port ring-resonator circuit with loss and an active one with gain. We present numerical observations of temporal behavior of a Gaussian pulse passing through circuits having such properties. We also show that when the negative v_g is 'slow' ($|v_g|<<c$), there is enhanced sensitivity of the phase shift to the ring effective index changes, which suggests its potential for highly sensitive optical sensing applications.

1. Introduction

Besides the possibility to travel with low group velocity (v_g), light can also travel with large v_g (larger than the light velocity in vacuum c) or even with negative v_g [1]. In fact, the phenomenon where light travels with negative v_g has been theoretically studied by Brillouin and Sommerfeld [2] and recently experimentally demonstrated in active optical fibers [3]. Its consistency with causality has also been experimentally verified [4].

Recently, Heebner and Boyd [5] briefly reported that a lossy two-port ring-resonator (TPRR) circuit (as depicted in Fig. 1) can also exhibit such negative v_g phenomenon when operated in an undercoupled condition. However, since the group velocity is not the signal velocity [2] in such a phenomenon, there is no true signal advancement and hence regarded as physically meaningless [2] and can not be used in applications like telecom delay lines [6]. While at one side, the peculiar pulse temporal behavior in such a structure is interesting for scientific curiosity, at the other side, we believe that it is still can be beneficial for applications where an analytic form of input signal is used. In this paper, we studied TPRR circuit theoretically and observe the temporal behavior of Gaussian pulses passing through such structure in various regimes including the negative v_g and superluminal v_g regimes. We also show, that when the negative v_g is 'slow' (i.e. when $|v_g|<<c$), there is enhancement of sensitivity of the optical properties (like phase shift) to the effective index changes in the ring, which suggests the potential of such devices for sensing applications.

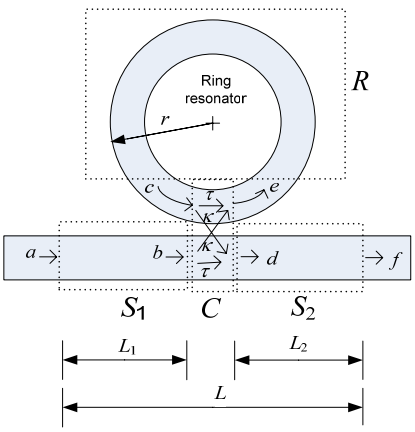

Figure 1. The two-port ring-resonator (TPRR) circuit and the notation used in the modeling.

2. Modeling method

To study the TPRR, we divided the structure into 4 sections as shown in Fig. 1. In this study, we have assumed that the coupler and straight waveguide sections are lossless, while the resonator can have loss or gain. For simplicity, we assume that both the ring resonator and straight waveguides are single mode waveguides.

By assuming a time dependence of exp(iωt), the transfer function of the straight waveguide section for a wave traveling from left to right in Fig. 1 can be expressed as $S_1 = b/a = \exp\left(-i\beta_{\text{straight}} L_1\right)$ and $S_2 = f/d = \exp\left(-i\beta_{\text{straight}} L_2\right)$, where a to f are variables representing the fields at corresponding positions as illustrated in the figure; β_{straight}, L_1, and L_2 are the propagation constant of the mode of the straight waveguide, the length of the first and the second sections of the straight waveguide, respectively.

The properties of the coupler section can be described using a scattering matrix

$$\begin{bmatrix} d \\ e \end{bmatrix} = \mathbf{S}\begin{bmatrix} b \\ c \end{bmatrix} = \begin{bmatrix} \tau & \kappa \\ \kappa & \tau \end{bmatrix}\begin{bmatrix} b \\ c \end{bmatrix} \tag{1}$$

with τ and κ representing the through and cross port amplitude coupling constant of the directional coupler, respectively. The transfer function of the ring is

$$R = c/e = \exp\left(-i\theta\right) \tag{2}$$

with $\theta = \left(\beta_{\text{res}} - i\alpha_{\text{res}}\right) L_{\text{round-trip}} = \left(\beta_{\text{res}} - i\alpha_{\text{res}}\right) 2\pi r$, where β_{res}, α_{res}, $L_{\text{round-trip}}$, and r represent the (linear) propagation constant, the attenuation constant, the effective round trip propagation length, and the effective radius of the ring resonator, respectively. Using eq. (1) and (2), we obtain $C = d/b = \left[\tau + \left(\kappa^2 - \tau^2\right)\exp\left(-i\theta\right)\right] / \left[1 - \tau\exp\left(-i\theta\right)\right]$. Hence, the transfer function of the TPRR circuit can be written as

$$T = f/a = \left(f/d\right)\left(d/b\right)\left(b/a\right) = S_2 C S_1 = \exp\left[-i\beta_{\text{straight}}\left(L_1 + L_2\right)\right]\left[\tau + \left(\kappa^2 - \tau^2\right)\exp\left(-i\theta\right)\right] / \left[1 - \tau\exp\left(-i\theta\right)\right].$$

By making use of the unitary property ($\mathbf{SS}^{\text{H}}=\mathbf{I}$, where superscript H denotes conjugate transpose) of the scattering matrix as a consequence of power conservation of the lossless coupler, with purely imaginary κ and real τ, the transfer function of the structure can then be written as $T = \exp\left(-i\beta_{\text{straight}} L\right) C$, where $L = L_1 + L_2$ and $C = \left[\tau - \exp\left(-i\theta\right)\right] / \left[1 - \tau\exp\left(-i\theta\right)\right]$.

Using the complex transmission coefficient approach [7], we can treat T as a complex quantity and rewrite it as $T = |T|\exp\left[-i\phi\right]$, where the effective phase shift $\phi = -\arctan\left[\text{Im}\left(T\right)/\text{Re}\left(T\right)\right] \pm 2\pi p$ can be used to calculate the group velocity defined as $v_g \equiv \left\{\partial\beta_{\text{eff}}/\partial\omega\right\}^{-1} = \left\{\partial\left(\phi/L\right)/\partial\omega\right\}^{-1}$ and other phase related parameters of the structure. In the ϕ expression, p is an integer. The complex transmission spectrum $T(\lambda)$ of the TPRR can then be calculated. For a known input pulse $a(t)$, by the help of Fourier transform, we can then get the shape of the output pulse $f(t)$ to study the pulse temporal behavior in the TPRR.

3. Numerical observations and discussions

For numerical observations, we take a TPRR circuit with $n_{\text{eff,straight}}=n_{\text{eff,res}}=2$ for the effective indices of the straight and ring waveguides, respectively; α_{res} 1dB/cm,

0dB/cm, and -1dB/cm for lossy TPRR, lossless TPRR, and TPRR with gain, respectively; r= 300μm, and L=1 cm.

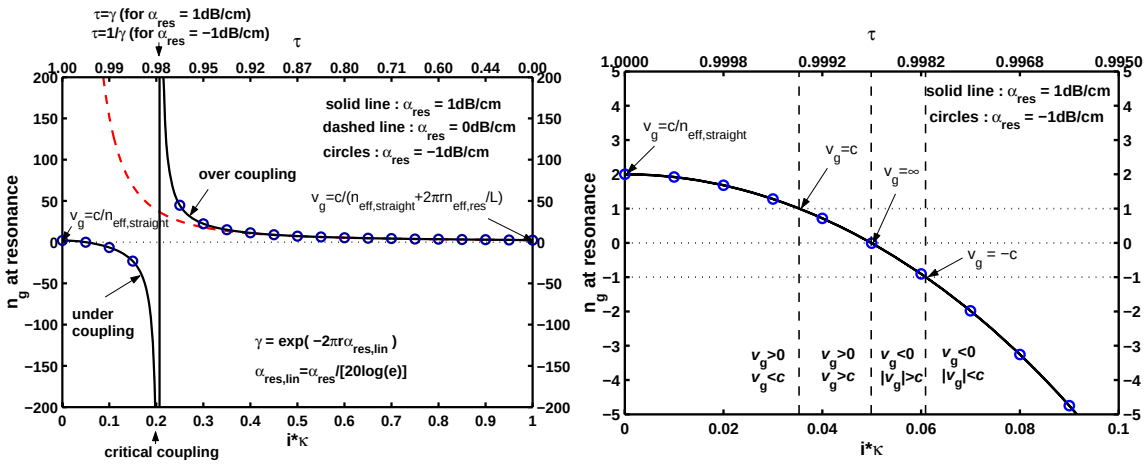

(a) (b)

Fig. 2. (a). n_g at resonant wavelength as function of the coupling constant for lossy TPRR, lossless TPRR, and TPRR with gain as specified in the text. (b). A zoomed plot of part of figure (a) showing the four possible regimes of v_g. The plot for α_{res}=1dB/cm coincides with α_{res}=-1dB/cm.

Fig. 2a shows the group index $n_g = c/v_g$ at the resonant wavelength as one varies the coupling constant. The figure clearly shows that negative v_g can occur in both TPRR with loss and gain operating in the under coupling condition, but can not occur in lossless TPRRs. It also shows that for TPRR with loss or gain, in the over coupling condition, v_g is always positive and slow i.e. $0<v_g<c/(n_{eff,straight}+2\pi r n_{eff,res}/L)$ (see [8]). However, Fig. 2b shows that in the under coupling condition, there are 4 possible operating regimes, i.e. $c/n_{eff,straight}<v_g<c$, $v_g>c$, $v_g<(-c)$, and $0>v_g>(-c)$ which we referred to as 'slow' light with positive v_g, 'fast' light with positive v_g, 'fast' light with negative v_g, and 'slow' light with negative v_g, respectively. Note that our definitions are slightly different than the widely accepted definitions [1]. Detail analysis on classification of such regimes is reported elsewhere [8].

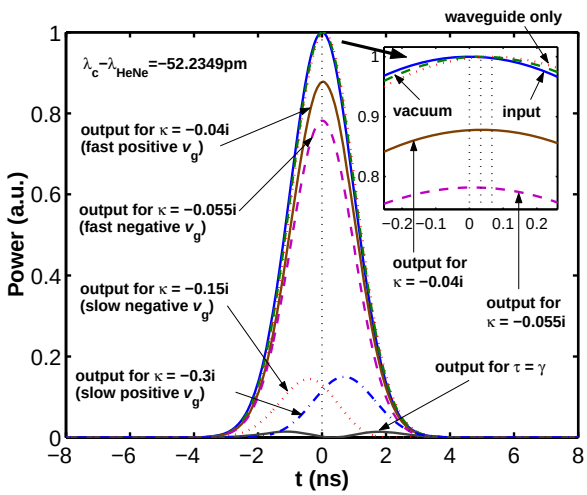

Fig. 3. The power of output pulses of the lossy TPRR circuit operating in various regimes, exited by a Gaussian pulse. For reference, the input pulse, the output pulse if it would travel through vacuum and straight waveguide only of length L, are also plotted together with vertical dotted lines to indicate their peak positions.

Fig. 3 shows the temporal behavior when the lossy TPRR is excited with a Gaussian input pulse $a(t) = \exp\left[-(t/t_d)^2\right]\exp(i\omega_c t)$ with t_d=2ns, $\omega_c = 2\pi c/\lambda_c$ where λ_c is the resonant wavelength of the ring nearest to 6328nm (λ_{HeNe}) at several sampled points representing the four operation regimes. Here, we have assumed that the straight waveguide is not dispersive. For 'slow'-light regimes, the pulses experience

considerable delay and insertion loss (as an indication of intensive light-matter interaction). For 'slow' negative v_g, the pulse experiences negative delay, where the peak of the output pulse appears earlier than the peak of the input pulse. Since the leading edge of the strong input pulse already exists before the weak output pulse with negative v_g, the energy of such output pulse indeed comes from the energy of the input pulse as has been discussed in the literature [1]. Besides, the leading edge of the output pulse if it would travel in vacuum also already exists before the output pulse with negative v_g. Hence, the energy velocity is positive and not faster than c. Since the Gaussian pulse is analytic, it is infinitely differentiable. Through Taylor's expansion, it is possible to exactly predict the pulse in the 'future' using the information available in the neighborhood of a point in the 'past'. So, the information velocity is also positive, since the information is in fact already available in the 'past'. Hence, there is no violation to the causality in such negative v_g phenomenon. Fig. 4 shows that as the light is 'slow' (either with positive or negative v_g), there is enhanced sensitivity of the phase shift to the ring effective index change $S \equiv \partial\phi / \partial n_{eff,res}$, which suggests its potential for sensing applications. The S of the 'slow' light in the figure corresponds to sensor effective interaction length of around 10 cm. Since we can opt to work with continuous wave (which is analytic), we believe that the exploitation of 'slow' light with negative v_g for sensing application is possible. The experimental verification of this application will be part of our future topics.

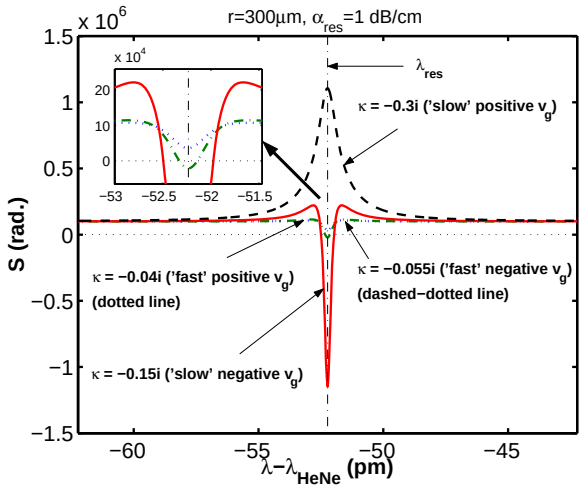

Fig. 4. The sensitivity of the phase shift to the changes in the effective index of the resonator.

Acknowledgements

This work is supported by STW Technology Foundation through project TOE.6596.

References

[1] R. W. Boyd and D. J. Gauthier, "'Slow' and 'fast' light", in Prog. in Optics, ed. E. Wolf, Vol. 43, pp. 497-530, 2002.

[2] L. Brillouin, Wave propagation and group velocity, New York: Academic Press Inc., 1960.

[3] K. Y. Song, M. G. Herráez, and L. Thévenaz, "Observation of pulse delaying and advancement in optical fibers using stimulated Brillouin scattering," Opt. Express, Vol. 13, No. 1, pp. 82-88, 2005.

[4] M. D. Stenner, D. J. Gauthier, and M. A. Neifeld, "The speed of information in a 'fast-light' optical medium," Nature, Vol. 425, pp. 695-698, 2003.

[5] J. E. Heebner and R. W. Boyd, "Slow and fast light in resonator-coupled waveguides," J. Modern Opt., Vol. 49, No. 14/15, pp. 2629-2636, 2002.

[6] L. Zhuang, Time-delay properties of optical ring resonators, master thesis, Univ. Twente, 2005.

[7] J. M. Benedickson, J. P. Dowling, and M. Scalora, "Analytic expressions for the electromagnetic mode density in finite, one-dimensional, photonic band-gap structure," Phys. Rev. E, Vol. 53, No. 4, pp. 4107-4121, 1996.

[8] H. P. Uranus and H. J. W. M. Hoekstra, "Modeling of loss and gain-induced superluminal and negative group velocity in a two-port ring-resonator circuit," in preparation.

Deep etching of DBR gratings in InP using Cl_2 based ICP processes

B. Docter, E.J. Geluk, M.J.H. Sander-Jochem, F. Karouta and M.K. Smit

COBRA Inter-University Research Institute on Communication Technology
Eindhoven University of Technology
Faculty of Electrical Engineering
Opto-Electronic Devices Group
P.O.Box 513, 5600 MB Eindhoven, The Netherlands

We present the progress on deep etching of InP for the fabrication of DBR gratings in Photonic Integrated Circuits (PICs). Various etching chemistries were investigated using an Inductively Coupled Plasma (ICP) etching system. It is shown how the different process settings determine the etched profile and sidewall roughness. Different masking techniques were also investigated. Hard masks using SiN_x and SiO_2 layers are discussed, as well as a three-level masking technique using hard baked photoresist or polyimide. Special attention is paid to applying Electron Beam Lithography (EBL) in the fabrication of the etching mask. A combination of Aluminum lift-off and SiO_2 shows the best results.

Introduction

Dry etching processes are widely used in the fabrication of Photonic Integrated Circuits (PICs) in InP. New devices like Distributed Bragg Reflector (DBR) gratings and photonic crystal structures demand deep etching processes that are able to etch high aspect ratio trenches and mesas with straight and smooth sidewalls [1][2]. But also deep etched waveguides are interesting applications because the increased lateral contrast allows smaller devices and thus the possibility to integrate more devices on a single chip. Side wall roughness is one of the key parameters for this application.

An Inductively Coupled Plasma (ICP) machine is one of the most suitable etching systems for fabricating deep (>2 um) and high aspect ratio structures. In such a system the plasma is generated using a separate induction coil which enables the user to control the ion density (ICP power) separately from the ion energy (RF power). This allows a better process flexibility.

The quality of the etched structures depends very much on the chemistry of the etching gasses. Several chemistries are possible, but in this paper we will concentrate on chlorine based processes. We will discuss a pure Cl_2 process, a Cl_2-CH_4-H_2 process and a Cl_2-Ar-H_2 process. Each process has its advantages and disadvantages.

The sidewall roughness is not only depending on the ICP etching process, but also on the used mask. In general, when using high power ICP processes, we need a thick mask with a good selectivity with respect to InP. But we must also keep in mind that the dimensions of the structures are becoming smaller and smaller and feature sizes are already well below 1 um. This means that the mask must be fabricated using Electron Beam Lithography (EBL). Three different EBL masking techniques will be discussed, 1) direct E-beam writing in ZEP e-beam resist on a SiN mask, 2) a three level process with a hard-baked photoresist buffer layer and 3) an aluminium lift-off process using PMMA e-beam resist on SiO_2.

Etching chemistries

Most etching process used in ICP etching of InP are based on chlorine. The Cl_2 ions react with the indium and phosphide atoms creating $InCl_3$ and PCl_3 and PCl_5 atoms, which are quite volatile under low process conditions. However, if the process temperature is too low (<150 ºC) the $InCl_3$ tends to induce micro-masking that results in rough etched surfaces [3].

The simplest process to etch InP is to use a pure chlorine plasma. This chemistry results in very smooth surfaces and the selectivity of the InP with respect to the etching mask (SiO_2 or SiN_x are suitable materials) is usually more than 20:1. However, etch rates are generally low (< 1 µm/min) and the shape of the etched structures tends to be smaller at the bottom. This shape can be improved slightly by adjusting the process pressure and the gas flow, but it can never be completely straight. Although this is a problem for high aspect ratio structures with very narrow openings, for deep etched waveguides a wider waveguide foot is not a big problem, because the waveguide film is usually less than 2 µm below the top of the waveguide.

To increase the etch rate and improve the directionality of the etching process, some argon can be added to the process chamber. The argon ion bombardment adds energy to the etching process. This increases the etch rate and improves the etched profile. However, the argon also causes the mask to degrade quicker. Some faceting on the corners of the mask is observed and if the etch time is too long, this faceting will cause extra roughness on the etched sidewalls.

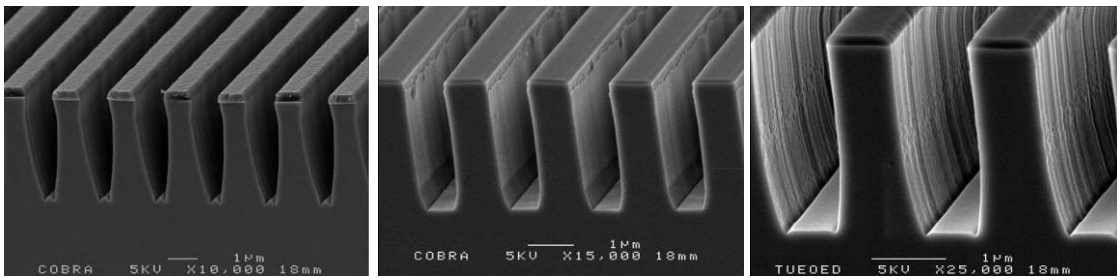

Cl_2 Cl_2-Ar-H_2 Cl_2-CH_4-H_2

Figure 1: Different etching chemistries result in different etch profiles

Adding hydrogen to the chemistry results in some passivation of the etched surface. It decreases the under etch and results in smoother sidewalls. The ratio between Cl_2 and H_2 should be chosen carefully. The best results were obtained using a Cl_2:Ar:H_2 ratio of 7:4:12 sccm and a pressure of 4 mTorr.

Another way to passivate the sidewalls of the waveguides, and thus to decrease the roughness, is to add some methane to the process. The CH_4 creates a polymer coating that protects the sidewall to further etching by the Cl_2 species. This results in smoother sidewalls and lower waveguide losses [4]. However, etch rates are also lower, while mask erosion is more or less the same as in the Cl_2:Ar:H_2 case. The roughness visible in fig. 1 is mostly caused by this mask erosion. The optimal gas flow was found to be Cl_2:CH_4:H_2 7:8:5.5 sccm and 4 mTorr process pressure.

2-level masks using SiN_x

The conclusion of the investigation of the different chemistries is that there are different ways to improve the sidewall roughness by adding passivating species. However, the passivation also brings down the etch rate. This means that to obtain a deep etch, a thicker mask is required. In most dry etching processes it is common to use SiN_x or SiO_2 as etching mask, because photoresist does not withstand the plasma sufficiently. The SiN_x or SiO_2 is opened with photoresist as a mask. However, in the case of electron beam lithography (EBL), the resist layer thickness is limited. In a 30 kV EBL system the maximum thickness in which small structures can be defined with enough accuracy is about 300 nm. This limits the thickness of the SiN_x or SiO_2 to about 400 nm, although thinner masks give better results (less roughness).

3-level masks

Another way of making thick masks is using a 3-level masking method, instead of the 2-level method described before. In this method, first a thick layer (~ 1.5 µm) of photoresist or polyimide is spun on the InP, which is completely hard-baked. Next a thin layer (~100 nm) of SiO_2 is deposited on the hard-baked resist. This thin SiO_2 can then be opened by RIE using an EBL pattern. In the next step the hard-baked resist is opened with an O_2:Ar plasma in the ICP machine. The result is a thick high aspect ratio photoresist mask that can be used for further ICP etching of the InP.

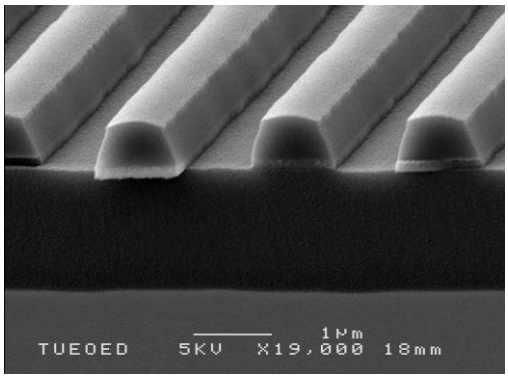

InP substrate – hard baked resist – SiO_2 – photo resist

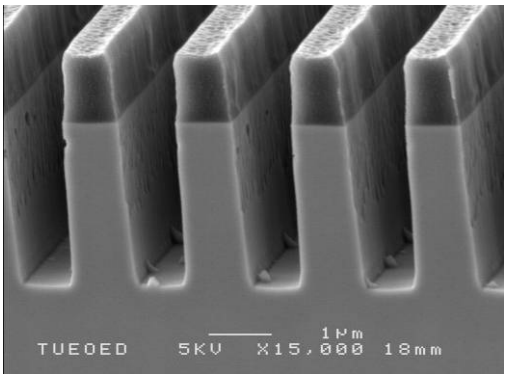

Trenches in InP with hard baked resist as a mask

Figure 2: SEM photographs of the 3-level mask method

The main problem with this etching process is that the hard baked resist does not withstand elevated temperatures. Especially very small structures have this problem. But, as mentioned before, a certain temperature is needed to make sure that all the etch species are removed, so this is a difficult trade-off. Also the lateral etching is higher than in the case of SiN_x or SiO_2 hard masks.

Aluminium lift-off on SiO_2

Another approach to obtain thick masks is to find an alternative to open a thick SiN_x or SiO_2 layer. These materials are usually etched in an RIE system using a CHF_3 plasma, but the standard resists are not sufficiently thick to withstand long etching times. However, there is some good experience using titanium as a mask to open SiN_x layers

[5] and using aluminium has an even higher selectivity with respect to SiO_2 in a CHF_3 chemistry.
The process that was developed using aluminium as a mask is as follows: First a 530 nm layer of SiO_2 is deposited by PECVD and then a 200 nm layer of PMMA 950K A4 EBL resist was spun on the sample. The sample is exposed at a relatively low acceleration voltage of 20 kV, which increases the forward scattering of the electrons in the resist. This causes a slight undercut in the resist profile, which is necessary for the lift-off process. After development a 70 nm layer of aluminium is deposited by electron beam evaporation. Then the PMMA is removed by acetone and the exposed structure remains as an aluminium mask. The SiO_2 mask is then opened in a CHF_3 RIE process which is then used as an etch mask in a Cl_2:Ar:H_2 ICP process.

In fig. 3 two 1 µm wide waveguides are shown. One with a DBR grating that goes through the whole waveguide and one with a grating depth of 50 nm. The etch depth is 3.9 µm and the etched sidewalls are very steep. The side wall roughness is caused by the roughness of the aluminium mask. To improve this roughness we need to optimize the aluminium thickness and the deposition process.

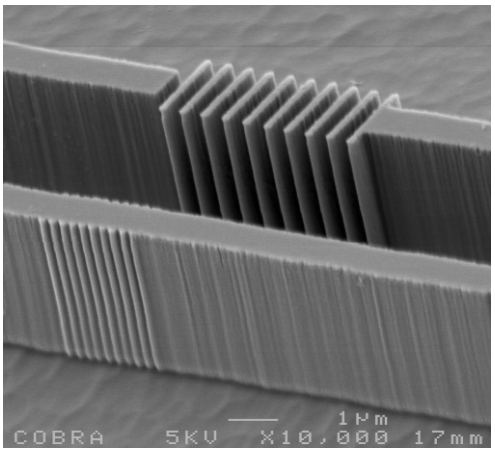

Figure 3: SEM photograph of DBR gratings in 1 µm wide waveguides

Conclusion

To obtain high aspect ratio structures, the chemistry of the etching process is very important. A Cl_2:Ar:H_2 chemistry gives the most vertical sidewalls, but requires very thick masks. The fabrication of these thick masks is difficult, especially using a low voltage EBL system. A process using a 70 nm aluminium lift-off process on top of a 530 nm SiO_2 layer allows us to etch 3.9 µm deep with high aspect ratio. This process seems very promising for the fabrication of DBR gratings and other sub-micron, deep-etched structures like photonic crystals.

References

[1] T. Segawa et al., “Fast Tunable Optical Filter Using Cascaded Mach–Zehnder Interferometers With Apodized Sampled Gratings”, IEEE Phot. Tech. Lett., Vol. 17, pp. 139-141, 2005

[2] C.F. Carlström et al., “Cl_2/O_2-inductively coupled plasma etching of deep hole-type photonic crystals in InP”, J. Vac. Sci Technol. B, Vol 24, pp. 6-9, 2006

[3] F. Karouta et al., “Role of Temperature and Gas-Chemistry in micro-masking of InP by ICP Etching”, Proc. 18th annual IEEE/LEOS 2005, pp.987-988

[4] Y.C. Zhu et al., “ICP Etching of InP and its Applications in Photonic Circuits”, Proc. IEEE/LEOS Benelux 2003, pp.81-84

[5] A.A.M. Kok et al., “Two-dimensional photonic crystals based on InP rods”, Proc. IEEE/LEOS Benelux 2005, pp. 273-276

A Mach-Zehnder interferometric switch within the POLarization based Integration Scheme (POLIS)

A.J.G.M. van de Hulsbeek[1], U. Khalique[1], J.J.G.M. van der Tol[1], F.H. Groen[1], M.K. Smit[1], H.H. Tan[2] and C. Jagadish[2]

[1]COBRA Research Institute
Opto-Electronic Devices Group
Eindhoven University of Technology
Eindhoven, The Netherlands

[2]Australian National University
Group of Electronic Materials Engineering
Canberra, Australia

We present an electro-optical switch operating on TM polarized light in POLIS. All relevant electro-optical effects, including bandgap shrinkage, bandfilling, intra-band and inter-valence band absorption are modeled, properly accounting for the magnitude of these effects at various doping levels. Based on the results of the model switches were realized on POLIS material, and by optimizing the doping profile a decrease in switching voltage from 4.6 V to 2.8 V was obtained. A good agreement between the model and measurements was found. The switches have 3 mm long phase shifters and show low crosstalk values of -17 dB.

Introduction

In enabling fast, low-cost and reliable optical communication, optical integrated circuits will play a vital role. In these circuits a variety of optical components is needed, including passive structures like waveguides and couplers and active structures such as light sources and detectors. The integration of these different devices puts different requirements on the material used, and to meet these requirements an additional processing step (e.g. regrowth) is needed. In the POLarization Based Integration Scheme (POLIS) this issue is overcome by having a material that can offer both passive and active properties, depending on the polarization of the light. In this scheme, TE polarized light is used for active components (absorbing) and TM polarized light for passive components (transparent) [1]. The material responsible for this behavior contains one or more compressively strained quantum wells, resulting in different bandgaps for TE and TM due to band splitting. The change between active and passive behavior can be achieved with polarization converters [2], defined during device processing.

One of the key components in optical integrated circuits is the electro-optical switch. By applying an electric field, it is capable of changing the path followed by a confined light wave. Its main applications are the generation of optical data by modulation of a continuous optical signal and the routing of signals in an optical network. Various designs are possible, but a Mach-Zehnder interferometer (MZI) based switch has the advantages of operating under reverse bias and of using multi-mode interference (MMI) couplers, which are fabrication tolerant. The electro-optical switch presented here fits into the POLIS scheme and operates on TM polarized light. Because the polarization state of the light in a POLIS circuit is always defined, the polarization dependence that limits other designs, does not play a role here.

Principle of operation

The MZI based switch features 2 MMI's and two branches connecting these (figure 1). In applying a phase shift to the light in one of the two branches, we can arrive at

constructive or destructive interference at either of the two output ports. In our case, the phase shift is generated by applying a reverse bias over the p-n junction that is formed by the doping profile of the POLIS material. The applied field results in both field-induced and carrier related refractive index change mechanisms. The latter are due to the removal of carriers under the influence of the reverse bias.

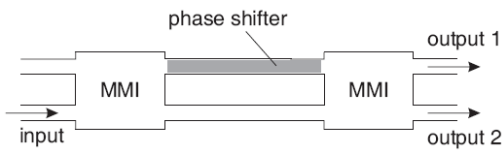

Figure 1: MZI based electro-optical switch

Model

The only field-induced mechanism that has to be considered is the Kerr or quadratic electro-optic effect. As we are operating on TM polarized light, the Pockels (linear electro-optic) effect does not contribute to a change in refractive index for the field and crystal orientations used. The quantum confined Stark effect only plays a role in quantum wells and is neglected here because of the small optical verlap with the thin quantum well (less than 0.5%).

The magnitude of the Kerr effect has a quadratic dependence on the applied field strength. It is modeled according to the model in reference [3], where the relevant coefficients for our material have been determined by fitting to experimental data.

Two carrier induced effects usually simultaneously referred to as the plasma effect are intra-band absorption and inter-valence band absorption. The first describes the transition of a carrier to a higher energy level in the same band, whereas the second describes the transition of a hole from one valence band to another. In modeling the refractive index change due to the plasma effect, other works only consider the intra-band absorption. In this work, we extended the model by applying the Kramers-Kronig transform to experimentally fitted data of the inter-valence band absorption from reference [4].

The two last effects that were considered are bandgap shrinkage and bandfilling. These effects both describe a change of the absorption around the band edge of the material due to Coulomb interaction of carriers (bandgap shrinkage) and the occupation of available energy states (bandfilling). For the bandgap shrinkage, we adopt an analytically obtained model valid at T = 300 K for all doping levels [5]. The bandfilling is modeled according to the model given in reference [6]. To accommodate for experimental results indicating that the absorption doesn't increase at energies more than 0.2 eV above the bandgap, we add a quickly decaying exponential to limit the magnitude of these effects at high photon energies.

The absorption around the bandgap is described using a square-root law [6], fitted to experimental data from reference [7]. The dependence of the magnitude of the Urbach tail on the doping level is accounted for by assuming a Gaussian distribution of the absorption strength.

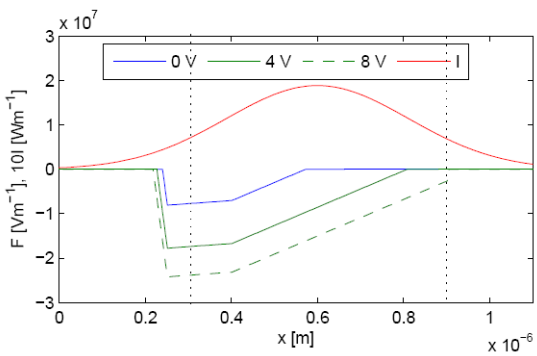

Figure 2: Field distributions of a POLIS wafer

With the distribution of the electric field and all refractive index change mechanisms modeled, the effective change in refractive index that the light experiences was determined by calculating the overlap of the local optical intensity with the local refractive index change due to the electric field (figure 2).

Layer stack design

The original layer stack design (figure 3, A) has the strained quantum well in the middle of an undoped waveguide. The simulations based on the model described above showed that a slight intentional n-type doping of the waveguide would be advantageous for the switching efficiency. However, the series resistance of the layer stack would increase in this case, due to a reduced mobility of holes in this region. Therefore a second wafer (B) was grown with a displaced quantum well (towards the p-contact) and a slightly n-type doped waveguide below the quantum well.

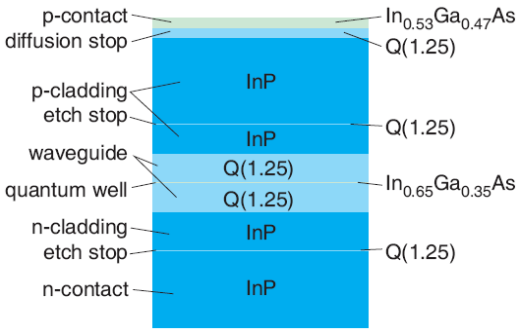

Figure 3: POLIS layer stack design for wafer A

Realization

A series of switches with 3 mm phase shifters was realized on both wafers. The processing consisted of 6 lithography steps. The complete realization was done with established in-house techniques. The various regions defined during processing are: shallow waveguides, thin cladding waveguides for electrical isolation of two phase shifter branches, deeply etched MMI's, contact pads, p-contacts on top of the phase shifters and n-contacts. In figure 4 microscope and SEM pictures are given of the realized switches.

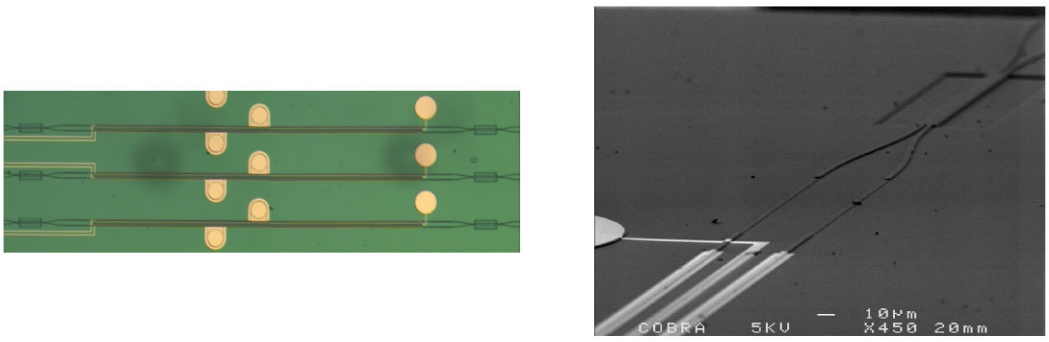

(a) (b)

Figure 4: Microscope (a) and SEM (b) pictures of the realized switches

Characterization

The characterization was performed by coupling light from an EDFA (after passing through a bandwidth filter) into one input port of a switch on the chip and collecting the light from both output ports. A chopper together with a lock-in amplifier is used to reduce noise levels and probes were used to apply a bias to the phase shifter. A typical switching curve for sample A is given in figure 5.

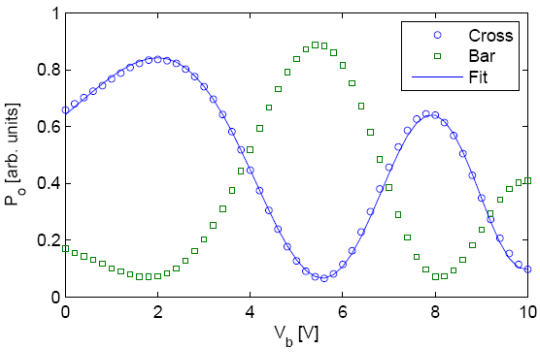

Figure 5: Typical switching curve for a switch realized on wafer A

We fitted this measurement data to the description of an MZI with one perturbed branch, relating it directly to a number for the

imposed refractive index change at various bias voltages. The refractive index change obtained in this way is given in figure 6, with the simulation results for both samples.

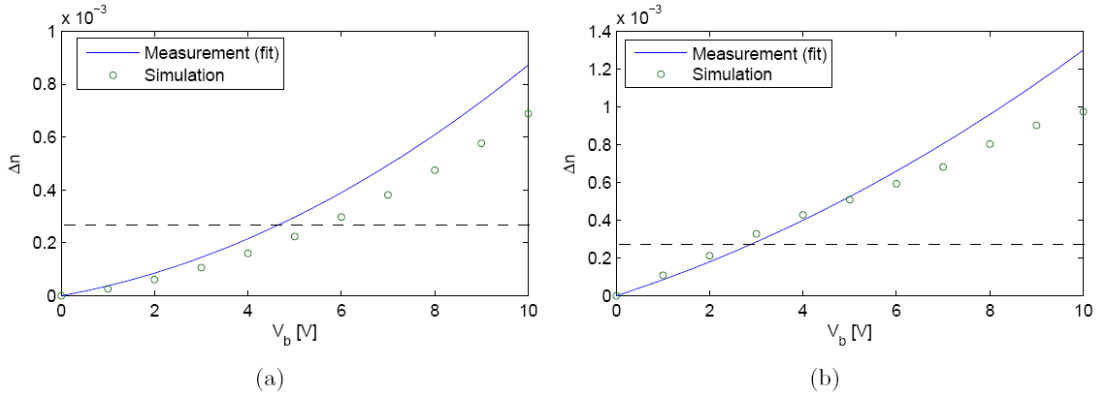

Figure 6: Refractive index change from fitting and simulation for sample A (a) and B (b)

Discussion

The simulation and measurements are seen to give a good agreement, but the total effect is underestimated by the simulations at higher reverse biases. This is most likely due to a slight deviation in the strength of the Kerr effect for our material.

The switching voltage is determined to be 4.6 V and 2.8 V for sample A and B respectively, corresponding to a switching efficiency of 13.0 °/Vmm and 21.4 °/Vmm. The adjusted doping profile of sample B is seen to give a large improvement on the switching efficiency. Unfortunately, displacing the quantum well is seen to give additional losses. The losses of the switch are high, most likely due to diffusion of the p-type dopant (silicon) towards the waveguide region.

Obtained crosstalk values are -11.8 dB and -17.2 dB at 1550 nm, for sample A and B respectively; the difference in these values is attributed to a small fabrication error during the processing of sample A.

Conclusion

Mach-Zehnder switches with 3 mm phase shifters, showing a switching voltage as low as 2.8 V and a crosstalk value of -17 dB have been demonstrated on POLIS material. All relevant refractive index change mechanisms were modeled to arrive at an improved design for the layer stack. A good agreement between simulations and measurements was found.

References

[1] J.J.G.M. van der Tol and J.E.M. Haverkort, “A novel polarization based integration technique for photonic circuits: POLIS”, in Proceedings of the Conference LEOS Benelux Chapter, 1999, pp. 69-72.

[2] Y.C. Zhu, U. Khalique, J.J.G.M van der Tol, F.E. Geluk, F.H. Groen, F. Karouta and M.K. Smit, “Ultrashort polarization converter on InP/InGaAsP”, in Proceedings of the Conference LEOS Benelux Chapter, 2004, pp. 115-118.

[3] D.H.P. Maat, “InP-based integrated MZI switches for optical communication”, doctoral dissertation, Delft University of Technology, 2001.

[4] C.H. Henry, R.A. Logan, F.R. Merritt and J.P. Luongo, “The effect of intervalence band absorption on the thermal behavior of InGaAsP lasers”, Journal of Quantum Electronics, vol. 19, pp. 947-952, 1983.

[5] D. Botteldooren and R. Baets, “Influence of band-gap shrinkage on the carrier-induced refractive index change in InGaAsP”, Applied Physics Letters, vol. 20, pp. 1989-1991, 1989.

[6] B.R. Bennett, R.A. Soref and J.A. Del Alamo, “Carrier-induced change in refractive index of InP, GaAs and InGaAsP”, Journal of Quantum Electronics, vol. 26, pp. 947-952, 1983.

[7] H. Burkhard, H.W. Dinges and E. Kuphal, “Optical properties of $In_{1-x}Ga_xP_{1-y}As_y$, InP, GaAs and GaP determined by ellipsometry”, Journal of Applied Physics, vol. 53, pp. 655-652, 1982.

Defect Grating Simulations: Perturbations with AFM-like Tips

R. Stoffer and M. Hammer

MESA+ Institute for Nanotechnology, AAMP group, University of Twente,
P.O. Box 217, 7500 AE Enschede, The Netherlands

A defect grating in a silicon on insulator waveguide is simulated. We consider spectral changes in the optical transmission when a thin silicon nitride or silicon tip is scanned across the defect. The tip perturbs the resonance field, moving its peak wavelength and possibly changing its shape and quality factor. For the nitride tip, the influence is mostly a spectral shift; for silicon, the change of the resonance shape is pronounced. In particular for the nitride tip we observe a close correspondence between the wavelength shift as a function of tip position, and the local intensity in the unperturbed structure.

Introduction

Photonic crystals have the property that in a perfect crystal, a band of wavelengths is unable to propagate through the crystal. By introducing defects, extra states can be created which allow light to be transmitted; for example, a row of holes may be removed to create a photonic crystal waveguide. The crystal may be engineered to offer more functionality; for example, an extra defect may be created near or inside the waveguide, which can cause strongly wavelength-dependent behaviour and high local field intensities. These resonances can be very sensitive to perturbations. [1] shows that probing a photonic crystal microcavity by a silicon nitride or silicon AFM (Atomic Force Microscopy)-like tip can cause strong variations in the transmitted power.
In this paper, we perform simulations on a grating with a defect in a two-dimensional silicon on insulator waveguide structure. A very thin silicon nitride or silicon tip is scanned over the surface of the grating, and the transmitted, reflected and scattered powers are analyzed. We will show that there is both a wavelength shift of the resonance and a deformation of the spectrum, and that the wavelength shift can be correlated very well with the local intensity at the location of the end of the tip in the unperturbed structure.

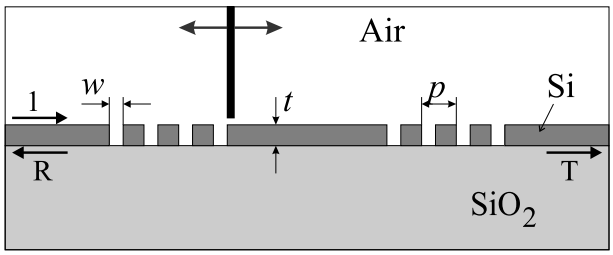

Figure 1: Silicon on Insulator waveguide structure. The refractive indices are: Si - 3.4, Si_3N_4 - 2.0, SiO_2 - 1.0, Air - 1.0. The waveguide thickness t is 220 nm, the grating hole width w 150 nm, and the grating period p 380 nm. The width of the rectangular perturbing Si_3N_4 or Si tip is 40 nm. The defect is four filled holes long (so the length of the waveguide between the inner holes is $(4*0.38+0.23)\,\mu\text{m} = 1.75\,\mu\text{m}$).

Figure 1 shows the waveguide structure under consideration. Simulations are performed by means of a Quadridirectional Eigenmode Propagation (QUEP) method [2]. This method divides the structure into horizontal and vertical slices, and uses eigenmodes of these

slices to describe the complete field. The horizontally and vertically propagating fields are coupled at the boundaries of the computational window, such that the boundaries are transparent for outgoing radiation and for influx of the the desired fields.

Simulations

Into the structure of Figure 1 we insert the guided TE-polarized slab mode from the left, and analyze the transmitted and reflected modal powers T and R. Since the waveguide is monomodal, the scattered power S is equal to $1-R-T$. The spectrum of these quantities is shown in Figure 2.

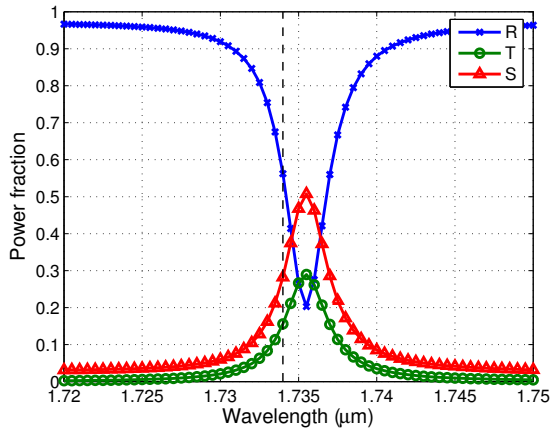

Figure 2: Spectrum of the structure of Figure 1 for unit input from the left; R is the reflected modal power, T is the transmitted modal power, and S is the scattered (lost) power.

In order to make sure the changes due to perturbations are as large as possible, we tune the wavelength to the left flank of the resonance, at 1.734 μm (the dashed vertical line). At this wavelength, Figure 3 shows the absolute value of the field.

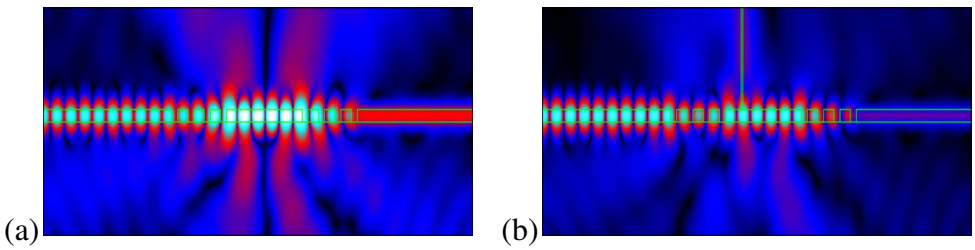

Figure 3: Logarithm of absolute value of the principle dielectric component of the field in the defect grating at a wavelength of 1.734 μm. a: without tip; b: with silicon tip

A 40 nm wide rectangular silicon nitride or silicon tip is scanned horizontally across the surface of the structure, at a height of 10 nm above the waveguide. The most pronounced perturbation of the resonance occurs when the tip is placed close to the field maxima visible in Figure 3a; Figure 3b shows an example. By evaluating R, T and S at each location of the tip, Figure 4 is obtained. The tip switches, or at least modulates, the transmission through the structure. Obviously, the tip moves the transmission further out of resonance (increase of R, decrease of T and S), with a pattern that relates (nonlinearly) to the local intensity in Figure 3a [1].

[1] At a wavelength of e.g. 1.737 μm, the opposite effect can be observed; the tip moves the transmission into resonance, and R is decreased while T and S increase.

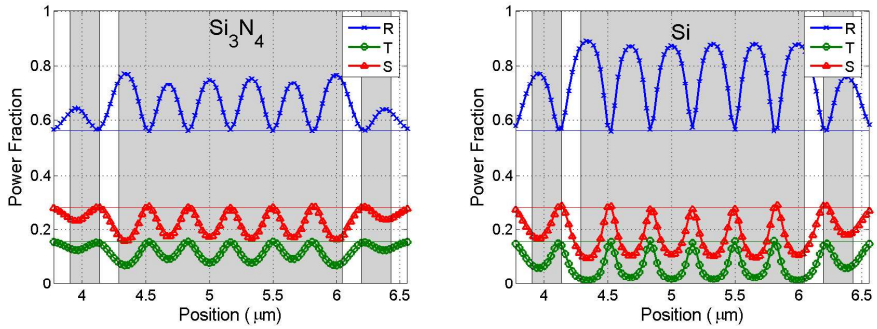

Figure 4: Reflected, transmitted and scattered power as a silicon nitride (left) or silicon (right) tip is scanned over the surface around the central defect (gray patches: high index regions). The horizontal lines denote the values without the tip.

We now look at the spectral properties of the perturbation. In first approximation, we assume that the only effect of the perturbation is a wavelength shift of the resonance. Under that assumption, each of the curves of Figure 4 can be directly related to a wavelength shift by finding the wavelength difference needed in Figure 2 to obtain the altered values of the three powers. These estimations are shown in Figure 5.

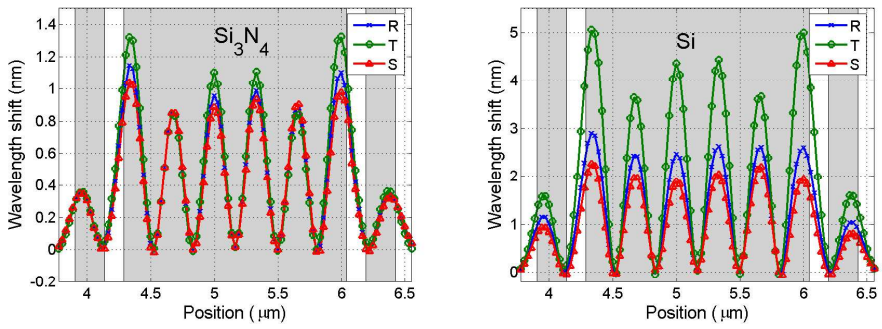

Figure 5: Estimated wavelength shift of the resonance for the silicon nitride (left) and silicon (right) tips; each line is the wavelength shift estimated by only considering the R, T or S curve in Figure 4. Note the different scales of the shifts in the two graphs.

If the assumption of a pure wavelength shift would hold, all three curves predicted by the three powers would yield the same resonance shift. For the silicon nitride tip, this is well satisfied at some tip positions; for the silicon tip, the three curves do not agree well anywhere.

As an example, the full spectrum of the structures with the tip at location 4.6664 μm, which is at the top of the third peak in Figure 5, is shown in Figure 6, and it is indeed clear that the spectrum at this location only shifts for the nitride tip, while it is significantly distorted for the silicon tip; the resonance is broadened and less pronounced.

Clearly, positioning the tip where the field intensity is negligible should not change the transmission. Conversely, at a position with a strong local intensity, a pronounced effect on the transmission and on the spectral properties can be expected. This is investigated in Figure 7, where we - admittedly rather arbitrarily- plot the average value of the estimated wavelength shift from the three curves in Figure 5, as well as the absolute value squared of the local electric field that would be at the end of the tip if there were no tip present.

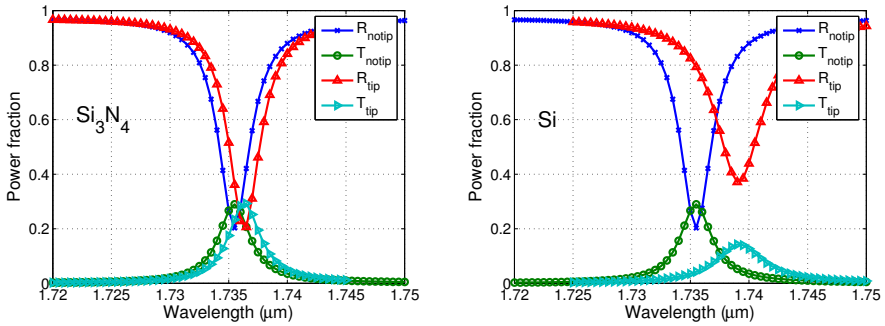

Figure 6: Spectra of the structure without and with a silicon nitride (left) or silicon (right) tip at location 4.6664 μm.

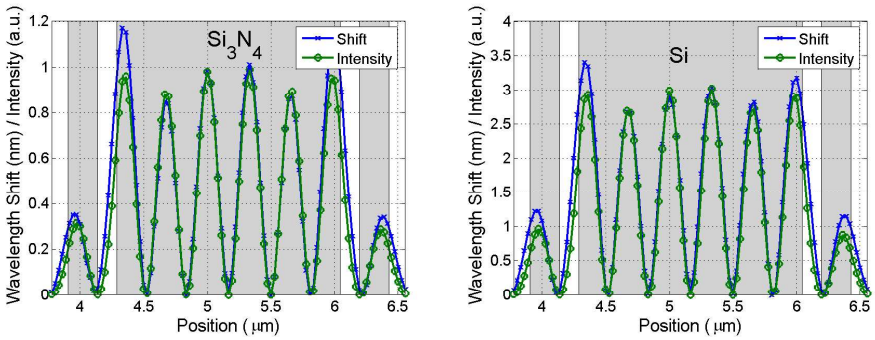

Figure 7: Comparison of the average wavelength shifts of Figure 5 to the intensity in the unperturbed structure; the intensity has been scaled to obtain a good fit. Left: silicon nitride tip; right: silicon tip.

Conclusions

Two-dimensional calculations show that perturbing a defect grating with a thin silicon nitride or silicon tip shifts the resonance wavelength significantly, and may also perturb the shape (and thus the quality factor) of the resonance. The wavelength shift turns out to be almost directly proportional to the local light intensity at the location of the tip in the unperturbed structure. The silicon tip perturbs the shape of the resonance much more strongly than the nitride tip. These simulations confirm measurements reported in [1].

References

[1] W.C.L. Hopman, K.O. van der Werf, A.J.F. Hollink, W. Bogaerts, V. Subramaniam and R.M. de Ridder, ”Nano-mechanical tuning and imaging of a photonic crystal micro-cavity resonance ”, *Optics Express*, vol 14, issue 19, pp. 8745-8752, 2006.

[2] M. Hammer, ”Quadridirectional eigenmode expansion scheme for 2-D modeling of wave propagation in integrated optics”, *Optics Communications*, vol 235 (4-6), pp. 285-303, 2004.

Metal mask free dry-etching process for integrated optical devices applying highly photostabilized resist

G. Sengo, H. van Wolferen, K. Wörhoff and A.Driessen

Integrated Optical Micro Systems MESA+ Research Institute; University of Twente
P.O. Box 217, 7500 AE Enschede, The Netherlands, E-mail: g.sengo@utwente.nl

Photostabilization is a widely used post lithographic resist treatment process, which allows to harden the resist profile in order to maintain critical dimensions and to increase selectivity in subsequent process steps such as reactive ion etching. In this paper we present the optimization of deep UV-curing of 0,3-3.3 μm thick positive resist profiles followed by heat treatment up to 280 ^{0}C. The effectiveness of this resist treatment allows for metal mask free reactive ion etching with selectivity up to 6 for silicon structures, thermal silicon oxide and silicon oxynitride. This procedure is demonstrated by the results obtained in etching of various integrated optical structures.

Introduction

Positive photo resist is not only widely used as a mask for patterning structures in the semiconductor industry but also for manufacturing of a wide range of optical devices. In contrary to electronic devices, where many patterning steps involve small lateral dimensions in combination with a small step height, the main challenge in the patterning of optical devices consists in the high lateral resolution together with mostly a large step height. In our research group a large variety of optical devices based on Si, Si_3N_4, SiO_2 and SiO_xN_y waveguides have been designed, realized and tested.[1,2] For optical waveguide fabrication, the majority of those applications require a steep, vertical step which can be up to several microns high. In order to realize low loss optical waveguides, side walls with low roughness are crucial. When applying reactive ion etching (RIE) on standard processed resist structures, the imposed ion bombardment often causes damage to the resist profile resulting in increased sidewall roughness. In addition, when exceeding the glass transition temperature (Tg) of the resist; re-flown masking material will disturb the maintenance of dimensions.

In order to make the resist structure thermally stable and strong so that it can withstand high temperatures which occur during the RIE and Ion Implantation, several resist treatment methods have been proposed. Deep UV hardening followed by -or in combination with heating[3,4,5], the plasma resist stabilization technique[6], and photoresist polymerization through pulsed photomagnetic curing[7] have been proposed to strengthen the resist profile. In addition, hard baking of the resist structure at high temperature is also necessary to increase the resist selectivity during the RIE.

Of the proposed resist treatment methods, deep UV-curing and thermal heating is a widely used post lithographic process, to harden the resist profile in order to maintain critical dimensions and increase the resist selectivity necessary during the subsequent process steps such as RIE and ion implantation. In the following we apply this method to several integrated optics structures with critical dimensions.

Resist treatment procedure

1- Experiments

The experiments were carried out with various wafers. Blank silicon wafers, thermal and PECVD oxide, thermal nitride and SiON of various thicknesses were used. The resist types used were the positive resist OIR 907/12, diluted resist of 500 nm, OIR 907/17 and OIR 908/35 of Arch Chemicals. After standard cleaning and resist spinning; the wafers were exposed with the Electronic Visions EV620 Mask aligner with 12 mW/mm^2 conventional G-line (436 nm) light source. Different laser written masks were used with amongst others waveguide structures of various dimensions, ranging from 0,9 -4 μm. For the photonic crystals and gratings OIR 907/12 was diluted to obtain a thickness of 300 nm. The resist was single exposed with a period of 500 nm by a Laser Interference Lithography (LIL) system (266 nm) for the gratings and double exposed for the photonic pillars.
In contrast to the standard DUV-curing process, mostly in nitrogen or oxygen atmosphere[8], the wafers were first intensely irradiated in an air filled chamber after which they were baked at temperatures of 180-280 ^{0}C for 1-3 hours.
After DUV-curing and a hardbake step, the structures were etched in Elektrotech Twin System PF 340 Reactive Ion Etching, Plasmatherm 790 parallel plate Reactive Ion Etching or Alcatel Adixen DE Inductive Coupled Plasma machines. The profiles were measured with Dektak 8 of Digital Instrument Veeco Metrology Group and examined with the Scanning Electron Microscope of JEOL, type JSM-5610/5610LV.

2- Results and discussion

In figure 2 the process optimization is presented for resist 907/17, 1.2 μm and diluted resist of 300 and 500 nm. Figure 2 (a) is a picture of the resist profile after development in the OPD4262 positive resist developer. Figure 2 (b) is the optimized result of DUV-curing followed by hardbake at 250 ^{0}C for 2 hours. The integrity of the resist profile is retained quite well, including the line width control and the sidewall angle.
Figure 2 (c) is the result of a hardbake at 280^{0}C for 1 hour. The profile shrinkage is more pronounced in the width as well as in the height compared to figure 2 (b). Thus to maintain the integrity of the resist profile, the hardbake should be applied below 280^{0}C. Figure 2 (d) is 300 nm DUV cured and hardbaked resist at 180^{0}C for 2 hours used for etching of gratings. Figure 2 (e) is 500 nm hardbaked resist at 180^{0}C for 2 hours used for amongst others etching of silicon oxynitride.

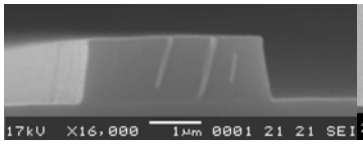

Figure 2(a)

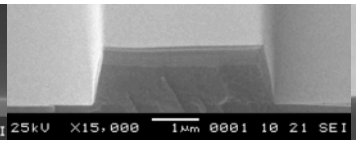

Figure 2(b)

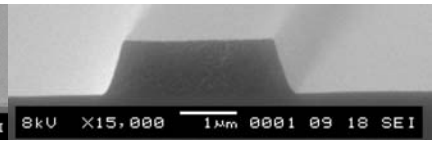

Figure 2(c)

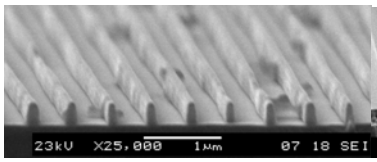

Figure 2(d)

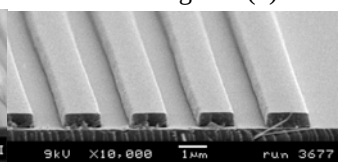

Figure 2(e)

The hardbake should be carried out step by step to the final temperature of 180^{0}C or higher in order to maintain the integrity of the resist profile.
Obviously the thicker the resist, the longer the irradiation and also a proper optimization is required. Characterizing and determining the proper sequence of UV exposure and

thermal rise to a final temperature are paramount to the success of photostabilization[8]. In Figure 3 the process optimization is presented for resist 908/35, 3.3 µm.

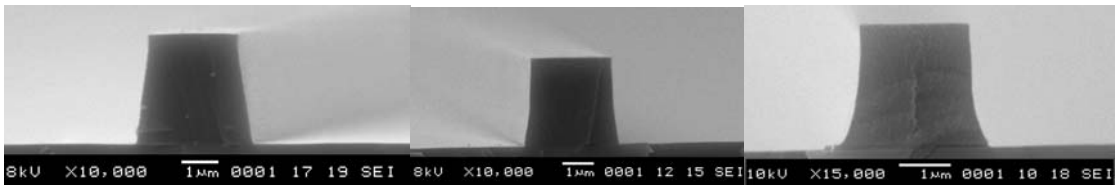

Figure 3(a) Figure 3(b) Figure 3(c)

Experiments have been carried out with resist 908/35 which gives profile heights around 3,3 µm. In figure 3 (a) a SEM picture is presented of resist 908/35 after development. Figure 3 (b) is the result of optimized hardbake at 180^0C for 2 hours after DUV-curing. Figure 3 (c) is a similar resist profile baked at 280^0C for 1 hour. As can be seen, the integrity of the profile is still well maintained, although the forming of the so-called "foot", as observed in figure 2 (c) as well, is clearly present. It appears that the bottom of the profile is slightly broader than the top which is of course partly inherent to the lithographic process, as can be seen in picture 3 (a) whereby the difference between broadness of the top and bottom is around 0.8 µm for this type of resist. The behavior of a so-called "foot" is also clearly observed by I. Pollentier et al.[9]

3-Etch selectivity

Experiments have been carried out with resist baked at 180 and 280^0C to investigate the etch selectivity. There was no noticeable difference measured between resist baked at 180 and 280^0C. Therefore, for the further experiments, the resist profiles were standard hardbaked at 180^0C for 2 hours.

For silicon oxynitride layers of 1.5 -2.5 µm deposited on silicon and etched in the Plasmatherm 790 dry etching machine, a selectivity of 5 was obtained. For layers of 1.5 -2.5 µm SiON deposited on 8 µm thermal oxide a selectivity of 6 was obtained. For silicon a selectivity of 4-5 is obtained for etching controlled structures of 200 - 1000 nm in the PF 340 Reactive Ion Etching twin system. For oxide, a selectivity of 4 was obtained in the Plasmatherm 790 and a selectivity of 6 was obtained in the Alcatel Adixen DE Inductive Coupled Plasma etching machine. In addition, the silicon nitride selectivity never has been a problem; it is quite high.

4-Examples of optical structures in SiON, SiO_2 and Si

Initial experiments have been carried out with silicon oxynitride (SiON) layers ranging from 1.0- 2.5 µm, because from the lithographic point of view, SiON is the most difficult material in achieving high resolution and high etching steps. If the process could be optimized for SiON; other materials like oxide, nitride and silicon would form no problem.

Figure 4 (a) is an arbitrary SiON waveguide of 1.5 µm etched in the Plasmatherm 790 reactive ion etching machine using resist thickness of 1.2 µm. Figure 4 (b) is a microring resonator of SiON with waveguide width of 0.9 µm and the gap between the ring and waveguide of 0.6 µm. Under specific conditions it is possible for conventional contact mask lithography with a source wavelength of 436 nm, to open gaps of 0.6 µm between the waveguide and the resonator with 2.5 µm SiON on 8 µm thermal oxide

using diluted resist of 500 nm. The etch step in figure 4 (b) is 1.7 µm in SiON of 2.5 µm.

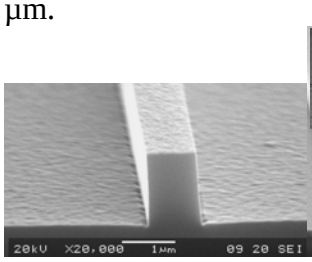

Figure 4(a)

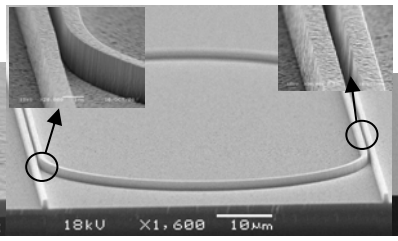

Figure 4(b)

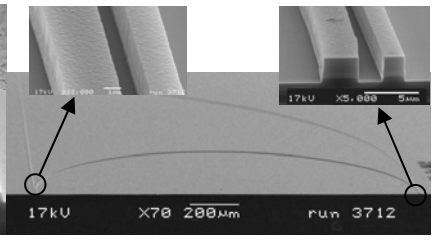

Figure 4(c)

Figure 4 (c) is a micro ring resonator of 2.5 µm height in SiON etched in the Plasmatherm 790, using resist of 0.9 µm. The gap is around 1.0 µm.

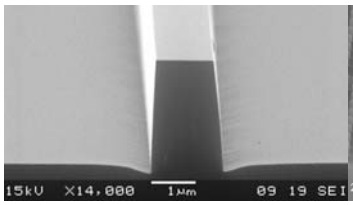

Figure 4(d)

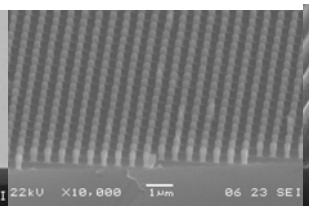

Figure 4(e)

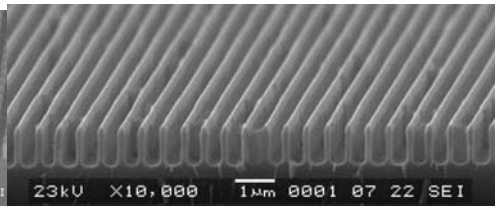

Figure 4(f)

Figure 4 (d) is a waveguide of 2.3 µm height etched in thermal silicon oxide in Alcatel Adixen DE Inductive Coupled Plasma (ICP) etching machine, using 1.2 µm resist. It would be possible with the same amount of resist to etch around 6 µm thermal oxide.
Figure 5 (e) is an example of photonic pillars of 750 nm etched in silicon and figure 4 (f) is an example of a grating of 750 nm height in silicon with 160 nm resist still on top of the structure.

As demonstrated in the aforementioned examples; optimization of UV radiation and temperature treatment after exposing provide a meaningful tool to produce a broad range of critical optical structures in silicon, thermal silicon oxide, nitride and silicon oxynitride.

[1] R. M. de Ridder, K. Wörhoff, A. Driessen, P. V. Lambeck, and H. Albers, “Silicon Oxynitride Planar Waveguiding Structures for Application in Optical Communication”, IEEE Journal in Selected Topics in Quantum Electronics, vol. 4, pp. 930-937, 1998

[2] C. Roeloffzen, “Passband flattened binary-tree structured add-drop multiplexers using SiON waveguide technology”, Ph.D. thesis, Enschede, 2002.

[3] R. Allen, M. Foster and Y.T. Yen, "Deep U.V. Hardening of Positive Photoresist Patterns," Journal for Electrochemical Society. vol. 129, pp. 1380, 1982.

[4] R. Mohondro, J. Eisele, D. Whiteside, T. Romig and M. Bishop, “Photostabilization: the process of improvement”, Future Fab International”, vol. 3, pp. 235-247, 1997.

[5] G. Jordhamo and W. Moreau, “Deep UV Hardening of deep UV resist”, International Society for Optical Engineering, vol. 2724, pp. 588-600, 1996

[6] W.H.L. Ma, "Plasma Resist Image Stabilization Technique (PRIST) Update" International Society for Optical Engineering, vol. 333, pp. 19-23, 1982.

[7] Paul A. Ruggerio, “Positive Photoresist Polymerization Through Pulsed Photomagnetic Curing”, Solid State Technology, vol. March 1984, pp. 165-169, 1984

[8] R. Mohondro, “Photostabilization: Comparing DUV and I-line”, Solid State Technology, vol. February 2003, 2003

[9] I. Pollentier, P. Jaenen, C. Baerts, and K. Ronse, “Sub-50nm Gate Patterning Using CD Trim Techniques and 248nm or 193nm Lithography”, Future Fab International, vol. 12, 2002

Al_2O_3 and Y_2O_3 Thin Films for Active Integrated Optical Waveguide Devices

J.D.B. Bradley, F. Ay, K. Wörhoff and M. Pollnau

Integrated Optical MicroSystems Group, University of Twente,
P.O. Box 217, 7500 AE Enschede, The Netherlands

Al_2O_3 and Y_2O_3 are both very promising host materials for active integrated optics applications such as rare-earth ion doped waveguide lasers. In this paper, a reactive co-sputtering process for stable, target condition-independent deposition of Al_2O_3 layers with high optical quality is discussed. The loss of as-deposited Al_2O_3 waveguides in the near infrared wavelength range was 0.3 dB/cm. Reactive ion etching of both Al_2O_3 and Y_2O_3 thin films for defining channel waveguide structures was investigated and compared using CF_4/O_2, BCl_3, HBr and Cl_2 inductively coupled plasmas.

Introduction

Thin films of amorphous aluminum oxide (Al_2O_3) and yttrium oxide (Y_2O_3) offer very promising platforms for active integrated optics applications [1]. In particular, rare-earth-ion doped Al_2O_3 waveguides for integrated optical amplifiers and tunable light sources have been demonstrated [2]. For large scale realization of such active devices, the development of stable, reproducible and straightforward methods resulting in as-deposited low-loss Al_2O_3 layers are required. Sputtering is known to result in fast, well-controlled, uniform deposition over a large substrate area. Er:Al_2O_3 slab waveguides fabricated by DC-driven reactive co-sputtering [3], for example, were optimized to an estimated loss value of about 0.25 dB/cm. The main drawback of the DC-driven method is however a poor process stability and reproducibility due to a strong dependence on the exact condition of the sputtering target.

Low-loss planar optical waveguides of Y_2O_3 deposited by various techniques have also been demonstrated recently [4]. In contrary to the successful channel definition in Al_2O_3 [5] by reactive ion etching (RIE), the utilization of Y_2O_3 channel waveguides is still hampered by the absence of a reliable patterning process. Due to its high chemical stability, structuring of Y_2O_3 has been primarily limited to entirely physical etching techniques [6], [7]. The physical methods often result in high waveguide losses due to poor sidewall quality and severely limit the profile of waveguide structures. RIE, which combines physical and chemical etching, generally allows for low-cost, high resolution structuring of channel waveguides with smooth sidewalls.

In this paper, results on DC- and rf-based reactive co-sputtering of Al_2O_3 films and the reactive ion etching behaviour of Y_2O_3 in various plasma chemistries are presented.

Experimental Set-up

For the Al_2O_3 layer deposition, an AJA ATC 1500 sputtering system has been applied. The substrates are fixed on a rotating substrate holder and heated up to a maximum temperature of 800 ºC. The system is equipped with three Ar sputtering guns for 2-inch sputtering targets, which can be driven by either rf- or DC power supplies, both having a maximum range of 500 W. An oxygen flow is connected to a gas inlet at the chamber, allowing for reactive co-sputtering of metallic targets. For sputtering of Al_2O_3 layers, a high-purity 2-inch Al target was mounted to one of the sputtering guns and deposition

was carried out on 100-mm Si wafers, either bare or thermally oxidized to a thickness of 8 µm. The film properties, including refractive index, layer thickness and uniformity, and loss values, were measured by ellipsometry and prism coupling.
For studying the etching behavior of Y_2O_3, an Oxford Plasmalab 100 inductively-coupled plasma (ICP) reactive ion etch system was used. The ICP source was controlled by a 3 kW, 13.56 MHz generator, while substrate bias was controlled separately by a 600 W, 13.56 MHz RF generator. Various standard process gases and combinations of these gases were used, including BCl_3, BCl_3-HBr (50:50), CF_4/O_2 (90:10), and Cl_2. Y_2O_3 films of approximately 900 nm thickness were reactively sputtered on Si substrates using a separate DC sputtering system for the etch experiments. The etch rate of the Y_2O_3 films was determined by measuring the film thickness before and after the etch process with a spectroscopic ellipsometer.

Results and Discussion

Sputter-deposition of Al_2O_3 thin films

The impact of various processing parameters (temperature, pressure, power, total flow and oxygen percentage in flow) on the layer properties (deposition rate, refractive index, film density, stress, material birefringence and optical loss) has been studied for both, DC and rf-driven sputtering. Based on this study, it was found that the optimum deposition conditions include high substrate temperature, high sputtering power, low pressure and higher total gas flow. The optimized films had high refractive index and high density, and a sufficiently large deposition rate for depositing waveguide layers of typical thickness (5.5 nm/min for the optimized rf-sputtered films). The most striking difference found between rf- and DC-sputtering was in the process stability and the optical loss of the waveguides. In the case of DC sputtering the optical quality is highly dependent on the exact condition of the sputtering target. Oxidation of the target surface results in release of large particles from the target due to arcing. In case of all waveguide samples fabricated by the DC sputtering process no propagation could be observed after coupling of light with a 633-nm wavelength. In contrary, the rf sputtering process was highly stable and reproducible, without the occurrence of arcing. Figure 1 (a) shows the refractive index of the optimized Al_2O_3 as a function of wavelength, with low material birefringence based on TE and TM polarization measurements. The refractive index is reproduced within $\pm 10^{-3}$. The thickness uniformity, as shown in Figure 1 (b), is within the 1-2% range over an area 4 cm wide in the centre of the wafer. The uniformity of films in the optimized parameter range was also significantly better for the rf-deposited films.
Figure 2 a) shows the optical loss of rf-deposited Al_2O_3 slab waveguides at 633nm as a function of deposition temperature (a), and the optical loss as a function of wavelength for both optimized and non-optimized layers. The film quality is improved significantly as the temperature is increased towards the higher range. In (b), the optical loss throughout the near IR wavelength range of 1200-1600 nm for optimized 660 nm thick rf-sputtered film is about 0.3 ± 0.15 dB/cm. For the optimized rf-process, the absorption peak at 1400 nm (caused by the presence of O-H bonds in the film) is not observed. For rare-earth doping applications, O-H free deposition is required, because these bonds form one of the major quenching sources and largely diminish the gain efficiency.

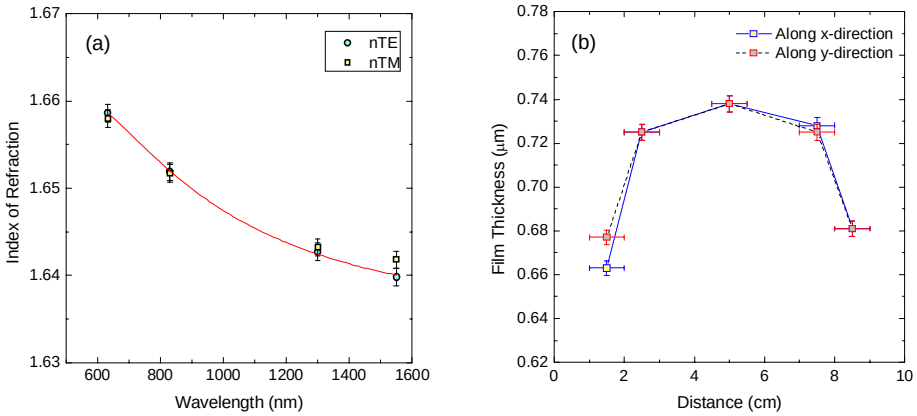

Fig. 1. (a) Variation of the refractive index of optimized Al_2O_3 layer as a function of wavelength. (b) 9-point scan of layer thickness along two perpendicular directions on the 100-mm wafer.

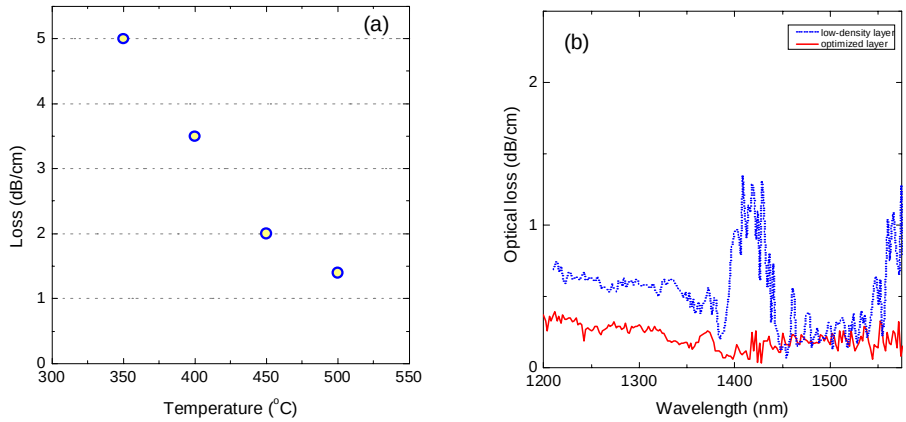

Fig. 2. (a) Change of optical loss of Al_2O_3 slab waveguides at 633 nm as a function of deposition temperature. (b) Optical loss spectrum for both low-density and optimized Al_2O_3 layers in the IR region.

Y_2O_3 thin film etching

The etch rate of the Y_2O_3 films was investigated as a function of applied RF power for various plasma compositions. Figure 3 (a) shows the resulting etch rate as a function of RF power for CF_4/O_2 (90:10%), BCl_3 (100%), BCl_3/HBr (50:50%) and Cl_2 (100%) gases. From these results, it can be seen that with the exception of Cl_2, the various etch chemistries do not significantly impact the etch rate. This indicates that a primarily physical etch process is involved for these process gases. All values were almost an order of magnitude lower than those obtained for the optimized sapphire-etching process in BCl_3-based plasmas [5]. The possible etch products of Y_2O_3 (such as YCl_3, YBr_3, with the exception of YF_3) are generally known to be much less volatile than those of Al_2O_3, indicated by much higher melting points. We therefore expect lower etch rates for Y_2O_3, with primarily physical mechanisms dominating. Of all the process gases used to etch Y_2O_3, Cl_2 clearly exhibits the highest etch rates, with a maximum value of 53 nm/min observed at 400 W RF power. This indicates that perhaps a stronger chemical component is involved in the purely Cl-based etch process.

In the initial studies, it was found that the surface quality of the etched films, as measured by the quality of the ellipsometric measurement fitting parameters, varied significantly for the different chemistries. Specifically, films etched in CF_4/O_2, were

found to have significantly higher surface quality. Therefore a study was undertaken to optimize the etch rate in CF_4/O_2 plasma. As shown in figure 3 (b), it was found that the lowest obtainable chamber pressure (~10 mTorr), highest ICP power and highest RF power resulted in the highest etch rate, all trends indicative of strong physical etching. The highest etch rate for this chemistry was still lower than that obtained for the un-optimized etch rate in Cl_2. The poor surface quality in the case of Cl_2 could in fact be attributed to formation of non-volatile etch products, such as YCl_3, by chemical reactions on the surface [8]. As some chemical component is required in order to enhance the etch rate, Cl_2 seems to be the best choice as a process gas for optical waveguide fabrication in Y_2O_3.

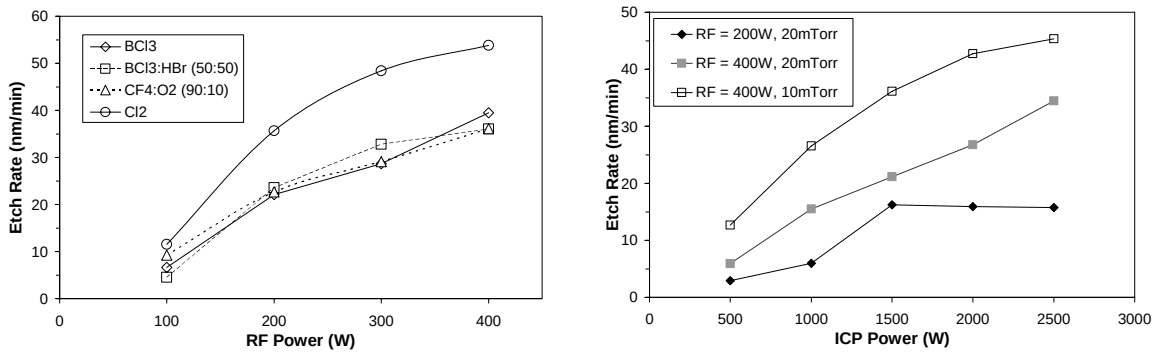

(a) (b)

Fig. 3. (a) Comparison of etch rate and RF bias as a function of RF power for 100% BCl_3, BCl_3:HBr (50:50), CF_4:O_2 (90:10) and Cl_2 at a total flow rate of 50 sccm. (b) Etch rate as a function of ICP power in CF_4/O_2 (90:10) plasma at a total flow rate of 50 sccm, for varying RF chuck power and chamber pressure.

Conclusion

An rf-based reactive co-sputtering process, which resulted in stable, target condition-independent deposition of uniform Al_2O_3 layers with high optical quality, has been developed. The optical loss of waveguides based on the optimized material is 0.3 ± 0.15 dB/cm throughout the near IR wavelengths ranging from 1200 to 1600 nm. Reactive ion etching of Y_2O_3 thin films was also studied using various plasma chemistries and parameters. A maximum etch rate of >50 nm/min was measured using Cl_2 plasma, which is sufficiently high for the controlled etching of optical waveguide structures to a depth of several hundred nm. Further work will continue towards the realization of active integrated optical devices in both materials.

References

[1] A. Polman, J. Appl. Phys., vol. 82, pp. 1-39, 1997.
[2] G.N. van den Hoven, et al, Appl. Opt., vol. 36, pp. 3338-3341, 1997.
[3] S. Musa, et al, IEEE J. Quant. Electr., vol. 36, pp. 1089-1097, 2000.
[4] O. Pons-Y-Moll, et al, J. Appl. Phys., vol. 92, pp. 4885-4890, 2002.
[5] C.H. Jeong, et al, Surf. Coat. Technol., vol. 171, pp. 280-284, 2003.
[6] T.H. Hoekstra, et al, Electron. Lett., vol. 29, pp. 581-583, 1993.
[7] S.O. Barros, et al, IEEE T. Semiconduct. M, vol. 14, pp. 173-176 2001.
[8] Y.-C. Kim, et al, J. Vac. Sci. Technol. A, vol. 19, pp. 2676-2679, 2001.

Thin film InGaAs MSM photodetectors integrated onto silicon-on-insulator waveguide circuits

Joost Brouckaert, Gunther Roelkens, Dries Van Thourhout and Roel Baets

Photonics Research Group, Dept. of Information Technology, Ghent University – IMEC, Sint-Pietersnieuwstraat 41, 9000 Gent, Belgium

Joost.Brouckaert@intec.UGent.be

Silicon-on-insulator (SOI) is rapidly emerging as a versatile platform for a variety of integrated nanophotonic components. High density waveguide circuits can be fabricated using standard CMOS processing techniques. However, light detection in the near-infrared wavelength range (1550 nm) is not possible in silicon which is naturally transparent in this region. One possibility for overcoming this is the integration of III-V semiconductors. We present simulation results of a very compact thin film InGaAs metal-semiconductor-metal (MSM) detector integrated on an SOI waveguide. These photodetectors can be fabricated on a wafer scale and efficiencies of +90% are predicted for wavelengths up to 1650 nm.

Introduction

The SOI material system possesses unique optical properties due to the large refractive index difference between silicon (n = 3.45) and silica (n = 1.45). This allows the creation of very compact and high density waveguide circuits including so-called photonic wires with bend radii as small as 1 μm [1] and photonic crystals. Moreover, these waveguide structures can be fabricated on a wafer scale using standard CMOS processing techniques, including deep ultraviolet lithography [2]. Keeping in mind the worldwide silicon fabrication infrastructure available, it is clear that this evolution could revolutionize the photonics industry [3]. As silicon is transparent for wavelengths above 1.1 μm, photodetection at wavelengths typically used for optical communications is not possible in silicon. One possibility for overcoming this problem is epitaxial growth of germanium on top of silicon waveguides [4]. Another possibility is the heterogeneous integration of thin film III-V compound semiconductors. We believe that this approach can lead to higher performances: InGaAs has an unchallenged position in low dark current, high speed and high sensitivity integrated near-infrared photodetectors. On top of that, for the fabrication of SOI waveguide integrated laser diodes [5], integration of III-V material is the only viable solution and detectors and sources could be fabricated in the same processing steps, using the same wafer scale III-V technologies.

Thin film heterogeneous integration

This integration approach consists of bonding multiple unprocessed III-V dies (epitaxial layers down) onto a processed SOI wafer using a polymer, BCB as a bonding agent. After bonding, the III-V substrate is removed leaving unprocessed epitaxial III-V layers bonded onto the SOI waveguide substrate. From now on, photodetectors can be processed on a wafer scale. This adhesive die-to-wafer bonding approach is clearly described elsewhere [5]. The main advantage as compared to other hybrid integration techniques is that it allows processing the InGaAs photodetectors on a wafer scale.

Photodetector design

We previously reported two types of integrated p-i-n photodetectors based on the same thin film heterogeneous integration technique [5,6]. The advantages of the detector design discussed in this paper are its high theoretical quantum efficiency, large spectral bandwidth, easy processing and compact size.

The design we propose in this paper is based on the principle of coupled mode theory. By using a thin BCB bonding layer (~200 nm) in between the SOI waveguide and detector and by proper design to obtain phase-matching between the optical mode in the SOI waveguide and the detector waveguide mode, optical coupling between guide and detector will occur. A schematic picture of the design is shown in figure 1(a), a cross-section view in figure 1(b).

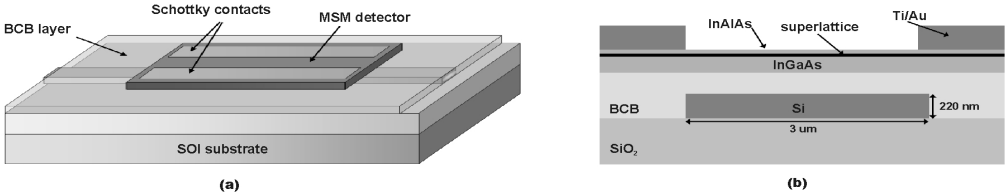

Fig. 1(a). Schematic- and (b) cross-section view of waveguide integrated MSM detector

The material structure of the thin film MSM detector consists of a 40 nm InAlAs Schottky barrier enhancement layer, 20 nm InAlAs/InGaAs superlattice layer to decrease carrier trapping by the bandgap discontinuity between $In_{0.52}Al_{0.48}As$ and $In_{0.53}Ga_{0.47}As$ and a 145 nm $In_{0.53}Ga_{0.47}As$ absorption layer. All layers are not intentionally doped and lattice matched to the InP substrate. Two Schottky electrodes (Ti/Au, 20nm/200nm) are deposited on top, with the same spacing as the SOI waveguide as can be seen in figure 1. Lateral confinement of the detector waveguide mode is obtained by the two Ti/Au Schottky electrodes. The large imaginary part of the refractive indices of Ti (4.62) and Au (9.81) at 1.55 μm lowers the effective refractive index of the fundamental slab mode of slices A as compared to slice B and this causes lateral confinement as can be seen in figure 2(b). As a consequence, absorption loss in the Ti/Au electrodes is small as will be calculated in this paragraph and on top of that, no waveguide ridge has to be defined, strongly simplifying the processing.

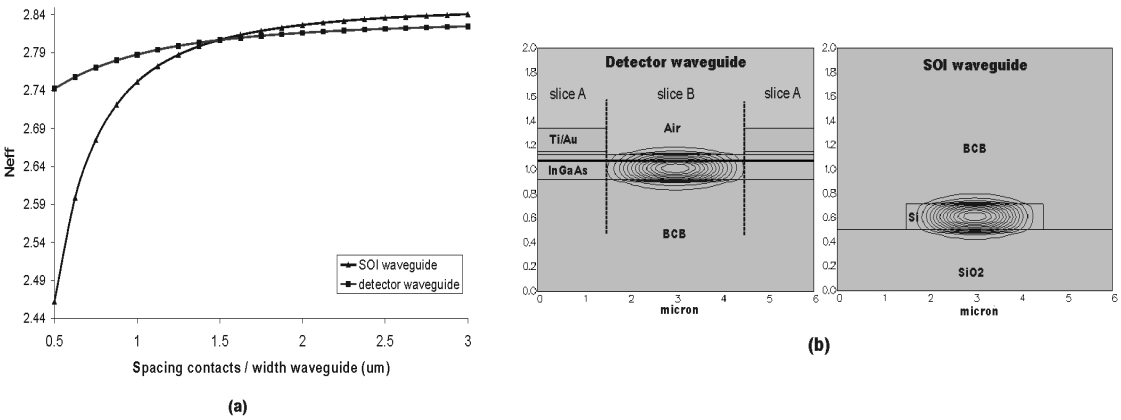

Fig. 2 (a) Real part of the effective refractive index of the TE ground modes of the decoupled detector waveguide and decoupled SOI waveguide in function of contact spacing and waveguide width respectively and (b) corresponding mode profiles.

Figure 2(a) shows the (real part of the) effective refractive index (N_{eff}) of the TE ground modes of the decoupled detector- and SOI waveguide in function of respectively Schottky contact spacing and waveguide width. Corresponding mode profiles are shown in figure 2(b). Using deep-UV lithography, contact spacings down to 200 nm are easily obtainable but here we limited ourselves to 1 µm, which is compatible with standard optical contact lithography. Phase-mismatch of the decoupled waveguide modes smaller than 1.3 % can be obtained with spacings/widths from 1 µm to 3 µm using the layer structure described above. As absorption resonances occur when the (real) propagation constants of the fundamental modes of the decoupled waveguides coincide, the smaller the phase-mismatch, the higher the detector absorption per unity of length. A fully vectorial 3D simulation tool based on eigenmode expansion has been used to calculate the absorbed power as a function of the detector length (figure 3). The simulated structure has a contact spacing and waveguide width of 3 µm. When having a 200 nm thick BCB bonding layer between the SOI waveguide and the detector, 95% of the power is absorbed for detector lengths as short as 11 µm. It is well know from coupled mode theory that when the spacing between the two waveguides increases, couple length will increase. As a consequence of that, the detector efficiency for a given length will decrease for increasing bonding layer thickness as can be seen in figure 3.

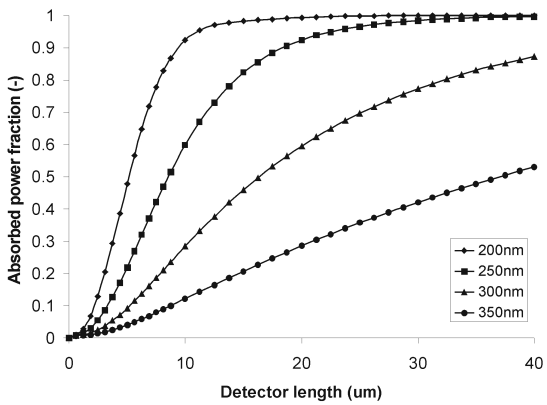

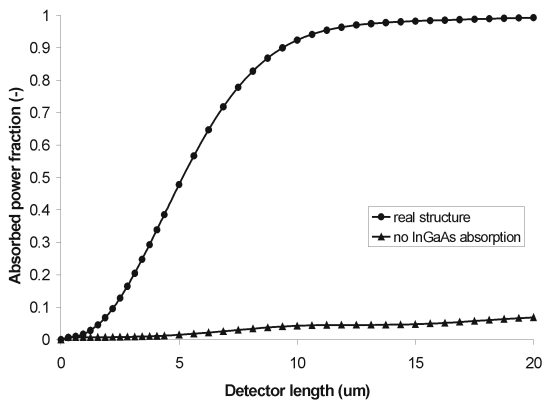

Fig. 3. (Left) Absorption as a function of detector length for different bonding layer thicknesses.
Fig 4. (Right) Influence of optical absorption in the Schottky contacts (Ti/Au).

To estimate the loss due to absorption in the Ti/Au Schottky contacts, we calculated the absorbed power as a function of detector length for both the real structure and the structure where we do only take into account absorption in the Schottky contacts and no absorption in the InGaAs layers. However, this is an approximation because setting the imaginary part of the refractive index of InGaAs to zero slightly influences the field profile. The results are shown in figure 4. When we only consider absorption in the Schottky contacts, power in the structure is lost, but at a very slow pace. From this approximated method, we can conclude that loss due to absorption in the Schottky contacts is limited (smaller than 10% of input power). This is caused by the fact that the contacts are used to obtain lateral waveguide confinement as explained earlier.

In figure 5, the absorbed power as a function of the wavelength is shown for detectors with a length of 10, 20 and 50 µm and with a 3 µm wide detector- and SOI waveguide. Dispersion relations of all the materials were taken into account in this simulation;

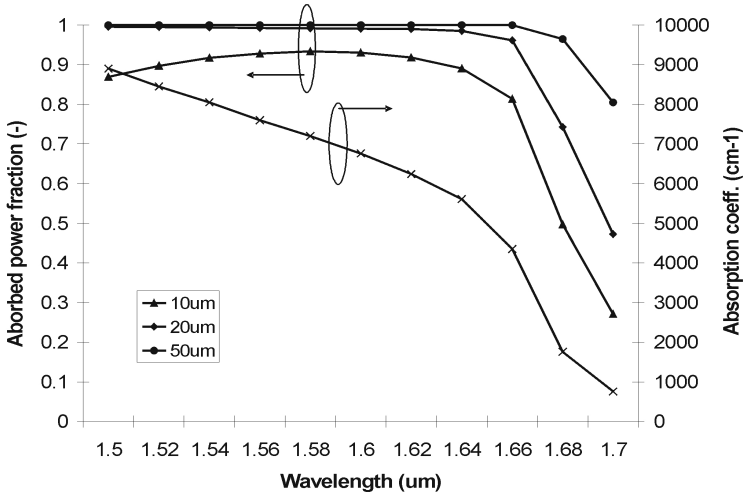

Fig. 5. Absorption coefficient of InGaAs and spectral bandwidth of the MSM detector, parameter is detector length.

however the main contribution is due to the lower absorption coefficient of InGaAs at larger wavelengths as can be seen in the figure. There is a sharp drop in absorbed power around 1.65 μm, which corresponds with the bandgap of InGaAs lattice matched to InP. By increasing the detector length the spectral bandwidth can be improved, however, detector capacitance and dark current will rise.

Conclusion and acknowledgement

We presented the design of an InGaAs MSM detector integrated on a silicon-on-insulator platform. It was shown that an internal quantum efficiency of more than 90% can be achieved for a 15 μm long device and a 200nm intermediate BCB bonding layer. The ultra-compact device offers a high spectral bandwidth and a very simple processing. By tuning the detector length or bonding layer thickness, a fraction of the optical power can be detected for power monitor applications.

This work was supported in part by the Institute for the Promotion of Innovation through Science and Technology (IWT Vlaanderen) under the SBO epSOC project. The work of G. Roelkens was supported by the Fund for Scientific Research (FWO).

References

[1] P. Dumon et al., "Basic photonic wire components in silicon-on-insulator", in Proceedings of the 2nd IEEE International Conference on GroupIV Photonics, 2005, pp. 189-191.

[2] W. Bogaerts et al., "Nanophotonic waveguides in silicon-on-insulator fabricated with CMOS technology", Journal of Lightwave Technology, vol. 23, pp. 401-412, 2005.

[3] R. Baets et al., "Silicon-on-insulator based nano-photonics: Why, How, What for?", in Proceedings of the 2nd IEEE International Conference on GroupIV Photonics, 2005, pp. 168-170.

[4] J. F. Liu et al., "Waveguide-Integrated Ge p-i-n Photodetectors on SOI platform", in Proceedings of the 3rd IEEE International Conference on GroupIV Photonics , 2006, pp. 173-175.

[5] G. Roelkens et al., "Laser emission and photodetection in an InP/InGaAsP layer integrated on and coupled to a Silicon-on-Insulator waveguide circuit", Optics Express, vol. 14, pp. 8154-8159, 2006.

[6] G. Roelkens et al., "Integration of InP/InGaAsP photodetectors onto Silicon-on-Insulator waveguide circuits", Optics Express, vol. 13, pp. 10102-10108, 2005.

Non-linear behavior in quantum-well polarization converters

M.J.H. Marell, U. Khalique, J.J.G.M. v.d. Tol, E.A.J.M. Bente, M.K. Smit
COBRA Research Institute, Eindhoven University of Technology
Postbus 513, 5600 MB Eindhoven, The Netherlands

The application of strain in quantum-wells leads to polarization dependence in their absorption characteristics. Material containing compressively strained quantum-well layers (such as used in the POLarization based Integration Scheme, POLIS) shows enhanced interaction with the TE polarization. Devices fabricated on such material are affected by the polarization dependence as well. For slanted side-wall polarization converters this leads to different effective conversion lengths for the TE and TM polarization. Simulations show that the polarization dependent absorption affecting these devices is saturable and therefore power dependent. The simulations have been confirmed by measurements on experimental devices.

Quantum well polarization converters

Slanted sidewall polarization converters operate on the principle that the light, applied at the input, is forced into two hybrid polarization states [1]. These hybrid states are linear combinations of the main polarization states TE and TM. The fraction of TE polarized light and TM polarized light in the two hybrid modes is dependent on the angle at which the two hybrid modes are placed with respect to the TE and TM polarization. This angle can be influenced by the angle of the slanted sidewall and the width of the converter waveguide.

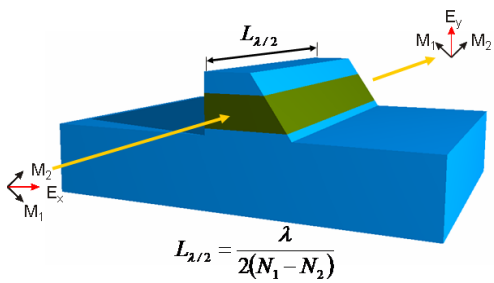

Figure 1: A slanted side-wall polarization converter

One tilted mode is dominantly polarized parallel with the slanted interface, while the second tilted mode is polarized perpendicular to that interface. Both tilted modes experience different propagation constants and dephase while propagating through the converter waveguide. At the end of the polarization converter light in the tilted modes is forced back in the TE and TM polarization. The fraction of light in both polarization states is determined by the phase difference the light gained while propagating in the tilted modes. The coupling between the two orthogonally polarized modes, which occurs in the polarization converter, can be described by means of the coupled mode theory.
Some applications require the slanted side-wall polarization converters to be fabricated on quantum-well material. This, for example, is the case in the POLIS (POLarization based Integration) scheme in which the polarization dependence of the material is used

for active/passive integration [2]. In these applications the quantum-well layer is part of the converter's waveguide region and it will therefore interact with the light passing through the converter. Depending on the wether the waveguide is pumped or not, the TE-polarized light is either amplified or absorbed.
The absorption of light, leads to the generation of free carriers. This two consequences. The first consequence is that, because of the limited number of states available in the quantum-well, the absorption is quickly saturated. This effect is enhanced by the fact that the free carriers are not removed from the well by means of an externally applied field. The other consequence is that the free carriers affect the refractive index of the material and therefore influence the operation of the converter. Both effects have been investigated by means of a computer model and were confirmed by measurements on experimental devices, of which the results are discussed in the remaining part of this paper.

Modeling of the devices

The model of the quantum-well polarization converters is based on the coupled mode theory. The coupled mode theory applies to a large class of mode interactions, when there are two guided modes with sufficient phase synchronism to allow a significant exchange of energy. Therefore, one can neglect all other modes and obtain simple coupled wave equations to describe the interaction between these modes [3].
For the polarization converters under consideration, the coupled mode equations are given below. The equations have been written as a set of four real differential equations, representing the power and phase of both polarizations. In these equations the variables κ, α and δ represent the coupling constant, the TE attenuation and the phase mismatch respectively. The rate equations were solved by means of a traveling wave model.

$$\frac{dP_{TE}(l)}{dl} = 2\kappa\sqrt{P_{TE}(l)P_{TM}(l)}\sin(\psi(l)-\phi(l)) - 2P_{TE}(l)\alpha \tag{1}$$

$$\frac{dP_{TM}(l)}{dl} = 2\kappa\sqrt{P_{TE}(l)P_{TM}(l)}\sin(\phi(l)-\psi(l)) \tag{2}$$

$$\frac{d\phi(l)}{dl} = -\kappa\sqrt{\frac{P_{TM}(l)}{P_{TE}(l)}}\cos(\phi(l)-\psi(l)) + \delta \tag{3}$$

$$\frac{d\psi(l)}{dl} = -\kappa\sqrt{\frac{P_{TE}(l)}{P_{TM}(l)}}\cos(\phi(l)-\psi(l)) - \delta \tag{4}$$

Incorporating the saturable quantum-well losses for the TE polarization can easily be done by replacing the factor α_{TE} in eq. 1 with the differential equation in eq. 5 that describes the amplification/absorption in the quantum well. The changes in phase caused by the fluctuating carrier density are accounted for by adding eq. 6, to the appropriate phase equation. The carrier density itself is represented by eq. 7.

$$\frac{dP_{TE}}{dl} = \frac{1}{v_g}\left[\frac{g(N)P_{TE}}{1+\varepsilon P_{TE}} - \alpha_{int}P_{TE}\right] \tag{5}$$

$$\frac{d\phi}{dl} = -\frac{1}{2v_g}\left[\alpha_N g(N) - \alpha_T\frac{g(N)P_{TE}}{1+\varepsilon P_{TE}}\right] \tag{6}$$

$$\frac{dN}{dl} = \frac{1}{v_g}\left[-\frac{N}{\tau_s} - BN^2 - CN^3 - \frac{g(N)P_{TE}}{1+\varepsilon P_{TE}}\right] \tag{7}$$

The results of the simulations with this model are shown in figures 2(a) and 2(b). Figure 2(a) shows the response of a partial polarization converter with TE losses for increasing power, while TM polarized light is applied at the input. Figure 2(b) shows the response of the same converter, but with TE polarized light applied at the input. In the first figure we can see an increase in the ratio between the amount of TE and TM polarized light. This can be explained by the fact that as the quantum-well saturates, more light is available for conversion and thus more TE polarized light appears at the output. The response of the second figure can be explained by the fact that for low power, the TE polarized light is converted as well as absorbed. As the power increases, the absorption saturates. More light is converted, but more TE light is present at the output as well.

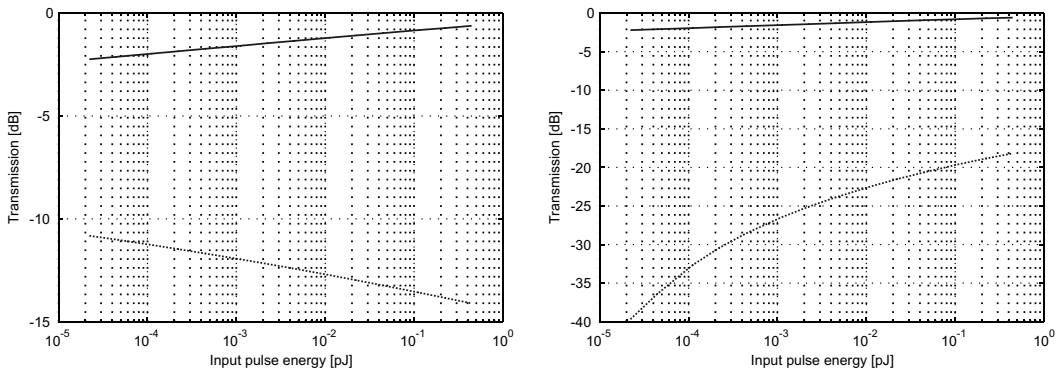

(a) (b)

Figure 2: Lossy conversion for a partial converter with TM input (a) and TE input (b). The dotted lines represent TM polarized light, the solid lines TE polarized light

Experimental verification of the model

To verify the results obtained with the simulations on the quantum-well polarization converters, measurements have been performed on experimental devices. The test structures consisted of a waveguide, connected to a polarization converter which was cleaved through the middle. The waveguide was used to couple the light in the polarization converters. By the cleaving of the converters both polarization states at the output could be monitored without suffering from waveguide losses. A schematic overview of the mea-

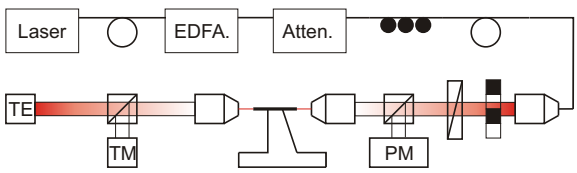

Figure 3: A schematic overview of the measurement setup, TE and TM indicate detectors for that polarization, PM is a power meter

surement setup is shown in figure 3. It consists of a tunable CW laser, coupled to an EDFA to provide enough power to saturate the quantum-well layer. The amount of power sent into the device under test is regulated by a computer controlled attenuator and was continuously monitored by a free space power meter. The polarization of the light applied to the input waveguide was set to TM with an external polarizer, to prevent absorption in the waveguide. After having passed through the teststructures, the polarization states of the light are separated by means of a polarization beam splitting cube. The light in both polarization states is then monitored by two free space detectors.
In the measurements, the input power of the polarization converter was swept over a large range, while the polarization of the output light was continuously monitored. This measurement has been performed for several lengths of polarization converters fabricated on material containing a quantum-well, as well as on material containing no quantum-well. The results of these measurements are shown in figures 4(a) and 4(b). In these figures the ratio of the TM polarized light over the TE polarized light is shown.
With increasing power, this ratio should not change, if the operation of the polarization converter is not influenced by absorption or index changes. This is the case for converters fabricated on bulk material (figure 4(a)). For the converters fabricated on quantum-well material, the ratio between the amount of TM and TE power decreases; indicating an increase in the amount of TE power, a decrease in the amount of TM power or both at the same time. This implies that the absorption of TE polarized light is saturated.

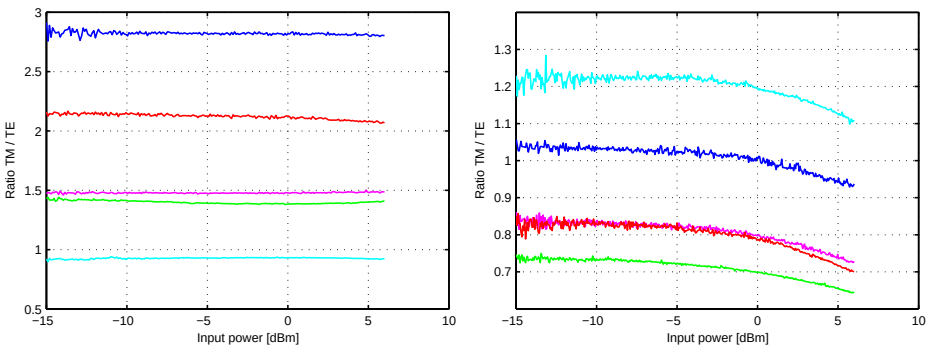

(a) (b)

Figure 4: Power dependence of a polarization converter on bulk material (a) and POLIS material (b). The different lines correspond to converters of different lengths

Conclusions

We have shown that the saturability of the absorption in quantum-well polarization converters leads to power dependent behavior of the converters. With increasing input power, the effective conversion length of the converter changes and the behavior of the device approaches the behavior without no absorption.

References

[1] El-Refaei, H. and D. Yevick, T. Jones, "Slanted-Rib waveguide InGaAsP-InP polarization converters", in *Journal of Lightwave Technology*, Vol. 22 (2004), No. 5, p. 1352-1357

[2] U. Khalique et al., "Polarization based Integration Scheme (POLIS) for Active and Passive Components", *ECIO Proc.*, Vol. 1, pp. 137-140, March 2003

[3] H. Kogelnik, "Theory of optical waveguides", in *Guided-Wave Optoelectronics*, Springer-Verlag, Berlin, Germany, 1988, pp. 79-80

Phase-locking on the beat signal of a two-mode 2.7 terahertz metal-metal quantum cascade laser

J.N. Hovenier[1], A.J.L. Adam[1], I. Kašalynas[1,a)], J.R. Gao[1,b)], and T.O. Klaassen[1], A. Baryshev[2] , B.S. Williams[3], S. Kumar[3], and Q. Hu[3], J. L. Reno[4]

1 Kavli Institute of NanoScience, Faculty of Applied Sciences, Delft University of Technology, Lorentzweg 1, 2628 CJ, Delft, The Netherlands; a) permanent address: Semiconductors Physics Institute, A. Gostauto 11, LT-01108 Vilnius, Lithuania. b) also with SRON Netherlands Institute for Space Research, Utrecht, The Netherlands.
2 SRON Netherlands Institute for Space Research, Landleven 12, 9747 AD Groningen, The Netherlands; 3 Department of Electrical Engineering and Computer Science and Research Laboratory of Electronics, Massachusetts Institute of Technology, Cambridge MA 02139, U.S.A; 4 Sandia National Laboratories, Albuquerque, NM 87185-0601, U.S.A.

Abstract:

We have studied the linewidth and phase-locking of a 2.7 THz quantum cascade laser by using a superconducting bolometer mixer. The 8 GHz beat signal is compared with a microwave reference with a feedback to the laser bias current. Phase locking has been demonstrated, resulting in an extremely narrow beat linewidth of less than 10 Hz. Under frequency-stabilization conditions we find that the line profile is virtually Lorentzian with a long-term minimum linewidth of the THz modes of about 6.3 kHz. Temperature dependent measurements suggest that this linewidth does not approach the Schawlow-Townes limit.

Significant progress in the development has made quantum cascade lasers[1] (QCLs) promising coherent solid-state THz sources for various applications. As demonstrated, a THz QCL can be applied as local oscillator (LO) for heterodyne receivers operating at several THz frequencies,[2,3] which are crucial for astronomical and atmospherical high-resolution spectroscopic sensing. For those applications a narrow emission linewidth of a QCL under frequency stabilization or phase locking is essential. In the case of a heterodyne space interferometer,[4] phase locking to an external reference is absolutely required. Here we report the first demonstration of phase locking of the beat signal of a two lateral-mode THz QCL to a microwave reference. Under frequency stabilization conditions, we are able to study the emission spectrum of a THz QCL in a systematic way, which previously was impossible. We use a QCL-device based on the resonant phonon design.[8] The active region contains 176 $GaAs/Al_{0.15}Ga_{0.85}As$ quantum-well modules, with a total thickness of 10 μm. The cavity of the QCL is a double-sided metal-semiconductor-metal waveguide, which is 40 μm-wide and 1 mm-long. When operated in a CW mode at a cold plate temperature of below 15 K, the emission spectrum measured by a Fourier-transform spectrometer (FTS) shows two closely spaced lines at 2.742 THz and 2.749 THz, respectively. They correspond to two different lateral lasing modes with unequal intensities. Their intensities and frequencies depend on the bias current of the QCL and the cold plate temperature. Furthermore, the effective indexes of refraction corresponding to the two modes are different and should also have a different temperature or current dependence. The maximum lasing output power per facet is roughly 1 mW.

To obtain the beat signal of the QCL, we use a spiral antenna coupled NbN hot electron bolometer (HEB) mixer, which can be operated up to at least 3-4 THz. The HEB is similar to those described in Ref. 9 and has a comparable sensitivity.

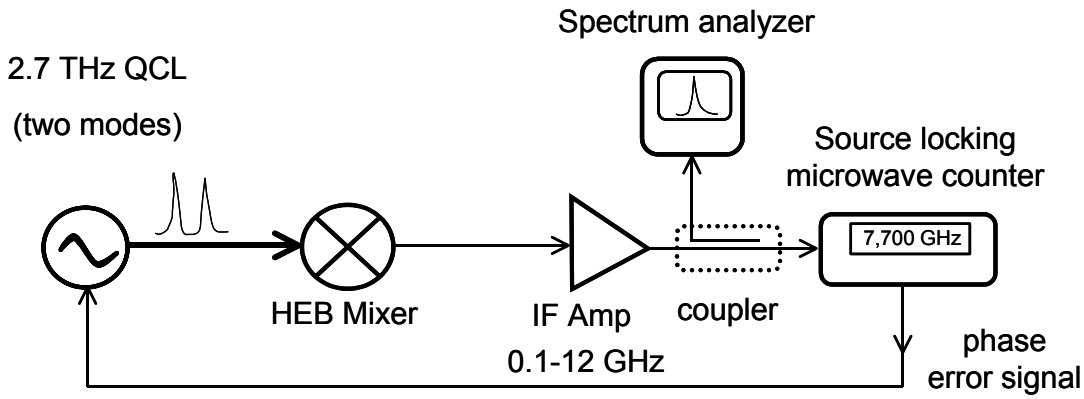

FIG.1. Schematic diagram of the experimental setup to phase lock of a two-mode THz QCL.

Figure 1 shows a schematic diagram of our measurement setup. The output beam of the QCL is focused onto the quasi-optically coupled HEB mixer. The IF (beat) output is fed into an EIP 575 source-locking microwave counter. The phase error correction signal of this counter is fed back into the bias-current circuit of the QCL using a variable resistor. We create a phase lock condition by using the PLL with a high loop gain with a maximum regulation bandwidth of 10 kHz. Figure 2 shows a typical set of power spectra of the beat signal recorded by the spectrum analyzer using a fixed video bandwidth (VBW), but different resolution bandwidths (RBW). Apart from the phase error correction signal from the EIP 575, both the temperature of the cold plate and the DC bias current are fixed. The spectra in figure 2 are actually power spectra of the phase difference between QCL beat and reference signal. As indicated in the figure, the linewidth seems to be reduced with reducing the RBW of the spectrum analyzer. Apparently the linewidth is too small, e.g. smaller than 10 Hz, to be measurable due to the limited RBW of 10 Hz. The data demonstrate that for an offset from the center frequency less than the PLL regulation bandwidth most of the signal power is located in a central peak of (near-) zero bandwidth. *This is a clear indication of phase locking.* The spectra are reproducible and stable for an arbitrary-long time. Experimentally, we can show that the QCL behaves as a current controlled oscillator, which is the key to enable phase locking. As shown in the inset of figure 2, the beat frequency decreases monotonically with increasing bias current for a given cold plate temperature, e.g., from 7.9 to 7.5 GHz with the rate of roughly 10 MHz/mA. This means that phase locking conditions can be realized for all bias points, and moreover that stabilization of the beat frequency implies stabilization of the THz frequencies of both laser modes. The second part of our studies involves the study of the free running laser line profile and linewidth. Starting from phase locking conditions we now reduce the loop gain such that the central frequency of the beat signal remains the same but the line shape is no longer influenced by the phase locking. Under this frequency-stabilization, we are able to measure the power spectrum of the beat signal of the QCL in a systematic way, e.g. as a function of the cold plate temperature or the bias current. Figure 3 shows a measured beat signal with the minimum linewidth observed in this experiment, fitted with a Lorentzian curve. We draw attention to several interesting features. The fit shows the spectrum to be predominantly Lorentzian, as expected if the

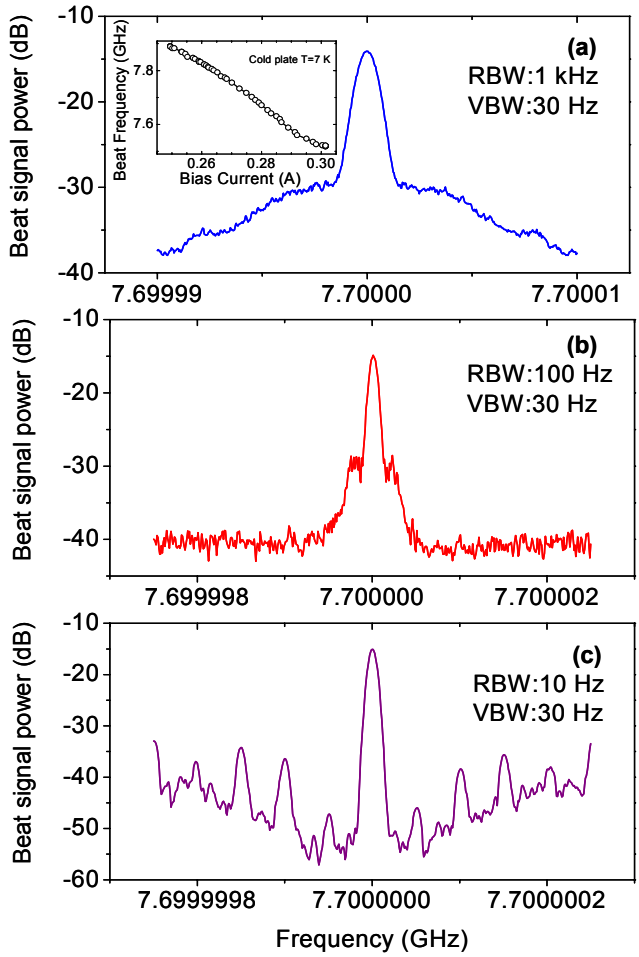

noise is due to spontaneous emission. In some other cases, we find that a Voigt function gives a better fit than the Lorentzian, suggesting the coexistence of other noise sources, e.g. 1/f noise and noise interference pick up.

The minimum (FWHM) linewidth is found to be 12.6 kHz. Knowing that this beat signal results from a convolution of two similar lines and assuming that their profiles are virtually Lorentzian, the lower limit of the linewidth of *an individual emission line* should be 6.3 kHz. Note that this is the narrowest linewidth ever reported in THz QCLs and is actually a few orders of magnitude smaller than required for astronomical and atmospheric observations. The linewidth of a THz QCL should be limited by quantum noise through spontaneous emission and is expected to be described by the Schawlow-Townes limit .

FIG. 2 The power spectra of the beat signal of two lateral-mode THz QCL that is phase locked to a microwave reference around 7.7 GHz recorded with different resolution bandwidths (RBW), but a fixed video bandwidth (VBW) in the spectrum analyser. Other lines appeared in (c) are due to the pick-up of 50 Hz signals. The inset in (a) shows the beat frequency as a function of bias-current of the QCL at cold plate temperature of 7K.

$$\Delta\nu_{ST} = \left(\frac{N_2}{N_2 - N_1}\right)\frac{(2\pi h\nu)(\Delta\nu_c)^2}{P}$$

(1)

Here $N_{1,2}$ are the populations in the upper and lower laser states; $\Delta\nu_c$ is the cold cavity waveguide and mirror losses ($\alpha = \alpha_w + \alpha_m$); P is the internal power in the mode relating linewidth and equals $\alpha v_g/2\pi$ with the group velocity v_g and the total loss α of the to P_{out} by $P_{out} = (\alpha_m / \alpha)P$. We assume eq. 1 to be valid for each of the two emission lines. Using the following inputs: $N_2/(N_2-N_1)$=1.3, α_w ~10 cm^{-1} at 2.7 THz, α_m =2.2 cm^{-1}, and P_{out} ~1 mW, we derive a Schawlow-Townes linewidth $\Delta\nu_{ST}$ = 0.7 KHz, which seems to be 10 times smaller than the measured linewidth. In view of large uncertainties in these input parameters, the result is not conclusive yet. Nevertheless, this represents a first serious attempt to investigate the ultimate linewidth of a THz QCL.

Eq. 1 suggests that the linewidth should be inversely proportional to the laser power. To test this, we have studied the linewidth of the beat signal as a function of cold plate temperature. The results are shown in figure 4.

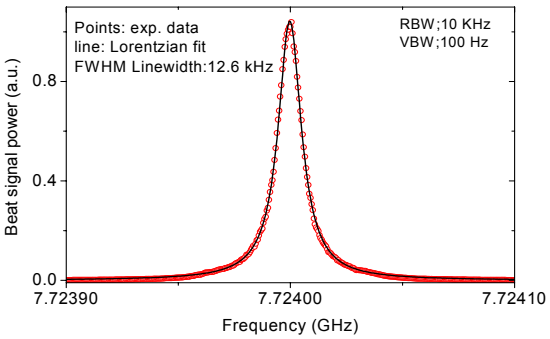

FIG. 3 Measured power spectrum of the beat signal under frequency stabilization (data points)[11]. The curve is a fit with a Lorentzian profile.

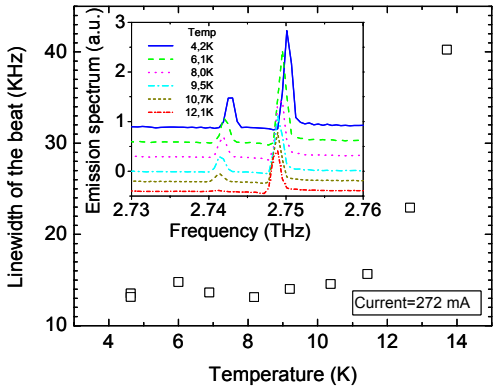

FIG. 4 Linewidth of the beat signal as a function of the cold plate temperature of the QCL. The inset shows emission spectra of the two-mode QCL taken at several temperatures. For clarity an offset in the intensity for each spectrum is introduced.

We notice that, despite that the intensity (considered to be equivalent to the power) of both emission lines decreases monotonically (see the inset of figure 4), the linewidth remains virtually independent of temperature up to 12 K. Clearly the linewidth does not follow Eq. 1 and consequently does not approach the quantum-noise limit.

In summary, we have succeeded in achieving phase stabilization of a 2.7 THz QCL through the beat signal of its two lateral-modes, demonstrating the feasibility of phase-lock of the THz signal itself. Under frequency-stabilization conditions we have been able to study the lineshape and linewidth of the free running QCL in a controllable manner and found the narrowest linewidth of 6.3 kHz.

The authors acknowledge M. Hajenius and J.J.A. Baselmans for the use of their HEB mixer, and T.M. Klapwijk for his support and stimulating discussion. This work is supported partly by Radionet. The work at MIT is supported by AFOSR, NASA and the NSF. Sandia is a multi-program laboratory operated by Sandia Corporation, a Lockheed Martin Company, for the US Dept. of Energy under Contract DE-AC04-94AL85000.

References

[1] R. Köhler, A. Tredicucci, F. Beltram, H.E. Beere, E.H. Linfield, A.G. Davies, D.A. Ritchie, R.C. Iotti, and F. Rossi, Nature (London) **417**, 156(2002).

[2] J.R. Gao, J.N. Hovenier, Z.Q. Yang, J.J.A. Baselmans, A. Baryshev, M. Hajenius, T.M. Klapwijk, A.J.L Adam, T.O. Klaassen, B.S. Williams, S. Kumar, Q. Hu, and J.L Reno, Appl. Phys. Lett. **86**, 244104 (2005).

[3] H.-W. Hübers, S. G. Pavlov, A. D. Semenov, R. Köhler, L. Mahler, A. Tredicucci, H. E. Beere, D. A. Ritchie and E. H. Linfield, Optics Express, **13**, 5890(2005).

[4] Th. de Graauw, *et al*, Proc. SPIE **5487**, 1522 (2004).

[5] J.J.A. Baselmans, M. Hajenius, J.R. Gao, T.M. Klapwijk, P.A.J. de Korte, B. Voronov, and G. Gol'tsman, Appl. Phys. Lett, **84**, 1958 (2004).

[6] We notice that the beat frequency of this QCL has shown a down-shift of about 0.6 GHz after the measurements in figure 2.

[7] A. Yariv, Quantum Electronics, 3rd ed., New York : Wiley, 1989.

[8] G. M. Stéphan, T. T. Tam, S. Blin, P. Besnard, and M. Têtu, Phys. Rev. **A71**, 043809(2005).

Mode structure of a vertical-cavity surface-emitting laser subject to optical feedback

K. Green[1], B. Krauskopf[2] and D. Lenstra[3]

[1]Quantum Electronics Theory and Laser Centre, Vrije Universiteit Amsterdam, The Netherlands
[2]Department of Engineering Mathematics, University of Bristol, UK
[3]Faculty of Electrical Engineering, Mathematics and Computer Science,
Delft University of Technology, The Netherlands

We present an analysis of the external cavity mode (ECM) structure of a vertical-cavity surface-emitting laser subject to optical feedback. We consider a model in which two transverse optical modes are excited. Furthermore, we allow weak coupling of the modes via the feedback term. (In addition to the coupling through the inversion.) We use numerical continuation techniques to find and follow solutions of the governing partial, delay differential equations. This approach allows us to show how the ECM structure depends on the key parameters of feedback strength, feedback phase and the amount of coupling via the feedback term.

Vertical-cavity surface-emitting lasers (VCSELs) can support a number of transverse optical modes. Under external influence, such as pump modulation [1], optical injection [2] or optical feedback [3], these modes may interact resulting in complex dynamics. In this study, we investigate a VCSEL model in which the first two, rotationally symmetric, linearly polarised optical modes (LP_{01} and LP_{02}) are excited [3]. We include a general form of optical feedback in which the electric fields of the two modes can couple via the external-cavity round-trip. This is in contrast to previous studies in which each field receives feedback only from itself [3]. More specifically, we study the external-cavity mode (ECM) structure of a VCSEL with a small amount of feedback induced cross-coupling between the electric fields. The ECMs underpin the more complicated dynamics and, as such, a detailed analysis of their dependence on parameters is needed to fully understand a VCSEL subject to optical feedback.

In dimensionless form, our VCSEL model [1] can be described by the following system of delayed partial differential equations

$$\frac{dE_n}{dt} = (1+i\alpha)\left[\int_0^1 \psi_n N\, r dr\right] E_n + \kappa F_n(t,\tau)e^{iC_p}, \quad n=1,2, \tag{1}$$

$$T\frac{\partial N}{\partial t} = d_f\left[\frac{1}{r}\frac{\partial}{\partial r}\left(r\left(\frac{\partial N}{\partial r}\right)\right)\right] - N + J - \sum_{n=1,2}\left(\left(1+2\left[\int_0^1 \psi_n N\, r dr\right]\right)\psi_n |E_n|^2\right) \tag{2}$$

describing the evolution of the two complex electric fields $E_1(t)$ and $E_2(t)$, associated with the radial profiles $\psi_1(r)$ and $\psi_2(r)$ of the LP_{01} and LP_{02} modes, respectively, and the evolution of the spatial carrier distribution $N(r,t)$. Dimensionless parameters are the linewidth enhancement factor $\alpha = 3.0$, the diffusion coefficient $d_f = 0.05$, the ratio between the carrier lifetime and the photon decay rate $T = 750.0$, the pump applied to the cladding region $J_{\min} = 0.0$ and to the core (with radius $a = 0.3$) region $J_{\max} = 2.0$. This value of pump current was chosen well above threshold so that the system is lasing. The

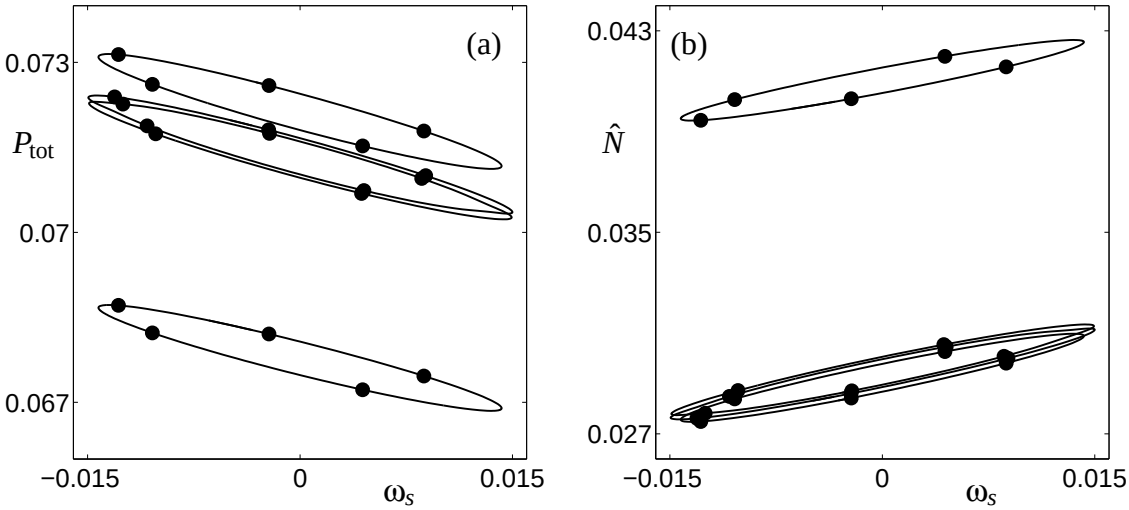

Figure 1: ECM-components for $\eta = 0.9$ with ECMs for $C_p = 0$, shown in the $(\omega_s, P_{\text{tot}})$-plane (a) and the $(\omega_s, \hat{N})$-plane (b).

feedback terms $\kappa F_n(t,\tau)e^{iC_p}$ involve the dimensionless (weak) feedback rate $\kappa = 0.005$, and the dimensionless propagation time $\tau = 500$ between the VCSEL and an external reflector; corresponding to a physical distance of approximately 10 cm. Furthermore, C_p represents the feedback phase, which can be controlled experimentally by varying the length of the external cavity on the scale of the optical wavelength, so that τ remains unchanged [6].

In past studies the feedback function in Eq. (1) has been given as $F_n(t,\tau) = E_n(t-\tau)$. In other words, there is no coupling of the two electric fields through optical feedback. In this study, we consider the following, more general, feedback terms

$$F_1(t,\tau) = \eta E_1(t-\tau) + (1-\eta)E_2(t-\tau)e^{i\Delta}, \quad (3)$$

$$F_2(t,\tau) = (1-\eta)E_1(t-\tau)e^{-i\Delta} + \eta E_2(t-\tau). \quad (4)$$

This allows the two fields to couple through the external-cavity round-trip. The amount of coupling is given by the *coupling parameter* η. For $\eta = 1$, Eqs. (3) and (4) reduce to the zero-coupling case, that is, both fields receive feedback only from themselves. Conversely, for $\eta = 0$, the electric fields are cross-coupled, that is, the first electric field receives feedback from the second field, and vice versa. Finally, we note that Δ describes the difference between the optical frequencies of the two fields in the absence of feedback. In this study, we fix $\Delta = 0$.

In order to employ numerical methods, we first need to discretise (2) in the radial direction r. To this end, we consider 100 intervals, over the radius of the VCSEL, that is, $r \in [0,1]$. At $r = 0$ we use zero Neumann boundary conditions, and at $r = 1$ we use zero Dirichlet boundary conditions. This results in a large-scale delay differential equation (DDE) of size 105, which presents quite a challenge for an analytical investigation. In fact, even simulated results obtained from direct numerical integration of Eqs. (1) to (4) are very time-consuming to produce. In this study, we use numerical continuation techniques which allow us to find and follow in parameters branches of steady state solutions, irrespective of their stability [7, 5]. These techniques are not generally used for systems

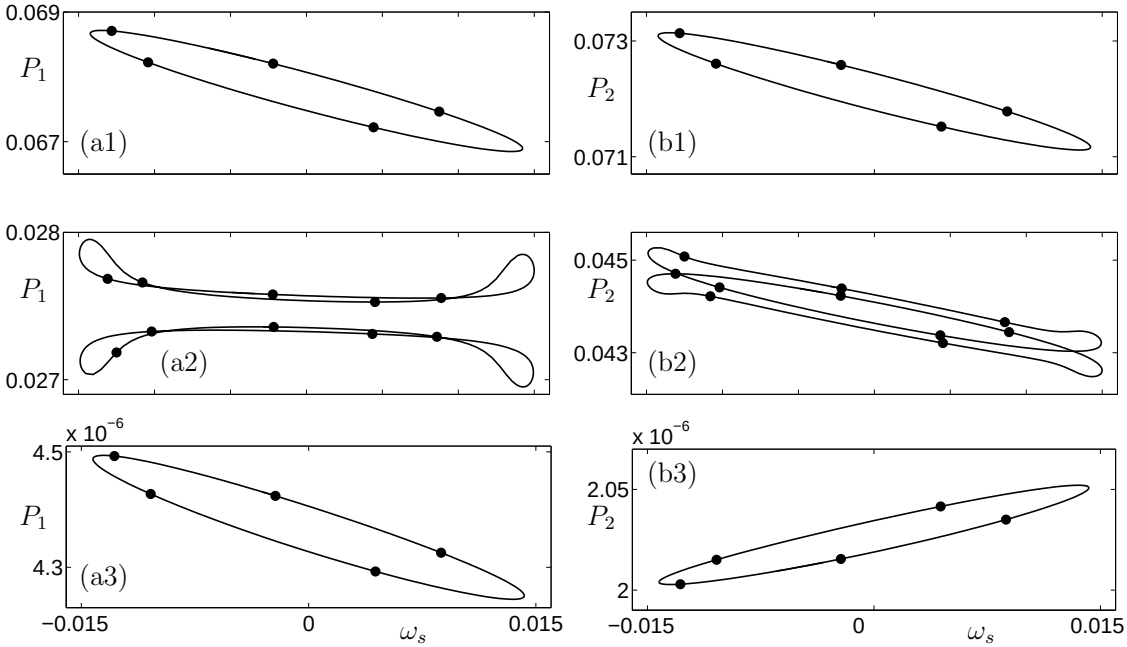

Figure 2: ECM-components for $\eta = 0.9$ with ECMs for $C_p = 0$, shown in the (ω_s, P_1)-plane (a1) to (a3), and (ω_s, P_2)-plane (b1) to (b3).

of this size and, hence, this study also acts as a test-case for the efficiency of such tools in analysing large-scale DDEs.

The basic steady state solutions of Eqs. (1) to (4) are the so-called *external cavity modes* (ECMS). They are given as

$$(E_1(t), E_2(t), N(r,t)) = (R_1 e^{i\omega_s t}, R_2 e^{i\omega_s t + i\Phi}, N_s(r)), \tag{5}$$

where $R_n = |E_n|$ $(n = 1,2)$ are the amplitudes of the two fields, ω_s is the frequency of the output light, Φ is a fixed phase difference, and $N_s(r)$ is a fixed level of inversion in both space and time. Note that the field intensities are given as $P_1 = R_1^2$ and $P_1 = R_2^2$. We denote the total field intensity as $P_{\text{tot}} = P_1 + P_2$, that is, $P_{\text{tot}} = |E_1|^2 + |E_2|^2$.
Typically, in finding the steady state solutions of lasers with feedback [4], one first finds an analytical expression for the frequency ω_s which is used to obtain the values of amplitude, inversion and phase difference. However, due to its spatial nature, this approach is not possible when solving for the ECMs of Eqs. (1)–(4). Therefore, we turn to the aforementioned numerical continuation techniques.
As for conventional optical feedback (COF) [6] and filtered optical feedback (FOF) [4], a continuous change of the feedback phase C_p over 2π traces the path from one ECM of Eq. (5) to the next. Using the continuation package `DDE-BIFTOOL` [7] with C_p as a free parameter, we can trace out closed curves on which the steady-state ECM solutions of Eqs. (1) to (4) lie. We refer to these closed curves as the *ECM-components*.
Figure 1 shows the ECM-components of Eqs. (1)–(4) and the ECMs for $C_p = 0$ (shown as large dots). The cross-coupling parameter was fixed at $\eta = 0.9$. Panel (a) shows the ECM-components in the $(\omega_s, P_{\text{tot}})$-plane, and panel (b) shows them in the $(\omega_s, \hat{N})$-plane, where $\hat{N}$ is the mean value of $N(r)$ over the radial distance $r \in [0,1]$. The laser's intensity

and inversion are in direct competition with one another. For example, the lower solutions in Fig. 1(a) correspond to the upper solutions in Fig. 1(b). Furthermore, for our parameter choice, the ECMs are shown to lie on four separate ECM-components which, like for the COF laser, have the shape of an ellipse. (For the COF laser, one always finds a single ECM-component.)
Figure 2 shows the same ECM-components for $\eta = 0.9$ and ECMs for $C_p = 0$ but now in terms of the intensity contributions of the individual fields P_1 (a1)–(a3) and P_2 (b1)–(b3). Three panels are used due to the position of the ECM-components on the y-axes. We now find that, while the ECM-components shown in Fig. 1(a) have similar values of total intensity P_{tot}, the individual intensities of the two fields E_1 and E_2 can be quite different. Specifically, we have three types of solutions. In the first, the field E_1 dominates, while E_2 hardly contributes to the total intensity; see the ECM-components shown in Figs. 2(a1) and (b3). These solutions make up the lowermost ellipse shown in Fig. 1(a). Conversely, we have a solution in which the field E_2 dominates, while E_1 hardly contributes to the total intensity. This corresponds to Figs. 2(a3) and (b1), the uppermost ellipse of Fig. 1(a). Finally, we have solutions in which both fields E_1 and E_2 contribute to the total intensity. These solutions lie on the ECM-components shown in Figs. 2(a2) and (b2). They correspond to the two intermediate ellipses of Fig. 1(a).

In summary, it has been shown that, while the total intensities of the ECMs on each of the ECM-components are very similar, the individual contributions of the two fields can be quite different. For example, we find solutions in which one of the two fields hardly contributes to the total intensity. How these ECM-components depend on other parameters, in particular on a variation of κ and η is presently being investigated and will be discussed elsewhere.

References

[1] A. Valle, “Selection and modulation of high-order transverse modes in vertical-cavity surface-emitting lasers”, *IEEE J. Quantum Electron.*, vol. 34, pp. 1924–1932, 1998.

[2] J. Y. Law, G. H. M. van Tartwijk, and G. P. Agrawal, “Effects of transverse-mode competition on the injection dynamics of vertical-cavity surface-emitting lasers”, *Quantum Semiclass. Opt.*, vol .9, pp. 737–747, 1997.

[3] M. S. Torre, C. Masoller, and P. Mandel, “Transverse-mode dynamics in vertical-cavity surface-emitting lasers with optical feedback”, *Phys. Rev. A*, vol. 66, 053817, 2002.

[4] K. Green and B. Krauskopf, “Mode structure of a semiconductor laser subject to fi ltered optical feedback”, *Opt. Commun.*, vol. 258, pp. 243–255, 2006.

[5] B. Krauskopf, “Bifurcation analysis of lasers with delay”, in *Unlocking dynamical diversity: Optical feedback effects on semiconductor lasers*, D. M. Kane and K. A. Shore, Eds., Wiley, 2005, pp. 147–183.

[6] T. Heil and I. Fischer and W. Elsäßer and B. Krauskopf and K. Green and A. Gavrielides, “Delay dynamics of semiconductor lasers with short external cavities: Bifurcation scenarios and mechanisms”, *Phys. Rev. E*, vol. 67, 066214, 2003.

[7] K. Engelborghs, T. Luzyanina, and D. Roose, “Numerical bifurcation analysis of delay differential equations using DDE-BIFTOOL”, *ACM Trans. Math. Softw.*, vol. 28, pp. 1–21, 2002.

Frequency Doubled Er/Brillouin All-Fiber Laser

Andrei A. Fotiadi [1, 4], Olivier Deparis [1, 3], Patrice Mégret [1],
Costantino Corbari [2], Albert Canagasabey [2], Morten Ibsen [2] and Peter G. Kazansky [2]

[1]Service d'Electromagnétisme et de Télécommunications, Faculté Polytechnique de Mons, 31 boulevard Dolez, B-7000 Mons, Belgium

[2]Optoelectronics Research Centre, University of Southampton, Southampton SO17 1BJ, UK

[3]Now with Laboratoire de physique du solide, FUNDP, 61 Rue de Bruxelles, B-5000 Namur, Belgium

[4]Also with Ioffe Physico-Technical Institute of RAS, St.Petersburg, Russia

25 mW output power Er/Brillouin oscillator and a periodically poled optical fiber with a quasi phase matching resonance at ~1.56 µm are the simplest way to realize nanosecond, all-fiber laser sources operating at ~778 nm and ~389 nm. 25 W peak power pulse train generated at ~778 nm with 120 mW diode pumping is reported.

Introduction

Nanosecond pulse laser sources with extended wavelength diversity are of great interest for numerous applications. The use of fiber lasers for second harmonic generation allows combining efficient wavelength conversion with the possibility to keep all-fiber format. Second-order nonlinear optical processes can be implemented in all-fiber configurations by using a periodically poled fiber as second-order nonlinear medium with quasi-phase-matching [1,2] and a fiber laser as pump source. In the past, second-harmonic generation (SHG) was demonstrated in periodically poled fibers using solid-state lasers [1, 3] or master-oscillator-power-amplifier (MOPA) configurations as pump sources [4]. In order to fully exploit the advantages of all-fiber configurations (low-cost, robustness, compactness, flexibility) and to optimize nonlinear wavelength conversion processes in the periodically poled silica fiber (PPSF), a fiber laser with appropriate characteristics is needed. The requirements for the fiber laser (to be used as pump source for e.g. SHG) are as follows: 1) it must deliver high-peak power pulses in order to obtain high conversion efficiency of the pump; and 2) its optical spectrum must be located inside the quasi-phase-matching (QPM) resonance band of the PPSF, which is about ~1 nm for a 10 cm long device. A self-Q-switched erbium fiber laser employing stimulated Brillouin scattering (SBS) [5] can potentially meet all these requirements and, moreover, can bring simplicity of configuration and possibility of wavelength tuning. Providing a typical recovery time for the population inversion in the doped fiber as long as hundreds of microseconds (i.e. the repetition rate as low as several kHz) such lasers are able to emit nanosecond pulses with record values of the peak/average power contrast ranging up to ~10^5 that makes them very efficient for nonlinear conversion in fibers [6].

Here we present a low-cost solution for all-fiber frequency-doubled laser sources by combining two ingredients: 1) a self-Q-switched erbium/SBS fiber laser that generates ~5 ns pulses with a bandwidth of ~0.25 nm and a peak/average power contrast up to ~1 kW/25 mW; and 2) a periodically poled fiber with QPM resonance around ~1556 nm. We demonstrate that, in spite of the low average power (~250 µW) associated with the random nature of erbium/SBS laser pulsation [5], the peak power of second-harmonic pulses at ~778 nm lies within the ten-watts-scale and is high enough to generate the

fourth harmonic at ~389 nm in a cascade process. In practice, simple bending of fiber allowed us to completely suppress the residual pump and to select the second and fourth harmonic signals. The advantage of the proposed solution relies in the specific suitability of the nanosecond pulses generated through the multi-cascade SBS process for nonlinear interaction. Since the optical spectrum of the pulses contains several SBS components (the SBS shift is ~11 GHz) locking between them could considerably enhance values of peak power available for SHG.

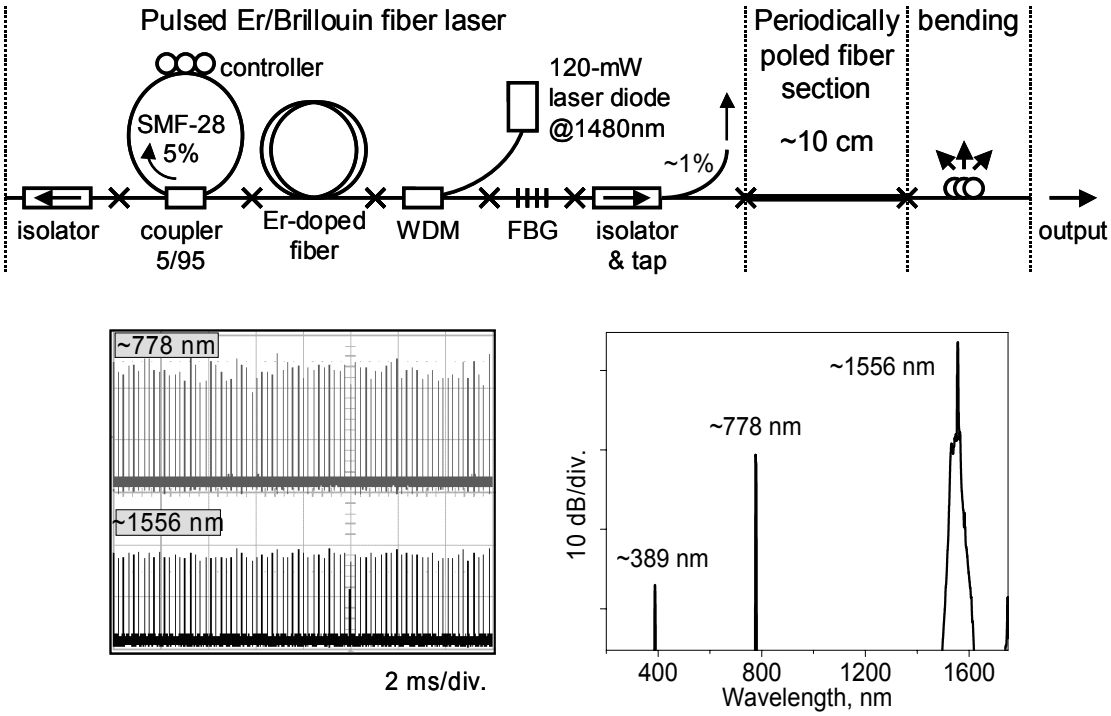

Fig.1. Configuration of the all-fiber frequency-doubled laser source(a).
Typical oscilloscope traces (b) and an optical spectrum (c) recorded with the laser.

Experimental setup

The scheme of the frequency doubled Er/Brillouin laser is shown in Fig.1(a). The all-fiber format of the configuration is maintained by direct splicing of standard low-cost telecom components. The configuration is pumped by a 120-mW laser diode at ~1480 nm. The Er/Brillouin oscillator [5] generates a pulse train with a repetition rate of ~4 kHz (Fig.1(b)). Most of the laser intensity is emitted through few SBS components localized near the Stokes side of the FBG reflection spectrum within ~0.25 nm (see Fig.2(a)). A ~40-GHz-bandwidth FBG used in the cavity sets the fundamental laser frequency precisely at ~1556.25 nm, which is close to the QPM resonance peak of the periodically poled fiber. The ~10-cm long PPSF was fabricated from a twin-hole fiber by point-to-point UV-erasure of the second-order nonlinearity induced by uniform thermal poling (T=250 ^{o}C, ~30 minutes with ~4 kV applied). The fiber geometry, the poling and erasure parameters were described in ref. [2]. The fiber laser is fusion spliced to the PPSF and the laser polarization is optimized in order to get the maximum SH power. The splice between the twin-hole fiber and the SMF28 is not optimized and estimated to be around ~3 dB, thus reducing the input fundamental average/peak power in the poled fiber to

about ~12 mW / 500 W. Gigantic pulses initiated through multi-cascade SBS induce second-harmonic generation in the periodically poled fiber around the QPM resonance.

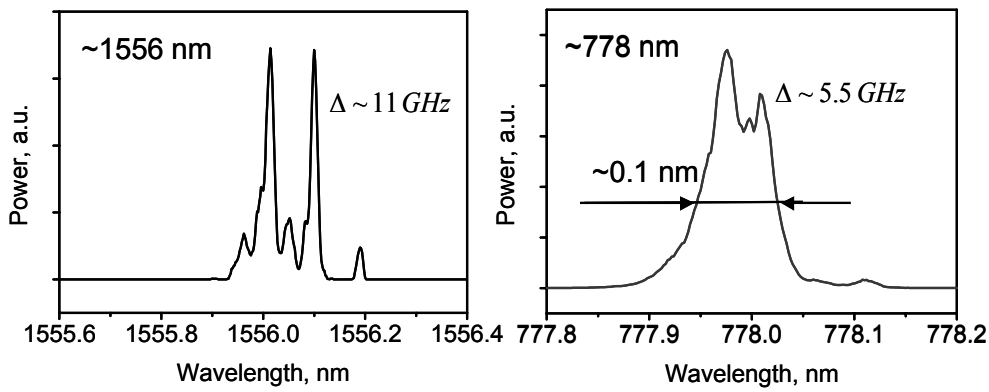

Fig.2. Typical optical spectra of the fundamental (a) and SH (b) radiation.

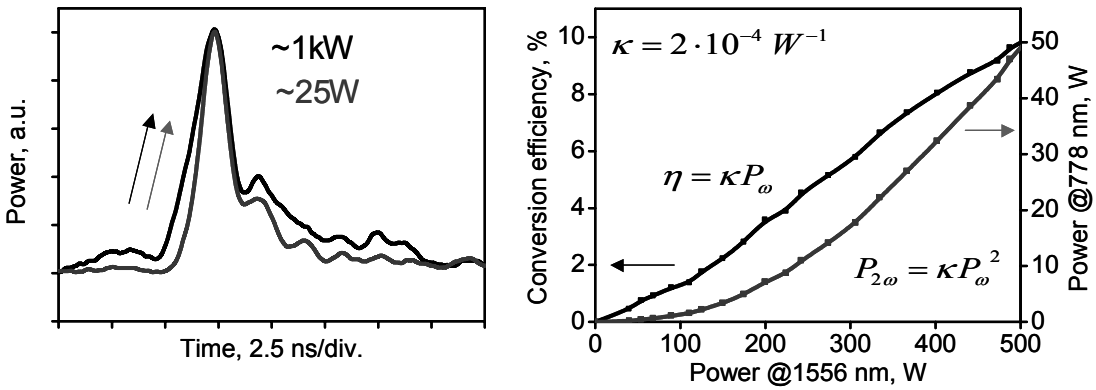

Fig.3. Typical oscilloscope traces of the fundamental (black) and SH (grey) pulses (a). Conversion efficiency (black) and SH pulse peak power (grey) as dependences on the fundamental pulse peak power (b). The dependencies (b) are calculated from the oscilloscope traces (a).

Results and discussion

A typical optical spectrum of the output radiation covering almost the full range of the optical spectrum analyzer is shown in Fig. 1(c). One can see that not only the second harmonic is generated but also the fourth harmonic. Whereas the former originates from QPM of the fundamental radiation, the latter is likely to be due to SHG of the former through modal phase matching. Fine structures of the spectral lines at 1556 nm and 778 nm are shown in Fig. 2. Both structures exhibit clear signatures of the stimulated Brillouin scattering that is the origin of the laser operation. Whereas the Brillouin laser generates two spectral peaks with the spacing of ~11 GHz (that is the Brillouin shift) the SHG results in two peaks with the spacing of ~5.5 GHz (that is half of the Brillouin shift). All presented spectra were recorded with an optical spectrum analyzer Ando AQ-6317B operating in a pulse low-pass-filter (LPF) mode (the filter time constant is ~2 ms).

Typical pulse trains generated at ~778 and ~1556 nm are shown in Fig. 1 (b). Since the first train is a result of the frequency doubling of the second train, it exhibits slightly larger fluctuations of the pulse amplitude. Insight into the dynamics of the SHG process was obtained by attenuating the radiation emitted by the source and by detecting it using two fast photodiodes. The laser pulses were registered simultaneously from the main output (SH pulses) and from the ~1% tap (pump pulses). The bandwidths of registration channels are ~1 GHz. Typical oscilloscope traces of pump and SH pulses are shown in Fig. 3(a). One can see that the SH pulse is narrower than the pump pulse. Besides, the Fig. 3(b) shows that for the reported operation the SH power is precisely proportional to the square of the pump power $P_{2\omega} = \kappa P_{\omega}^{2}$ (see, Fig. 3(b)), as it usually takes place with SH generation. The maximal SH average power was ~250 μW corresponding to ~25 W SH peak power, and resulting in a peak conversion efficiency of $\eta = \kappa P_{\omega}$ ~10% inside the PPSF. Further increase of the conversion efficiency exceeding ~50% could be ensured by using longer PPSF and optimization of the splice loss.

Conclusion and acknowledgements

The proposed configuration offers simple solution for all-fiber frequency-doubled laser sources. The solution opens the potential to produce nanosecond pulses through the complete visible spectrum employing as a pump the rare-earth doped fiber lasers commonly operating in the infrared. Owing to the low chromatic dispersion, the periodically poled silica fiber used in our configuration had a QPM bandwidth of about ~1 nm for a ~10 cm long device (10 times larger than in typical nonlinear crystals such as $LiNbO_3$). The Brillouin lasers delivering ns pulses with the linewidth less than ~0.25 nm will be suitable for frequency doubling up to ~50 cm interaction lengths. Therefore, an increase of the conversion efficiency above 50% may be achieved by utilizing the total available power budget for the fiber laser in conjugation with the use of long PPSF. Additional advantages of such sources are compactness, robustness, low cost and their all-fiber integrated format.

The research was supported by Interuniversity Attraction Pole program (IAP V 18) of the Belgian Science Policy and also funded by FRFC 2.4622.04.

References:

[1] P. G. Kazansky, V. Pruneri and P. St. J. Russell, “Blue-light generation by quasi-phase-matched frequency doubling in thermally poled optical fibers”, Opt. Lett. , vol. 20, pp. 843-845, 1995.

[2] C. Corbari, A. Canagasabey, M. Ibsen, F. Mezzapesa, C. Codemard, J. Nilsson, P. G. Kazansky, “All-fiber frequency conversion in long periodically poled silica fibers”, Techn. Digest of OFC’05, 2005, OFB3.

[3] V. Pruneri, G. Bonfrate, P. G. Kazansky, C. Simonneau, P. Vidakovic, J. A. Levenson, “Efficient frequency doubling of 1.5 mm femtosecond laser pulses in quasi-phase-matched optical fibers”, Appl. Phys. Lett., vol. 72, pp.1007-1009, 1998.

[4] V. Pruneri, G. Bonfrate, P. G. Kazansky, D. J. Richardson, N. G. Broderick, J. P. deSandro, C. Simonneau, P. Vidakovic, J. A. Levenson, “Greater than 20% efficient frequency doubling of 1532-nm pulses in quasi-phase-matched germanosilicate fibers”, Opt. Lett., vol. 24, pp.208-210, 1999.

[5] A. A. Fotiadi, P. Mégret, M. Blondel, “Dynamics of self-Q-switched fiber laser with Rayleigh – stimulated Brillouin scattering ring mirror”, Opt.Lett., vol.29, pp.1078-1080, 2004.

[6] A. A. Fotiadi, P. Mégret, “Self-Q-switched Er-Brillouin fiber source with extra-cavity generation of a Raman supercontinuum in a dispersion shifted fiber”, Opt.Lett., vol.31, pp.1621-1623, 2006.

InAs/InP Quantum Dot Fabry-Pérot and Ring Lasers in the 1.55 µm Range using Deeply Etched Ridge Waveguides

Y. Barbarin, S. Anantathanasarn, E.A.J.M. Bente, Y.S. Oei, M.K. Smit and R. Nötzel

COBRA, Eindhoven University of Technology Den Dolech 2,
P.O. Box 513, 5600 MB, Eindhoven, The Netherlands

In this paper we report on the fabrication and characterization of InAs/InP (100) quantum dot Fabry-Pérot and ring lasers, lasing in the 1.55 µm wavelength range and employing narrow deeply etched ridge waveguides (1.65 µm width). Sidewall recombination effects at the deeply etched waveguides appear not to affect the performance of the lasers. Narrow deeply etched ridge waveguides can be mono-mode and allow for a small bending radius to realize compact integrated devices. As a demonstration we present results on a compact ring laser.

Introduction

Quantum dot (QD) lasers and amplifiers are of great interest for optical telecommunication. QD lasers have a very low transparency current density per dot layer, a wide gain bandwidth and can have a much lower threshold current density [1] compared to bulk or quantum well lasers. For the use of QD lasers and amplifiers in optical integrated circuits for telecommunication, there are two important aspects. The first is the operation in the C and L band; the second is the option to have deeply etched mono-mode ridge QD waveguide amplifiers which allow for significantly more compact devices. QD material has the advantage over other active materials with respect to the spreading and sidewall recombination [2] of injected carriers. It has been reported in [3] that PL intensities of 1.2 µm InAs QDs deeply etched mesas depend weakly on the mesa size down to 200 nm. Deeply etched InAs/GaAs QD lasers have been reported with waveguide mesa widths down to 1 µm in the 1.3 µm wavelength range [4]. A ring laser at 1.3 µm has also been reported [5], with a 10.28 mm long ring shallowly etched. In this paper we present first results on InAs/InP (100) QD lasers, lasing in the 1.55 µm wavelength range, with mono-mode deeply etched waveguides (1.65 µm width). The presented lasers are Fabry-Pérot (FP) and ring cavity types. All our high contrast deeply etched QD lasers have the same threshold current density as shallowly etched ones and do not deteriorate over many hours of operation. It appeared that due to the low absorption of the QDs, the output waveguides of the ring lasers do not need to be contacted and injected with current for operation with reasonable output power. This shows that for specific applications QD active materials offer the possibility to integrate active and passive devices on a single chip in a uniform layer stack.

Fabrication process

The QD laser structure was grown on n-type InP (100) substrates by metal organic vapor-phase epitaxy (MOVPE). In the active region, five-fold stacked InAs QD layers separated by 40 nm thick InGaAsP (Q = 1.25 µm; Q1.25) were placed in the center of a

500 nm thick lattice-matched Q1.25 waveguide core. The choice of the Q1.25 waveguide core is the result of an optimization made with regards to the application of this material in active/passive photonic integration using selective area regrowth [6]. It is a compromise between the maximum confinement energy of the QDs for temperature stability of active devices, a large electro-optic effect for phase modulators in passive areas, and maintaining a large refractive index contrast for strong vertical optical mode confinement. The nominal InAs amount for QD formation was 3.5 monolayers (MLs). One ML GaAs interlayer was inserted underneath each QD layer to suppress unwanted As/P exchange reactions during QD growth to tune the QD emission wavelength into the 1.55 µm region [7]. Bottom and top claddings of the laser structure are 500 nm n-InP buffer and 1.5 µm p-InP completed by a compositionally graded 75 nm p-InGaAsP contact layer. The device performance of shallowly etched narrow ridge waveguide QD lasers processed from the same material is reported in [8]. The waveguides have been processed using Reactive Ion Etching (RIE). For electrical isolation between contacted waveguides, the contact layer and part of the top cladding were removed. Before contacting, the waveguides have been planarized by polyimide.

Fabry-Pérot laser results

The cavity length of the 1.65 µm wide deeply etched FP QD laser is 2.0 mm, defined by cleaving. The cleaved facets are un-coated. Comparison with the shallowly etched QD lasers shows that lasing occurs on the QD ground states [8]. The threshold current density in continuous wave (CW) operation is 3.3 kA/cm² at 15°C, which is the average value for eight different lasers. Most remarkable, the threshold current density is the same as that of the 2 µm wide shallowly etched ridge QD lasers which are on the same chip. This demonstrates that the performance of the deeply etched lasers does not suffer from surface recombination at the etched sidewalls due to the three-dimensional confinement of injected carriers in the QDs [2]. The QD lasers did not degrade with time as compared with bulk lasers fabricated in the same way, where lasing stops after one hour when pumped at twice the initial threshold current.

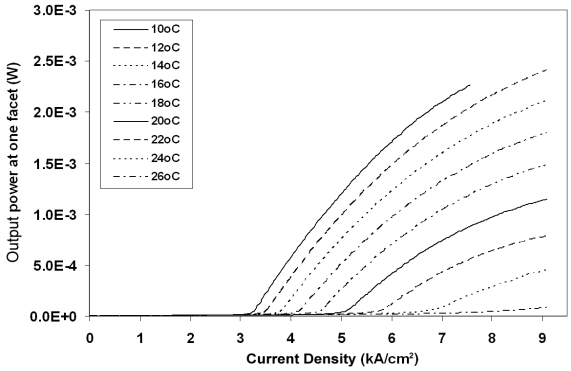

Figure 1: Output power at one facet of the deeply etched FP QD laser as a function of current density for different temperatures. The light was collected using an objective lens (NA = 0.65).

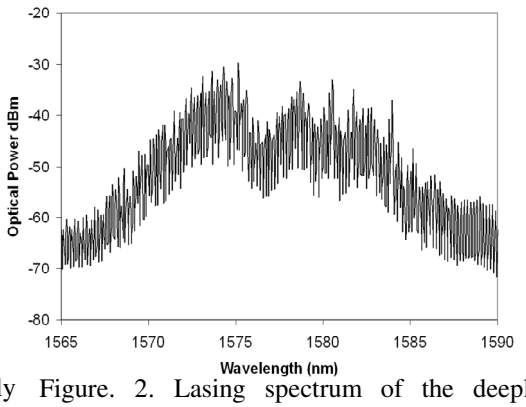

Figure. 2. Lasing spectrum of the deeply etched FP QD laser for I = 300 mA and T = 12°C, (resolution 0.1 nm).

The optical output power of the FP QD laser from one facet as a function of the current density for different temperatures in CW operation is plotted in figure 1. The light was collected using an objective lens (NA = 0.65). Output powers up to a few milliwatts are obtained. From the PI curves a value of the characteristic temperature T_0 of 20 K at room temperature is determined, the same value as that for shallowly etched lasers. This

relatively low T_0, for CW operation, is dominated by thermionic emission of carriers from the QDs to the Q1.25 barriers. Figure 2 shows a typical lasing spectrum. The wide lasing spectrum is due to the 80 nm gain bandwidth [8] and the inhomogeneous character of the QD gain medium. For the eight lasers measured, the central wavelength varies from 1565 nm to 1595 nm.

Ring laser results

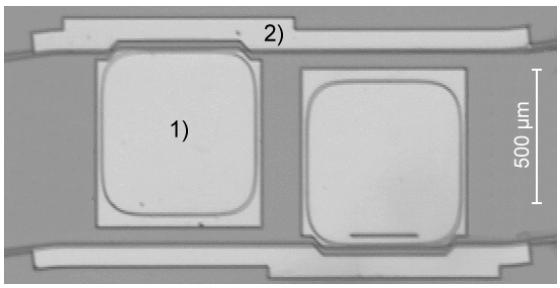

Figure 3: Top view of two QD ring lasers with two separate electrical contacts, 1) for the ring and the directional couplers and 2) for the output waveguides.

A photograph of two realized compact QD ring lasers is presented in figure 3. The deeply etched waveguides are visible as dark lines. The rings are 2.0 mm long. The bends have a radius of curvature which decreases adiabatically down to 100 µm in order to avoid offsets between straight and curved waveguides which can give rise to reflections. The directional coupler is double-etched with the gap shallowly etched and the outer ridges deeply etched to increase the fabrication tolerances [9]. The coupler is 200 µm long and the gaps vary from 0.9 to 1.2 µm in width resulting in output coupling efficiency between 25 and 50 %. The reflectivity of the cleaved facets of the output waveguides is reduced by the 7° angle and anti-reflection coating. The lasers have two separate electrical contacts, one for the rings and the directional couplers and another one for the two output waveguides.

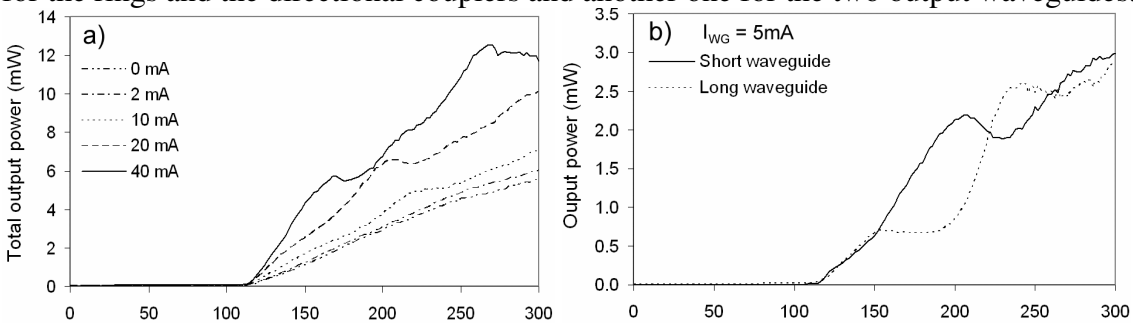

Figure. 4: a) Total optical output power as a function of I_{Ring} for different I_{WG}. b) Short and long output waveguides power as a function of I_{Ring} for I_{WG} = 5mA. The output powers are corrected for coupling and optical isolator losses. T = 12°C. The directional coupler gap is 1.2 µm.

In figure 4 a), the total optical output power from the long and short output waveguides of the QD ring laser with a directional coupler gap of 1.2 µm is plotted as a function of ring current (I_{Ring}), for different current values in the output waveguides (I_{WG}). Operation is in CW mode at 12°C. The output powers are corrected for lensed fiber coupling and optical isolator losses. The total current for transparency of the QD gain material in the output waveguide is estimated at 3 mA [8]. The low absorption of the QDs allows for use of the ring laser without pumping the output waveguides. In unpumped FP lasers, an optical loss of 10 dB/cm ± 1dB around 1555 nm has been measured by injecting 1 mW from an EDFA broadband source. The presented light versus current (LI) curves are not linear above 10 mA pump current in the output waveguides due to the spontaneous emission generated there injected into the ring. In figure 4 b) output powers are plotted from the two outputs separately as a function of I_{Ring} for I_{WG} = 5 mA. The laser is operating bi-directional; however, above 150 mA some

power is transferred between the clockwise and counter clockwise modes. The lasing spectra of the ring laser are similar to those of the FP lasers, but with a 40 GHz FSR.

Conclusion

We have presented the results on InAs/InP QD Fabry Pérot and ring lasers using narrow deeply etched waveguides (1.65 µm width) and lasing in the 1.55 µm wavelength range. We have observed that the performance of such lasers does not suffer noticeably from surface recombination of injected carriers. The deeply etched lasers have the same threshold current densities as shallowly etched ones and do not deteriorate with time. These observations show that more compact integrated photonic devices can be realized through the use of deeply etched bends with a small radius of curvature. This was demonstrated by the realization of small ring lasers. The measurements performed with unpumped output waveguides of the ring lasers, due to the low absorption and transparency current densities, reveal that QD gain materials offer further increased flexibility for photonic integration for specific applications. Short sections of unpumped waveguides are easily bleached with limited power loss. One can consider to integrate lasers, photodetectors and passive waveguides for interconnection, using the same layer stack and thus avoiding sophisticated active-passive integration technology.

References

[1] M.V. Maksimov, Y.M. Shernyakov, N.V. Kryzhanovskaya, A.G. Gladyshev, Y.G. Musikhin, N.N. Ledentsov, A.E. Zhukov, A.P. Vasil'ev, A.R. Kovsh, S.S. Mikhrin, E.S. Semenova, N.A. Maleev, E.V. Nikitina, V.M. Ustinov and Z.I. Alferov "High-power 1.5 µm InAs-InGaAs quantum dot lasers on GaAs substrates" Semiconductors, Vol. 38, No. 6, pp. 732–735, 2004.

[2] S.A. Moore, L. O'Faolain, M.A. Cataluna, M.B. Flynn, M.V. Kotlyar, T.F. Krauss, "Reduced Surface Sidewall Recombination and Diffusion in Quantum-Dot Lasers" IEEE Photon. Technol. Lett., Vol. 18, Issue 17, pp.1861-1863,2006

[3] N.N. Ledentsov, M.V. Maximov, P.S. Kop'ev, V.M. Ustinov, M.V. Belousov, B.Ya. Meltser, S.V. Ivanov, V.A. Shchukin, Zh.I. Alferov, M. Grundmann, D. Bimberg, S.S. Ruvimov, W. Richter, P. Werner, U. Gösele, U. Heidenreich, P.D. Wang and C.M. Sotomayor Torres "Optical spectroscopy of self-organized nanoscale heterostructures involving high-index surfaces" Microelectronics Journal 26, pp.871-879 (1995)

[4] M Kuntz, G Fiol, M Lämmlin, D Bimberg, M G Thompson, K T Tan, C Marinelli, A Wonfor, R Sellin, R V Penty, I H White, V M Ustinov, A E Zhukov, Yu M Shernyakov, A R Kovsh, N N Ledentsov, C Schubert and V Marembert "Direct modulation and mode locking of 1.3 µm quantum dot lasers" New J. Phys. 6 181, 2004.

[5] H. Cao, H. Deng, H. Ling, C. Liu, V.A. Smagley, R.B. Caldwell, G.A. Smolyakov, A.L. Gray, Z. Laser, L.F. Lester, P.G. Eliseev, M. Osińskia "Highly unidirectional InAs/InGaAs/GaAs quantum-dot ring lasers" Applied Physics Letters 86, 203117 2005.

[6] E.A.J.M Bente and M.K. Smit, "Ultrafast InP optical integrated circuits", Proc. Photonics West 2006, Integrated Optoelectronic Devices, 21-26 January 2006, San Jose, California, vol. 6124.

[7] S. Anantathanasarn, R. Nötzel, P.J. van Veldhoven, F.W.M. van Otten, T.J. Eijkemans, and J.H. Wolter, "Stacking and polarization control of wavelength-tunable (1.55-µm region) InAs/InGaAsP/InP (100) quantum dots", Applied Physics Letters, vol. 88, 2006, pp. 063105.

[8] S. Anantathanasarn, R. Nötzel, P.J. van Veldhoven, F.W.M. van Otten, Y. Barbarin, G. Servanton, T. de Vries, E. Smalbrugge, E.J. Geluk, T.J. Eijkemans, E.A.J.M. Bente, Y.S. Oei, M.K. Smit and J.H. Wolter, "Lasing of wavelength-tunable (1.55-µm region) InAs/InGaAsP/InP (100) quantum dots grown by metalorganic vapor phase epitaxy", Applied Physics Letters, vol. 89, 2006, pp. 073115.

[9] G. Griffel, J.H. Abeles, R.J. Menna, A.M. Braun, J.C. Connolly, M. King,"Low-threshold InGaAsP ring lasers fabricated using bi-level dryetching" IEEE Photonics Technology Letters, Vol. 12, Issue 2, pp. 146-148, 2000.

Complete rate equation modelling for the dynamics of multi-mode semiconductor lasers.

S. Beri, M. Yousefi, P. C. De Jager, D lenstra, and M. K. Smit

COBRA Research Institute Den Dolech 2, 5612AZ Eindhoven, The Netherlands

We propose a rate equations model for the description of a multilongitudinal mode semiconductor laser. We show how usually disregarded effects such as parametric interaction, carrier-diffusion and interference between the fields of the different longitudinal modes play an important role in the final operating characteristics of the laser. Parametric interaction induces a non-trivial distribution of spectral power among different cavity modes. Interference results in nonlinear gain terms in the equations, which favour longer wavelengths versus shorter ones. Carrier-diffusion is regulating the magnitude of such effects. In the limit of very strong diffusion, previous rate equations models are recovered.

Introduction

Nonlinear dynamics in semiconductor lasers is nowadays a hot topic in laser research From an experimental point of view, a broad variety of dynamical regimes have been reported, for instance bystablility and mode hopping, sequential mode switching, and transitions to chaos [1]. Compared to other classes of laser, semiconductor devices have a particular tendency to display multimode dynamics. A recent experiment showed a resonant external cavity semiconductor laser operating in chaotic regime with more than 100 active external cavity modes [2].

From the theoretical point of view, one aims to develop a model that reliably describes the features of the dynamics even in the most complicated regimes such as chaos. Rate equations models are very suitable for this task, as they deal with a limited number of dynamical variables that evolve according to a set of ordinary differential equations (ODE). However, developping a reliable rate equations model for devices operating in multimode regime is a challenging task. In the models available in literature, the mode coupling is described as a simple depletion of a common gain, whereas phase effects induced by the interference between field components in different modes are usually neglected. This rules out important effects related to the parametric interaction. Moreover, other mechanisms of mode coupling induced by spatial hole burning or diffusive processes are often disregarded.

In this paper we propose a set of rate equations for the description of multimode dynamics of semiconductor lasers, which takes into account in a consistent way the phase effects induced by the interference of the electrical fields in different modes, the diffusion of carriers and the spatial hole burning. We predict parametric interaction and symmetry breaking between long and short wavelengths.

Model

For sake of concreteness, we discuss here the model in the case of a single-transverse and multi-longitudinal mode Fabry-Pérot semiconductor laser. It will be clear from the

derivation that the principles presented here are more general and work for a generic class B laser.
For a class B laser, the electric field inside the cavity evolves according to the following differential equation:

$$\frac{\partial}{\partial t}E(z,t) = \sum_j \frac{1}{2}\left(-\Gamma_j + 2i\omega_j + G_j(z,t)\right)E_j(t)\psi_j(z)e^{i\omega_j t}, \tag{1}$$

where $\psi_i(z)$ are the spatial profiles of the cold cavity modes, $E_i(t)$ are the modal amplitudes of the electric field, $G_i(z,t)$ is the modal gain, Γ_i the modal losses and ω_i are the eigenfrequencies of the cavity modes.
The gain profile $G_i(z,t)$ depends on the properties of the semiconductor material and can have a complicate dependence on the carrier inversion $N(z,t)$. In what follow we will consider a device operating not too far from its threshold for which a linear dependence on the inversion applies: $G_i(z,t) = g_i + \xi_i(1+i\alpha_i)N(z,t)$, where g_i is the gain of the mode i when the laser is at threshold, ξ_i is the differential gain and α_i is the linewidth enhancement factor [3]. $N(z,t)$ is the inversion level relative to the laser threshold.
Assuming the eigenfunctions $\psi_i(z)$ to be orthonormal, a set of ODEs for the dynamics of E_n can be obtained by projection of Eq. (1) on the cavity modes:

$$\frac{dE_n}{dt} = -\frac{\Gamma_n E_n}{2} + \frac{1}{2}\sum_j \left(\int_0^L dz\left(g_j + \xi_j\left(1+i\alpha_j\right)N(z,t)\right)\psi_n^*(z)\psi_j(z)e^{i\omega_{jn}t}\right)E_j \tag{2}$$

where the frequencies $\omega_{ij} = \omega_i - \omega_j$ indicate the detunings between different modes.
The integral in Eq. (2) regulates the coupling between different modes; one sees that the coupling intensity is regulated by the overlap of the interference term $\psi_n^*\psi_j$ with the carrier profile $N(z,t)$.
In order to express the dynamics of the modal amplitudes E_i, the evolution of the carrier density $N(z,t)$ must be known. The carrier dynamics is assumed to be described by:

$$\begin{aligned}\frac{\partial}{\partial t}N(z,t) &= J(z,t) - \frac{N(z,t)}{T} + D\frac{\partial^2}{\partial z^2}N(z,t) \\ &- \frac{1}{2}\left[\sum_{nj}\left(\left(g_j + \xi_j\left(1+i\alpha_j\right)N\right)\psi_n^*(z)\psi_j(z)e^{i\omega_{jn}t}\right)E_n^*(t)E_j(t) + c.c.\right]\end{aligned} \tag{3}$$

Here $J(z,t)$ describes the pumping of carriers in the laser junction; the second term on the right hand side describes phenomenologically the spontaneous decay of the inversion, with T being a phenomenological carrier lifetime which summarises a range of different decay processes such as spontaneous radiative decay (decay with emission of radiation), non-radiative decay (for example after interaction with phonons) and Auger recombination (collision of different electrons leading to a loss of energy available for stimulated emission). The third term accounts for the spatial diffusion of the carriers in the active layer, with D the diffusion coefficient. The last terms describe the loss of inversion due to the stimulated emission of photons in the laser. To achieve energy balance, this term must equal the number of stimulated emission photons in (2). Note that, when more field components are present in the cavity, their interference terms contribute to the formation of oscillating gratings in the spatial inversion profile. On the other hand, the presence of

diffusion tends to wash away such gratings, driving the carrier distribution towards a flat profile. The actual spatial profile of the inversion results from the competition of these two effects. In general, one has to expect that the diffusion will be very efficient in washing away spatial profiles containing many ripples and less efficient for smoother profiles.
We choose to expand the carrier distribution on an orthonormal set of base functions ϕ_n: $N(z,t) = \sum_j N_j(t)\phi_j(z)$. The diffusive kernel in Eq. (3) introduces a diffusion-induced decay of the different components N_j; in particular, N_j decays fast if the corresponding profile ϕ_j contains many ripples; on the other hand, when ϕ_j is relatively flat, the corresponding N_j decays more slowly. Thus, during the operation of the device, the actual inversion profile will be sufficiently smooth to be reliably described with a finite number of components N_j. From the dynamical point of view, we can state that only a limited number of N_j can actively participate in the laser dynamics.
Performing the projection of Eq. (3) on the base functions ϕ_n, one obtains the following set of coupled ODEs:

$$\frac{dN_n}{dt} = J_n - \frac{N_n}{T} + \int dz D \frac{\partial^2 N}{\partial z^2}\phi_n - \frac{1}{2}\sum_{jk} g_j f_{jkn} e^{i\omega_{kj}t} E_j^* E_k - \frac{1}{2}\sum_{jk} g_j f_{kjn} e^{i\omega_{jk}t} E_k^* E_j$$
$$+\frac{1}{2}\sum_{jkh} \xi_j \left(1+i\alpha_j\right) N_h f_{jknh} e^{i\omega_{kj}t} E_j^* E_k + \frac{1}{2}\sum_{jkh} \xi_j \left(1-i\alpha_j\right) N_h f_{kjnh} e^{i\omega_{jk}t} E_k^* E_j. \quad (4)$$

Where the phase matching coefficients f_{ijk} and f_{ijkh} have been defined as $f_{ijk} = L\int \psi_i^* \psi_j \phi_k dz$, $f_{ijkh} = L\int \psi_i^* \psi_j \phi_k^* \phi_h dz$. With these definitions, the final set of equations for the modal fields amplitudes is:

$$\frac{d}{dt}E_n = -\frac{1}{2}\left(\Gamma_n - g_n\right)E_n + \frac{1}{2}\sum_{jk} f_{njk}\xi_j \left(1+i\alpha_j\right) N_k E_j e^{i\omega_{jn}t}, \quad (5)$$

which, in combination with Eq. (4) is the complete set of multimode laser rate equations.

Numerical investigation of the model

Consider the case of a two-mode system. We assume the diffusion to be fast enough to wash away all components of the carrier density except the two first. The component N_0 describes a common gain available for both modes; the component N_1 regulates the parametric coupling between the modes.
Let the modal parameters be the same for both modes; the equations for the two modes are then completely symmetric and can be distinguished only by their optical frequency. It can be verified from Eqs. (4) and (5) that the following single mode operation scenarios are possible: $|E_{1,2}|^2 = \frac{J_0}{\Gamma}$, $|E_{2,1}|^2 = 0$, $N_0 = 0$ and $N_1 = 0$.
As expected by the symmetry in the device equations, both solutions correspond to the same lasing intensity; however, the stability for these two solutions is different: the solution corresponding to operation in the longer wavelength mode is robust versus fluctuations in the other mode, whereas, the operation in the shorter one is unstable: a fluctuation in the mode with longer wavelength will grow until the short wavelength operation will be completely suppressed. We illustrate this effect in Fig. 1 (left), where we show a 80ns time series obtained by direct integration of (4,5) by predictor-corrector algorithm. The system switches spontaneously from operation at short wavelength to operation at long

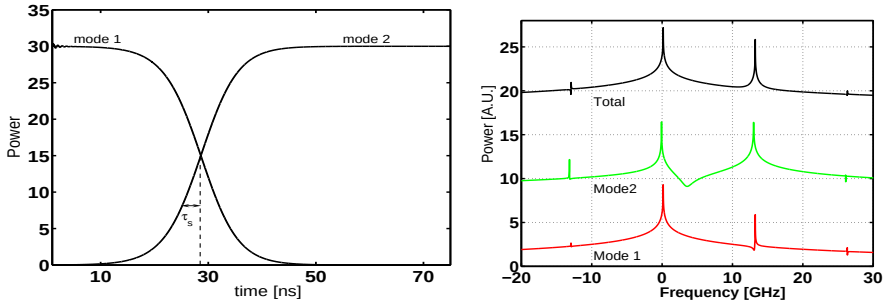

Figure 1: (Left) Switch of lasing mode due to modal interaction: the frequency detuning between the two modes is chosen to be 80GHz. The diffusion time for the grating is $T_1 = 100$ps. Mode 1 correspond to the shortest wavelength. The switching time τ_s is indicated by the double arrow. (Right) Mode resolved spectra and total optical spectrum.

wavelength. In Fig. (1) (right) we show the optical spectrum of the laser when two modes are contemporary lasing in the cavity. As expected, two peaks are present in the total spectrum, however, despite the gain being the same for both modes, the spectral amplitudes are different and the laser favours the longer wavelength over the shorter one. This result is consistent with the experimental work of Bogatov et al. [4]. When the spectral contents of the cavity modes are considered, it appears that both eigenfrequencies are present in the dynamics of each of the modal profiles, in accordance with Eq. (5).

Conclusions

We presented a set of rate equations for the description of a generic class B laser operating in multimode regime. The intrafield interactions and the field-inversion interaction take into account the interference terms between different modes. We predict a different stability for different wavelengths, an asymmetric optical spectrum where the longer frequencies are enhanced compared to the short ones, and a non-trivial distribution of optical power among the different frequencies. The diffusion coefficient regulates the magnitude of these effects.

Previous rate equations models can be obtained from Eq. (4,5) by taking the limit of very strong diffusion. In this case, only the inversion component N_0 survives in Eq. (4) and the effects of parametric interaction, spatial hole burning and diffusion disappear.

The authors acknowledge financial support by the Dutch Science Foundation (NWO) through the Dutch Technology Foundation (STW) within the STW-TWICE program and the NRC-Photonics program of the Dutch Ministry of Economic Affairs.

References

[1] A.M. Yacomotti, *et al.* “Dynamics of multimode semiconductor lasers”, Phys. Rev. A **69**, pp. 053816 (2004); L. Furfaro, *et al.* IEEE J. Quantum Electron. **40**, pp 1365 (2004); C. O. Weiss and J. Brock, Phys. Rev. Lett. **57**, pp 2804-2806 (1986)

[2] Michael Peil, Ingo Fischer, and Wolfgang Elsäßer, Phys. Rev. A **73**, 023805 (2006)

[3] C. Henry, IEEE J. Quantum Electron., **QE-19**, pp. 1391 (1983).

[4] A. P. Bogatov, P. G. Eliseev, and B. N. Sverdlov, IEEE JQE **11** pp. 510–515 (1975)

Ultrafast all-optical wavelength conversion in Silicon-on-Insulator waveguides by means of Cross Phase Modulation using 300 femtosecond pulses.

R.Dekker[1)], J. Niehusmann[2)], M. Först[2)] and A. Driessen[1)].

[1)] MESA+ Institute for Nanotechnology, Integrated Optical Micro Systems, University of Twente, Faculty of Electrical Engineering, Mathematics and Computer Science, P.O.Box 217, 7500 AE Enschede, The Netherlands. Phone: +31-53-489 4440; E-mail: R.Dekker@utwente.nl.

[2)] RWTH Aachen University, Institut für Halbleitertechnik, 52074 Aachen, Germany.

In this paper we report the ultrafast all-optical wavelength conversion in Silicon-on-Insulator (SOI) waveguides. We used a pump-probe setup with 300 femtosecond pulses to demonstrate large temporal phase-shifts, caused by the Kerr effect and free carrier generation. Large wavelength shifts of a 1683nm probe signal have been observed. The wavelength conversion, ranging from 10nm redshifts to 15nm blueshifts, depending on the time delay between the pump and probe pulses, is caused by the pump induced Cross Phase Modulation. Furthermore, an all-optical switching scheme using SOI microring resonators is discussed. These results enable ultrafast all-optical switching using SOI microring resonators.

Introduction

Silicon integrated photonics has received a lot of attention in the last couple of years, because of its compatibility with CMOS electronics [1]. In recent years, many new types of nonlinear active silicon-based photonic devices have been developed. Substantial progress has been achieved in the field of Raman amplification, in both continuous-wave [2] and pulsed pump-probe [3,4] experiments. Other nonlinear effects like two-photon absorption (TPA) [5], self-phase modulation (SPM) [6-8], cross-phase modulation (XPM) and continuum generation [9], four-wave mixing (FWM) [10] and the Kerr coefficient [11] have been successfully demonstrated and thoroughly investigated.

In this paper, we present experimental results of femtosecond pump-probe experiments in Silicon-on-Insulator (SOI) waveguides by means of XPM. Large Kerr-induced wavelength shifts of the probe signal have been observed, whereas the free carrier contribution did not substantially contribute. Since the ultra-fast Kerr effect is the dominating mechanism, this method of wavelength conversion is suitable for ultra-fast all-optical switching.

Theory

The refractive index of SOI waveguides is changed mainly by two nonlinear effects when strong pump pulses with a FWHM pulse duration of 300fs propagate through the silicon wire. The first one is the instantaneous Kerr effect, inducing a refractive index increase of $\Delta n_{Kerr} = n_2 \cdot I$ [11]. Secondly, free carriers (FCs) are generated by TPA causing a refractive index decrease that can be empirically described by

$\Delta n_{FC} = -(8.8\cdot 10^{-22}N + 8.5\cdot 10^{-18}N^{0.8})$ [12], with N the free carrier density. In Figure 1 the contribution to the total induced refractive index change of both the Kerr nonlinearity and the free carrier dispersion is shown for a Gaussian pulse with a maximum intensity of I_{max}~150TW/m^2. It can be seen that the Kerr contribution is dominant, while the effect of the free carrier accumulation is limited because the pulses are short.

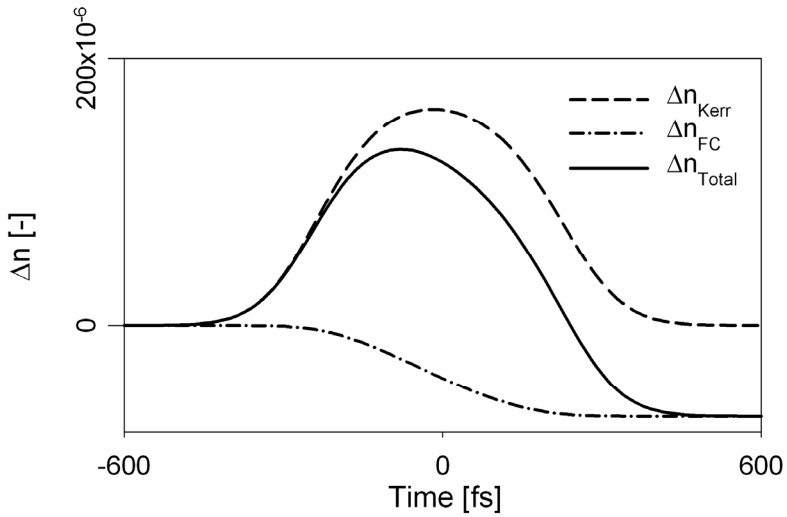

Figure 1: Modelled Kerr and free carrier induced refractive index change for 300fs pulses with an average power of 500μW in 300×450nm SOI waveguides.

The temporal shape of the pump pulse is influenced by several mechanisms like TPA, Free Carrier Absorption and the dispersion [13]. Since both the Kerr and free carrier induced refractive index changes are intensity dependent, they both change with the envelope of the pump pulse, resulting in a temporal phase shift $\Delta\phi(t)=2\pi L_{int}\Delta n(t)/\lambda$. Here, L_{int} is the interaction length of pump and probe pulses. Consequently, this temporal phase shift causes a frequency shift $\Delta\omega(t)=d\Delta\phi(t)/dt$, which is the basis for SPM and XPM. In this paper we will only focus on the XPM induced frequency shift causing a wavelength shift of the probe pulses, which is defined as [13]:

$$\lambda_s = \frac{\lambda_0}{1 - \frac{L_{\text{int}}}{c}\cdot\frac{\Delta n(t,z)}{dt}} \tag{1}$$

Experimental results

Both the pump (1554nm) and probe (1683nm) pulses with a FWHM pulse duration of 300fs are delivered by an optical parametric oscillator (OPO) with a repetition rate of 80MHz. The time delay between pump and probe pulses is controlled with a free-space optical delay line with 6.6 femtosecond accuracy. Both beams are combined using a beam splitter and coupled into a 10cm piece of polarization maintaining fiber (PMF) using a microscope objective. The output of the PMF (30mW average power for the pump and 3mW for the probe) is used to facilitate the simultaneous coupling of the TM polarized pulses into our SOI waveguides having a 450nm×300nm (w×h) cross section (by design) and a length L of 7mm. No spectral broadening due to the fiber nonlinearities has been observed at the output of the fiber, prior to entering the SOI

waveguide. After propagation through the SOI waveguide the transmitted pulses are coupled out using a single mode fiber, which is attached to an optical spectrum analyzer. By this means, both intensity and spectral characteristics of the transmitted pump and probe pulses can be detected simultaneously.
In Figure 2 the experimentally observed center wavelength of the probe pulses are plotted as function of delay time. Here a negative delay time means that the probe pulses are running ahead of the pump pulses, *i.e.* are overlapping with the leading edge of the pump pulse. The discrepancy between the experimental results and the simulations is caused by the fact that dispersion effects are not included in the model [13]. We observed a 10nm redshift at negative delay times, indicating that the nonlinearities are dominated by the Kerr effect in case of femtosecond pulses. This is in contrast to the blueshift that is normally observed in pump-probe experiments with longer ps pulses [4], where the free carrier dispersion effect is dominant due to the fact that ps pulses are long enough to build up a sufficient amount of free carriers.

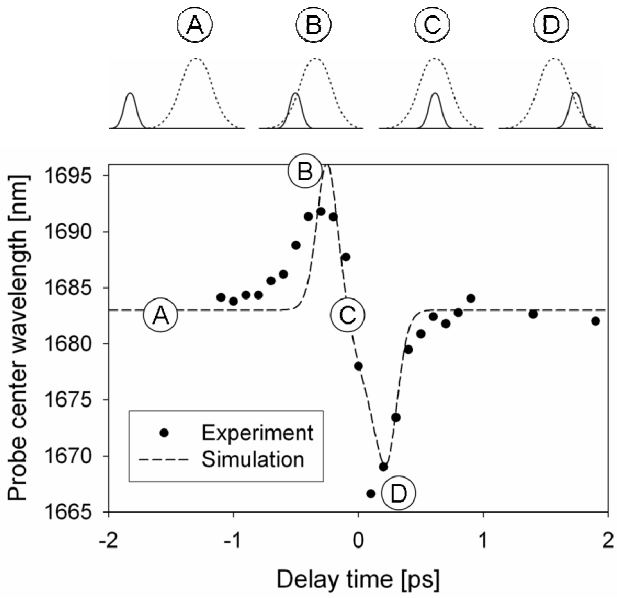

Figure 2: Center wavelength vs. delay time.

Ultrafast all-optical switching can be achieved in case that the frequency shifted probe pulse is redirected by a wavelength selective device. In our case we propose a SOI waveguide combined with a SOI microring resonator filter. The wavelength conversion of 10nm taking place in the active port waveguide is in the order of the free spectral range (FSR) of a passive ring resonator with a radius of 10μm. This means that the probe signal can be tuned over the full FSR of the ring by adjusting the time delay. Low Q resonators having short loading and unloading times can be used as passive space switches, because of the large XPM induced wavelength shift. Since the wavelength conversion is determined by the time derivative of the Kerr induced refractive index change, the switching time of such a switch is related to the width of the pump pulse [4], which is in the order of 300fs. This is in contrast to the all-optical switching mechanisms that rely on the FC dispersion, where the switching speed is limited by the FC lifetime in the order of ns.

Conclusions

We have shown that both 10nm blue and red shifts in SOI waveguides using a pump-probe setup with 300fs pulses are feasible. The XPM is dominated by the Kerr effect, since the pulses in the femtosecond regime are too short to accumulate a sufficient amount of free carriers to have considerable free carrier dispersion. This means that the temporal refractive index changes are mainly caused by the instantaneous Kerr effect and thus both the wavelength up and down-conversion takes place in a sub-picosecond timeframe. The ultrafast wavelength conversion can be exploited for all-optical switching when combined with microring resonator filters.

Acknowledgments

This research is supported by the Freeband Impulse technology program of the Ministry of Economic Affairs of the Netherlands and the European Network of Excellence on Photonic Integrated Components and Circuits (ePIXnet FAA5/WP11). The authors would like to thank AMO GmbH in Aachen, Germany, for the fabrication of the silicon-on-insulator waveguides.

References

[1] G. T. Reed, "Optical age of silicon," Nature **427**, 595-596 (2004).

[2] V. Raghunathan, R. Claps, D. Dimitropoulos, and B. Jalali, "Parametric Raman Wavelength Conversion in Scaled Silicon Waveguides," J. Lightwave Technol. **23**, 2094-2102 (2005).

[3] A. Liu, H. Rong, M. Paniccia, O. Cohen, and D. Hak, "Net optical gain in a low loss silicon-on-insulator waveguide by stimulated Raman scattering," Opt. Express **12**, 4261-4268 (2004).

[4] Q. Xu, V. R. Almeida, and M. Lipson, "Time-resolved study of Raman gain in highly confined silicon-on-insulator waveguides," Opt. Express **12**, 4437-4442 (2004).

[5] T. K. Liang, H. K. Tsang, I. E. Day, J. Drake, A. P. Knights, and M. Asghari, "Silicon waveguide two-photon absorption detector at 1.5µm wavelength for autocorrelation measurements," Appl. Phys. Lett. **84**, 2745-2747 (2002).

[6] O. Boyraz, T. Indukuri, and B. Jalali, "Self-phase-modulation induced spectral broadening in silicon waveguides," Opt. Express **12**, 829-834 (2004).

[7] R. Dekker, E. J. Klein, J. Niehusmann, M. Först, F. Ondracek, J. Ctyroky, N. Usechak, and A. Driessen, "Self Phase Modulation and Stimulated Raman Scattering due to High Power Femtosecond Pulse Propagation in Silicon-on-Insulator Waveguides.," presented at the Symposium IEEE/LEOS Benelux Chapter, Mons, Belgium, (2005).

[8] E. Dulkeith, Y. A. Vlasov, X. Chen, N. C. Panoiu, R. M. Osgood Jr., “Self-phase-modulation in submicron silicon-on-insulator photonic wires”, Opt. Express **14**, 5524-5534, (2006).

[9] O. Boyraz, P. Koonath, V. Raghunathan, and B. Jalali, "All optical switching and continuum generation in silicon waveguides," Opt. Express **12**, 4094-4102 (2004).

[10] H. Fukuda, K. Yamada, T. Shoji, M. Takahashi, T. Tsuchizawa, T. Watanabe, J. Takahashi, and S. Itabashi, "Four-wave mixing in silicon wire waveguides," Opt. Express **13**, 4629-4637 (2005).

[11] M. Dinu, F. Quochi, and H. Garcia, "Third-order nonlinearities in silicon at telecom wavelengths," Appl. Phys. Lett. **82**, 2954-2956 (2003).

[12] R. A. Soref and B. R. Bennett, "Electrooptical Effects in Silicon," IEEE J. Quantum Electron. **QE-23**, 123-129 (1987).

[13] R. Dekker, T. Wahlbrink, C. Moormann, J. Niehusmann, M. Först and A. Driessen, "Ultrafast Kerr-induced all-optical wavelength conversion in silicon waveguides using 1.55 µm femtosecond pulses", Opt. Express **14**, 8336-8346, (2006).

Investigations on Electronic Equalization for Step-Index Polymer Optical Fiber Systems

F. Breyer(1), N. Hanik(1), S. Randel(2), B. Spinnler(2)

(1) Institute for Communications Engineering (LNT), Munich University of Technology (TUM), Munich, Germany, email: florian.breyer@tum.de

(2) Siemens AG, Corporate Technology, Information & Communications, Munich, Germany

Electronic equalization can allow for significant mitigation of impairments induced by modal dispersion in the step-index Polymer Optical Fiber. In this work we show the performance of digital T-spaced equalizer technologies like Feed Forward Equalization (FFE) and Maximum Likelihood Sequence Estimation (MLSE) with data rates from 100 Mbit/s to 500 Mbit/s. The simulations are based on a channel model, which combines all three major fiber effects of modal attenuation, modal dispersion and mode coupling.

1. Introduction

The standard 1 mm PMMA Polymer Optical Fiber (SI-POF) is a highly attractive candidate for wired communication links in application scenarios such as industrial automation, automotive and in-building networking. Its unique advantage is the easiness of handling, allowing large alignment and dimensional tolerances for components and connectors together with the possibility of field installation by non-professionals. Probably the most critical disadvantage of the 1 mm SI-POF is the limitation of its bandwidth-length product to approximately 35 MHz×100 m mainly due to modal dispersion. In this paper, we present first investigations on electronic equalization to overcome this limitation. Simulations are carried out with a new simulation model [1] which includes the three major fiber effects in Polymer Optical Fibers: the mode-dependant attenuation, the modal dispersion and the mode coupling process.

2. System Simulation Model

Figure 1 shows the system simulation model. In the Bit Source, a pseudorandom bit sequence is generated. A Light Emitted Diode (LED) is used as the transmitter (TX), which is modeled as a simple low pass filter with bandwidth B_{TX}.

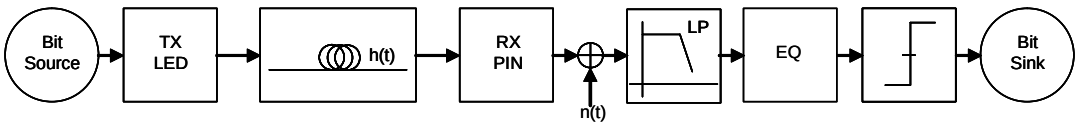

Figure 1 : Block diagram system model

As launch condition into the fiber, uniform mode distribution (UMD) is assumed, which approximates an LED quite well. The POF channel h(t) corresponds to a new simulation model [1], which is presented in the next chapter in details. At the receiver (RX), the optical signal power is converted to an electrical current by means of a simple

multiplication with the responsitivity *S*. After that, thermal noise resulting from the PIN-diode and the amplifier is added as additive white Gaussian noise (AWGN) to the system. The distorted signal is then passed through a low pass filter with bandwidth B_{RX} to reduce the impact of noise. Finally, this signal is fed into the equalizer or directly into the decision device.

3. Simulation model for the impulse response

Here the principle of the simulation model is shown, for more details see [1]. The starting point is the time-dependant power flow equation (1) depicted by Gloge [2]:

$$\frac{\partial P}{\partial z} = -\alpha(\theta)P - \tau(\theta)\frac{\partial P}{\partial t} + \frac{D}{\theta}\frac{\partial}{\partial \theta}\left(\theta \frac{\partial P}{\partial \theta}\right) \tag{1}$$

where $P = P(\theta, z, t)$ is the power distribution in angle θ with respect to the fiber axis, in z along the fiber and the time t. $\alpha(\theta)$ is the mode-dependant attenuation [3-5], given in Eq. 2. $\tau(\theta)$ is the delay (modal dispersion) for modes excited at angle θ (Eq. 3). *D* is the diffusion constant for mode coupling, which is modeled as a diffusion process.

$$\alpha(\theta) = \frac{\alpha_{core}}{\cos(\theta)} + \frac{\tan(\theta)}{2a}\ln(1-T) + \frac{\alpha_{clad}}{a\cos(\theta)}\frac{\lambda}{2\pi\sqrt{n_{core}^2\cos^2(\theta) - n_{clad}^2}} \tag{2}$$

$$\tau(\theta) = \frac{n_{core}}{c_0}\left(\frac{1}{\cos(\theta)} - 1\right) \tag{3}$$

$\alpha_{core}, \alpha_{clad}$ and n_{core}, n_{clad} are respectively the attenuation coefficients and the refractive indices of the core and the cladding. *a* is the core radius and *T* is the transmission factor of the core-cladding interface. λ is the mean wavelength and c_0 is the speed of light in vacuum. So equation (1) relates all three major fiber effects: the mode-dependant attenuation, the modal dispersion and the mode coupling.

To solve equation (1), it is transformed into the frequency domain, resulting in

$$\frac{\partial p}{\partial z} = \underbrace{-\left(\alpha(\theta) + j\omega\tau(\theta)\right)p}_{\tilde{L}\cdot p} + \underbrace{\frac{D}{\theta}\frac{\partial}{\partial \theta}\left(\theta\frac{\partial}{\partial \theta}p\right)}_{\tilde{N}\cdot p}. \tag{4}$$

The solution of equation (4) is approximated by solving the two part $\tilde{L}$ and $\tilde{N}$ separately. So the solution of this equation for a small fiber step size Δz is

$$p(\theta, z+\Delta z, \omega) \approx \exp\left\{\frac{\Delta z}{2}\tilde{L}\right\}\exp\left\{\Delta z\tilde{N}\right\}\exp\left\{\frac{\Delta z}{2}\tilde{L}\right\}p(\theta, z, \omega). \tag{5}$$

At the end of the fiber, the impulse response is calculated by integrating the power distribution in the time-domain over the angle θ:

$$h(t)\big|_{z=z_0} = \int P(\theta, z_0, t)d\theta \tag{6}$$

4. Equalizer schemes

In this work, we consider two types of equalizers: a Feed Forward Equalizer (FFE) and a full-state Maximum Likelihood Sequence Estimation (MLSE). The filter coefficients of the FFE are calculated by solving the Wiener-Hopf-Equation [6]. For all data rates a 15 T-spaced FFE is applied. As reference, the MLSE implemented in MATLAB® is used.

5. Simulation results

Impulse Response

In Figure 2, the simulated impulse responses for different lengths of standard 1mm Step-Index Polymer Optical Fiber (SI-POF) are shown. The resulting fiber parameters including bandwidth and overall attenuation are given in Table 1.

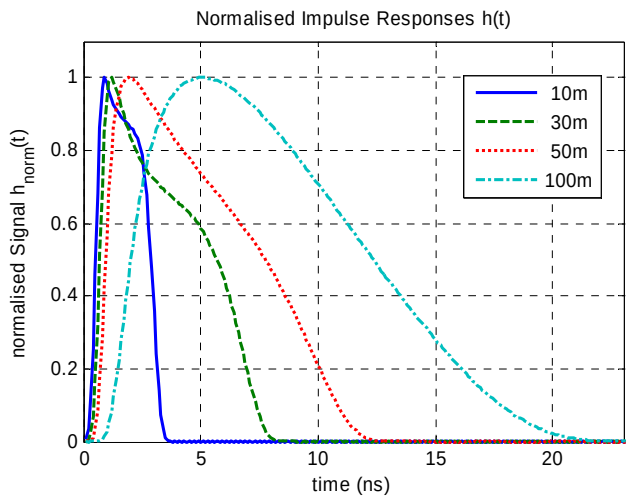

Figure 2: Normalised Impulse Responses

Length (m)	BW_{3dB} (MHz)	Att (dB)
10	200	2,1
30	89,9	5,1
50	65,7	8,1
100	43,1	15,5

Table 1: Fiber Parameters

So the impulse response used in the simulations has a bandwidth-length product of 43 MHz×100 m and an overall attenuation of 15.5 dB at a fiber length of 100 m.

System Simulations

For evaluating the performance of the different equalizers, we did Monte-Carlo simulations for bitrates R of 100 MBit/s, 250 MBit/s and 500 MBit/s. The launch power is 0 dBm and the transmitter bandwidth $B_{TX} = R$ is equal to the bitrate. The receiver has a responsitivity of $S = 0.4$ A/W and a bandwidth of $B_{RX} = R/0.707$. Only thermal noise is added as white gaussian noise with a noise figure of $F_N = 4$. The number of transmitted bits is 4×10^6.

In Figures 3a,b and d, the BER values versus fiber length are shown for the three different data rates. The equalization gain given in reached fiber length is measured at a BER of 10^{-5}. The results are shown in Figure 3c.

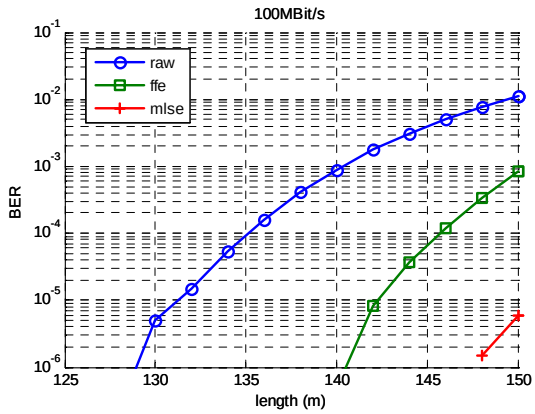

(a)

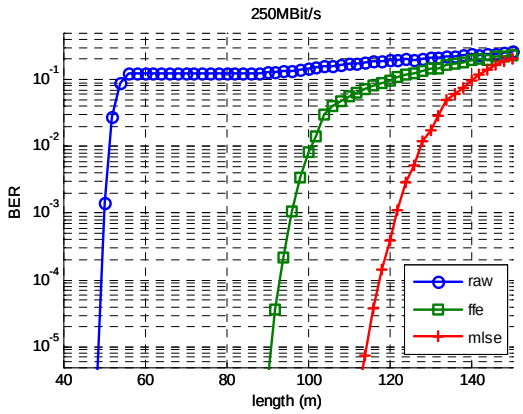

(b)

Bitrate	FFE gain	MLSE gain
100 MBit/s	1.07	1.15
250 MBit/s	1.88	2.3
500 MBit/s	3.4	5.2

(c)

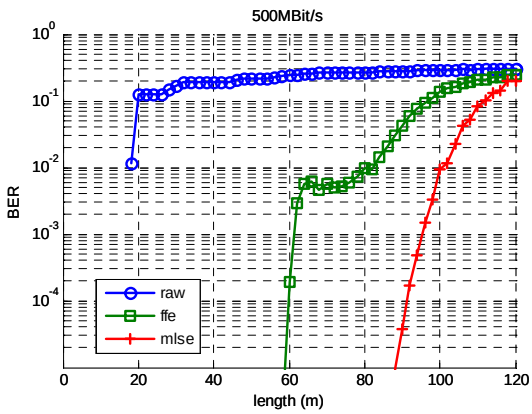

(d)

Figure 3: BER versus fiber length

6. Conclusions

The simulation results show the performance bounds of electronic equalization techniques for SI-POF. The MLSE shows the best achievable performance, at the cost of highest complexity. The FFE is a relatively simple equalizer with low complexity, but achieves less performance. Nevertheless, it can be seen from the results that even the relatively simple linear FFE can obtain good performance gains in a SI-POF system.

7. References

[1] F. Breyer, N. Hanik, C. Cvetkov, S. Randel, B. Spinnler, "Advanced Simulation Model for the Impulse Response of Step-Index Polymer Optical Fiber", in Proc. International Conference On Plastic Optical Fiber 2006, P-2, 2006.

[2] D. Gloge, "Impulse Response of Clad Optical Multimode Fibers", B.S.T.J. Vol. 52 No. 6, 1973, pp. 801-816.

[3] A.W. Snyder and J.D. Love, "Optical Waveguide Theory", Chapman and Hall, 1983.

[4] U. Paar, W. Ritter, K.F. Klein, "Excitation dependent losses in plastic optical fibers", SPIE Vol. 1799, 1992.

[5] Kapany and Burke, "Optical Waveguides", Academic Press 1972

[6] S. Haykin, "Adaptive Filter Theory", 4th Edition, Prentice Hall, 2002

Transmission of QAM Signals Over 100m Step-Index PMMA Polymer Optical Fiber with 0.98mm Core Diameter

M.S. Alfiad, X. Li, J. Yang, A.M.J. Koonen, H.P.A. van den Boom,
COBRA Institute, Eindhoven University of Technology, The Netherlands
P.O. Box 513, NL 5600 MB Eindhoven, The Netherlands
phone +31 40 2473444, fax +31 40 2455197, e-mail m.s.alfiad@student.tue.nl

Polymer Optical Fiber (POF) is severely bandwidth-limited; to overcome this problem Quadrature Amplitude Modulation (QAM) was chosen for reaching high data rates because of its spectrum efficiency. In this paper we present Digital Video Broadcasting for Cables (DVB-c) transmission using 16-, 64- and 256-QAM modulation over up to 100m Step-Index PMMA POF. An LED as well as a laser source have been investigated. Because a commercially available DVB-c modulator was used for generating the QAM signal, the symbol rate was limited to 7MSps, so bit rates up to 56 Mbps are achieved. The experimental results have been compared with simulation results and match very well. Error Vector Magnitude (EVM) readings as low as 1.65% with 256-QAM were achieved in the experiment, which is promising for further increase in the symbol rate and the fiber length.

Introduction

The great potential of POF is mainly due its large core diameter (typically 750 or 1000 µm) compared to the very small diameter of a silica fiber (8-100 µm), which makes it easy to handle without the need for an accurate alignment [1]. In particular step-index POF with 1 mm core diameter is interesting for cheap short-reach data links, and may become suited for do-it-yourself network installation. A number of problems are associated with using the SI-POF including its severely limited bandwidth. Using Quadrature Amplitude Modulation (QAM) was the idea to overcome the bandwidth limitation for POF because of its spectral efficiency [2].

Digital Video Broadcasting-Cable is the DVB European consortium standard for the broadcast transmission of digital television over cable. The modulation used in DVB-c is QAM with 16, 32, 64, 128 or 256 points in the constellation diagram [3], which makes it a good candidate to be used in the POF transceiver. The wide acceptance for the DVB-c standard in the whole world and especially in Europe produced a large volume market for its products; which made it possible to find commercial DVB-c modems for QAM demodulation at very low prices, and QAM modulators for DVB-c head-ends at moderate prices. It was interesting to investigating the performance of a POF transmission system benefiting from this availability for DVB-c equipments to provide the QAM signal, which also uses an extremely inexpensive system of couplers and photo detectors to couple the light into the POF and to detect it.

System Setup

A commercially available PCI-card for generating DVB-c QAM signal was used in the experiment. The PCI-card QAM modulator is controlled using a software installed in the PC where the PCI-card is plugged in to generate 16- , 32-, 64- , 128- or 256-QAM signals at frequencies ranging from 400 to 862 MHz. This frequency range for the generated signal is far beyond the frequencies that can be used with POF, so a down conversion mixer was always used at the transmitting side as can be seen from Figure 1 which illustrates the system setup.

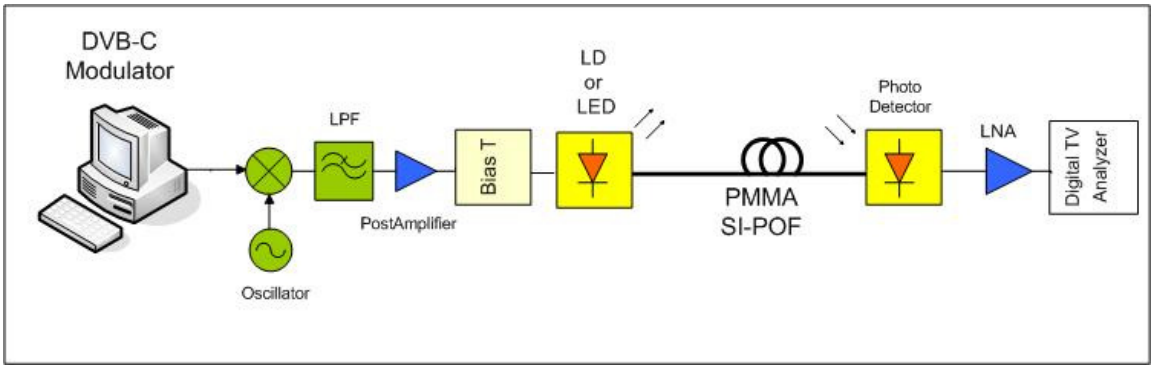

Fig. 1 System Setup for Generating and Transporting DVB-c Signals over POF

The down-converted QAM signal is amplified using a post amplifier with a gain of 20dB to be able to drive the light source, because the output power of the PCI-card QAM modulator is fixed to -25dBm. In the system shown in Figure 1, a laser and an LED were tested. The laser is a red light laser, emitting at a wavelength of 655nm with a linewidth of 2nm, at an output power of 6mW. The LED used is a low cost green light LED, emitting at a wavelength of 510nm with a linewidth of 35nm, at an output power of 5mW.
The transmission medium used in this experiment is a Polymethylmethacrylate (PMMA) Step Index-POF fiber with a diameter of 1 mm, and a length of 100 meters. A very simple plastic connector is used for coupling the light from the light source to the POF. At the end of the POF, a Si Photodiode with an active area of 0.81 mm^2 is used for light detection.

In this experiment, 16-, 64-, and 256-QAM signals were used. The DVB-c standard is limited to 7 MSps transmission rate; which limited the experiment to a maximum bit rate of 56 Mbps when using 256-QAM modulation. A Digital TV Analyzer for demodulating the received QAM signal, and measuring its Error Vector Magnitude (EVM) value.

Experimental Results

The carrier frequency for the generated DVB-c signal out from the down-converter was swept between 20 and 80MHz. The EVM for the received signal at the photodetector was measured at these frequencies, and an EVM Versus carrier frequency plots were made for the 16- 64- and 256-QAM signals using both the red laser and the green LED; the plots can be seen in figure 2.

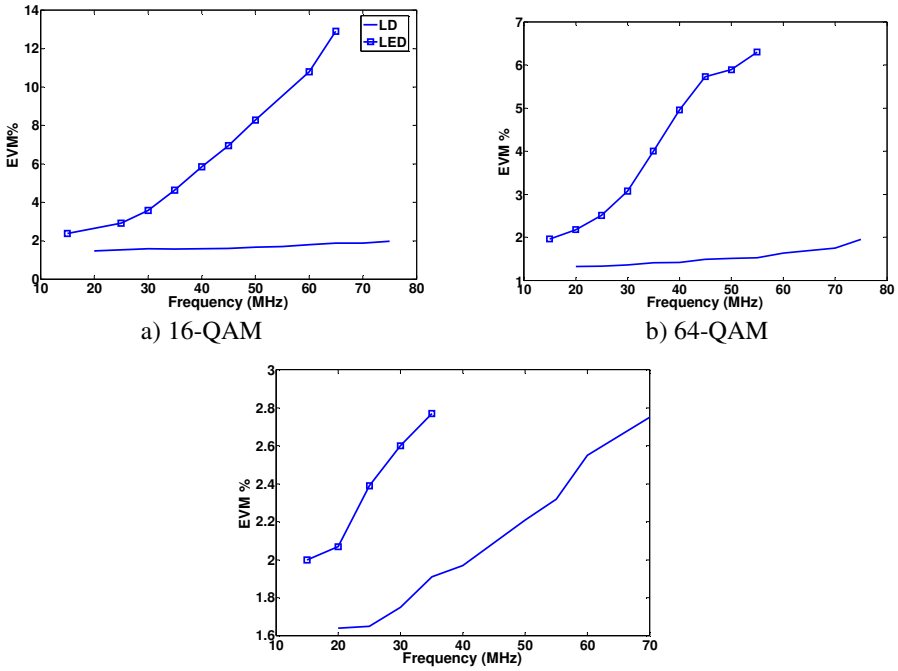

a) 16-QAM b) 64-QAM

c) 256-QAM

Fig. 2 EVM versus carrier frequency for a DVB-c Signal over 100 meters of 1 mm core SI-POF

No EVM requirements are specified for the DVB-c standard, so the EVM requirements for the IEEE802.11a were used to qualify the signal because of the similarity in symbol rates used in both standards. The EVM requirements in IEEE802.11a for a QAM-16 system (EVM<11.2%) and of a QAM-64 signal (EVM<5.6%), but not specified for 256-QAM so it was considered (EVM<2.5%) which can be considered realistic compared to the requirements for 16- and 64-QAM; from the plots in figure 2 it can be seen that these values can be met using the red laser and the Green LED.

Despite that the green light has a lower attenuation in POF than the red light (attenuation for green is 90dB/km; for red is 150dB/km), but the EVM for the LED was rapidly degraded with increasing the carrier frequency; which indicates that the link bandwidth of the LED-based system is lower than that of the laser-based system; this may be attributed to the large mode volume excited by the LED [2].

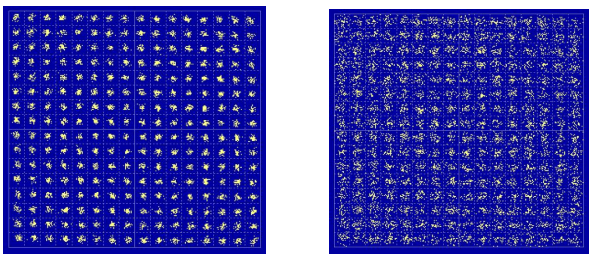

a) fc= 20MHz b) fc= 70MHz

Fig. 3 Constellation diagrams for the detected QAM signal after 100 meters of 1 mm core SI-POF

Constellation diagrams for the 256-QAM signal transmitted using laser and probed after the photodetector at carrier frequencies of 20 and 70MHz are shown in figure 3.

Simulation Results

Simulations have been made using VPI Transmission Maker for QAM signals with a symbol rate of 7MSps over 100 meters POF with a laser source to compare their results with the experimental results obtained. The performance of the simulated system is plotted in figure 4; which shows a similar behavior to the system in figure 1, with some differences in the EVM values due to the use of different POF model in the simulation.

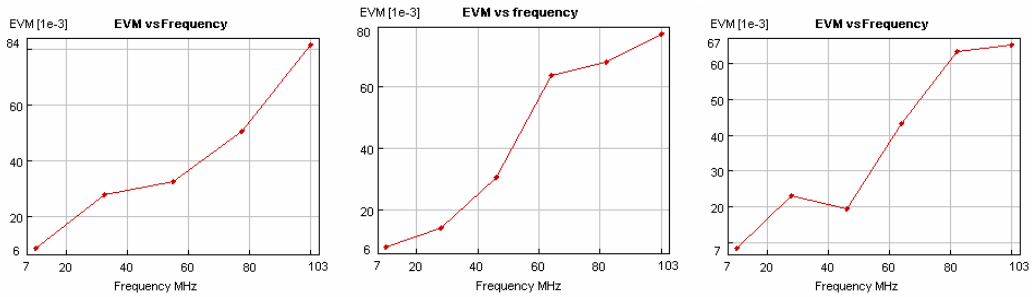

a) 16-QAM b) 64-QAM c) 256-QAM

Fig. 4 EVM versus carrier frequency for QAM Signals at a Symbol Rate of 7MSps

Conclusions

A completely commercially available QAM transmission system over 100 meters POF was realized and tested successfully, which can be considered as a start to further increase the length of the fiber and the bit rate to achieve a cheap, easy to install Fiber to the home (FTTH) system. A cheap green light LED was tested and showed a good performance despite of its wide linewidth, and this can be attributed to the relatively low attenuation POF has at green light wavelengths. Simulations for QAM transmission systems showed similar behavior to the tested system.

References

[1] Iracema A. Suassuna de Oliveira and Marlino Bonfim, “Plastic Optical Fibers in Telecommunications: Analysis, Comparison and Applications”, in Proceedings of the Conference SBMO/IEEE MTT-S IMOC, 2003, pp. 651-655.

[2] Ton Koonen, Jia Yang, Xinkai Li, Mohammad Alfiad, Jianming Zeng, Henrie van den Boom, “High Capacity Data Transport over Highly Dispersive Plastic Optical Fibre Links using Quadrature Modulation”; in Proceedings of the Conference POF/MOC, 2006.

[3] European Telecommunications Standards Institute (ETSI): Digital Video Broadcasting (DVB); Framing structure, channel coding and modulation for cable systems.

Optimisation of optical bandpass filters for semiconductor optical amplifier-based all-optical wavelength conversion using genetic algorithms

J. Molina Vázquez, Z. Li, Y. Liu, E. Tangdiongga, S. Zhang, D. Lenstra, G.D. Khoe and H.J.S. Dorren

Eindhoven University of Technology, P.O. Box 513, 5600 MB, Eindhoven, The Netherlands

(Email: j.molina.vazquez@ieee.org)

We use genetic algorithms to numerically optimise optical bandpass filters for non-inverted wavelength conversion based on semiconductor optical amplifiers. Output signal eye openings greater than 30 dB are obtained using a Hermite-Gaussian sum series to describe the filter's amplitude transfer function. We show that this can be implemented experimentally using an asymmetric Mach-Zehnder interferometer combined with a Gaussian optical bandpass filter. Finally, we explore the possibility of using a Sech-Hermite sum series to describe the filter and compare the results with those obtained for the Hermite-Gaussian filter.

1 Introduction

Wavelength conversion has been investigated extensively in the past several years as it will play an important role in future wavelength division multiplexing optical networks [1]. Wavelength conversion techniques based on semiconductor optical amplifiers (SOA) have attracted considerable attention [2]. However, relatively long carrier lifetimes ($\sim$10-100 ps) result in significant pattern effects limitting the maximum pattern-effect-free bit rate.

Different approaches have been proposed to reduce the pattern effects in high-speed SOA-based wavelength converters [3–6] demonstrating operation speeds as high as 320 Gbit/s. All these similar techniques can be generalised as a structure composed of a SOA followed by an optical filter. The filter transfer function is critical in determining the output signal quality and therefore one needs to find the optimum filter transfer function that can produce good output signal quality.

In this paper we use genetic algorithms, a multi-parameter optimisation technique used in evolutionary computing, inspired by Darwin's theory of evolution [7]; to optimise the filter transfer function used for non-inverted wavelength conversion. We explore the possibility of using Gaussian-Hermite (GH) and Sech-Hermite (SH) series to define the filter transfer function and investigate how these filters compare. We find that the GH filter gives a better signal quality than the SH filter, with output signal eye openings greater than 30 dB for the former and less than 30 dB for the latter. Finally, we investigate the effect of variations in the SOA's and input signals' properties on the output signal quality.

In Section 2 we briefly introduce the model used in our simulations and the criteria used to evaluate the filters during the optimisation. Results are given in Section 3. Finally, a summary is given in Section 4.

2 Model

An extended rate-equation model that accounts for ultrafast carrier dynamics, gain dispersion and group velocity dispersion in bulk SOAs [8, 9] is used to simulate 160 Gbit/s non-inverted wavelength conversion of 1550 nm Gaussian pump pulses onto a 1535 nm continuous wave probe. The output of the SOA model is then used as the input to the filter optimisation algorithm.

2.1 Filter Optimisation

To optimise the filter transfer function we use a common genetic algorithm technique and proceed as in [10]. During the filter optimisation, the input to the filter, i.e. the SOA output, is kept constant.

The average peak power of the '1' bits, given by $\overline{P^1}_{\max} = [\sum_{i=1}^{N_1}(P^1_{\max})_i]/N_1$, where N_1 is the number of '1' bits and $P^1_{\max}$ is the peak power of a given '1' bit; is used as one of the criteria when optimising the filter instead of using the pulse amplitude fluctuations (PAF) as in [10].

In addition, we investigate the use of the SH function, given by

$$T(\nu) = \left\{\cosh\left[\frac{(\nu-\delta\nu)^2}{\Delta\nu^2}\right]\right\}^{-1} \sum_{i=0}^{4} a_i \mathrm{H}_i \left[\frac{\nu-\delta\nu}{\Delta\nu}\right], \tag{1}$$

where $\delta\nu$ and $\Delta\nu$ are the filter detuning and bandwidth, respectively; to define the filter transfer function instead of a GH function, as in [10], and compare the results obtained with each.

2.2 Filter Test

We investigate the optimum filter's sensitivity to changes in the SOA's and signals' properties. For this we use the SOA model to simulate wavelength conversion for different values of linewidth enhancement (α-) factor, current, input pump pulse energy, and probe power. The first two modify the SOA structure, whereas the last two alter the light inputs into the SOA. In all cases, the interaction between the light and SOA will be different affecting the gain and chirp dynamics of the system, and therefore affecting the performance of the wavelength conversion.

3 Results

3.1 Filter Optimisation

Fig. 1 shows the optimum filters together with Guassian and Sech filters with no optimisation having the same detuning and bandwidth as the optimum filters for comparison. Also shown is the SOA output spectrum before going through the filter. Fig. 2 shows their corresponding output signals. One can see that both the GH and SH optimum filters show similar features. In particular, there is a dip in the filters' transfer functions at the probe frequency. This ensures that the probe d.c. component is removed. In contrast, the output

signals from the non-optimum filters, which do not have this dip, show a non-zero d.c. component to the point where, for the non-optimum Sech filter the output signal begins to become inverted. The output from the optimum SH filter has a larger average peak power however, the signal quality is significantly degraded. For the GH filter, the output has an EO of 35.7 dB whereas the SH filter gives an EO of 29.2 dB. The GH and SH non-optimum filters have EOs of 11.9 dB and 1.43 dB, respectively. It has been shown in [10] that the optimum GH filter can be implemented experimentally using an asymmetric Mach-Zehnder interferometer (AMZI) combined with a Gaussian filter, which, in fact, has been used already in [5, 6, 11].

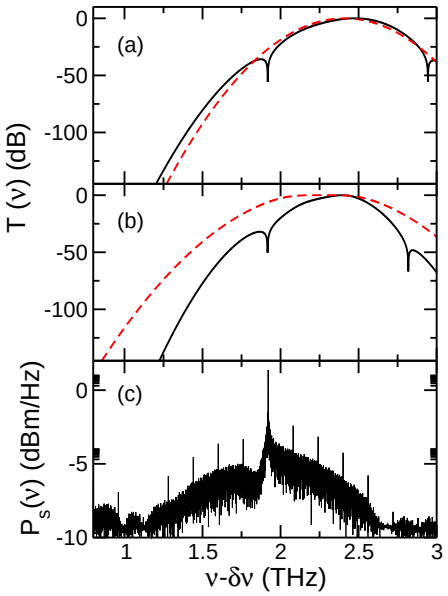

Fig. 1. Optimised (solid) and non-optimised (dashed) filter transfer functions for a (a) GH filter, and (b) SH filter. (c) Shows the SOA output signal spectrum prior to the filters.

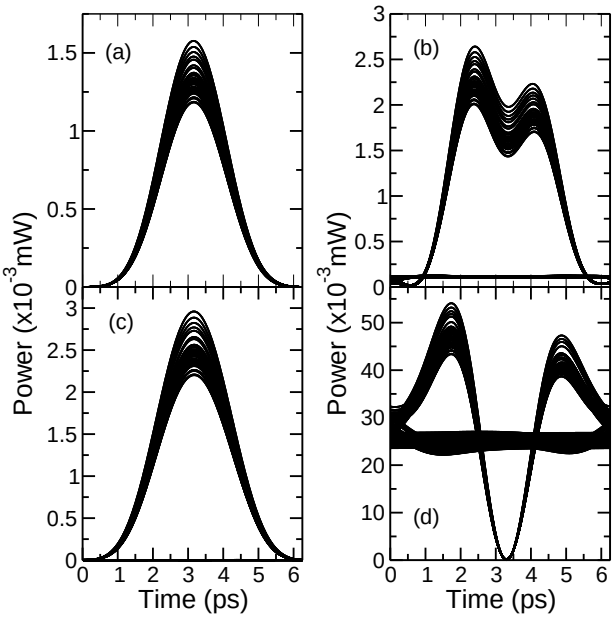

Fig. 2. Optimised (a), (c), and non-optimised (b), (d) wavelength converted output signals from the (a), (b) GH filters, and (c), (d) SH filters.

3.2 Filter Test

Fig. 3 shows the dependence of the output signal's quality factor $[Q = (\overline{P^1}_{\max} - \overline{P^0})/(\sigma_1 + \sigma_0)$, where $\overline{P^0}$ is the average power of the '0' bits, and σ_1 (σ_0) is the standard deviation of the '1' ('0') bits] and extinction ratio $[ER = 10\log_{10}(\overline{P^1}_{\max}/\overline{P^0})]$ for the GH and SH filters as a function of the α-factor, current, probe power and pump energy. One can see that all parameters bar the pump energy can be modified significantly without considerable changes in the output signal's quality. The behaviour in all cases is the same for both the GH and SH filters with only a difference in magnitude of the Q-factor and ER. Finally, the quality of the signal improves with increasing α-factor and probe power, and with decreasing current and pump power. This behaviour is a direct consequence of the pattern effects in the signal, we find (not shown) that the effect of PAF affects the signal Q more significantly than the difference in power between the '1' and '0' bits.

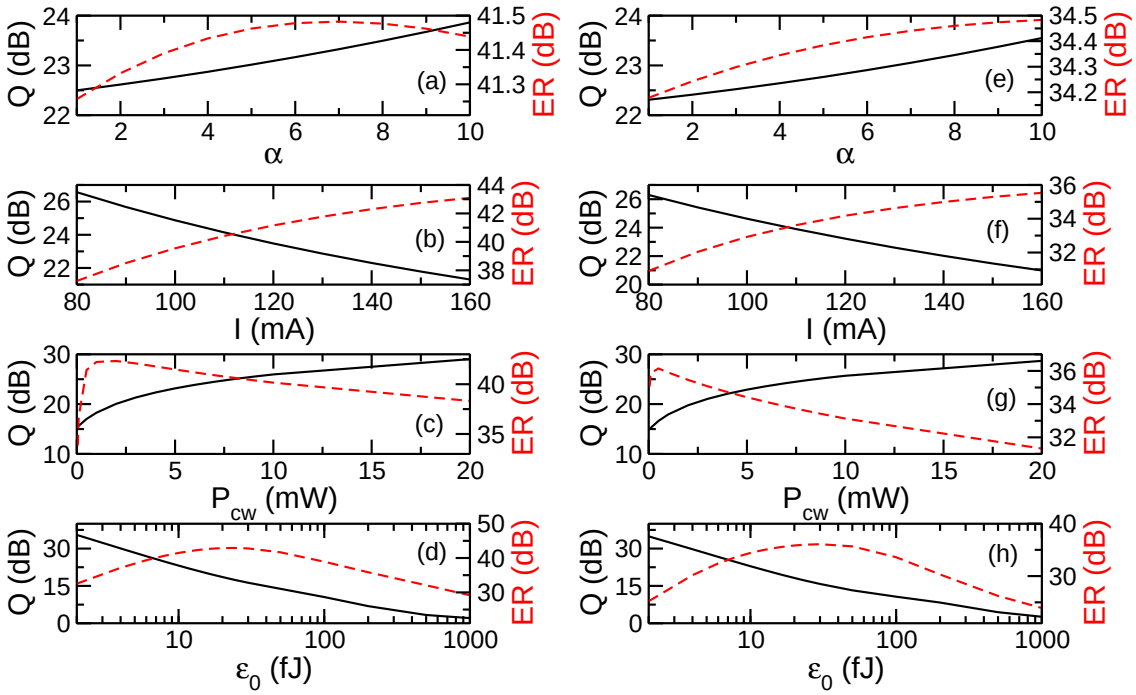

Fig. 3. Q-factor (solid) and ER (dashed) for the (a)-(d) GH filter, and (e)-(h) SH filter, as a function of (a), (e) α-factor, (b), (f) current, (c), (g) probe power, and (d), (h) pump energy.

4 Conclusion

Genetic algorithms have been used to optimise filters used in SOA-based wavelength conversion. Output signals with eye openings greater than 30 dB were obtained. It was found that the output signal's quality is not significantly affected when the SOA's and input signals' properties change.

References

[1] C. Nuzman, *et al.*, *IEEE/OSA J. Lightwave Technol.*, 21:648–663, 2003.
[2] S. J. B. Yoo, *IEEE/OSA J. Lightwave Technol.*, 14:955–966, 1996.
[3] K. Taijima, *Jpn. J. Appl. Phys.*, 32:L1726–L1749, 1993.
[4] H. Y. Yu, *et al.*, *IEEE/OSA J. Lightwave Technol.*, 17:308–315, 1999.
[5] S. Nakamura, *et al.*, *IEEE Photon. Technol. Lett.*, 13:1091–1093, 2001.
[6] Y. Liu, *et al.*, *Optical Fiber Communication Conference*, PD28, 2006.
[7] D. E. Goldberg, *Genetic Algorithms in Search, Optimization and Machine Learning*, Addison-Wesley, Amsterdam, 1989.
[8] N.K. Das, *et al.*, *IEEE J. Quantum Electron.*, 36:1184–1192, 2000.
[9] X. Yang, *et al.*, *Opt. Commun.*, 223:169–179, 2003.
[10] J. Molina Vázquez, *et al.*, *IEEE J. Quantum Electron.*, In Press, 2006.
[11] J. Leuthold, *et al.*, *Electron. Lett.*, 40:554–555, 2004.

Demonstration of an All-Optical Data Vortex Switch node base on MZI-SOA gates

Hyun-Do Jung, Idelfonso Tafur Monroy, A.M.J. Koonen

The COBRA Research Institute, Eindhoven University of Technology, Eindhoven, 5600 MB, Netherlands
E-mail : h.d.jung@tue.nl

We have proposed and demonstrated the fully all-optical operation of a data vortex switch node based on MZI-SOA gates. All-optical self-routing of WDM 10Gbps optical packets has been successfully achieved.

Introduction

The current and forecast increase in the Internet traffic and the growth of new and diverse kind of services are calling for higher data rates and flexibility that current network cannot offer. Optical packet switching has emerged as a solution for these demands by means of increasing the throughput, efficiency, transparency and flexibility. In order to meet these promising expectations, it is required to perform the routing and switching operations in the optical domain. At the current level of development of photonic technology, hybrid optical-to-electronic configurations are used to process the label information due to the immaturity of optical techniques to perform those operations. Moreover, operations easily performed electronically such as packet buffering and intelligent control are still challenging to be realized all-optical and solution need to be searched in order to realize the so longed all-optical packet switching.

A new packet routing architecture called the Data Vortex[1] was proposed that is uniquely free of an optical buffer and enables a simple routing strategy for large scale low latency packet switch fabrics. So far, several researches[2,3] have reported operation of Data Vortex switch structures. In their approaches, an electrical decision circuit for performing the routing decision was employed. However, electrical signal processing may introduce performance loss and latency, especially at higher data rates.

In this paper, we have proposed and demonstrated a fully all-optical operation of a data vortex switch node. All-optical self-routing decision are obtained by an optical AND logic operation between a routing and an optical control signal. WDM 10Gbps packet routing through the proposed node structure has been successfully achieved.

Proposed Data Vortex node structure

The proposed all-optical Data Vortex node (Fig. 1) consists of two Mach-Zehnder Interferometers with SOA (MZI-SOA). The upper and lower MZI-SOA act as an optical AND gate and an optical switch respectively. A WDM-encoding technique for the optical packets payload and headers[2] was used, which increases the network capacity. In addition, encoding the header bits by WDM substantially simplifies the routing strategy at the node. As each cylinder in a Data Vortex switch decodes a specific header bit in a binary tree fashion, passive wavelength filtering can be implemented in the nodes to perform the routing operations.

If a WDM-header encoded optical packet comes into the switch node, a small portion of header signal is extracted by the optical band pass filter with a particular wavelength

which is uniquely dedicated to a particular cylinder. The extracted header signal interacts with the control signal from an inner cylinder node at the upper MZI-SOA. The output signal of this upper MZI-SOA controls the switching function of the lower MZI-SOA gate. The output signal of the upper MZI-SOA is only 'on' when both control and routing signals are of '1'-state, resulting in routing of the packet to the inner cylinder. This self-routing decision is an *AND* logical operation successfully performed by the upper MZI-SOA gate. In the case of the output of the upper MZI-OSA being 'off', the input optical packet passes to the same cylinder.

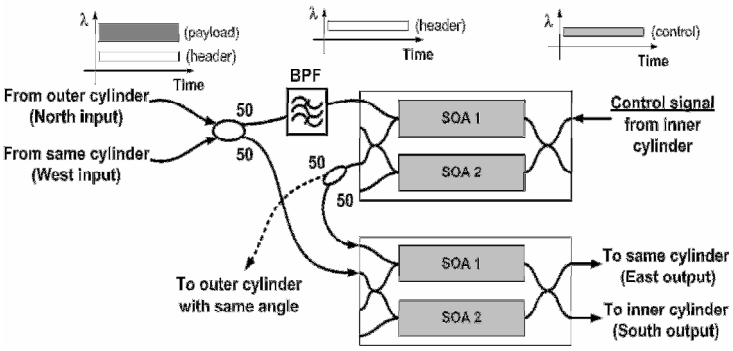

Fig. 1 Configuration of the proposed all-optical Data Vortex node employing MZI-SOA gates

Experiment setup

Fig. 2 shows the experimental setup. The setup consists of two parts: the optical packet generator and the Data Vortex switch node. The optical packet comprised two payload signals (10G, optical clock(1552.52nm) and LD1(1557.36nm)) and a header signal (LD2(1554.13nm)). Electrical data of payload and header bits was generated by a pulse pattern generator (PPG1). The packet length was 16ns, including 2.4 ns guard time as shown in fig. 4. In the experiment, the payload and header had contained the same data by using the same intensity modulator to simplify the time aligning between the payload and header signals. The control signal was generated by the PPG2 and delayed to align it with the extracted header signal at the upper MZI-SOA.

To emulate packets propagating across multiple node hops, a re-circulating configuration was used. For this purpose, the signal from (S)outh output was connected to the (N)orth input with two time slot delay: see Fig. 2. A fiber bragg grating (FBG) was employed to eliminate the control signal from (S) due to the co-propagation configuration used in the lower MZI-SOA. The packet routing was observed at (E)ast deflection output port.

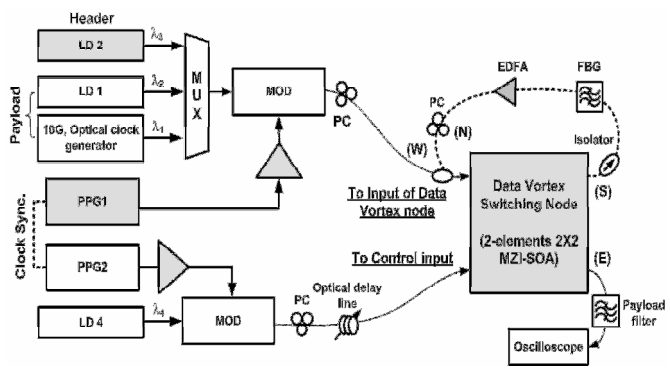

Fig. 2 Experiment setup. The black box of Data Vortex switching node has the architecture in Fig. 1

Experiment results

To verify the successful routing function, we examined the signal trace at each input and output port. The inset (1) of fig. 4 shows the initial input sequence. We programmed an initial pattern sequence ”001100 100011 001100 110011 000000 000000” and this same pattern was repeated continuously. Among these bits, the last twelve ’0’ bits were inserted to distinguish a given sequence from the following one.

A portion of the input packet signal power was tapped and sent to the first MZI-SOA to perform the AND logic decision logic operation. Out of this input packet, the header signal was extracted (filtered) and AND gated with the input control signal as shown in the inset (2) of fig. 4. The only ’on’ bits at the output of the upper MZI-SOA are those when both the header and control bit were simultaneously ’1’. The input packet is routed either to the same or inner cylinder node in accordance with these control output bits. The routing result is shown in the insets of (4), (5) of fig. 4. The bits shown in the inset (5) are the result of routing to the (S) port at the lower MZI-SOA and were used as the re-circulation input signal. The bits shown in the inset (4) are the deflected ones to port (E). The spike signal shown in the inset (4), after four bits are due to the mis-alignment between the control output from the first MZI-SOA and the input packet signal.

The (S)outh output signal (inset (5)) was connected to the (N)orth input and the result are shown in the inset (6) of fig. 4. The signal after recirculation is observed somewhat noisy due to the sub-optimal input optical power level to the MZI-SOA (after recirculation) and added ASE noise. This situation causes the variation of switching condition of MZI-SOA as the power level of the probe and pump signal is changed. Consequently, each bit showed somewhat different switching performance. Nevertheless, the routing of both of the single and re-circulation path was successfully achieved and its performance can be improved by further optimization of operation conditions.

Conclusions

In this paper, we have proposed and demonstrated a fully all-optical data vortex switch node. All-optical self-routing decision are performed as a AND logic operation in a MZI-SOA switch between an optical routing and control signal. The output of this AND operation controls, all-optically, a second of MZI-SOA completing in this way all-optical packet routing. Successful experimental demonstration of WDM 10 Gb/s packet routing through the proposed structure has been achieved.

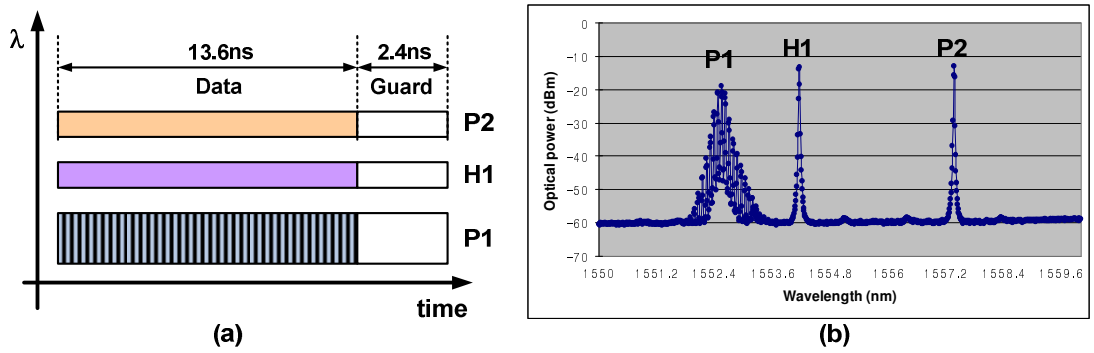

Fig. 3 Structure of the optical packet (P1: first payload (1552.52nm), P2: second payload (1557.36nm), H1: header (1554.13nm))

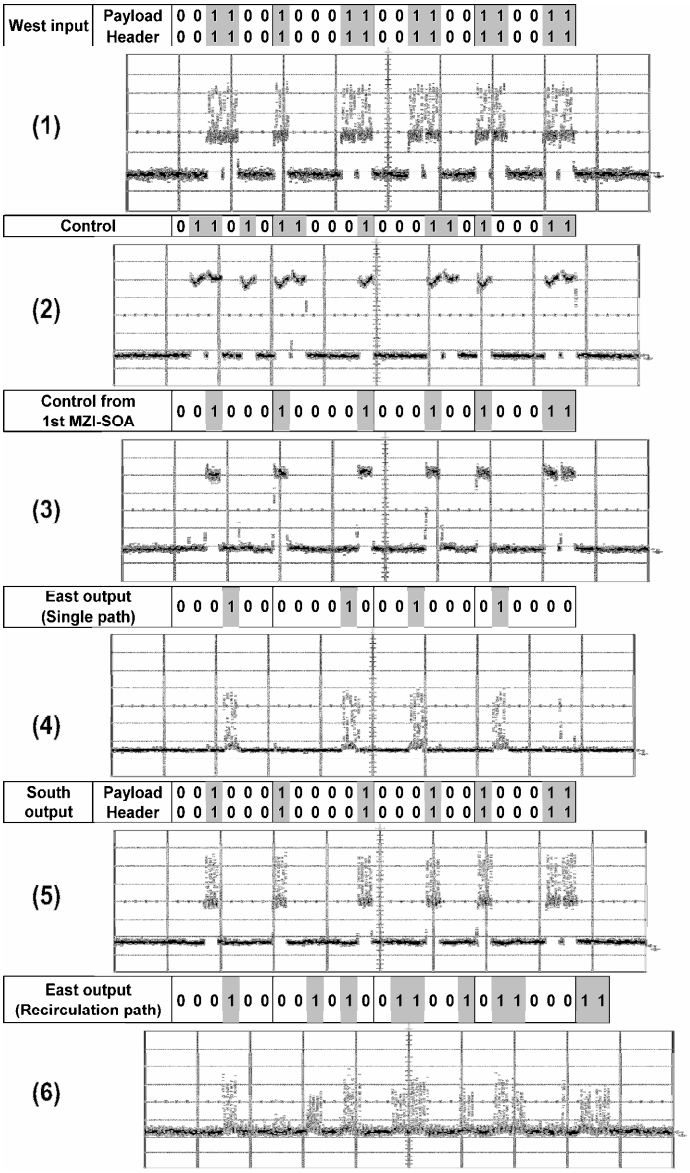

Fig. 4 Signal traces at each input and output port

Acknowledgements

This works has been partly funded by the IST project MUFINS.

References

[1] C. Reed, "Multiple level minimum logic network", U.S. Patent 5996020, Nov. 30. 1999.

[2] Qimin Yang et al., "WDM Packet Routing for High-Capacity Data Networks," J. Lightwave Technology, vol. 19, pp. 1420, 2001.

[3] Qimin Yang et al., "Traffic Control and WDM Routing in the Data Vortex Packet Switch," IEEE Photon. Technol. Lett., vol. 14, pp. 236, 2002.

Spectral Slicing for Data Communications

M S Leeson[1], B Luo[1] and A J Robinson[2]

[1]School of Engineering, [2]Department of Physics,
University of Warwick, Gibbet Hill Road,
Coventry, CV4 7AL, UK

Abstract: *In short range data communications, the cost of terminal equipment is borne by the user so low- cost wavelength generation methods are desirable. One option is to use an optical filter to provide narrow slices of a broadband noise source producing an approach commonly known as spectral slicing (SS). This provides a cost-effective alternative to laser diode sources but introduces excess intensity noise due to the source incoherence. This paper addresses the bit error rate performance of SS systems and their capabilities. Consideration is given also to the impact of different modulation formats and performance improvement using error correcting codes.*

Introduction

Wavelength division multiplexing (WDM) is finding its way into access networks where the cost of expensive components is shared by a relatively small number of customers. One low cost option for implementing WDM is to use an optical filter to provide narrow slices of a broadband noise source, known as spectral or spectrum slicing (SS) [1]. Recent developments in, for example, superluminescent LEDs [2] have greatly increased slice output powers in recent years. However, the excess intensity noise in SS compared to laser diodes due to the source incoherence remains, producing a power penalty in exchange for the inexpensive nature of the source.

System Model

The SS system, shown schematically in Figure 1, is assumed to operate in the C-band and thus linear dispersion is dominant. The broadband optical source may be modeled as white Gaussian noise of two-sided power spectral density (PSD) $N_0/2$. Slices are taken from it with an unapodized arrayed waveguide grating (AWG) with impulse response $\propto \exp(-\alpha t^2)$ [3], where the parameter α is half the mean squared coherence time. This produces noise that is Gaussian but no longer white because of the effect of the filter on the PSD. The slices are assumed to be narrow in comparison with the approximately rectangular passbands of the WDM multiplexer (MUX) and demultiplexer (DEMUX), which then have a negligible effect on the Gaussian spectrum of the SS source. On-off keyed (OOK) data drives a polarization-insensitive intensity modulator of ideal extinction ratio such that the optical field has an envelope $s(t)$. The modulated signal travels through an optical fiber path of length z, having linear dispersion β_2 (here taken as -20 ps^2 per kilometer). A trade off between the dispersive spreading of the pulses generated using a wide filter, causing intersymbol interference (ISI), and the increasingly detrimental effect of the excess noise with narrowing filter bandwidth occurs.

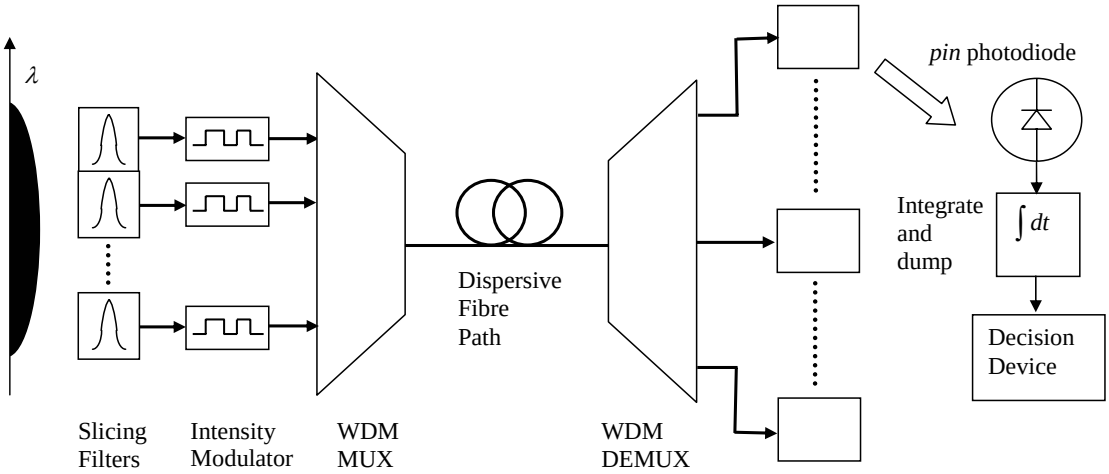

Figure 1: Schematic Representation of a Transmission System Employing Spectral Slicing.

For a bit time T_b, the current at the input to the decision circuit may be expressed as [4]

$$I = \frac{1}{2T_b}\int_0^{T_b}\left[x^2(t) + y^2(t) + \tilde{x}^2(t) + \tilde{y}^2(t)\right]dt + I_n \tag{1}$$

where $x^2(t), y^2(t), \tilde{x}^2(t)$ and $\tilde{y}^2(t)$ are independently identically distributed baseband Gaussian processes with variance σ^2, equal to the photocurrent contributed by each of the two orthogonal polarizations. That is to say they represent the in-phase and quadrature components of each polarization of the sliced signal. The term I_n represents the thermal noise current induced in the electrical part of the receiver (here taken to be 255 nA). The mean signal photocurrent, σ^2, is obtained from the photodiode quantum efficiency η, the electronic charge q, the mean number of photons per bit $\overline{N_p}$, and the bit rate R_b via $\sigma^2 = \overline{Np}\eta q R_b$. Taking the amplitude of the modulating waveform to be Gaussian of the form $s(t) = \exp[-t^2/2T_o^2]$, where T_0 is the half-width at the e^{-1} intensity points, permits a tractable expressions to be derived. The bit error rate (BER) is obtained using the saddlepoint approximation (SPA) [5] or the Gaussian approximation.

Sensitivity Results

The SS system is assumed to operate at a wavelength of 1550 nm, and the spectral slice and slice power spectral density are taken as Gaussian waveforms as above. To accommodate ISI, pulses either side of the received pulse are considered, with the sequences 010 and 101 representing the worst case scenarios. A bit rate of 2.5 Gbps and a photodiode of efficiency 70% are also assumed.

OOK

Using OOK, the 10^{-9} sensitivity of a single WDM channel as a function of the slice full width at half maximum (FWHM) appears as depicted by the black symbols on Figure 2.

The appearance of a minimum is apparent for the 15 km results, and operation at approximately 0.35 nm FWHM is optimum.

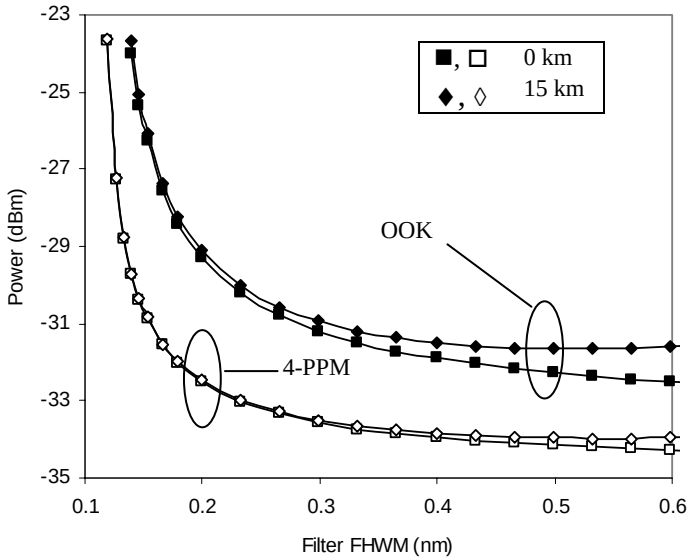

Figure 2: Sensitivity of SS as a function of slice width in the presence of dispersion [6], [7]

Pulse Position Modulation (PPM)

Digital PPM uses a single pulse, representing *M* bits (the PPM coding level), to convey information by its position, and the format exchanges bandwidth for receiver sensitivity. The SS-PPM system considered uses maximum likelihood detection (MLD), i.e. integration over each time slot. Assuming perfect extinction, only thermal noise is present in the off state and the Gaussian approximation may be employed to compare the relative performance of PPM and OOK. The 10^{-9} sensitivity of 4-PPM is shown by the white diamonds and squares on Figure 2. It may be observed that this modulation scheme offers an improvement in sensitivity of approximately 3 dB.

Forward Error Correction (FEC)

Recent work in Japan [8] has illustrated that substantial benefits accrue for SS by the use of FEC codes. As an example, a preliminary Monte Carlo simulation of a (15, 11) Hamming code applied to a slice width of ~0.07 nm is shown in Figure 3. It may be seen that even this simple code offers a benefit of several dBs, and this area is one for further study using more powerful codes.

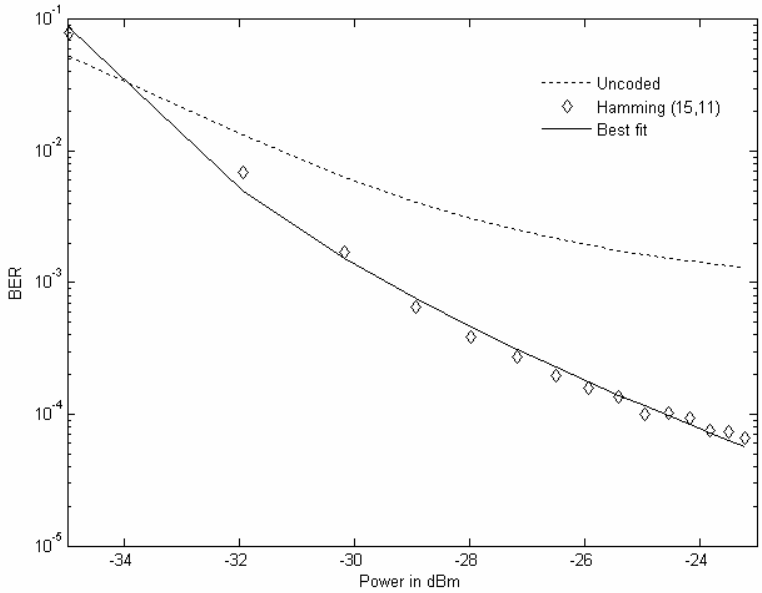

Figure 3: BER for SS system with and without FEC

Conclusions

SS lightwave systems have been considered for high speed data communications. The appearance of an optimum slicing width of ~ 0.35 nm for a bit rate of 2.5 Gbps has been illustrated. PPM has been shown to offer a 3 dB sensitivity advantage for SS over OOK. The emerging area of FEC for SS has been introduced with promising initial results and the prospect of considerable further work.

References

[1] J. Kani, K. Iwatsuki and T. Imai, “Optical Multiplexing Technologies for Access-Area Applications”, IEEE J. Sel. Topics in Quantum Electron., vol. 12, no. 4, pp. 661-668, 2006.

[2] T. Yamatoya, S. Sekiguchi and K. Iga, “High-Power CW Operation of GaInAsP/InP Superluminescent Light-Emitting Diode with Tapered Active Region”, Jpn. J. Appl. Phys, vol. 40, no. 7A, pp. L678-L680, 2001.

[3] M. C. Parker and S. D. Walker, “Design of Arrayed-Waveguide Gratings Using Hybrid Fourier-Fresnel Transform Techniques”, IEEE J. Sel. Topics in Quantum Electron., vol. 5, no. 5, pp. 1379-1384, 1999.

[4] M. S. Leeson, “Performance Analysis of Direct Detection Spectrally Sliced Receivers Using Fabry–Perot Filters”, J. Lightwave Technol., vol. 18, no. 1, pp. 13-25, 2000.

[5] G. Einarsson, Principles of Lightwave Communications: Wiley, 1996, ch. 5.

[6] M. S. Leeson, “Spectrally Sliced Transmission with Burst Mode Operation”, IEE Proc. Optoelectron., vol. 151, no. 4, pp. 211-218, 2004.

[7] M. S. Leeson, “Pulse Position Modulation for Spectrum Sliced Transmission”, IEEE Photon. Technol. Lett., vol. 16, no. 4, pp. 1191–1193, 2004.

[8] S. Kaneko, J. Kani, K. Iwatsuki, A. Ohki, M. Sugo and S. Kamei, “Scalability of Spectrum-Sliced DWDM Transmission and Its Expansion Using Forward Error Correction”, J. Lightwave Technol., vol. 24, no. 3, pp. 1295-1301, 2006.

Switched DWDM Ethernet Passive Optical Networks

R. Roy, G.G.H. Roeloffzen, *Member IEEE* and W van Etten, *Senior Member IEEE*

Telecommunication Engineering, University of Twente,
8202 Hogekamp, PO 217, Enschede, 7500 AE, the Netherlands

The IEEE Ethernet Passive Optical Networks (EPON) standard is a leading Time Division Multiplex (TDM) standard for PONs. The paper investigates the operation of an EPON based system in a Dense Wavelength Division Multiplex (DWDM) environment. It extends the concept of a multi-wavelength system from being merely a stack of independent PONs to that of a stack of a switched set of PONs. The functioning of the switching elements within the scope of EPON operation are investigated and qualitatively described. The architecture of the "Switched DWDM EPON" system is presented.

Introduction

The IEEE EPON standard is a TDM protocol for operation in PONs. The downstream transmission form the Optical Line Termination Unit (OLT) at the head-end to the Optical Network Unit (ONU) at the user is a broadcast transmission, the upstream transmission, from the ONU to the OLT, on the other hand is a TDM arbitrated transmission. EPON specifies WDM operation only for multiplexing the upstream (1.31 μm) and downstream transmission (1.49 μm) over a single fiber. EPON as such does not have a specification for use in a multi-wavelength environment. DWDM can also be used as a contention avoidance mechanism in PONs but this is not a practically scalable idea and is not discussed further. The following sections examine the operation of a switched EPON in a multi-wavelength environment.

DWDM PON

Figure 1 illustrates the concept of stacking up PONs to increase the aggregate bandwidth with use of multiple wavelengths. The aggregate bandwidth supported by the network scales up linearly with the number of wavelengths used. Each such PON is an independent network with only the fiber resources being shared by all the networks.

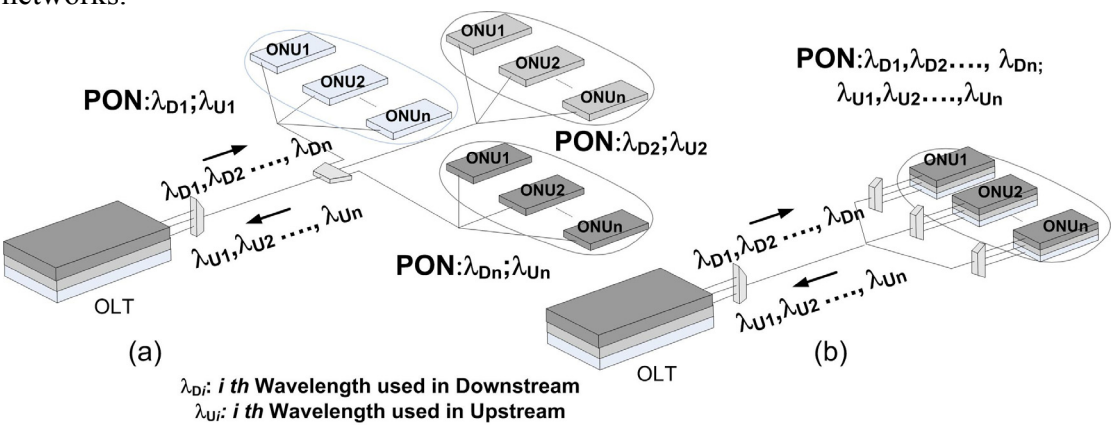

Figure 1: DWDM PON (a) Increasing number of users; (b) Increasing bandwidth per user

The increase in the bandwidth can be used in either increasing the number of users (horizontal stack) or in increasing the bandwidth provided per user (vertical stack). A dynamic switched combination of the two approaches is an interesting proposition.

Switched DWDM EPON Configuration

The use of multiple wavelengths opens up an added dimension which can be used to not just increase the aggregate bandwidth of the network but to also increase the dynamic re-configurability and the resiliency of the network. To achieve a dynamic switched combination of a horizontal and a vertical stack of PONs at the same time it should be possible to drop any or all wavelengths towards all the ONUs and that the ONUs are wavelength agnostic. To do this we consider a reconfigurable wavelength switch instead of passive (de)multiplexer, this device can output any set of wavelengths towards any of its ports. The control of the device will be done out of band [2]. The Client and WAN interfaces do not see the PON as a stack of separate PONs and the switching intelligence is in-built in the PON network.

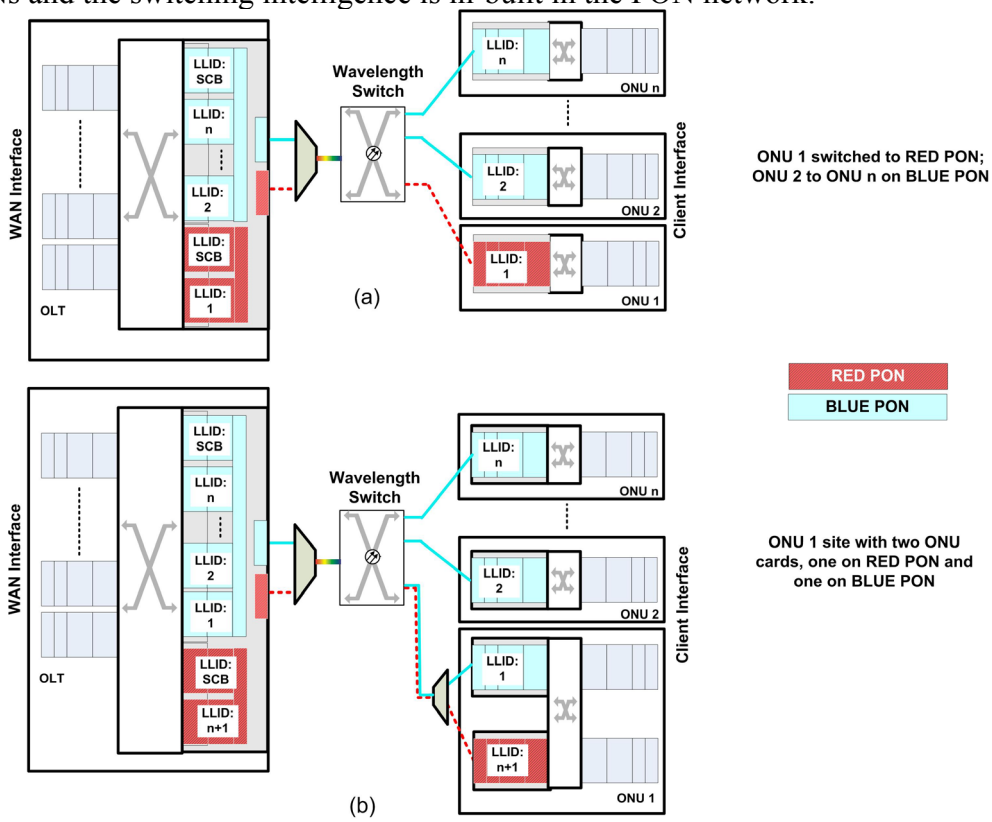

Figure 2: Switched DWDM EPON
(a) Switching an ONU to a new wavelength (b) Using additional wavelengths at a single ONU site

In EPON operation to emulate a point to point topology in a point to multipoint scenario each ONU is allocated a Logical Link Identity (LLID) and the MAC instantiation in the ONU has a corresponding MAC instantiation in the OLT. An additional MAC called the Single Copy broadcast (SCB) MAC is used for broadcast from the OLT to the ONUs. In a single PON with n ONUs there will be n+1 corresponding MAC instantiations in the OLT. If additional bandwidth or a different service is required for a set of ONUs, it can be switched to a different wavelength pair. Figure 2 illustrates the concept. The switching to a different wavelength pair, switches the transmission on to a different logical PON but the MAC instantiation still remains in the same chipset. The figure 2a illustrates two logical PONs; the red PON and the blue PON; ONU 1 is switched to the Red PON while ONU 2 to ONU n are left in the blue PON. The SCB MAC is also duplicated for both the logical PONs. Thus now the OLT instantiates n MACs for the blue PON and 2 MACs for the red PON. Figure 2b illustrates a configuration when additional wavelengths are used at a

particular ONU site. In this case the additional ONU card will have its own unique MAC identity. At ONU 1 site two wavelength pairs are used, the new card on the red PON is given a new LLID, thus the blue PON retains n+1 MACs and 2 MACs are instantiated for the red PON. The OLT should be able to instantiate as many MACs as is the number of LLIDs floated, and as many SCB MACs as the number of logical PONs. Having separate logical PONs for different wavelength pairs also allows for different line rates on the separate PONs. This way the cost of physical components for ONUs wanting higher line rates is not imposed on ONUs wanting to operate at lower line rates.

Concept implementation

The switching logic implementation will be carried out in the MAC Control Client block which is beyond the scope of the EPON specifications. There will be a single MAC Control Client interface for all the logical PONs. There are minimal modifications to the current MAC Control block specifications. Figure 3 illustrates the interfacing of the MAC Control Client interface with the modified MAC Control Client block.

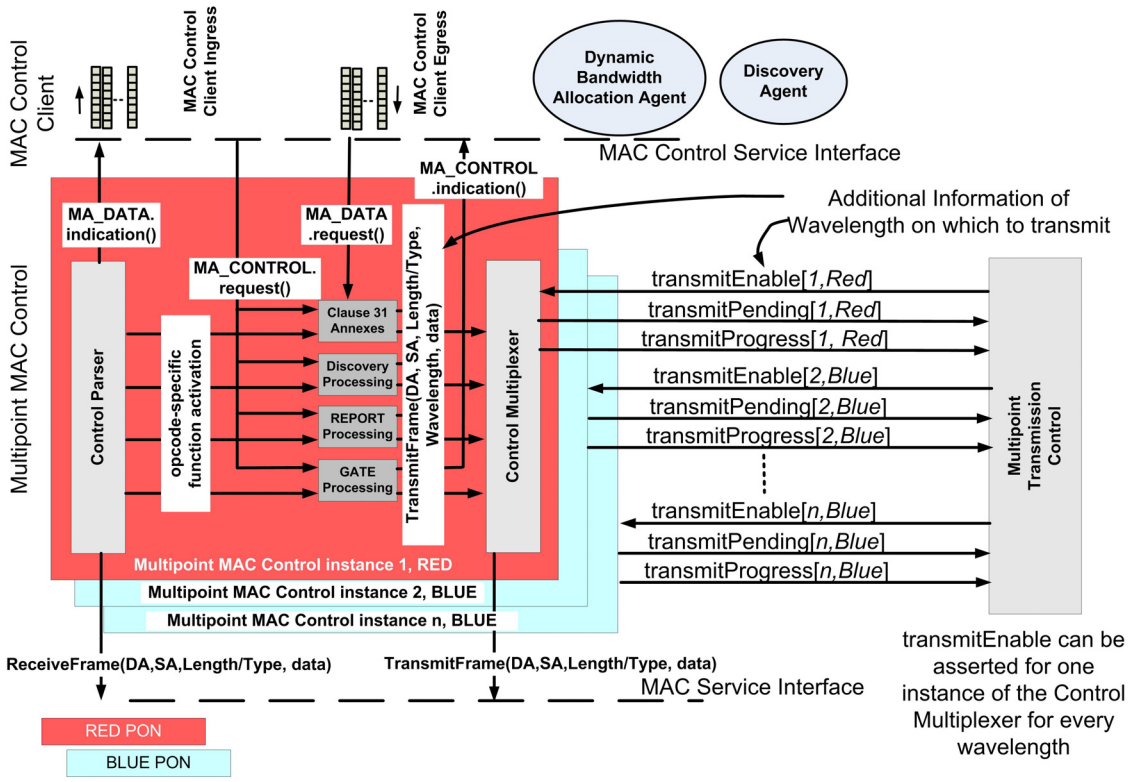

Figure 3: Multipoint MAC Control Block in a DWDM EPON

The Dynamic Bandwidth Allocation (DBA) agent takes care of the resource allocation and decides on the modalities for switching between the logical PONs. The agent has a complete overview of the resources available and the resources allocated. The switching initiation can be autonomous based on a pre-determined bandwidth allocation scheme, or an operator triggered event. The discovery agent initiates a discovery round periodically to detect and range the ONUs. It is envisaged that in a multi-wavelength configuration it is possible that the split ratio for a single wavelength will not have sufficient optical power budget for all the ONUs that might be connected. At initial start up, the discovery agent will ensure that the splitting ratio for every wavelength is controlled at the wavelength switch and thus if k wavelength

pairs are used there will be *k* parallel discovery rounds. In the operational state the discovery agent has the information about the wavelength allocations on all the ports and will run the discovery round without reallocation of wavelengths.

The *MA_Data.request* and the *MA_CONRTOL_request* primitives are used for transfer of data to the MAC entity or the MAC control entity respectively. The primitive should be able to carry additional information on the wavelength on which it is operating. The *Multipoint Transmission Control* block generates the *transmitEnable* to allow for transmission from one of the *Multipoint MAC Control* instance in a single PON, however with multiple logical PONs operating; the *Multipoint Transmission Control* block should be able to enable parallel transmissions on different wavelengths and will enable multiple transmissions as long as the transmissions from the *Multipoint MAC Control* instance are on different wavelengths. We envisage the logic of operation of the *Multipoint Transmission Control* block to be controlled by the DBA agent. To receive data from the MAC instances, the *ReceiveFrame( )* function call is continuously asserted. For a single PON there is always a single packet reception from one of the MAC instances which is forwarded to the MAC Control Client for data packets. In the current scenario there can be more than one packet receipts at the same time on different logical PONs. The MAC Control Client will have the provision to receive multiple data streams and to process them independently. At the OLT the Reconciliation Sublayer (RS) will be separate for the logical PONs. For one logical PON at a given instance only one *PLS_DATA.request* primitive (not illustrated) from any one of the multiple MAC instantiations to the RS, is active; this is ensured by the *Multipoint Transmission Control* Block. To enable parallel transmission on the different wavelengths there will be specific instantiations of the RS for each logical PON. The RSs interface to the PHYs which drive the DWDM optics. The ONU is wavelength agnostic and no changes are required.

Conclusions

An architecture for extension of EPON operations in a multi-wavelength environment is presented. The emphasis is to present an architecture which can be practically realized with minimum modifications to the existing EPON standards. The network is a dynamic switched combination of a horizontal and a vertical stack of PONs which can be used to exploit the best features of both kinds of networks. The solution minimizes the cost increase at the ONU site, instead increasing the associated complexity at the OLT site to distribute the cost addition over multiple users. The cost-performance characterization of such a network needs to be elaborated and will form part of future study.

Acknowledgements

The work is funded by the Dutch Ministry of Economic affairs through the BSIK Freeband Broadband Photonics Project under contract BSIK 03025. The authors acknowledge the contribution of the project partners.

References

[1] IEEE 802.3-2005, Part1-Part5, Carrier sense multiple access with collision detection (CSMA/CD) access method and physical layer specifications, *IEEE Standard*.

[2] R. Roy et al, “Control and Management Scheme in a DWDM EPON, Tu.D1.6, ICTON2006, Nottingham, UK

[3] Kramer, G., *Ethernet Passive Optical Networks*, New York: Mc-Graw Hill, 2005

Ultrafast optical differentiators based on asymmetric Mach-Zehnder interferometer

Z. Li, S. Zhang, J. Molina Vázquez, Y. Liu, G.D. Khoe, H.J.S. Dorren and D. Lenstra

COBRA Research Institute, Eindhoven University of Technology, P. O. Box 513, 5600 MB Eindhoven, The Netherlands. D. Lenstra is also with Laser Centre Vrije Universiteit, Amsterdam, The Netherlands.
Telephone: +31 40 247 5066, E-mail: lizhonggui@ieee.org

An ultrafast all-optical differentiator based on an asymmetric Mach-Zehnder interferometer is proposed. The device has a simple structure and can be integrated. Differentiation operations for Gaussian and super-Gaussian optical pulses are numerically shown successfully with very small deviation from the ideal differentiator output. The working speed of the device is only limited by the size of the device.

Introduction

Optical differentiators have received considerable attention recently due to their potential applications in all-optical analog-digital signal processing circuits, optical pulse shaping and optical sensing [1-3]. Several approaches have been proposed based on an integrated-optic transversal filter structure [1] or long period fiber gratings [2-3]. These approaches are complicated in terms of the optimization of the design parameters and they show large relative deviation (error) from the ideal differentiator. In this letter we propose a simple optical differentiator based on an Asymmetric Mach-Zehnder Interferometer (AMZI). AMZI is very useful in all-optical signal processing and has been extensively investigated in the framework of Differential Interferometer Signal Converter (DISC) [4, 5]; however, it has not been recognized as an optical differentiator. We explain how the device works and numerically demonstrate the differential operation with low relative error. Higher order derivatives can also be realized by cascading AMZIs and the device can be integrated.

Operation principle

he proposed logic differentiator [inset in Fig. 1(a)] is composed of an AMZI, in which a delay τ is introduced in one arm and a π phase shift is introduced in another arm. Suppose the input optical electrical field is $E_{in}(t)\exp(i\omega t)$, where ω is some optical frequency and $E_{in}(t)$ is a slowing varying amplitude, representing the function to be differentiated. The optical electric field $E_{out}(t)\exp(i\omega t)$ at the AMZI output can be expressed as

$$E_{out}(t) = [E_{in}(t) - E_{in}(t-\tau)\exp(-i\omega\tau)]/2 = \tau\dot{E}_{in}(t)/2, \tag{1}$$

when τ is small. Hence by adjusting τ we obtain

$$I_{out}(t) \propto |E_{out}(t)|^2 = \frac{\tau^2}{4}\left|\frac{dE_{in}(t)}{dt}\right|^2, \tag{2}$$

and the output signal intensity is directly proportional to the square of the absolute value of the differentiation of the input electrical field.

Simulation results

The proposed differentiator is simulated in the frequency domain using a Fast Fourier Transform (FFT) algorithm. An assumed input electrical field is Fourier transformed into the frequency domain, multiplied by the transfer function of the AMZI and transformed back into the time domain. In both Fig. 1 and Fig. 2 the delay τ in the differentiator is fixed at 5 ps. Fig. 1 shows a comparison between the simulated and ideal (analytic) output signals for the 1st and 2nd order differentiation. The latter is achieved by cascading two 1st order differentiators. The differentiation of 100ps and 10ps Gaussian input pulses are shown in Fig. 1(a) and Fig. 1(b), respectively. The pulse width here is referred to full

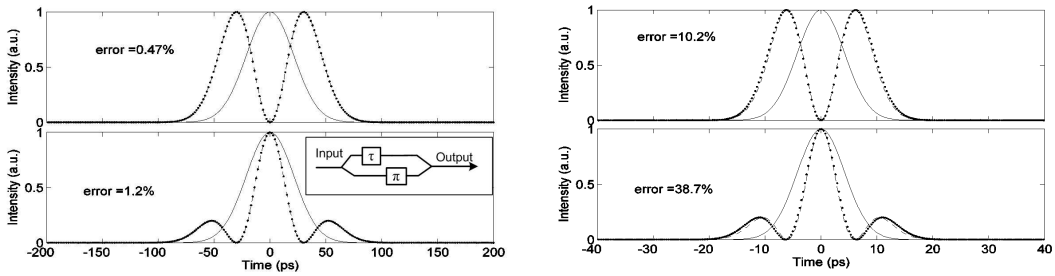

(a) (b)

Figure 1: Simulated output temporal waveforms (dash-dotted) and analytical output (dotted) for input Gaussian pulses with a FWHM of (a) 100 ps, and (b) 10 ps. Upper panels: 1st order derivative, and lower panels: 2nd order derivative. The inset in (a) shows the proposed device.

width at half maximum (FWHM). The estimated errors or deviations are indicated in Fig. 1, estimated from the relative difference between the normalized optical intensities that correspond to the numerically obtained and the ideal temporal derivatives over a temporal window where the signals exhibit nonzero intensity [2]. In Fig. 2 similar results are shown for 3rd order Super Gaussian pulses of 200 ps (a) and 100 ps (b). There is good agreement

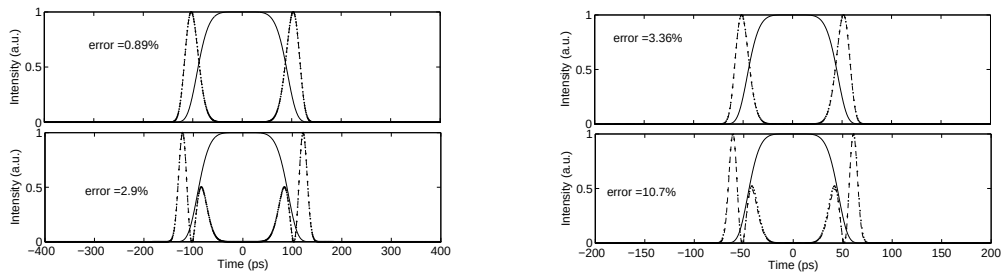

(a) (b)

Figure 2: Simulated output temporal waveforms (dash-dotted) and analytical output (dotted) for input 3rd order Supergaussian pulses with a FWHM of (a) 200 ps, and (b) 100 ps. Upper panels: 1st order derivative, and lower panels: 2nd order derivative.

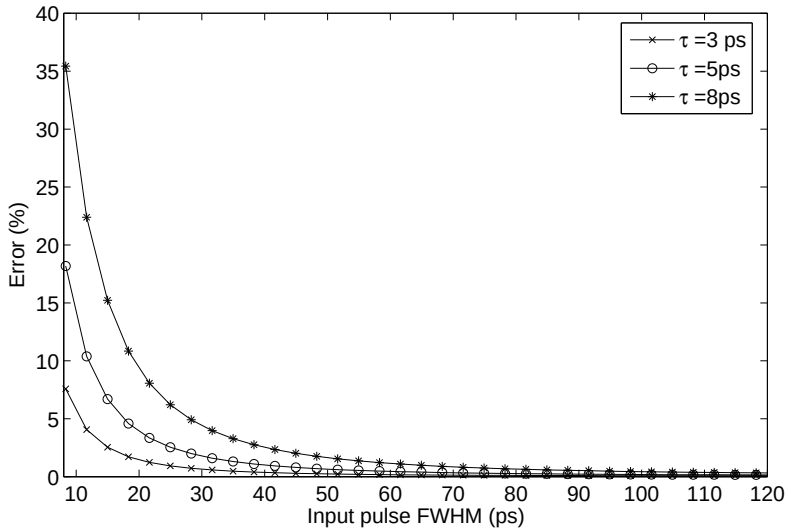

Figure 3: Error dependence on (a) input pulse FWHM and delay in the differentiator for Gaussian input pulses.

between the numerical and the analytic results. The error increases with decreasing pulse width and with increasing differentiation order. The main reason for this is the deviation of the transfer function from an ideal linear transfer function. As explained, the transfer function of the proposed differentiator is linear only around the frequency origin. Hence, as the signal bandwidth increases, the transfer function of the differentiator within the signal spectrum shows considerable deviations from an ideal linear function. A differentiator is a high-pass filter and therefore the error increases for higher differentiation order because the outputs spectrum from the previous differentiator shows more pronounced high frequency components. Fig. 3 shows the error dependence on the Gaussian pulse FWHM. The error decreases with increasing input pulse width (equivalent to decreasing the input pulse bandwidth), as expected. For input pulses of equal FWHM, the error is lower for a shorter delay τ in the differentiator since the bandwidth over which the transfer function is linear increases.

Since a differentiator works like a high-pass filter, the output signal is weak after the 1st order differentiation decreasing the optical signal-to-noise ratio (SNR). Since differentiation is very sensitive to noise [6], the device performance dependence on the noise level is also investigated. Uniformly distributed noise is added to the input waveform (200 ps, 3rd order Super Gaussian pulse) and the error for the differentiated signal is calculated. The error increases and it shows instability when the variance of the added noise increases, as shown in Fig. 4. In principle, the proposed differentiator can work for arbitrarily broadband signal if the delay in the differentiator can be made arbitrarily small. AMZIs with a delay of several picoseconds have been demonstrated [5], indicating the ability to deal with ultrafast input signals. Higher order differentiation can be realized by cascading several AMZIs at the expense of increased error. The cascadability is limited by both the delay τ in the AMZI and the SNR. It is important to note that the proposed differentiator can be integrated with planar lightwave circuit (PLC) technology [4].

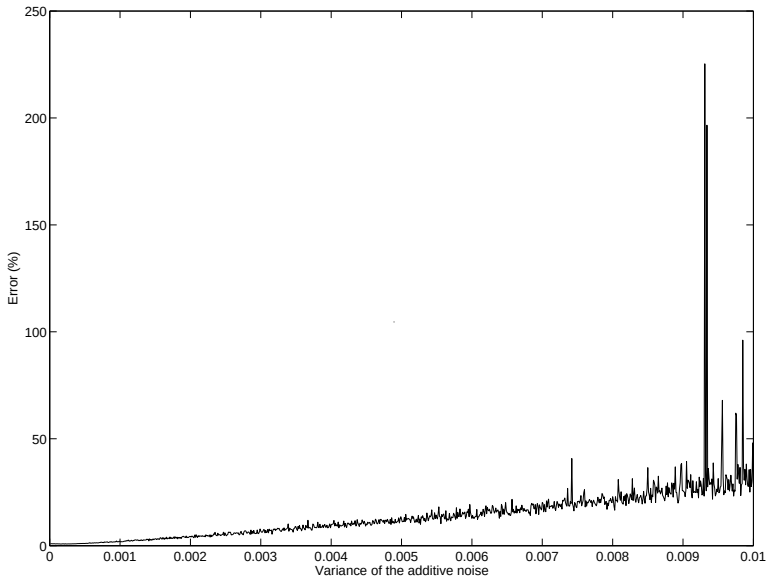

Figure 4: Error dependence on the level of added noise carried by the input signal. The input signal is a 200 ps 3rd Super Gaussian pulse.

Conclusion

A simple, low error differentiator based on an AMZI is proposed. The device can be cascaded to realize higher order derivatives at the cost of reduced SNR. The device can be integrated.

Acknowledgement

This work was supported by the Netherlands Organization for Scientific Research (NWO), the Technology Foundation STW and the Ministry of Economic Affairs through respectively the NRC Photonics grant, the “Innovational Research Incentives Scheme Program” and the technology program “Towards Freeband Communication Impulse”.

References

[1] N.Q. Ngo, S.F. Yu, S.C. Tjin and C.H. Kam,”A new theoretical basis of higher-deriative optical differentiators”, *Optics Communications*, 2004, 230, pp. 115-129.

[2] M. Kulishov and J. Azaña, ”Long-period fi ber gratings as ultrafast optical differentiators”,*Optics Letters*, 2005, 20(30), pp.2700-2702.

[3] J. Azaña and M. Kulishov, ”All-fi bre ultrafast optical differentiator based on π phase-shifted long-period grating”, *Electronics Letters*, 2005,41(25), pp.1368-1369.

[4] J. Leuthold et al., ”3.8THz wavelength conversion of picosecond pulses using a semiconductor delayed-interference signal-wavelength converter (DISC)”, *Photonics Technologies Letters*, 1998, 10(3), pp.346-348.

[5] R. Allen and D. Mills, ”Signal analysis: time, frequency, scale and structure”, Wiley-Interscience, 2004.

Fiber Bragg Gratings for In-line Dispersion Compensation in Cost-effective 10.7-Gbit/s Long-Haul Transmission

D. van den Borne[1], V. Veljanovski[2], E. Gottwald[3], G. D. Khoe[1] and H. de Waardt[1]

1: COBRA institute, Eindhoven University of Technology, The Netherlands
(e-mail: d.v.d.borne@tue.nl), 2: Siemens AG, Program and System Engineering, Munich, Germany, 3 : Siemens AG, Communications, Fixed networks, Munich, Germany.

Among the promising new developments towards cost-effective long-haul transmission are chirped multi-channel Fiber Bragg Gratings (FBG). In this paper we discuss the feasibility of long-haul WDM optical transmission using only FBGs for in-line dispersion compensation. We show successful transmission of 32x10.7-Gbit/s NRZ modulated channels over 3,800-km using low group delay ripple slope-matched FBGs.

Introduction

Dispersion compensating fiber (DCF) is currently used as the standard solution for dispersion compensation in long-haul transmission links, since it yields colorless, slope-matched dispersion cancellation with negligible cascading impairments. However DCF is also limited in optical input power to avoid nonlinear impairments, has a relatively high insertion loss and is bulky.

Chirped FBGs could possibly replace DCF as the standard solution for in-line dispersion compensation. Chirped FBGs have a negligible nonlinearity, low insertion loss and small size [1-2]. This potentially allows simpler erbium-doped fiber amplifier (EDFA) design by cascading the FBG and transmission fiber without a mid-stage amplifier, resulting in a significant cost reduction. The main drawback of FBGs is that they suffer from distortions in their phase response, better known as the group delay ripple (GDR) [3]. This is caused by imperfections in the gratings fabrication process and limits the number of FBGs that can be cascaded. Improved fabrication processes have however gradually reduced the GDR of state-of-the-art slope-matched FBGs, which significantly increases the number of FBGs that can be cascaded [4].

In this paper we show, to the best of our knowledge for the first time, long-haul WDM optical transmission using only FBGs for in-line dispersion compensation. We successfully transmit 32x10.7-Gbit/s NRZ modulated channels over 3,800 km using low-GDR slope-matched FBGs to compensate for the group-velocity dispersion (GVD).

Chirped multi-channel fiber Bragg gratings

Chirped multi-channel FBGs can compensate for the group velocity dispersion of single-mode fibers due to a frequency dependent group delay. The dispersion compensation module (DCM) consists of a circulator and a FBG, as depicted in Fig. 1. The FBGs used in the experiments have a 100-GHz channel spacing and Fig. 2b and 2c show the amplitude and phase response for a single WDM channel of the FBG, respectively. The group delay is relatively linear over

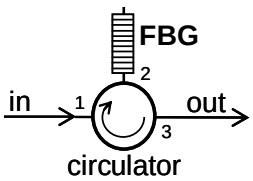

Fig. 1: Layout of the FGB-based DCMs

approximately a 70-GHz bandwidth within the 100-GHz WDM channel spacing . The FBG ‘s GDR can be computed by taking a linear fit of the group delay, and computing the deviations from this linear fit (Fig. 2c). The FBGs used in the described experiments have an average peak-to-peak GDR of 15.5 ps within a 35-GHz bandwidth around the channel’s center.

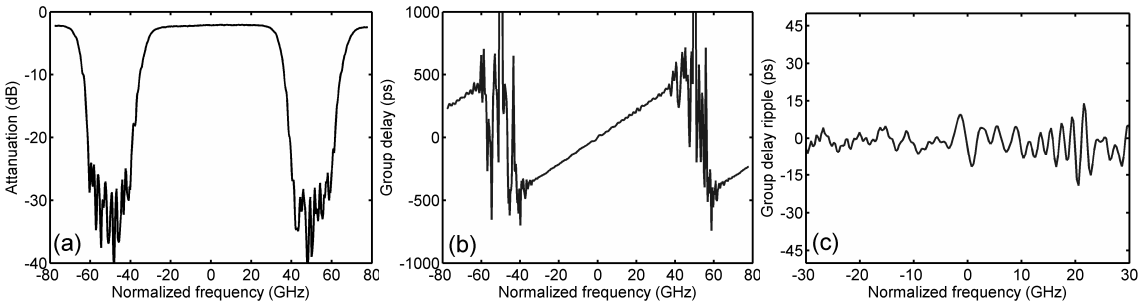

Fig. 2: Measured response of a chirped multi-channel FBG for one particular WDM channel;(a) attenuation, (b) group delay and (c) group delay ripple.

Experimental setup

Fig. 3 depicts the re-circulating loop setup. In this experiment 32 distributed feedback laser (DFB) outputs are combined on a 100-GHz ITU grid, from 1538.2 THz to 1563.0 THz. Using a standard Mach-Zehnder modulator (MZM) the signals are NRZ-OOK modulated with a 10.7-Gbit/s 2^{31}-1 pseudo-random bit sequence (PRBS). The re-circulating loop used in the transmission experiment consist of 8 x 95-km SSMF spans. The average loss of the SSMF spans is 19.5 dB and the FBG-based DCMs have an average insertion loss of 2 dB. EDFA-only amplification is used, with double-stage EDFAs to control the tilt of the WDM spectrum. The SSMF input power is 3 dBm per WDM channel. A double periodic dispersion map is used in the transmission experiments. This has the advantage that the accumulated dispersion after every eight spans is close to zero [5]. Before the first span a FBG-based DCM with -1020 ps/nm of GVD (at 1550 nm) is used as pre-compensation. For inline dispersion compensation, the DCMs have a GVD equivalent to 80 km (-1345 ps/nm, 5x) or 100 km of SSMF (-1681 ps/nm, 3x). Loop-induced polarization effects are reduced using a loop-synchronous polarization scrambler (LSPS). Power equalization of the DWDM channels is provided by a channel-based dynamic gain equalizer (DGE). At the receiver the desired WDM channel is selected using a narrowband 18-GHz channel-selection filter (CSF) and the residual GVD is per-channel optimized with a tunable dispersion compensator (TDC) (DCF/SSMF-based). Afterwards the signal is fed to a standard 10.7-Gbit/s receiver (Rx) and evaluated using a bit-error rate (BER) tester.

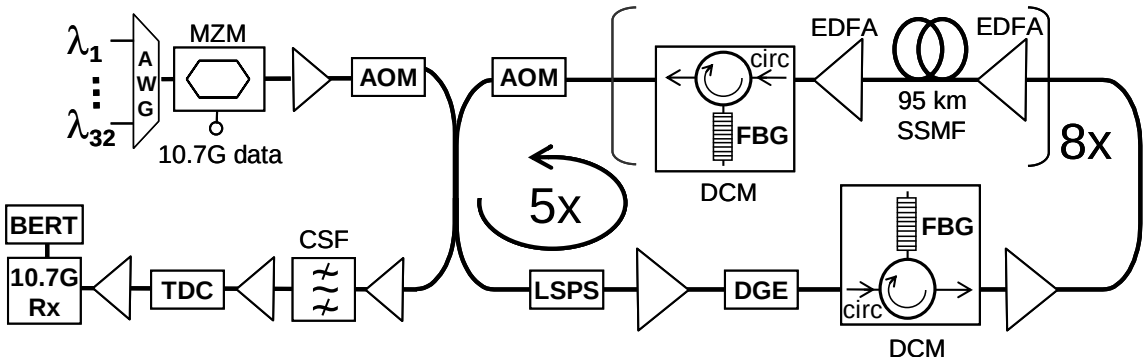

Fig. 3: Experimental setup; circ: Circulator, AOM: acoustic optical modulator.

Experimental results

Fig. 4a and 4b show the measured Q-factor after 3,040-km and 3,800-km of transmission, cascading 36 and 45 FBGs, respectively. The influence of GDR-related impairments is apparent through the large (~5 dB) spread in performance between the WDM channels. For a similar DCF-based transmission experiment the spread in Q-factor is expected to be in the range of ~1 dB (see for example [6]). Yet after 3,040-km transmission the measured Q-factor for the worst channel is still 2.5-dB above the correction limit of a concatenated FEC code with a 7% overhead (BER $2.4 \cdot 10^{-3}$ or Q-factor 9.0 dB). And even for a 3,800-km transmission distance the measured Q-factor is above the FEC limit for all 32 channels.

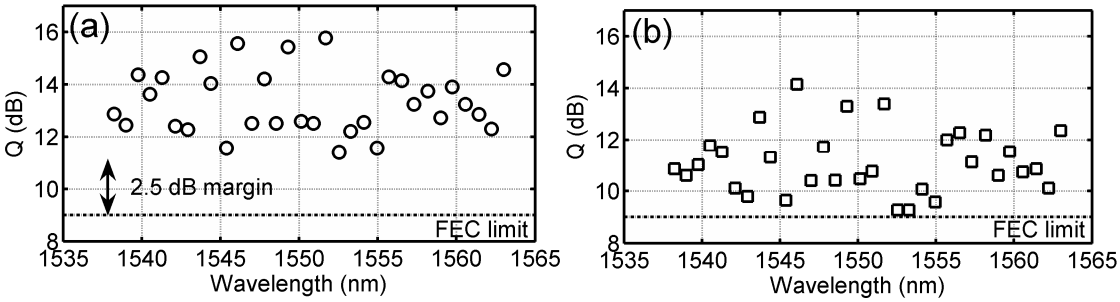

Fig. 4: Measured Q-factor for 32 WDM channels after (a) 3,040-km and (b) 3,800-km transmission.

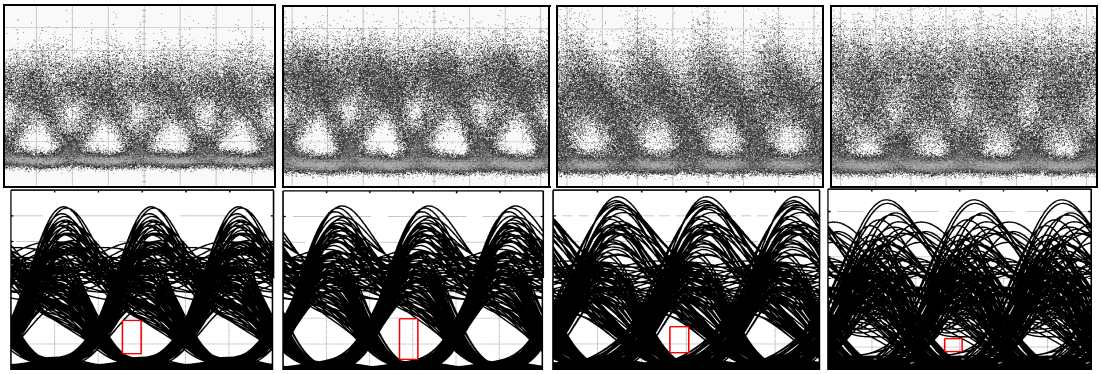

(a) 1543.7nm **(b) 1551.7nm** **(c) 1552.5nm** **(d) 1554.1nm**

Fig. 5: upper row: Eye diagrams after 3,800 km with small (a and b) and large (c and d) GDR related penalties, lower row: simulated eye diagrams using measured amplitude and phase response.

Fig. 5 shows in the upper row the measured eye diagrams after 3,800-km of transmission for several WDM channels. The eye diagrams at 1543.7 nm (a) and 1551.7 nm (b) show WDM channels where the GDR has a relatively small influence. On the other hand, for the channels at 1552.5 nm (c) and 1554.1 nm (d) a severe influence of GDR is evident, limiting the feasible transmission distance to 3,800 km. The lower row in Fig. 5 shows the eye diagrams for the same WDM channels when the amplitude and phase response of the cascaded FBGs is simulated. In the simulations the measured amplitude and phase response of the FBGs are used, but no transmission is simulated ("back-to-back"). Hence, the simulation shows only the GDR related impairments resulting from the cascaded FBGs. Both the simulated and measured eye diagrams in Fig. 5 show a strong broadening of the '1'-rail through phase distortions. Based on this similarity we conjecture this result mainly from GDR induced penalties.

Back-to-back, the required optical signal-to-noise ratio (OSNR) is 9.7 dB and 15.3 dB for a Q-factor of 9.8 dB (BER 10^{-3}) and 15.6 dB (BER 10^{-9}), respectively. After transmission the average OSNR is 19.7 dB and 18.8 dB, for respectively a 3,040-km

and 3,800-km transmission distance. The OSNR penalty is computed by comparing the required OSNR back-to-back and after transmission for the best-case and worst-case measured Q-factor. After 3,040 km transmission the OSNR penalty is between 4 dB and 8.5 dB, and for a 3,800-km transmission distance the penalty ranges from 5 dB to 10 dB. Fig. 6a and 6b shows the Q-factor decrease with transmission distance for respectively a channel with small and large GDR penalties. The Q-factor decreases with ~6.5 dB when the transmission distance is doubled, in comparison to 3 dB for an ideal (linear) transmission line. As a result the GDR related impairments become more severe with an increasing number of cascaded FBGs.

In the re-circulating loop experiments the measured penalty is however artificially increased due to the cascade of the same FBGs, resulting in a correlated GDR. For arbitrary cascaded FBG the GDR is uncorrelated and as a result the influence of the GDR grows statistically (square-root) [7]. However in this transmission experiment 8 FBGs are cascaded in a re-circulating loop and the optical signal is thus passed multiple times through the same FBG. Consequently, the peak-to-peak GDR grows linearly, tremendously worsening the associated penalty. Hence, we conjecture that for arbitrary cascaded FBGs the drop-off with transmission distance is less steep and a significant larger number of FBGs can be cascaded with acceptable GDR impairments.

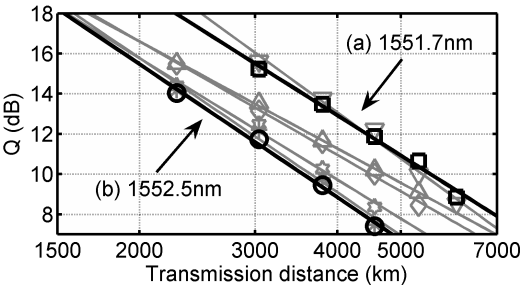

Fig. 6: Measured Q-factor versus distance for a channel with small (a) and large (b) GDR penalties as well as several arbitrary WDM channels (grey).

Conclusions

We showed long-haul 10.7-Gbit/s WDM transmission with only FBG-based DCMs for in-line dispersion compensation. Using low-GDR FBGs we successfully transmit NRZ modulated data over 40 x 95 km, cascading 45 FBG units. The penalties associated with cascading a large number of FBGs (>30) implies that FBGs are not yet suitable for ultra long-haul applications. But it shows that FBG fabrication technology has matured into an appealing alternative for cost-sensitive links, up to approximately 2000 km.

References

[1] K. O. Hill and G. Meltz, “Fiber Bragg Grating technology fundamentals and overview” J. Lightwave Technol., vol. 15, pp. 1263-1276, 1997.

[2] H. S. Fews, et. al, “Experimental Comparison of Fibre and Grating-Based Dispersion Compensation Schemes for 40 channel 10Gb/s DWDM systems”, ECOC 2006, paper Th3.2.5.

[3] C. Scheerer, et al., “Influence of Filter Group Delay Ripples on System Performance”, ECOC 1999, pp. I-410.

[4] Y. Painchaud, et al., “Low-penalty cascade of low-ripple FBG-based dispersion compensators”, ECOC 2006, paper Th4.2.7.

[5] S. Banerjee, et al., Doubly periodic dispersion maps for 10 and 40 Gbit/s ultra-long-haul transmission”, Electronic Letters, vol. 40, pp. 1287-1288, 2004.

[6] D. van den Borne, et al., "1.6-b/s/Hz Spectrally Efficient 40 x 85.6-Gb/s Transmission Over 1.700 km of SSMF Using POLMUX-RZ-DQPSK, OFC 2006, PDP34.

[7] M. H. Eiselt, et al., “Performance Characterization of Components With Group Delay Fluctuations”, Photonic Technology Letters, vol. 15, pp. 1076-1078, 2003.

Towards a reliable RoF infrastructure for broadband wireless access

M. Garcia Larrode and A.M.J. Koonen

Eindhoven University of Technology,
Den Dolech 2, 5600 MB Eindhoven, The Netherlands

Radio-over-Fiber (RoF) distribution antenna systems have been identified as a flexible option for the access architecture of the emerging wireless access networks, especially inside buildings, as a means of reducing infrastructure cost and antenna site complexity. Exploiting the features of the Optical Frequency Multiplication (OFM) technique, a reliable RoF physical layer can be designed, comprising bidirectional RF transmission, increased cell capacity allocation, multi-standard support, remote LO delivery and an in-band control channel for dynamic radio link adaptation and remote antenna controlling. The proposed scheme can be easily integrated in WDM-PON architectures, allowing a flexible convergence of wireless services with broadband access optical networks.

Introduction

One major application of microwave photonics research is radio-over-fiber (RoF) distribution antenna systems, in which radio signals are generated at a remote central station (CS) and distributed transparently to several simplified antenna stations (AS) via optical fiber. The main goal of these RoF systems is to reduce infrastructure cost and to overcome the capacity bottleneck in wireless access networks, allowing at the same time a flexible merging with conventional optical access networks. Thus, in order to design a reliable RoF-based access infrastructure, RoF techniques must (a) be capable of generating the microwave signals and (b) allow a reliable microwave signals transmission over the optical link. The Optical Frequency Multiplication (OFM) method [1] satisfies these two main requirements by generating the microwave signals with a single laser source and low frequency electronics and presenting high tolerance to dispersion impairments in transmission over single mode [2] and multimode [3] fiber links. In this paper, we summarize a number of functionalities enabled by the OFM technique, which make possible the design of a reliable RoF-based infrastructure for broadband wireless access.

Optical Frequency Multiplication (OFM)

The Optical Frequency Multiplication (OFM) principle is based on harmonics generation by FM-IM conversion through a periodic band pass filter. At the CS, a continuous wave laser source ω_0 is frequency modulated (FM) by a sinusoid with sweep frequency f_{sw}, intensity modulated by the radio signal (data) at low frequency subcarrier $f_{sc} < f_{sw}/2$, passed through a periodic band pass filter (e.g., a Mach-Zehnder interferometer (MZI)), launched into the optical fiber link and recovered at the AS by a photodetector (fig. 1(a)). At the output of the photodetector, radio frequency components at every harmonic of f_{sw} are obtained ($f_{harmonic} = n \cdot f_{sw}$) (fig. 1(b), no data), with relative amplitudes depending on f_{sw}, the frequency modulation index and the free spectral range (FSR) of the MZI. When radio data is applied, the radio signals are obtained up-converted double-sided along with

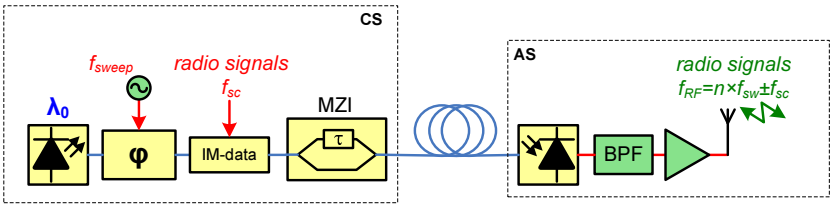

(a) OFM implementation schematic

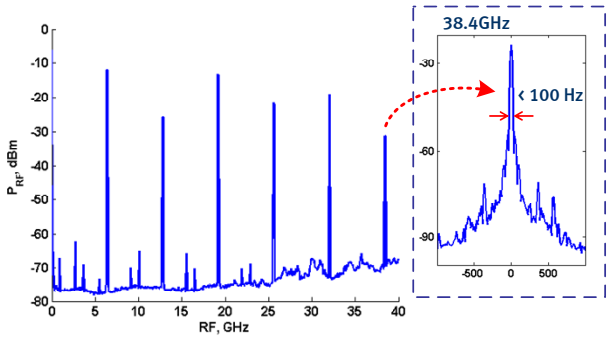

(b) harmonics generation with f_{sw}=6.4GHz [2]

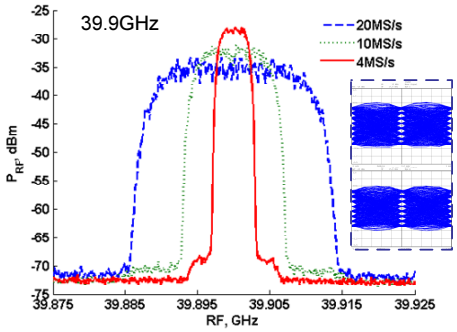

(c) QAM signals at f_{RF}=39.9GHz (6th harmonic of f_{sw}=6.4GHz, f_{sc}=1.5GHz) [2]

Figure 1: Optical Frequency Multiplication technique

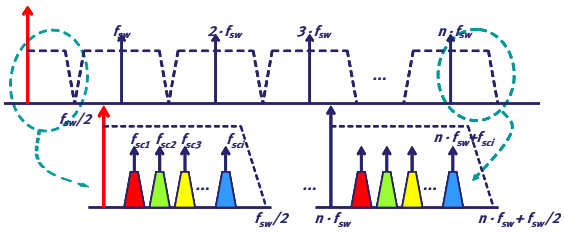

(a) RF bandwidth capacity

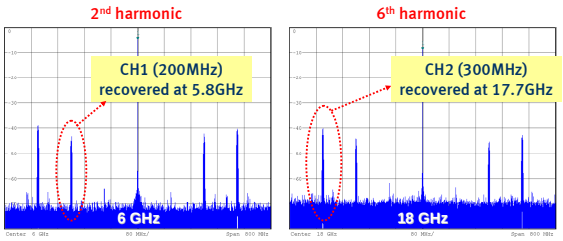

(b) simultaneous transmission/upconversion of QAM signals to 5.8GHz and 17.7GHz (f_{sw}=3GHz, f_{sc_1}=200MHz, f_{sc_2}=300MHz)

Figure 2: RF bandwidth capacity and multistandard support

the generated harmonics at $f_{RF} = n \cdot f_{sw} \pm f_{sc}$ (n indicates the nth harmonic), at the AS (fig. 1(c)).

Increased cell capacity allocation and multi-standard support

As explained before, in a RoF link employing OFM, any radio signal at low frequency subcarrier $f_{sc} < f_{sw}/2$ can be introduced by intensity modulation at the CS, transparently transmitted to the AS, and recovered up-converted along with the desired harmonic. On the condition that the maximum RF bandwidth ($f_{sw}/2$) is not exceeded, different wireless signals can be transmitted simultaneously in a subcarrier multiplexing (SCM) scheme [4] (fig. 2(a)). Hence, at the AS, the obtained up-converted signals can be selected at the same or at different harmonics bands. This opens the possibility of *increasing the cell capacity* of a wireless system at the AS, when the signals are selected in the same harmonic band. Also, a proper election of the f_{sw} and f_{sc}'s at the CS enables the simultaneous recovery of

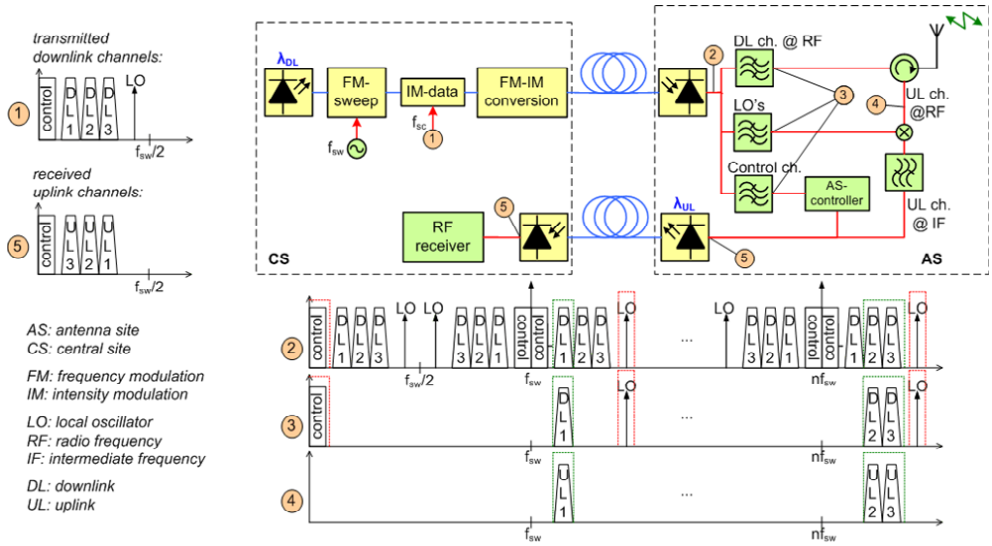

Figure 3: Bidirectional RoF link employing OFM [5]

the wireless signals at different harmonic bands (fig. 2(b)). In this way, *multiple wireless standards* can be simultaneously and transparently transmitted to the same AS, e.g. WiFi and WiMax, in a single OFM link, employing only one laser source and and low frequency electronics at the CS.

Dynamic radio link adaptation with OFM

Dynamic radio link adaptation to the physical medium is a key feature in wireless transmission to guarantee system performance. Thus, a RoF link has to support this adaptability without incurring in additional signal degradation along the optical path, being as independent as possible of the radio link adaptation procedures. Whereas link/MAC and baseband adaptation can be controlled from the CS, the RF adaptation may occur either at the CS or at the AS. In this last case, adaptive remote AS configuration might be necessary. Hence, a trade-off between AS-simplicity and minimum level of AS-intelligence needed arises. OFM enables a flexible mechanism for the dynamic radio link adaptation support [4]:

- *Dynamic carrier frequency allocation* can be easily performed from the CS by tuning low frequency subcarriers.
- *Transmit power* can be remotely controlled from the CS and adjusted at the AS, to alleviate optical dynamic range requirements in the RoF link; for this purpose, an *in-band control channel* has to be transmitted simultaneously with the wireless data channel from the CS to the AS.

In a more general approach, an in-band control channel in the same optical link may enable other mechanisms for remote antenna configuration and controlling during network optimization and dynamic resource allocation.

Bidirectional RoF link employing OFM

Figure 3 shows a schematic of a bidirectional RoF link employing OFM [5]. At the CS, a pilot subcarrier $f_{sc_{pilot}}$ can be also multiplexed together with the downlink radio chan-

nels and the control channel. At the photodetector output, this subcarrier is up-converted together with the RF channels to $f_{LO} = n \cdot f_{sw} \pm f_{sc_{pilot}}$, and can be used as a local oscillator (LO) at the AS. In this way, the uplink RF channels arriving at the AS are mixed with the remotely delivered LO's and down-converted to low intermediate frequency (IF) $f_{UL} = |f_{LO} - f_{RF}|$. The resulting IF uplink signals can modulate the intensity of a low cost light source and be directly transmitted to the CS, where they can be further processed by a low frequency RF receiver.

Flexible wireless-optical convergence

OFM has the advantage of generating microwave carriers with the use of one single laser source. When considering bidirectional transmission, two separate wavelengths (λ_{DL} and λ_{UL}) compose the RoF link. Thus, the extension of this OFM-based RoF link towards a distribution antenna system design implies the multiplexing of wavelength pairs per AS. This scheme can be easily integrated in wavelength division multiplexing passive optical network (WDM-PON) architectures, which are nowadays very popular in fibre-to-the-home (FTTH) broadband access [5].

Conclusions

Optical Frequency Multiplication is a flexible and cost-effective RoF technique that enables multiple functionalities required for the support of wireless access systems. Increased cell capacity allocation, multi-standard support, remote LO delivery and in-band control channel for dynamic radio link adaptation and remote antenna controlling can be provided with a single laser source and low frequency electronics at the CS. Additionally, RoF distribution antenna systems based on OFM can be smoothly merged with broadband access optical networks like WDM-PON, allowing a flexible convergence of optical fiber's high capacity and wireless access flexibility.

References

[1] A. M. J. Koonen and A. Ngoma, *Broadband Optical Access Networks and Fiber-to-the-Home: System Technologies and Development Strategies*. Wiley & Sons, 2006, ch. 11: Integrated Broadband Optical Fibre/Wireless LAN Access Networks.

[2] M. G. Larrode, A. M. J. Koonen, J. J. V. Olmos, E. J. M. Verdurmen, and J. P. Turkiewicz, "Dispersion tolerant radio-over-fibre transmission of 16 and 64 QAM radio signals at 40 GHz," *IEE Electronics Letters*, vol. 42, no. 15, pp. 872–874, July 2006.

[3] M. G. Larrode, A. M. J. Koonen, and J. J. V. Olmos, "Overcoming modal bandwidth limitation in radio-over-multimode fiber links," *IEEE Photonics Technology Letters*, (accepted for pub.) 2006.

[4] ——, "Fiber-based broadband wireless access employing optical frequency multiplication," *IEEE Journal of Selected Topics in Quantum Electronics*, vol. 12, no. 4, pp. 875–881, July 2006.

[5] M. G. Larrode and A. M. J. Koonen, "Physical layer design for RoF-based wireless access networks," in *Proc. 31st European Conference on Optical Communication, ECOC*, Sep. 2006.

The Effect of Passive Optical Components in Multimode Fibre Links Using Mode Group Diversity Multiplexing

C. P. Tsekrekos and A. M. J. Koonen

COBRA Research Institute, Eindhoven University of Technology

P. O. Box 513, 5600 MB Eindhoven, The Netherlands, e-mail: C.Tsekrekos@tue.nl

In short-reach multimode fibre (MMF) links, mode group diversity multiplexing (MGDM) can be used to create parallel, independent communication channels. Each channel uses a different subset of the propagating modes in the MMF. To allow for network topologies beyond the basic point-to-point scenario, passive components, such as optical splitters, are required. Such components may affect the modal spectrum of the MGDM channels and therefore the performance of the communication link. This paper presents an experimental investigation of the effect of passive optical components on an MGDM link.

Introduction

Multimode fibre (MMF) is extensively used in in-building and campus networks. Its large core diameter, in comparison to the single-mode fibre (SMF), facilitates its installation and handling. In MMFs, monochromatic light propagates in a multitude of modes. Each mode has a different spatial intensity distribution and propagation delay. Mode group diversity multiplexing (MGDM) is an intensity-modulation (IM), direct-detection (DD), multiple-input, multiple-output technique that uses groups of propagating modes to create independent, parallel communication channels. N lasers excite N different groups of modes and M detectors $(M \geq N)$ selectively respond to the optical power at the MMF output. The mixing among the channels is mitigated electronically [1, 2]. In short-reach networks, the effect of dispersion can be neglected when the bandwidth requirements are not very high. The transmission bandwidth can still be in the range of a few GHz for MMF links up to 100 m long [3]. In this case, the electrical output signals are related to the electrical input ones via a real-valued $M \times N$ transmission matrix $\mathbf{H}$. The matrix elements $h_{i,j}$ express the amount of optical power in the jth channel that is received by the ith detector.

MGDM requires mode-selective components to launch and detect the mode groups. Design considerations for graded-index (GI) MMFs have been presented [4], with radially offset beams at the GI-MMF input and a multi-segment detector with annular segments responding to the near field pattern (NFP) at the GI-MMF output. The intensity distribution of the NFPs of the MGDM channels determines the geometry of the detector. In particular, the areas of the detector's segments are chosen so as to minimize the crosstalk among the channels. In local area networks, bus, star and ring topologies are often deployed (Figure 1). To apply MGDM in such network topologies, passive optical components, such as optical couplers, are required. In this paper, we present an experimental investigation of the effect of several passive optical components on the NFP of GI-MMF links under selective excitation with an SMF.

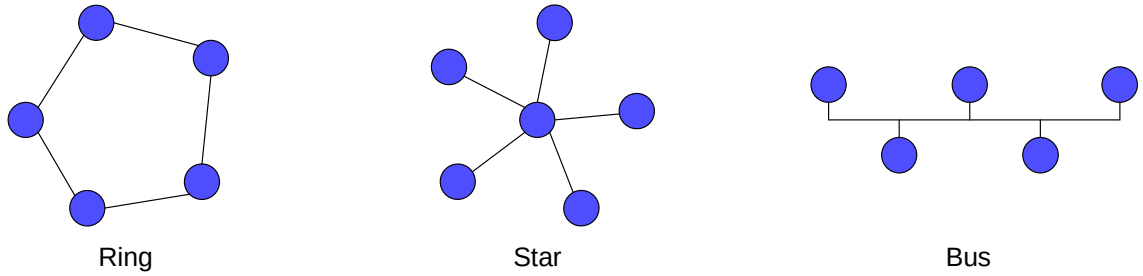

Figure 1: Common topologies in local area networks.

Experimental Results

The experimental investigation of the NFP was realized with the set-up illustrated in Figure 2. An external cavity type tunable semiconductor laser was used to selectively excite a 1 m long GI-MMF with core/cladding diameter of 50/125 μm and central numerical aperture (NA) 0.2. The wavelength of the laser was tuned at 1310 nm and its linewidth was 85 kHz. The laser was pigtailed with an SMF of 9.3 μm mode field diameter at 1310 nm wavelength. The SMF and GI-MMF axes were parallel and their lateral distance was set by computer-controlled translational stages. The axial distance between the SMF and the GI-MMF ends was in the order of a few microns to allow for the movement of the stages. The 1 m long GI-MMF was connected to a GI-MMF passive optical component followed by a 100 m long GI-MMF, both of the same type with the 1 m GI-MMF. The optical components were connected with FC/PC adapters. At the output of the 100 m long GI-MMF, the NFP was observed with an infrared vidicon camera and a microscope (magnification 50×, NA 0.75). An image of the NFP was grabbed with video-processing software.

The intensity distribution of the NFP was observed when the radial offset of the SMF axis with respect to the GI-MMF one was 0, 12 and 21 μm, and for different passive optical components. The obtained NFP images are shown in Figure 3 for several cases, described in Table 1. A 2 m long GI-MMF, a monolithical 50/50 coupler, a monolithical 90/10 coupler and a 3-port circulator were tested. The couplers and the circulator are optimized for use at 1310 nm. When the 2 m long GI-MMF was tested (case 2), the overall shape of the NFP was very similar to the corresponding NFP at the output of the 1 m GI-MMF (case 1). This is meant to show the limited effect of the FC/PC adapters, present in every case. The NFP in 3, 4 and 5 appears to be nearly as in 1 and 2. In 7 and 8, the intensity distribution of the NFP for 0 μm radial offset at the input is slightly expanded, while for

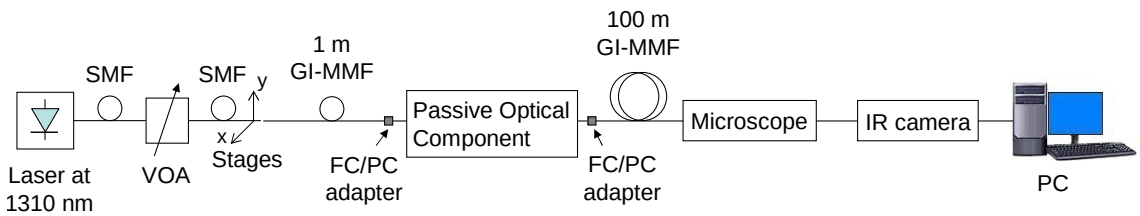

Figure 2: Experimental set-up for the investigation of the effect of passive optical components on the NFP of GI-MMF links.

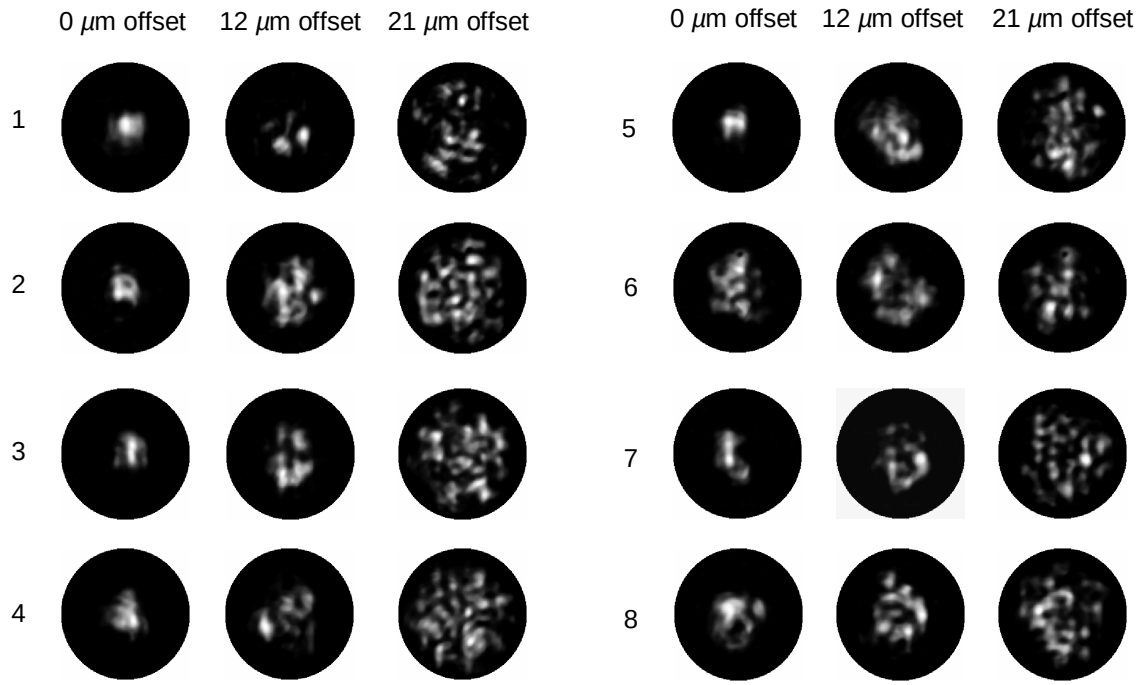

Figure 3: Intensity distribution of the NFP at the output facet of (1) the 1 m long GI-MMF (2-8) the 100 m long GI-MMF used in the set-up of Figure 2. The passive components used in 2-8 are described in Table 1.

the other two offsets it remains similar. Finally, in 6, the shape of the NFP seems to be independent of the offset of the input beam.

In order to use passive optical components in an MMF network with selective excitation, these components should not alter significantly the modal distribution and furthermore their specifications, such as the coupling ratio and the insertion loss, should be maintained. Apart from MGDM, this is of interest for the offset launch technique, which has been proposed to increase the bandwidth of IM-DD, single-input, single-output MMF links [5]. From the components we tested, only the circulator maintained its specifications for all offsets. The couplers did not exhibit a consistent coupling ratio, even though in several cases they did not change the overall shape of NFP.

Table 1: Description of the cases presented in Figure 3

Case	Passive component
2	2 m long 50/125 μm GI-MMF
3	monolithical 50/50 coupler, input 1 to output 1
4	monolithical 50/50 coupler, input 1 to output 2
5	monolithical 90/10 coupler, input 1 to output 1
6	monolithical 90/10 coupler, input 1 to tap 1
7	3-port circulator, port 1 to port 2
8	3-port circulator, port 2 to port 3

From the above investigation, standard MMF passive components do not seem to be suitable for MMF networks with techniques using selective excitation. Laser optimized components would be required [6]. The primary reason is that standard components, although in most cases they do not change dramatically the modal distribution, they do not respond according to their specifications. These specifications are usually given for overfilled launch conditions. This can be achieved with a source of high angular divergence, e.g. an LED, or a mode scrambler at the GI-MMF input [7].

Conclusions

We have presented an experimental investigation of the intensity distribution of the NFP at the output of a GI-MMF link comprising a 1 m long GI-MMF, a GI-MMF passive optical component and a 100 m long GI-MMF. We examined standard components, i.e. not ones designed for laser optimized operation. We have shown that in several cases the overall NFP remains similar with the NFP at the output of the 1 m GI-MMF. In some cases, the NFP is slightly affected when light is launched at the lower order modes at the input of the GI-MMF link. In most cases, though, these passive components did not seem to introduce a dramatic change in the mode distribution. This is very important for MGDM links. However, when MMF couplers were tested, the coupling ratio did not maintain its value according to the specifications. This hampers the use of such components in MMF networks with selective excitation.

Acknowledgment

Funding from the Freeband Impulse programme of the Ministry of Economic Affairs of the Netherlands is gratefully acknowledged.

References

[1] T. Koonen, H. P. A. van den Boom, I. T. Monroy, and G. D. Khoe, “High Capacity Multi-service In-house Networks Using Mode Group Diversity Multiplexing,” *Proc. of OFC 2004*, Los Angeles, CA, Feb. 22-27, paper FG4.

[2] C. P. Tsekrekos, M. de Boer, A. Martinez, F. M. J. Willems, and A. M. J. Koonen, “Demonstration of a Transparent 2-Input 2-Output Mode Group Diversity Multiplexing Link,” *Proc. of ECOC 2006*, Cannes, France, Sep. 24-28, paper We3.P.145.

[3] C. Carlsson, A. Larsson, and A. Alping, “RF Transmission Over Multimode Fibers Using VCSELs-Comparing Standard and High-Bandwidth Multimode Fibers,” *J. Lightwave Technol.*, vol. 22, no. 7, pp. 1694-1700, Jul. 2004.

[4] C. P. Tsekrekos, A. Martinez, F. M. Huijskens, and A. M. J. Koonen, “Design Considerations for a Transparent Mode Group Diversity Multiplexing Link,” accepted for publication in *IEEE Photon. Technol. Lett.*.

[5] L. Raddatz, I. H. White, D. G. Cunningham, and M. C. Nowell, ”An Experimental and Theoretical Study of the Offset Launch Technique for the Enhancement of the Bandwidth of Multimode Fiber Links,” *J. Lightwave Technol.*, vol. 16, no. 3, pp. 324-331, March 1998.

[6] http://www.fiberdyne.com/

[7] *Mode Scrambler Requirements for Overfilled Launching Conditions to Multimode Fibers*, FOTP-54, ANSI/TIA/EIA-455-54-2001, Dec. 2001.

Distributed measurement of parametric oscillations in WDM systems

G. Ravet[(1)], F. Vanholsbeek[(2,3)], P. Emplit[(2)], M. Wuilpart[(1)], P. Mégret[(1)]

[(1)]Faculté Polytechnique de Mons, Electromagnetism and Telecommunications department
31 bld Dolez 7000 Mons, Belgium

[(2)] Université Libre de Bruxelles, Service d'Optique et Acoustique,
CP 194/5, Av. F. D. Roosevelt 50, B-1050, Bruxelles, Belgium

[(3)] The University of Auckland, Department of Physics,
Private Bag 92019, Auckland, New Zealand

We describe the implementation of an optical time domain reflectometry technique to characterize the power evolution of wavelength division multiplexed (WDM) channels in single-mode optical fibers. Thanks to this non-destructive method, we have observed the parametric oscillations due to four-wave mixing and how the power exchanges are distributed along the fiber. Comparison of the agreement between experiment and numerical simulation based on both coupled mode equations and nonlinear Schrödinger equation is also provided. As the period of the oscillation partially depends on the fiber dispersion, our technique is promising for its determination along the fiber length.

Introduction

In today's optical telecommunication system with still higher demand in capacity, wavelength division multiplexing (WDM) has proven to be a very efficient technique to increase the bandwidth. By simply coupling together in a single optical fiber several sources at various wavelengths, it is possible to multiply the capacity by the number of channels. While optical amplification is making progress every day in order to meet the requirement of long haul transmission systems, the power of channels can be higher and higher. The optical fibers can exhibit high optical nonlinearities inside their core due to the high confinement that light undergoes while being guided, leading to interactions between the different wavelengths. Because of the crosstalk between the channels in those high power WDM transmission systems, this has become a limiting impairment.

In a previous paper [1], we have demonstrated the implementation of a new multi-wavelengths optical time domain reflectometric (OTDR) experimental set-up that enables the distributed measurement the nonlinear interactions between several WDM channels inside an optical fiber. The measurement of parametric amplification of a channel was provided and so were numerical simulations generated with the coupled modes model (CMM) giving account for it.

In this report, we show how to enhance the set-up so that we can highlight other physical phenomena such as the parametric oscillations generated by the interplay between the nonlinear Kerr effects and the dispersion of the fiber that were predicted in [2] by the CMM. Indeed, these two features induce the four-wave mixing of the channels that propagate along the fiber through phase-matched power exchanges requiring both good chromatic dispersion and optical power conditions.

Principle

If we couple powerful OTDR-like pulses at different wavelengths in a fiber, those will interact together through various nonlinear effects such as stimulated Raman scattering (SRS) and four-wave mixing (FWM). Thanks to Rayleigh backscattering it is possible to follow the evolution of the power at each wavelength along the fiber. One can show that the power evolution of the channels of a WDM system can be either modeled by [2]:

$$P_{NL} = \varepsilon_0 \chi_K^{(3)} E^3(t) + \varepsilon_0 E(t) \int_{-\infty}^{t} \chi_R^{(3)}(t-t') E^2(t') dt' \tag{1}$$

$$\frac{\partial P_j(z,t)}{\partial z} = -2\gamma_j \sum_{k,l,m=1}^{N} \left[\Re\left(H_{jklm}\right)\cos(\theta) + \Im\left(H_{jklm}\right)\sin(\theta) \right] \sqrt{P_j P_k P_l P_m} - \alpha P_j \tag{2}$$

where P_{NL} is the nonlinear polarization, $\Re$ and $\Im$ denote real and imaginary parts, P_j is the optical power of channel j, $\chi_R^{(3)}$ and $\chi_K^{(3)}$ are respectively the Raman and Kerr susceptibilities, θ is the phase mismatch, α is the linear attenuation coefficient, γ is the nonlinear coefficient and:

$$H_{jklm} = \eta_{jkl} \frac{\varepsilon_{jjjj}}{\varepsilon_{jklm}} \tag{3}$$

$$\eta_{jjk} = \varepsilon_0 \left(3\chi_K^{(3)}/4 + \chi_R^{(3)}(\omega_j - \omega_k)\right)$$
$$\eta_{jkl} = \varepsilon_0 \left(3\chi_K^{(3)}/2 + \chi_R^{(3)}(\omega_k - \omega_l) + \chi_R^{(3)}(\omega_j - \omega_l)\right) \tag{4}$$

$$\theta = -\Delta k.z + \varphi_k + \varphi_l - \varphi_m - \varphi_j$$
$$\Delta k = k_k + k_l - k_m - k_j \tag{5}$$

where k is the wave number, φ_j is the optical phase of channel j, ε_0 is the dielectric constant in a vacuum. In equation (1) and (2), the first term is related to optical Kerr effect and its consequences such as FWM, self- and cross-phase modulation and the second term is related to SRS effects. The other way to model such kind of nonlinear interactions can be made through the generalized nonlinear Schrödinger equation (GNLSE) :

$$\frac{\partial A}{\partial z} + \frac{\alpha}{2} A + \beta_1 \frac{\partial A}{\partial t} + \frac{i\beta_2}{2}\frac{\partial^2 A}{\partial t^2} - \frac{\beta_3}{6}\frac{\partial^3 A}{\partial t^3} = i\gamma \left(1 + \frac{i}{\omega_0}\frac{\partial}{\partial t}\right)\left(A(z,t).\int_{-\infty}^{+\infty} R(t')\left|A(z,t-t')\right|^2 dt' \right) \tag{7}$$

$$g_R(\Delta\omega) = \frac{\omega_0}{cn_0} f_R \chi^{(3)} \operatorname{Im}[\tilde{h}_R(\Delta\omega)] \tag{8}$$

$$h_R(t) = \frac{\tau_1^2 + \tau_2^2}{\tau_1 \tau_2^2} \exp(-t/\tau_2)\sin(t/\tau_1) \tag{9}$$

where A(z,t) is the amplitude the slowly varying envelope of the electric field [5].

Experimental set-up and results

Our experimental set-up, shown on figure 1, was initially derived from the set-up proposed in [3,4]. It based on a commercial OTDR whom output signal is directed to a PIN photodiode through a circulator. The resulting electrical signal is used to drive an acousto-optic modulator (AOM) via a pulse generator. This AOM modulates four external cavity tunable lasers source (TLS) that are coupled together with the use of a 3 dB coupler. Consequently the narrow lasing lines of the four ECL replace the classical OTDR broadband source. Pulses are launched into the fiber through a second circulator and are then continuously Rayleigh backscattered when they propagate down the fiber. The circulators then direct the backscattered signal to the OTDR detector. A tunable

band-pass filter is placed between the two circulators in order to select one wavelength at a time. As an ECL is less powerful than a classical OTDR source, we need to amplify the lasers in order to have enough power to detect the backscattered signal. This amplification is provided using a high power erbium doped fiber amplifier (EDFA) with +23 dBm output power. As we use narrow linewidth lasers, we see the appearance of a coherence noise due to the interferences between components of the pulses arriving at the same time at the OTDR detector [4]. In order to prohibit stimulated Brillouin scattering (SBS) that would limit the propagating power inside the fiber, cross-phase-modulation of the sources is provided thanks to a Raman fiber amplifier (RFA) to broaden their spectrum. This spectral broadening of the sources also reduces the coherence noise.

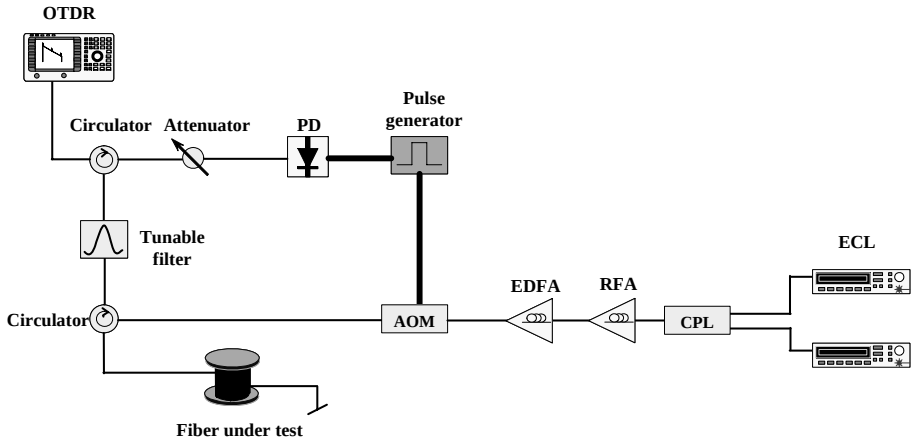

Fig 1 Experimental set-up

We performed measurements with our experimental set-up on a dispersion-shifted fiber (DSF) that has its zero-dispersion wavelength near 1550 nm. Figure 2 shows spectra recorded at the input and at the output of the fiber with an optical spectrum analyzer. We can see that, beside the two lines of the TLS, two others are generated through FWM inside the EDFA. The newly generated wavelengths are nearly equally spaced 1 nm apart. On figure 2, we denote n°1–6, the six channels around 1550 nm from highest to lowest wavelength, n°2–5 being the four wavelengths et the input of the fiber. After propagation inside the fiber, there has been a power exchange between wavelength n°2–5 and n°1 and 6 that were generated from the EDFA ASE noise through FWM.

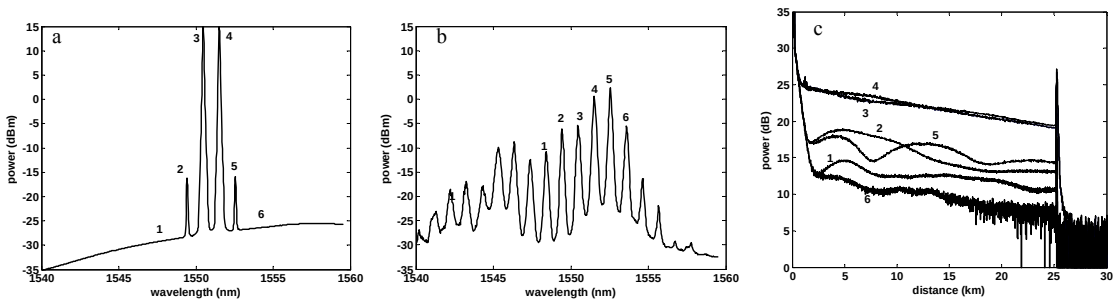

Fig 2 (a) Input spectrum, (b) output spectrum, (c) distribution of the power of channels 1-6

Thanks to our modified OTDR, we could measure the power distribution along the fiber for the different wavelengths. Results are presented on figure 2.
Numerical simulations based on both equations (2) and (7) were performed. Results are presented on figure 4. Comparing to the experiment, one can notice that qualitative behaviors could be reproduced. However, the simulations exhibit some disagreement with our measurement. This can be explained by the fact that we did not take the zero-dispersion wavelength variation along the fiber into account [7].

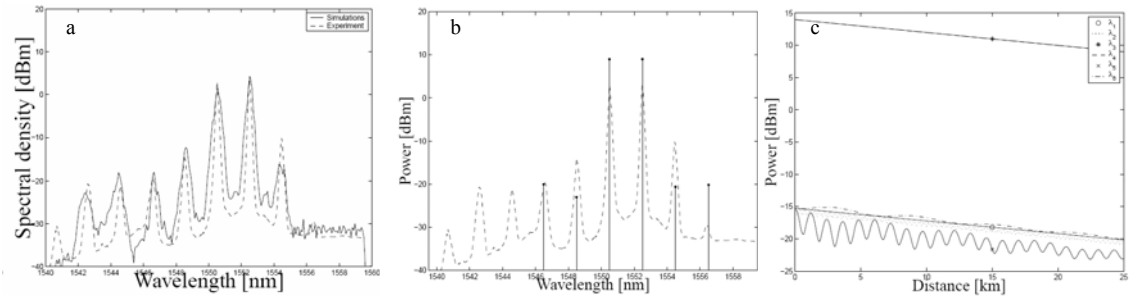

Fig 3 (a) Spectrum produced by simulation of GNLSE, (b) spectrum produced by simulation of the CMM, (c) distribution of the power produced by simulation of the CMM

Conclusions

We have demonstrated a new kind of reflectometry technique for WDM systems characterization. It is based on a multi-wavelength tunable OTDR. This method can be useful to characterize nonlinear effects in WDM systems. We have emphasized the applicability of this method to the study of the interactions between several channels leading to parametric oscillations due to FWM.

Acknowledgements

This research was supported by the Interuniversity Attraction Pole ~IAP V/18 program of the Belgian Science Policy.

References

[1] G. Ravet et al., “Distributed measurement of nonlinear interactions in WDM systems”, in Proceedings of the IEEE/LEOS Benelux Chapter Conference, 2003, pp 245-248.

[2] F. Vanholsbeeck et al., “Dynamics of stimulated Raman scattering and four-wave mixing process in WDM systems”, in Proceedings of the Optical Amplifiers and their Applications Conference, 2001, OTuE18.

[3] G. Ravet et al., “Measurement of the distributed Raman gain spectrum in single-mode optical fibers”, in Proceedings of the IEEE/LEOS Benelux Chapter Conference, 2002, pp 242-245

[4] M. Wuilpart et al., “Distributed measurement of Raman gain spectrum in concatenation of optical fibres with OTDR”, IEE Electronics Letters Vol. 39, 2003, pp88-89.

[5] G. P. Agrawal, Non-linear fiber optics 3rd ed., Academic Press, 2001.

[6] G. Ravet et al., “Suppression of Stimulated Brillouin scattering with a Raman Fiber Amplifier”, in Proceedings of the IEEE/LEOS Benelux Chapter Conference, 2004, pp. 199-202.

[7] M. Karlsson, “Four-Wave Mixing in Fibers with Randomly Varying Zero-Dispersion Wavelength”, J. Opt. Soc. Am. B Vol. 15, pp. 2269-2275, 1998.

Subcarrier Modulated Transmission over Silica and Polymer Multimode Fibres

J. Zeng[1], A. Ng'oma[1], S.C.J. Lee[1], Y. Watanabe[2],

H.P.A. van den Boom[1] and A.M.J. Koonen[1]

[1]COBRA Institute, Eindhoven University of Technology, P.O. Box 513, 5600 MB, Eindhoven,The Netherlands, Email: j.zeng@tue.nl

[2]Lucina Div., Asahi Glass Co., Ltd., 520 Imazato Susono-city, Shizuoka 410-1104, Japan

Multimode fibre (MMF) is a suitable medium for constructing a cost-effective converged access network. Compared with single mode fibre the bandwidth of the baseband of MMF is limited. The transmission capacity of MMF can however be increased due to the existence of passbands in the higher frequency region above the -3dB baseband. Multiple subcarrier modulation may explore efficiently the passband characteristics of MMF. In this paper, we demonstrate the transmission of 1.25 Gb/s binary phase shift keying (BPSK) modulated data over 4.4 km 50µm-core- diameter silica MMF and 100 m 50µm-core-diameter graded-index perfluorinated polymer optical fibre (GI POF) by using a single subcarrier channel centered at 3 GHz. Eye diagram and bit error rate measurement results will be presented. Experiments with different subcarrier frequencies indicate the possibility for Subcarrier Multiplexing (SCM) to transport various broadband signals through a common infrastructure with one laser source.

Introduction

In the final link to the user premises there are various services with widely ranging characteristics and accordingly, dedicated infrastructures to deliver these services, e.g. coaxial cable bus networks for television and radio broadcasting, and twisted copper pair point-to-point links for voice telephony. This situation hampers the introduction of new services and the communication functionalities among these services. Graded index MMF (GIMMF), either silica or polymer, is a preferable alternative to single mode fibre (SMF) for building a common infrastructure to provide different services in a full-service access network.

In a short range MMF-based access network the modal dispersion dominates chromatic dispersion and mode coupling is normally assumed negligible (especially for silica MMF). Under these circumstances, the impulse response of the MMF can be assumed to consist of a number of delta functions which correspond to groups of modes traveling at different speeds. Therefore bandpass lobes at higher frequency region may exist in the transfer function [1]. Fig. 1 shows the frequency response of the silica MMF and POF used for the transmission experiments. By means of subcarrier multiplexing (SCM), these passband regions have the potential to host additional transmission channels for integrating different services into a common MMF link with each service modulated onto a separate carrier frequency.

SCM over MMF demonstration was first reported by Raddatz et al. in 1998 [2] with the transmission of a 200 Mb/s signal on one subcarrier-modulated channel over a 1 km 62.5 µm core silica MMF. Since then this technique has been explored for even higher capacity/speed transmission, together with more spectrally efficient modulation

schemes, i.e. quadrature phase-shift keying (QPSK) [3][4]. However, this technique has not been demonstrated on a POF system yet.
We have presented a system concept of a MMF-based point-to-multipoint access network by using SCM techniques [1][5]. The work in this paper is the first step toward realizing such system using a passband for transmission of 1.25 Gb/s over both silica and polymer MMF link.

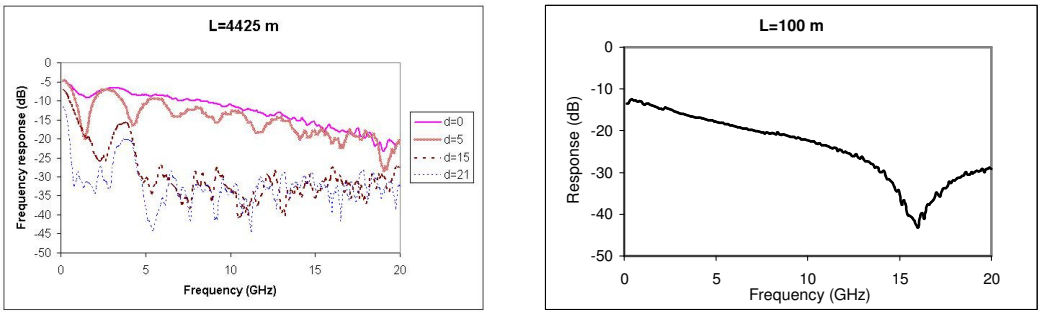

a) b)

Figure 1: Frequency responses of a)the 4.4 km silica MMF obtained with different offset lauching positions d and b)the 100 m 50 µm core diameter graded index perfluorinated POF measured with central lauching. All were with a 1300 nm DFB laser.

Setup for the transmission experiment

The experimental setup is shown in Fig. 2. At the transmitter end, a bit pattern generator (BPG) is used to produce a 1.25 Gb/s, nonreturn-to-zero (NRZ), 2^7-1 pseudo-random binary sequence (PRBS) data stream. Through a double-balanced microwave mixer, this baseband PRBS data is up-converted onto the 3 GHz subcarrier which is generated by an RF signal generator. Either a BPSK or an amplitude shift keying (ASK) signal can be produced at the output of the mixer by setting the BPG properly. The up-converted subcarrier channel signal then directly modulates a 1300 nm Distributed Feedback (DFB) laser. The modulated light is butt-coupled from the single mode laser pigtail into the MMF link. The core diameters of both this 4.4 km silica MMF and 100 m POF are 50 µm. Afterwards the transmitted optical signal is detected by a 50 µm core MMF pigtailed photodiode which has 25 GHz bandwidth. At the receiver end an identical mixer as used for up-conversion at the transmitter was used for demodulation. The RF signal generator is connected to the second mixer through a phase shifter, which is used to correct the phase change after transmission. After the low pass filter (LPF) the down-converted signal was sent to the BER tester and oscilloscope.

Experimental results

Eye diagrams for both the BPSK and ASK schemes were obtained first. Fig. 3 shows the results of the transmission with the 100 m POF. For these eye diagrams, the optical power into the photodiode was kept the same at -10 dBm. Obviously, the eyes for the BPSK scheme are much more open than those of the ASK, both with the back-to-back and after the transmission of 100 m POF. For the 4.4 km silica MMF, we obtained similar eye diagrams.
This observation is in good agreement with the BER measurement. For the transmission over the 4.4 km silica MMF, as shown in Fig. 4a, we can see that a BER lower than 10^{-9} was obtained for each case and there exists a power penalty around 1 dB for both BPSK

and ASK at BER of 10^{-9}. While compared with BPSK, the ASK format resulted in an extra 2.7 dB penalty at the BER of 10^{-9}.

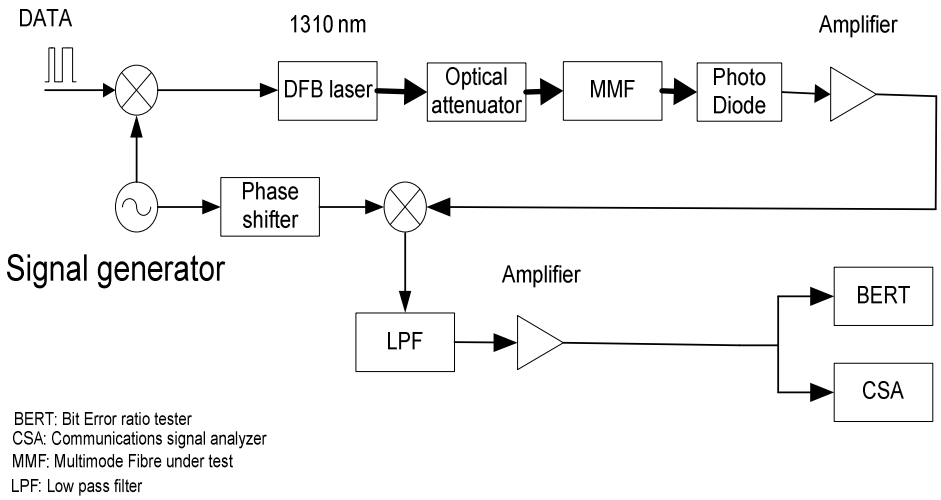

Figure 2: Experimental setup for the one channel 1.25 Gb/s subcarrier modulated transmission over MMF link.

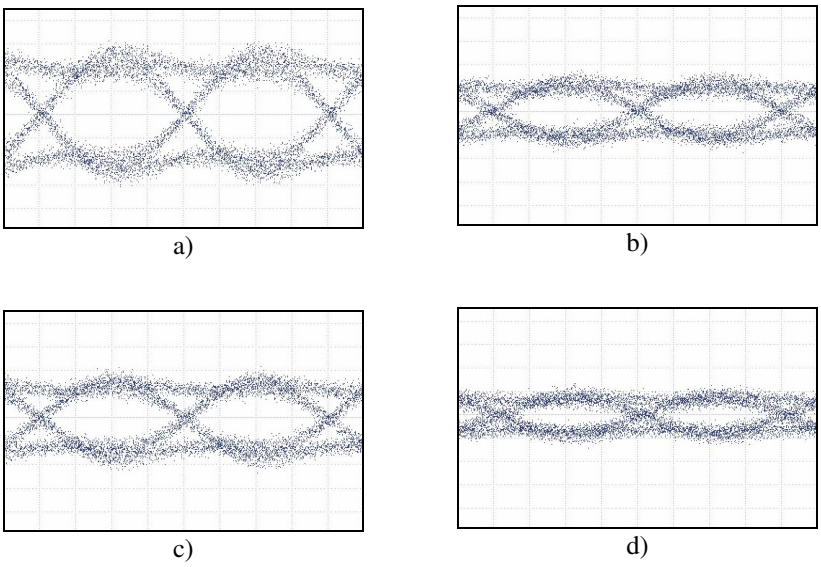

Figure 3: Received eye diagrams of the 1.25 Gb/s subcarrier-modulated channel (200ps/div, 50mV/div). a) back-to-back with BPSK, b) back-to-back with ASK, c) after 100 m 50µm core PF POF with BPSK and d) after 100 m 50µm core PF POF with ASK.

For the 100m POF experiment (results shown in Fig. 4b), the reception is still error-free for the BPSK signal with received power level of -10 dBm, while for the ASK signal, the BER increased to about 10^{-8} after transmission. Compared to the back-to-back scenario, at BER of 10^{-9} there was a power penalty of around 1.5 dB after transmission for both BPSK and ASK. Compared with BPSK, the ASK scheme resulted in an extra 3.4 dB penalty at the BER of 10^{-9}.

Furthermore, for both BPSK and ASK schemes error-free transmission was achieved with either the silica MMF link or the POF link.

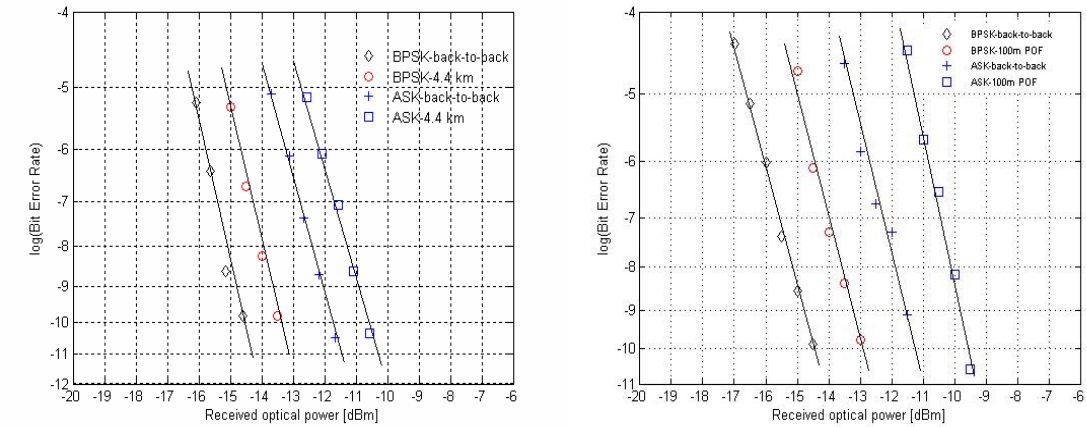

Figure 4. BER comparison between BPSK and ASK subcarrier modulated transmission. a) results of the 4.4 km silica MMF and b) results of the 100 m PF POF.

In addition, experiments with combination of other subcarrier frequencies and bit rates were conducted. The tested subcarrier frequencies were 2.2 GHz, 2.5 GHz and 2.8 GHz for the 4.4 km silica MMF, and were 4.0 GHz, 3.5 GHz and 2.5 GHz for the 100 m POF. The bit rates were 450 Mb/s, 625 Mb/s and 1 Gb/s. Error-free transmission was observed for all these combinations of frequencies and bit rates. This indicates that it is possible to apply SCM techniques onto a silica MMF, or a POF system for delivering different services.

Conclusions

1.25 Gb/s transmission experiments over 4.4 km silica MMF and 100 m 50µm core diameter GIPOF were conducted with the use of subcarrier modulation techniques. Combinations of different subcarrier frequencies and bit rates were tested for transport in a subcarrier channel. Error-free transmissions were achieved for both BPSK and ASK modulation formats. This experiment demonstrates the feasibility of integrating different services into one silica or polymer MMF system by SCM techniques.

Acknowledgement

This work is supported by the Dutch Ministry of Economic Affairs under the Innovation Oriented Research Program (IOP GenCom) "Full service access networks using multimode fibre".

References

[1] A.M.J. Koonen, *et. al.*, "Integration of service in short-range multimode polymer optical fibre networks by exploiting the higher-order fibre passbands", in Proceedings of the International Conference on Plastic Optical fiber 2004, pp.90-97.

[2] L. Raddatz, *et. al.*, "High bandwidth multimode fiber links using subcarrier muitiplexing in vertical-cavity surface-emitting lasers", in Proceedings of the OFC 1998, pp. 358-359.

[3] P. Kourtessis, *et. al.*, 0.6 Tb/s/km multimode fiber feasiility experiments using 40 channel DWDM over quadrature-subcarrier transmission, Electronics Letters, Vol. 38, pp.813-815, 2002.

[4] E.J. Tyler, *et. al.*, "Toward terabit-per-second capacities over multimode fiber links using SCM/WDM techniques", IEEE Journal of lightwave technology, Vol. 21, pp.3237-3243, 2003.

[5] A.M.J. Koonen, *et. al.*, "Recent developments in broad service delivery techniques for short-range networks", in Proceedings of NOC 2004, pp. 86-93.

High Capacity Switched Optical Interconnects for Low-Latency Packet Routing

K.A. Williams[1]

[1]Eindhoven University of Technology
Inter-University Research Institute COBRA on Communication Technology
Department of Electrical Engineering,
P.O. Box 513, 5600 MB Eindhoven, The Netherlands.

High-capacity switched interconnects based on semiconductor optical amplifier switches are studied for low-latency data networking applications. Capacity is scaled through the use of wavelength multiplexed packets to show a sublinear dependence of power penalty on data capacity and sufficient power margin for scaling to 8x8 port interconnection at 100Gb/s aggregate capacity per port. Good agreement with test-bed data is achieved and a route to switched terabit/second capacity optical interconnection circuits is identified.

Introduction

Advances in high performance signal processing have been predominantly driven by improved microprocessor speeds and transistor miniaturization. However the rapid increase in the power consumption within these circuits and the delays in transmission between processors and memory incur formidable bottlenecks. Switched electronic interconnects are approaching their limits in terms of tolerable size, power consumption, crosstalk and thermal dissipation and this is leading to renewed interest in photonic techniques. However power consumption and complexity are paramount in the deployment of high-capacity photonic solutions.

The parallel transmission of multiple wavelengths has been proposed in optical interconnection [1] and exploited more recently in packet-switched optical interconnects [2,3] with a view to facilitating order of magnitude reductions in power consumption and component count. While aggregate data capacity of order 100Gb/s is achieved, there is evidence of signal impairment and little simulation study has been performed to quantify and explore the origins of power penalty or assess the potential limitations in terms of ultimate capacity and connectivity. This simulation study explores data capacity limits and connectivity for broadcast and select switch networks. Scaling in aggregate capacity is quantified in terms of power penalty for varied numbers of wavelength channels. The input power dynamic range is explored to facilitate power map assessment for increased numbers of splitter stages in larger interconnection networks. Cross-comparison is made with test bed data using commercially available components.

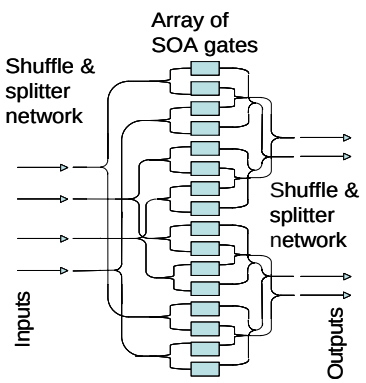

Figure 1: Example schematic of a 4 x 4 broadcast and select switch fabric

Simulation

The interconnect architecture studied is a broadcast and select fabric with cascaded splitters which fan out to an array of semiconductor optical amplifiers. Outputs are subsequently recombined at the output side. Figure 1 shows an example layout for a four input and four output (4x4) switch architecture with shuffle networks on both the input and output side.

Wavelength multiplexed sources are implemented with up to ten wavelength channels, and are modulated with 10Gb/s pseudo random bit streams with a simulation-limited pattern length of 2^7-1 and an extinction ratio of 10dB. The data streams are decorrelated in time, and spaced with a 100GHz channel separation. Multiplexing is performed in the Fourier domain before defining the time resolved input field to the SOA model. The simulated SOA output is subsequently filtered using the amplitude response of a commercial demultiplexer. Signal integrity is assessed initially in terms of Q factor before deriving power penalty.

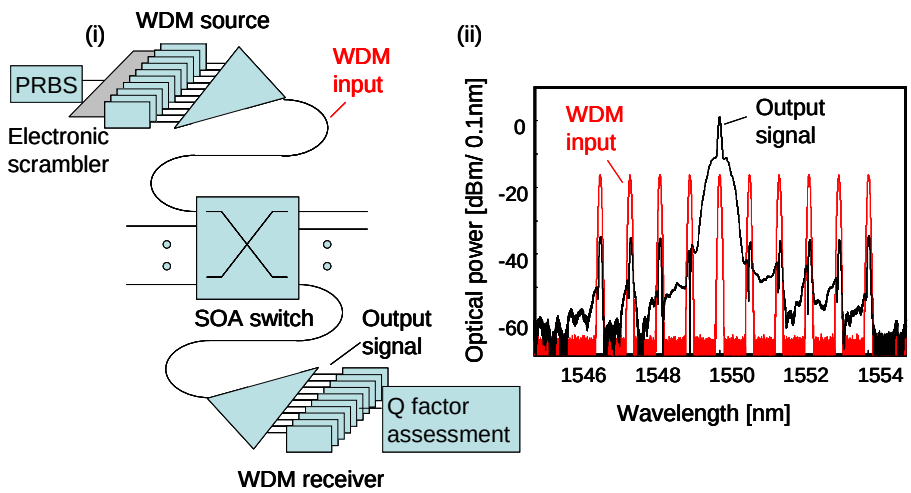

Figure 2: Assessment of the capacity of an SOA based interconnect and inset right, the simulated input spectrum and received spectrum for 100Gb/s aggregate operation

Received data for the central 1550nm wavelength channel is presented in the right inset of figure 2 along with the wavelength multiplexed input. The output time resolved field is assessed with a receiver model [4] using an analysis of the eye diagram, and estimations are made for the Q-factor from the probability distribution functions for the ones and zero level voltages at the receiver. Bit error rate is subsequently estimated as a function of receiver sensitivity. Figure 3 shows the bit error rate performance of the switch for 100 Gb/s aggregate data transmission on ten wavelength channels.

Bit error rate performance is estimated initially for the input signal to the switch and subsequently for the amplified signals outputted from the switch fabric. A reduction in the receiver sensitivity is noted for the case of -25dB into the SOA, and further degradation to a total power penalty of 1dB is observed for the case of -20dBm input power. An increased curvature in the bit error rate dependency on received power is also observed as the error performance deviates away from noise limited sensitivity and power dependent distortion in the amplifier becomes more important. This is also

evident in the eye diagram in the right inset (ii), where a resulting broadening in the one level rail is attributable to insufficiently fast gain dynamics.

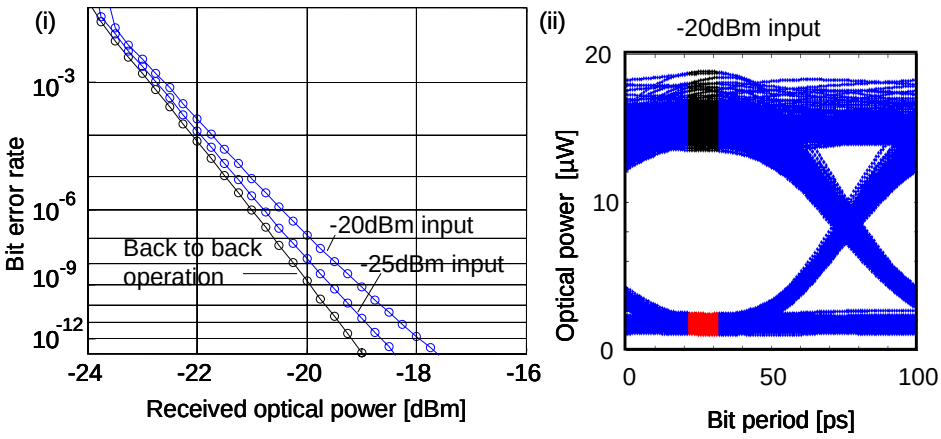

Figure 3: Simulated bit error rate characteristics for the SOA switch element operating at based interconnect and inset right, the simulated input spectrum and received spectrum for 100Gb/s aggregate operation

Capacity scaling

To explore the role of the data capacity on switch performance, the number of wavelength channels and the input power per wavelength channel into the switch is varied and the power penalty is extracted from Q-factor estimation. Figure 4 summarizes the power penalty and gain for the broader range of operating conditions.

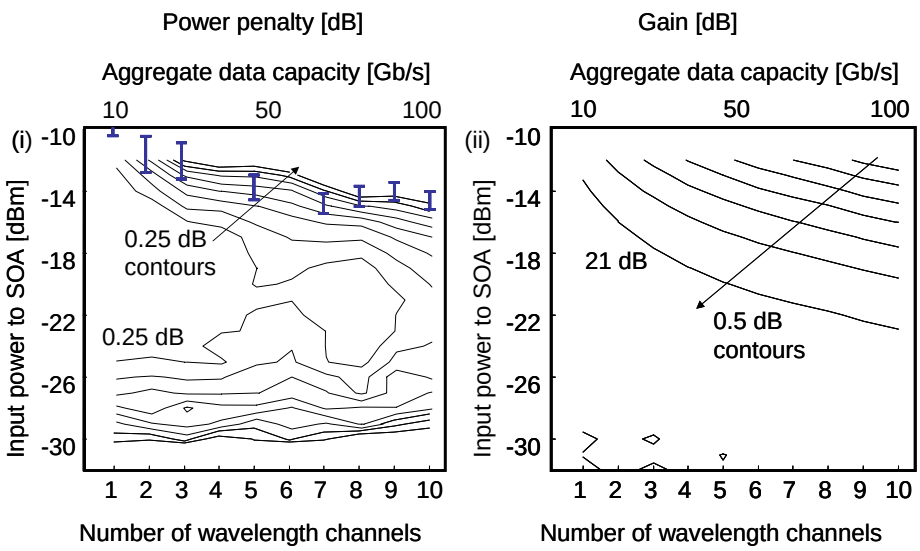

Figure 4: (i) Power penalty at bit error rate 10^{-9} and (ii) gain as a function of the number of wavelength channels and the input power per channel into the SOA switch. Also included in inset (ii) are experimental data points taken from [2] to show the experimentally measured maximum operating input power

The contour plots in figure 4(i) show the power penalty extracted from Q factor assessments as a function of both number of input wavelengths and for a range of input powers into the switch. The power penalty data indicate that power penalties of below 0.25dB are readily achieved for low numbers of wavelength channels, but as the

capacity is increased, the power range for which this is feasible drops. The right inset figure shows the gain for the measured conditions and therefore shows the correlation between power penalty and gain saturation at high operating powers. The degradation in power penalty at low power is attributable to poorer signal to noise ratio. Experimental data taken from [2] are also included in figure 4 to show good correlation with measured test-bed data. The maximum tolerated input power is observed to increase sublinearly with the number of wavelengths, indicating that further scaling in capacity is still feasible.

Connectivity scaling

The interconnection of the switch fabric presented in figure 1 and 2 indicates that the power map is determined primarily by the tolerated splitter and multiplexer losses. Assuming fixed losses of 7dB for the wavelength multiplexer and splices, and splitter losses of 3.4 $\log_2 N_p$ dB for a switch fabric of N_p input/ output pairs allows an estimate to be made for the connectivity scaling for a 100Gb/s/port switch fabric. A margin for fabrication tolerance and variations in system implementation may also be included. The data presented in figure 3 and 4 indicate a maximum input power of -18dBm into the switch, a receiver sensitivity of -20dBm and 18dB SOA gain with 1dB power penalty. The power map for these values indicates a margin of order 1dB even for an 8 x 8 architecture with each input potentially operating at 100Gb/s.

Conclusions

The scaling performance of broadcast and select switch fabrics is studied to identify the limits to performance in terms of capacity and connectivity scaling. The trends are in close agreement with test-bed data, indicating that performance is primarily limited by the design of the SOA switch implemented. Performance enhancement may be anticipated for SOAs which are further optimized for the switch architecture. However 100Gb/s/port is already achieved for an architecture which is scaleable to 8x8 interconnection, indicating a route to Terabit/second aggregate routing for a moderately sized photonic interconnect circuit.

Acknowledgements

The support a Marie Curie Chair mobility award is acknowledged. Prof Ian White at the Cambridge University Engineering Department and Dr Madeleine Glick at Intel Research Cambridge are thanked for stimulating discussions.

References

[1] M.L. Loeb and G.R. Stilwell, "High-speed data transmission on an optical fiber using a Byte-wide WDM system", IEEE Journal of Lightwave Technology, 6, 1306-1311, 1988.

[2] T. Lin, K. A. Williams, R.V. Penty, I. H. White, M. Glick and D. McAuley, "10x10Gb/s packet routing with single stage SOA switch for multi-port interconnects", IEEE Photonics Technology Letters, 18, 691-694, 2006

[3] K.A. Williams, G.F. Roberts, T. Lin, R.V. Penty, I.H. White, M. Glick and D. McAuley, "Monolithic 2x2 optical switch for wavelength multiplexed interconnects", IEEE Journal of Selected Topics in Quantum Electronics, 11, 78-85, 2005

[4] S. Gee, H. Lage, C. Park, K.A. Williams, R.V. Penty, I.H. White, and J. Barnard, "Modelled optimisation and experimental verification of a low dispersion source for long haul 2.488Gb/s systems", Hewlett Packard Journal, 48, 5, 91-106, 1997

Sensitivity Analytic Calculation of Rib Waveguides for Sensing Applications

F. Dell'Olio, V. M. N. Passaro and F. De Leonardis°

Politecnico di Bari, Dipartimento di Elettrotecnica ed Elettronica,
via Edoardo Orabona n. 4, 70125 Bari, Italy.

° Dipartimento di Ingegneria dell'Ambiente e per lo Sviluppo Sostenibile,
viale del Turismo n. 8, 74100 Taranto, Italy

To calculate sensitivity of rib waveguides designed for integrated optical sensors, an analytic approach based on well-known Effective Index Method has been developed. To validate the proposed formalism, sensitivity of different rib guiding structures in CMOS compatible technologies has been calculated by developed formulas and by a numerical procedure based on Finite Element Method. Agreement is demonstrated to be good in all considered cases.

Introduction

Integrated optical devices are increasingly being used in a great number of sensing applications. This interest is due to their immunity to electromagnetic interference, high sensitivity, good compactness and robustness and high compatibility with fiber networks.

In the last years, different kinds of guided-wave optical sensors have been designed and fabricated, adopting different architectures such as those based on directional couplers [1], Mach–Zehnder interferometers [2-3], grating-coupled waveguides [4], and micro-resonators [5]. A lot of these devices have been fabricated using CMOS compatible technological processes.

In integrated optical sensors the shift in measured chemical/physical quantity produces a change of cover medium refractive index. This change affects the propagating mode effective index. Then, optical field distribution in the guiding structure cross section heavily affects the device sensitivity, so one of the most important design task is the waveguide optimization in order to maximize this parameter.

In a number of integrated optical sensors, a rib waveguide having a width w, a total height h_1 and an etch depth h_1-h_2, is adopted, as shown in Fig. 1(a).

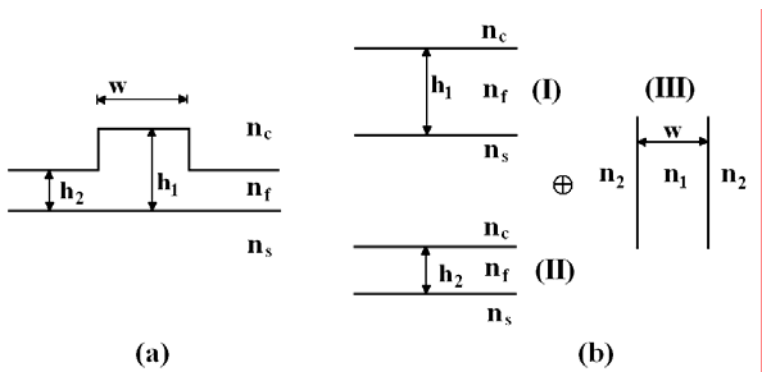

Fig. 1. (a) Rib waveguide structure; (b) Effective-index method applied to the rib waveguide.

Waveguide sensitivity is usually expressed as:

$$S_w = \frac{\partial N}{\partial n_c} \tag{1}$$

where N is the effective index of a mode propagating in the rib waveguide and n_c is the refractive index of cover medium. In [6], a normalized analytic formalism has been introduced to optimize the sensitivity of slab waveguides.
In this paper we propose an analytic procedure to calculate the sensitivity of a rib waveguide, to be included in an integrated optical sensor. Our approach is based on the application of Effective Index Method (EIM) to the guiding structure (see Fig. 1(b)). Results are compared with those derived by a numerical rigorous procedure carried out by full-vectorial Finite Element Method (FEM) [7].

Analytic estimation of sensitivity

Two analytic expressions for rib waveguide sensitivity can be obtained by applying EIM [8] for quasi-TE and quasi-TM polarization, respectively:

$$S_w^{TE} = \frac{1}{N}\frac{Q + k_0 w n_2^3 A_1^{TE}\left(n_1 a_2\sqrt{a_2} + n_2 a_1\sqrt{a_2}\right)}{k_0 w n_2^3\sqrt{a_2}\left(n_2 a_1 + n_1 a_2\right) + 2a_1^2 a_2^2\left(a_1 + a_2\right)} \tag{2}$$

$$S_w^{TM} = \frac{1}{N}\left[A_1^{TM} + \frac{2a_1\left(A_2^{TM} - A_1^{TM}\right)}{\left(a_1 + a_2\right)\left(2 + k_0 w\sqrt{a_2}\right)}\right] \tag{3}$$

and

$$Q = 4a_1 a_2 A_2^{TE} n_1^2 - 4a_1 a_2 A_1^{TE} n_2^2 + 2a_2 A_1^{TE} a_1^2 a_2^2 + 2a_1 A_2^{TE} a_1^2 a_2^2 \tag{4}$$

$$a_1 = n_1^2 - N^2 \tag{5}$$

$$a_2 = N^2 - n_2^2 \tag{6}$$

$$A_i^{TE} = \frac{n_c}{\sqrt{c_i}\left(1 + \frac{c_i}{f_i}\right)\left(h_i k_0 + \frac{1}{\sqrt{c_i}} + \frac{1}{\sqrt{s_i}}\right)} \qquad \text{i=1,2} \tag{7}$$

$$A_i^{TM} = \frac{\left(2c_i + n_c^2\right)\left(\frac{c_i n_f^4 + f_i n_c^4}{f_i n_c^4}\right)^{-1}\frac{1}{n_c^3\sqrt{c_i}}}{\left[\frac{h_i k_0}{n_f^2} + \frac{\left(c_i + f_i\right)n_c^2}{\left(c_i n_f^4 + f_i n_c^4\right)\sqrt{c_i}} + \frac{\left(s_i + f_i\right)n_s^2}{\left(s_i n_f^4 + f_i n_s^4\right)\sqrt{s_i}}\right]} \qquad \text{i=1,2} \tag{8}$$

$$c_i = n_i^2 - n_c^2 \qquad \text{i} = 1,2 \tag{9}$$

$$s_i = n_i^2 - n_s^2 \qquad \text{i} = 1,2 \tag{10}$$

$$f_i = n_f^2 - n_i^2 \qquad \text{i} = 1,2 \tag{11}$$

where k_0 is the vacuum wave-number, n_1 is the effective index of a mode propagating in the slab waveguide with height h_1 (waveguide I in Fig. 1(b)), n_2 is the effective index of a mode propagating in the slab waveguide with height h_2 (waveguide II in Fig. 1(b)), n_c, n_f and n_s are rib waveguide cover, core and substrate refractive indices, respectively.

Analytic method validation

Rib waveguide sensitivity, as defined in (1), can be also numerically estimated by a Finite Element Method (FEM) based approach. This approach is based on rigorous calculation of cover medium refractive index n_c change in a narrow range and the relevant shift of effective index N. To estimate the effective index N, the full-vectorial FEM has been used.

To validate the proposed analytical method, sensitivity of two waveguides adopting silicon oxide (SiO_2) as substrate and silicon oxynitride (SiON) and silicon nitride (Si_3N_4) as guiding film, has been investigated. As cover medium water (whose refractive index can be changed by mixing it with ethanol [3]) has been considered. An operating wavelength $\lambda = 633$ nm has been assumed in both cases.

For quasi-TE and quasi-TM modes, waveguide sensitivity dependence on etch depth ($ED = h_1 - h_2$) has been investigated by proposed analytic formula and by FEM-based numerical approach. Comparisons are sketched in Fig. 2 and Fig. 3.

Waveguide sensitivity calculated by both analytical and numerical approaches exhibits similar dependence as a function of etch depth. Moreover, the moderate difference between results obtained by both methods remains quite constant. For silicon nitride waveguides, we obtain a maximum difference of 15% for quasi-TE and 10% for quasi-TM.

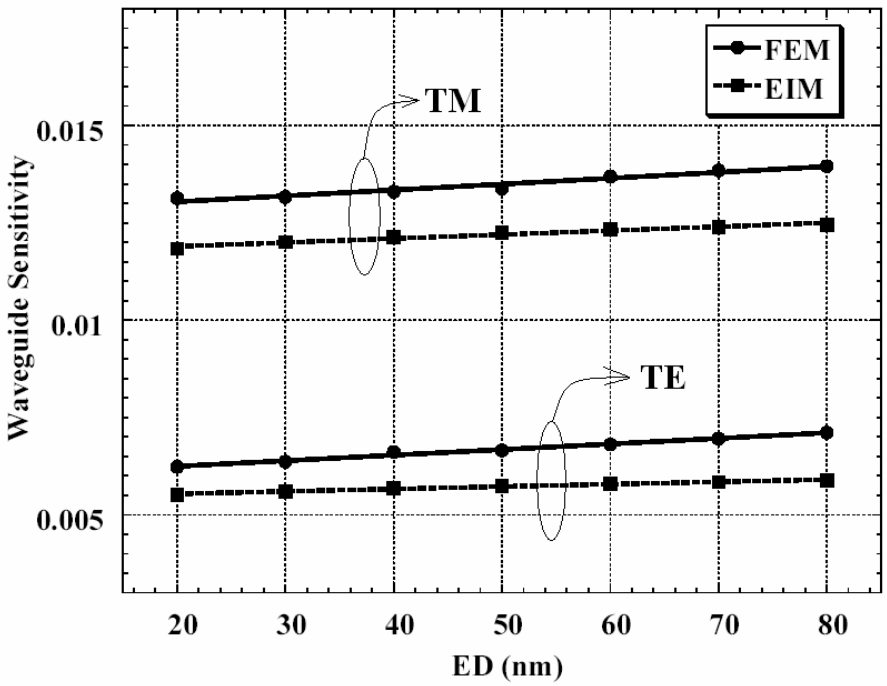

Fig. 2. Silicon nitride waveguide sensitivity dependence on *ED*, estimated by proposed analytic approach and by FEM-based numerical method, for quasi-TE and quasi-TM modes. Other parameters are w= 1000 nm, h_1 = 600 nm, n_s = 1.46, n_f = 2 and n_c = 1.33.

In case of silicon oxynitride waveguides, we have a maximum difference of 11% for quasi-TE and 10% for quasi-TM. It is clear that the behavior with polarization still remains the same for smaller index contrast structures (as in Fig. 3).

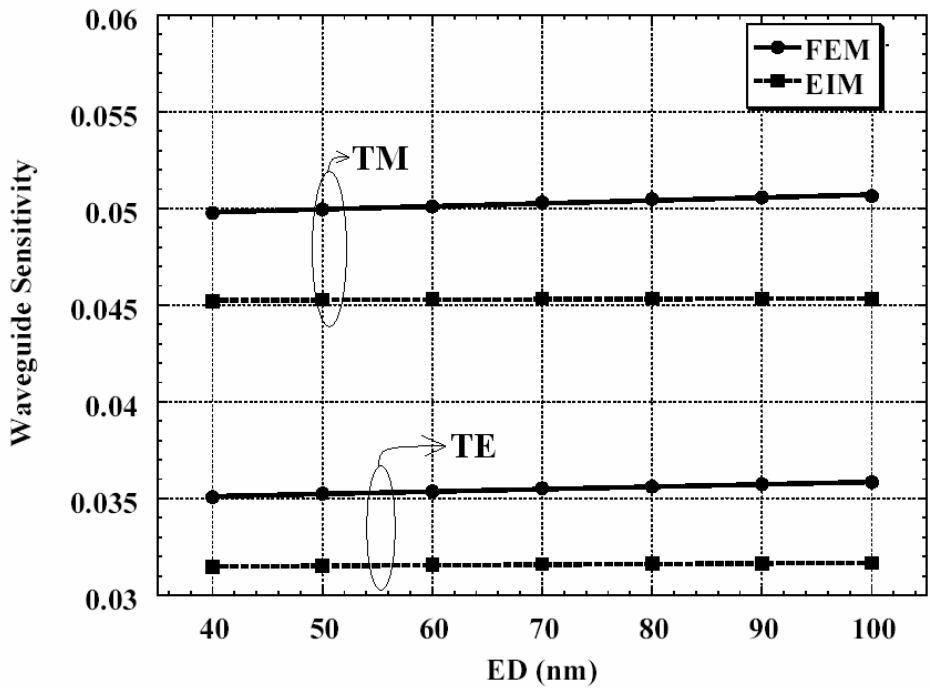

Fig. 3. Silicon oxynitride waveguide sensitivity dependence on *ED*, estimated by proposed analytic approach and by FEM-based numerical method, for quasi-TE and quasi-TM modes. Other parameters are w = 2000 nm, h_1 = 500 nm, n_s = 1.46, n_f = 1.55 and n_c = 1.33.

Conclusion

In this paper an analytic approach based on effective index method is applied for the estimation of sensitivity to cover refractive index change in rib waveguides for sensing applications. The results are in good agreement with those obtained by a rigorous numerical approach based on full-vectorial finite element method.

References

[1] B. J. Luff, R. D. Harris, J. S. Wilkinson, R. Wilson, and D. J. Schiffrin, "Integrated-optical directional coupler biosensor," Opt. Lett., vol. 21, pp. 618–620, 1996.

[2] R. G. Heideman, and P. V. Lambeck, "Remote opto-chemical sensing with extreme sensitivity: design, fabrication and performance of a pigtailed integrated optical phase-modulated Mach–Zehnder interferometer system", Sensors and Actuators B, vol. 61, pp. 100–127, 1999.

[3] F. Brosinger, H. Freimuth, M. Lacher, W. Ehrfeld, E. Gedig, A. Katerkamp, F. Spenser, and K. Camman, "A label-free affinity sensor with compensation of unspecific protein interaction by a highly sensitive integrated optical Mach-Zehnder interferometer on silicon", Sensors and Actuators B, vol. 44, pp. 350–355, 1997.

[4] E. Krioukov, D. J. W. Klunder, A. Driessen, J. Greve, and C. Otto, "Integrated optical microcavities for enhanced evanescent-wave spectroscopy", Opt. Lett., vol. 27, pp. 1504–1506, 2002.

[5] C.-Y. Chao, W. Fung, and L. J. Guo, "Polymer Microring Resonators for Biochemical Sensing Applications", IEEE J. Sel. Top. in Quantum Electron., vol. 12, pp. 134–142, 2006.

[6] O. Parriaux, and G. J. Veldhuis, "Normalized Analysis for Sensitivity Optimization of Integrated Optical Evanescent–Wave Sensors", J. Lightwave Technology, vol. 16, pp. 573–582, 1998.

[7] Comsol Multiphysics by COMSOL ©, ver. 3.2, single license, 2005.

[8] F. Dell'Olio, V.M.N. Passaro, F. De Leonardis, "Sensitivity Analysis of Rib Waveguides for Integrated Optical Sensors," submitted to Optics Express.

Sensitivity of Polarization Maintaining Fibres to Temperature and Strain for Sensing Applications

C. Crunelle, M. Wuilpart, P. Mégret

Service d'Electromagnétisme et de Télécommunications
Faculté Polytechnique de Mons
Boulevard Dolez 31 – B7000 Mons (Belgium)

The sensitivity of a polarization maintaining fibre (PMF) to external effects has been investigated. Using a polarimeter, the evolution of the state of polarization (SOP) on the Poincaré sphere was observed for the light transmitted into a PMF as a function of temperature and longitudinal strain. In theses conditions, the SOP describes a circle on the Poincaré sphere. Temperature and strain have proven to communicate a linear behaviour to the rotation angle described by the SOP on the Poincaré sphere. The authors also discuss the feasibility of a distributed sensor exploiting this phenomenon.

Work position

On today's industry market, sensors are no more important but mandatory. Their applications are sparse: manufacturing monitoring, people and goods security, smart structures, etc. Within all these possible applications, the demand for distributed sensors is continuously increasing.

This paper proposes to analyze the sensitivity of Polarization Maintaining Fibres (PMF) to temperature and strain for sensing applications. The analysis has been performed using a polarimeter. Results are presented and are supported by simulations. An interesting issue exploiting the PMF sensitivity is discussed and concerns the distributed measurement of the temperature or strain via a reflectometry technique.

Polarization in PMF – Theoretical background

In electrodynamics, *polarization* is the property of electromagnetic waves, such as light, that describes the direction of their transverse electric field. More generally, the state of polarization (SOP) is the pattern drawn in the transverse plane by the extremity of the electric field vector as a function of time at a fixed position in space. That pattern represents an ellipse that can degenerate into a circle (circular polarization) or a straight line (linear polarization).

The *birefringence* in optical fibres is defined as the difference in refractive index between a particular pair of orthogonal polarization modes (called the eigenmodes) and results from the presence of asymmetries in the fibre section.

The Polarization Maintaining Fibre (PMF) intentionally creates consistent linear birefringence pattern along its length, prohibiting coupling between the two orthogonal polarization directions.

Two parameters are needed for the representation of linear polarization in optical fibres: δ, the phase retardance between the two orthogonal linear states, and q, the azimuth of the fastest linear polarization mode with respect to *Ox*.

The *beat length* is a length of fibre through which the polarization SOP is recovered whatever the input SOP (i.e. the polarized light undergoes a complete revolution of polarization). PMF exhibit a beat length of about 3 mm.

Polarization effects can be described by a mathematical formalism based on a matrix representation. In the Stokes formalism, a state of polarization is represented by a four-dimensional vector S, called the Stokes vector.

$$S = \begin{pmatrix} S_0 \\ S_1 \\ S_2 \\ S_3 \end{pmatrix} \quad \text{where} \quad \begin{aligned} S_0 &= \textit{Total amount of power} \\ S_1 &= P_0 - P_{\frac{\pi}{2}} \\ S_2 &= P_{\frac{\pi}{4}} - P_{\frac{-\pi}{4}} \\ S_3 &= P_{CR} - P_{CL} \end{aligned}$$

where P_θ denotes the power of the light passed through a linear polarizer set at an angle θ with the x axis. P_{CR} and P_{CL} represent the optical powers of the light after passing though a right- or left-handed circular polarizer, respectively.

It is generally more common to work with the normalized Stokes parameters, where $s_i = S_i / S_0$ (for i=1 ..3). Consequently, the normalized Stokes parameters vary from -1 to +1. They can be assigned to the Cartesian coordinates *xyz*. Then, any given state of polarization, i.e. any given triplet (s_1, s_2, s_3), corresponds to a unique point on or within a sphere: the Poincaré sphere. That sphere is a powerful and elegant graphical tool for describing states of polarization transformation induced by optical systems. It is represented on figure 1. The two poles of the sphere represent left and right-hand circularly polarized light. Points on the equator indicate linear polarizations. All other points on the sphere represent elliptical polarization states

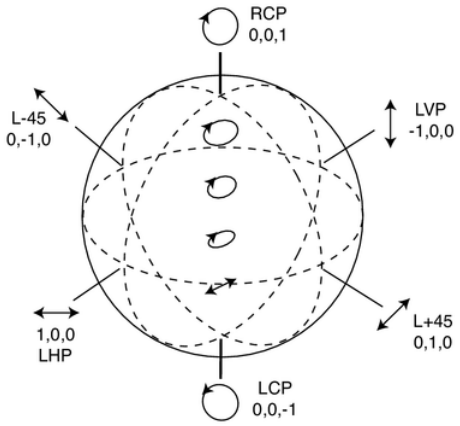

***Figure 1**: Poincaré Sphere. Any given polarization state corresponds to a unique point on the sphere. The two poles of the sphere represent left- and right-hand circularly polarized light (LCP and RCP respectively). Points on the equator indicate linear polarizations (L)*

Experimental results

The experimental setup is presented in figure 2. During operation, the laser source injects a light signal into the PMF via a linear polarizer in order to fix the state of polarization of the light launched into a 2 meters long bow tie fibre. The outgoing signal is then analyzed with the polarimeter. A *polarimeter* is an instrument indicating on the Poincaré sphere the state of polarization of a given light signal.

Depending on the physical effect under study, the PMF is either placed into a temperature controlled oven, or subject to controlled longitudinal strain.

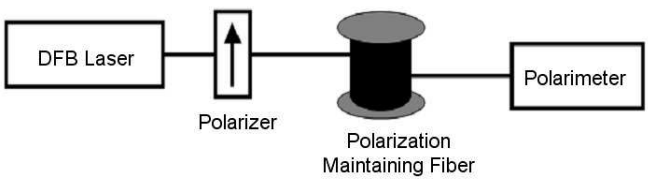

***Figure 2**: The polarimeter permits one to visualize on the Poincaré sphere the evolution of the light signal going out of the PMF.*

The figures 3a and 3b represent two snapshots of the same Poincaré sphere illustrating the SOP evolution of the light outgoing the PMF when the latter is placed into the temperature controlled oven between 0°C and 60°C. At 0°C, the SOP occupies a fixed position on the sphere. When temperature increases till 60°C, the SOP describes a certain number of circles. The rotation angle behaves linearly with temperature and its evolution is represented on figure 5. The behaviour of the PMF has proven to be very sensitive to temperature: 2.73 rad/°C.

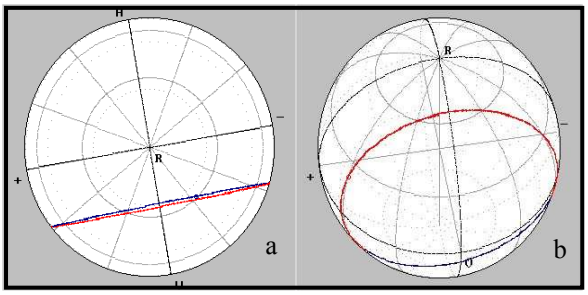

***Figure 3 (a, b)**: Two snapshots of the evolution of the SOP of the light outgoing the PMF subject to a temperature variation between 0°C and 60°C.*

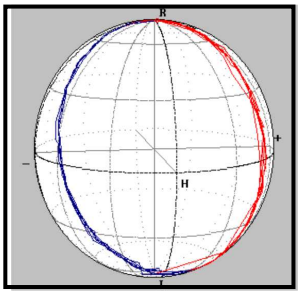

***Figure 4**: Evolution of the SOP of the light outgoing the PMF subject to longitudinal strain*

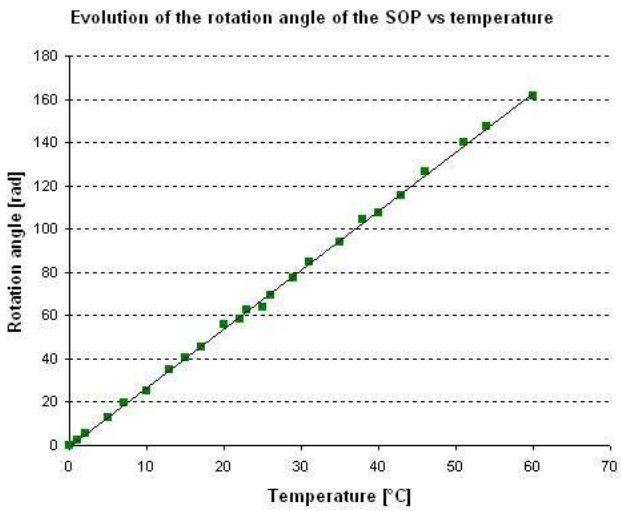

***Figure 5:** Evolution of the rotation angle of the SOP on the Poincaré sphere when the PMF is subject to temperature*

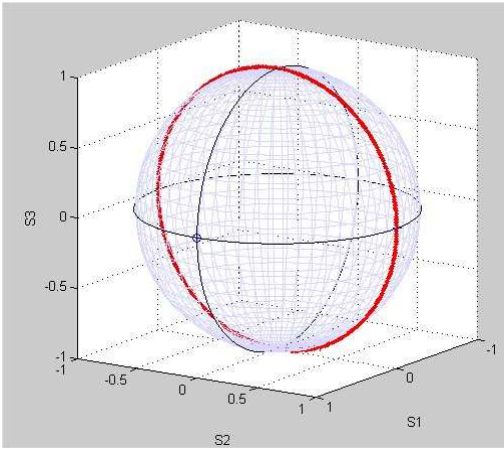

***Figure 6:** Simulation of the evolution of the rotation angle of the SOP on the Poincaré sphere*

Similarly, figure 4 represents the evolution of the SOP of the light signal outgoing the PMF when the latter is subject to a controlled longitudinal strain. Here, again, the SOP clearly describes a circle. But the setup doesn't permit to quantify the strain.

In the Stokes formalism, the transmission matrix of an optical system is represented by a 4x4 matrix of real numbers, the Mueller matrix. It relates the input and output Stokes vectors of the optical device. For a given PMF of length L and whose polarization parameters are δ and q, the corresponding Mueller matrix can be written as [1]:

$$M = \begin{pmatrix} 1 & 0 & 0 & 0 \\ 0 & \cos^2\frac{\delta L}{2} + \sin^2\frac{\delta L}{2}\cos 4q & \sin^2\frac{\delta L}{2}\sin 4q & -2\sin\frac{\delta L}{2}\cos\frac{\delta L}{2}\sin 2q \\ 0 & \sin^2\frac{\delta L}{2}\sin 4q & \cos^2\frac{\delta L}{2} - \sin^2\frac{\delta L}{2}\cos 4q & 2\sin\frac{\delta L}{2}\cos\frac{\delta L}{2}\cos 2q \\ 0 & 2\sin\frac{\delta L}{2}\cos\frac{\delta L}{2}\sin 2q & -2\sin\frac{\delta L}{2}\cos\frac{\delta L}{2}\cos 2q & \cos^2\frac{\delta L}{2} - \sin^2\frac{\delta L}{2} \end{pmatrix}$$

In the case of a PMF whose eigenmodes are properly placed with respect to the coordinates system (q=0), the matrix reduces to:

$$M = \begin{pmatrix} 1 & 0 & 0 & 0 \\ 0 & 1 & 0 & 0 \\ 0 & 0 & \cos\delta L & \sin\delta L \\ 0 & 0 & -\sin\delta L & \cos\delta L \end{pmatrix}$$

With properly chosen input Stokes vector - representing light linearly polarized at $\pi/4$ with respect to *Ox* (s_1=s_3=0, s_2=1), the corresponding output Stokes vector reduces to (s_1=0, s_2= *cos* δL, s_3= -*sin* δL), without loss of generality.
Therefore, the linear variation of the rotation angle of the circle described by the SOP on the Poincaré sphere directly corresponds to a linear variation of the δ parameter. In other words, in PMF, the birefringence is directly proportional to temperature.
Simulations have also been undertaken. The PMF was modelled as a 5 meters long fibre, with a 3 mm beat length and with various q angles. Various input angles were considered. Results were presented on a Poincaré sphere, as the example illustrated on figure 6 where the polarizer at the fibre's input is oriented at $\pi/4$ with respect to the fast axis of the modelled PMF. The linear behaviour of the rotation angle of the SOP was observed when δ was subject to a linear increase.

Conclusion - Discussion

This paper presents the experimental and simulation study of the sensitivity of PMF to external physical effects like temperature and longitudinal strain.
In our experiments, the birefringence in PMF has exhibited a linear behaviour with respect to temperature with a high sensitivity (2.73 rad/°C). A direct measurement of a temperature change is therefore possible through analysis of the SOP. Longitudinal strain measurements did also led the SOP to describe circles, but the current setup doesn't allow us to quantify the applied strain and therefore to draw conclusions.
Distributed sensors usually deal with reflectometry techniques. In the past, we have developed a Polarization OTDR (Optical Time Domain Reflectometer) allowing the distributed measurement of the birefringence along an optical fibre [2]. As small resolution lengths are needed for the PMF study (as the beat length is about 3 mm), OFDR (Optical Frequency Domain Reflectometry) technique should be used instead of OTDR, as it permits to decrease the resolution length to the sub-centimetre scale. A distributed temperature or strain measurement is then possible along a PMF.

Acknowledgments

C.Crunelle is supported by the Fonds pour la Formation à la Recherche dans l'Industrie et dans l'Agriculture. The authors thank the Belgian Scientific Policy through IAP/V18.

References

[1] A.J. Rogers, Y.R. Zhou, V.A. Handerek, "Computational polarization-optical time domain reflectometry for measurement of the spatial distribution of PMD in optical fibres" Proceedings OFMC'97, Teddington, UK, September 1997.

[2] M. Wuilpart, 'Distributed measurement of polarization properties in single-mode optical fibres using a reflectometry technique', Thèse de Doctorat, Faculté Polytechnique de Mons, Septembre 2003.

Time-of-flight Optical Ranging Sensor Based on a Current Assisted Photonic Demodulator

D. Van Nieuwenhove, W. Van der Tempel, R. Grootjans and M. Kuijk

Vrije Universiteit Brussel, Electronics and Informatics Department ETRO (LAMI),
Pleinlaan 2, 1050 Brussel, Belgium

The presented optical ranging sensor utilizes a current assisted photonic demodulator (CAPD) in combination with an integrating circuit to measure time-of-flight. The distance information is obtained by correlating received modulated light with the sent-out signal. Simulations and measurements show that the structure is suitable as a pixel in a real-time 3D-camera setup. A CMOS prototype is presented showing 0.25 A/W infrared photo-responsivity, nearly 100% detector demodulation efficiency and good linearity. Different design aspects and possibilities are discussed and evaluated. With averaging, real time sub-cm resolution is achieved at a modulation speed of 20 MHz and using NIR 860 nm light.

Introduction

Distance measurement devices have long been investigated. The recent revival in continuous time-of-flight (TOF) research has opened the way to fulfilling the aim of building a robust and high resolution real-time 3d-camera. Previous attempts using triangulation, interferometry or structured light projection all suffer downsides found in either speed, robustness, cost, accuracy or dynamic range. Research of the last years [1], [3], [4] has shown that time-of-flight might hold the keys to solve above problems emphasizing it as a 3D-camera-of-the-future candidate and an interesting research subject. In this paper a sensor is described that can be used as a pixel for such a camera having the promising capacity of improving above mentioned shortcomings. The basis of the pixel is a very efficient in-substrate demodulator, called current assisted photonic demodulator (CAPD). All displayed measurements in this paper where conducted using NIR light (λ = 860nm), since it is invisible and detectable in normal silicon making it the ideal type of light for the application.

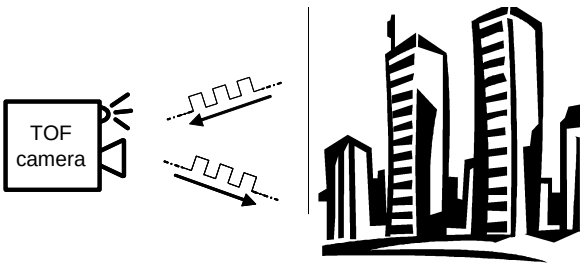

Figure 1 Illustration of the time-of-flight principle

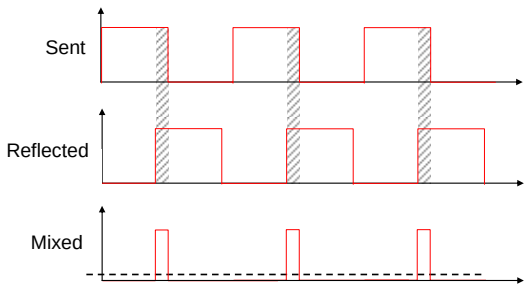

Figure 2 Phase measurements by averaging mixed reflected and sent-out waveforms

Time-of-flight principle

The continuous time-of-flight principle is illustrated in fig. 1: the camera sends out modulated light and measures its reflections on the scene. Within each pixel this reflected signal is mixed with the sent-out signal to obtain the phase shift, as shown in fig. 2. This phase shift can easily be translated in the distance between the

pixels and the different points in the scene. This simple technique has many advantages:

- capable of delivering complete images at once, no scanning is needed
- real-time images possible
- robust, without moving components
- high accuracy : the technique is based on the lock-in principle
- scalable accuracy : several parameters influence the signal-to-noise ratio, such as modulated light intensity, integration interval and modulation frequency.
- high dynamic range
- no expensive materials are used

Few drawbacks/constrains exist, most important are the degradation of accuracy proportionate to background light and the limited distance range due to the periodicity of the modulation signal.

Principle of a CAPD

A current assisted photonic demodulator utilizes a guiding current to accelerate electrons towards detecting junctions. Whilst in standard photo detection diffusion is the main transport mechanism, a CAPD uses a current induced guiding drift field. As shown in fig. 3 the photo-generated electron hole pairs are separated: the hole becomes part of the flowing majority current and starts moving towards the p+ region with the lowest voltage, the electron is accelerated in the opposite direction and will, due to the built-in potential barrier of the p^-substrate/p^+ junction, choose to enter the detector node. Mixing is achieved by alternating the current so that correlated amounts of the light-induced carriers arrive at the different detecting junctions [2]. The field amplitude and extension in the substrate are the key factors determining the demodulator qualities. In a CAPD the drift field is spread very well over the substrate resulting in high demodulation contrast and high speed. Further the amplitude of the field is proportionate to the applied substrate voltage and thus scalable.

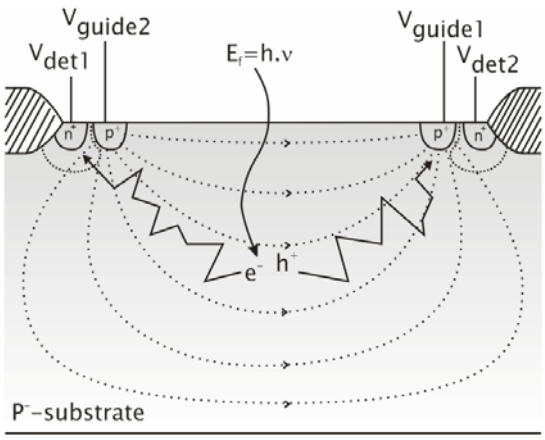

Figure 3 Current Assisted Photonic Demodulator (CAPD), the configurable current determines towards which detecting junction the minority carriers are driven

CMOS Implementation

In fig. 4 layouts are shown of possible 0.35µm CMOS CAPD implementations. Two possible configurations are shown: a centralized and a linear. The centralized setup has a minimal detecting junction size, and thus a

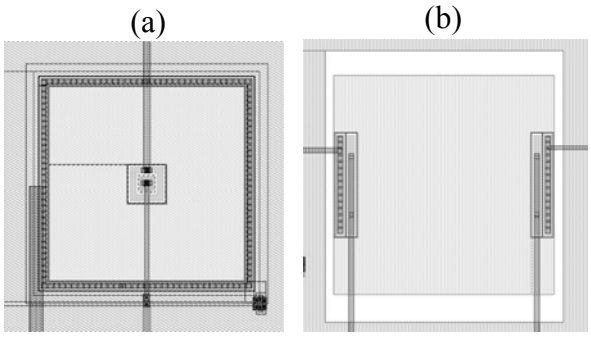

Figure 4 Layout of a centralized (a) and linear (b) shaped CAPD

minimal capacitance. Drawback is the high current density in the center, resulting in a higher resistance and, due to this non-uniform conductivity, the applied drift field will not be spread equally over the sensitive area, lowering the speed of the device. The linear implementation is an alternative for this problem: no current concentration occurs, so that the applied field is evenly distributed, but at the cost of a larger detector node. Choosing between both structures has to be done having this speed to detector capacitance trade-off in mind.

Measurements

Figure 5 shows measurements performed on a centralized 30x50 μm^2 and a linear 50x50 μm^2 prototype. It can be seen that both perform very well in DC having nearly 100% demodulation contrast from very low guiding field voltages on. The centralized CAPD slightly outperforms the sensitivity of the linear. This is probably due to the presence of surrounding nwells, placed there to isolate the pixel and prevent it to be distorted by

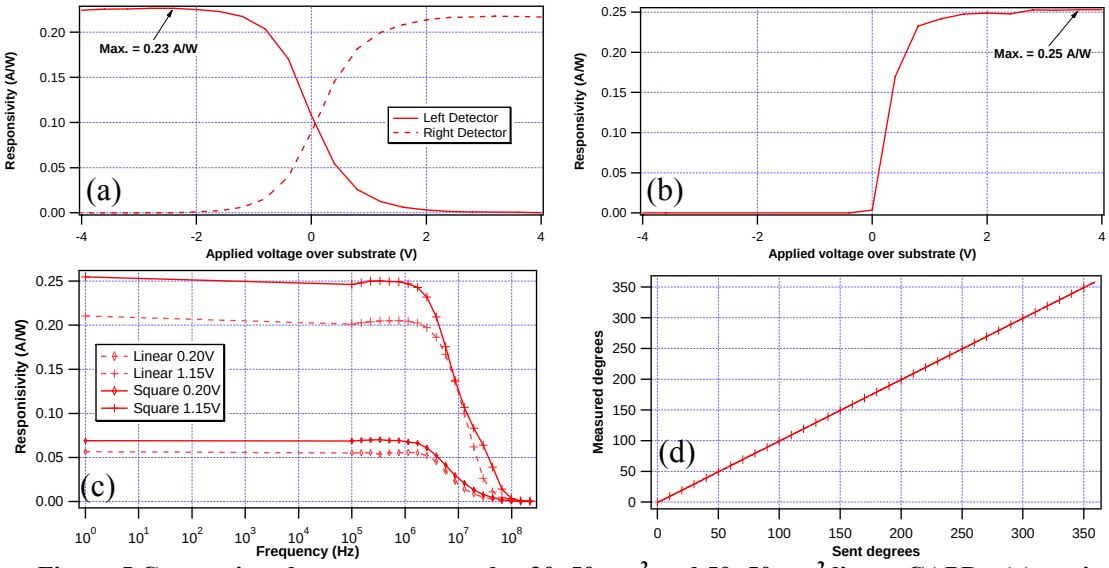

Figure 5 Comparison between rectangular 30x50 μm^2 and 50x50 μm^2 linear CAPD: (a) static measurements of linear CAPD (b) static measurements of rectangular CAPD (c) dynamic measurements (d) linearity measurements performed at a modulation frequency of 1MHz

illumination coming from outside of the pixel. In the linear setup electrons are guided closer to these nwells causing some of the carriers to be lost. In the centralized setup all used carriers are guided to the center. In fig. 5c dynamic results of both CAPD's are shown for two different substrate voltages. It can be seen that the increase in guiding field strength has a double effect: a sensitivity and a bandwidth improving effect. Again there is a difference in sensitivity between both CAPD's as a consequence of the surrounding nwells. At 0.2V substrate voltage bandwidths are respectively 4.5 MHz for the centralized and 4.9 MHz for the linear CAPD, at 1.15V bandwidth is 5.6 MHz and 7.6 MHz. Figure 5d shows the measured to the sent-out phase for a shift of one period at 1 MHz,

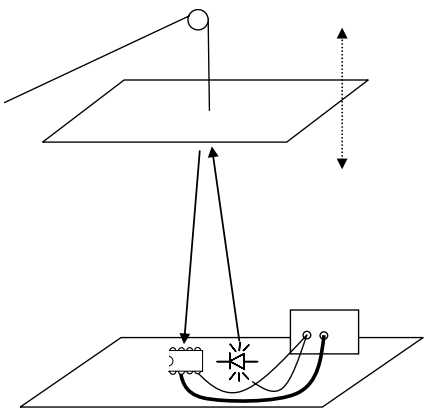

Figure 6 Measurement setup

illustrating the linearity properties of the device.
In fig. 6 our lab setup to perform a first set of distance measurements is shown. A plate, adjustable in height, was mounted above a CAPD pixel, consisting of a CAPD and a simple integrating circuit, and a modulated light source, built using 16 LED's and generating a total light output of 0.5 W. We used 20 MHz as modulation frequency. The pixel was calibrated at 70 cm. A total integration interval of 8 ms was used in combination with an averaging step over 25 samples, resulting in a refresh rate of 5 Hz. Figure 7 shows measurement results of a distance sweep from 40 to 100 cm. At the shortest distance sub-cm accuracy is achieved. The rather large systematic error is due to the limited effort done in these proof-of-principle measurements to reduce the non-linear effects beyond the -3dB frequency of the demodulator. Further changes, like replacing the used square with sinusoidal modulation and improving the optical side of the setup, should be completed to enhance these results.

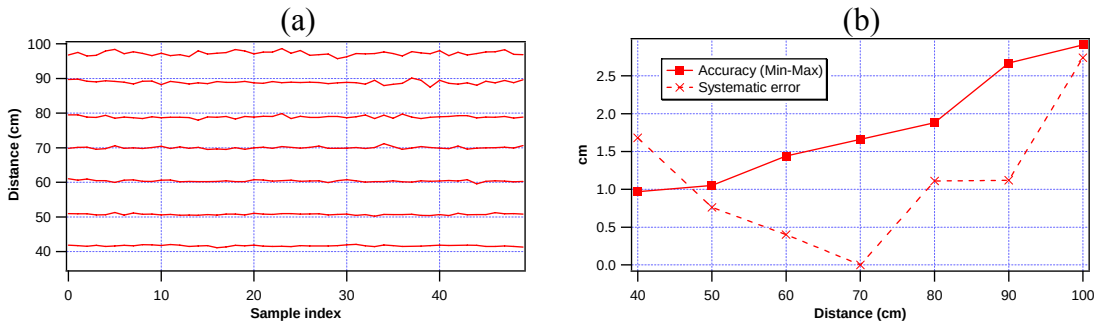

Figure 7 Distance measurements showing values (a) and accuracy/error information (b)

Conclusion

We have illustrated the efficacy of an optical ranging sensor based on the time-of-flight principle. Measurements show that the used current assisted photonic demodulator has good properties and forms an efficient pixel opening perspectives for sub-cm resolution real time 3D-cameras. Expansion of this proof-of-principle to more accurate results and eventually matrices is needed to further develop this technology.

Acknowledgment

The research activities described in this paper were funded by the Fund for Scientific Research-Flanders (FWO-Flanders).

References

[1] P. Gulden, D. Becker, M. Vossiek, "Novel optical distance sensor based on MSM technology," IEEE Sensors Journal, vol. 4, pp. 612-618, October 2004

[2] D. Van Nieuwenhove, W. van der Tempel, and M. Kuijk "Novel standard CMOS detector using majority current for guiding photo-generated electrons towards detecting junctions", in proc. 10th Annu. Symp. of the IEEE/LEOS Benelux Chapter, Mons, 2005, pp. 229-232

[3] R. Schwarte, " Dynamic 3D Vision", in Proceedings of the Conf. IEEE EDMO, 2001, pp. 241-248

[4] R. Lange and P. Seitz, "Solid-State Time-Of-Flight Range Camera", IEEE Journal of Quantum Electronics, vol. 37, NO. 3, March 2001.

Optical Biosensor based on Silicon-on-Insulator Microring Resonators for Specific Protein Binding Detection

K. De Vos, I. Bartolozzi*, P. Bienstman, R. Baets, E. Schacht*

Ghent University - IMEC, Department of Information Technology Sint-Pietersnieuwstraat 41, 9000 Gent, Belgium

*Ghent University, Polymer Chemistry and Biomaterials Research Group, Krijgslaan 281 (S4 Bis), 9000 Gent, Belgium

Optical label-free biosensors to detect biomolecular interaction attempt to overcome the drawbacks of commercialized systems relying on the detection of labeled biomolecules. We propose an integrated Silicon-on-Insulator optical biosensor, fabricated with Deep UV-lithography, based on resonant microring cavities. The shift of resonance wavelength that occurs when the dielectric surroundings of a cavity is changed, can be used for sensing. An SOI optical microring resonator with a radius of 5 micron is capable of detecting bulk refractive index changes of 10^{-4}. *We use the avidin/biotin high affinity couple to demonstrate good repeatability and the detection of avidin concentrations down to 50 ng/ml.*

Introduction

Sensing of biomolecules is gaining interest due to its applications in many areas such as bacterial and virus detection, medical diagnostics, drug development, food and evironmental control. Most commercialized biosensors rely on detection of labeled molecules. The intermediate labeling step however complicates the detection process and decreases reliability so there is a growing need for label-free detection methods, enabling the monitoring of the dynamics of molecular reactions and quantitative concentration measurements. Different approaches for integrated optical biosensors based on Surface Plasmon Resonances (SPR) [1], interferometers [2] and resonant cavities [3][4] are previously reported. Often these components still require relatively large amounts of analyte and are not suited for cheap high throughput fabrication. The integrated Silicon-on-Insulator (SOI) optical biosensor we propose combines fast sample preparation, real time and quantitative measurements and reduced analyte quantities with a high throughput fabrication method using standard microelectronics processing, in particular deep UV lithography. SOI offers a high refractive index contrast suitable for the fabrication of optical cavities of very high quality. The shift of resonance wavelength that occurs when the surroundings of such a cavity is changed, can be used for sensing. Integrated in a microfluidic setup thousands of cavities can be lined up in arrays for multiparameter sensing within a few square millimeters.

Direct sensing of proteins is based on affinity between protein couples; a protein (ligand) fixed to the sensor's surface forms a complex with a complementary protein (analyte). In this work we used the avidin/biotin protein couple which gives a very specific and stable interaction. Anchoring biotin to the sensor requires a chemical modification of the semiconductor surface which has to be chemically and morphologically homogeneous, and has to prevent from non-specific protein adsorption.

1 Silicon-on-Insulator microrings for sensing purposes: design and fabrication

When light with a wavelength $\lambda = \frac{n_{eff}L}{m}$, $m = 1, 2, ...$ and L being the circumference, couples to a microring resonator whispering gallery modes occur. This results in a sharp dip in the transmission. A change in the refractive index of the ring's environment shifts the resonance spectrum, which can be monitored by scanning the wavelength and by measuring the intensity profile at one well chosen wavelength. For both techniques the sensitivity increases with increasing quality factors Q of the resonator. The Q-factor expresses the peak's width: $Q = \frac{\delta\lambda_{3dB}}{\lambda_{resonance}}$. Q-factors over 20,000 are easily achievable with our fabrication process and optimized design. The pass and drop spectra of a $5\mu m$ racetrack resonator are shown in Fig. 1. We observe a 3dB peak width of 7.5pm.

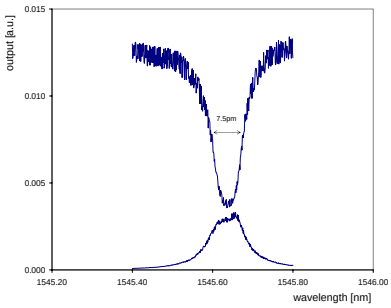

Figure 1: Measured pass and drop spectrum.

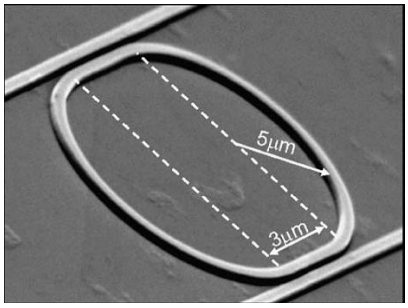

Figure 2: SEM picture of the device.

Deep ultraviolet (UV) lithography, the technology used for advanced complementary metal-oxide-semiconductor (CMOS) fabrication offers both the required resolution and the throughput needed for commercial applications. This was previously reported in [5]. A SEM picture of the device is shown in Fig. 2.

2 Surface functionalization

Silanization of the surface is used to provide a suitable biointerface between the transducer element and the biological medium. In the present work we used the avidin/biotin system which has a high affinity constant ($K_a = 10^{15} M^{-1}$) and therefore has a stable and specific interaction, as a model of biomolecular interaction. Biotin was immobilized on the aminofunctionalized silicon surface and the biotinylated surface was exposed to an avidin solution to allow the complex formation. X-ray Photoelectron Spectroscopy (XPS) confirmed the success of both the aminosilanization and the biotin anchoring step. Contact angle and ellipsometry suggested the formation of multilayers where the amino functional groups might be partially buried. However, the modification was effective to provide a biotinylated surface which was used in binding experiments with avidin.

3 Measurements

A schematic drawing of the proof-of-principle measurement setup is given in Fig.3. Optical

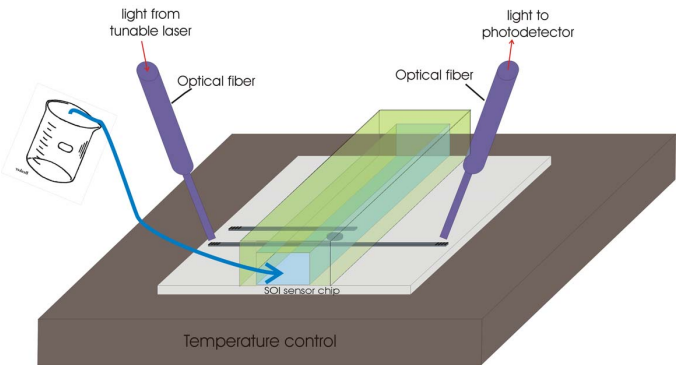

Figure 3: Measurement setup.

fibers are vertically coupled to the in- and output integrated waveguides through grating couplers [5]. This allows for easy coupling with high alignment tolerances.

3.1 Bulk refractive index sensing

Liquids with varying refractive indices (aqueous solutions of NaCl) are flown across the ring resonator in order to characterize the sensor for bulk refractive index sensitivity. Fig.4a shows a linear shift of the resonance wavelength with increasing refractive index units (RIU) of 70nm/RIU. A minimal detectable wavelength shift of 7.5pm, one tenth of the peak broadness, corresponds to a minimal detectable refractive index shift of $1 * 10^{-4} RIU$.

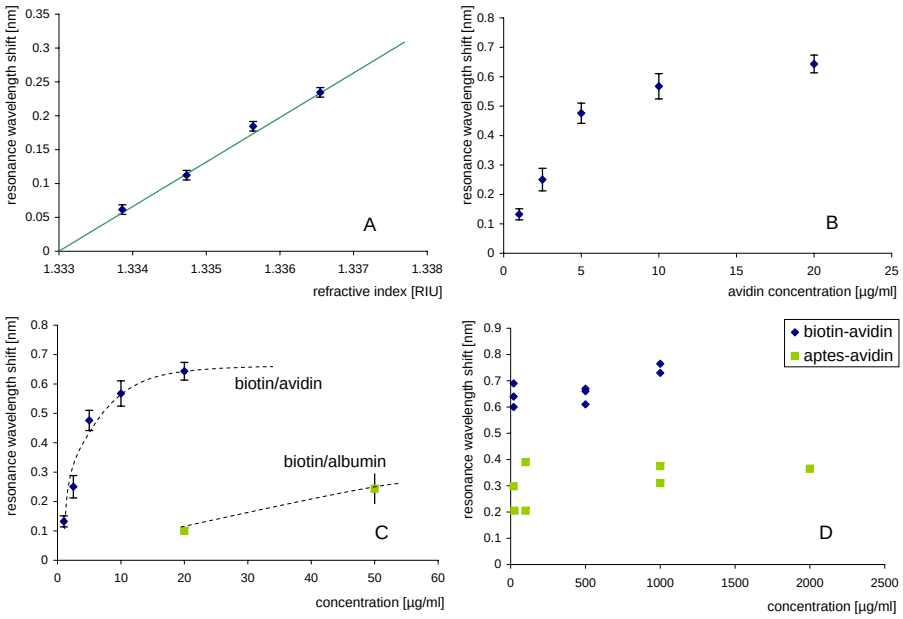

Figure 4: a) Resonance wavelength shift versus bulk refractive index change. b) Quantitative avidin/biotin detection with an SOI microring cavity. c) Nonspecific binding test biotin/albumin. d) Nonspecific binding test aptes/avidin.

3.2 Surface sensing of biotin/avidin coupling

We compare the resonance wavelength of the cavity immersed in Phosphorate Buffer Solution (PBS), before and after being in contact with avidin solution. The evolution of the wavelength shift for different avidin concentrations is shown in Fig.4b. For high avidin concentrations all binding sites are occupied and the curve saturates. For low avidin concentrations the wavelength shift corresponds to the concentration. The estimated lowest detectable concentration, for a minimal detectable wavelength shift of 7.5pm, is 50ng/ml. Furthermore two nonspecific binding tests are accomplished (Fig.4c and d). Firstly Bovine Serum Albumin (BSA), a protein with similar molecular weight to avidin but with low affinity to biotin, is brought into contact with the biotin layer. Secondly avidin is brought into contact with the aminosilanized surface without biotin. Both measurements resulted in a smaller wavelength shift due to a decreased molecular interaction, proving the specificity of the sensor.

4 Conclusions and Perspectives

We have demonstrated a highly miniaturized optical label-free biosensor based on a Silicon-on-Insulator microring cavity with high Q-factors and fabricated with Deep UV lithography, a high-throughput fabrication method. Measurements reveal proper operation of the device, being able to detect in a specific way avidin concentrations down to 50ng/ml, which compares favorably with commercial biosensors. Further improvements will be made to increase the sensitivity, by increasing the cavity's Q-factor and reduce its size. The microrings are suitable for lining up in arrays to perform multiarray molecular detection.

Acknowledgments

The author thanks the Flemish Institute for the Promotion of Innovation through Science and Technology (IWT) for a specialization grant.

References

[1] Čtyrocký J et al., "Theory and Modelling of Optical Waveguide Sensors Utilising Surface Plasmon Resonance", *Sens. Actuators B*, vol. 54, pp.66, 1999.

[2] Hradetzky D et al., "Interferometric label-free biomolecular detection system", *J. Opt. A: Pure Appl. Opt.*, vol. 8, pp. S360-S364, 2006.

[3] Boyd R.W., Heebner J.E., "Sensitive disk resonator photonic biosensor"', *Applied Optics*, vol. 40, pp. 5742, 2001.

[4] Yalçin A et al., "Optical Sensing of Biomolecules Using Microring Resonators", *IEEE J. Sel. Topics Quantum Electron.*, vol. 12, pp. 148, 2006.

[5] Bogaerts W et al., "Nanophotonic Waveguides in Silicon-on-Insulator Fabricated With CMOS Technology", *J. Lightwave Technology*, vol. 23, pp. 401, 2005.

Improved Modulation Techniques for Time-Of-Flight Ranging Cameras using Pseudo Random Binary Sequences

R. Grootjans; W. van der Tempel; D. Van Nieuwenhove; C. de Tandt; M. Kuijk

Vrije Universiteit Brussel, Electronics and Informatics Department ETRO (LAMI),
Pleinlaan 2, 1050 Brussel, Belgium

A Current Assisted Photonic Demodulator (CAPD) correlates received modulated light with the original modulating signal and can be used as pixel in real-time 3D cameras. We show how the use of well-chosen Pseudo-Random Binary Sequences (PRBS) as modulating signals allows multiple 3D cameras to operate in the same area by reducing crosstalk and increases the maximal unambiguously measurable distance. Simulated results are compared to measurements performed on a CAPD-based circuit developed in our lab. The influence of parameters such as the length and base frequency of the PRBS on the measurements is also discussed.

Introduction

Ever since the first working model of the radar was demonstrated in 1936, scientists have continued research on distance measuring devices. Most efforts have been focused on improving performance of devices that measure the distance to a single point. Several applications, however, require complete 3D information analogous to human vision about their surroundings. Many attempts to provide such 3D information, including stereovision, depth-from-focus and structured light, fall short in providing both high framerates, high accuracy, high dynamic range and a low cost implementation. Recent breakthroughs in research on CAPD structures [1] predict a promising future for Time-Of-Flight based 3D cameras, which could outperform other approaches in all areas mentioned above.

Principle of operation

Three-dimensional information about the environment is gathered by means of the Time-Of-Flight principle, which is illustrated by Figure 1. A continuously modulated near-infrared (NIR) light wave is sent out by the camera, which travels towards the scene and is reflected. These reflections are focused on the newly developed camera chip, where they are correlated with the original waves. From these correlation values, the total traveling time of the light wave can be extracted. Because the NIR light is transmitted towards the whole scene, every pixel of the camera continually receives reflections. This allows all pixels to perform their correlations concurrently, making the 3D camera useful for real-time applications.

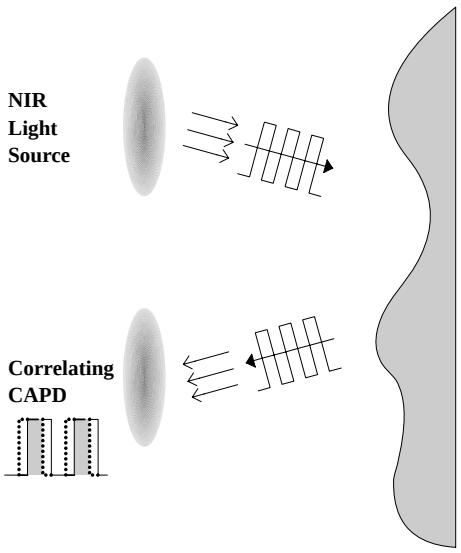

Figure 1: 3D camera based on the Time-Of-Flight principle

Correlation models of modulating signals

Correlation between the original modulating signal and the reflected modulated signal is performed by the CAPD. As the distance to the object increases, the phase shift between the original modulating and the received signal increases, and the correlation between them decreases. The trajectory of this correlation value for varying phase shifts follows the autocorrelation function of the modulating signal.

A straightforward approach would be to use a square wave as modulating signal. Figure 2 displays the theoretic autocorrelation function of a square wave, compared to measurements performed on one of our CAPD enabled devices. The result was obtained by artificially shifting the phase of the reflected signal, and displays the normalized correlation between the original modulation signal and the reflected modulated signal, with B indicating the amount of phase shift corresponding to 1 bit. In order to obtain the measurement below, a 500 kHz square wave was used as modulating signal.

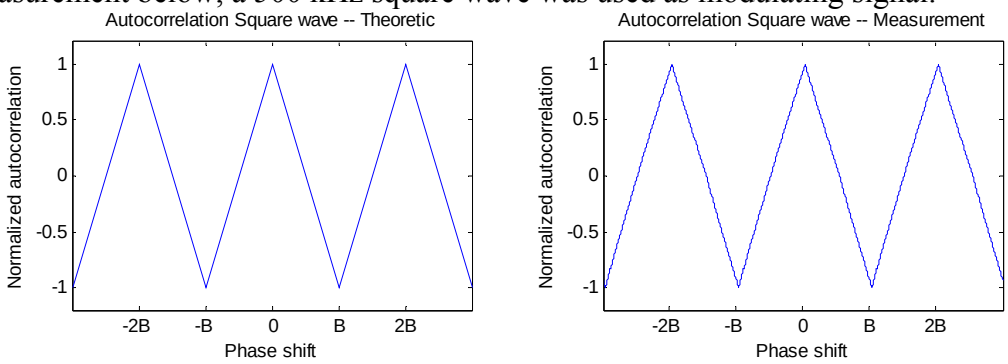

Figure 2: Theoretic and measured autocorrelation function of a square wave

From any normalized value δ found within the [0, B] region, one can easily find the corresponding distance D the light has traveled using Equation 1, where c is equal to the speed of light and f indicates the frequency of the modulating signal.

$$D = \frac{(1-\delta)}{2} \cdot \frac{c}{f}.$$

Equation 1: converting correlation to distance

Using a square wave as modulating signal, one can define 2 problems:

1. Every correlation value $x = \delta + k \cdot B$ corresponds to the same distance as δ corresponds to. This means the measured distance is not unambiguously defined.
2. In the event of 2 cameras operating in the same neighborhood, crosstalk will occur if both cameras are using the same modulating square wave.

In order for the Time-Of-Flight based 3D camera to be of general interest, both problems need to be solved. These problems of autocorrelation have been identified in the field of communications [2] , and certain results of research on that area can be reused here. Figure 3 displays the theoretic autocorrelation function on the left of the image for a maximal-length PRBS sequence (m-sequence) of 15 bits. On the right, a measurement is shown where the same m-sequence was used as modulating signal. The normalized correlation was plotted against the applied phase shift.

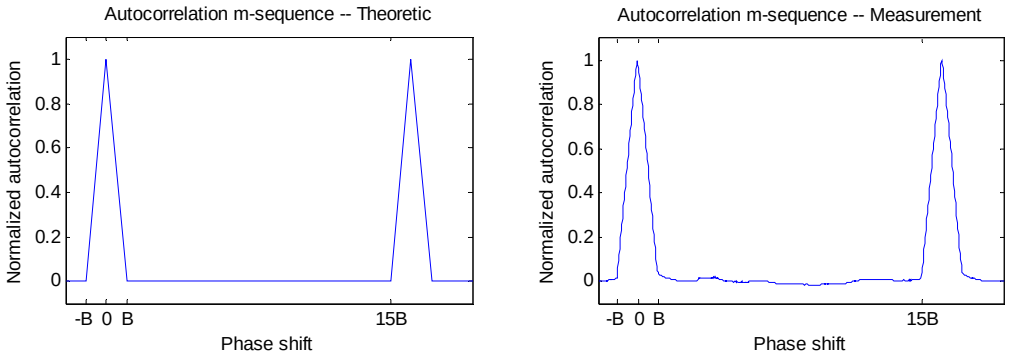

Figure 3: Theoretic and measured autocorrelation function of a maximal-length sequence of 15 bits

However, to obtain the normalized correlation, multiple measurements need to be conducted. Using the approach described in [3], 4 signals are required. These signals consist of the correlation between the original modulating signal and the reflection light modulated by:

- the original modulating signal, yielding S0 (see also Figure 3)
- the inverse of the modulating signal, yielding ~S0
- the original modulating signal, shifted by one bit, yielding SB
- the inverse of the original modulating signal, shifted by one bit, yielding ~SB

The simulation of these correlation values is shown in the left part of Figure 4. Measurements of those 4 signals on a CAPD enabled device are shown on the right part.

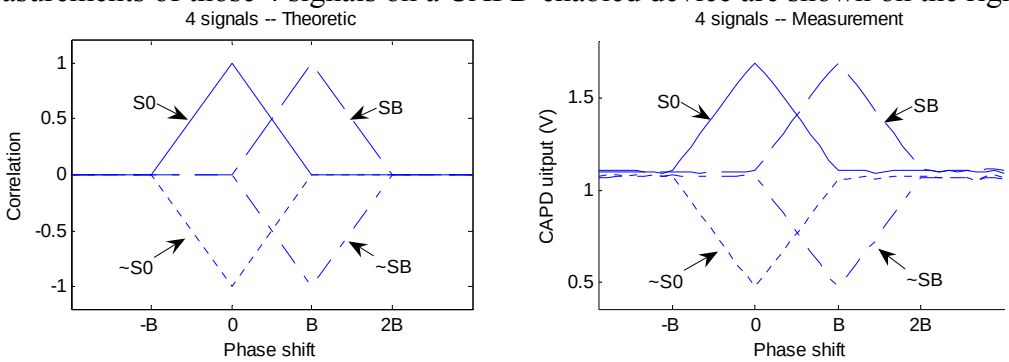

Figure 4: Theoretic and measured correlation functions of the 4 m-sequences

One can notice the slight offset between the positive and inverse signal in the measurements. This offset is due to the fact that a complete m-sequence of $2^n - 1$ bits contains 2^{n-1} '1' bits and only $2^{n-1} - 1$ '0' bits. Hence, averaged over a complete m-sequence, the correlation with a positive signal will be higher than the correlation with an inverse signal. Because of this, the offset decreases as the length of the m-sequence increases, which is shown in Figure 6.

By subtracting the inverse signals from the corresponding positive signals, one obtains the nil-referenced discriminator signals C1 and C2. The difference between C1 and C2, D, must be divided by the normalization factor N, which is the sum of C1 and C2, to obtain the normalized function F, which is linear in the [0, B] region. Each value in this interval corresponds to exactly 1 distance, which can be calculated using Equation 1.

The simulated functions for D and N are shown on the left side of Figure 5. On the right side, you find the measured values, as well as the normalized discriminator characteristic for the [0, B] region, which has a standard deviation of only 0.54%.

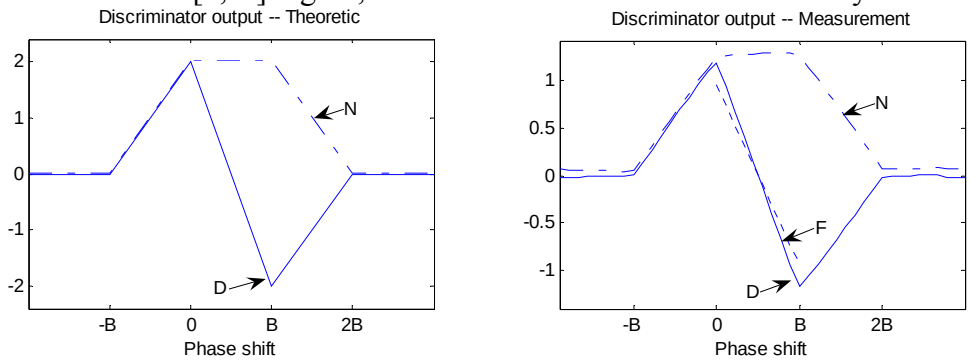

Figure 5: Theoretic and measured discriminator functions of the 4 m-sequences

Discussion & Future work

M-sequences can be used as modulating signal for Time-Of-Flight based 3D cameras. When the base frequency of those m-sequences is raised, the linearity of the discriminator function suffers, as displayed in Figure 7. Future research is necessary to model the causes of these non-linearities, and to find a way of correcting them.

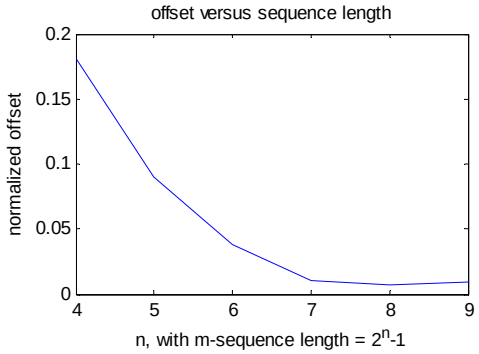

Figure 6: Correlation offset between positive and inverse signals versus m-sequence length

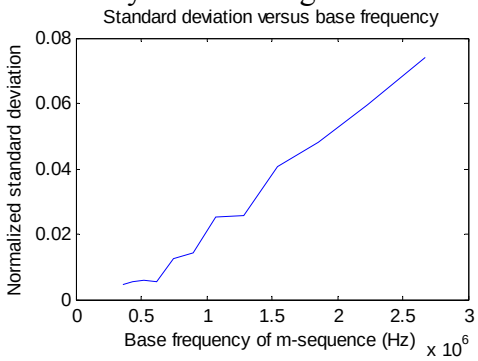

Figure 7: Normalized standard deviation between the [0,B] region versus base frequency

Acknowledgements

R. Grootjans is indebted to the Institute for the Promotion of Innovation through Science and Technology in Flanders (IWT-Vlaanderen) for the financial support. The research activities described in this paper were partially funded by the Fund for Scientific Research-Flanders (FWO-Flanders).

References

[1] D. Van Nieuwenhove, W. van der Tempel and M. Kuijk, “Novel Standard CMOS Detector using Majority Current for guiding Photo-Generated Electrons towards Detecting Junctions”, in Proc. of the Symposium IEEE/LEOS Benelux Chapter, 2005, pp. 229-232.

[2] J.G. Proakis, “Digital Communications”, Third Edition, New York, McGraw Hill, 1995P.Q. Roberts, "Title of chapter in book", in Title of Book, R.E. Dak and T. Euren, Eds., Amsterdam: North-Holland, 1991, pp. 123-456.

[3] X. Luan, “Experimental Investigation of Photonic Mixer Device and Development of TOF 3D Ranging Systems Based on PMD Tecnhology”, Siegen Univ., Diss., 2001

16 channels optical interface utilizing InP-based mode adapters combined with 30 µm intervals spaced fibre pitch converters

J. H. C. van Zantvoort, F. M. Soares, F. Karouta, M. K. Smit, S. Zhang, G. D. Khoe, A.M.J. Koonen and H. de Waardt

COBRA Research Institute, Eindhoven University of Technology,
Den Dolech 2, 5600 MB Eindhoven, The Netherlands

The performance of an optical connection is determined between 16 single mode fibres and an InP-based chip. The optical interface consists of a fibre pitch converter in combination with on-chip spot-size converters. All optical transitions are uniform spaced at 30 µm intervals. The coupling efficiencies are 3 dB / channel and the 1-dB alignment tolerances are 1.2 µm for both linear lateral x- and transversal y-translations. The rotational 1-dB tolerance for the θ_z roll position is ± 0.3°, measured at the outermost points of the fibres in the optical bus.

Introduction

The high refractive index contrast between InP-based waveguides and cleaved single-mode fibres result in optical coupling losses of 10 dB for each optical connection. Therefore mode-shape matching is necessary to reduce the optical losses due to mode mismatch of the small elliptical widely divergent field of the waveguide compared to the ten times larger circular field of a single mode fibre with a narrow angle of acceptance. In this paper, the mode-shape matching is accomplished by spot-size converters (SSC's) [1] in combination with a fibre spacing concentrator (FSC). Hence, practical issues are described as well as the optical performance of the coupling method. Subsequently, the results are compared and discussed with the coupling approach of lensed fibre arrays.

Optical coupling system

The "standard" fibre pitch spacing of 250 µm is converted to 30 µm intervals by means of a commercially available FSC, which end facet is polished at an angle of 8° from top to bottom in order to reduce optical reflections. The measured mode field diameter (MFD) of the waveguides at the end facet is 9.5 µm with a numerical aperture of 0.1 at the 5% intensity level. The insertion loss of the FSC is 0.4 ± 0.1 dB / channel and the dimensions are 45 mm (l) x 6.5 mm (w) x 3 mm (h). The FSC is shown in figure 1, while the on-chip SSC is sketched in figure 2. The most critical component of the SSC is the 1.5 mm long vertical taper, which is used to adiabatically couple the light from the 600 nm primary guiding layer to a 5 µm secondary guiding layer underneath. More details about the SSC can be read in reference [1]. The optical mode is expanded from the regular 3 µm device waveguide (MDF of 2.7 µm x 0.9 µm) to the 6 µm wide waveguide (MDF of 6.5 µm x 5.8 µm). Owing to this increase in mode size, the loss due to mode mismatch from the SSC to a single mode fibre is reduced from 10 dB to 0.9 dB.

Alignment procedure

In contrast with lensed fibre arrays, aligning the FSC is more complicated due to the following reasons: first the positions of the waveguides of the FSC must be localised for the coarse aligning in the lateral x-direction. Next, as a consequence of the polished end

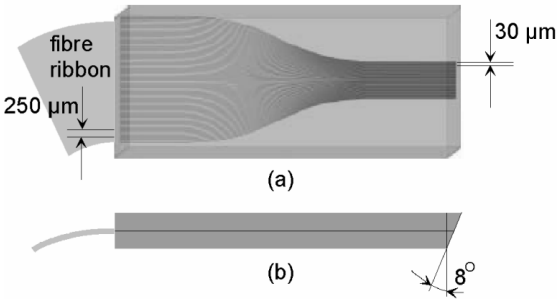

Fig.1 (a) Top view FSC, 16 fibers with 250 µm interval spacing are converted to 30 µm spaced intervals. (b) Side view FSC, the end facet is polished at an angle of 8°.

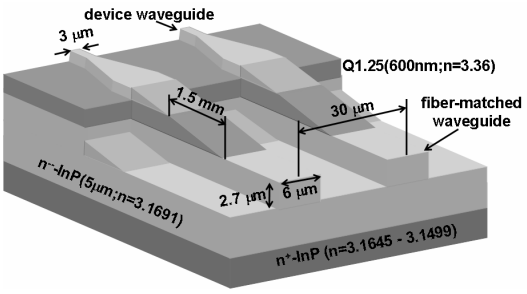

Fig. 2 Schematic representation of the SSC's (not to scale).

facet (see figure 1(b)) is the distance between the chip facet and FSC can not be visualized. This limited view makes the aligning in the transversal y-direction, just as the rotational θy-yaw alignment more difficult. Furthermore, the small air gab between the FSC and chip facet results in an interference phenomenon with an oscillating optical power fluctuation in the order of 1 – 1.5 dB. To perform the alignment, the FSC is mounted on a 6-axis piezo-electric controlled manipulator and positioned in front of an InP-based optical chip. The chip is a compact InP-based True Time Delay beam former with integrated SSC's [1]. A section of the chip is provided with a looped waveguides structure purposed for the investigation of the optical coupling performance. The section of the waveguide structure is shown in figure 3 (b). On the left-side are the SSC's, spaced at 30 µm intervals. The outer four looped waveguides are single looped waveguides, whereas the four inner looped waveguides are connected two by two through a 50/50 splitting ratio multimode interference (MMI) coupler. The positions of the waveguides of the FSC are observed with a microscope from the topside by illumination the FSC at the underside. A capture of the microscope view is given in figure 3 (a). The numbers 1 to 16 denotes the in- and output fibre connections of the FSC. Fibres 1 to 8 are connected to optical power meters, while fibres 9 to 16 are connected to an optical source. The height position of the FSC waveguides can be localised at both side views of the FSC. Namely, the waveguides are sandwiched between a top cover and substrate, both made from glass. A photograph is shown in figure 4. After the coarse visible alignment in the lateral x-, transversal y- and longitudinal z-direction, the FSC is fine positioned using active alignment of the outer waveguide loop. Due to the interference phenomenon which is related to the thickness of the air gab between the SSC and FSC, a broadband source is used. A typical plot is shown in figure 5. After physical contact between the FSC and chip facet at distance 0, the FSC is adjusted back until the first maximum power of the oscillating phenomenon is registered. This position is sketched with the mark (P) in figure 5. The position (P) is stable with the used broadband source. By using sources with longer coherence lengths, point (P) became instable. To determine the optimum roll θ_z position, the FSC is varied in the rotational θ_z direction. The relation between the θ_z roll position of the FSC and the chip facet is shown in figure 6. In this graph the two outermost fibre pair combination is observed, namely fibre 1 and fibre 16. The alignment tolerances for the 1-dB level are ± 0.3°. The FSC is aligned at an angle θ_z roll position of 0° and varied in the θ_x pitch direction. As a result of the polished end facet of 8°, the light is deviated from the optical z-axis. The dependence of the angular variation is shown in figure 7. If the FSC

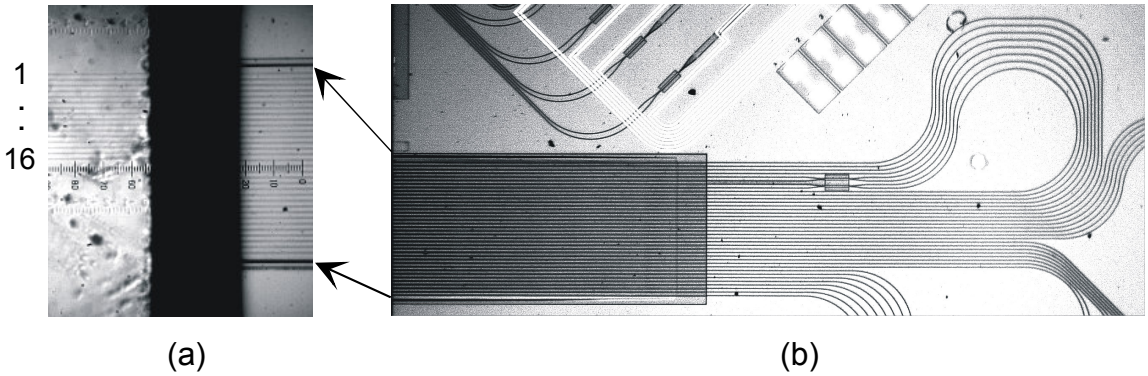

Fig. 3 (a) View of a microscope used for the coarse aligning in the lateral x-direction. The black colored area between the optical chip facet (right) and the FSC (left) is the shadow of the FSC as a consequence of the polished end facet of the FSC. The right photograph (b) shows the top view of the optical chip with looped waveguides combined with SSC's. The inner four waveguide loops are connected two by two through a 50/50 splitting ratio multimode interference (MMI) coupler.

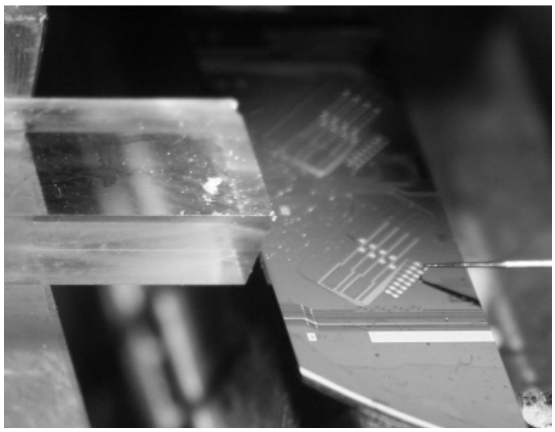

Fig. 4 Side view of the FSC and chip facet used for passive coarse alignment in the transversal y-direction.

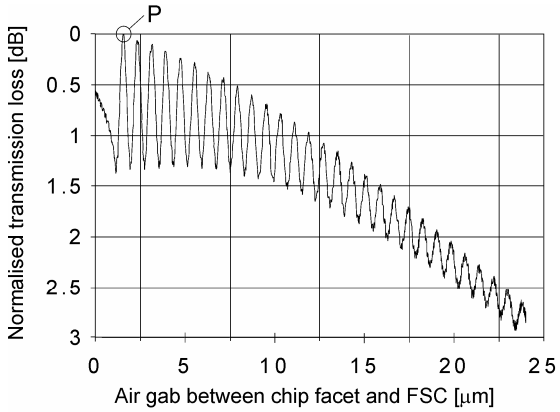

Fig. 5 Oscillating interference phenomenon because of the air gab between the FSC and chip fact. All measurements are registered at point P.

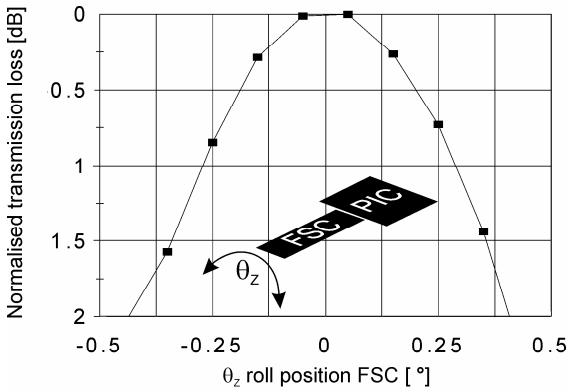

Fig. 6 Normalised additional transmission loss increment as a function of the rotational roll position of the FSC compared with the chip facet.

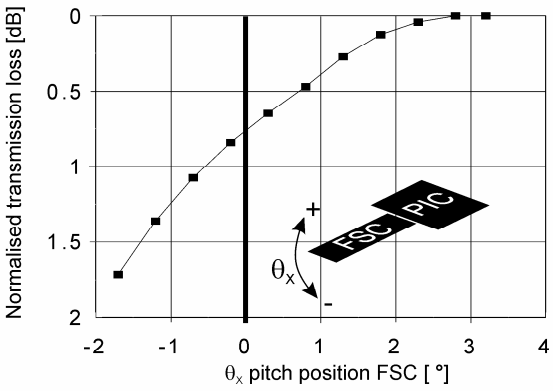

Fig. 7 Normalised optical coupling loss transmission as function of the pitch position between the FSC and chip facet

is rotated 3° with respect to the longitudinal z-alignment, the coupling efficiency is improved with 0.75 dB. The FSC is adjusted back at the 0° pitch position and the coupling efficiencies are determined for all 16 optical connections simultaneously.

Results

The FSC is linear translated from the optimum alignment in the lateral x- and transversal y-direction meanwhile all 8 optical transmission circuits are measured. The relative power loss increment as function of linear shift in x- and y-direction is plotted in figure 8 and figure 9, respectively. These figures show excellent channel spacing uniformity between the waveguide pitches of the FSC and SSC's. The transmission losses of all channels are listed in the last row of table 1, showing a transmission loss of 11.6 ± 0.4 dB / transmission circuit. These losses are composed as follows; 0.9 dB/cm shallow-waveguide propagation, 1.5 – 2 dB internal losses of the SSC, mode mismatch between the SSC and FSC is 0.9 dB / channel, insertion loss FSC is 0.4 dB / channel and 0.8 dB for the MMI coupler. An antireflection (AR) coating was not applied to the chip facet, so the remaining losses of 2.5 – 3 dB are introduced by the internal reflection losses of the chip facets.

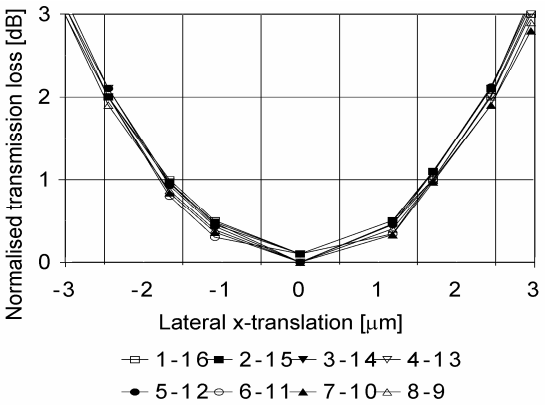

Fig. 8. Additional loss increment as function of lateral x-displacement.

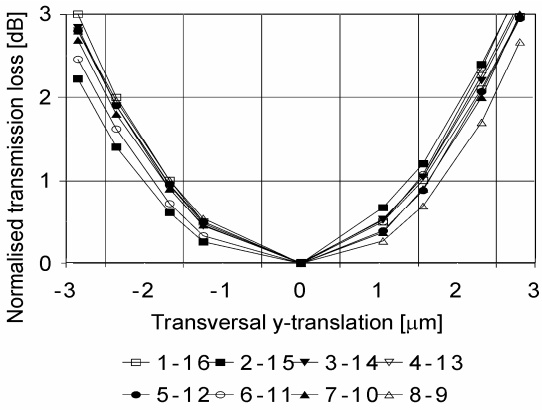

Fig. 9. Additional loss increment as function of transversal y-displacement.

Fibre pair [-]	1-16	2-15	3-14	4-13	5-12	6-12	5-11	6-11	7-10	8-10	7-9	8-9
Loss [dB]					17.0	16.3	14.6	14.1	14.9	14.2	13.7	14.6
Total loss [dB]	11.7	11.8	12.3	11.5	13.6		11.3		11.5		11.1	

Table 1. Measured coupling loss of the fibre pair combinations. The values of the middle row are measured after both MMI branches, whereas the last row shows the total transmission losses of all fibre pair combinations.

Discussion

The coupling efficiency of the waveguide-SSC-FSC-fibre system is determined to be -3 ± 0.3 dB / channel. For this 16 channel coupling system, the 1-dB alignment tolerances are 1.2 μm for both lateral x- and transversal y-translations and ± 0.3° for the θ_z rotational position. The coupling interface shows excellent channel spacing uniformity. In contrast, the inaccuracy of commercially available lensed fibre arrays are in the order of 1 – 2 μm, resulting in a coupling efficiency of -6.5 dB measured for eight fibres simultaneously in combination with waveguides without SSC's [2]. In conclusion, this coupling approach has the potential of increasing the number of fibre-chip connections. The interference effects can be reduced by applying an AR-coating on the chip facet and using an index matching material between the FSC and SSC's.

References

[1] F.M. Soares et al in Proc. IPRA Conference USA, paper IMF5, 24-26 April 2006.

[2] J.H.C. van Zantvoort et al IEEE/JSTQE Sept/Okt 2006.

Fiber Array to Photonic Integrated Circuit Assembly Method with Post-Weld-Shift Compensation

J. H. C. van Zantvoort, S.G.L. Plukker, E. Smalbrugge, M.T. Hill, E.C.A. Dekkers, G.D. Khoe, A.M.J. Koonen, and H. de Waardt

COBRA Research Institute, Eindhoven University of Technology,
Den Dolech 2, 5600 MB Eindhoven, The Netherlands

A mechanical subassembly is presented enabling fine positioning and fixation of an array of lensed fibers to multiport photonic integrated circuits. To demonstrate the functionality, two Indium Phosphide based photonic integrated circuits are pigtailed; an integrated two-state multi-wavelength laser chip, operating at 25 ºC and a coupled Mach-Zehnder interferometer chip, operating at 10 ºC. Both devices functions as a one-bit optical memory element with optical set and reset functions. Successful post-weld-shift compensation, in the order of 0.1 µm – 3 µm, is established, using laser supported adjustment. The mechanical alignment stability is proven to be smaller than 25 nm / ºC, measured in a temperature range between 10 ºC and 30 ºC.

Introduction

In opto-electronic device packaging, the fixation technology is a very challenging task and laser welding is acknowledged at present as the most stable fixation technology. During the welding process, the melting of metal parts that fuse together upon solidification and consequently forming a weld joint, causes shrinkage forces during this solidification. The shrinkage forces produce misalignment between the two welded parts and these shifts are the so-called post-weld-shifts (PWS's). In this paper, the PWS is minimized by the design of the subassembly and alignment of the fiber array can be accomplished in four degrees of freedom. Subsequently, after the permanent fixation process, post-weld-shift compensation is possible by re-position of the fiber array by metal deformation based on laser welding induced local heat.

Assembly procedure

The subassembly consists of a mechanical actuator part, on which the fiber array is mounted and a chip mounting platform. A photograph of the subassembly is shown in figure 1. After aligning the fiber array to the optimum position, using temporary connected piezo-electric actuators, the mechanical actuator part is welded in position using an alignment frame. Subsequently, the piezo-electric actuators are disconnected and compensation for PWS's can be performed by deformation of the tuning frame at positions A, B, C, or D using laser induced local heat (fig 1, b). Detailed information about the subassembly can be read in reference [1]. To demonstrate the functionality, two indium phosphide based photonic integrated circuits (PIC's) are pigtailed; an integrated two-state arrayed waveguide grating (AWG) based multi-wavelength chip and a coupled Mach-Zehnder interferometer. The mask layouts are shown in figure 2. Description of the working principle of both devices can be read in references [2] and [3]. Commercially available lensed fiber arrays, composed of fibers with lens radii of 15.0 µm ± 1.0 µm, are used to reduce the coupling loss to 4.4 dB – 5.5 dB. The fiber arrays are fine aligned actively, by measuring the optical spontaneously emission power of the semi-conductor optical amplifiers (SOA's) at the fiber pigtails simultaneously. When the fiber array is optimal aligned, the received optical powers for all fibers are

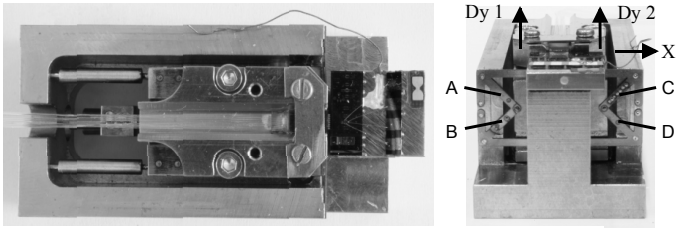

(a) (b)

Fig. 1 Top view (a) and front view (b) of the realized sub-assembly. PWS compensation can be performed using laser adjusting at positions A, B, C, or D of the alignment frame.

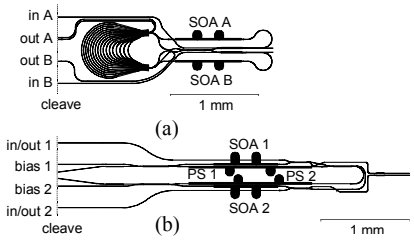

Fig. 2 Mask layouts of a two state AWG-based multi-wavelength laser PIC1 (a) and a coupled Mach-Zehnder interferometer chip PIC2 (b).

PIC (a)	Dx [µm]	Dy1 [µm]	Dy2 [µm]	In A [%]	Out A [%]	Out B [%]	In B [%]
I Initial position	0	0	0	100	100	100	100
II fixation	+ 0.3	- 0.2	- 0.1	100	84	83	94
III disconnection	- 0.4	+ 0.4	+ 0.2	93	106	108	100
PIC (b)	Dx [µm]	Dy1 [µm]	Dy2 [µm]	In/Out 1 [%]	Bias 1 [%]	Bias 2 [%]	In/Out 2 [%]
I Initial position	0	0	0	100	100	100	100
II fixation	- 2.8	- 0.3	+ 0.7	2	11	12	9
III disconnection	+ 4.3	+ 1.6	- 2.2	12	29	21	16
IV laser adjusting	- 1.6	- 1.4	+ 1.2	95	100	89	80

Table 1. Displacement in x- and y-direction and accompanying normalized optical power in % at initial position (I), after the fixation step (II), after removing the connection pins between the piezo-actuator and the sub-assembly (III) and the net displacement after the laser-adjust process (IV).

normalized to 100 %. Next, the actuator part is welded to the tuning frame simultaneously, with equal laser energies of 5 J. The optical output signals and the absolute position of the fiber array are measured during the welding process. In table 1 are shown the process of the concerned PIC, the relative positions of the fiber array in the lateral x-direction, (Dx) and the transversal y-direction, measured at two positions (Dy 1) and (Dy 2). The position and the definition of the translations are also sketched in figure 1b, using the right handed coordinate system. Next, the normalized received optical powers are given of the in- and out-put ports. The shift of the fiber array as a result of the PWS is for the two-state AWG-based multi wavelength chip (PIC (a)) 0.3 µm and 0.2 µm in the lateral x- and transversal y-direction, respectively. These small shifts lead to an optical power decrease of 6 % for the (In B) port. The two inner fibers of fiber array have a deviation difference of 0.6 µm approximately in the fiber pitch of 250 µm. This causes more relative optical power decrease of the two inner (Out A) and (Out B) channels of about 15 %. Next, the displacement pins are disconnected from the subassembly. This mechanical disconnection releases the internal stresses in the subassembly, which results in a shift of 0.4 µm in the negative x-direction. Consequently, the fiber array is translated to the initial x-position. Also a small shift in the positive y-direction produces a higher coupling efficiency improvement of the (Out A) and (Out B) ports compared with the initial position. The coupling efficiency of the fourth (In B) port is also recovered to the maximum value. Compared with the normalized received optical powers at the initial position, re-adjusting the fiber array using the tuning frames was not necessary to execute. In contrast, the coupled Mach-Zehnder interferometer is also actively aligned and all measured optical powers of the waveguides are normalized to 100 %. During the fixation welding process, the measured values of the displacement transducers are 2.8 µm in the negative x-direction, 0.3 µm in the negative y-direction at position (Dy 1) and 0.7 µm in the positive y-direction at position (Dy 2). Consequently, the received optical powers of all waveguides-to-fibers transitions are reduced with 10 dB approximately. After disconnecting the displacement pins between the piezo-actuators and subassembly, the internal stress build up in the

subassembly forces the adjustable inner part back in the positive x-direction, resulting in coupling losses of 7 dB average for all fiber waveguide transitions. Therefore the adjustable inner part of the subassembly is laser adjusted in the negative x-direction over a net translation range of 1.6 µm. Simultaneously, the fiber array is also rotated in the θ_z-direction, measured the net linear translations of 1.4 µm in the negative y-direction at position (Dy 1) and 1.2 µm in the positive y-direction at position (Dy 2). During the laser adjust process, the received optical powers are recovered to 95%, 100%, 89% and 80% for the (In/Out 1), (Bias 1), (Bias 2), and (In/Out 2) ports, respectively. The PWS is compensated by deform the tuning plate at 22 positions. The alignment step can varied from 0.2 µm to 2 µm, depending on the laser energy, which is in the range of 0.8 J – 2.8 J with a weld time of 5 ms. The most shrinkage is applied 7 times at position C of the tuning frame to realize the rotational translation in the θ_z-direction (see figure 1b). Positions B and C are heated up 6 times, while position A is heated up 3 times.

Thermal stability characterization

Both subassemblies are mounted onto a 16.6 W thermo-electric cooler (TEC) and fixed unambiguously on a three-point support in a package [1]. The package is hermetic sealed and filled with dry nitrogen gas using two integrated small valves in the package. The stability between the fiber tips and chip facet is determined by measuring the average spontaneous emission power of all four ports of both PIC's by supplying a current of 20 mA to the SOA's. The chip temperature of both devices is varied from 10 ºC to 30 ºC by controlling the TEC. For both devices is measured an increase of spontaneous emission power as a function of decreasing chip temperature. For the two-state multi-wavelength laser chip, the measured optical output of both SOA's shows optical power dependence with the same linear slope for all four fiber-to-waveguide transitions. The relation between received optical powers as function of the chip temperature is shown in figure 3. In addition, the dependence between the spontaneous emission power and the chip temperature is measured on a SOA with the same length of 750 µm between 10 ºC and 40 ºC. The relation between the emitted optical power and chip temperature is determined to be –0.06 dB / ºC. Refer to figure 3, it can be concluded that the coupling is stable for the measured temperature range. The normalized output power as function of the chip temperature of the coupled Mach-Zehnder interferometer is shown in figure 4. From this figure can be concluded that, analogous to figure 3, the coupling between the (Bias 1) port and the fiber is stable. From this reference, at a chip temperature of 30 ºC, an extra additional loss of 0.5 dB and 0.8 dB for the (Bias 2) and (In/Out 2) ports are measured at the fiber pigtails, respectively. The In/Out 1 port shows an improvement in coupling efficiency. The transmission curves as function of transversal displacement in the y-direction, measured just before the fixation process are shown in figure 5. This figure explains the difference between measured curves of figure 4; the top of the (Bias 1) curve is located at the position y = 0, whereas the top of the (In/Out 1) curve is located at position y = -1 µm. Similarly, the maximum optical power transfer of the (Bias 2) and (In/Out 2) ports are located at 0.5 µm intervals in the y-direction. At position y = 0, the difference in average coupling efficiency of all four fiber transitions are within 0.5 dB. However, if the aligning between the waveguides and fiber array translates in the negative y-direction over a range of 0.5 µm as a result of temperature changes between 10 ºC and 30 ºC, the coupling efficiencies of the (In/Out 1) port increases, while the coupling efficiency of the (Bias 1) port remain the same value and the coupling efficiencies of the other (Bias

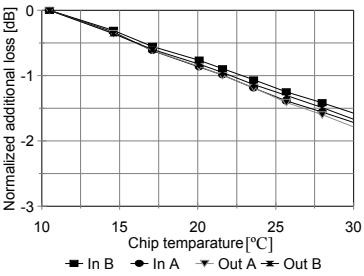

Fig. 3 Measured spontaneously emission power as function of chip temperature of PIC 1.

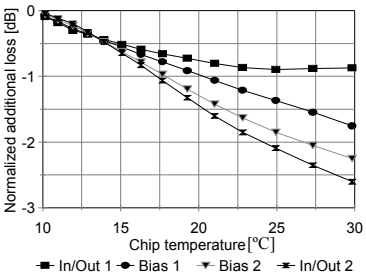

Fig. 4 Measured spontaneously emission power as function of chip temperature of PIC 2.

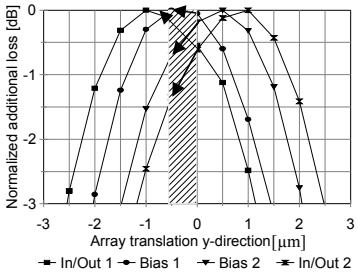

Fig. 5 Measured received spontaneously emission power as a function of the transversal y-position of the fiber array.

2) and (In/Out 2) ports decrease. This tendency agrees with additional coupling efficiency curves of + 0.5 dB, - 0.5 dB and - 0.8 dB for the waveguide ports (In/Out 1), (Bias 2), and (In/Out 2), respectively. In conclusion, concerning the subassembly of PIC 2, the fiber array shifts apparently 0.5 μm in the negative y-direction measured over a temperature range between 10 ºC and 30 ºC. In contrast, the subassembly of PIC 1 shows excellent thermal stability. The difference between these two subassemblies is the fact that during the assembly process, the pre-aligning of PIC 1 is performed more accurate in the x-direction with respect to the neutral position of the fiber array. Therefore, as a result of small absolute translations of the fiber array, the external forces cause relative small strain in the subassembly. After pre-aligning and attaching PIC 2 to the chip mounting platform, the fiber array has to be aligned over a relative longer distance. During the fixation process, this a-symmetrical initial position of the middle part of the subassembly, related to the tuning frame can cause differ in the local temperature profile of the two welded parts, resulting in a PWS. The higher forces, applied on the adjustable middle part of the subassembly, to obtain the optimum alignment of the fiber array to the waveguides, can build up residual stress in the subassembly after disconnecting the displacement pins. During the laser tuning of the alignment frame for the PWS compensation process, the plastic material deformation of the branches in the alignment frame create also stress in the material. It is plausible that residual stress in the subassembly as well as the generated strain in the alignment frame can causes the thermal mechanical stability dependence of 25 nm / ºC in the temperature range of 10 ºC to 30 ºC.

Conclusions

A mechanical subassembly is realized to align and fix a lensed fiber array in 4 degrees of freedom to a two-state multi wavelength laser chip and a coupled Mach-Zehnder interferometer chip. The design minimizes PWS's and permanent fixation is performed using a well-balanced laser set-up. The optimum position of the fiber array is laser welded resulting in minimum and neglect able PWS of 0.1 μm to 0.3 μm for the two-state multi-wavelength laser chip. This device shows excellent thermal stability. During the assembly process of the coupled Mach-Zehnder interferometer successful PWS compensation, in the order of 0.1 μm to 3 μm is established. The mechanical alignment stability of this device is proven to be smaller than 25 nm / ºC from 10 ºC to 30 ºC.

References

[1] J.H.C. van Zantvoort et al, in IEEE, LEOS Benelux, 2005, pp. 217-220.

[2] M.T. Hill et al, IEEE, Photon. Technol. Letters, vol 17, no 5, 2005 pp. 956-958.

[3] M.T. Hill et al, OPTICS LETTERS, vol. 30, July 1, 2005, pp. 1710-1712.

Optical interconnections embedded in flexible substrates

E. Bosman, G. Van Steenberge, P.Geerinck, W.Christiaens, J.Vanfleteren and P. Van Daele

Ghent University, TFCG-Microsystems, Technologiepark Building 914A, 9052 Zwijnaarde, Belgium, affiliated with IMEC, Kapeldreef 75, 3001 Leuven, Belgium

The need for flexible electrical circuits has increased significantly over the past few years. This paper focuses on the integration of optical data interconnections in such flexible substrates. Optical waveguides, micro-mirrors and opto-electronic chips are embedded and stacked between two flexible Polyimide layers to increase the mechanical stability and the reliability. Three different optical materials (Truemode™ Backplane Polymer, Ormocer® and Epoxies) have been studied as well as different schemes for applying the Polyimide layers (spin-coating and lamination). Ongoing research focuses on the embedding of opto-electronic components and the mechanical- and optical characterization of the module.

I. Introduction

The ever increasing telecommunication sector results in a continuously growing demand for higher communication speeds and data-rates, forcing the step towards optical data transmission. This step is already established for long distance communication, but the increasing density and integration of electronic components on boards forces the market to integrate optical interconnections on the boards.

Together with this trend, the demand for flexible substrates for electronic applications has doubled in the last 5 years [1]. Because of their flexible behavior, the use of these substrates can significantly lower the over-all substrate thickness and weight. Moreover they can ease the assembly, increase the module compactness and can be applied to a curved surface, and even to a dynamic one.

Both increasing trends and needs will result in applications which combine the advantages of optical interconnections and flexible substrate technologies.

This paper focuses on the fabrication of flexible substrates with embedded active opto-electronic components and passive optical interconnections based on multimode waveguides, 45˚-turning mirrors and aligning structures. The definition of these structures is done by photolithography and laser ablation. Later on, the fabrication of a proof-of-principal demonstrator is intended, in means of a functional alone-standing opto-electrical flexible module.

II. Materials

The material for the optical transmission medium needs to show low light propagation losses for the common wavelengths for data communication (850 nm) and telecommunication (1.3 or 1.55 µm) and must have the right properties in means of UV-crosslinking ability, spin-coating, temperature- and chemical resistance and mechanical brittleness.

Truemode Backplane™ Polymer [2], Ormocer® [3] and Epocore are materials which meet these requirements and have shown good results when applied on rigid substrates in the past [5].

The material for the flexible substrate itself is Polyimide (PI) which is the dominant material in the flexible circuits industry because of its good electrical, chemical, temperature and mechanical behavior [4]. Precautionary steps had to be taken to assure the adhesion of the PI with the optical materials because of the chemical inertness of Polyimide (PI).

III. Stacking of optical- and Polyimide-layers

The creation of waveguides consists of the stacking of an undercladding,-, core- and uppercladding layer by spin-coating. The optical materials are however not flexible and strong enough to be bended without cracking or damaging. Therefore these layers are sandwiched between two spin-coated Polyimide layers, one at the top and one at the bottom, which absorb all stress and pressure during bending, protecting the inner optical layers from breaking.

Stacking of materials with such a different chemical and mechanical behavior demands special measures like CTE (Coefficient of Thermal Expansion) matching to avoid curling and bad adhesion, and low cure-temperatures for the PI to protect the layers underneath from reaching their glass transition temperature.

As an alternative way to fabricate the stack, lamination of the optical layers between prefabricated commercially available PI-foil was proposed and studied. This method has the advantage that the PI-foil and the optical layers can be handled and cured separately since the lamination step is one of the last steps in the process flow. A semi cured adhesive, fixed on a ceramic substrate by dubbelsided tape is used as a carrier for the spincoating of the optical layers and acts as a release layer later in the process by peeling of this adhesive.

When creating the stack special care must be taken to ensure no outgassing of remaining solvents in underlying layers appears during cure steps.

IV. Fabrication of passive optical interconnections

A. Fabrication of optical waveguides

Creating a core transmission channel, isolated inside a bulk cladding material with a lower refractive index results in an optical waveguide which captures the light due to total internal reflection.

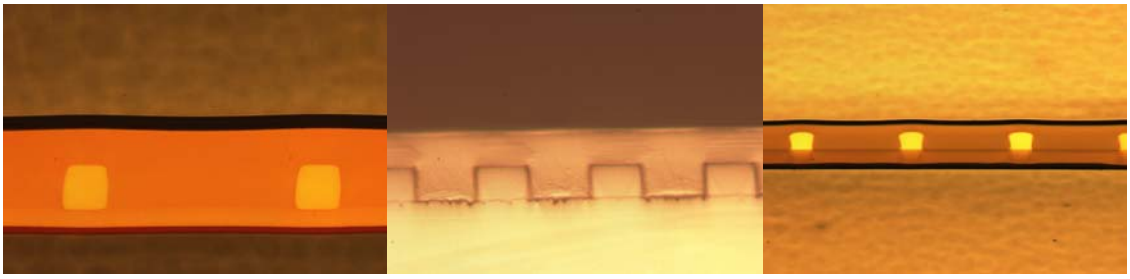

Figure 1: Complete stack with photolithographic waveguides in *left:* Ormocer®, *middle:* Epocore (on FR4-material) and *right:* Truemode Backplane Polymer™

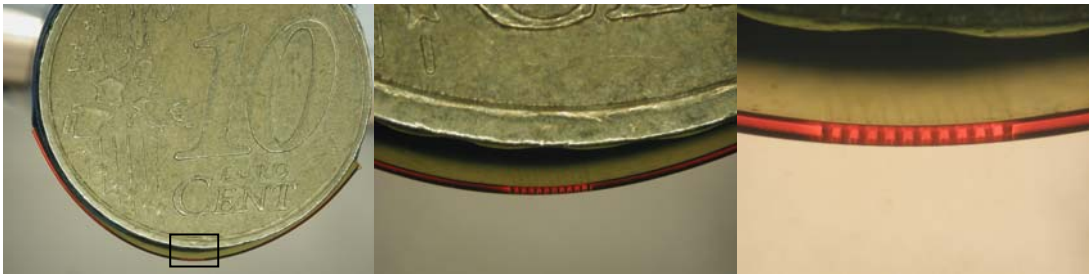

Figure 2: Complete stack with laser ablated waveguides in Truemode Backplane™ Polymer, using a 248 nm wavelength Kr-F Excimer laser, bended with a radius of 1cm.

This isolation can be done by patterning the core-layer with a standard photolithographic process with selective exposure of the waveguides to UV-light (Figure 1) and in an alternative way by laser ablation, removing the core-material at both sides of the waveguide (Figure 2).

B. Fabrication of 45 degrees out of plane turning mirror

The data-carrying light can be vertically coupled in- and out of the waveguides with 45 degrees out of plane deflecting micro-mirrors, terminating the waveguides and connecting them with laser diodes, receivers, optical fibers, open air or optical elements. These mirrors are realized by laserablation with a Kr-F Excimerlaser (248 nm wavelength) [5].

C. Fabrication of alignment structures for a proof-of-principle demonstrator

This research not only focuses on the optical assembly of flexible circuits but the combination of optical and electronic assembly on the same module. This means that the positioning of the VCSEL's and receivers on one hand and optical fiber-arrays, optical elements and deflecting micro-mirrors on the other hand is crucial. Alignment structures like alignation holes, mechanical stand-offs and fiducials are therefore needed and fabricated using the laser ablation technique .

A proof-of-principle demonstrator will be fabricated in the future, including all the elements which have been discussed in this paper to create a standalone flexible module with embedded optical interconnections and electrical assembly on top of the Polyimide.

V. Embedding of active optoelectronic devices

Experiments have been done with success to embed ultra thin dummy chips into the optical layers by implementing a cavity with photolithography. Later in the research functional opto-electronic chips, thinned down to 30 µm thickness [6], will be embedded. Micro-via's will be ablated using a frequency tripled Nd:YAG laser (355 nm wavelenght) and metallized by sputtering and plating to fan out the contacts on the top PI layer where all other electrical assembly can be done with standard flex assembly processes. The optical layers have proven to stand the temperature cycles during these procedures.

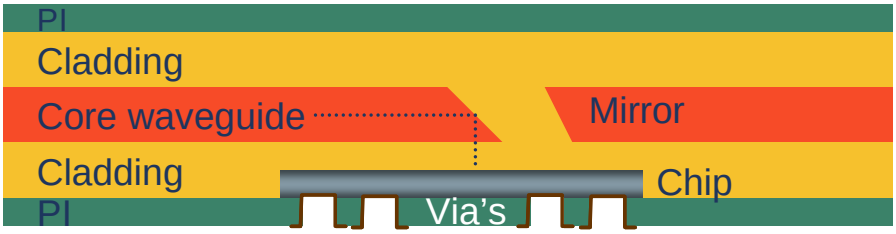

Figure 3: Schematic representation of the embedding, alignment and electrical connection of active components and waveguides in the optical layers.

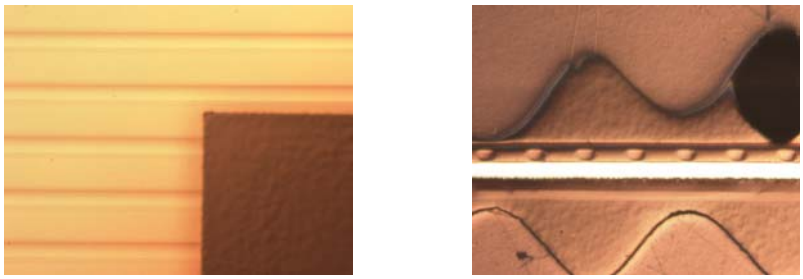

Figure 4: Embedded 5x5 cm^2 dummy chip and waveguides in Ormocer® material. *left:* Top view *right:* Cross section.

VI. Acknowledgements

This work is partly supported by the European 6th Framework Programme "Network of Excellence on Micro-Optics" (Nemo).

VII. Conclusion

The increasing need for flexible modules and the integration of photonics on boards results in a challenging and competitive research which combines both needs by embedding passive optical interconnections and active optoelectronic devices on flexible Polyimide substrates.

A complete autonomous opto-electrical and flexible module will be demonstrated.

References

[1] www.bpaconsulting.com
[2] www.exxelis.com Truemode Backplane™ Polymer data sheets
[3] http://www.microresist.de Ormocer® material datasheets
[4] Joseph Fjelstad, "An engineer's guide to flexible circuit technology", Elektromechanical Publications LTD, 1997
[5] G. Van Steenberge, N. Hendrickx, E. Bosman, J. Van Erps, H. Thienpont, P. Van Daele "Laser Ablation of Parallel Interconnect Waveguides", IEEE Photonics Technology Letters, Vol. 18, No. 9, May 2006.
[6] W. Christiaens, M. Feil, T. Loeher, J. Vanfleteren, "Embedded ultra-thin Chips in Flex", Proceedings of Forum for Flexible Electronic Systems, Munich, November 2005.

Technology Demonstrator of an Optical Board-to-Board Data-Link

T. Lamprecht, C. Berger, R. Beyeler, R. Dangel, L. Dellmann, F. Horst, N. Meier, T. Morf and B.J. Offrein

IBM Research GmbH, Zurich Research Laboratory, 8803 Rüschlikon, Switzerland

Compared with electrical interconnects, optical interconnects offer several advantages, such as higher channel bandwidth and density, longer reach, and insensitivity to electro-magnetic interference. We developed an optical printed circuit board (PCB) technology platform and demonstrate a 12 × 10 Gbps optical link between boards. Embedded polymer waveguides guide the optical signals, which are generated and detected by 12-channel optoelectronic modules. A polymer waveguide flex is used as optical link between boards. All connections between elements are based on passively aligned, standard MT interfaces, keeping costs low and providing compatibility with parallel fiber optics. The technology is also compatible with standard PCB processes.

Optical Interconnects

The increasing performance of microprocessors leads to higher bandwidth requirements for the data flow to and from the processor. Today, all signaling on a PCB is performed electrically, using copper lines that are integrated in the board. However, issues such as propagation loss and interchannel crosstalk, limit the scalability of electrical interconnects to ever higher bandwidth densities. A possible solution for these issues is the implementation of optical interconnects. Optical interconnects feature a higher bandwidth × length product, are more power-efficient and enable a higher channel density than electrical interconnects above a certain data rate. It is especially this higher channel density of optics that drives the research on optical PCB technology for inter-system interconnects [1]. However, we expect that before optical interconnects can find widespread use in PCBs, first the following two requirements have to be met: First, passive alignment, whereby the optical elements are simply plugged into the board without the need for optical monitoring and/or further fine adjustment, and, secondly, compatibility of optical PCB production with standard PCB manufacturing processes.

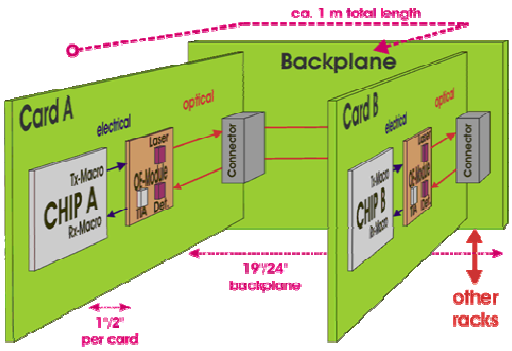

Fig. 1: Schematic drawing of an optical interconnect system

The schematic in Fig. 1 shows a basic optical interconnect configuration, in which chips A and B, mounted on daughter cards A and B, are connected via a backplane. The required building blocks for such a link are **optoelectronic modules**, which are mounted close to the chips and convert signals between the electrical and optical domain. In addition, **polymer optical waveguides** in the board are used to transmit the optical signals. Finally, an **optical connection system** is required to connect the individual optical elements, such as optoelectronic modules to daughter cards, daughter cards to backplanes, and backplanes to flexible optical waveguides or optical fiber bundles for connection to other racks. To achieve

reliable data transmission at 10 Gbps, the overall optical losses should not exceed 15 dB for a link. Besides the propagation losses in the waveguides, the losses in the optical connections between elements are the main contributors to the overall system loss. Thus, finding a cost-effective method for achieving low-loss optical connections is an important requirement for a successful implementation of optics in the PCB world.
After a brief introduction to waveguide technology and of the optoelectronic modules, we will focus on our solution to connect optical elements to PCBs and on its impact.

Waveguide technology

Because of the precision and smoothness requirements for optical waveguides, the patterning of the actual waveguides cannot be performed using standard PCB processing equipment. Therefore, we implemented a direct laser writing tool for large-scale waveguide patterning [2]. Thick-film cladding and core layers are applied on a board substrate using doctor-blading, spray-coating or inkjet printing. Waveguides having core sizes ranging from 35 to 50 µm, pitches between 62.5 and 250 µm, and propagation loss values below 0.04 dB/cm have been realized. To increase the density of the waveguides at the board edge, two-dimensional waveguide arrays with up to four waveguide layers were built.

Optoelectronic modules

The optoelectronic modules are butt-coupled to the waveguide facet in the PCB, while the electrical signals are transmitted through an electrical flex that provides a 90° bend in the electrical domain. The 12 channel transmitter and receiver elements consist of a 1×12 VCSEL array and a laser driver or a 1×12 photodiode array and a TIA (trans-impedance amplifier), respectively, developed in collaboration with IntexyS Photonics [3].

Mechanical alignment reference for optics

The implementation of optics into PCBs necessitates a proper connection of optical elements to an optical PCB. Precise mechanical alignment features in the PCB are required to enable a pluggable connection to the board. During the assembly, these alignment features have to be positioned passively in the PCB. The major obstacle to achieving precise passive alignment is the large discrepancy in positioning tolerances between the optics and the PCB world. In standard PCB processing, manufacturing tolerances of more than 100 µm are acceptable. However, the multimode waveguides we use allow an alignment tolerance of only 8 µm to keep the optical loss due to misalignment to less than 0.5 dB.
We chose an interface based on the MT standard, using two guiding pins with a diameter of 700 µm. This also enables compatibility with standard parallel optical fiber equipment.
In this paper, we propose a passive alignment concept that fulfills the following requirements: First, the alignment structures are created and compatible with standard PCB manufacturing processes. Second, they enable a passive assembly of a mechanical element within an 8 µm alignment tolerance with respect to the waveguides.
These alignment structures are formed by standard PCB photolithography in a copper layer on the board substrate, and we will therefore refer to them as “copper markers”. The laser writing tool we use for waveguide definition provides the flexibility to compensate for substrate distortions for each PCB individually, simply by adapting the waveguide pattern to the position of the copper markers. The next step is to use these

copper markers also for mechanical alignment. The surface of the copper acts as vertical alignment reference, and a slot in the copper acts as horizontal reference, see Fig. 2.
Because these copper markers are laminated into the PCB together with the waveguides, they have to be retrieved. First, a laser drill process is used to retrieve and clean the surface of the copper. The laser beam is reflected by the copper, and only material above the copper layer will be removed. However, in the copper marker we placed a photolithographically defined opening, through which the laser drilling continues into the polymer underneath the copper. This generates a slot in the copper marker, which can be used as horizontal reference. As the copper acts as a mask for the laser beam, the position of the slot is defined by the original opening in the copper marker and not by the relatively inaccurate laser drilling process.
In summary, the optical waveguides are aligned with the copper markers thanks to the direct laser writing. In addition, also the vertical and horizontal reference planes for the mechanical alignment are defined by the copper markers. Thus we have created a mechanical reference system that is precisely aligned with respect to the waveguides. Fig. 3 shows a set of copper markers with illuminated waveguides.

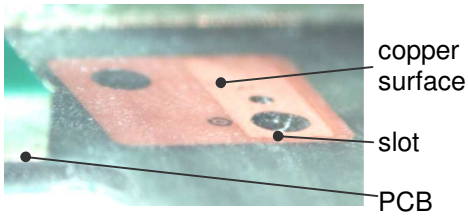

Fig. 2: Copper marker

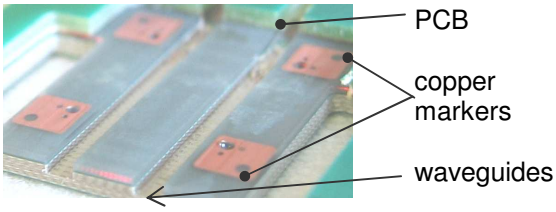

Fig. 3: Set of copper markers with waveguide facet

A mechanical adapter acts as a bridge between the copper alignment markers and the required MT guiding pins. Fig. 4 shows the details of the mechanical alignment of such an MT adapter. Fig. 5 shows an MT adapter passively inserted into an optical PCB with the illuminated waveguide array between the guiding pins.

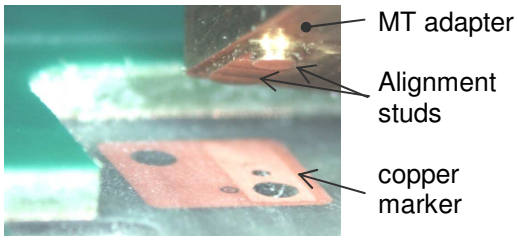

Fig. 4: Adapter insertion into copper structures

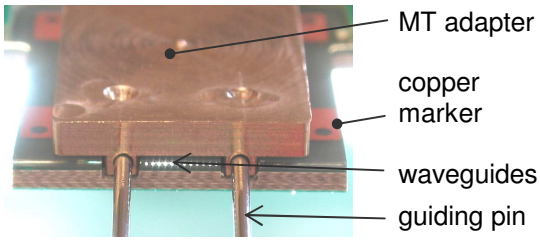

Fig. 5: Passive aligned MT adapter with optical facet

Alignment inspection

We developed an inspection system to measure the passive alignment precision with respect to the waveguides in order to improve the performance of the fabrication process. The inspection concept is based on a mechanical gauge with reference markers at the target center position of the waveguides and alignment holes corresponding to the standard MT interface. After mounting the gauge on the MT adapter, which is assembled onto the board, pictures of the waveguides and the reference markers are taken while the waveguides are illuminated from the backside. Subsequent image processing yields the offset values of the waveguides relative to the reference markers. We achieved standard deviations below 4 µm for vertical and horizontal alignment. As

this is below the required 8 µm alignment tolerance, less than 0.5 dB loss per interface due to misalignment is expected.

Demonstrator Results

A demonstrator, as shown in Fig. 6, was built to test the performance of the proposed technology. A transmitter and a receiver module are inserted into optical PCBs, which provide polymer optical waveguides to the board edge. A fiber bundle with MT connectors is used as substitution for a backplane to connect the two board edges. Both the connections of the optoelectronic modules in the boards and of the fiber bundles to the board edges use the passive alignment system with MT interface proposed in the preceding sections.

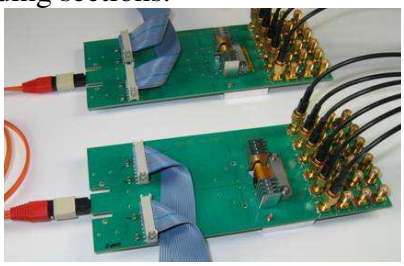

Fig. 6: Twelve-channel board to fiber to board link

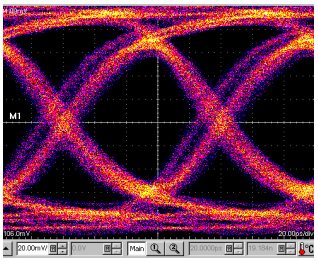

Fig. 7: Eye-diagram (channel 9) at 10 Gbps

A pulse pattern generator is used to create the signals, which are detected by a signal analyzer after the transmission through the optical link. Fig. 7 shows the open eye-diagram of one channel (all 12 channels operating), demonstrating the capability of data transmission at 10 Gbps per channel. Conservatively estimated, the optical losses are below 9 dB, which is well below the limit of 15 dB.

Summary

A passive alignment system that uses one set of copper markers for both optical and mechanical alignment is introduced. The fabrication of this alignment system is compatible with standard PCB processes. Using the system, we can precisely integrate an optical connector (MT standard) into an optical PCB. We achieved alignment tolerances below 4 µm, leading to an optical loss due to misalignment below 0.5 dB.

A system demonstrator based on this passive alignment system successfully transmitted signals over 12 channels, each at a data rate of 10 Gbps, from board to board via an optical fiber cable, through four passively aligned optical interfaces. The calculated optical losses are below 9 dB for this link. A board-to-board link via an optical backplane is the next target.

References

[1] Christoph Berger, Bert Jan Offrein and Martin Schmatz, “Challenges for the introduction of board-level optical interconnect technology into product development roadmaps”, in Proc. SPIE, Vol. 6124, 61240J (Mar. 3, 2006)

[2] T. Lamprecht, et al., “Passive Alignment of Optical Elements in a Printed Circuit Board”, in Proceedings of the ECTC 2006, ISBN: 1-4244-0152-6

[3] S. Bernabé, et al., “Highly Integrated VCSEL-Based 10Gb/s Miniature Optical Sub-Assembly”, in Proceedings of the ECTC 2005, ISBN: 0-7803-8907-7

Membrane couplers and photodetectors for optical interconnections on CMOS ICs

P.R.A. Binetti[1], X.J.M. Leijtens[1], M. Nikoufard[1], T. de Vries[1], Y.S. Oei[1], L. Di Cioccio[2], J-M. Fedeli[2], C. Lagahe[3], R. Orobtchouk[4], C. Seassal[5], P.J. van Veldhoven[1], R. Nötzel[1], M.K. Smit[1]

We introduce a compact photodetector (PD) suitable for photonic interconnections on silicon ICs. In such applications, the optical sources and detectors are linked via waveguides in an interconnection layer which is on top of CMOS circuitry. The photonic devices are fabricated with wafer scale processing steps, guaranteeing compatibility towards future generation electronic IC processing.

In our approach, the optical signals propagating through the waveguides in the interconnection layer are coupled into the PDs via InP membrane waveguides. These coupling structures were designed using 3D modal analysis. Device simulation and fabrication are described in this paper.

Introduction

For future generation electronic ICs, a bottleneck is expected at the interconnect level. The integration of optical sources, waveguides and detectors forming a photonic interconnect layer on top of the CMOS circuitry is a promising solution, providing bandwidth increase, immunity to EM noise and reduction in power consumption [1, 2]. This solution is investigated within the European project PICMOS[6]. In that context, the interconnect layer is built as a passive Si optical wiring layer and the InP based photonic sources and detectors are fabricated with wafer scale processing steps [3]. A possible integration technique, which assures compatibility towards future generation electronic ICs, is based on a die-to-wafer bonding technology [4, 5].

In this paper we present a compact photodetector structure that can be used for the above mentioned optical interconnections. One of the main difficulties in the detector design is achieving a good optical coupling from the photonic wiring layer to the PD. In our structure, an InP membrane waveguide is used to couple the optical signal out of the Si wiring layer. Coupler design and fabrication are described further in this paper.

Detector design

In our approach, the optical coupling from the photonic wiring layer to the PD is realized via an InP membrane input waveguide on top of a SiO_2 bonding layer, like shown

[1]COBRA Research Institute, Technische Universiteit Eindhoven, Postbus 513, 5600 MB Eindhoven, The Netherlands

[2]CEA-LETI, France

[3]TRACIT Technologies, France

[4]LPM - UMR CNRS 5511, France

[5]LEOM, Ecole Centrale de Lyon, France

[6]Photonic Interconnect Layer on CMOS by Wafer-Scale Integration (PICMOS), http://picmos.intec.ugent.be

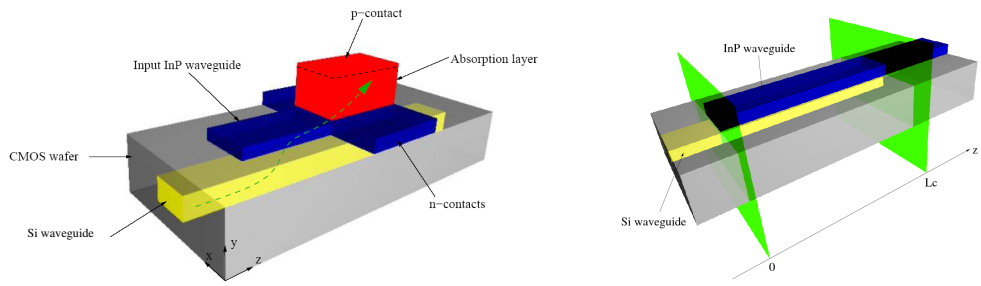

Figure 1: Photodetector structure (left): the dashed arrow indicates how the coupling from the photonic wiring (Si waveguide) layer to the PD takes place by means of an InP membrane input waveguide. The detector is stacked on top of that and the optical power is detected in the absorption layer. The membrane coupler (right) was studied with a 3D modal analysis, considering the three sections shown in the figure.

schematically in Fig. 1. The PD structure is built as a 700 nm InGaAs absorption layer sandwiched between a highly p-doped InGaAs contact layer and a highly n-doped InP layer, which is also used for realizing the membrane waveguide.

The coupling between the InP and the Si waveguides was studied performing a 3D modal analysis. First, the mode indices of the fundamental mode propagating in the Si and InP waveguides and of the even and odd system modes excited in the coupling structure were calculated. Then, the excitation coefficients were calculated by overlapping the Si waveguide fundamental mode and the even/odd system mode. The system modes propagate along the coupling region with different propagation constants $\beta_{\text{even/odd}}$, and after a distance $L_c = \frac{\pi}{\Delta\beta}$, defined as coupling length, the maximum transfer of optical power occurs from the Si to the InP waveguide. The difference $\beta_{\text{even}} - \beta_{\text{odd}}$ is responsable for the system dynamics: by varying the waveguide geometry, different system modes are supported, with different propagation constants. Thus, the mode beating changes and, accordingly, the coupling length. As a last step, the coupling efficiency η_c was calculated by overlapping the fundamental mode guided by the InP waveguide with the field at the section $z = L_c$ (see Fig. 1, right). The calculations were done with the Finite Difference (FD) and the Film Mode Matching (FMM) calculation methods implemented in two different full vectorial mode solvers: Selene, by C2V, and FIMMWAVE, by Photon Design, respectively. Fig 2 (left) shows the mode indices for the coupled waveguides calculated with those two methods. By properly choosing the InP waveguide dimensions, mode matching can be achieved with the Si waveguide, which is 500 nm wide and 220 nm thick. We fixed the InP waveguide thickness to 250 nm, which leads to a predicted optimum waveguide width of 1 μm (0.8 μm), calculated with the FD (FMM) method. When choosing a thinner InP waveguide, e.g. 200 nm, simulations show that the mode matching does not occur. On the other hand, going for a larger thickness would lead to a narrower waveguide, which is more difficult to fabricate. According to the simulations, the predicted coupling length varies between 12 and 14μm, depending on the calculation method used, and a power coupling efficiency of more than 80% can be achieved with a tolerance of $\pm$100 nm for the InP waveguide width (see Fig. 2, right), which is well within the current technology limitations. The PD structure shown in Fig. 1 allows the fabrication of laterally tapered membrane waveguides without additional processing steps, which provides an increase of the alignment tolerance between the waveguides. The device fabrication is described

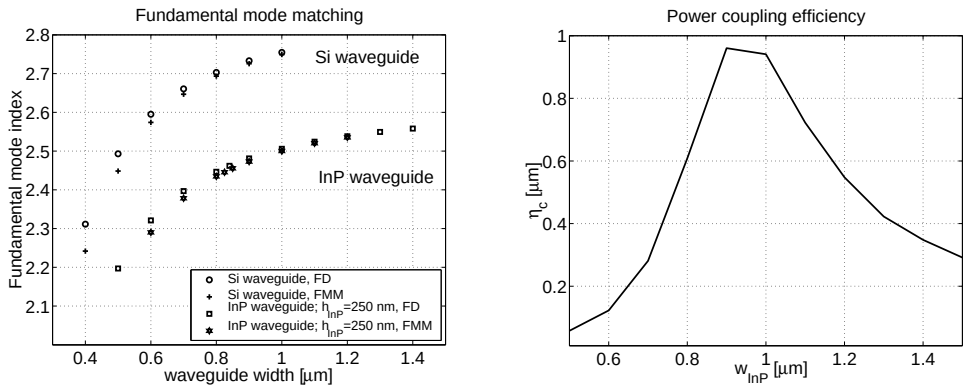

Figure 2: Left: Mode index. Right: Coupling efficiency as a function of the InP waveguide width. The thickness of the membrane waveguide is 250 nm. In this configuration, a power coupling efficiency of more than 80% can be achieved with a tolerance for the InP waveguide width of ± 100 nm.

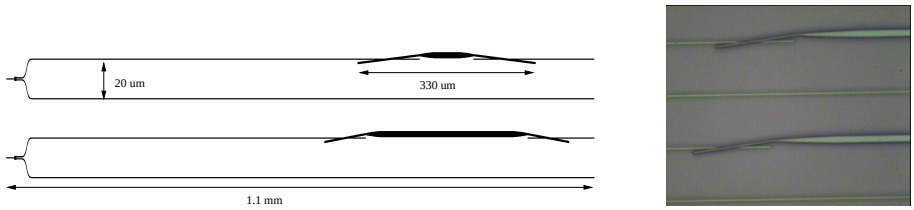

Figure 3: Left: a zoom of the coupler mask layout is shown, overlapped with the Si waveguide pattern. The Si waveguides are split into the upper test branch, over which the InP couplers were fabricated, and the lower reference arm. Slanted coupler layouts are shown in this figure. Right: photograph of the fabricated slanted membrane couplers taken with optical microscope.

in the next section.

Coupler fabrication

Several types of couplers were designed, including straight, laterally tapered, and slanted waveguides. Moreover, couplers with different width, length and lateral offset with respect to the Si waveguides were designed to compensate possible fabrication errors and simulation discrepancies. For the ease of the measurements, the Si waveguides are split into two branches, one of which is used as a reference arm, as can be seen in Fig. 3, left.

The waveguide structure was epitaxially grown on a 2 inch InP substrate. The wafer was then bonded upside down on a SOI wafer, in which the Si wiring had been defined. A 300 nm SiO_2 layer had been deposited at the bonding interface in order to achieve molecular bonding. Afterwards, the InP wafer substrate was wet-chemically removed and the bonded wafer diced. The die processing started with a RIE step to open the alignment markers in the Si layer, underneath the bonded area. Those markers were then used to align the membrane waveguides over the Si wires. This was the most critical step, due to the small waveguide dimensions and the step height between the waveguide layers. After waveguide lithography, the couplers were fabricated by using a combination of wet and dry etching steps. The characterization of the devices is currently under way.

Processing of full PDs like the one shown schematically in Fig. 1 is also currently being done. Two InP-based 2 inch wafers with, respectively, PD and laser layer stacks

were grown and diced in 9×7 mm^2 pieces.

The dies were then bonded upside down on a SOI wafer, in which the Si waveguide pattern had been defined, and the die substrate was wet-chemically removed. Afterwards, samples containing both source and PD dies and test samples with only the source or the detector die were sawn. Sources and PDs patterns were defined by e-beam lithography and transferred to a 150 nm thick SiO_2 hard mask. The same hard mask was then used to dry-etch the membrane waveguides and the PD bottom contact areas, which share the same n-InP layer. The PD mesas were wet-chemically etched (see Fig. 4). We are currently working on the final passivation and metallization processing steps, after which the device characterization will start.

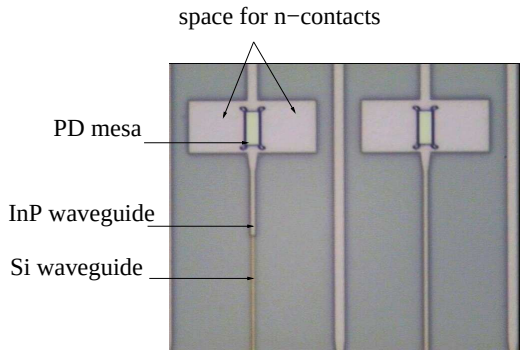

Figure 4: Two PDs are shown in this picture taken with optical microscope. The detector input InP waveguides are aligned over the Si wires and tapered out towards the absorption area underneath the mesas.

Conclusions and acknowledgement

We presented the design of a photodetector structure suitable for integration on an optical interconnect layer on top of CMOS ICs. The device uses an InP membrane input waveguide to couple the optical signal out of the interconnect layer. A 3D modal analysis was performed to design the membrane coupler and predict its performance. It is shown that a 250 nm thick by 14 μm long coupler has a predicted efficiency of more than 80% with a fabrication tolerance for the waveguide width of $1\,\mu\text{m} \pm 150\,\text{nm}$. We are currently working on the device characterization and the PD fabrication.

We acknowledge the support by the EU through the IST-PICMOS project.

References

[1] *International Technology Roadmap for Semiconductors (ITRS)*. http://public.itrs.net.

[2] C. Piguet, J. Gautier, C. Heer, I. O'Connor, and U. Schlichtmann, "Extremely low-power logic," in *Proc.of the Design, Automation and Test in Europe Conference and Exhibition (DATE'04)*, vol. 1, pp. 656–661, Feb. 16-20 2004.

[3] D. Van Thourhout, P. Dumon, W. Bogaerts, G. Roelkens, D. Taillaert, G. Priem, and R. Baets, "Recent progress in SOI nanophotonics waveguides," in *Proc. 31st Eur. Conf. on Opt. Comm. (ECOC '05)*, pp. 241–244, Glasgow, Scotland, Sep. 25–29 2005.

[4] D. Van Thourhout, G. Roelkens, J. Van Campenhout, J. Brouckaert, and R. Baets, "Technology for on-chip optical interconnects," in *LEOS Annual Meeting 2005*, Sydney, Australia, Oct. 2005.

[5] H. Hattori, C. Seassal, E. Touraille, P. Rojo-Romeo, X. Letartre, G. Hollinger, P. Viktorovitch, L. Di Cioccio, M. Zussy, L. E. Melhaoui, and J. Fedeli, "Heterogeneous integration of microdisk lasers on silicon strip waveguides for optical interconnects," *IEEE Photon. Technol. Lett.*, vol. 18, pp. 223–225, Jan. 2006.

Focused-ion-beam fabrication of slanted fiber couplers in silicon-on-insulator waveguides

J. Schrauwen, F. Van Laere, D. Van Thourhout, R. Baets

Photonics Research Group, Department of Information Technology,
Ghent University - IMEC, 9000 Gent, Belgium

The ability for forming complex three dimensional shapes is one of the prime advantages of focused ion beam based micromachining. We have used this technique to fabricate slanted fiber couplers in silicon on insulator. Simulations show coupling efficiencies of up to 63% for fiber couplers with 167 nm slits under an angle of 59° to the surface normal. We have fabricated these devices with focused-ion-beam. The dimensions of the fabricated structures are similar to the design, but we have not measured efficiencies larger than 20%. The difference with the simulated value is probably caused by ion induced damage in the Si crystal.

Introduction

Microfabrication with focused-ion-beam (FIB) consists of hitting a substrate locally with high energy ions; in most commercial systems these are gallium ions with energies around 30 keV. If the substrate is crystalline this process induces lattice damage, makes the top layer amorphous, and implants ions deeper into the substrate [4, 5]. These effects cause optical losses and make the direct fabrication of low-loss photonic devices non-trivial. Nevertheless, FIB remains a promising process due to the flexibility with which we can make photonic devices, e.g. for the fabrication of slanted fiber couplers.
The silicon-on-insulator (SOI) platform is a promising candidate for future ultra-compact photonic integrated circuits because of its compatibility with CMOS technology [1]. The high index contrast in this material system allows for the fabrication of short waveguide bends and thus circuits with a high degree of integration. The SOI wafers we use have a thin top Si layer of 220 nm and a bottom oxide thickness of 1 μm. One of the difficulties of a high contrast platform is the coupling of light from optical fibers, due to the large mode-size mismatch. This problem can be solved by using tapers or grating couplers. The latter are shallow gratings in broad waveguides that diffract light out of the waveguides into vertically positioned single-mode fibers. In previous work we have fabricated these shallow grating couplers with a CMOS compatible process (248 nm deep UV lithography and Inductively Coupled Plasma etching) and optimized the parameters for optimal coupling efficiency (25% and more [2]) and 1550 nm operation [3]. Recently another design was proposed for grating couplers [6], with a theoretical efficiency of over 50%. These structures consist of a series of very narrow slits in the top silicon layer, under an angle of about 60° with the surface normal. Due to this complicated design the structures can't be fabricated with standard CMOS processing, and no fabrication method was proposed so far [6]. In this paper we report on the fabrication of similar structures with FIB. In the first section we detail the design of the slanted fiber couplers with Finite Difference Time Domain (FDTD) methods, and in the second section the fabrication with FIB is evaluated. In previous work grating couplers were designed with various geometries [3]. In the simplest form, completely CMOS compatible, these are shallow etched gratings. They

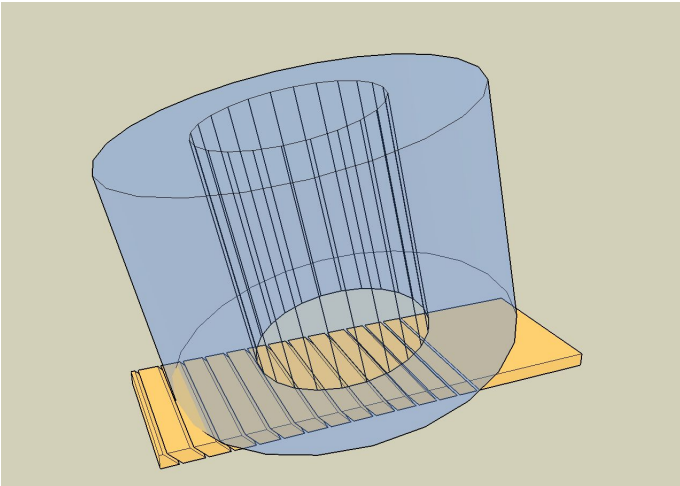

Figure 1: Schematic drawing of the slanted fiber coupler.

have efficiencies of about 25% [2]. When going to more complex fabrication methods, the efficiency of these couplers can be greatly enhanced: by adding a bottom gold mirror by means of bonding, an efficiency of 69% was obtained for the same gratings [7]. All grating couplers from our previous work were designed for coupling of 1550 *nm* infrared light form a waveguide into a fiber positioned at an angle of 10° with respect to the surface normal. This choice was made to reduce reflection by back diffraction into the second order mode. When using slanted gratings, the fraction of light coupled into the second order mode depends on the slant angle of the slits, and can thus be minimized without the necessity of tilting the fiber. However, due to measuring convenience in our setup, we have chosen to design a slanted fiber coupler for coupling to a fiber with 10° tilt, as shown in Figure 1. The advantage of a slanted coupler, as compared to the bottom mirror gratings from [7], is fast fabrication. The slanted couplers can be fabricated with FIB in less than 10 minutes, in situ, anywhere on a wafer.

Simulation

The optimum design has 167 *nm* wide slits, under 59.06° to the surface normal, with a period of 675 *nm*, showed in Figure 2. First we optimized the grating position, then a global scanning of the parameter space and a fine optimization was used to determine slit width, period and angle. This optimization was performed in a simulation environment of 25 μm by 14 μm, with grid cells of 10 *nm* and a PML thickness of 8 cells. A mode was excited in the fiber, and the power coupled to the waveguide mode was calculated, in a two-dimensional approximation and for the polarization with the electric field parallel to the grating slits. The fraction of the measured mode power to the excited power was optimized for 1550 *nm*. For the optimal structure in Figure 2 it is 63.2%.

Fabrication with focused-ion-beam

In previous work we have demonstrated that low-loss fiber couplers can be fabricated with FIB [8]. By using Al_2O_3 as hard mask and I_2 as selective etchant the loss by crystal

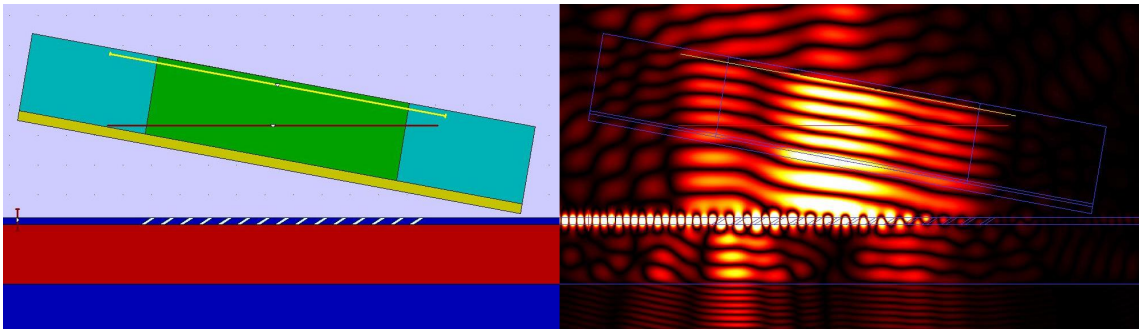

Figure 2: Part of the FDTD simulation environment of the optimal grating with 63.2% efficiency, at the right the magnitude of the electric field parallel to the grating slits is plotted for 1550 *nm* operation.

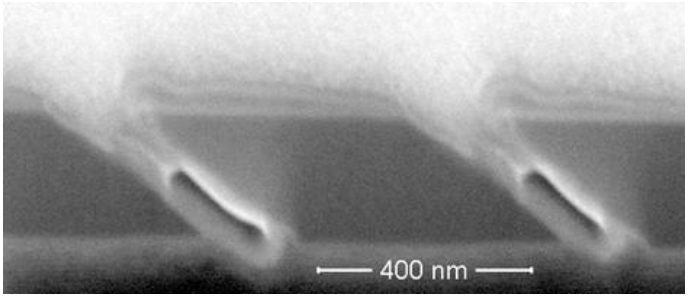

Figure 3: Cross section of two slits of the slanted grating coupler. There is a good agreement with the FDTD designed grating.

damage was minimized. To etch narrow slanted slits we have mounted the sample under 59° relative to the ion beam, and scanned lines under an iodine atmosphere. The etching was performed in an FEI Dualbeam 600. The dose was optimized to etch down to the oxide layer. A cross section of the grating is shown in Figure 3.

Results and discussion

The cross section images of the fabricated gratings are in good agreement with the optimal slanted coupler design. To determine the coupling efficiency we use a fiber-to-fiber transmission measurement for TE polarization. The structure consists of an input coupler, a 10 μm wide waveguide, and an output coupler. We assume that both couplers are identical. We have not measured efficiencies higher than 20%, in contrast to 63% as expected from the simulations. The optical losses are most likely caused by damage to the Si crystal. This result proves that the process proposed in [8] can not straightforward be applied to the etching of slanted grating couplers. We assume that this is caused by the limited iodine etch enhancement due to the difficult placement of the gas injection needle, and due to slow adsorption of iodine on the Si surface in the narrow grooves. Further investigation will show whether slower etching solves this problem.

Conclusions

We have fabricated slanted fiber couplers in silicon-on-insulator with a focused-ion-beam. The etched structures are in good agreement with the FDTD simulated optimal design. However, the measured efficiencies are a factor of three lower than expected. We think that this is caused by a bad penetration of gas molecules in the narrow grooves.

References

[1] W. Bogaerts, R. Baets, P. Dumon, V. Wiaux, S. Beckx, D. Taillaert, B. Luyssaert, J. Van Campenhout, P. Bienstman and D. Van Thourhout, "Nanophotonic Waveguides in Silicon-on-Insulator Fabricated with CMOS Technology", *Journal of Lightwave Technology*, vol. 23(1), pp. 401-412, 2005.

[2] P. Dumon, G.R.A. Priem, L.R. Nunes, W. Bogaerts, D. Van Thourhout, P. Bienstman, T.K. Liang, M. Tsuchiya, P. Jaenen, S. Beckx, J. Wouters and R. Baets, "Linear and nonlinear nanophotonic devices based on silicon-on-insulator wire waveguides", *Japanese Journal of Applied Physics*, vol. 45(8B), pp. 6589-6602, 2006.

[3] D. Taillaert, P. Bienstman and R. Baets, "Compact efficient broadband grating coupler for silicon-on-insulator waveguides" ,*Optics Letters*, vol. 29(23), pp. 2749-2751, 2004.

[4] S. Rubanov and P.R. Munroe, "FIB-induced damage in silicon", *Journal of Microscopy-Oxford*, vol. 214, pp. 213-221, 2004.

[5] A.A. Tseng, "Recent developments in micromilling using focused ion beam technology", *Journal of Micromechanics and Microengineering*, vol. 14(4), pp. R15-R34, 2004.

[6] B. Wang, J.H. Jiang and G.P. Nordin, "Embedded, slanted grating for vertical coupling between fibers and silicon-on-insulator planar waveguides", *IEEE Photonics Technology Letters*, vol. 17(9), pp. 1884-1886, 2005.

[7] F. Van Laere, G. Roelkens, J. Schrauwen, D. Taillaert, P. Dumon, W. Bogaerts, D. Van Thourhout and R. Baets, "Compact grating couplers between optical fibers and Silicon-on-Insulator photonic wire waveguides with 69% coupling efficiency", *OFC 2006, United States*, p. PDP15, 2006.

[8] J. Schrauwen, D. Van Thourhout and R. Baets, "Focused-ion-beam fabricated vertical fiber couplers in silicon-on-insulator waveguides", *Applied Physics Letters*, vol. 89, pp. 141102, 2006.

The Asymptotic Properties of Electromagnetic Pulse Transmission in Photonic Crystals by Saddle-point Analysis

R. Uitham and B.J. Hoenders

University of Groningen and Materials Science Centre,
Nijenborgh 4, 9747 AG Groningen, The Netherlands

We calculate the initial electromagnetic field that has been transmitted through a finite one dimensional photonic crystal in terms of the parameters of the crystal. The shape of the Sommerfeld precursor merely depends on the spatial average of the refractive indices of the homogeneous constituents of the crystal, whereas the shape of the Brillouin precursor depends in a complicated manner on the index contrast.

Introduction

A photonic crystal (PC) [1] is a spatially repeated geometrical structure (crystal) of various material compounds that each individually have in general a different interaction strength with an applied electromagnetic (EM) field. Therefore this field experiences a periodically varying potential. Exactly as in the case of electrons in interaction with a periodic atomic lattice where there are band-gaps in the electron dispersion relation due to Bragg scattering, the lattice of material compounds in PCs gives rise to photonic band-gaps (PBGs). Therefore, with a PC, it is in principle possible to manipulate the propagation of an EM field at the very small scale of its own wavelength.

In order to quantify the effect of a PC on a transmitted EM-pulse, the dependence of the shape (instantaneous amplitude and period) of the transmitted pulse in terms of the parameters of the PC must be calculated. However, since the frequency integral equation for the transmitted field is not analytically solvable, one is directed to search for approximate solutions which usually give good results for the transmitted field only in a restricted range of the time domain.

In the case of pulse propagation in a *homogeneous* medium [2], the saddle-point method is a successful technique to calculate approximately the so-called asymptotic field after a certain propagation distance in the medium. Here with asymptotic field is meant the initial field, immediately behind the wavefront: this is the restriction in the time domain that results from the choice to consider only those frequency components that interact weakly with the system. The saddle-point technique can be extended to *inhomogeneous* media with the concept of equivalent homogeneous index of refraction [3]. Thus we derive an expression of the asymptotic transmitted field in terms of the parameters of the PC.

A substantial drawback of our approach is that it gives only accurate results for the initial transmitted field; we did not obtain results for the more interesting 'main part' of the pulse, where usually the strong interaction with the crystal takes place.

Model

Our model for a one dimensional PC is the rectangular N-layer dielectric, nonmagnetic medium (NLM), depicted in Fig. 1. It is surrounded by another dielectric nonmagnetic

medium.

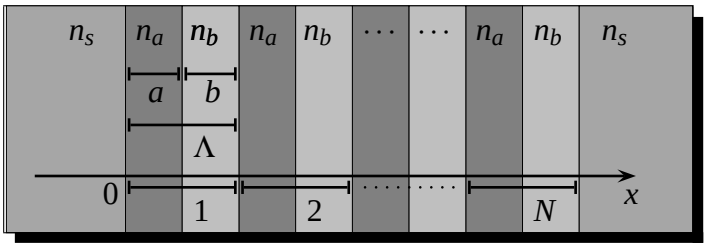

Figure 1: The N-layer medium and its surroundings.

The parameters of this system can be divided into two types. There are *geometrical* parameters that scale the interaction due to scattering of the EM-field at interfaces: these are the slab widths a and b, that add up to the layer width, $a+b=\Lambda$, and N, the total number of layers. The other type of parameters are *material* parameters that describe the (macroscopic) interaction of the EM-field with the atoms: these are the permittivity ε for the electric component and the permeability μ for the magnetic component, or, equivalently, the refractive index $n=\sqrt{\varepsilon\mu}$ and the impedance $Z=\sqrt{\frac{\mu}{\varepsilon}}$. However, for nonmagnetic media, $\mu=1$ and the material interaction can be stated in terms of the refractive index only. The homogeneous refractive indices of the slabs are n_a and n_b and of the surrounding medium is n_s.

In information technology, often mentioned as a significant application area for PCs, information is usually encoded in *optical* EM-pulses. We will therefore consider optical applied pulses and PCs that have a PBG in the optical range of the frequency spectrum. In order to obtain a band-gap in the visible part of the EM-spectrum, where the frequency $\omega\sim 10^{15}$rad/s, Λ should be of the order of 10^{-7}m, assuming that all refractive indices are of order 10^0.

The two restrictions that we impose on our applied EM-pulse, coming in from the left-hand-side of Fig. 1, are that it lasts a finite amount of time T (measured at the entrance plane $x=0$) and that its amplitude is finite. An example pulse is depicted in Fig. 2.

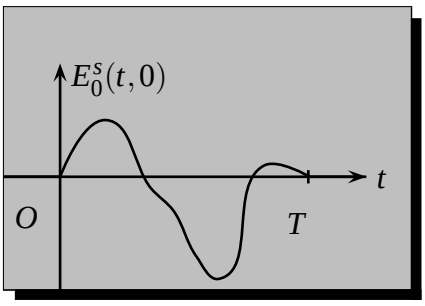

Figure 2: Time dependence of electric field component, evaluated at entrance plane of NLM, of an example applied pulse

The electric component of the EM pulse is in a plane wave decomposition

$$E_0^s(t,x)=\int \mathrm{d}\omega \tilde{E}_0^s(\omega)\mathrm{e}^{-\mathrm{i}\omega(t-n_s(\omega)x/c)}, \tag{1}$$

where the spectral density is

$$\tilde{E}_0^s(\omega)=\frac{\sum_m}{2\pi}\frac{\omega_m E_{0m}}{\omega^2-\omega_m^2}\left((-1)^m\mathrm{e}^{\mathrm{i}\omega T}-1\right). \tag{2}$$

Here, E_{0m} denotes the amplitude at carrier frequency

$$\omega_m=\frac{m\pi}{T}. \tag{3}$$

For purely optical pulses, the E_{0m} takes on nonzero values only at carrier frequencies that lie in the optical range.

Theory

The exact expression for the transmitted field, evaluated at the plane $x=N\Lambda$, is, in mono-exponential form,

$$E_N^s(t,N\Lambda)=\int \mathrm{d}\omega \tilde{E}_0(\omega)\mathrm{e}^{\frac{N\Lambda}{c}\nu_N(\omega)}, \tag{4}$$

in which the propagation is described by the function

$$v_N = -\mathrm{i}\omega\left(\Theta_N - n_N\right) \equiv X_N + \mathrm{i}Y_N \tag{5}$$

with X_N, Y_N real. Here, $\Theta_N = \frac{ct}{N\Lambda}$ is the time in natural units and

$$n_N = \frac{-\mathrm{i}c}{N\Lambda}\frac{1}{\omega}\log t_N \tag{6}$$

is the equivalent homogeneous index of refraction for the NLM, with t_N the transmission coefficient.

The integration path in Eq. (4) is deformed such that X_N is minimal. Denote the deformed path as S. This path S has been sketched in Fig. 3 in a small environment (circle) around the SP, taken on at frequency ω_s. On S, the SP of X_N are crossed along lines of steepest descent (SD). Dominant contributions in Eq. (4) then come from the peaks of X_N around SP. These peaks are sharp when the scaling parameter $\frac{N\Lambda}{c}$ is 'large'. Denote the locations of SPs in the complex frequency plane as ω_s. When ω_s is not too close to the optical ω_m where E_{0m} is nonzero, then the spectral density $\tilde{E}_0^s$ is nearly constant around this SP (that is, for $\omega \simeq \omega_s$) and satisfies $\tilde{E}_0^s(\omega) \simeq \tilde{E}_0^s(\omega_s)$. In that case, Eq. (4) is approximately equal to a Gaussian integral,

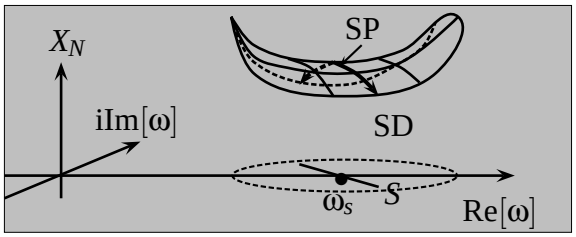

Figure 3: The integration path S near a saddle-point

$$E_N^s(t, N\Lambda) \simeq \tilde{E}_0(\omega_s)\mathrm{e}^{\frac{N\Lambda}{c}v_N(\omega_s)}\int_S \mathrm{d}\omega \mathrm{e}^{\frac{N\Lambda}{c}v_N''(\omega_s)(\omega-\omega_s)^2}. \tag{7}$$

This approximation does therefore not give contributions from frequency components close to, or inside, the optical PBG.

Results

For the very large-frequency components (near SP with $|\omega_s| >>$optical frequencies), the effective index may be expanded about infinite frequency. Up to second order, this series is

$$n_N(\omega) = n_N(\infty) + \left(-\omega^2 n_N'\right)|_{|\omega|=\infty}\omega^{-1} + \frac{1}{2!}\left(\omega^3\left(\omega n_N'' + 2n_N'\right)\right)|_{|\omega|=\infty}\omega^{-2}. \tag{8}$$

For Lorentz type slab refractive indices, we have calculated,

$$n_N(\infty) = 1, \quad \left(-\omega^2 n_N'\right)|_{|\omega|=\infty} = 0, \quad \left(\omega^3\left(\omega n_N'' + 2n_N'\right)\right)|_{|\omega|=\infty} = \omega_{p\Lambda}^2, \tag{9}$$

where $\omega_{p\Lambda}^2 \equiv \frac{a\omega_{pa}^2 + b\omega_{pb}^2}{\Lambda}$ is the average plasma frequency squared. These components give rise to the Sommerfeld precursor, starting at times $\delta_N^S \equiv \Theta_N - n_N(\infty) \geq 0$. Its amplitude is found as

$$E_N^s(t, N\Lambda) = \sum_m \frac{\omega_m}{\omega_{p\Lambda}} E_{0m}\sqrt{2\delta_N^S} J_1\left(\omega_{p\Lambda}\frac{N\Lambda}{c}\sqrt{2\delta_N^S}\right), \tag{10}$$

where J_1 denotes the first order Bessel function.

For the very small-frequency components (near SP with $|\omega_s| <<$optical frequencies), n_N may be expanded about zero frequency,

$$n_N(\omega) = n_N(0) + n'_N(0)\omega + \frac{1}{2!}n''_N(0)\omega^2, \quad |\omega| << \text{optical frequencies} \tag{11}$$

where we have calculated the coefficients as

$$n_N(0) = \left(\frac{n_\Lambda^2 + n_s^2}{2n_s}\right)\Big|_{\omega=0}, \qquad \left(n_\Lambda^2 \equiv \frac{an_a^2 + bn_b^2}{\Lambda}\right) \tag{12}$$

$$n'_N(0) = \left(\frac{n_\Lambda^2 + n_s^2}{2n_s}\right)'\Big|_{\omega=0} + \frac{\mathrm{i}N\Lambda}{2c}\left(\frac{n_\Lambda^2 - n_s^2}{2n_s}\right)^2\Big|_{\omega=0}, \tag{13}$$

$$n''_N(0) = \left(\frac{n_\Lambda^2 + n_s^2}{2n_s}\right)''\Big|_{\omega=0} + \frac{\mathrm{i}N\Lambda}{c}\left(\left(\frac{n_\Lambda^2 - n_s^2}{2n_s}\right)^2\right)'\Big|_{\omega=0} \tag{14}$$

$$-\frac{2}{3}\frac{N^2\Lambda^2}{c^2}\left(\frac{n_\Lambda^2 + n_s^2}{2n_s}\right)\left(\frac{n_\Lambda^2 - n_s^2}{2n_s}\right)^2\Big|_{\omega=0} + \frac{ab}{3c^2}\left(n_a^2 - n_b^2\right)\left(\frac{\frac{an_a^2 - bn_b^2}{\Lambda} - \frac{a-b}{\Lambda}n_s^2}{2n_s}\right)\Big|_{\omega=0}. \tag{15}$$

Note that the slab index difference is only in term $n''_N(0)$. The small-$|\omega|$-components give rise to the Brillouin precursor at times $\delta_N^B \equiv \delta_N^S - n_N(0) \geq 0$,

$$E_N^S(t, N\Lambda) \simeq \sqrt{\frac{2c}{\pi N\Lambda\sqrt{D_N}}}\sum_m \frac{E_{0m}}{\omega_m}\mathrm{e}^{\frac{N\Lambda}{c}X_N(\omega_s)}\cos\left(\frac{N\Lambda}{c}Y_N(\omega_s) + \pi/4\right), \tag{16}$$

where the SP-location $\omega_s = \mathrm{i}\left(\frac{2\mathrm{i}n'_N(0)}{3n''_N(0)}\right) + \frac{\sqrt{D_N}}{3n''_N(0)}$ with $D_N = 4n'_N(0)^2 + 6n''_N(0)\delta_N^B$.

Conclusions

We have calculated the initially transmitted field through an NLM, expressed in the parameters of the NLM. As in the case of a homogeneous medium, the wave-front propagates at the speed of light c, immediately followed by the Sommerfeld precursor. This precursor experiences the spatial average of the slab indices: it is not influenced by the slab contrast. The arrival time of the Brillouin precursor is also not influenced by the slab contrast, but its shape is: roughly, its amplitude and period decrease with contrast.

References

[1] J.D. Joannopoulos, R.D. Meade and J.N. Winn, Photonic Crystals, Princeton University Press, Princeton, 1995.

[2] L. Brillouin, Wave propagation and group velocity, Academic Press, New York and London, 1960

[3] M. Centini, C. Sibilia, M. Scalora, G. D'Aguanno, M. Bertolotti, M.J. Bloemer, C.M. Bowden and I. Nefedov, *Phys. Rev. E.* Vol. 60, Nr. 4-B, 1999.

Semiconductor Optical Bloch Equations Explain Polarization Dependent Four Wave Mixing Quantum Beats in Bulk Semiconductors

W. Wang[1], J. Zhang[2] and D. Lenstra[1]

Department of Physics and Astronomy, Vrije Universiteit Amsterdam,
De Boelelaan 1081, 1081HV, Amsterdam, The Netherlands[1], IMR, Salford University, Manchester, U.K.[2]

We re-examined the semiconductor Bloch equations (SBE) and found that, excluding the many-body electron Coulomb interaction, SBE do not reduce to the optical Bloch equations (OBE). By applying OBE on semiconductors straightforward, we propose an explanation for the polarization dependent four wave mixing (FWM) quantum beats, which could not be explained by the conventional SBE but attributed to bi-exciton processes. We suggest that this effect is simply a coherent process rather than due to electron-electron Coulomb interaction; the coherence transfer between the excited states accounts for the FWM in the configuration with pump and probe in orthogonal polarization states.

Introduction

Polarization-dependent four wave mixing (FWM) quantum beats [1–4] have been observed after simultaneous excitations of two optical transitions, i.e. heavy-hole and light-hole. The signal magnitude and its beat phase depend on the polarization of the pump and probe with respect to each other. This phenomenon has been analyzed with applying semiconductor Bloch equations (SBE) for excitations in a six-band model by broad spectrum pump-probe pulses. [1, 2] However this theory predicts *identical* FWM intensities for the two polarization configurations: pump and probe have either parallel or perpendicular linear (circular) polarizations. Since then, a great effort has been devoted to theoretically explain this phenomenon. One of the successful explanations is the bi-exciton theory. [3, 4] However, why the optical Bloch equation (OBE) can do very well in atomic optics, but the SBE fails in this specific investigation is an interesting question, and it should not be, without constructive considerations, simply answered by the fact that SBE formalism does not include exciton-exciton processes or a Hartree-Fock approximation is not capable to describe quasi-stationary of the excited semiconductor. [5]

The SBE is developed as the similar basis as the OBE. [6, 7] The main extra efforts of the former theory are its focusing on the electron many-body effects, such as semiconductor band gap renormalization, excitonic effects, phase-space filling, etc, which do not exist in OBE. However, in the present work we will completely neglect the Coulomb interaction between the carriers, which means that no excitonic effects are considered. Based on this assumption, we compare the SBE and OBE formalism. We find that the SBE do not reduce to the OBE formalism, contrary to what one would expect.

In an electron two-level system with vacuum state is defined as $|0_a 0_b\rangle$, i.e. an electron can be in two states: $|a\rangle$ and $|b\rangle$. In case of the resonant light excitation, the *system* of the electron can be inverted from the electron system ground state $|g\rangle$ which gives $|0_a 1_b\rangle$, to the system excited state $|e\rangle$ which gives $|1_a 0_b\rangle$. Correspondingly, in the SBE, the states of the electron system $|e\rangle$ and $|g\rangle$ will be given as $|1_c 0_v\rangle$ and $|0_c 1_v\rangle$, in case that an electron in semiconductors can only be in two states: $|c\rangle$ and $|v\rangle$.

In the normal formalism of SBE, what one finds are a coupled equations between polarization P_{cv} and the occupation probabilities for the electron in the state $|c\rangle$ and $|v\rangle$: n_c and n_v. [7, 8] However, to be consistent with the OBE formalism, the coupled equations should be between the electron system polarization P_{eg} and the occupation probabilities of the *electron system* in the state $|e\rangle \equiv |1_c 0_v\rangle$ and $|g\rangle \equiv |0_c 1_v\rangle$: n_e and n_g. Although n_c (n_v) incidently equals n_e (n_g) in the electron two-level system, the physical meaning is completely different and will result in errors in case that complicated many-level system is considered.
In this work, we strictly follow OBE formalism, discard the electron many-body effects. By this semiconductor OBE, we derive the polarization dependent FWM quantum beats in semiconductors without introducing any bi-exciton interaction effects. In this way we suggest that FWM quantum beats might be a purely coherent light-matter interaction effect, rather than due to something, such as electron-electron interaction process.

Modelling

In this work we do not consider the electron Coulomb interaction, we simply treat the semiconductor as a many-level atomic model with considering electron spin states. The ground state of the heavy-hole electron system, as well as those of the light-hole electron system, are described as

$$|hg\rangle = a_{h1}^{\dagger} a_{h2}^{\dagger} |0_h\rangle \,, |lg\rangle = a_{l1}^{\dagger} a_{l2}^{\dagger} |0_l\rangle \,. \tag{1}$$

Next, by Eq.(1) we derived the excited stats $|ex\rangle$ and $|ey\rangle$ of the semiconductor in case of x and y polarized light excitation, only resonant excitation are taken into account

$$\begin{aligned}
|ex\rangle &= \sum_{\theta,\phi} \Bigg\{ \Big[-a_{c1}^{\dagger} a_{h2}^{\dagger} bu - a_{c1}^{\dagger} a_{h1}^{\dagger} (wR_h - cu) + a_{c2}^{\dagger} a_{h2}^{\dagger} (uc^* - wR_h) + a_{c2}^{\dagger} a_{h1}^{\dagger} ub^* \Big] |0_h\rangle \\
&\quad + \Big[a_{c1}^{\dagger} a_{l2}^{\dagger} (uR_l + wc^*) + a_{c1}^{\dagger} a_{l1}^{\dagger} wb - a_{c2}^{\dagger} a_{l2}^{\dagger} wb^* + a_{c2}^{\dagger} a_{l1}^{\dagger} (wc + uR_l) \Big] |0_l\rangle \Bigg\} + c.c. \\
|ey\rangle &= \sum_{\theta,\phi} i \Bigg\{ \Big[-a_{c1}^{\dagger} a_{h2}^{\dagger} bu + a_{c1}^{\dagger} a_{h1}^{\dagger} (wR_h + cu) - a_{c2}^{\dagger} a_{h2}^{\dagger} (wR_h + uc^*) - a_{c2}^{\dagger} a_{h1}^{\dagger} ub^* \Big] |0_h\rangle \\
&\quad + \Big[a_{c1}^{\dagger} a_{l2}^{\dagger} (uR_h - wc^*) - a_{c1}^{\dagger} a_{l1}^{\dagger} wb - a_{c2}^{\dagger} a_{l2}^{\dagger} wb^* - a_{c2}^{\dagger} a_{l1}^{\dagger} (uR_l - wc) \Big] |0_l\rangle \Bigg\} + c.c.
\end{aligned} \tag{2}$$

with $u = -\sqrt{1/2}$ and $w = \sqrt{1/6}$; b, c, R_h and R_l are defined as in [9]. Here, the summation of θ and ϕ gives the total transition magnitude, or the full transition matrix, from electron valence state $|v\rangle$ to electron conduction state $|c\rangle$. From Eq.(2), one can find the excited states essentially are pairs of electrons in both conduction bands and valence bands but with difference phase.
The system Hamiltonian is

$$H_0 = \varepsilon_{ex} a_{ex}^{\dagger} a_{ex} + \varepsilon_{ey} a_{ey}^{\dagger} a_{ey} + \varepsilon_{hg} a_{hg}^{\dagger} a_{hg} + \varepsilon_{lg} a_{lg}^{\dagger} a_{lg}. \tag{3}$$

The energy ε_{ex}, ε_{ey}, ε_{hg} and ε_{lg} are defined for a single electron. For simplicity, we assume the energy $\varepsilon_{ex} = \varepsilon_{ey} = 0$, thereby ε_{hg} and ε_{lg} are the photon resonant energies but with minus sign. The states energy difference of $|hg\rangle$ and $|lg\rangle$ is ε_{lh} defined as $\varepsilon_{hg} - \varepsilon_{lg}$.

The dipole coupling to a laser field is described as

$$H_I = -\mathcal{E}(t)\left(a_{ex}^{\dagger}a_{hg}e^{i\alpha_1} + a_{ey}^{\dagger}a_{hg}e^{i\alpha_2} + a_{ex}^{\dagger}a_{lg}e^{i\beta_1} + a_{ey}^{\dagger}a_{lg}e^{i\beta_2} + h.c.\right). \tag{4}$$

The modulus of the optical transitions between $|g\rangle \rightarrow |ex\rangle$ and $|g\rangle \rightarrow |ey\rangle$ are equal in both $|hg\rangle$ and $|lg\rangle$ cases, but the phase, α_1, α_2, β_1, and β_2 are different. We derived a relation between the phases of the optical transition matrixes,

$$\exp[i(\alpha_1 - \alpha_2)] = -\exp[i(\beta_1 - \beta_2)]. \tag{5}$$

After some straightforward algebra, we obtain for the third-order nonlinear optical polarization, origin of the FWM signal. For polarization configurations of pump and probe parallel and orthogonal.

$$\begin{aligned}
\mathcal{P}_{\parallel}^{(3)}(t) &= -4i\Theta(t)\Theta(-\tau)E_pE_pE_t\left(e^{-i(\varepsilon_h - i\gamma_2)t} + e^{-i(\varepsilon_l - i\gamma_2)t}\right)\left(e^{i(\varepsilon_h - i\gamma_2)\tau} + e^{i(\varepsilon_l - i\gamma_2)\tau}\right) \\
\mathcal{P}_{\perp}^{(3)}(t) &= -i\Theta(t)\Theta(-\tau)E_pE_pE_t\left(e^{-i(\varepsilon_h - i\gamma_2)t} + e^{-i(\varepsilon_l - i\gamma_2)t}\right)\Big(e^{i(\varepsilon_h - i\gamma_2)\tau}e^{i(\alpha_1 - \alpha_2)} + \\
&\quad e^{i(\varepsilon_l - i\gamma_2)\tau}e^{i(\beta_1 - \beta_2)}\Big)
\end{aligned} \tag{6}$$

By the relation in Eq.(5), one can easily find that the two cases in Eq.(6) are different by a sign in the last term and different magnitudes with a factor 1/4, thereafter the ratio of the intensities of FWM signal in the two cases will be 1/16. In case of $\tau = 0$, $\mathcal{P}_{\parallel}^{(3)}$ is on the peak of the beats, but $\mathcal{P}_{\perp}^{(3)}$ on the bottoms of the beats. There is an exact phase difference π between the two cases as shown in Fig.(1).
The calculation of Fig.(1) are based on some parameters: the phase relaxation time $\gamma_2 = 4$ ps; the resonant optical transitions of $|hg\rangle \rightarrow |e\rangle$ is at wavelength 810 nm. The difference of the energy between $|hg\rangle$ and $|lg\rangle$ is 4.2 meV. The beats modulation depth is adjusted by a parameter f_{lh}. In the idea case, the optical transitions are equally taken place at $|hg\rangle$ and $|lg\rangle$, namely $f_{lh} = 1$, the modulation depth will between modulated 1 and 0. In this calculation, we adopt $f_{lh} = 0.75$ to avoid zero point. However, we do not attribute this unbalance to the heavy-hole and light-hole optical transition matrixes. [1, 2] As we have shown that the modulus of the optical transition matrixes are just equal. The reason might be the state-density dependent optical excitations of heavy-hole and light-hole bands. Also the detuning optical excitations and the summation of the optical transitions with different positions $\vec{k}$ could contribute to this by phase interference to mitigate the beats modulation depth. However it is not within the aim of this work in this stage.

Conclusion

In conclusion, we have re-examined the semiconductor Bloch equations (SBE) and found that, excluding the many-body electron Coulomb interaction, SBE do not reduce to the optical Bloch equations (OBE). We applied OBE on bulk semiconductors straightforward, neglecting electron-electron Coulomb interaction, and proposed an explanation for the polarization dependent four wave mixing (FWM) quantum beats, which could not be

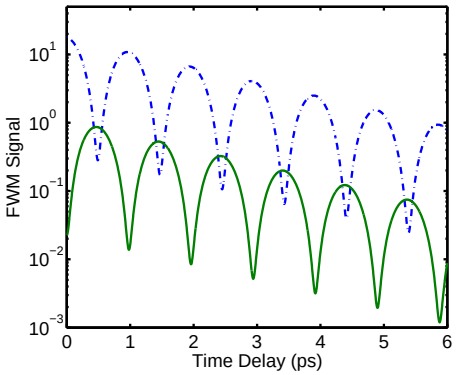

Figure 1: The FWM signal quantum beats as a function of pump-probe time delay. The dash-dotted and solid lines for parallel and orthogonal polarized pump-probe configurations.

explained by the conventional SBE but attributed to bi-exciton processes. We suggest that this effect might be simply a coherent process rather than due to electron-electron Coulomb interaction.

In case of a configuration with pump and probe in orthogonal polarization states, FWM can be generated due to the coherence transfer between the two excited states. In the investigates of polarization dependent FWM quantum beats, this coherence transfer could make the main role in the reproducing experimental results.

References

[1] D. B. Stefan Schmitt-Rink, Volker Heuckeroth, Peter Thomas, Peter Haring, Gerd Maidorn, Huib Bakker, Karl Leo, Dai-Sik Kim and Jagdeep Shah, ”Polarization dependence of heavy- and light-hole quantum beats,” Phys. Rev. B, vol. 46, p. 10460, 1992.

[2] D. Bennhardt, P. Thomas, R. Eccleston, E. J. Mayer, and J. Kuhl, ”Polarization dependence of four-wave-mixing signals in quantum wells,” Phys. Rev. B, vol. 47, p. 13485, 1993.

[3] E. J. Mayer, G. O. Smith, V. Heuckeroth, J. Kuhl, K. Bott, A. Schulze, T. Meier, D. Bennhardt, S. W. Koch, P. Thomas, R. Hey, and K. Ploog, ”Evidence of biexcitonic contributions to four-wave mixing in GaAs quantum wells,” Phys. Rev. B, vol. 50, p. 14730, 1994.

[4] T. Aoki, G. Mohs, M. Kuwata-Gonokami, and A. A. Yamaguchi, ”Influence of Exciton-Exciton Interaction on Quantum Beats,” Phys. Rev. Lett., vol. 82, p. 3108, 1999.

[5] W. Schäfer, D. S. Kim, J. Shah, T. C. Damen, J. E. Cunningham, K. W. Goossen, L. N. Pfeiffer, and K. K ohler, ”Femtosecond coherent fields induced by many-particle correlations in transient four-wave mixing,” Phys. Rev. B, vol. 53, p. 16429, 1996.

[6] M. Lindberg and S. W. Koch, ”Effective Bloch equations for semiconductors,” Phys. Rev. B, vol. 38, p. 3342, 1992.

[7] W. W. Chow, S. W. Koch, and M. S. III, Semiconductor-laser physics. Berlin: Springer, 1994.

[8] H. Haug and S. W. Koch, Quantum Theory of the Optical and Electronic Properties of Semiconductors, 3 ed. Singapore: World Scientific, 1994.

[9] W. Wang, K. Allaart, and D. Lenstra, ”Correlation between electron spin and light circular polarization in strained semiconductors,” Phys. Rev. B, vol. 74, p. 073201, 2006.

Judd-Ofelt Analysis of $Nd(TTA)_3Phen$-doped 6-FDA/Epoxy Planar Waveguides

J. Yang, M.B.J. Diemeer, L.T.H. Hilderink, R. Dekker, and A. Driessen

University of Twente, Integrated Optical Microsystems Group, P.O. Box 217, Enschede, the Netherlands

The fluorescent complex $Nd(TTA)_3Phen$ (TTA = thenoyltrifluoroacetone, Phen = 1, 10-phenanthroline), was doped into the host material 6-FDA epoxy (6-fluorinated-dianhydride cured epoxy). The room-temperature absorption spectrum of Nd^{3+} transitions was experimentally obtained, with which the Judd-Ofelt model was applied to determine the Judd-Ofelt parameters. These parameters are used to calculate the emission probabilities of transitions and branching ratios of the Nd^{3+} from the excited-state $^4F_{3/2}$ to lower-lying manifolds. The radiative lifetime of $^4F_{3/2}$ was obtained from the emission probabilities. The results of the analysis indicate this Nd (III) complex doped polymer material is promising to be used in planar waveguide lasers and amplifers.

Introduction

There has been much interest in rare-earth-doped polymer planar optical waveguide for applications in amplifiers and lasers. Polymers are promising host candidates for these applications because of their excellent properties such as high transparency, low cost, and easy fabrication. One way to incorporate rare-earth ions into a polymer is to encapsulate the ions in organic chelates and dope these complexes directly. Recently, work has been done on rare-earth-doped polymer planar waveguides [1, 2]. In our work, $Nd(TTA)_3Phen$ was synthesized and doped in to the fluorinated host 6-FDA epoxy. The ligands with fluorine and the fluorination of the host material can improve the luminescent quenching from C-H and water.

Knowledge of the transition intensities of 4f-4f transitions and of the absorption and emission cross sections is the first step in investigating the performance of the rare-earth-doped waveguides. In this paper, we used the Judd-Ofelt method [3, 4] to analyse the measured absorption spectrum of Nd^{3+} transitions. This method is successfully applied for the calculation and characterization of the optical transitions in rare-earth doped materials [5~8]. The results of the analysis indicate this Nd (III) complex doped polymer material is promising to be used in planar waveguide lasers and amplifers.

Experimental procedure

The $Nd(TTA)_3Phen$ was synthesized according to the procedure as described in [9]. A film of $Nd(TTA)_3Phen$ doped 6-FDA epoxy was spin-coated on an thermally oxidized wafer. The refractive index and the thickness as determined with a prism coupler were 1.53 (at 632.5nm) and 4.3 μm, respectively. The concentration was 1.1×10^{19} Nd/cm^3.

White light was coupled into the film and coupled out after propagating a certain distance through the film using a prismcoupler. Varying the propagation distance and collecting the light from the outcoupling prism by a spectrum analyzer Spectro320, the room-temperature loss spectrum of Nd^{3+} in 6-FDA epoxy was recorded. After subtraction of the background loss, the absorption spectrum of Nd^{3+} in 6-FDA epoxy was obtained from the recorded

spectrum (Fig. 1).

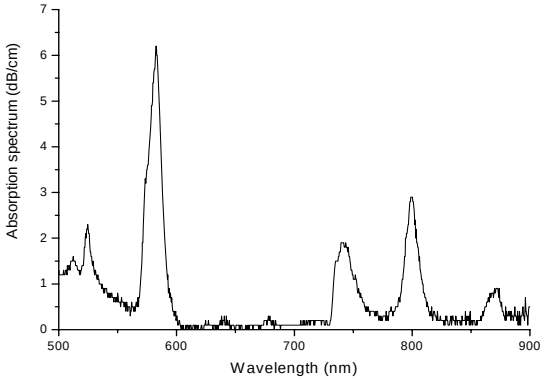

Fig. 1. Room temperature absorption spectrum of Nd^{3+} in 6-FDA epoxy from 450nm to 900nm.

Data analysis

The electric dipole line strength S is adopted to describe the transition between two of the eigenstates of the ion in the Judd-Ofelt theory. The line strength S between initial state J characterized by (S, L, J) and the final state J' given by (S', L', J') can be written as [5~8]:

$$S_{calc}(J \to J') = \sum_{t=2,4,6} \Omega_t \left| \left\langle (S,L)J \left\| U^{(t)} \right\| (S',L')J' \right\rangle \right|^2 = \Omega_2 \cdot \left[U^{(2)}\right]^2 + \Omega_4 \cdot \left[U^{(4)}\right]^2 + \Omega_6 \cdot \left[U^{(6)}\right]^2 \quad (1)$$

where Ω_t (t=2,4,6) are the Judd-Ofelt parameters, and $U^{(t)}$ (t=2,4,6) are the doubly reduced matrix elements depend only on angular momentum. As $U^{(t)}$ (t=2,4,6) are independent of the host, the values can be obtained from some former papers. [5, 10]

The parameters Ω_t (t=2,4,6) are determined by measuring the line strength for a number of ground-state transition. Four absorption peaks can be observed from Fig 1 and the four peak wavelengths of the Nd^{3+} bands are given in Table 1.

The measured line strengths $S_{meas}(J \to J')$ of the bands are determined using following expression:

$$S_{meas}(J \to J') = \frac{3ch(2J+1)n}{8\pi^3 \lambda e^2 N_0} \left[\frac{9}{(n^2+2)^2} \right] \Gamma \quad (2)$$

where c is the velocity of light, h is the Planck's constant, e is the elementary charge, J is the angular momentum, N_0 is the density of ion, λ is the mean wavelength of the absorption bands, n is the wavelength-dependent refractive index which is determined from Sellmeier's dispersion equation, and $\Gamma = \int \alpha(\lambda) d\lambda$ is the integrated absorption coefficient. The results

Table 1. Values of reduced matrix elements for the absorption transitions of Nd^{3+} in 6-FDA epoxy at 300K.

Transition (from $^4I_{9/2}$)	λ (nm)	n	$\left[U^{(2)}\right]^2$	$\left[U^{(4)}\right]^2$	$\left[U^{(6)}\right]^2$
$^4G_{5/2}$+$^2G_{7/2}$	580	1.5316	0.9710	0.5897	0.0663
$^4F_{7/2}$+$^4S_{3/2}$	740	1.5239	0.0010	0.0448	0.6582
$^4F_{5/2}$+$^2H_{9/2}$	795	1.5221	0.0100	0.2431	0.5148
$^4F_{3/2}$	865	1.5206	0	0.2296	0.0563

Table 2. Measured and calculated line strengths of Nd^{3+} in 6-FDA epoxy at 300K.

Transition (from $^4I_{9/2}$)	λ (nm)	n	Γ (nm cm^{-1})	S_{meas} (10^{-20} cm^2)	S_{calc} (10^{-20} cm^2)
$^4G_{5/2}+^2G_{7/2}$	580	1.5316	18.7295	22.1520	22.1570
$^4F_{7/2}+^4S_{3/2}$	740	1.5239	8.4009	7.8329	8.1997
$^4F_{5/2}+^2H_{9/2}$	795	1.5221	10.3377	8.9276	8.4069
$^4F_{3/2}$	865	1.5206	2.7888	2.2300	2.6969

of S_{meas} are given in Table 2.

From the least-squares fitting of S_{meas} to S_{calc}, the values of the three parameters Ω_t (t=2,4,6) can be obtained as follows:

$$\Omega_2 = 16.64\times10^{-20}cm^2, \Omega_4 = 8.85\times10^{-20}cm^2, \Omega_6 = 11.83\times10^{-20}cm^2$$

We used them to recalculate the transition line strengths of the absorption bands from Eq. (1) and the results are in Table 2.

Next, they were applied in Eq. (1) to calculate the transition line strength of the upper state transitions which are give in Table 3. Then, we obtained the corresponding radiative decay rate, radiative lifetime and fluorescence branching ratio.

The radiative decay rates $A(J \to J')$, for electric dipole transitions between an excited states (J) and the lower-lying terminal manifolds (J') were calculated from:

$$A(J \to J') = \frac{64\pi^4 e^2}{3h(2J+1)\lambda^3}\frac{n(n^2+2)^2}{9}S_{calc}(J \to J') \quad (3)$$

From the radiative decay rates, the radiative lifetime τ_r for an excited state (J) and the fluorescence branching ratios $\beta(J \to J')$ were obtained from:

$$\tau_r = \frac{1}{\sum A(J \to J')} \quad (4)$$

$$\beta(J \to J') = \frac{A(J \to J')}{\sum A(J \to J')} = A(J \to J')\tau_r \quad (5)$$

All results are given in Table 3.

Table 3. Predicted fluorescence line strength, radiative decay rates, radiative lifetimes, and branching ratios of Nd^{3+} in 6-FDA epoxy at 300K.

Transition	S_{calc} (10^{-20} cm^2)	$A_{JJ'}$ (s^{-1})	τ_{rad} (ms)	$\beta_{JJ'}$
$^4F_{3/2} \to {}^4I_{9/2}$	2.6969	1.9491	0.18259	0.3559
$^4F_{3/2} \to {}^4I_{11/2}$	6.0710	2.9168		0.5326
$^4F_{3/2} \to {}^4I_{13/2}$	2.5080	0.5812		0.1061
$^4F_{3/2} \to {}^4I_{15/2}$	0.3313	0.0297		0.0054

Discussion of results

With the standard Judd-Ofelt method, the analysis of absorption spectrum of Nd^{3+} in 6-FDA epoxy has been performed.

It has been shown that Ω_2 is quite sensitive to the metal-ion environment [11]. A large value of Ω_2 indicate the presence of covalent bonding between the Nd^{3+} ions and the

surrounding ligands. Compared with the values of the Judd-Ofelt parameters of Nd^{3+} in other hosts as shown in Table 4, our Nd-doped material has a large Ω_2. That means the optical transition is dominated by electrical dipole transition in this system and the emission is strong.

The radiative lifetime τ_{rad} for Nd^{3+} in our material is comparable to that in deuterated (-d_8) PMMA, but smaller than the values in the hosts of PF (perfluorinated) plastic solution and ZBAN ($ZrFr$-BaF_2-LaF_2-ALF_3). The reason is that the latter two materials don't contain C-H bonds which cause quenching.

Table 4. Judd-Ofelt parameters of Nd^{3+} for different hosts.

host	$\Omega_2 (10^{-20} cm^2)$	$\Omega_4 (10^{-20} cm^2)$	$\Omega_6 (10^{-20} cm^2)$	$\tau_{rad} (ms)$
6-FDA epoxy	16.64	8.85	11.83	0.183
PF plastic solution [6]	10.6	6.51	4.72	0.548
PMMA-d_8 [6]	9.45	2.70	5.27	0.187
$ZBAN^{51}$ [6]	3.1	3.7	5.7	0.419

Conclusion

A Judd-Ofelt analysis was applied to the measured absorption spectrum of a $Nd(TTA)_3Phen$ doped 6-FDA epoxy planar waveguide. The results show that $Nd(TTA)_3Phen$ doped 6-FDA epoxy has good potential to be used as planar waveguide in the laser or amplifier.

Acknowledgement

The authors acknowledge the financial support of STW (TOE 6986).

References

[1] S. Lin, R. J. Feuerstein, and A.R. Mickelson, "A study of neodymium-chelate-doped optical polymer waveguides", J. Appl. Phys., vol. 79, pp.2868-2874, 1996.

[2] L. H. Slooff, A. van Blaaderen, A. Polman, G. A. Hebbink, S. I. Klink, F. C. J. M. Van Veggel, D. N. Reinhoudt, and J. W. Hofstraat, "Rare-earth doped polymers for planar optical amplifiers", J. Appl. Phys., vol. 91, pp. 3955-380, 2002.

[3] B. R. Judd, "Optical absorption intensities of rare-earth ions", Phys. Rev., vol. 127, pp.750-761, 1962

[4] G. S. Ofelt, "Intensities of crystal spectra of rare-earth ions", J. Chem. Phys., vol. 37, pp. 511-520, 1962.

[5] W. F. Krupke, "Induced-emission cross sections in neodymium laser glasses", IEEE J. Quantum Electronics, vol. QE-10, pp. 450-457, 1974.

[6] K. Kueki and Y. Koike, "Plastic optical fiber lasers and amplifiers containing lanthanide complex", Chem. Rev., vol 102, pp. 2347-2356, 2002.

[7] D.K.Sardar, J. B. Gruber, B. Zandi, J.A. Hutchinson and C. W. Trussell, "Judd-Ofelt analysis of the Er^{3+} ($4f^{11}$) absorption intensities in phosphate glass: Er^{3+}, Yb^{3+}", J. Appl. Phys., vol. 93, pp. 2041-2046, 2003.

[8] Y. Hasegawa, Y. Wada, S. Yanagida, "Strategies for the design of luminescent lanthanide (III) complexes and their photonic applications", J. Photochemistry Rev., vol 5, pp. 183-202, 2004.

[9] L. R. Melby, N. J. Rose, E. Abramson, and J.C. Caris, "Synthesis and fluorescence of some trivalent lanthanide complex", J. Am. Chem. Soc., vol. 86, pp. 5117-5125, 1964.

[10] W. T. Carnall, P. R. Fields, and K. Rajnak, "Electronic energy levels in the trivalent lanthanide aquo ions", J. Chem. Phy., vol.49, pp. 4424-4442, 1968.

[11] R. Reisfeld, C.K. Jørgensen, Lasers and Excited States of Rare Earths, Berlin: Springer-Verlag, 1977.

Near Field Pattern Simulations of Graded-Index Multimode Fibres

R.W. Smink, C.P. Tsekrekos, B.P. de Hon, A.M.J. Koonen and A.G. Tijhuis

Eindhoven University of Technology, P.O. Box 513, 5600 MB Eindhoven,
The Netherlands. E-mail: r.w.smink@tue.nl

To compute the near field pattern (NFP) of a silica graded-index multimode fibre, a full-wave model has been implemented. A single-mode fibre pigtail, with possible angular tilt and radial offset, excites the wavefield. The amplitudes of the propagating modes are computed by overlap integrals. The graded-index α-profile has been determined by matching differential mode delay simulations to measurements. Differential mode attenuation and mode-mixing are introduced through a power-flow equation. Only minor parameter adjustments suffice to obtain a satisfactory match between measurements and simulations. To gain a better understanding of the phenomena, NFPs have been determined for a range of excitation positions and angles.

Introduction

In short-range optical communication networks, e.g. in-building networks, the multimode fibre (MMF) is widely accepted as a means to transfer data. In comparison with a single-mode fibre (SMF), the MMF benefits from its large core diameter, since splicing is easier and the use of expensive high-precision connectors is not required. However, the capacity of MMFs regarding their bandwidth is limited due to differential mode delay (DMD). This disadvantage can be mitigated considerably by using a well-chosen graded refractive index-profile in the fibre core. Moreover, by a selective excitation of a subset of propagating modes, the bandwidth can be increased even further, due to reduced propagation time differences [1]. By exciting different subsets simultaneously, parallel independent transmission channels can be created in the MMF, which is a technique known as mode group diversity multiplexing (MGDM) [2].

We have implemented a full-wave model to compute the near field pattern (NFP) at the output of a graded-index multimode fibre (GI-MMF) [3]. A continuous wave laser, pigtailed to a SMF, serves as excitation of the modefield in the GI-MMF. The possibility exists to perform a selective excitation by employing an angular tilt and/or radial offset. We have compared simulated NFPs with measured ones and determined the effects of differential mode attenuation (DMA) and mode-mixing, with the aid of a power flow equation.

Theoretical Investigation

To compute the modal propagation coefficients in the GI-MMF, we assume that the fibre under consideration is circularly symmetric, isotropic and translationally invariant. The fibre consists of a radially inhomogeneous core and an infinite homogeneous cladding. A three-term Sellmeier dispersion equation is used to characterise the permittivity of the fibre material $\varepsilon(r,\omega)$, with an $e^{j\omega t}$ time-dependence [4]. A full-vectorial field model has been implemented and the modal electromagnetic fields $\mathbf{E}^{m,n}$ and $\mathbf{H}^{m,n}$, where $m =$

$0,1,2,...$ and $n = 1,2,...$ denote the azimuthal and radial modal indices, respectively, are determined for each modal propagation coefficient $k_z^{m,n}$. In a cylindrical coordinate system $\{r,\phi,z\}$, with corresponding unit vectors $\{\mathbf{u}_r,\mathbf{u}_\phi,\mathbf{u}_z\}$, the electromagnetic fields in a z-directed fibre can be expressed as

$$\begin{bmatrix} \mathbf{E}(r,\phi,z) \\ \mathbf{H}(r,\phi,z) \end{bmatrix} = \sum_{m,n} A^{m,n} \begin{bmatrix} \mathbf{E}^{m,n}(r) \\ \mathbf{H}^{m,n}(r) \end{bmatrix} e^{-jm\phi} e^{-jk_z^{m,n}z}. \tag{1}$$

The modal fields are normalised to unit power. We excite the GI-MMF at the plane $z = 0$. There, the modal amplitudes $A^{m,n}$ of the corresponding excited modes are determined by an overlap integral [6],

$$A^{m,n} = \frac{1}{2}\int_{r=0}^{\infty}\int_{\phi=-\pi}^{\pi} \mathbf{u}_z \cdot \left\{\mathbf{E}^i(r',\phi') \times [\mathbf{H}^{m,n}(r,\phi)]^*\right\} r d\phi dr, \tag{2}$$

where $\mathbf{E}^i(r',\phi')$ is the electric field of the SMF. The primed coordinates $\{r'(r,\phi),\phi'(r,\phi)\}$ denote the transverse cylindrical polar coordinates about the SMF axis.
At the receiver end of the fibre, at $z = \ell$, the intensity distribution I of the NFP is given by

$$\mathrm{I}(r,\phi,\ell) = \frac{1}{2}\mathrm{Re}\left\{\mathbf{E}(r,\phi,\ell) \times [\mathbf{H}(r,\phi,\ell)]^* \cdot \mathbf{u}_z\right\}. \tag{3}$$

So far, we have neglected the influence of DMA and mode mixing on the NFP. To simulate these effects, we employ a set of coupled power equations [7]

$$\frac{dP_\mu}{dz} = -\gamma_\mu P_\mu + \sum_\nu h_{\mu\nu}(P_\nu - P_\mu), \tag{4}$$

where P_μ and γ_μ are the power and the attenuation coefficient of the corresponding mode μ, respectively, and $\mu = \nu = 1,2,3....$ The elements in the coupling matrix $h_{\mu\nu}$ are a measure of the probability per unit length of a transition occurring between modes μ and ν.
In order to reduce the set of coupled power equations in Eq. (4), we introduce principal mode groups (PMGs). PMGs are determined by the difference in the propagation coefficient between adjacent modes. If this difference is relatively small, modes belong to the same PMG. Consequently, mode mixing occurs between modes within a mode group, which is called intra-group mode mixing, and between mode groups themselves, called inter-group mode mixing. Since intra-group mode mixing is faster than the inter-group one, we may safely neglect the latter in short-range communication networks [5].
Further, we distinguish between a region near the launch end, where intra-group mode mixing is still negligible, a transition region and a region where intra-group mode mixing is at an advanced stage. In this latter region, it is acceptable to assume that the power within a mode group is approximately equally divided among the modes of the group. Since the modal amplitudes $A^{m,n}$ at $z = 0$ are known, the average amplitude of each mode in a PMG reads

$$|A_{PMG}^{m,n}|_{ave} = \sqrt{\frac{\sum_{m,n}|A_{PMG}^{m,n}|^2}{N_{PMG}}}, \tag{5}$$

where N_{PMG} denotes the amount of modes in a mode group. The phase of $A_{PMG}^{m,n}$ is chosen randomly, with a uniform distribution within $[0,2\pi)$, as it is mixed in a random fashion with the other modes within the group. Moreover, the phase noise, due to the finite linewidth of the laser, also contributes to a random phase.

Since we have neglected the coupling between PMGs, the coupling matrix $h_{\mu,\nu}$ in Eq. (4) diagonalises, and consequently $P_\mu(z) = P_\mu(0)\exp(-\gamma_\mu z)$, where the index μ is now related to PMGs instead of separate modes. Note that we could have included the exponential as an imaginary part of $k_z^{m,n}$ in Eq. (1). However, then prior knowledge of the modes belonging to a PMG would have to be available. Under the weakly guiding approximation, we can use the concept of LP-modes, where a relation between the PMG and the modal indices exists. For an arbitrary index profile such relation is not available, and hence, computation of the real part of $k_z^{m,n}$ is necessary to distinguish between the PMGs. The γ_μ-dependence is added in the computation of the modal power.
For mode group μ, a matched formula for the attenuation coefficient γ_μ for silica fibres is given by [8]

$$\gamma(\mu,\lambda) = \gamma_0(\lambda) + \gamma_0(\lambda) I_\rho \left[\eta \left(\frac{\mu - 1}{M_{PMG}} \right)^{2\alpha/(\alpha+2)} \right], \tag{6}$$

where $\rho = 9$, $\eta = 7.35$, I_ρ denotes the modified Bessel function of order ρ, and γ_0 is the intrinsic fiber attenuation at a specific wavelength λ, which is equal for all PMGs. Further, M_{PMG} denotes the total number of PMGs, whereas α is the exponent of the graded-index power-law profile. Observe that the higher-order PMGs are attenuated more than the lower-order ones.

Experimental Results

A Fabry-Perot laser, with a cental wavelength at $\lambda = 660$nm, is pigtailed to a 1m SMF. The SMF has a numerical aperture (NA) of 0.12 and a mode-field diameter of 4.2µm. In order to excite the GI-MMF with a possible offset, a computer controlled set-up with transitional stages is used. The circularly symmetric GI-MMF has a core/cladding diameter of 62.5/125µm, and NA=0.275. It is designed for use at $\lambda = 850$nm. Having performed several DMD simulations, the corresponding α-parameter of the graded-index profile is found to be $\alpha = 2.06$ [3]. At the receiver end of the fibre, the NFP is observed with a charge-coupled device (CCD) camera through a microscope.
For various radial offsets (ro) and angular offsets (ao), the simulated and measured NFPs at $z = 1$m are shown in Figure 1. Intra-group mode mixing has not been included, which seems reasonable as the power has not yet been equally divided among the modes in a PMG. The measured and simulated intensity patterns look similar, which confirms that there is no significant mixing within the PMGs. Observe the ring-like shape of the field as we excite the GI-MMF with ro=13µm and ao=6.5°.
Next, we investigate the influence of intra-group mode mixing on the NFPs. In Figure 2(a), simulated and measured intensity patterns at $z = 75$m and $z = 1$km for ro=13µm are shown. We observe that mode mixing produces a more blurred simulated NFP compared to the ones in Figure 1. In Figure 2(b), an additional ao=6.5° is inserted. At $z = 75$m simulations and measurements are in good agreement. However, at $z = 1$km, the simulated fields move outward, which effect is absent in the measurements. Now, we recall that DMA attenuates the higher-order modes more than the lower-order ones. Simulation results at $z = 1$km without and with DMA are shown in Figure 3. We see that with DMA the NFPs give a better agreement with the measurements in Figure 2.

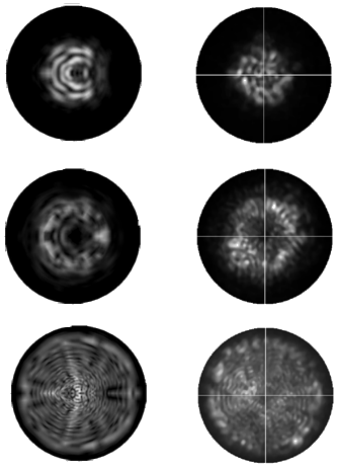

Figure 1: Simulations (left) and measurements (right) at $z = 1$m. Upper: ro=13µm; centre: ro=13µm and ao=6.5°; bottom: ro=26µm.

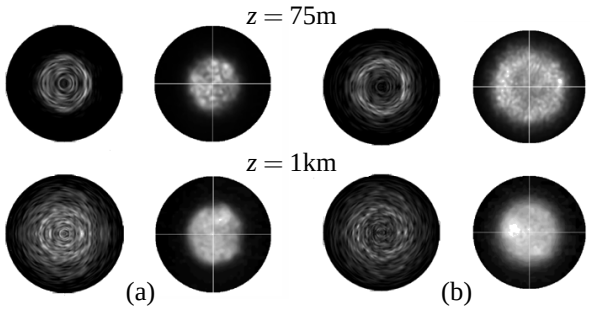

Figure 2: Simulations (left) and measurements (right) at $z = 75$m and $z = 1$km (a): for ro=13µm; (b): for ro=13µm and ao=6.5°.

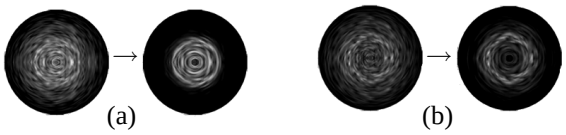

Figure 3: Simulations without (left) and with (right) DMA at $z = 1$km for (a) ro=13µm; (b): ro=13µm and ao=6.5°.

Conclusions

We have developed a full-wave model to compute intensity patterns in a lossless circularly cylindrical MMF. A straightforward analysis shows that (intra-group) mode mixing and DMA can be easily implemented to obtain NFPs that are in reasonable agreement with measurements. We have performed these measurements with a GI-MMF, excited by a pigtailed SMF. For short GI-MMFs, intra-group mode mixing, in combination with possible phase noise, generate a blurry NFP. It is shown that DMA causes the higher-order modes to be attenuated more than the lower-order ones. By generating NFPs at several distances, we have gained insight in where these effects occur.

References

[1] L. Raddatz, I.H. White, D.G. Cunningham and M.C. Nowell, ”An Experimental an Theoretical Study of the Offset Launch Technique for the Enhancement of the Bandwidth of Mulitomde Fiber Links”, *J. of Lightw. Techn.*, vol. 16, pp. 324-331, 1998.

[2] T. Koonen, H. van den Boom, I.T. Monroy and G.D. Khoe, ”High Capacity Multi-Service In-House Networks using Mode Group Diversity Multiplexing”, in *Proceedings of OFC2004; Los Angeles, CA*, 2004, paper FG4.

[3] M. Bingle and B.P. de Hon, ”Differential Mode Delay - Full-Wave Modelling and Various Levels of Approximations”, in *Proceedings. of the XXVIIth General Assembly of the International Union of Radio Science; URSI, Maastricht*, vol. 24, 2002, pp. 1-4.

[4] W. Hermann and D.U. Wiechert, ”Refractive Index of Doped and Undoped PCVD Bulk Silica”, *Mat. Res. Bull.*, vol. 24, pp. 1083-1097, 1989.

[5] S. Kawakami and H. Tanj, ”Evolution of Power Distribution in Graded-Index Fibres”, *Electr. Lett.*, vol. 19, pp. 100-102, 1983.

[6] E.G. Neumann, Single-Mode Fibers, Fundamental, Berlin: Springer, 1988, pp. 170-174.

[7] D. Marcuse, Theory of Dielectric Optical Waveguides, Sec. Ed., San Diego: Academic Press, 1991.

[8] G. Yabre, ”Comprehensive Theory of Dispersion in Graded-Index Optical Fibres”, *J. of Lightw. Techn.*, vol. 18, pp. 166-176, 2000.

Variational effective index mode solver

O. V. Ivanova, M. Hammer, R. Stoffer, E. van Groesen

MESA+ Institute for Nanotechnology, University of Twente, Enschede, The Netherlands

A variational approach for the modal analysis of dielectric waveguides with arbitrary piecewise constant rectangular 2D cross-section is developed. It is based on a representation of a mode profile as a superposition of all modes of the constituting slab waveguides times some unknown continuous coefficient functions, defined on the entire lateral coordinate axis. The propagation constant and the lateral functions are found from a variational principle. It appears that this method, while preserving the computational efficiency of the standard effective index method, provides more accurate estimates for propagation constants, as well as well-defined continuous approximations for mode profiles.

Introduction

The effective index method (EIM) is one of the most popular among the many approaches for the modal analysis of dielectric optical waveguides [1]. While being rather intuitive and computationally very efficient, the inherent approximations limit the range of applicability of the EIM. For example, if all modes of some slab region are below cut-off, heuristics have to be applied to provide the necessary effective indices, and mode profiles are not defined. As an alternative to other approaches for improvements (e.g. [2], [3]), here we propose a variational effective index method (VEIM) which overcomes these problems by means of a modified ansatz for the modal field, together with the use of a variational principle. The procedure is applicable in practice for an arbitrary, piecewise constant rectangular permittivity distribution.

Problem definition

Figure 1(a) shows the cross-section of a typical waveguide structure with piecewise constant rectangular refractive index distribution $n = n(x,y)$. Given the semi-vectorial TE and TM mode equations for the dominant electric $E = E_y(x,y)$ and magnetic $H = H_y(x,y)$ field components at vacuum wavelength $\lambda = 2\pi/k_0$, searching for square integrable solutions in the form of profiles propagating in the z - direction with propagation constant β, leads to the following eigenvalue problems:

$$\Delta E + k_0^2 n^2 E = \beta^2 E \quad \text{(TE)}, \qquad \nabla\left(\frac{1}{n^2}\nabla H\right) + k_0^2 H = \beta^2 \frac{1}{n^2} H \quad \text{(TM)}. \tag{1}$$

It can be shown that these problems are equivalent to finding the critical points of the functionals:

$$-\beta^2 = \text{crit}\left\{ \int_{R^2} \left\{ |\nabla E|^2 - k_0^2 n^2(x,y) E^2 \right\} dx\,dy \;\middle|\; \int_{R^2} E^2\,dx\,dy = 1 \right\} \quad \text{(TE)}, \tag{2}$$

$$-\beta^2 = \text{crit}\left\{ \int_{R^2} \left\{ \frac{1}{n^2(x,y)} |\nabla H|^2 - k_0^2 H^2 \right\} dx\,dy \;\middle|\; \int_{R^2} \frac{1}{n^2(x,y)} H^2\,dx\,dy = 1 \right\} \quad \text{(TM)}. \tag{3}$$

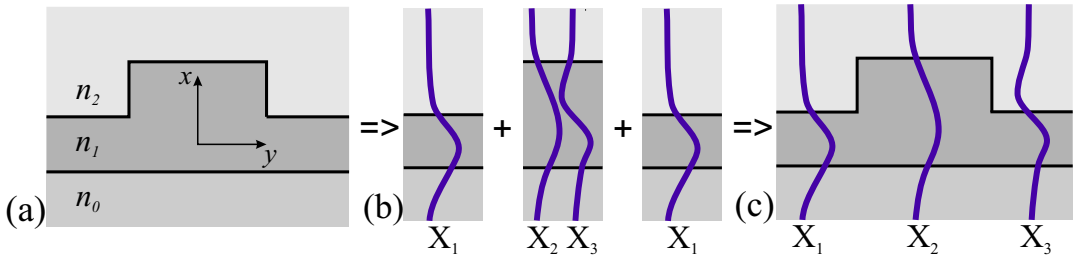

Figure 1: (a) Cross-section of a typical waveguide structure; (b) Constituting slab waveguides with corresponding mode profiles; (c) Original waveguide with all slab modes $X_1(x),\ldots,X_N(x)$ (in this case $N=3$).

Method of Solution

We represent the principal field component $E_y(x,y)$ and $H_y(x,y)$ respectively as a superposition of guided TE and TM modes $X_1(x),\ldots,X_N(x)$ of the constituting slab waveguides (Figure 1), times unknown continuous coefficient functions $Y_1(y),\ldots,Y_N(y)$:

$$E_y(x,y)=\sum_{i=1}^{N}X_i(x)Y_i(y)\quad\text{(TE)},\qquad H(x,y)=\sum_{i=1}^{N}X_i(x)Y_i(y)\quad\text{(TM)}. \tag{4}$$

Note, that the functions $Y_i(y)$ are meant to be continuous and defined on the entire y axis (in contrast to what is common in formulations of the EIM).
Restricting the functionals (2) and (3) to the trial field (4) and requiring this functional to become stationary leads to a vectorial differential equation for the unknown function $\boldsymbol{Y}(y)=(Y_1(y),\ldots,Y_N(y))$:

$$\boldsymbol{Y}''(y)+\boldsymbol{F}^{-1}\boldsymbol{M}(y)\boldsymbol{Y}(y)=\beta^2\boldsymbol{Y}(y)\quad\text{(TE)}, \tag{5}$$

$$\big(\boldsymbol{F}(y)\boldsymbol{Y}'(y)\big)'+\boldsymbol{M}(y)\boldsymbol{Y}(y)=\beta^2\boldsymbol{F}(y)\boldsymbol{Y}(y)\quad\text{(TM)}. \tag{6}$$

With continuity of

$$\boldsymbol{Y}(y)\quad\text{(as an essential condition)}, \tag{7}$$

and

$$\boldsymbol{Y}'(y)\quad(TE)\quad\text{and}\quad\boldsymbol{F}(y)\boldsymbol{Y}'(y)\quad(TM)\quad\text{(as a natural condition)} \tag{8}$$

as interface conditions. Here matrices $\boldsymbol{F}$ and $\boldsymbol{M}$ have a dimension $N\times N$ and consist of elements

$$M_{g,h}(y)=\int_R\left(k_0^2n^2(x,y)X_g(x)X_h(x)-X_g'(x)X_h'(x)\right)dx,\quad F_{g,h}=\int_R X_g(x)X_h(x)\,dx\quad\text{(TE)},$$

$$M_{g,h}(y)=\int_R\left(k_0^2X_g(x)X_h(x)-\frac{1}{n^2(x,y)}X_g'(x)X_h'(x)\right)dx,$$

$$F_{g,h}(y)=\int_R\frac{1}{n^2(x,y)}X_g(x)X_h(x)\,dx\quad\text{(TM)}.$$

Modes X_i need to differ sufficiently, i.e. modes of equal slices should be introduced only once, otherwise matrices $\boldsymbol{M}$ and $\boldsymbol{F}$ become singular.
It can be easily seen that in each constituting slab matrices $\boldsymbol{M}$ and $\boldsymbol{F}$ do not depend on y and (5), (6) become vectorial mode equations with interface conditions (7) and (8). Searching for square integrable solutions of these problems we obtain a resonance condition. By identifying roots of that expression one finds propagation constants and the unknown coefficient functions, i.e. the field distributions (4).

Results and comparisons

As examples, we applied this method for the analysis of the rib waveguide and 3D coupler of Figure 2.

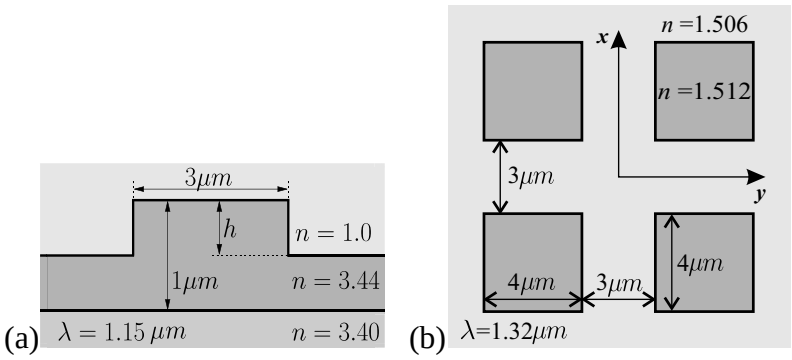

Figure 2: (a) Rib waveguide; (b) 3D coupler structure.

Effective indices $N_{\text{eff}} = \beta/k_0$ of the former structure in case of TE and TM polarizations are compared with results obtained by more sophisticated methods in the Figure 3. It can be seen that in cases where the outer slab region supports a guided mode, including this mode into expansion (4) leads to a better approximation of the effective index. Moreover, according to the principle of eigenvalue comparison the effective index of the fundamental mode will approach its exact value from below.

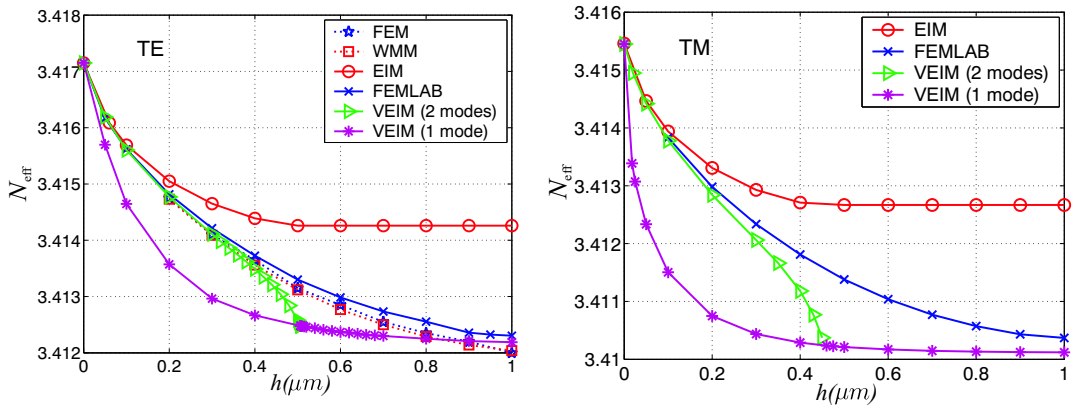

Figure 3: Rib waveguide: effective indices of TE - and TM - like modes versus rib depth h; FEMLAB: semivectorial mode equations, vectorial FEM, WMM: reference results [4], EIM: effective index method, VEIM: the present method. Note that curve VEIM (1 mode) was obtained using in expansion (4) only the fundamental mode of the central slice, while in expansion for VEIM (2 modes) the fundamental mode of the outer slice was used as well (obviously, such an expansion is possible only when the outer slices are above cut-off).

A similar comparison for the latter structure is given in Table 1. Apparently the VEIM results agree better with the data from rigorous methods, than the ”standard” EIM results.

	β_{00}/k	β_{01}/k	β_{10}/k	β_{11}/k
FEM	1.5075807	1.5067966	1.5067966	1.5060260
WMM	1.5078966	1.5071085	1.5071092	1.5064697
EIM	1.5080433	1.5072134	1.5075570	1.5067277
VEIM	1.5077912	1.5069894	1.5069690	1.5061836

Table 1: Effective indices of the TE modes of the 3D coupler; FEM, WMM: reference results [4], EIM: effective index method, VEIM: the present method.

Figure 4 illustrates the VEIM mode profiles for the propagation constants of Table 1. Note that, in contrast to EIM, field profiles, obtained using VEIM, are well-defined and continuous.

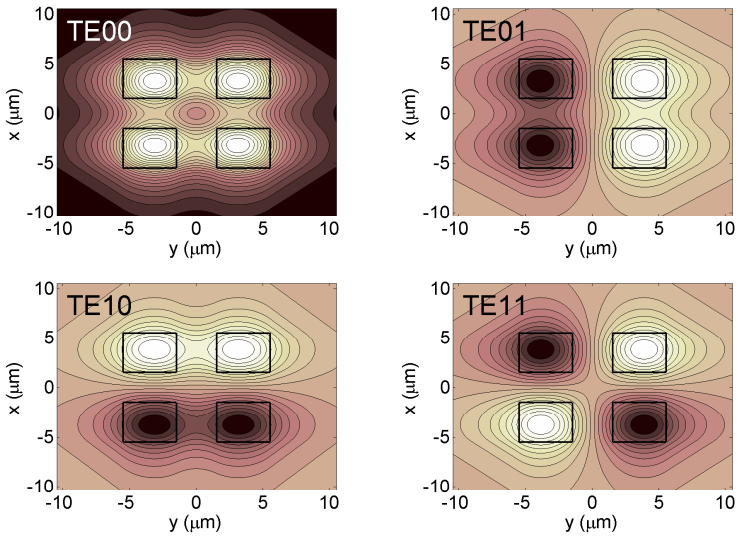

Figure 4: Mode profiles for the 3D coupler of Figure 2(b): dominant electric component of semivectorial TE fields.

Conclusions

In conclusion, while the VEIM approach allows to estimate propagation constants with reasonable accuracy and provides continuous, well-defined mode profiles, it largely preserves the simplicity and the computational efficiency of the ”standard” EIM. In principle it should be possible to include into the expansion of the field not only the guided, but, for example, also radiation modes.

References

[1] K.S. Chiang, ”Review of numerical and approximate methods for the modal analysis of general optical dielectric waveguides”, *Opt. Quantum Electron.*, vol. 26, pp. S113 - S134, 1994.

[2] K.S. Chiang, ”Analysis of rectangular dielectric waveguides: effective-index method with built-in perturbation correction”, *Electron. Lett.*, vol. 28, pp. 388 - 390, 1992.

[3] T.M. Benson and R.J. Bozeat and P.C. Kendall, ”Rigorous effective index method for semiconductor rib waveguides”, *IEE Proc. J.*, vol. 139, pp. 67 - 70, 1992.

[4] M. Lohmeyer, PhD Thesis ”Guided waves in rectangular integrated magnetooptic devices”, Univ. Osnabrück, ch. 4, pp. 41 - 57, 1999.

Spatial Effects in the Emitted Field of Zero Diffraction Resonators

P. Tassin,[1] M. Tlidi,[2] G. Van der Sande,[1,2] I. Veretennicoff,[1] and P. Kockaert[3]

[1]Department of Applied Physics and Photonics, Vrije Universiteit Brussel, Pleinlaan 2, B-1050 Brussel, Belgium

[2]Optique non linéaire théorique, Université Libre de Bruxelles, CP 231, Campus Plaine, B-1050 Bruxelles, Belgium

[3]Service d'optique et acoustique, Université Libre de Bruxelles, CP 194/5, 50, Av. F. D. Roosevelt, B-1050 Bruxelles, Belgium

In a previous work, we have devised a way to eliminate diffraction from optical resonators by introducing left-handed materials – or negative index materials – in an optical cavity. Such zero diffraction resonators are promising devices, because they can potentially generate sub-diffraction-limited light beams. However, when diffraction vanishes completely, other physical effects will determine the spatial structure of the emitted field. In this work, we derive models to describe these effects and we study the dynamical behaviour of zero diffraction resonators. We address two different contributions: the inherent nonlocality of the left-handed metamaterial and higher order cavity effects.

Introduction

Metamaterials, i.e. materials with an artificial internal structure, promise to provide previously unexplored electromagnetic behaviour. In recent years, researchers have been able to fabricate metamaterials with negative permittivity and permeability (see Ref. [1] for an overview of these so-called left-handed materials). Exotic electromagnetic wave propagation such as negative refraction in left-handed materials has been predicted [2] and demonstrated [3]. Moreover, metamaterials offer possibilities for new applications, such as sub-wavelength imaging [4] and electromagnetic cloaking of objects [5].

Left-handed materials can also be used to improve optical devices. In previous work [6], we have proposed a double layered nonlinear Fabry-Perot resonator containing both right-handed and left-handed materials (see also Fig. 1). We have derived a mean-field model for this resonator, according to which the time evolution of the envelope A of the electric field of the output field is given by

$$\frac{\partial A}{\partial t} = A_{\text{in}} - (1+\mathrm{i}\Delta)A + \mathrm{i}|A|^2 A + \mathrm{i}\alpha\nabla_\perp^2 A. \tag{1}$$

In this equation, A_{in} is the amplitude of the incident wave and Δ is the detuning between the frequency of the optical carrier and the nearest cavity mode. We have shown that diffraction acts in the left-handed material layer with the opposite sign as in the right-handed layer. Therefore, it is possible to tune the value of the diffraction coefficient α to either positive or negative values. By careful adjustment of the layer thicknesses l_{R} and l_{L}, it should also be possible to achieve complete diffraction compensation between the layers, thus eliminating diffraction from the resonator. In this case, the diffraction coefficient α in Eq. (1) becomes zero.

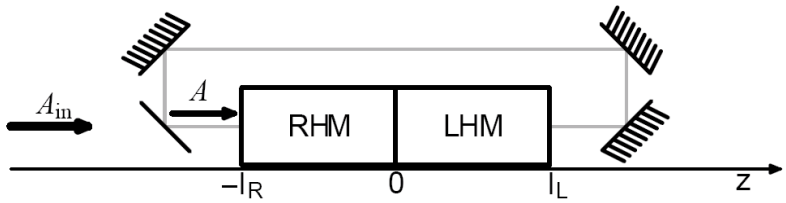

Fig. 1: Scheme of an optical resonator with diffraction compensation between the layer of left-handed material (LHM) and the layer of right-handed material (RHM).

Sub-Diffraction-Limited Light Beams

A nonlinear optical resonator, such as the ring cavity depicted in Fig. 1, is a dissipative system far from equilibrium, in which the interaction between diffraction and nonlinearity can result in modulational – or Turing – instability. This means that small fluctuations can lead to the formation of dissipative structures in the emitted field of the resonator [7]-[8]. In such systems, the typical feature size of the emerging structures is not determined by the boundary conditions, but rather by the strength of diffraction. From the scaling of the space coordinates in Eq. (1), it can be seen that the larger the diffraction coefficient α, the larger the size of the patterns. By tuning the diffraction coefficient to arbitrarily small values as discussed above, one could generate dissipative structures with ever smaller feature sizes.

However, the Lugiato-Lefever equation [Eq. (1)] is no longer appropriate for small values of α. Indeed, the derivation of this equation relies on two consecutive perturbation expansions [5]. In a first step, the fast optical oscillations of the light field are separated from the slower variations of the field envelope A. In a second step, the time evolution of this envelope is expanded with respect to the cavity length under the assumption of small changes during one roundtrip. In both expansions, all but the first-order terms are neglected. When diffraction – which is the only spatially dependent first-order term – is eliminated, higher order terms should be taken into account. In particular, we have identified two physical effects contributing to these higher terms: the inherent nonlocality of the left-handed material and higher-order cavity effects.

Nonlocal Interactions in the Left-Handed Material

Most left-handed materials contain a large number of very small resonators interacting with the electromagnetic fields, e.g. tiny wires and split-ring resonators in Smith's first metamaterial [3]. These interactions contribute to the value of the permittivity and permeability and can make them negative. Typically, the resonators are spaced extremely closely, resulting in interactions between neighbouring resonators. Consequently, metamaterials should be modelled with nonlocal constitutive relations:

$$\mathbf{D}(\mathbf{r}) = \varepsilon_0 \iiint \varepsilon_r(\mathbf{r}-\mathbf{r}')\mathbf{E}(\mathbf{r}')\,\mathrm{d}\mathbf{r}', \quad \mathbf{B}(\mathbf{r}) = \mu_0 \iiint \mu_r(\mathbf{r}-\mathbf{r}')\mathbf{H}(\mathbf{r}')\,\mathrm{d}\mathbf{r}'. \tag{2}$$

When these relations are introduced in Maxwell's equations and the optical carrier is removed from the model with a multiple scales analysis, one finds the classical nonlinear Schrödinger equation with a number of additional terms. However, symmetry considerations reveal that many of these terms vanish. Applying the normal mean-field approximations, we have finally found the following generalisation of Eq. (1):

$$\frac{\partial A}{\partial t} = A_{\text{in}} - (1+\mathrm{i}\Delta)A + \mathrm{i}|A|^2 A + \mathrm{i}\alpha\nabla_\perp^2 A + \mathrm{i}\beta\nabla_\perp^4 A. \tag{3}$$

The nonlocality thus gives rise to a bilaplacian with real coefficient. Gelens *et al.* have shown that this equation has localised solutions and have investigated the size limits on these solutions imposed by the new term [9].

Higher Order Cavity Effects

When the typical space scales of nonlinearity and diffraction are larger than the cavity length, the nonlinear Schrödinger equation can be integrated approximately by considering its right-hand side as constant. The propagation operator for the field envelope obtained in this way can then be expanded as a Taylor series in the layer widths l_R and l_L:

$$e^{i(\mathrm{D}+\mathrm{N})l_{R,L}} = 1 + \mathrm{i}\, l_{R,L}\,\mathrm{D} + \mathrm{i}\, l_{R,L}\,\mathrm{N} - \frac{1}{2} l_{R,L}^2\,\mathrm{D}^2 + \ldots, \tag{4}$$

where D and N are operators associated to diffraction and nonlinear effects (which we assume here to be Kerr-like), respectively:

$$D = \frac{\mathrm{i}}{2k_{R,L}}\nabla_\perp^2, \qquad N(A) = |A|^2. \tag{5}$$

In the mean-field approximation, only the first three terms of Eq. (4) are kept in the analysis. However, when the second term vanishes due to elimination of diffraction, the next higher order spatially dependent term should also be taken into account. This leads to the following generalised mean-field equation:

$$\frac{\partial A}{\partial t} = A_{\text{in}} - (1+\mathrm{i}\Delta)A + \mathrm{i}|A|A + \mathrm{i}\alpha\nabla_\perp^2 A - \frac{1}{2}\alpha^2\nabla_\perp^4 A. \tag{6}$$

The correction due to higher cavity effects thus leads to a bilaplacian term in the mean-field equation too, be it in this case with a real coefficient. It is important to note that the coefficient of the bilaplacian is proportional to α^2. This means that this effect will not change the traditional scaling law of dissipative structures: their typical width is proportional to the square root of the diffraction coefficient α. However, the stability will of course be altered.

Stability Analysis

We have carried out the linear stability analysis of the mean-field equation with either of both corrections. The stability of Eq. (3) with an imaginary bilaplacian term has been studied in detail in Ref. [9], where also the size limitation on localised solutions of this equation are investigated.

We have also analysed the linear stability of Eq. (6), which has a real bilaplacian term. The effect of this term is mainly to stabilise the homogeneous solution. For $\Delta < 1.44$, the homogeneous solution is now completely stable. For higher values of the detuning, the marginal stability curve (see Fig. 2) closes, reducing the range of unstable modes and stabilising the homogeneous solution for high intensities.

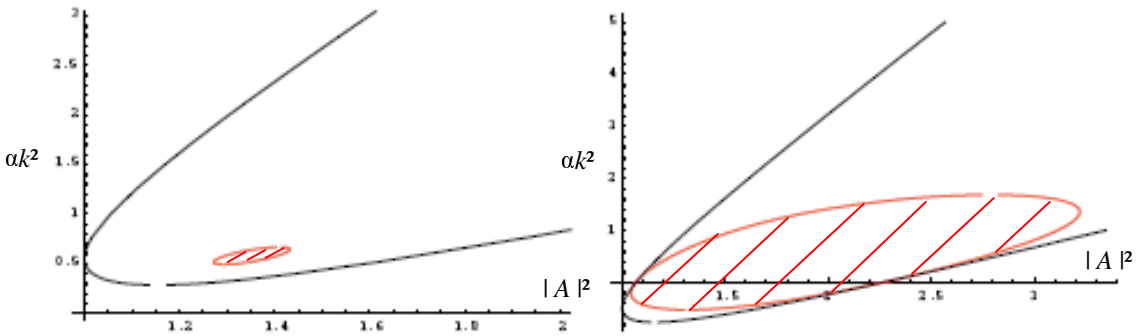

Fig. 2: Marginal stability of the mean-field equation. The open curves correspond to the original equation [Eq. (1)], whereas the closed curves are for the equation with the real bilaplacian term [Eq. (6)]. The detuning is taken equal to Δ = 1.45 (left graph) and Δ = 2.5 (right graph). Unstable regions are hatched.

Conclusions

We have studied the zero diffraction regime of a nonlinear optical resonator containing right- and left-handed materials. When the strength of diffraction in this system is tuned to very small values, the Lugiato-Lefever equation breaks down, and other spatial effects come into play. We identified two contributions, coming from the nonlocal interaction in the left-handed material between the polarisation field and the electric field of light, and from higher order cavity effects. Only the first effect changes the size scaling law of optical patterns and localised structures explicitly, but both influence their formation by changing the stability of the homogeneous solution.

Acknowledgements

This work was supported by the Belgian Science Policy Office under grant no. IAP-V18. P. T. is a PhD Fellow of the Research Foundation – Flanders (FWO). M. T. is a Research Associate of the Fonds national de la recherche scientifique (FNRS). G. V. is a Postdoctoral Fellow of the Research Foundation – Flanders (FWO).

References

[1] C. Soukoulis, “Bending back light: The science of negative index materials,” Optics and Photonics News, vol. 17, no. 6, pp. 18-21 (2006).

[2] V. Veselago, “The Electrodynamics of Substances with Simultaneously Negative Values of ε and μ,” Sov. Phys. Usp., vol. 10, pp. 509-514, 1968.

[3] R. Shelby, D. Smith and S. Schultz, “Experimental Verification of a Negative Index of Refraction”, Science, vol. 292, pp. 77-79, 2001.

[4] J. Pendry, “Negative Refraction Makes a Perfect Lens”, Phys. Rev. Lett., vol. 85, pp. 3966, 2000.

[5] J. B. Pendry , D. Schurig, and D. R. Smith, “Controlling Electromagnetic Fields,” Science 312, pp. 1780-1782.

[6] P. Kockaert, P. Tassin, G. Van der Sande, I. Veretennicoff, and M.Tlidi, “Negative diffraction pattern dynamics in nonlinear cavities with left-handed materials,” Phys. Rev. A, vol. 74, 033822, 2006.

[7] P. Mandel and M. Tlidi, J. Opt. B: Quantum Semiclassical Opt., vol. 6, pp. R60, 2004.

[8] W. J. Firth, G. K. Harkness, A. Lord, J. M. McSloy, D. Gomila, and P. Colet, J. Opt. Soc. Am. B, vol. 19, pp. 747-752, 2002

[9] L. Gelens, P. Tassin, G. Van der Sande, I. Veretennicoff, P. Kockaert, M. Tlidi, D. Gomila,, and J. Danckaert, “Beyond the Size Limit on Cavity Solitons with Left-Handed Materials,” in Proceedings of the Annual Symposium of the IEEE/LEOS Benelux Chapter, 2006.

Author Index